

CRANFIELD UNIVERSITY

SCHOOL OF APPLIED SCIENCES

PhD THESIS

Academic Year 2009-2010

Nuno Vasco da Costa Pépe

Advances in Gas Metal Arc Welding and Application to Corrosion Resistant Alloy Pipes

Supervisor

David Yapp

March 2010

“Intuition is the source of scientific knowledge”

Aristotle

To my parents, Fátima and José

ABSTRACT

According to recent estimations, the construction of pipelines will continue to increase during the next thirty years, in particular as a result of oil and gas discoveries in remote locations. Significant advances in welding technology during the last ten years have potential to provide improvements in productivity, quality and structural integrity of pipe girth welds.

In this thesis, several new processes Lincoln STT, Lincoln RapidArc, Fronius CMT, Fronius CMT-P and Kemppi FastROOT have been compared the first time to the GMAW-P to understand how these new waveforms operate for pipe welding. The process setting parameters have been analysed to understand their effect on metal transfer and arc stability control, and on bead shape characteristics. Although all waveforms present similar burn-off ratios, individual waveforms differ considerably, and especially the arc voltage waveform. This leads to considerable differences in the mechanism of metal transfer and the stability of the processes under similar experimental conditions. Understanding of these new waveforms in terms of the effect of setting parameters in the mechanism of metal transfer, process stability and melting phenomena provides a basis for assessing the potential of these processes for a range of applications, and in particular application to CRA pipe root welding

Since the arc energy is the overall energy delivered from the power source at the contact tip of the torch, and part of that energy is not absorbed by the workpiece, research was performed to measure the process efficiency associated with some of these waveforms and process setting conditions. The study led to a better understanding of the potential errors in calculating process efficiency. The results obtained show that all the short-circuiting waveforms analysed (i.e. CMT, STT and FastRoot) had a similar process efficiency of $90\pm 3\%$, while pulse spray waveforms (GMAW-P, CMT-P and RapidArc) are characterized by lower process efficiency, approximately $78\pm 3\%$.

The application of these waveforms to the welding a narrow groove pipe with a "J" groove design was investigated. These analyses were focused on the variation of bead shape characteristics and welding quality performance based on the analysis of the conditions that result in lack of penetration and top bead defects, such as lack of side wall fusion or undercutting. It was observed that RapidArc and CMT-P are able to satisfy the quality requirements, i.e. full penetration and absence of defects for the specific conditions described in this thesis. High welding speeds (up to 1m/min) were achieved with these processes, four times the typical speed 0.25m/min.

Finally, the shielding gas plays an important role in terms of quality and weld bead performance. This led to an optimization of the shielding gas composition used, based on mixtures of carbon dioxide, argon and helium. Statistical modelling was undertaken to optimize the shielding gas mixtures using RapidArc and CMT-P waveforms. In parallel, a new purging shielding gas device was designed to achieve a weld root free of oxidation.

ACKNOWLEDGMENTS

This doctoral thesis is the conclusion of a research programme sponsored by BP at Cranfield University. During this research work I have been helped by so many individuals.

This thesis would not have been possible without the support, help and patient of my supervisor, Mr. D. Yapp. His unsurpassed knowledge and experience led this project with innovation and enthusiasm. I would like therefore to thank Mr. D. Yapp for giving me the opportunity to pursue this doctoral programme and his friendly attitude, encouragement and continuous advice.

I would also like to thank Prof. S. Williams for several constructive discussions and advice. Prof. A. Scotti contributed to many discussions on heat and metal transfer and welding process characteristics. I am extremely grateful by his enthusiasm and invaluable knowledge he demonstrates, which led to important achievements during his internship at Cranfield.

My appreciation goes to Prof. L. Coutinho for at first introducing me to Cranfield University, and also for her support and encouragement during the doctoral period. This is highly appreciated.

Thanks are due to the technical staff and colleagues of WERC at Cranfield who have contributed in many different ways. I would like to thank Mr. J. Savill for his support in the beginning of the first experiments, and Mr. F. Nielson and Mr. B. Brookes for all help and support during the experimental research. I would like to mention a special thanks to Mr. B. Brookes for his patience and brilliant talent in metal construction and in creating experimental set-ups in many ways during this work.

I also wish to acknowledge the financial support of this project funded by BP which allowed me to work in a very demanding and innovative engineering domain.

I would also like to thank Mrs M. Yapp for her support and kindness.

I would also like to thank all colleagues I have met at WERC. A special thank to G. Lopes and W. Suder who have helped me several times in the experimental work. I would like to emphasize the dedication of G. Lopes towards everything and everyone, always with a very friendly attitude.

A special mention of gratitude for all support and friendship, especially during the last months of this doctoral programme goes to P. Marmelo, M. Pinheiro, J. Palacz, E. Costa, T. Sousa, W. Suder, P. Almeida, E. Assunção and J. Alonso. I would also like to mention other colleagues that have helped several times in many different ways at WERC, T. Liratzis, A. Varughese, C. Kong, T. Nagy, N. Stone, H. Wang and M. Rush.

I am very grateful to all my old and new friends for their permanent encouragement, especially M. Violeta, C. Girard, F. Abdi, M. Lourenço, A. Pereira, A. Chícharo, C. Gomes, P. Santos, A. Lopes, C. Lopes, M. Pinheiro, F. Pereira, J. Travessa and R. Rodrigues.

Finally, I could not forget my parents, brothers and grandmothers for their support during this long journey. A special thank goes to my brother B. Pépe; his joy and energy were a huge support during the last years!

TABLE OF CONTENTS

ABSTRACT	V
ACKNOWLEDGMENTS	VII
TABLE OF CONTENTS.....	IX
LIST OF APPENDICES.....	XIII
LIST OF FIGURES.....	XV
LIST OF TABLES	XXI
LIST OF NOMENCLATURE	XXIII
LIST OF ABBREVIATIONS	XXV
1. INTRODUCTION	1
1.1. BACKGROUND	2
1.2. OVERVIEW OF CRA PIPELINE WELDING	4
1.2.1. Pipelines Industry	4
1.2.2. Materials Development	5
1.2.3. Welding Processes Innovation.....	6
1.2.4. Summary	8
1.3. MOTIVATION FOR THE RESEARCH PROJECT	10
1.4. AIMS AND OBJECTIVES	12
1.5. STUCTURE OF THE THESIS.....	13
2. PROCESS CHARACTERISTICS AND METAL TRANSFER CHARACTERIZATION	15
2.1. LITERATURE REVIEW	16
2.1.1. Introduction.....	16
2.1.2. Modes of Metal Transfer and their Classification	16
2.1.3. Effect of Processes Characteristics on Metal Transfer Phenomena	19
2.1.4. Forces acting during welding Metal Transfer.....	19
2.1.5. Characterization of the Mechanisms of Metal Transfer.....	21
2.1.6. Characterization of GMAW	27
2.1.7. Pulsed GMAW – Process Characteristics	29
2.1.8. Innovative GMAW Technologies	34
2.1.9. Summary	39
2.2. RESEARCH OBJECTIVES.....	40
2.3. MATERIALS AND METHODS.....	41
2.3.1. Materials	41
2.3.2. Welding Processes.....	42
2.3.3. Methods	45
2.4. RESULTS.....	52
2.4.1. Introduction.....	52
2.4.2. Analysis of the Effect of Setting Parameters on the Arc and Waveform Characteristics	55
2.4.3. Arc Characteristics.....	69
2.4.4. Analysis of Metal Transfer.....	74
2.4.5. Analysis of Arc Stability Control using Current – Voltage Diagrams	102
2.5.6. Analysis of Bead Shape Characteristics	116
2.5. DISCUSSION OF RESULTS	128

2.5.1. Introduction.....	128
2.5.2. Waveform Design and Characteristics	128
2.5.3. Mechanism of Metal Transfer	131
2.5.4. Arc Stability Control.....	136
2.5.5. Arc Energy	138
2.5.6. Bead Shape Characteristics	138
2.6. CONCLUSIONS	142
3. PROCESS EFFICIENCY AND HEAT TRANSFER CHARACTERIZATION	143
3.1. LITERATURE REVIEW	144
3.1.1. Heat Flow in Arc Welding.....	144
3.1.2. Heat Losses during Arc Welding.....	151
3.1.3. Process Efficiency	152
3.1.4. Power, Arc Energy and Heat input Calculations.....	158
3.1.5. Summary	160
3.2. RESEARCH OBJECTIVES.....	162
3.3. MATERIALS AND METHODS.....	163
3.3.1. Materials.....	163
3.3.2. Welding Processes.....	163
3.3.3. Methods	163
3.4. RESULTS	169
3.4.1. Introduction.....	169
3.4.2. Assessment of Experimental Errors.....	169
3.4.3. Characterization of the Effect of Welding Parameters on the Process Efficiency	172
3.4.4. Welding Processes Comparison.....	179
3.5. DISCUSSION OF RESULTS	181
3.5.1. Introduction.....	181
3.5.2. Calorimetric Test Method and Experimental Errors	181
3.5.3. Characterization of the Effect of Setting Parameters on Process Efficiency Results	184
3.5.4. Characterization of Process Efficiency using Different Waveform Systems	186
3.6. CONCLUSIONS	188
4. CHARACTERIZATION OF NARROW GROOVE PIPE WELDING.....	191
4.1. LITERATURE REVIEW	192
4.1.1. Introduction.....	192
4.1.2. Narrow Groove Welding.....	192
4.1.3. Weld Bead Quality.....	193
4.1.4. Weld Imperfections and Defects in Arc Welding	195
4.1.5. Characterization of Imperfections and Defects in Arc Welding.....	195
4.1.6. Summary	198
4.2. AIMS AND OBJECTIVES	199
4.3. MATERIALS AND METHODS.....	200
4.3.1. Materials.....	200
4.3.2. Welding Processes.....	200
4.3.3. Methods	200
4.4. RESULTS.....	205
4.4.1. Introduction.....	205
4.4.2. Analysis of Bead Shape Analysis.....	205
4.4.3. Analysis of Penetration Maps.....	214
4.4.4. Analysis of Defects	214

4.5. DISCUSSION OF RESULTS	221
4.5.1. <i>Introduction</i>	221
4.5.2. <i>Depth of Penetration</i>	221
4.5.3. <i>Height Bead Shape</i>	223
4.5.4. <i>Width Bead Shape</i>	224
4.5.5. <i>Welding Quality and Desirability Conditions</i>	224
4.6. CONCLUSIONS	226
5. EFFECT OF SHIELDING GAS MIXTURES ON WELD BEAD SHAPE CHARACTERISTICS	229
5.1. LITERATURE REVIEW	230
5.1.1. <i>Introduction</i>	230
5.1.2. <i>Effect of Shielding Gas in Arc Welding</i>	230
5.1.3. <i>Characteristics of Common Gases</i>	231
5.1.4. <i>Physical-Chemical Properties of the Gases</i>	232
5.1.5. <i>Effect of Shielding Gas Mixtures on Process Characteristics</i>	234
5.1.6. <i>Gas Flow Control</i>	236
5.1.7. <i>Effect of Oxygen in Arc Welding</i>	236
5.1.8. <i>Summary</i>	238
5.2. AIMS AND OBJECTIVES	239
5.3. MATERIALS AND METHODS.....	240
5.3.1. <i>Materials</i>	240
5.3.2. <i>Welding Processes</i>	240
5.3.3. <i>Methods</i>	240
5.4. RESULTS.....	246
5.4.1. <i>Introduction</i>	246
5.4.2. <i>Root Shielding Quality</i>	246
5.4.3. <i>Analysis of Arc Length</i>	247
5.4.4. <i>Modelling Analysis</i>	248
5.5. DISCUSSION OF RESULTS	251
5.5.1. <i>Introduction</i>	251
5.5.2. <i>Effect of Arc Length</i>	251
5.5.3. <i>Analysis of the Modelling Responses</i>	252
5.5.4. <i>Analysis of Desirability and Optimum Solutions</i>	254
5.6. CONCLUSIONS	256
6. CONCLUSIONS AND PERSPECTIVES FOR FURTHER WORK	257
6.1. CONCLUSIONS.....	258
6.2. PERSPECTIVES FOR FURTHER WORK	260
7. REFERENCES	261
APPENDICES.....	277

LIST OF APPENDICES

I.	PIPE MATERIAL CHEMICAL ANALYSIS CERTIFICATE	279
II.	SETTING PROCESS PARAMETERS APPLIED TO THE BEAD ON PIPE TESTS.....	281
III.	ARC LENGTH MEASUREMENTS FOR THE BEAD ON PIPE TESTS.....	295
IV.	RESULTS OF WAVEFORM CHARACTERISTICS FOR THE BEAD ON PIPE TESTS	309
V.	WAVEFORM PARAMETERS FOR THE BEAD ON PIPE TESTS.....	323
VI.	GRAPHICAL ANALYSIS OF THE EFFECT OF PROCESS SETTING PARAMETERS ON WAVEFORM AND ARC CHARACTERISTICS	319
VI.1.	CHARACTERIZATION OF WAVEFORM CHARACTERISTICS AND ARC LENGTH FOR GMAW-P	326
VI.2.	CHARACTERIZATION OF WAVEFORM CHARACTERISTICS AND ARC LENGTH FOR RAPIDARC	331
VI.3.	CHARACTERIZATION OF WAVEFORM CHARACTERISTICS AND ARC LENGTH FOR STT	336
VI.4.	CHARACTERIZATION OF WAVEFORM CHARACTERISTICS AND ARC LENGTH FOR CMT	341
VI.4.1.	<i>13% Chrome Supermartensitic Stainless Steel</i>	341
VI.4.2.	<i>Mild Steel</i>	341
VI.5.	CHARACTERIZATION OF WAVEFORM CHARACTERISTICS AND ARC LENGTH FOR CMT-P.....	351
VI.6.	CHARACTERIZATION OF WAVEFORM CHARACTERISTICS AND ARC LENGTH FOR FASTROOT	358
VII.	GRAPHICAL ANALYSIS OF THE EFFECT OF SETTING PROCESS PARAMETERS ON WAVEFORM PARAMETERS.....	365
VII.1.	CHARACTERIZATION OF WAVEFORM PARAMETERS FOR GMAW-P.....	366
VII.2.	CHARACTERIZATION OF WAVEFORM PARAMETERS FOR RAPIDARC	369
VII.3.	CHARACTERIZATION OF WAVEFORM PARAMETERS FOR STT.....	372
VII.4.	CHARACTERIZATION OF WAVEFORM PARAMETERS TO CMT.....	376
VII.5.	CHARACTERIZATION OF WAVEFORM PARAMETERS FOR CMT-P	380
VII.6.	CHARACTERIZATION OF WAVEFORM PARAMETERS FOR FASTROOT.....	384
VIII.	ARC CURRENT AND VOLTAGE WAVEFORMS.....	389
IX.	BEAD SHAPE CHARACTERISTICS FOR BEAD ON PIPE TESTS	397
X.	GRAPHICAL ANALYSIS OF THE EFFECT OF SETTING PROCESS PARAMETERS ON BEAD SHAPE CHARACTERISTICS.....	411
X.1.	CHARACTERIZATION OF BEAD SHAPE CHARACTERISTICS FOR GMAW-P	412
X.2.	CHARACTERIZATION OF BEAD SHAPE CHARACTERISTICS FOR RAPIDARC.....	418
X.3.	CHARACTERIZATION OF BEAD SHAPE CHARACTERISTICS FOR STT	425
X.4.	CHARACTERIZATION OF BEAD SHAPE CHARACTERISTICS FOR CMT	431
X.5.	CHARACTERIZATION OF BEAD SHAPE CHARACTERISTICS FOR CMT-P	440
X.6.	CHARACTERIZATION OF BEAD SHAPE CHARACTERISTICS FOR FASTROOT	448
XI.	RESULTS OF BEAD SHAPE CHARACTERISTICS OBTAINED FOR NARROW GROOVE WELDING	455
XII.	EQUATION MODELS OBTAINED FOR THE DIFFERENT WELDING WAVEFORMS, RESPONSES AND SHIELDING GAS MIXTURES APPLIED.....	467
XII.1.	EQUATION MODELS OBTAINED FOR GMAW-P	467
XII.2.	EQUATION MODELS OBTAINED FOR RAPIDARC.....	469
XII.3.	EQUATION MODELS OBTAINED FOR STT	471

XII.4. EQUATION MODELS OBTAINED FOR CMT.....	473
XII.5. EQUATION MODELS OBTAINED FOR CMT-P	475
XII.6. EQUATION MODELS OBTAINED FOR FASTROOT	476
XIII. VALIDATION ANALYSIS	477
XIV. GRAPHICAL ANALYSIS OBTAINED FROM THE STATISTICAL MODELLING	481
XIV.1. GRAPHICAL RESULTS OBTAINED FOR THE DEPTH OF PENETRATION (DP) MODEL RESPONSES.....	481
XIV.2. GRAPHICAL RESULTS OBTAINED FOR THE HEIGHT RATIO (HR) MODEL RESPONSES.....	483
XIV.3. GRAPHICAL RESULTS OBTAINED FOR THE ROOT WIDTH (RW) MODEL RESPONSES.....	485
XIV.4. GRAPHICAL RESULTS OBTAINED FOR THE TOP WIDTH (TW) MODEL RESPONSES	487
XV. DIAGRAMS OF THE DESIRABILITY CRITERIA APPLIED FOR DIFFERENT WAVEFORMS.....	489
XVI. DESIRABILITY GRAPHIC ANALYSIS OBTAINED FROM STATISTICAL MODELLING	493
XVII. ARC LENGTH MEASUREMENTS	497
XVIII. BEAD SHAPE CHARACTERISTICS OBTAINED FOR RAPIDARC AND CMT-P	503
XIX. EQUATION MODELS OBTAINED FOR GAS MIXTURES STUDY.....	505
XIX.1. EQUATION MODELS OBTAINED FOR THE MIXTURES DESIGN WITH RAPIDARC	505
XIX.2. EQUATION MODELS OBTAINED FOR THE MIXTURES DESIGN WITH CMT-P	506
XX. DESIRABILITY CRITERIA ESTABLISHED FOR THE MIXTURE DESIGNS	507

LIST OF FIGURES

FIGURE 1.1 – WORLD ENERGY DEMAND (SOURCE: IEA) (CORNOT-GANOLPHE, ET AL. 2003).	4
FIGURE 1.2 – DEEP WATER OFFSHORE TECHNOLOGY (COURTESY OF SHELL) (INTERNATIONAL ENERGY AGENCY 2005).	5
FIGURE 1.3 – DIAGRAM OF THE STRUCTURE DEFINED FOR THE RESEARCH DEVELOPED IN THIS THESIS.....	11
FIGURE 2.1 – PULSE WAVEFORM OF SYNERGIC CONTROL.....	28
FIGURE 2.2 – PULSE WAVEFORM OF SELF-REGULATING CONTROL.....	29
FIGURE 2.3 – REPRESENTATION OF A CHARACTERISTIC SQUARE PULSED WAVEFORM.....	29
FIGURE 2.4 - SCHEMATIC DIAGRAM OF OPERATIONAL AREA FOR RAPIDARC WAVEFORM (LINCOLN ELECTRIC 2005).	35
FIGURE 2.5 - SCHEMATIC DIAGRAM OF METAL TRANSFER MECHANISM FOR RAPIDARC WAVEFORM (LINCOLN ELECTRIC 2005).....	35
FIGURE 2.6 – SCHEMATIC DIAGRAM OF METAL TRANSFER MECHANISM FOR STT WAVEFORM (LINCOLN ELECTRIC 2006).	36
FIGURE 2.7 – PRINCIPAL PHASES DURING THE TRANSFER MECHANISM OF CMT PROCESS (FRONIUS 2005).	37
FIGURE 2.8 – CURRENT (I) AND VOLTAGE (U) WAVEFORM IN CMT WELDING (HIMMELBAUER 2005).....	38
FIGURE 2.9 – DIAGRAM OF CURRENT WAVEFORM AND SYNCHRONIZED METAL TRANSFER HIGH SPEED IMAGES (UUSITALO 2007). ..	38
FIGURE 2.10 – PIPE SECTIONS OF SUPERMARTENSITIC STAINLESS STEEL.	42
FIGURE 2.11 – VIEW OF THE RIG USED FOR WELDING THIN SHEETS.	46
FIGURE 2.12 – VIEW OF THE RIG USED FOR PIPE WELDING USING A ROTATOR MACHINE.....	46
FIGURE 2.13 – CALIBRATION CURVE FOR THE WELDING SPEED SETTING ON THE ROTATOR.	47
FIGURE 2.14 – OSCILLOSCOPE USED FOR THE CURRENT AND VOLTAGE WAVEFORM AND WFS SIGNAL RECORDINGS.	48
FIGURE 2.15 – VIEW OF HIGH SPEED CAMERA AND BACK LIGHT SYSTEM ALIGNED IN OPPOSITE DIRECTIONS TO THE WELDING ZONE (PIPE SPECIMEN REMOVED)	48
FIGURE 2.16 – DIAGRAM OF SET-UP FOR THE EXPERIMENTS DESCRIBED IN THIS CHAPTER.	49
FIGURE 2.17 – CALIBRATION CURVE FOR THE ACTUAL WFS USING VOLTAGE MEASUREMENTS FROM A TACHOMETER.....	49
FIGURE 2.18 – MACROGRAPH ILLUSTRATING THE BEAD SHAPE MEASUREMENTS, RESPECTIVELY A) HEIGHT BEAD; B) PENETRATION BEAD; C) WIDTH BEAD; D) REINFORCEMENT AREA AND E) DILUTION AREA.	51
FIGURE 2.19 – ARC CURRENT AND VOLTAGE WAVEFORMS USING WFS OF 6M/MIN FOR: A) GMAW-P; B) RAPIDARC; C) STT; D) FASTROOT; E) CMT AND F) CMT-P.	53
FIGURE 2.20 – ARC CURRENT AND VOLTAGE WAVEFORMS USING WFS OF 8M/MIN FOR: A) GMAW-P; B) RAPIDARC; C) STT; D) FASTROOT; E) CMT AND F) CMT-P.	54
FIGURE 2.21 – COMPARISON OF ACTUAL AND SET WFS FOR ALL WELDING PROCESSES CONSIDERED.	56
FIGURE 2.22 – AVERAGE AND RMS VARIATION OF ACTUAL WFS (WFS SET OF 6M/MIN) FOR ALL WAVEFORMS, WHEN ADJUSTING ARC LENGTH PARAMETER WAS CHANGED FROM ITS MINOR TO UPPER LIMITS (IN FIVE STEPS).	56
FIGURE 2.23 – EFFECT OF CTWD ON ACTUAL WFS, FOR WELDING OF MILD STEEL IN CMT.	57
FIGURE 2.24 – COMPARISON OF BURN-OFF RATIO FOR DIFFERENT WELDING WAVEFORMS.....	58
FIGURE 2.25 – TRANSITION REGION OF BURN-OFF RATIO FOR RAPIDARC WAVEFORM.	58
FIGURE 2.26 – VARIATION OF PEAK AND BACKGROUND CURRENT WITH ACTUAL WFS TO THE DIFFERENT WAVEFORMS.	59
FIGURE 2.27 – VARIATION OF SHORT CIRCUITING AND PULSE FREQUENCIES WITH WFS FOR CMT-P USING 2.5%CO ₂ 97.5%AR... 60	
FIGURE 2.28 – COMPARISON OF THE AVERAGE AND RMS VARIATION (BARS) OF MEAN ARC CURRENT FOR DIFFERENT WAVEFORMS, OBTAINED BY CHANGING THE ARC LENGTH ADJUSTING PARAMETER (IN FIVE STEPS FROM LOWER TO UPPER LIMITS).....	61
FIGURE 2.29 – COMPARISON OF AVERAGE AND RMS VARIATION (BARS) OF MEAN ARC CURRENT FOR DIFFERENT WAVEFORMS, OBTAINED BY CHANGING CTWD IN THREE STEPS (11, 13.5 AND 16MM).	62
FIGURE 2.30 – COMPARISON OF THE VARIATION OF MEAN ARC CURRENT WITH SHIELDING GAS FOR ALL WAVEFORMS (WFS SET OF 6M/MIN).	62
FIGURE 2.31 – COMPARISON OF THE VARIATION OF MEAN ARC CURRENT WITH WFS/TS RATIO FOR ALL WAVEFORMS (WFS SET OF 6M/MIN).	63
FIGURE 2.32 – VARIATION OF MEAN ARC VOLTAGE WITH ACTUAL WFS FOR ALL WAVEFORMS.....	63
FIGURE 2.33 – VARIATION OF ARC VOLTAGE WITH ACTUAL WFS FOR RAPIDARC, USING DIFFERENT SHIELDING GASES.....	64

FIGURE 2.34 – RELATIONSHIP BETWEEN WFS AND PEAK AND BACKGROUND ARC VOLTAGE FOR DIFFERENT WELDING WAVEFORMS.	65
FIGURE 2.35 – COMPARISON OF THE AVERAGE AND RMS VARIATION (BARS) OF MEAN ARC VOLTAGE FOR DIFFERENT WAVEFORMS, OBTAINED BY CHANGING THE ARC LENGTH ADJUSTING PARAMETER (IN FIVE STEPS FROM LOWER TO UPPER LIMITS).	66
FIGURE 2.36 – COMPARISON OF AVERAGE AND RMS VARIATION (BARS) OF MEAN ARC VOLTAGE FOR DIFFERENT WAVEFORMS, OBTAINED BY CHANGING CTWD IN THREE STEPS (11, 13.5 AND 16MM).	67
FIGURE 2.37 – COMPARISON OF THE VARIATION OF MEAN ARC VOLTAGE WITH SHIELDING GAS FOR ALL WAVEFORMS (WFS SET AT 6M/MIN).	67
FIGURE 2.38 – COMPARISON OF THE VARIATION OF MEAN ARC VOLTAGE WITH WFS/TS RATIO FOR ALL WAVEFORMS (WFS SET AT 6M/MIN).	68
FIGURE 2.39 – VARIATION OF ARC ENERGY WITH ACTUAL WFS FOR ALL WAVEFORMS.	68
FIGURE 2.40 – VARIATION OF ARC POWER WITH ACTUAL WFS FOR ALL WAVEFORMS.	69
FIGURE 2.41 – VARIATION OF ARC LENGTH WITH ACTUAL WFS (MEASURED) FOR ALL WAVEFORMS.	70
FIGURE 2.42 – COMPARISON OF THE VARIATION OF ARC LENGTH WITH ACTUAL WFS (MEASURED) FOR RAPIDARC FOR DIFFERENT SHIELDING GASES AND WFS/TS RATIOS.	70
FIGURE 2.43 – COMPARISON OF AVERAGE AND RMS VARIATION OF ARC LENGTH FOR ALL WAVEFORMS, OBTAINED BY CHANGING THE ARC LENGTH ADJUSTING PARAMETER (IN FIVE STEPS FROM THE MINOR TO UPPER LIMITS) FOR TWO DIFFERENT SHIELDING GASES (WFS SET OF 6M/MIN).	71
FIGURE 2.44 – COMPARISON OF THE VARIATION OF ARC LENGTH WITH THE ARC VOLTAGE, OBTAINED WHEN ARC LENGTH ADJUSTING PARAMETER WAS VARIED IN FIVE STEPS FROM THE LOWER TO UPPER LIMITS (WFS SET OF 6M/MIN).	72
FIGURE 2.45 – COMPARISON OF THE VARIATION OF ARC LENGTH WITH THE ARC VOLTAGE OBTAINED WHEN WFS SET WAS VARIED FROM LOW (AROUND 3-4M/MIN) TO HIGH LEVELS (AROUND 8-10M/MIN) USING NOMINAL ARC LENGTH ADJUSTING PARAMETERS FOR ALL WAVEFORMS.	72
FIGURE 2.46 – COMPARISON OF THE AVERAGE AND RMS VARIATION OF ARC LENGTH FOR ALL WAVEFORMS, OBTAINED BY CHANGING CTWD (AT THREE LEVELS: 11, 13.5 AND 16MM) (WFS SET OF 6M/MIN).	73
FIGURE 2.47 – SYNCHRONIZED ARC CURRENT AND VOLTAGE WAVEFORMS WITH HIGH SPEED VIDEO-IMAGES OBTAINED FROM GMAW-P FOR TEST BG08.	76
FIGURE 2.48 – SYNCHRONIZED ARC CURRENT AND VOLTAGE WAVEFORMS WITH HIGH SPEED VIDEO-IMAGES OBTAINED FOR GMAW-P (TEST BG42).	77
FIGURE 2.49 – SYNCHRONIZED ARC CURRENT AND VOLTAGE WAVEFORMS WITH HIGH SPEED VIDEO-IMAGES OBTAINED FOR GMAW-P (TEST BG42).	78
FIGURE 2.50 – SYNCHRONIZED ARC CURRENT AND VOLTAGE WAVEFORMS WITH HIGH SPEED VIDEO-IMAGES OBTAINED TO GMAW-P (BG30).	79
FIGURE 2.51 – SYNCHRONIZED ARC CURRENT AND VOLTAGE WAVEFORMS WITH HIGH SPEED VIDEO-IMAGES OBTAINED FOR RAPIDARC (TEST BR22).	81
FIGURE 2.52 – SYNCHRONIZED ARC CURRENT AND VOLTAGE WAVEFORMS WITH THE HIGH SPEED VIDEO-IMAGES OBTAINED FOR RAPIDARC (BR06).	82
FIGURE 2.53 – SYNCHRONIZED ARC CURRENT AND VOLTAGE WAVEFORMS WITH HIGH SPEED VIDEO-IMAGES OBTAINED FOR RAPIDARC (BR56).	83
FIGURE 2.54 – SYNCHRONIZED ARC CURRENT AND VOLTAGE WAVEFORMS WITH HIGH SPEED VIDEO-IMAGES OBTAINED FOR STT (BS13).	85
FIGURE 2.55 – SYNCHRONIZED ARC CURRENT AND VOLTAGE WAVEFORMS WITH HIGH SPEED VIDEO-IMAGES OBTAINED FOR STT (BS10).	86
FIGURE 2.56 – SYNCHRONIZED ARC CURRENT AND VOLTAGE WAVEFORMS WITH HIGH SPEED VIDEO-IMAGES OBTAINED FOR STT (BS26).	87
FIGURE 2.57 – SYNCHRONIZED ARC CURRENT AND VOLTAGE WAVEFORMS WITH HIGH SPEED VIDEO-IMAGES OBTAINED FOR CMT (BC13).	89
FIGURE 2.58 – SYNCHRONIZED ARC CURRENT AND VOLTAGE WAVEFORMS WITH HIGH SPEED VIDEO-IMAGES OBTAINED FOR CMT (BC66).	90

FIGURE 2.59 – SYNCHRONIZED ARC CURRENT AND VOLTAGE WAVEFORMS WITH HIGH SPEED VIDEO-IMAGES OBTAINED FOR CMT (BC66).....	90
FIGURE 2.60 – SYNCHRONIZED ARC CURRENT AND VOLTAGE WAVEFORMS WITH HIGH SPEED VIDEO-IMAGES OBTAINED FOR CMT (BC15).....	91
FIGURE 2.61 – SYNCHRONIZED ARC CURRENT AND VOLTAGE WAVEFORMS WITH HIGH SPEED VIDEO-IMAGES OBTAINED FOR CMT (BC40).....	92
FIGURE 2.62 – SYNCHRONIZED ARC CURRENT AND VOLTAGE WAVEFORMS WITH HIGH SPEED VIDEO-IMAGES OBTAINED FOR CMT-P (BP13).....	94
FIGURE 2.63 – SYNCHRONIZED ARC CURRENT AND VOLTAGE WAVEFORMS WITH HIGH SPEED VIDEO-IMAGES OBTAINED FOR CMT-P (BP11).....	95
FIGURE 2.64 – SYNCHRONIZED ARC CURRENT AND VOLTAGE WAVEFORMS WITH HIGH SPEED VIDEO-IMAGES OBTAINED FOR CMT-P (BP11).....	95
FIGURE 2.65 – SYNCHRONIZED ARC CURRENT AND VOLTAGE WAVEFORMS WITH HIGH SPEED VIDEO-IMAGES OBTAINED FOR CMT-P (BP28).....	96
FIGURE 2.66 – SYNCHRONIZED ARC CURRENT AND VOLTAGE WAVEFORMS WITH HIGH SPEED VIDEO-IMAGES OBTAINED FOR FASTROOT (BF08).	99
FIGURE 2.67 – SYNCHRONIZED ARC CURRENT AND VOLTAGE WAVEFORMS WITH HIGH SPEED VIDEO-IMAGES OBTAINED FOR FASTROOT (BF06).	100
FIGURE 2.68 – SYNCHRONIZED ARC CURRENT AND VOLTAGE WAVEFORMS WITH HIGH SPEED VIDEO-IMAGES OBTAINED FOR FASTROOT (BF53).	101
FIGURE 2.69 – SYNCHRONIZED ARC CURRENT AND VOLTAGE WAVEFORMS WITH HIGH SPEED VIDEO-IMAGES OBTAINED FOR FASTROOT (BF13).	101
FIGURE 2.70 – WAVEFORM (A) AND UI DIAGRAM (B) CORRESPONDENT FOR A GENERIC GMAW PROCESS.	102
FIGURE 2.71 – UI DIAGRAMS OF THE VARIATION WITH WFS FOR GMAW-P, USING WFS/TS RATIO OF 16: A) 2.5%CO ₂ 97.5%Ar; B) 1.5%CO ₂ 54%He 44.5%Ar.....	103
FIGURE 2.72 – UI DIAGRAM OF THE VARIATION WITH WFS FOR GMAW-P, USING WFS/TS RATIO OF 18.	104
FIGURE 2.73 – UI DIAGRAM OF THE VARIATION WITH TRIM FOR GMAW-P.	104
FIGURE 2.74 – UI DIAGRAM OF THE VARIATION WITH CTWD FOR GMAW-P.	105
FIGURE 2.75 – UI DIAGRAMS OF THE VARIATION WITH WFS FOR RAPIDARC, USING WFS/TS RATIO OF 16: A) 2.5%CO ₂ 97.5%Ar; B) 1.5%CO ₂ 54%He 44.5%Ar.....	105
FIGURE 2.76 – UI DIAGRAM OF THE VARIATION WITH WFS FOR RAPIDARC, USING WFS/TS RATIO OF 18.	106
FIGURE 2.77 – UI DIAGRAM OF THE VARIATION WITH TRIM FOR RAPIDARC.	106
FIGURE 2.78 – UI DIAGRAM OF THE VARIATION WITH CTWD FOR RAPIDARC.	107
FIGURE 2.79 – UI DIAGRAMS OF THE VARIATION WITH WFS FOR STT, USING WFS/TS RATIO OF 16: A) 2.5%CO ₂ 97.5%Ar; B) 1.5%CO ₂ 54%He 44.5%Ar.	107
FIGURE 2.80 – UI DIAGRAM OF THE VARIATION WITH WFS FOR STT, USING WFS/TS RATIO OF 18.	108
FIGURE 2.81 – UI DIAGRAM OF THE VARIATION WITH TRIM FOR STT.....	108
FIGURE 2.82 – UI DIAGRAM OF THE VARIATION WITH CTWD FOR STT.	109
FIGURE 2.83 – UI DIAGRAMS OF THE VARIATION WITH WFS FOR CMT, USING WFS/TS RATIO OF 16: A) 2.5%CO ₂ 97.5%Ar; B) 1.5%CO ₂ 54%He 44.5%Ar.	109
FIGURE 2.84 – UI DIAGRAM OF THE VARIATION WITH WFS FOR CMT, USING WFS/TS RATIO OF 18.....	110
FIGURE 2.85 – UI DIAGRAM OF THE VARIATION WITH ALC FOR CMT.....	110
FIGURE 2.86 – UI DIAGRAM OF THE VARIATION WITH DC FOR CMT.	111
FIGURE 2.87 – UI DIAGRAM OF THE VARIATION WITH CTWD FOR CMT.....	111
FIGURE 2.88 – UI DIAGRAMS OF THE VARIATION WITH WFS FOR CMT-P, USING WFS/TS RATIO OF 16: A) 2.5%CO ₂ 97.5%Ar; B) 1.5%CO ₂ 54%He 44.5%Ar.	112
FIGURE 2.89 – UI DIAGRAM OF THE VARIATION WITH WFS FOR CMT-P, USING WFS/TS RATIO OF 18.	112
FIGURE 2.90 – UI DIAGRAM OF THE VARIATION WITH ALC FOR CMT.....	113
FIGURE 2.91 – UI DIAGRAM OF THE VARIATION WITH PC FOR CMT-P.	113

FIGURE 2.92 – UI DIAGRAM OF THE VARIATION WITH CTWD FOR CMT-P.	114
FIGURE 2.93 – UI DIAGRAMS OF THE VARIATION WITH WFS FOR FASTROOT, USING WFS/TS RATIO OF 16: A) 2.5%CO ₂ 97.5%Ar; B) 1.5%CO ₂ 54%He 44.5%Ar.	114
FIGURE 2.94 – UI DIAGRAM OF THE VARIATION WITH WFS FOR FASTROOT, USING WFS/TS RATIO OF 18.	115
FIGURE 2.95 – UI DIAGRAM OF THE VARIATION WITH BASE CURRENT FOR FASTROOT.	115
FIGURE 2.96 – UI DIAGRAM OF THE VARIATION WITH FORMING PULSE FOR FASTROOT.	116
FIGURE 2.97 – UI DIAGRAM OF THE VARIATION WITH CTWD FOR CMT-P.	116
FIGURE 2.98 – VARIATION OF DEPTH OF PENETRATION WITH ACTUAL WFS FOR ALL WAVEFORMS.	117
FIGURE 2.99 – COMPARISON OF THE AVERAGE AND RMS VARIATION OF DEPTH OF PENETRATION FOR ALL WAVEFORMS, BY CHANGING ARC LENGTH CORRECTION PARAMETER (IN FIVE STEPS FROM LOWER TO UPPER LIMITS) FOR TWO SHIELDING GAS MIXTURES (WFS SET OF 6M/MIN).	118
FIGURE 2.100 – COMPARISON OF THE EFFECT OF ARC CURRENT ON DEPTH OF PENETRATION FOR ALL WAVEFORMS.	119
FIGURE 2.101 – COMPARISON OF THE EFFECT OF ARC POWER ON DEPTH OF PENETRATION FOR ALL WAVEFORMS.	119
FIGURE 2.102 – EFFECT OF PEAK CURRENT ON DEPTH OF PENETRATION FOR ALL WAVEFORMS.	120
FIGURE 2.103 – VARIATION OF DEPTH OF PENETRATION WITH ACTUAL WFS FOR ALL WAVEFORMS.	120
FIGURE 2.104 – VARIATION OF DILUTION RATIO WITH ACTUAL WFS FOR ALL WAVEFORMS.	121
FIGURE 2.105 – COMPARISON OF THE VARIATION OF DILUTION RATIO WITH ARC CURRENT AT DIFFERENT ALC FOR CMT.	122
FIGURE 2.106 – COMPARISON OF THE VARIATION OF DILUTION AREA WITH ARC CURRENT FOR ALL WAVEFORMS.	122
FIGURE 2.107 – COMPARISON OF THE VARIATION OF DILUTION AREA WITH ARC POWER FOR ALL WAVEFORMS.	123
FIGURE 2.108 – COMPARISON OF THE VARIATION OF DILUTION AREA WITH PEAK CURRENT FOR ALL WAVEFORMS.	123
FIGURE 2.109 – VARIATION OF WIDTH BEAD WITH ACTUAL WFS FOR ALL WAVEFORMS.	124
FIGURE 2.110 – COMPARISON OF THE AVERAGE AND RMS VARIATION OBTAINED FOR WIDTH BEAD BY CHANGING ARC LENGTH ADJUSTING PARAMETER (IN FIVE STEPS FROM MINOR TO UPPER LIMIT) FOR ALL WAVEFORMS.	124
FIGURE 2.111 – VARIATION OF HEIGHT BEAD WITH ACTUAL WFS FOR ALL WAVEFORMS.	125
FIGURE 2.112 – COMPARISON OF THE VARIATION OF HEIGHT BEAD WITH ARC LENGTH ADJUSTING PARAMETER (FIVE STEPS FROM MINOR TO UPPER LIMIT) FOR ALL WAVEFORMS.	125
FIGURE 2.113 – VARIATION OF DEPTH OF PENETRATION WITH ACTUAL WFS FOR ALL WAVEFORMS.	126
FIGURE 2.114 – COMPARISON OF THE AVERAGE AND RMS VARIATION OBTAINED FOR HEIGHT TO WIDTH RATIO WITH BY CHANGING ARC LENGTH ADJUSTING PARAMETER (IN FIVE STEPS FROM MINOR TO UPPER LIMIT) FOR ALL WAVEFORMS.	126
FIGURE 2.115 – EFFECT OF ARC ENERGY ON CONVEXITY INDEX (HEIGHT TO WIDTH RATIO).	127
FIGURE 2.116 – COMPARISON OF STABILITY DIAGRAMS FOR ALL WAVEFORMS: A) GMAW-P; B) STT; C) CMT-P; D) CMT; E) RAPIDARC; AND F) FASTROOT.	130
FIGURE 3.1 – POWER DENSITY FOR DIFFERENT WELDING PROCESSES (LANCASTER 1984).	147
FIGURE 3.2 – MEASUREMENT OF PROCESS EFFICIENCY IN GTAW: A) CALORIMETER; B) VARIATION OF WATER TEMPERATURE AS A FUNCTION OF TIME.	154
FIGURE 3.3 – A) SCHEMATIC SKETCH OF SEEBECK CALORIMETER APPLIED TO MEASURE PROCESS EFFICIENCY; B) OPERATING PRINCIPLE OF A GRADIENT LAYER CALORIMETER.	155
FIGURE 3.4 – A) ALUMINIUM SPECIMENS USED IN THE EXPERIMENTS WITH THE APPROXIMATE LOCATION OF THERMOCOUPLES (MARKED BY AN “X”); B) SCHEMATIC REPRESENTATION OF THE CALORIMETER.	156
FIGURE 3.5 – LIQUID NITROGEN CALORIMETRIC TESTS: A) CONTAINER DURING CALORIMETRIC TEST; B) SPECIMENS AFTER CALORIMETRIC TESTS.	164
FIGURE 3.6 – NORMAL VAPORIZATION RATE FOR LIQUID NITROGEN WITH TIME OBTAINED FOR THREE DIFFERENT TRIALS.	165
FIGURE 3.7 – COMPARISON BETWEEN NORMAL VAPORIZATION RATE OF LIQUID NITROGEN WITH VAPORIZATION FROM THE WELDING AND ROOM TEMPERATURE.	167
FIGURE 3.8 – CORRELATION OF THE MASS OF THE SPECIMENS AND THE AMOUNT OF LIQUID NITROGEN LOST, BETWEEN ROOM TEMPERATURE AND LIQUID NITROGEN BOILING TEMPERATURE.	168
FIGURE 3.9 – EFFECT CLAMPING BARS MATERIAL ON PROCESS EFFICIENCY FOR CMT, USING PLATES WITH DIFFERENT THICKNESSES.	170
FIGURE 3.10 – EFFECT OF WELDING DURATION TIME ON PROCESS EFFICIENCY FOR CMT.	171

FIGURE 3.11 – EFFECT OF THE NUMBER OF OSCILLATIONS DURING THE HOLING TRANSFER TIME ON PROCESS EFFICIENCY FOR CMT.	171
FIGURE 3.12 – EFFECT OF DELAY TIME ON PROCESS EFFICIENCY FOR CMT: A) FIRST 900SEC FOR 2MM THICKNESS PLATES; B) FIRST 60SEC COMPARING PLATES WITH DIFFERENT THICKNESSES.....	172
FIGURE 3.13 – EFFECT OF DIFFERENT WAVEFORM CHARACTERISTICS ON PROCESS EFFICIENCY FOR CMT, USING DIFFERENT WFS/TS RATIOS AND 2MM THICKNESS PLATES: A) MEASURED WFS; B) ARC CURRENT; C) ARC VOLTAGE AND D) ARC POWER.....	174
FIGURE 3.14 – EFFECT OF WFS ON PROCESS EFFICIENCY FOR CMT, USING CONSTANT WFS/TS RATIO OF 15.6 AND PLATES WITH DIFFERENT THICKNESSES.	174
FIGURE 3.15 – EFFECT OF WELDING SPEED ON PROCESS EFFICIENCY FOR CMT, USING PLATES WITH DIFFERENT THICKNESSES.	175
FIGURE 3.16 – EFFECT OF THE ARC LENGTH CORRECTION (ALC) ON PROCESS EFFICIENCY FOR CMT, AT DIFFERENT SETTING CONDITIONS (THICKNESS PLATES AND WFS LEVELS).	175
FIGURE 3.17 – EFFECT OF HOT START (HS) ON PROCESS EFFICIENCY FOR CMT, USING 4MM THICKNESS PLATES AND CONSTANT WFS (4M/MIN).	176
FIGURE 3.18 – EFFECT OF CTWD ON PROCESS EFFICIENCY FOR CMT.....	176
FIGURE 3.19 – EFFECT OF SHIELDING GAS COMPOSITION (I.E. AMOUNT OF CARBON DIOXIDE) ON PROCESS EFFICIENCY FOR CMT, USING PLATES WITH DIFFERENT THICKNESSES.	177
FIGURE 3.20 – EFFECT OF WFS ON PROCESS EFFICIENCY FOR RAPIDARC, USING CONSTANT WELDING SPEED OF 0.5M/MIN AND PLATES WITH DIFFERENT THICKNESSES.	177
FIGURE 3.21 – EFFECT OF PLATE THICKNESS ON THE PROCESS EFFICIENCY AT CONSTANT WFS/TS RATIO.	178
FIGURE 3.22 – EFFECT OF THE TRIM ON THE PROCESS EFFICIENCY.	178
FIGURE 3.23 – EFFECT OF SHIELDING GAS COMPOSITION ON PROCESS EFFICIENCY FOR RAPIDARC, AT DIFFERENT THICKNESS PLATES.	179
FIGURE 3.24 – EFFECT OF THE WFS/TS RATIO ON THE PROCESS EFFICIENCY FOR DIFFERENT WAVEFORMS.....	180
FIGURE 3.25 – SKETCH OF THE HEAT FLOW IN WELDING OF THIN PLATES, WITH THE INCREASE OF ARC ENERGY. THE RED ARROWS REPRESENT THE RADIATION LOSSES DURING WELDING, WHILE THE YELLOW ARROWS REPRESENT THE LOSSES BY RADIATION AFTER WELDING.	182
FIGURE 3.26 – VARIATION OF RADIATION LOSSES WITH THE INCREASE OF TEMPERATURE (NORMAND AND PELEG 2010).	183
FIGURE 4.1 – GROOVE DESIGN BASED ON “V” CONFIGURATION WITH A BEVEL ANGLE OF 30 DEGREES AND 1.5MM ROOT FACE.	201
FIGURE 4.2 – GROOVE DESIGN BASED ON MODIFIED “V” CONFIGURATION WITH 1.5MM ROOT FACE.....	201
FIGURE 4.3 – GROOVE DESIGN BASED ON “J” CONFIGURATION WITH 1.5MM ROOT FACE.....	201
FIGURE 4.4 – ADJACENT PURGING GAS DEVICE APPLIED TO THE ROOT PROTECTION: A) DETAIL OF THE APPLICATION; B) DETAIL OF THE FIRST DEVICE DEVELOPED WITH WIRE WOOL.....	202
FIGURE 4.5 – ADJACENT PURGING GAS DEVICES APPLIED TO THE ROOT PROTECTION: A) DEVICE WITH FIBRE GLASS AND WIRE MESH ON THE SURFACE; B) DEVICE WITHOUT ANY MATERIAL BUT BUILT WITH THREE INTERNAL PIPES.....	203
FIGURE 4.6 – FINAL SOLUTION OF PURGING GAS DEVICE APPLIED TO THE ROOT PROTECTION ACHIEVING LAMINAR GAS FLOW.....	203
FIGURE 4.7 – BEAD SHAPE MEASUREMENTS AT DIFFERENT SITUATIONS CONSIDERING THE FOLLOWING MEASURES: A) DEPTH OF PENETRATION; B1) HIGH HEIGHT BEAD (HH); B2) LOW HEIGHT BEAD (HL); C) TOP WIDTH BEAD; D) ROOT WIDTH BEAD; E) REINFORCEMENT AREA; F) DILUTION AREA; AND G) ROOT AREA.	204
FIGURE 4.8 – PENETRATION/ LACK OF PENETRATION MAPS OBTAINED BY THE VARIATION OF WFS AND WFS/TS RATIOS FOR DIFFERENT WAVEFORMS: A) GMAW-P; B) STT; C) RAPIDARC; D) FASTROOT; E) CMT-P AND F) CMT. THE CIRCLE REPRESENTS PENETRATION AND THE TRIANGLE LACK OF PENETRATION.....	215
FIGURE 4.9 – MACROSTRUCTURES ILLUSTRATING DEFECTS ON WELDING OF NARROW GROOVE PIPE USING GMAW-P.....	216
FIGURE 4.10 – MACROSTRUCTURES ILLUSTRATING DEFECTS ON WELDING OF NARROW GROOVE PIPE USING GMAW-P.....	217
FIGURE 4.11 – MACROSTRUCTURES ILLUSTRATING DEFECTS ON WELDING OF NARROW GROOVE PIPE USING STT.	218
FIGURE 4.12 – MACROSTRUCTURES ILLUSTRATING DEFECTS ON WELDING OF NARROW GROOVE PIPE USING CMT.	218
FIGURE 4.13 – MACROSTRUCTURES ILLUSTRATING DEFECTS ON WELDING OF NARROW GROOVE PIPE USING CMT-P.	219
FIGURE 4.14 – MACROSTRUCTURES ILLUSTRATING DEFECTS ON WELDING OF NARROW GROOVE PIPE USING CMT-P.	220
FIGURE 4.15 – WELD BEAD OBTAINED FOR GMAW-P USING WFS = 10M/MIN; TS = 0.83M/MIN; AND 1.5%CO ₂ 54%He44.5%Ar.....	225

FIGURE 4.16 – WELD BEAD OBTAINED FOR RAPIDARC USING WFS = 9M/MIN AND TS = 0.50M/MIN: A) 2.5%CO ₂ 97.5%AR; B) 1.5%CO ₂ 54%He44.5%AR.....	225
FIGURE 5.1 – ELECTRIC (A) AND THERMAL (B) CONDUCTIVITY OF GASES AT PRESSURE OF 1 ATM (SUBAN AND TUSEK 2001).	233
FIGURE 5.2 – MAP OF OXIDATION BASED ON COLORATION AND OXYGEN CONTENT MEASUREMENT ON AUSTENITIC STAINLESS STEEL, USING ARGON AS A PURGING GAS (HANSEN 1994).....	238
FIGURE 5.3 – FLOW LEVEL READ MEASUREMENTS OBTAINED FOR EACH GAS AT DIFFERENT SHIELDING RATES ON THE OUTLET OF THE GAS ANALYSER.	243
FIGURE 5.4 – FLOW LEVEL READ MEASUREMENTS OBTAINED FOR EACH GAS AT DIFFERENT SHIELDING RATES ON THE WELDING TORCH.	244
FIGURE 5.5 – VARIATION OF ARC LENGTH FOR DIFFERENT SHIELDING GAS MIXTURES FOR RAPIDARC. THE BARS REPRESENT THE RMS VARIATION WHEN TRIM WAS CHANGED.....	247
FIGURE 5.6 – VARIATION OF ARC LENGTH FOR DIFFERENT SHIELDING GAS MIXTURES FOR CMT-P. THE BARS REPRESENT THE RMS VARIATION WHEN ARC LENGTH CORRECTION WAS CHANGED.	247
FIGURE 5.7 – EFFECT OF SHIELDING GAS MIXTURES ON UNDERCUTTING FOR CMT-P.	252
FIGURE 5.8 – EFFECT OF SHIELDING GAS MIXTURES ON BEAD SHAPE CHARACTERISTICS FOR RAPIDARC: A) DEPTH OF PENETRATION; B) HEIGHT RATIO; C) ROOT WIDTH AND D) TOP WIDTH.	253
FIGURE 5.9 – EFFECT OF SHIELDING GAS MIXTURES ON BEAD SHAPE CHARACTERISTICS FOR CMT-P: A) DEPTH OF PENETRATION; B) HEIGHT RATIO; C) ROOT WIDTH AND D) TOP WIDTH.	254
FIGURE 5.10 – DESIRABILITY OBTAINED TO THE EFFECT OF SHIELDING GAS MIXTURE ON BEAD SHAPE CHARACTERISTICS A) RAPIDARC; B) CMT-P. A = CO ₂ ; B = HE AND C = AR.	255

LIST OF TABLES

TABLE 2.1 – CLASSIFICATION OF METAL TRANSFER PROPOSED BY I.I.W (LANCASTER 1984).	17
TABLE 2.2 – CLASSIFICATION OF CONTROLLED TRANSFER MODES (LUCAS ET AL. 2005).	18
TABLE 2.3 – CLASSIFICATION FOR EXTENDED OPERATING MODE TECHNIQUES (LUCAS ET AL. 2005).	18
TABLE 2.4 – PROCESSING ROUTE AND SPECIFICATIONS OF THE MATERIAL.....	41
TABLE 2.5 – CHEMICAL COMPOSITION FOR THE MILD STEEL WITHIN DIFFERENT THICKNESSES.....	41
TABLE 2.6 – CHEMICAL COMPOSITION OF 13% CHROMIUM SUPERMARTENSITIC STAINLESS STEEL.	42
TABLE 2.7 – TYPICAL MECHANICAL PROPERTIES FOR THE API X80 12Cr 6.5Ni 2.5Mo (LAURO AND MANDINA 2003)	42
TABLE 2.8 – CHEMICAL COMPOSITION OF THE FILLER WIRE SUPERDUPLEX STAINLESS STEEL ER2209	42
TABLE 2.9 – CMT AND CMT-P OPERATION MODE FOR DIFFERENT WELDING PROCESS AND CONSUMABLE CHARACTERISTICS SELECTED.	43
TABLE 2.10 – CMT AND CMT-P SETTING PARAMETERS VARIATION ACCORDING WITH THE OPERATION MODE SELECTED.	43
TABLE 2.11 – RAPIDARC, GMAW AND STT OPERATION MODE FOR DIFFERENT WELDING PROCESS AND CONSUMABLE CHARACTERISTICS SELECTED.....	44
TABLE 2.12 – RAPIDARC, GMAW-P AND STT SETTING PARAMETERS VARIATION ACCORDING WITH THE OPERATION MODE SELECTED.	44
TABLE 2.13 – FASTROOT OPERATION MODE FOR DIFFERENT WELDING PROCESS AND CONSUMABLE CHARACTERISTICS SELECTED....	45
TABLE 2.14 – FASTROOT SETTING PARAMETERS VARIATION ACCORDING WITH THE OPERATION MODE SELECTED.	45
TABLE 2.15 – SUMMARY OF THE WELDING SETTING PROCESS CONDITIONS ANALYSED FOR GMAW-P.	74
TABLE 2.16 – SUMMARY OF METAL TRANSFER AND ARC STABILITY RESULTS OBTAINED FOR GMAW-P.	75
TABLE 2.17 – SUMMARY OF THE WELDING SETTING PROCESS CONDITIONS ANALYSED FOR RAPIDARC.	78
TABLE 2.18 – SUMMARY OF METAL TRANSFER AND ARC STABILITY RESULTS OBTAINED FOR RAPIDARC.	80
TABLE 2.19 – SUMMARY OF THE WELDING SETTING PROCESS CONDITIONS ANALYSED FOR STT.....	83
TABLE 2.20 – SUMMARY OF METAL TRANSFER AND ARC STABILITY RESULTS OBTAINED FOR STT.....	84
TABLE 2.21 – SUMMARY OF THE WELDING SETTING PROCESS CONDITIONS ANALYSED FOR CMT.	88
TABLE 2.22 – SUMMARY OF METAL TRANSFER AND ARC STABILITY RESULTS OBTAINED FOR CMT.....	88
TABLE 2.23 – SUMMARY OF THE WELDING SETTING PROCESS CONDITIONS ANALYSED FOR CMT-P.....	92
TABLE 2.24 – SUMMARY OF METAL TRANSFER AND ARC STABILITY RESULTS OBTAINED FOR CMT-P.....	93
TABLE 2.25 – SUMMARY OF THE WELDING SETTING CONDITIONS ANALYSED FOR FASTROOT.....	97
TABLE 2.26 – SUMMARY OF METAL TRANSFER AND ARC STABILITY RESULTS OBTAINED FOR FASTROOT.	98
TABLE 2.27 – PROPOSAL FOR CLASSIFICATION OF CONTROLLED TRANSFER MODES.....	133
TABLE 2.28 – SUMMARY OF THE PROCESSES ANALYSED.	141
TABLE 3.1 – SUMMARY OF THE MAIN EXPERIMENTAL CONDITIONS APPLIED.	169
TABLE 3.2 – SUMMARY OF THE WELDING CONDITIONS APPLIED TO THE COMPARISON ON THE PROCESS EFFICIENCY TO CMT, RAPIDARC, STT AND FASTROOT WAVEFORMS.	179
TABLE 4.1 – SUMMARY OF WELDING ACCEPTANCE CRITERIA DEFINED IN BS EN 12732:2000, ISO 13847:2000(E) AND EN 14163:2001(E).....	194
TABLE 4.2 – RESULTS OF STATISTICAL ANALYSES OBTAINED FROM DOE SOFTWARE FOR THE DIFFERENT MODEL RESPONSES FOR GMAW-P.	208
TABLE 4.3 – RESULTS OF STATISTICAL ANALYSES OBTAINED FROM DOE SOFTWARE FOR THE DIFFERENT MODEL RESPONSES FOR RAPIDARC.	208
TABLE 4.4 – RESULTS OF STATISTICAL ANALYSES OBTAINED FROM DOE SOFTWARE FOR THE DIFFERENT MODEL RESPONSES FOR STT.	209
TABLE 4.5 – RESULTS OF STATISTICAL ANALYSES OBTAINED FROM DOE SOFTWARE FOR THE DIFFERENT MODEL RESPONSES FOR CMT.	209
TABLE 4.6 - RESULTS OF STATISTICAL ANALYSES OBTAINED FROM DOE SOFTWARE FOR THE DIFFERENT MODEL RESPONSES FOR CMT- P.	210

TABLE 4.7 - RESULTS OF STATISTICAL ANALYSES OBTAINED FROM DOE SOFTWARE FOR THE DIFFERENT MODEL RESPONSES FOR FASTROOT.	210
TABLE 4.8 – DESIRABILITY CRITERIA DEFINED FOR THE MODELS OPTIMIZATION.....	212
TABLE 4.9 – DESIRABILITY LIMITS SET FOR DIFFERENT WAVEFORMS.	212
TABLE 4.10 – SOLUTIONS OBTAINED FOR GMAW-P ACCORDING TO THE DESIRABILITY CRITERIA ESTABLISHED.	212
TABLE 4.11 – SOLUTIONS OBTAINED FOR RAPIDARC ACCORDING TO THE DESIRABILITY CRITERIA ESTABLISHED.	213
TABLE 4.12 – SOLUTIONS OBTAINED FOR STT ACCORDING TO THE DESIRABILITY CRITERIA ESTABLISHED.....	213
TABLE 4.13 – SOLUTIONS OBTAINED FOR CMT ACCORDING TO THE DESIRABILITY CRITERIA ESTABLISHED.....	213
TABLE 4.14 – SOLUTIONS OBTAINED FOR CMT-P ACCORDING TO THE DESIRABILITY CRITERIA ESTABLISHED.....	213
TABLE 4.15 – SOLUTIONS OBTAINED FOR FASTROOT ACCORDING TO THE DESIRABILITY CRITERIA ESTABLISHED.	213
TABLE 5.1 – GAS DENSITY AND IONISATION POTENTIAL FOR THE MOST COMMON GASES (MENZEL 2003).	232
TABLE 5.2 – OXIDATION CLASSIFICATION LEVELS ASSOCIATED WITH THE COLOUR OBSERVED.	238
TABLE 5.3 – SUMMARY OF WELDING CONDITIONS APPLIED TO THE RESEARCH DEVELOPED IN CHAPTER 5.	240
TABLE 5.4 – RANGE OF GAS COMPOSITION APPLIED TO THE RESEARCH DEVELOPED IN CHAPTER 5.	241
TABLE 5.5 – SHIELDING GAS MIXTURES SUGGESTED BY DOE SOFTWARE USING A MIXTURES DESIGN.	241
TABLE 5.6 – SHIELDING GAS COMPOSITION AS ACTUAL (OBTAINED) AND SET ON GAS ANALYSER AND RESPECTIVE FLOW LEVEL FOR EACH OF COMPONENT GASES APPLIED.	242
TABLE 5.7 – EXPECTED AND READ VALUES AT THE OUTLET OF THE GAS ANALYSER FOR DIFFERENT GAS MIXTURES, AND RESPECTIVE ERROR.....	243
TABLE 5.8 – EXPECTED AND READ VALUES AT THE WELDING TORCH FOR DIFFERENT GAS MIXTURES, AND RESPECTIVE ERROR.	244
TABLE 5.9 – VISUAL ILLUSTRATION OF A SECTION OF WELD ROOT SURFACE: A) WITHOUT PURGING SHIELDING PROTECTION; B) WITH PURGING SHIELDING PROTECTION USING PURE ARGON.	246
TABLE 5.10 – RESULTS OF STATISTICAL ANALYSES OBTAINED FROM DOE SOFTWARE FOR THE DIFFERENT MODEL RESPONSES OF MIXTURES DESIGN FOR RAPIDARC.....	249
TABLE 5.11 – RESULTS OF STATISTICAL ANALYSES OBTAINED FROM DOE SOFTWARE FOR THE DIFFERENT MODEL RESPONSES OF MIXTURES DESIGN FOR CMT-P.	249
TABLE 5.12 – DESIRABILITY CRITERIA DEFINED FOR THE MODEL OPTIMIZATION FOR RAPIDARC AND CMT-P.	250
TABLE 5.13 – SOLUTIONS OBTAINED FOR THE OPTIMIZATION OF THE DESIGNS ANALYSED FOR RAPIDARC AND CMT-P WAVEFORMS.	250

LIST OF NOMENCLATURE

ΔQ	Variation of Energy
ΔT	Variation of Temperature
Ar	Argon
CO ₂	Carbon Dioxide
C _p	Specific Heat Capacity
D.C.	Duty Cycle
f _o	Oscillation Frequency
f _p	Pulse Frequency
f _{sc}	Short-Circuiting Frequency
g	Thickness
H ₂	Hydrogen
He	Helium
I	Arc Current
I _{av}	Arc mean current
I _b	Background Current
I _{mean}	Arc mean current
I _p	Peak Current
I _{RMS}	Arc root mean square current
I _{sc}	Short-Circuiting Current
k	Thermal conductivity
k ₀	Bessel function
l	Arc length
L _v	Latent Heat of Vaporization
m	Mass
N ₂	Nitrogen
N _{p/sc}	Number of pulses per short-circuiting
O ₂	Oxygen
P _{arc}	Arc Power
P _{av}	Average Arc Power
P _{inst}	Instantaneous Arc Power
P _{RMS}	Root Mean Square Arc Power
Q _p	Heat transferred from the power source
r	radius

s	slope
T	Temperature
t_b	Background Time
t_{cycle}	Time Cycle
t_p	Peak Time
t_{sc}	Short-circuiting time
U	Arc Voltage
U_b	Background Voltage
U_{mean}	Arc mean voltage
U_p	Peal Voltage
U_{RMS}	Arc root mean square voltage
U_{sc}	Short-circuiting Frequency
U_{step}	Step Voltage
W	Burn-Off Ratio
x	distance
η	Process Efficiency
λ	Thermal diffusivity

LIST OF ABBREVIATIONS

3D	3 Dimensions
AC	Alternating Current
AE	Arc Energy
AL	Arc Length
ALC	Arc Length Correction
ANOVA	Analysis of Variance
AWS	American Welding Society
BC	Base Current
BP	British Petrol
CMT	Cold Metal Transfer
CMT-P	Pulsed Cold Metal Transfer
CRA	Corrosion Resistant Alloys
CTWD	Contact tip to the Workpiece Distance
DA	Dilution Area
DC	Dynamic Control
DC	Direct Current
DCEN	Direct Current Electrode Negative
DCEP	Direct Current Electrode Positive
DOE	Design of Experiments
DP	Depth of Penetration
DR	Dilution Ratio
FP	Forming Pulse
GMAW	Gas Metal Arc Welding
GMAW-P	Pulsed Gas Metal Arc Welding
GMAW-S	Short-Circuiting Gas Metal Arc Welding
GTAW	Gas Tungsten Arc Welding
HH	High Height Bead
HI	Heat Input
HL	Low Height Bead
HR	Height Ratio
HS	Hot Start
IIW	International Institute of Welding
MAG	Metal Active Gas
MIG	Metal Inert Gas

NGW	Narrow Groove Welding
ODPP	One Drop Per Pulse
PC	Pulse Control
RMS	Root Mean Square
RR	Reinforcement Ratio
RT	Room Temperature
RW	Root Width
SAW	Submerged Arc Welding
SC	Short-Circuiting
STT	Surface Tension Transfer
TIG	Tungsten Inert Gas
TS	Travel Speed (or welding speed)
TW	Top Width
TWI	The Welding Institute
U	Undercutting
WERC	Welding Engineering Research Centre (at Cranfield University)
WFS	Wire Feed Speed
WT	Welding Temperature

1. INTRODUCTION

Scope

This chapter will include the project background giving an overview about the main industrial application of the research developed and an overview of the main fields associated with the project. The motivation for the research undertaken, the aims and objectives of the project and the structure of thesis will also be presented.

1.1. BACKGROUND	2
1.2. OVERVIEW OF CRA PIPELINE WELDING	4
1.3. MOTIVATION FOR THE RESEARCH PROJECT	10
1.4. AIMS AND OBJECTIVES	12
1.5. STRUCTURE OF THE THESIS.....	13

1.1. BACKGROUND

Worldwide oil and gas consumption has been increasing during the last decade, and the exploration and access to oil and gas will continue to increase at least during the next twenty/ thirty years. New challenges in oil and gas exploration generate new engineering solutions as a result of improvements in technology, research and innovation. This industry depends fundamentally on metal construction and manufacturing engineering, and materials and welding comprise essential areas for research.

During the last ten years there have been significant developments in pipeline construction, and important achievements in mechanization and welding engineering have contributed to increased productivity and costs saving.

Technological innovation has always been considered a significant target for ambitious projects in the pipeline sector. In the offshore industry, leading companies face new demands where technological innovation and development have been necessary for more difficult applied environments, such as pipe applications in deep water and arctic conditions, combined with the need to increase productivity and structural integrity.

The increasing use of combined cycle power generation plants leads in part to the necessity of building new gas pipelines. For instance, in the United Kingdom about 40% of all electrical power produced comes from natural gas, and over 18 million homes use natural gas for heating (DragonLNG 2008).

Productivity issues in construction of pipelines have led to new research projects in welding engineering. In fact, construction of pipelines over long distances together with technological advances in welding require development of new welding techniques, and an understanding of how these new technologies work and can be applied in the pipeline industry.

In severe weather conditions the pipeline industry has had large developments, such as the projects running in Siberia and North Sea, where high strength pipeline steels, with high toughness and good weldability have been used. New grades of materials with higher strength have been developed from X65 to X120. Significant development has taken place for highly corrosive environments, and duplex stainless steel pipes with high strength, corrosive resistance and good weldability have been used. The supermartensitic stainless steel, often referred to as 13% Chrome, is a low carbon material with a good corrosion resistance, and commonly applied to intermediate corrosive environments.

In addition, weld integrity and quality are important criteria that influence the cost of pipelines and their implementation. In the last ten years innovative processes of welding have been developed with potential application to root pass welding of corrosion resistant alloys (CRA). Examples of this are the Surface tension Transfer (STT) and RapidArc from

Lincoln, Cold Metal Transfer (CMT) and pulsed CMT (CMT-P) from Fronius, and FastROOT MIG from Kemppi.

1.2. OVERVIEW OF CRA PIPELINE WELDING

1.2.1. Pipelines Industry

The pipeline industry has been expanding during the last three decades, and recent projections suggest continuing expansion for at least the next twenty years as shown in Figure 1.1, (Cornot-Ganolphé, et al. 2003) (International Energy Agency 2005) (Gower and Howard 2003). These studies reported that the oil and gas industrial sector is the main contributor for the expansion of this market, since gas has now overtaken the coal as a primary combustible for the new combined cycle power stations. Furthermore, the expectation of an increasing population in the developed and under development countries is likely to result in an expansion in energy consumption, for domestic and industrial uses, with continued demands on the pipeline market.

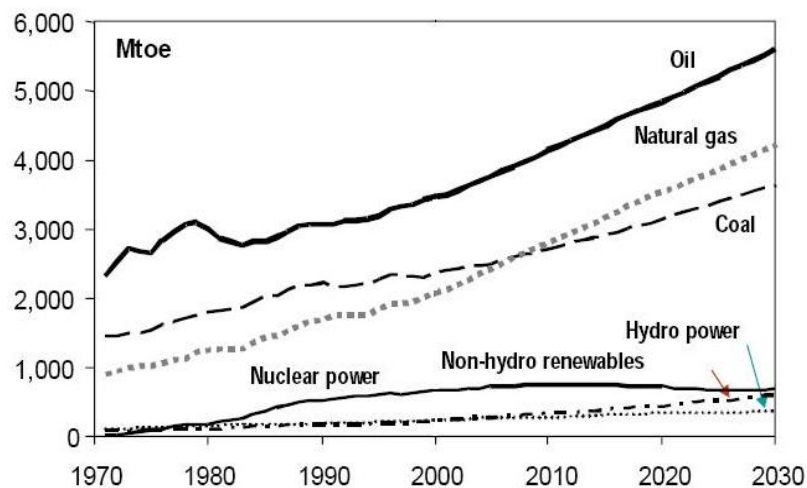


Figure 1.1 – World Energy Demand (Source: IEA) (Cornot-Ganolphé, et al. 2003).

The pipelines sector, both onshore and offshore, has existed for many decades. However it is the technological advances during the last thirty/ forty years that have most contributed to the current levels of expansion. The development of welding technology has made possible increased mechanisation to achieve high productivity for new pipeline installation.

Long onshore pipelines have been constructed with new advances in welding technologies, achieving high productivity at low costs, in projects carried out under difficult conditions, and in remote locations. The selection of high strength and toughness materials makes possible a reduction in wall thickness of pipelines. Welding methods have been developed for X100 steels (Yapp and Blackman 2003) (Liratzis 2007) (Hudson 2004). Work on even stronger steels such as X120 and composite reinforced pipe is ongoing (International Energy Agency 2005).

For offshore pipeline construction, exploration for oil and gas has moved to deeper water, with new requirements for technological advances, either in materials selection for strength and corrosion features, or technological aspects related to welding productivity, drilling, alignment, bevel preparation and machining operations (Figure 1.2) (International Energy Agency 2005).

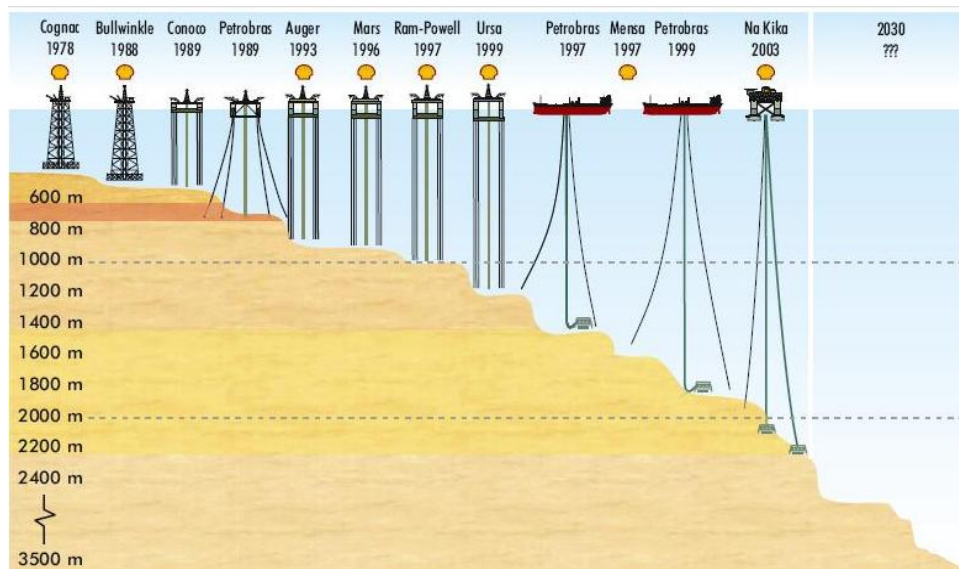


Figure 1.2 – Deep Water Offshore Technology (courtesy of Shell) (International Energy Agency 2005).

According to Perdure (2003), during the last decade offshore platforms that used to cost between 0.80 and 20 million Euros now cost between 400 million and 1.6 billion Euros. Bregagnollo (2005) reports that offshore exploration has led to challenges with increasing deep water pipeline construction and continued demands to increase productivity. The advancements in mechanized arc welding, pipe alignment and bevel preparation have met some of these challenges.

1.2.2. Materials Development

Materials selection for pipeline construction strongly depends on the application. Strength, toughness, corrosion and fatigue resistance must all be considered.

Materials in oil and gas onshore applications have requirements for strength and toughness, and considerable evolution has taken place during the last thirty years, moving from X70 to X100 steels. The increase in strength has been associated with the addition of different alloying elements, such as carbon, titanium, vanadium and molybdenum, and thermo-mechanical controlled processing (TMCP) (Liratzis 2007).

However, in the offshore construction of pipelines, high strength must be combined with acceptable corrosion properties. In offshore applications the materials used are corrosion resistance alloys (CRA), including austenitic stainless steels, duplex stainless steels and supermartensitic stainless steels.

Cumino et al. (2002) reported increasing corrosive environments in oil and gas wells associated with the partial pressure of carbon dioxide (CO₂) and high concentration of chlorides and hydrogen sulphide (H₂S), requiring use of CRA materials. Furthermore, the study concluded that the application of 13%Cr supermartensitic stainless steel is a good solution for corrosive environments, with high mechanical resistance and satisfactory weldability using GTAW, and with lower cost compared to duplex stainless steel materials.

Supermartensitic stainless steels used in oil and gas pipelines are commonly API 5L X80 12Cr 6.5Ni 1.5Mo and API 5L X80 12Cr 6.Ni 2.5Mo, with very low carbon and nitrogen contents. Lauro and Mandina (2003) pointed out that these materials have good weldability, and preheating is not required. Nevertheless, these materials are normally subjected to a post-weld heat treatment (PWHT) which can be applied at 650°C for 3 to 5 minutes. The application of PWHT greatly depends on the filler wire used during welding with a requirement to achieve a hardness level lower than 350 HV10. In addition, the toughness dramatically depends on oxygen content in the weld metal, which should be lower than 300ppm.

Yukio et al. (2006) added that the low carbon content in these materials is fundamental to ensure corrosion resistance against carbon dioxide, while additions of molybdenum are important to resist sulphide corrosion cracking.

Kvaale and Olsen (1999) considered that superduplex stainless steel filler wire consumables are the best option to weld supermartensitic stainless steels, due to the similar strength of these materials. This information is in agreement with the results obtained in the research study carried out by Miranda (1996).

However, other low cost solutions have also been considered in the last years. Yero (2006) has investigated the application of plastic lined materials to pipeline applications. Although it is not a generalized solution, this system provides important cost savings.

1.2.3. Welding Processes Innovation

The evolution of Gas Metal Arc Welding (GMAW) technologies has become more significant for automation and control of welding (Liratzis 2007) (Hudson 2004).

For the offshore pipelines sector, the welding of the root pass in narrow groove pipelines is particular significant, both in terms of quality requirements and productivity. Although the root pass is the slowest, it controls the rate at which the pipe can be laid. Hence the travel speed of the root pass is a critical factor in determining the overall productivity rate of pipe installation using mechanized welding. It is also the most difficult pass to make due to the requirement to ensure complete root fusion and good internal root profile (Mohamed 2005).

New welding approaches have been introduced during the last ten years, using new waveform control systems; the power supplies can generate more accuracy and precision

with substantial improvement in the control of the arc. In fact, the new generation of power supplies provide a more precise control of metal transfer with major benefits to arc stability.

Lincoln Electric (2006) developed a new welding technique called Surface Tension Transfer (STT), which consists in an advanced controlled short circuiting process, using a high frequency inverter power source. This process was firstly patented in 1988 and commercialized in 1994 (DeRuntz 2003).

After the development of this process pipeline contractors rapidly started to use this technology in root pass welding. The application of STT welding in open root of pipes used in the Alberta Oil Sands Projects made possible an increasing of travel speed with fewer defects when compared with traditional welding methods (Stava and Nicholson 2001).

A technical report published by Lincoln Electric (2006) claimed that STT eliminates the susceptibility to lack of fusion defects with a reduction in heat input, and generates less spatter and fumes, when compared to traditional short circuiting MIG/MAG processes. As described in the Lincoln Electric report, STT background current varies from 50 to 100A, which maintains the arc and heats the parent material. A reduction of current occurs during short-circuiting, followed by a pinch current, which promotes the detachment of the molten metal from the electrode to the weld pool. Then, a reduction in the current of about 50A is applied when the bridge between electrode and weld pool is broken, with further rise of the current to the peak level. Finally, an exponential tail-out is created (DeRuntz 2003) (Lincoln Electric 2006).

One of the most important issues in welding is how to achieve high quality weld beads when high productivities are required. In general, at very high speeds there is a point where lack of wettability on the weld bead occurs, with a consequent very short arc, instability, and wire stubbing (Fulmer 2004).

Lincoln Electric developed a RapidArc MIG/MAG process, which is intended for operation at low voltages, providing an increase of the range of application of pulsed GMAW (Lincoln Electric 2004) (Lincoln Electric 2005). Lincoln Electric (2004) (2005) claims that conventional pulse welding uses 23-26 V, while rapid arc welding can work at 16-19V, allowing the use of high welding speeds (Fulmer 2004). The increase of welding speed is associated with a reduction in the cycle time, allowing lower spatter emissions and heat input when compared with conventional MIG/MAG welding (Lincoln Electric 2005). Independent scientific investigations of this process have not been found in the literature.

A new system has been developed in Cranfield University to improve welding productivity, with up to the double the deposition rate. Michie (1998) described the first application of tandem GMAW-P to orbital narrow gap pipe welding using only one weld pool. Hudson (2004) and Liratzis (2007) have investigated the application of single and dual Tandem GMAW-P systems to high productivity welding of X100 pipe steels for onshore applications.

The dual torch approach was tested in mild steel pipelines (Kostrivas 1995) and further developed in what is now considered the dual tandem system CAPS (Cranfield Automated Pipeline System), which provides productivity increases of up to 400% compared with conventional single GMAW welding (Blackman 2001) (Blackman and Dorling 2002).

In 2005, Fronius (2005) introduced a revolutionary new arc welding process called Cold Metal Transfer (CMT). CMT is controlled mode of MIG/MAG welding process, where the droplet transfer is based on a mechanical oscillation of the wire (Himmelbauer 2005). Benefits of this new process include the possibility of simultaneous dip transfer and pulse arc welding, with heat input lower than conventional MIG/MAG welding (Fronius 2005). The special motion system for controlling the wire speed is incorporated into the waveform control and provides control of the molten metal detachment and arc length. As described by Fronius (2005), when the arc plasma is developed the filler wire moves to the weld pool until the wire touches the weld pool and short-circuiting takes place; then the current becomes lower and the electrode is retracted enhancing the droplet detachment. Although an important application of this new process is the joining of aluminium alloys with steel, a new range of applications has become possible with this new approach (Pickin and Young 2006) (Bruckner 2005).

More recently, Kemppi has developed a FastROOT welding technique which consists of a modified short arc process able to weld root pass and thin materials without spatter (Uusitalo 2007). Uusitalo (2007) pointed out that the application of this process in welding of stainless steel allowing positional welding with required penetration beads at higher welding speeds and productivity than TIG welding. The power source, in the FastROOT welding process, makes possible the digital control of arc current and voltage. In addition, the power source is able to monitor the short circuit and control the timing of droplet transfer. The accurate control of the waveform in respect to arc current and time is able to satisfy the spatter free condition, as is claimed by Uusitalo (2007). Uusitalo (2007) reported the wide application of this process in the Norwegian offshore industry where synergic curves for different shielding gas compositions have been developed for ferritic and duplex stainless steel. The results presented by Uusitalo (2007) indicated the importance of using a root gap (between 3 and 5 mm) and torch oscillation during narrow groove root pass welding of pipes.

1.2.4. Summary

Offshore pipeline construction faces new challenges regarding the application of corrosion resistance alloys (CRA), where high quality and reliability requirements are sometimes difficult to accomplish. Narrow groove root pass welding of pipelines is primarily significant in respect to the overall productivity and where corrosion and fatigue are highly important.

The recent advances in welding technologies provide opportunities to develop new welding procedures where integrity and productivity are significant issues. For applications using

these technologies, low heat input, spatter-free and high speed welding are the main claims made by the suppliers.

For these reasons, the research developed in this thesis was focused on the study of some of these new GMAW processes: RapidArc, CMT, CMT-P and FastROOT, including STT, and compared with the conventional GMAW-P. Other processes, such as Lincoln Power Mode, Tandem MIG welding, GTAW and hybrid laser could also be further considered. These processes were considered to have greatest potential for pipe root welding. It was regarded as essential to scientifically evaluate the potential of these new techniques, to understand how they work, and how they can be used to serve industrial needs, in particular regarding narrow groove root pass pipe welding. Although STT is already widely accepted in industry no deep scientific information has been found for this process.

Preliminary research work developed using Tandem MIG welding and Lincoln Power Mode showed very complex stability under the material and conditions studied and therefore were not consider in the research developed on this thesis.

1.3. MOTIVATION FOR THE RESEARCH PROJECT

A major challenge in high strength pipeline construction is production of high quality and high integrity welds at high welding speeds. This is fundamentally relevant in CRA materials where GTAW tends to be the most used process. GTAW is favourable in producing excellent welding quality, ideal for high corrosion resistance, but welding speed is typically slow. Further to this, the application of STT and GMAW-P has been considered, but productivity is still low. Moreover, the root pass of welding is the most important since it is the most critical in terms of corrosion and fatigue resistance.

In addition, the use of manual or mechanised GTAW in the root pass requires afterwards large amounts of filler metal to complete the groove, as a wide bevel is often used to allow TIG torch access the weld root. In the past ten years new technologies in GMAW have been developed. These new technologies claim the possibility to achieve high productivity and low heat inputs, combined with low spatter and high arc stability. However, no relevant scientific information has been published to describe how these new processes operate, and also to independently verify the potential benefits in applications such as pipe root welding.

The application of the innovative technologies described above might provide a reliable high productivity technique that could increase the welding speed of the root pass in construction of pipelines, particularly beneficial in deepwater pipes for J-lay applications, where welding is performed on a single work station.

The research project work scope was developed with the following main points, as illustrated in the Figure 1.3:

- Characterization of process current and voltage waveforms and understanding their impact in terms of arc energy, arc stability and weld bead quality and shape;
- Evaluation of actual heat input from process efficiency determination, using liquid nitrogen calorimetric tests, and consequently determining the heat input generated using different GMAW waveforms and arc parameters;
- Application of the knowledge of process behaviour to the root welding of CRA pipes, with understanding of how the different waveforms perform in terms of heat input, bead shape and quality, and productivity;
- Determination of how shielding gas composition affects weld shape, quality and productivity in root welding of CRA pipes.

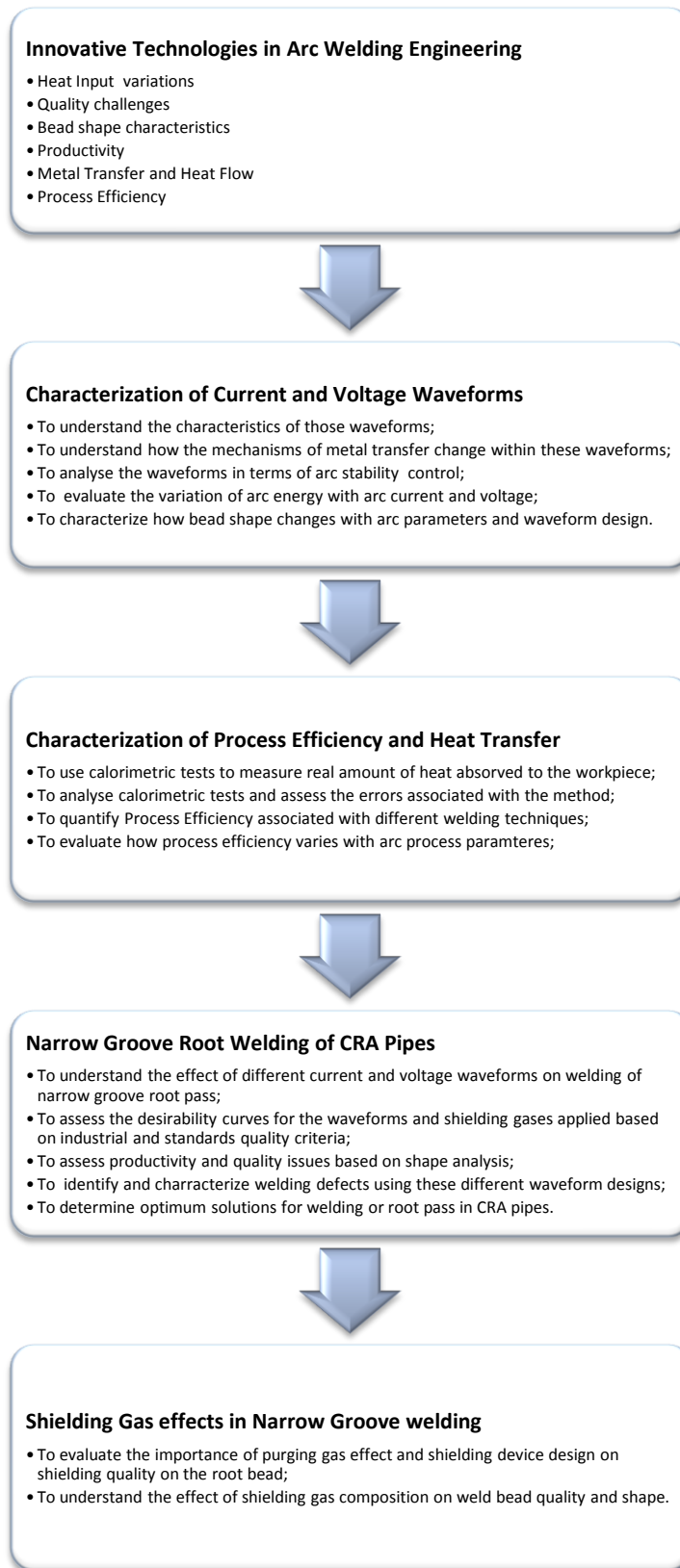


Figure 1.3 – Diagram of the structure defined for the research developed in this thesis.

1.4. AIMS AND OBJECTIVES

The main aim of this project is to understand how the arc current and voltage waveforms in GMA welding affect arc energy, bead shape and welding quality, and apply this knowledge to CRA root welds. All waveforms applied to this study were developed by different companies and have different characteristics which strongly affect their performance and their application ranges. From the aims defined, different main objectives are applied to the research developed in this thesis, as follows:

1. To characterize voltage and current waveforms for a range of process variants and relate these to metal transfer;
2. To measure process efficiency for these processes to differentiate between arc energy (energy supplied by the power source) and heat input (energy absorbed by the workpiece);
3. From (1) and (2) to develop a full understanding of how current and voltage waveform affect heat input;
4. To evaluate the effect of shielding gas composition and root purging gas protection on weld quality and shape;
5. To apply the fundamental knowledge obtained from (1) to (4) to establish how high productivity welds can be obtained with high quality for CRA root runs.

1.5. STUCTURE OF THE THESIS

This Thesis contains 7 chapters and appendices.

Chapter 1 presents an overview of the project, including an overview of the background associated with the industrial application of the project, a literature review associated with the main scientific fields of the research, the main aims and objectives of the research, and the structure and organization of the thesis.

Chapters 2, 3, 4 and 5 are the main chapters of this thesis, and are organized into different sections, each of which includes a specific literature review on the topic under consideration, the materials and methods applied, the results, and their analysis and discussion.

In Chapter 2, the operation of the different welding processes will be analysed. The mechanisms associated with the different waveform shapes for the processes considered will be evaluated in terms of process parameters and arc stability, and the bead shape characteristics obtained.

Chapter 3 will report the research developed on the process efficiency and heat transfer in arc welding. Process efficiency measurements will be presented based on liquid nitrogen calorimetric tests. Welding techniques and process parameters will be investigated in order to understand their effects on arc changes.

Chapter 4 will focus on narrow groove pipe welding comparing the processes investigated in Chapter 2. Fundamental research will be reported in this chapter regarding the bead profile characteristics and the control of defects associated with welding of root pass. Using established criteria based on international standards and industrial procedures, the range of parameters applied to welding of the root pass in narrow groove welding will be evaluated.

The research developed in the Chapter 5 will consist in the analysis of shielding gas effects on welding performance, in respect to the root quality and top surface characteristics. Back shielding devices developed in the project will be evaluated in relation to the root quality and appearance. The effect of shielding gas composition on narrow groove pipe welding will also be evaluated for CMT-P and RapidArc welding, including analysis of melting efficiency and welding quality.

Finally, Chapter 6 will present the main conclusions of the work developed and the recommendations for further work and Chapter 7 provides the references used in the thesis.

2. PROCESS CHARACTERISTICS AND METAL TRANSFER CHARACTERIZATION

SCOPE

Significant developments in welding technology commercialized in new processes such as RapidArc, STT, CMT, CMT-P and FastROOT justify intensive research to explore their capabilities and operational features. In addition, it is not known in detail how these recently developed waveforms work and how they can best be controlled to achieve the desired welding characteristics. It is fundamental to determine how arc parameters should be set to achieve desirable weld characteristics and arc stability.

This chapter presents an introduction related to the specialized literature, focused on process characteristics and metal transfer mechanisms, followed by the research objectives and materials and methods applied. Afterwards, the results and discussion are presented and followed by the conclusions.

2.1. LITERATURE REVIEW	16
2.2. RESEARCH OBJECTIVES.....	40
2.3. MATERIALS AND METHODS.....	41
2.4. RESULTS.....	52
2.5. DISCUSSION OF RESULTS	128
2.6. CONCLUSIONS	142

2.1. LITERATURE REVIEW

2.1.1. Introduction

Although GMAW was introduced more than sixty years ago, recent developments in power sources and waveform control systems have enabled innovations in arc welding processes, as was described earlier in Chapter 1.

In GMAW the electric arc between the electrode and workpiece creates molten drops which are transferred to the weld pool during welding. The process characteristics are strongly affected by the resulting mechanism of metal transfer. It has been identified that short circuit and free flight transfer are the main mechanisms, with main subdivisions: globular, spray and streaming transfer, under free flight transfer

The control of metal transfer depends on the different process parameters. Lesnewich (1958) (1958 b) first considered the importance of arc current, filler wire characteristics, polarity and arc length (sometimes defined in terms of electrode extension or stick-out). Later, the shielding gas was also found to have a dramatic effect on the mechanism of metal transfer (Smith 1966).

Furthermore, the interpretation of the forces acting during the droplet detachment can explain the mechanism of metal transfer.

During the following sub-sections a review will be presented about the principal modes of metal transfer and the physical phenomena and their characteristics, followed by the characterization of GMAW and process variables affecting metal transfer mechanisms and arc stability. Then, the new technologies will be reviewed regarding the technical-scientific knowledge published in the literature.

2.1.2. Modes of Metal Transfer and their Classification

The first classification of the modes of metal transfer for arc welding processes was proposed in 1976 in Commission XII of International Institute of Welding (IIW) (Anon 1976), as presented in the Table 2.1, which was further published by Lancaster (Lancaster 1984). He classified two main modes of welding metal transfer, the free flight and short circuiting transfer. A slag mode of transfer was also defined for other arc welding processes, such as submerged arc welding (SAW).

Short circuiting transfer was characterized by low current and low voltage and the transfer mechanism was associated with a bridge formed between the electrode (filler wire) and the weld pool.

Free flight transfer has been classified by the variation in droplet size; the droplet detaches from the filler wire and transfers across the arc plasma to the weld pool. This mechanism can occur within different time formations corresponding to different drop sizes. It is known

that increasing current density has an effect on the drops transferred, which become smaller as current increases. Lancaster (Lancaster 1984) explained that at moderate currents spheroidal drops are formed and these are aligned with the wire during detachment (globular transfer). At relatively high currents a conical electrode tip forms, and uniform drops transfer with relatively small size (projected spray transfer). When the current is increased, the drops formed become smaller, taking the form of a jet flow (streaming transfer). At very high currents a rotating spiral droplet mechanism (rotating transfer) was identified.

Other unstable transfer mechanisms were also defined associated with repulsion of large drops at lower currents (repelled transfer) and explosive small drops at very high current (explosive transfer).

Lancaster (1984) reported that the conductivity of the material affects the mechanism of transfer; materials such as copper and aluminium alloys with high conductivity have a much higher rate of drop detachment than steel at 200A. He reported 10 drops per second for steel, against 20 drops per second for copper and 170 drops per second for aluminium.

Table 2.1 – Classification of Metal Transfer proposed by I.I.W (Lancaster 1984).

Metal Transfer Mode		Application
Free Flight Transfer	Globular	1. Droplet 2. Repelled Low current GMAW CO ₂ Shielded GMAW
	Spray	1. Projected Intermediate Current GMAW
		2. Streaming Medium current GMAW
		3. Rotating High current GMAW
Explosive	SMA (coated electrode)	
Bridging Transfer	Short-circuiting	Short Arc GMAW
	Bridging without interruption	Filler wire addition
Slag-Protected Transfer	Flux wall guided	SAW
	Other modes	SMA, cored filler wire, electroslag

The advances in power sources control systems during the last two decades made possible more precise control of the arc stability. The power sources were designed to control the waveform ensuring a stable drop transfer.

Ma (1982) investigated the phenomena of metal transfer in GMAW and recognized the existence of a special mechanism of drop spray transfer in the region of transition current from globular to spray transfer.

Norrish (2003) reviewed the definition of the modes of transfer in GMAW considering three different categories, which are associated with the nature of the transfer mechanism: (1) natural metal transfer; (2) controlled transfer techniques; and (3) extended operating mode techniques. He included drop spray transfer in the natural metal transfer classification which was presented in the Table 2.1.

Tables 2.2 and 2.3 present the classification for controlled transfer and extended operating mode techniques, respectively, according with the classification proposed by Norrish (2003) and reviewed by Lucas et al. (2005).

Table 2.2 – Classification of Controlled Transfer Modes (Lucas et al. 2005).

Metal Transfer Mode	Application	Commercial Name
Controlled Spray	Pulsed transfer	GMAW using variable frequency pulse and drop spray transfer
Controlled Short Circuiting	Current controlled dip transfer	GMAW using current controlled power source
	Controlled wire feed short circuit mode	GMAW with wire feed oscillation

Table 2.3 – Classification for Extended Operating Mode Techniques (Lucas et al. 2005).

Metal Transfer Mode	Application	Commercial Name
Short Circuiting GMAW	Extended stick out GMAW	High deposition short circuit transfer GMAW
	Low frequency pulsed	Pulsed mean current for gap filling
Pulsed Transfer GMAW	Multi-wire	Multi-wire GMAW
	Low frequency pulsed	Modulated pulsed transfer welding of aluminium
	Variable polarity	Welding of thin sections and single sided root runs
Spray Transfer GMAW	Rotating spray	High current extended stick out
	Electrode negative	Fluxed cored wire or special gas mixture
Spray Transfer SAW	Electrode negative	
	Extended stick out	
	AC/ variable polarity	

However, during the last years other welding technologies based on new power source control systems, such as CMT welding, have been developed.

Recently, Iordachescu and Quintino (2007) reviewed the natural transfer classification, with a sketch of the mechanisms and a new grade of classification (A – short-circuiting, B – globular, C – spray). They included CMT welding in the controlled processes classification and defined two types of controlling processes, either simple controlled processes or real-time controlled processes.

2.1.3. Effect of Processes Characteristics on Metal Transfer Phenomena

The characterization of the effect of welding process parameters on metal transfer requires an experimental approach which can simultaneously identify the nature of transfer and the variation of arc parameters. Heald et al. (1994) proposed the study of metal transfer based on mapping arc current versus voltage for each instant of time, also known as cross plots. They found that the standard deviation of the current values can characterize the mechanism of metal transfer; with high standard deviations corresponding to short circuiting, moderate standard deviations for globular transfer and the lowest standard deviation values for spray transfer. They added that the sub-classifications can also be easily identified in those maps. The effect of CTWD on the transition between globular and spray transfer was also reported; they concluded that for a fixed voltage the transition current increases when CTWD increases.

Huang and Yapp (2000) also analysed the phenomenon of metal transfer in GMAW using cross plots. These maps revealed significant aspects during metal transfer phenomena, in particular in the transition between short-circuiting transfer and free flight transfer, where arc length seems to have an important effect; at low arc lengths the frequency of short circuits is higher. This research also found that the transition between mechanisms is gradual and involves mixed modes.

Most studies in this area have been carried out on using bead on plate welds and using mild steel materials. Scotti (2000) developed a map analysing system based on the correlation between arc length and arc current. This research was undertaken for stainless steel in a real groove instead of bead on plates, using two different shielding gases, Ar-1% O₂ and Ar-2% O₂. Within these maps it was possible compare for different shielding gas the variation of metal transfer mechanism associated with different arc length and current. Scotti (2000) found that increasing oxygen content in the shielding gas decreased the transition current between globular and spray transfer, and also affected droplet size and transfer rate.

2.1.4. Forces acting during welding Metal Transfer

Metal transfer in GMAW has been explained on the basis of force balance (Greene 1960) (Amson 1962). Surface tension is considered as a retaining force operating against the detaching forces, which include pinch electromagnetic field, gas plasma drag force, vapour jet forces, and gravitational forces. The relative contribution of these different forces is responsible for different actions in the mechanism of metal transfer, depending of the processes parameters applied (Lancaster 1984).

Arc pressure has been evaluated for long time in arc welding processes, especially in GTAW. Friedman (1978) proposed an analytical model to predict depression of weld pools considering the action of arc pressure and gravitational forces. Lin and Eagar (1983) first analysed the influence of welding current on the geometry of the weld pool by the action of

arc pressure but later (1985) they concluded that arc pressure only has a major impact when the current level is higher than 500 A. At intermediate currents convection flow can explain the depression of weld pools and could be responsible for the characteristic finger penetration. They found out that both surface tension and electromagnetic forces are responsible for the convective liquid flow on weld pool (1985).

The shielding gas has a strong effect on the arc plasma formed during welding. Lucas and Amin (1975) explained that the explosive metal transfer in GMAW is associated with the presence of oxygen in the filler wire. It has been reported that repelled metal transfer occurs in GMAW when helium is used as a shielding gas (Hazlett and Gordon 1957) (Jonsson, Eagar and Szekely 1995). This phenomenon is associated with repelling forces acting on the tip of the molten drop. Johnson et al. (1992) concluded that a strong electromagnetic force present in the cathode causes the repelling of the molten droplet which will be deposited randomly in the weld pool. Experimental results demonstrated that the effect of the cathode force becomes less significant with increasing arc current. This arc behaviour is due to the thermo-physical properties of the gases, in particular the higher ionization potential of the helium compared to the argon. Mondenesi and Nixon (1994) identified that the shielding gas composition can affect the bead shape geometry, electrical parameters and metal transfer. Costa et al. (2009) found out that instabilities generated in arc welding, such as repulsive behaviours of the arc and rapid short circuits, associated with the metal transfer, are due to the low oxidation potential of the gas and short arc lengths.

Jones et al. (1996) explained the effect of magnetic forces acting on a drop detachment when moderate and high currents are applied. These authors pointed out a temporal effect associated with the magnetic forces present during the period of drop detachment, which is responsible for the drop elongation until the complete detachment. The same authors (1997) investigated the Marangoni effect on weld pool flows and drop dynamics, and indicated that fluid flow has a major influence on weld quality.

It has been reported in the literature that drop size depends on the surface tension. The relevance of surface tension on the formation and detachment of liquid drops was studied by Subramaniam et al. (1998) for pulsed GMAW. They considered the effect of alloying elements on the temperature on the droplet and the composition of the arc plasma. They used an in situ technique during this investigation, and the results of surface tension measured in aluminium were in good agreement with the previous work (Lancaster 1984) (Kim and Eagar 1993 a) (1993 b). The authors also discussed the effect of small concentration of active elements such as sulphur on the surface tension. The influence of gases formed during welding, in particular oxides of nitrogen and vaporized elements associated with the arc plasma were also found to affect the surface tension.

2.1.5. Characterization of the Mechanisms of Metal Transfer

2.1.5.1. Dip Transfer Welding

The mechanism of short-circuiting transfer, also called dip transfer, in GMAW is determined by low arc current and voltage, and characterized by low heat input. The dominant forces controlling dip transfer short-circuiting welding are the surface tension and electromagnetic forces. A liquid metal drop is formed during the arc period, which touches the weld pool generating a liquid column bridge responsible for the short circuiting. The rupture of the liquid bridge re-establishes the arc and promotes a new waveform cycle. During the short circuiting period the arc is extinguished, which results in low heat input produced compared to other GMAW transfer mechanisms.

Instability in short-circuiting transfer is associated with different causes, such as:

- A failure in the arc re-establishment;
- A short time bridge formation with no metal transfer;
- Variations in wire feed speed.

Hermans and Ouden (1999) reported that short-circuiting frequency strongly depends on arc voltage and wire feed speed. In particular, increasing short-circuiting frequency is associated with the increase of wire feed speed and there is a critical value at which optimum stability is achieved.

Oscillations in weld pools have been identified as a significant phenomenon occurring in GTAW and short-circuiting GMAW. This has been extensively studied in GTAW and occurs during pulsed welding, due to the increase of arc pressure in the centre of the weld pool. Hermans and Ouden (1999) undertook a comprehensive study to understand the effect of weld pool oscillation on arc stability phenomena for GMAW. They suggested that the weld pool oscillation in short circuiting GMAW is due to the arc pressure generated immediately after the arc period, which is associated with a force input to the liquid metal transferred to the weld pool at the bridge rupture time. They found a proportional relationship between short circuiting frequency (f_{sc}) and weld pool oscillation frequency (f_o) for the higher arc stability conditions, corresponding to an optimum range of wire feed speed. They also concluded that:

- At low wire feed speeds the $f_{sc} < f_o$, the oscillating surface of the weld pool is not able to touch the growing liquid column at the end of the wire, and the stability is lower;
- At high wire feed speeds the $f_{sc} > f_o$ and the arc length becomes smaller and is associated with spatter projections, resulting in irregularities and unstable arcs.

Theories of Dip Transfer

Different numerical and analytical approaches have been dedicated to understanding and explaining the mechanism of dip transfer in short circuiting mode.

The effect of droplet size on the force balance in dip transfer welding was extensively studied by Bless (1974). This author suggested that a small droplet tends to create a stable meniscus between the electrode and the weld pool, and when this acquires a critical size, surface tension forces will support the transfer mechanism. Nonetheless, the breaking process was associated with a critical liquid column height, which must be larger than the filler wire diameter. Although his study reflects an important achievement in describing the critical meniscus, surface tension alone cannot explain the droplet transfer mechanism.

Allum (1985 a) (1985 b) developed an approach to characterize the viscous liquid column carrying surface charge, as a function of the current density and electromagnetic pinch field. This theory was the basis for later models of dip transfer welding. Ischenko (1993) developed a model to predict the velocity and acceleration of the liquid column associated with the surface tension energy, but effects of welding current were not considered.

Choi et al. (1998 a) developed a numerical model using the volume of fluid (VOF) method where electromagnetic forces were considered and current density was defined as a boundary condition. They pointed out that capillarity pressure acts in the first stages of the short circuiting transfer and electromagnetic forces play an important role during the rupture process. The rupture is favoured by high surface tension at high capillarity pressures. Also, arc current and initial drop volume have a major impact on pinch radius which is responsible for the rupture of the liquid column. Moreover, there is an optimum peak time associated with the peak current, where spatter can be reduced, which is associated with the reduction in electromagnetic forces.

More recently, some studies have been focused on the analysis of process characteristics based on the waveform analysis. Poloskov et al. (2002) used a controlled transfer power source to analyse the variation of the current at different times during the overall welding cycle on short circuiting transfer, proposing a new approach of process parameters limits in order to obtain high stability transfer.

Using power spectral density and time-frequency spectral techniques, Chu et al. (2004) analysed the process stability in short-circuiting GMAW. They found out that short circuiting frequency is a critical parameter which can be correlated with arc stability criteria to determine resulting weld quality. The time-frequency analyses performed were able to detect welding defects in real time. Oshima et al. (2004) proposed a development of a self-adjusting power source able to produce a stable short circuiting transfer using CO₂ GMAW.

Sagirov (2006) undertook a comprehensive study on short circuiting transfer regarding the reduction of heat input and spatter. He pointed out that inductance has a primary affect on control of waveforms and on the short circuiting transfer mechanism; the rupture of the liquid column depends of the intensity of electromagnetic forces, and the increase of short circuiting current through reduction of system inductance can improve the stability of the rupture. Luksa (2006) also explored causes for the unstable arc, which are related to the process parameters, specifically affecting shielding gas and arc length.

Recently, Feng et al. (2008) and Zhang et al. (2009) have studied the mechanism of metal transfer in Cold Metal Transfer (CMT) welding. These authors found that the critical stability condition of liquid bridge rupture is associated with the liquid drop attached to the filler wire, which has a size similar to its diameter. The stability of the short circuit is due to the mechanical motion system which retracts the filler wire at a low current level, assisting the rupture of the liquid bridge. They pointed out that in conventional short circuiting GMAW the explosion associated with the short circuit is due to the high current level present during this period.

2.1.5.2. Free Flight Transfer Welding

In GMAW the free flight transfer is associated with molten droplet detachment of the filler wire to the weld pool. The characteristics of the molten droplet, such as the arc current level and the detachment time and size, will determine a different mode of transfer, as presented earlier in the classification section.

During globular transfer the molten droplets formed are larger than the filler wire diameter and the transfer rate is low. This mechanism occurs at relatively low current levels.

Spray transfer mode occurs at moderate and high currents and the molten droplets formed are characterized by a diameter smaller than the filler wire and a higher transfer rates. Two main subdivisions can be observed in this transfer mode, associated with diameter similar to the filler wire size (projected) and much smaller drops in the form of streaming flow.

The metal transfer mechanism affects the bead shape quality and productivity, and the heat input is strongly dependent on the mode of transfer present.

Theories of Free Flight Transfer

The two principal theoretical models developed to characterize the free flight metal transfer mechanism in GMAW were the static force balance theory and the magnetic pinch instability theory.

The static force balance theory was firstly introduced by Greene (1960) who postulated that the drop detachment takes place when the static detaching forces are greater than the static retaining forces. The forces considered in this model were the surface tension, gravitational, electromagnetic and gas plasma drag force. In this approach while the surface

tension works as a retaining force, the other forces are responsible for detachment. Amson (1962) added the kinetic energy associated with the liquid metal and promoted by magnetic forces, which he called magneto-kinetic. This author quantified the different detaching forces acting on the droplet and concluded that the gas plasma drag force followed by magneto-kinetic force play a major role on the detaching mechanism for the whole range of currents considered (from 147A to 243A). The gravitational force appears to have minor impact. Waszink and Graat (1983) measured the liquid metal drop size considering the effect of electromagnetic, gravitational and gas plasma drag forces. The results obtained demonstrated that at very low currents the plasma drag force had the major effect on the detachment, while at currents where globular transfer was identified the electromagnetic force was dominant. These investigators also pointed out that this model did not apply to the spray transfer mechanism. Furthermore, this theory failed when considering a balance in axial direction solely, which did not include the effect of radial pinch field in the droplet detachment; and the molten droplets formed were assumed to be only spherical drops (Choi, Too and Kim 1998 b).

The pinch instability theory was initially proposed by Lancaster and further developed by Allum (1985 a) (1985 b) based on the model of Rayleigh for liquid column instability. This model was developed based in the principle of conservation of energy and considered that the spherical droplets have lower free energy than the liquid column. The theory assumes that the pinch force generated on the liquid column is determined by electromagnetic forces, which cause a disturbance responsible for breaking down the liquid column into drops. Thus, the model developed suggests that increasing arc current is associated with a reduction of the wavelength of the disturbance of the liquid column, which results in a decreasing drop size. However, it has been suggested that this theory fails if a liquid cylinder with infinite length and constant diameter is assumed (Choi, Too and Kim 1998 b).

These two theories described the decrease of the drop size when the arc current increases, following the specific physical models. However, they are not able to describe the abrupt transition between globular and spray transfer modes, as earlier described by Lesnewich (1958 b).

Kim and Eagar (1988) and Kim (1989) attempted to compare the static force balance and the pinch instability theories in different ranges of arc currents. Although the static force balance can reasonably predict the drop size at low currents, when globular metal transfer is identified, they suggested that the effects of the droplet movements should be included to improve the model prediction. On the other hand, the pinch instability model is only able to predict the drop size at streaming transfer currents. Kim and Eagar (1993 a) observed that the transition from globular to spray transfer is a gradual phenomenon, in contrast to earlier suggestions of a sharp transition.

Clark et al. (1989) noticed the existence of periodic large droplets followed by a stream jet of smaller drops in the globular current region. This investigation was then confirmed by Johnson et al. (1992), who described the existence of mixed modes

Watkins et al. (1992) proposed a model to predict droplet size and transfer frequency in free flight transfer modes, based in a water droplet model. This was further developed by Reutzel et al. (1995) with a more accurate simulation approach for streaming transfer.

The molten drop size has been considered one of the most important characteristics of metal transfer mechanism. Nemchinsky (1994) investigated the shape and size of the droplet during the detachment period including the effects of surface tension and electromagnetic pinch field. However, this model was not able to predict the dynamic changes associated with the droplet mechanism.

Dynamics have been considered for long time to have a strong impact on the mechanism of droplet detachment. Essers and Walter (1981) concluded that depth of penetration depends of droplet impulse. Waszink and Graat (1983) considered that the momentum is affected by the acceleration due to the shielding gas flow.

Murray and Scotti (1999) evaluated the importance of droplet transfer on depth of penetration, quantifying the momentum associated with the droplet detachment. This made possible the development of accurate models accounting for the momentum force present during detachment period.

Haidar and Lowke (1996) developed a time-dependent two dimensional model to characterize the size and frequency of the droplet in GMAW, where the arc characteristics and relations established between arc plasma and filler wire were accounted for. They obtained a reasonable agreement with experiments for the prediction of the transition current between globular and spray transfer modes. The model developed by these authors pointed out that at low currents mainly gravitational and surface tension transfer forces govern the globular transfer mode, while at high currents magnetic forces control the mechanism of the droplet formation in spray transfer mode.

Other investigators (Choi, Too and Kim 1998 b) developed a simulation model to predict the droplet transfer using a volume of fluid (VOF) method. They concluded that the axial flow and the electromagnetic effects are the primary forces affecting the transfer mechanism. Increasing arc current has the major impact on the axial flow, and the electromagnetic forces are more relevant during the detachment mechanism. This is in agreement with the work of Haidar and Lowke (1996). Also, in the spray mode of transfer the current density on the surface of the droplet strongly affects the drop size. Furthermore the model made possible the simulation of droplet size with accuracy and the estimation of the transition current between globular and spray transfer modes.

Some research work has indicated that fumes created during GMAW are due to evaporation of the molten droplet at the tip of the filler wire, which is controlled by the surface temperature of the droplet. Mendez et al. (2000) investigated fume formation during welding and concluded that is mainly caused by evaporation depending on the heat transfer phenomenon, which are associated with the surface temperature and liquid drop size. They concluded that surface temperature increases with the drop size, and smaller drop sizes generate less vaporization, which generates less fume emission. This behaviour was observed when spray or pulse transfer modes were identified.

It has been pointed out (Kim and Eagar 1993 b) that the best quality characteristics of metal transfer are associated with one drop per pulse (ODPP) condition. A precise setting of peak current, background current, peak time, background time, contact tip to the workpiece distance (CTWD) and wire feed speed can achieve the ODPP condition. Nevertheless, the control of these parameters is complex and dependent on shielding gas composition and filler wire characteristics.

Kim (1989) identified a taper effect at the end of the electrode with argon as a shielding gas in GMAW. This mechanism associated with droplet detachment was not observed when either pure helium or carbon dioxide was used as a shielding gas. Furthermore this phenomenon was observed in steels, aluminium and titanium alloys. This taper reduces the interfacial area of contact between electrode and molten droplet, producing a reduction in melting rate, since the melting rate is controlled by the heat transferred in that interface. At high currents the melting rate is then higher when helium and carbon dioxide were used, due to absence of the taper. The author pointed out that in Pulsed GMAW the taper formation can reduce the range of ODPP transfer. The droplet size decreases associated with the presence of taper, which can increase pulse frequency; when the taper is not present the range of pulse frequency to achieve ODPP transfer will expand.

Advances in technology with the introduction of inverter power sources and digital control techniques made possible special waveform characteristics. Wu et al. (2005) studied the effect of the waveform on metal transfer in pulsed GMAW. In addition to the peak current (I_p), peak time (t_p), background current (I_b) and background time (t_b), these authors introduced six other adjusting parameters to established a most precise and accurate control of the waveform. They found out that the ratio of peak time to the drop detachment time and the range of drop detachment current have a major influence in the control of one drop per pulse (ODPP) stable metal transfer. With the control of these parameters, it was possible to achieve stable conditions at much lower heat input and within a wider range of average current.

Wu and Kovacevic (2002) studied the droplet transfer mechanism associated with an additional mechanical force, by the use of an oscillating wire feeder. The results of this study revealed that the increase of oscillation frequency produced a decrease in droplet size and an increase in the transfer rate. In particular the spray transfer mode can occur at lower

currents, which has strongly stability benefits. However, this process is complex due to the introduction of two more variables, oscillation frequency and width, and also reduces the depth of penetration.

Miranda et al. (2007) developed a luminescence sensor with an electronic interface which was able to characterize the metal transfer mechanism and generate the necessary changes in the process characteristics to achieve the stable condition of ODPP. Good results were obtained for low carbon steel, stainless steel and particularly for aluminium.

More recently, Arif et al. (2008) investigated globular transfer using a modified force balance model, with the introduction of momentum flux considered as a function of the arc current and drop geometry. This study demonstrated that for low current range, associated with large drop size, the momentum flux has no significant impact on the drop detachment. However, as current increases, within decreasing drop size, the momentum flux effect, also increases, and is comparable to the electromagnetic force effect. Although, this model considerably improves the prediction of drop size, and is an important step in the characterization of drop size for globular metal transfer, the results obtained do not correspond completely with the experimental measurements of the drop size. Nevertheless, Scotti and Rodrigues (2008) have developed a methodology to predict the bead shape geometry based on dynamic and kinematic effects during metal transfer.

2.1.6. Characterization of GMAW

In GMAW, the electric arc heats the workpiece and melts the filler wire, which is transferred in the form of droplets to the weld pool. Conventional GMAW is typically in direct current (DC) mode and characterized by a continuous wire feed at a constant voltage. The main parameters to control in GMAW are the wire feed speed, arc length, shielding gas composition, and the filler wire material and diameter. The arc current is proportional to wire feed speed, while the arc voltage is dependent on the arc length and shielding gas composition, and also varies with CTWD. The filler wire characteristics change the burn-off rate and the arc length, due to the variation of melting rate and transfer mode.

The difficulty in controlling arc stability in GMAW is related to the complex physics involved in this technology and the wide range of variables present. Allum (1983) described the presence of poor fusion characteristics and spatter, in particular with an explosive behaviour associated with short-circuiting transfer. The stability of this process depends of the parameter control, and is particularly associated with the variation of arc length. Amin (1983) reported that the arc length stability depends on the relationship between wire feed speed and burn-off ratio. Moreover, he concluded that the stability is strongly associated with metal transfer mechanism and spray free flight transfer is preferable, with drop size in the order of the filler wire diameter.

The general arc instability associated with GMAW process and the high current levels in spray transfer mode, where heat input were is too high for some applications, prompted the

development of pulsed GMAW. In GMAW-P, droplet transfer mode could be achieved at lower mean current levels, enabling the quality of this transfer mode, but at lower heat input levels and with high arc stability.

Advances in terms of waveform control were assisted by the developments in power source technology. Norrish (1987) reported that advances in power source design improved significantly in respect to feedback control, fast response rates, and ability to change waveform design. In the so-called third generation of power supplies the control systems are associated with closed-loop feedback mechanisms. These systems can continuously monitor the process using feedback sensors systems, making possible self regulating control (Collard 1988).

Pulsed GMAW consists in a controlled spray transfer, characterized by drop spray transfer mechanism, where the current is maintained for a controlled time at a peak value, which initiates the droplet detachment from the wire. After the droplet is transferred, the current is changed to a background value which minimizes the heat input but is enough to maintain the arc.

2.1.6.1. Synergic and Self Regulating Control

With the new generation of new power supplies, The Welding Institute (TWI) was able to develop a synergic control mode of GMAW (Norrish 1987) (Amin 1981) (Allum 1983). Synergic mode consists in control of mean current through the wire feed speed setting. This relationship has been described as a burn-off rate control and consists in the synchronization between the power source and wire feeder to ensure arc stability

The use of synergic control mode was rapidly extended to pulsed GMAW, since it can simplify the wide range of variables associated with this process. Subramaniam et al. (1999) concluded that the wire feed speed, peak and background current, pulse frequency and duty cycle are the most important parameters in pulsed GMAW. It has been established that the condition of stability in GMAW-P correspond to one drop per pulse (ODPP) transfer, which is associated with low spatter emissions and fewer defects (Kim and Eagar 1993 b) (Allum 1983).

Using synergic pulsed GMAW with digital control of wire feed speed, pulse parameters are synchronized by a microprocessor system. In this system, only peak time is kept constant, with a dynamic increase of peak current, and changes of background current and time, as illustrated in Figure 2.1. This control system can produce multiple droplets detachment per pulse at higher mean currents (Allum 1983) (Praveen, Yarlagadda and Kang 2005).

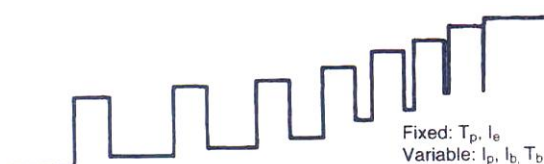


Figure 2.1 – Pulse waveform of synergic control.

Self-regulating control is another control mode, associated with voltage control of the mean current. Since the voltage changes accordingly with arc length, this operation mode responds by changing the arc length to keep voltage constant, which automatically varies the burn-off rate. In this system the pulse waveform is characterized by constant peak current and time, and background current, as can be observed in the Figure 2.2. Thus, only the background time can change (Praveen, Yarlagadda and Kang 2005). Nevertheless, Allum (1983) reported that the metal transfer characteristics produced with this system are not precisely controlled.

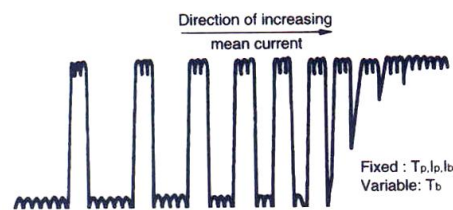


Figure 2.2 – Pulse waveform of self-regulating control.

2.1.7. Pulsed GMAW – Process Characteristics

Pulsed GMAW is characterized by a complex waveform, which involves different parameters affecting the overall transfer and resulting welding characteristics. The main parameters of pulsed GMAW are the peak current (I_p) and time (t_p) and background current (I_b) and time (t_b), as illustrated in Figure 2.3.

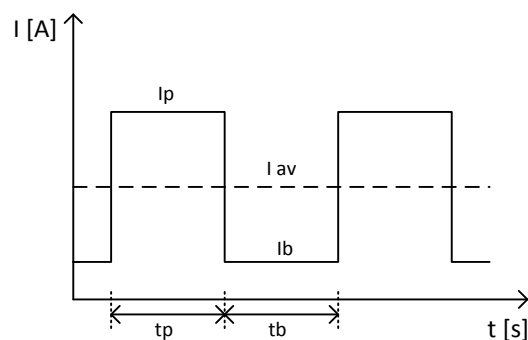


Figure 2.3 – Representation of a characteristic square Pulsed waveform.

However, other parameters such as pulse frequency (f_p) and duty cycle (DC) have also been described. In the following sub-sections the characteristics and control associated with the main process parameters for pulsed GMAW will be presented and discussed.

2.1.7.1. Arc Current

It has been reported that the burn-off relationship for GMAW-P defines the pulse characteristics in terms of a mean current. These pulse characteristics can be associated with the mean current through equation 2.1, considering a square wave form:

$$I_{av} = \frac{I_p t_p + I_b t_b}{t_p + t_b} \quad (2.1)$$

Amin (1983) pointed out that there was a relationship between the pulse parameters with wire feed speed, considering a specific mean current. He characterized several materials and defined the equation 2.2 to describe this linear behaviour between wire feed speed, w , and mean current:

$$I_{av} = s.w + k \quad (2.2)$$

Where s is the slope and k is a constant. It has been reported that if the pulse parameters remain constant, a relationship between the mean current and wire feed speed can be established, as occurs in conventional GMAW. In this case changes in wire feed speed can be associated with changes in frequency (Palani and Murugan 2006).

More complex relationships have been demonstrated considering trapezoidal and exponential waveforms (Praveen, Yarlagadda and Kang 2005).

2.1.7.2. Melting Rate Characteristics

Different authors have indicated that in GMAW the current depends directly on the burn-off rate. In stable conditions the wire feed speed is proportional to the melting rate (Norrish 1987) (Amin 1983). This stability criterion depends on the metal transfer phenomena. At low wire feed rates burn back (wire melting back to the contact tip) can occur, while at high feed rates the arc may extinguish associated with low arc lengths and short circuiting phenomena, resulting in stubbing (Smati 1986) (Palani and Murugan 2006).

Allum (1983) concluded that the arc current can affect process characteristics in respect to metal transfer, depth of penetration, wire melting efficiency and arc stability. He also added that to understand arc stability it is fundamental to consider the relationship between burn-off ratio (W), arc current (I) and the arc length (l), by the equation 2.3, below:

$$W = \alpha I + \beta l I^2 \quad (2.3)$$

where α is a factor accounting for localised arc heating at the wire tip and β describes the resistance heating along of the filler wire length. This expression was firstly proposed by Lesnewich (1958) and has been extensively accepted in the literature to describe the melting phenomena. Quintino and Allum (1984 a) (1984 b) have extended its application to pulse GMAW, as shown in equation 2.4:

$$W = (W_p t_p + W_b t_b) f_p \quad (2.4)$$

Where W_p is the wire melting rate at the peak current and W_b is the wire melting rate at the background current. However, this equation does not apply to all applications of GMAW, since it applies strictly to square waveforms. Subramaniam et al. (1999) found that the

background current and the duty cycle are the most important parameters affecting wire feed rate in pulsed GMAW.

More recently, Modenesi et al. (2005) studied the melting phenomena in GMAW observing a reduction in wire melting rate in the transition between drop spray and streaming metal transfer mechanisms. The authors believed that the transition behaviour is associated with metal vaporization of the filler wire by modification of the heat transfer condition in the electrode.

2.1.7.3. Peak Current and Time

Peak current has been considered the most important parameter in control of arc welding characteristics. It has been shown that dynamic effects responsible for drop detachment take place during the peak time. Amin (1983) and Praveen et al. (2005) found that pulse current affects the metal transfer mode, tapering of the filler wire and penetration bead, while the peak time influences the number of droplets detached per pulse and the droplet size.

Amin (1983) established a inverse relationship between the pulse amplitude and duration time; using experimental data for 1.2 mm filler wire in mild steel, the relationship between peak current and peak time for constant droplet volume is shown for in equation 2.5 for a constant slope of -2.3, as follow:

$$I_p^{-2.3} t_p = K_v \quad (2.5)$$

Where K_v was referred as a detachment parameter at constant volume.

Allum (1983) concluded that the detachment time of a droplet in pulsed welding is independent of the mass of the droplet for ODPP, resulting in equation 2.6:

$$I_p^n t_{pc} = \text{constant} \quad (2.6)$$

Where t_{pc} is the time of a critical pulse level, and with n approximately 2. This hyperbolic condition was also reported by Smati (Smati 1986), who observed that the peak current determines the rate of droplet detachment and peak parameters are associated with droplet frequency, and not with droplet volume as shown by Amin (1983).

Amin (1983) also reported the equation 2.7 for the relationship between peak current (I_p) and background current (I_b) at a specified mean current, should be used.

$$I_p = \left(\frac{t}{t_p}\right) I_{av} - \left(\frac{t}{t_p} - 1\right) I_b \quad (2.7)$$

Where the I_{av} can be obtained using the equation 2.2, where t is the cycle time.

Ueguri et al. (1985) concluded that pulse current should be set above a critical current value and pulse time should be adjusted in order to achieve the stable condition of ODPP. Long peak times are associated with large droplets while short peak times can result in no detaching occurring during each pulse. Furthermore, they recognized that the pulse duration time includes melting and detaching phases.

Rajasekaran and Kulkarni (1998) concluded that at high peak current and time, uniform arc length and droplet detachment control can be established; however, at lower peak current and high peak time those conditions are lost.

Subramaniam et al. (1999) developed a relationship between peak and background parameters in order to achieve the desirable ODPP condition, which could be presented in terms of peak time through the equation 2.8:

$$t_p = \left[496.1 \times (1 - e^{-0.003 \times I_b t_b}) + \frac{270.1}{\frac{(I_b t_b - 188.2)^2}{8423.5} + 1} \right] / I_p \quad (2.8)$$

They pointed out that this equation can be used to define a minimum peak time, which determines ODPP at a specified peak current.

2.1.7.4. Background Current and Time

The background current corresponds to the current necessary to maintain the arc in ignition, but not able to carry out droplet transfer. The background time is the time for which background current is established, affecting the pulse frequency and duty cycle parameters.

Amin (1983) defined a criterion to define a stable condition associated with the background current, expressed as $I_b > c$, where c correspond to a limit of background current as a function of the material (between 10A and 15A). Allum (1983) developed analytical expressions to show the dependence between the droplet size of molten wire and background conditions. He concluded that the expression $I_b t_b$ should be constant in order to achieve the stable condition of ODPP. It was also pointed out by Smati (1986) that the background welding characteristics are responsible for the droplet volume.

It is recognized that heat input can be controlled by the background current and time. These parameters have to be set according with the fusion characteristics needed. In contrast to the low values proposed by Amin (1983), Palani and Murugan (Palani and Murugan 2006) proposed values between 30 to 50A for mild steel, 50A for stainless steel and 20A for aluminium.

Subramaniam et al. (1999) demonstrated the importance of background parameters to obtain the stable condition of ODPP in metal transfer of aluminium. In contrast Vilarinho and Scotti (2000) reported that the background parameters do not affect the detachment mechanism or the one drop per pulse (ODPP) condition.

2.1.7.5. Pulse Frequency and Duty Cycle

Pulse cycle is defined as the period from the beginning of the pulse until the end of the background period, before the beginning of following pulse, and pulse frequency is determined by the equation 2.9, below:

$$f_p = \frac{1}{t_p + t_b} \quad (\text{Hz}) \quad (2.9)$$

Where the cycle time (t) can be defined by the equation 2.10,

$$t_{cycle} = t_p + t_b \quad (\text{s}) \quad (2.10)$$

Amin described the cycle time (t) as a dependant variable of the droplet volume to be transferred per cycle through equation 2.11:

$$t_{cycle} = \frac{240v}{\pi d^2 w} \quad (\text{ms}) \quad (2.11)$$

Where v is the required droplet volume, d is the filler wire diameter and w the wire feed speed.

Duty cycle (D.C.) can be defined as the ratio between pulse width and cycle time, within the Equation 2.12, followed:

$$D.C. = \frac{t_p}{t_p + t_b} \quad (\%) \quad (2.12)$$

The number of droplets detached per pulse is influenced by the pulse frequency and duty cycle. The pulse frequency also affects the mean current value (Praveen, Yarlagadda and Kang 2005). Furthermore, Amin (1981) found out that in synergic mode the variation of wire feed speed is proportional to the variation of pulse frequency for a specified pulse duration time. For a specified pulse frequency, the variation of wire feed speed is proportional to the background current and pulse duration changes.

The frequency of pulsing affects deposition rate by controlling the number of times in a given time interval at which these droplets are transferred. Uegui et al. (1985) showed that pulse frequency can vary from 30 to 500Hz. As duration time increases the frequency decreases at a constant wire feed rate, and this can result in an increase in arc length fluctuations.

2.1.7.6. Arc Voltage

The arc voltage is defined as the electrical potential between the electrode and the workpiece. It is also related to arc length, which suggests that is adjustable according with external welding parameters, such as shielding gas composition or CTWD. The arc voltage can be characterized by the sum of the voltage at the electrode, drop and electric arc column. The electric arc column voltage can be divided into the voltage associated with the arc column and the anode and cathode terms (Scotti and Ponomarev 2008) (American

Welding Society 2007). Smati (1986) reported that the arc voltage can be related to the metal transfer mechanism through its relationship with arc current.

2.1.7.7. Shielding Gas

The shielding gas has two main functions, protection of the molten droplet and pool from the atmospheric air and the development of arc plasma, which is responsible for the conduction of heat flow during the transfer mechanism.

Initially, the application of argon as a shielding gas was considered, and later on carbon dioxide was introduced. Nowadays mixtures of these gases have been commercialized, together with other gases, such as helium, oxygen and sometimes hydrogen.

Shielding gas mixture affects voltage and arc length control, resulting in variation of overall arc energy of the system and affecting process stability. The precise control of shielding gas can also be associated with defect free welding. The control of metal transfer has also been reported to be affected by the shielding gas used. In this context, Eagar (1981) has extensively studied the effect of helium and argon on the transfer mechanism.

The characteristics and effect of these gases on arc process characteristics will be discussed further in Chapter 5 of this thesis.

2.1.8. Innovative GMAW Technologies

The technological developments carried out in GMAW concerned the development of new power sources with different waveform designs, as was mentioned earlier in Chapter 1. These different processes will now be described in respect to the available technical and scientific information.

2.1.8.1. RapidArc

It has been claimed (Lincoln Electric 2004) (2005) that RapidArc welding consists in a refined pulse process, specially designed to achieve faster welding speeds comparable with the traditional pulse GMAW. The RapidArc waveform facilitates low voltage welding at high welding speeds, from 1 to 1.5m/min (40 to 60 in./min) as illustrated in the Figure 2.4. In traditional pulse the arc length is longer to avoid spatter, which limits the welding speed. The RapidArc waveform keeps arc length short and precise control of the short circuit cycle eliminates spatter.

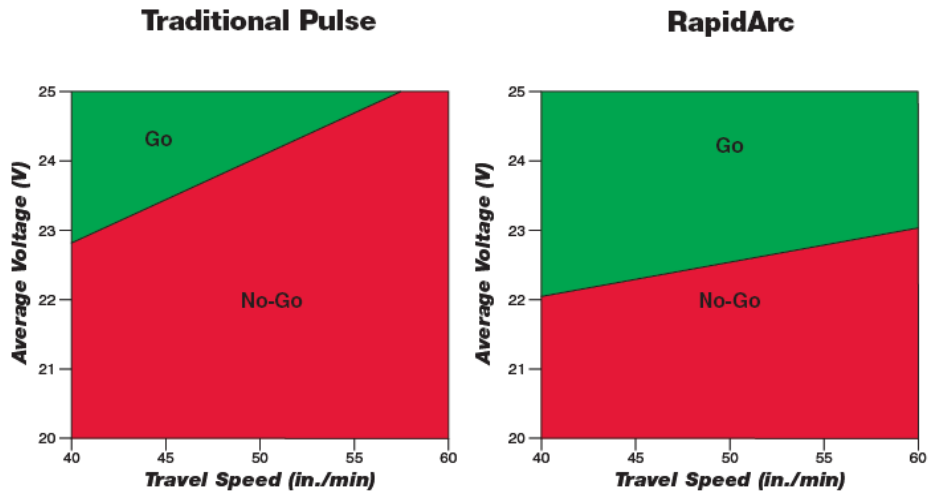


Figure 2.4 - Schematic diagram of operational area for RapidArc waveform (Lincoln Electric 2005).

The Figure 2.5 illustrates the characteristic waveform for RapidArc welding and the respective metal transfer mechanism.

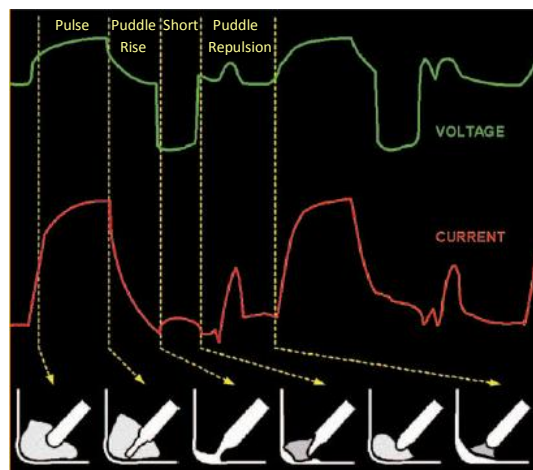


Figure 2.5 - Schematic diagram of metal transfer mechanism for RapidArc waveform (Lincoln Electric 2005).

The RapidArc waveform can be explained in four different phases, as follow:

- Pulse – characterized by an increase in current with a rise in arc energy, and formation and constriction of a molten drop at the electrode;
- Puddle Rise – a decrease in current reducing the plasma force, allowing the depressed weld pool to rise up towards the detaching droplet;
- Short – the arc is extinguished and the droplet touches the weld pool;
- Puddle Repulsion – immediately after the short circuit, a smooth arc pushes the weld pool away. This establishes a stable separation between electrode and weld pool.

Other advantages of this process compared with conventional GMAW are claimed to be a reduction of incidence of undercutting by 75%, and a reduction of 10 to 30% of the cycle time due to the higher welding speeds leading to cost savings. Furthermore, the lower spatter levels with this process can also reduce labour costs for post-weld part and fixture cleanup.

2.1.8.2. Surface Tension Transfer

STT welding is a dip transfer process which uses current controls to adjust the arc energy, independently of the wire feed speed. It allows changes in arc length without affecting the arc energy. Lincoln Electric (2006) claimed that the STT process is able to produce welds with low heat input, without overheating or burning through and can reduce distortion. Furthermore, they pointed out that spatter and fume emissions are minimized due to fact that the electrode does not overheat.

The Figure 2.6 illustrates the characteristic waveform and the metal transfer mechanism.

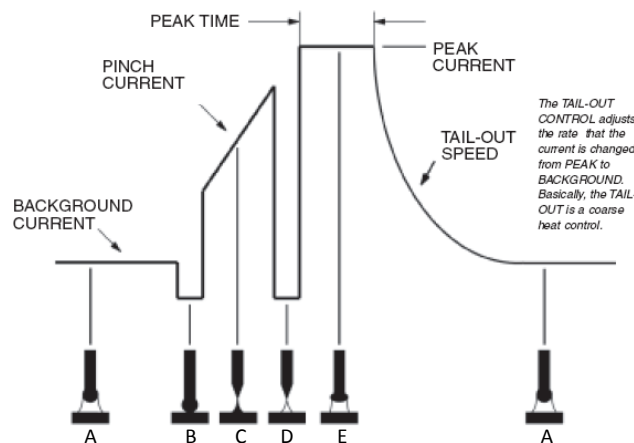


Figure 2.6 – Schematic diagram of metal transfer mechanism for STT waveform (Lincoln Electric 2006).

In STT the background current is kept between 50 and 100 A, which maintains the arc and contributes to the parent material heating. The mechanism of metal transfer in STT welding is described according with the Figure 2.6, as follow:

- Phase A – An uniform molten drop is formed and maintained until the drop touches the weld pool;
- Phase B – The drop touches the weld pool, the arc is extinguished, and the current is reduced to a low level allowing the molten drop to be absorbed by the weld pool;
- Phase C – A pinch current is applied to the remaining molten metal bridge. The short-circuit is near to break and the current is reduced to avoid spatter;
- Phase D – The short-circuit is broken and the arc is re-establishes at a low current level;

- Phase E – A peak current is applied which sets the proper arc length. Following peak current, internal control automatically switches to the background current, which serves as a fine heat control.

2.1.8.3. Cold Metal Transfer

CMT is also classified as a dip transfer process and characterized by low heat input when compared to the conventional GMAW (Fronius 2005). The CMT presents an innovative solution, which is determined by the motion of the electrode directly assisted by the process control mechanism. This forward and backward motion takes place at a frequency of up to 70 Hz. The control system detects the short-circuiting and then retracts the filler wire after droplet transfer (Figure 2.7).

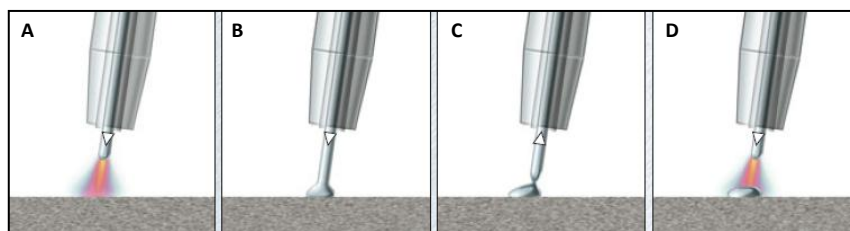


Figure 2.7 – Principal phases during the transfer mechanism of CMT process (Fronius 2005).

In CMT welding the mechanism of metal transfer occurs in phases A to D, and described below:

- Phase A – During the arc period, the filler metal is moved towards the weld-pool;
- Phase B – At the instant that the filler metal touches the weld pool the arc is extinguished and the short-circuit takes place. The current is reduced, and will be kept at background level;
- Phase C – The rearward movement of the wire will assist the droplet detachment mechanism during the short-circuiting. The current will be at low level;
- Phase D – The wire motion is reversed initiating the process again.

In addition, in CMT welding the arc energy supplied during the arc period is very brief, with an effect on the low arc energy produced with this process. Figure 2.8 illustrates the current and voltage waveform which characterize the CMT process.

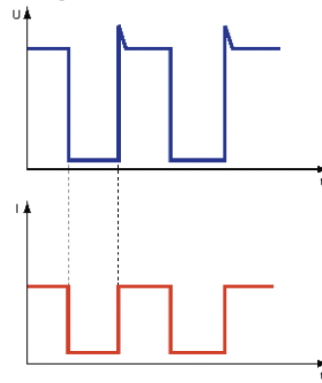


Figure 2.8 – Current (I) and voltage (U) waveform in CMT welding (Himmelbauer 2005).

Another important characteristic claimed for this process is the production of spatter free welds.

2.1.8.4. FastROOT

FastROOT welding process is a recent development in GMAW technology and is defined as a modified short-circuit process. It was developed to improve welding quality of pipe roots in mild steel and stainless steel materials (Uusitalo 2007). The principle of FastROOT welding is presented according with the Figure 2.9.

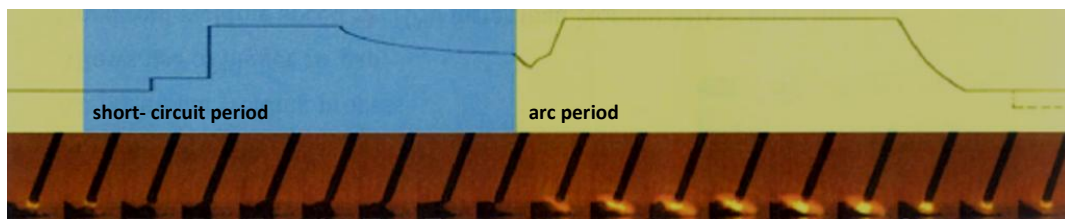


Figure 2.9 – Diagram of current waveform and synchronized metal transfer high speed images (Uusitalo 2007).

The metal transfer mechanism is characterized by short-circuit and arc periods, which involve the following stages:

- The filler wire touches the weld pool causing a short-circuit at a peak current time;
- During the short-circuit period the filler wire is transmitted to the weld pool. The rapid increase in current is responsible to the pinch force action which contributes to the droplet transfer mechanism;
- The detachment is ensured by a slow decrease in arc current;
- When the droplet is detached to the weld pool the current increases producing arc ignition and the beginning of the arcing period;
- During the arcing period the current is kept constant at peak level followed by a desirable “base current” level which can be controlled at the power source.
- The specified “base current” will ensure that the next droplet will be transferred during the next short-circuit period.

The increase in arc current during the arc period is responsible for achieving sufficient penetration.

2.1.9. Summary

This review has described the classification of metal transfer mechanisms into three different classes, respectively natural, controlled and extended operating modes.

The main mechanisms of metal transfer during welding have been described and the associated theories proposed according with the balance of forces present. Short-circuiting or dip transfer at low currents and voltages, and globular, spray and streaming transfer are the most recognized in ascending order of arc current. The mechanisms acting in GMAW during short-circuiting and pulsed waveforms are well understood

However, the new technologies introduced during the last ten years have not been extensively studied and the mechanisms for these processes are still not completely understood. Some technical information has been provided for these technologies by the respective companies and some of these techniques, such as STT and CMT, have already been quite well accepted industrially. Nonetheless, the lack of understanding about the metal transfer mechanisms and transition modes for these processes result in high costs associated with the developing of welding procedures and difficult in finding stable operating conditions for different materials and applications.

In respect of the waveform design and main related parameters, it was also found out that the most significant relationships were developed with the arc current for GMAW and GMAW-P. In fact, it has been pointed out that the current control, in relation to the main waveform parameters (peak and background current, and peak and background times) have a dramatic effect on arc stability and bead shape characteristics. However, the analysis associated with arc voltage is generally neglected or has been given lower importance. Nevertheless, it is well known that process stability is strongly associated with arc voltage control and this is affected by the external parameters, such as the CTWD, shielding gas composition, and filler wire diameter. In particular CTWD and shielding gas composition affect the arc length control and therefore the arc stability.

The effect of process parameters and power source characteristics should be understood for all of these processes in terms of arc stability control.

2.2. RESEARCH OBJECTIVES

The literature review introduced in the previous section shows that there is extensive knowledge about conventional GMAW and its variants, such as, short-circuit and pulsed modes. However, new waveform designs have been introduced recently and little understanding exists in respect to this innovative variants. The main objective of the research developed in this Chapter is to understand the how these different current and voltage waveforms work. In this perspective different research objectives can be described, as follow:

- The characterization of the current and voltage waveforms and the analysis of process variables associated with them;
- The analysis of metal transfer mechanisms associated with different waveforms analysed using current-voltage diagrams and high speed video images;
- The full understanding of how process parameters influence arc energy and melting rate using constant volume (WFS/TS ratio) parameters;
- The characterization of weld bead shape obtained on bead on pipe tests of CRA materials, using different waveform designs and welding parameters.

2.3. MATERIALS AND METHODS

2.3.1. Materials

Two different materials were used in the research developed during this stage, plates of mild steel and pipe sections of a supermartensitic stainless steel, frequently known as 13% Chromium. Particular emphasis will be given to the work developed with supermartensitic stainless steel, since the main application of the project developed is the welding of CRA pipes. However, work on mild steel is more often found in the literature, and therefore this material was also characterized for CMT and RapidArc welding. Another reason for the use of this material is due to the heat transfer and process efficiency research study, which is presented in the next chapter of this thesis, and which is focused on the use of mild steel plates.

Mild steel with the specification EN 440 G3Si1 - S355JR, and different thicknesses were used, respectively 2 mm, 4 mm and 5 mm thick according with the grade and processing routes mention in the Table 2.4.

Table 2.4 – Processing route and specifications of the material.

Thickness [mm]	Grade and Processing Route	Specification
2	S355JR +AR Normalised Pickled & Oiled	6HK12
4	S355JR +AR Normalised Dry	6HK10
5	S355JR Normalised Dry	6HK9

The dimensions for the specimens varied from 100 mm x 100 mm to 100 mm x 200 mm. The chemical composition of the material, as obtained from the supplier, for the different thicknesses considered, is given in the Table 2.5.

Table 2.5 – Chemical composition for the mild steel within different thicknesses.

Thickness [mm]	Chemical Composition [%]									
	C	P	S	Mn	Si	Mo	Cr	Ni	Al	Cu
2	0.163	0.013	0.015	1.115	0.001	0.001	0.019	0.020	0.046	0.017
4	0.179	0.023	0.020	0.998	0.003	0.002	0.024	0.017	0.060	0.020
5	0.119	0.013	0.009	1.094	0.007	0.003	0.023	0.020	0.017	0.035

The filler metal used for welding of mild steel followed the specification of EN ISO 14341: G42 3MG2Si1/ AWS A5.18/5.18M (EN 10025 – S355JR) from ElectroArco with 1 mm diameter. Different gas mixtures of carbon dioxide and argon blends were applied in the experiments, correspondingly 8%CO₂ 92%Ar, 20% CO₂ 80%Ar and 100% CO₂.

For bead on pipe welding using supermartensitic stainless steel, sections of pipe with an external diameter of 272 mm and 13 mm wall thickness were used (Figure 2.10).



Figure 2.10 – Pipe sections of supermartensitic stainless steel.

The chemical composition of the material was analysed by Bodycote Testing Ltd (Appendix I), and the results are presented below in the Table 2.6.

Table 2.6 – Chemical Composition of 13% Chromium supermartensitic stainless steel.

C	Cr	Ni	Mo	Mn	Si	P	S	Al	Cu	V	N
0.010	12.1	6.78	2.53	0.40	0.29	0.013	<0.003	0.03	0.05	0.03	0.006

The filler metal applied to this study was superduplex stainless steel from Lincoln Electric, Ltd LNM 4462 class AWS A5.9: ER2209 (EN 12071: G22 9 3NL) with 1 mm wire diameter. The chemical composition is in agreement with the supermartensitic stainless steel API X80 12Cr 6.5Ni 2.5Mo specification. The typical mechanical properties for this material are described in the Table 2.7 (Lauro and Mandina 2003).

Table 2.7 – Typical mechanical properties for the API X80 12Cr 6.5Ni 2.5Mo (Lauro and Mandina 2003)

Designation	R _s [MPa]	R _m [MPa]	A [%]	KV [J]		
				0°C	-20°C	-40°C
X80 12Cr 6.5Ni 2.5Mo	731	930	26	141	132	116

The chemical composition of the filler wire, according with EN 10204:2004, is presented in the Table 2.8.

Table 2.8 – Chemical Composition of the filler wire superduplex stainless steel ER2209

C	Cr	Ni	Mo	Mn	Si	P	S	Cu	N
0.01	23.1	8.6	3.1	1.59	0.50	0.02	0.001	0.1	0.16

Two different gas mixtures were applied during this research, respectively 2.5%CO₂ 97.5%Ar and 1.5%CO₂ 54%He 44.5%Ar.

2.3.2. Welding Processes

The welding processes studied were applied using three different power sources. The Fronius TransPulsSynergic 5000 CMT was used for the CMT and CMT-P welding techniques, while the Power Wave 455/ STT from Lincoln Electric was used for STT, RapidArc and

GMAW-P welding processes, and the Kemppi FastROOT was applied to FastROOT MIG welding.

2.3.2.1. Fronius

The Fronius TransPulsSynergic 5000 CMT is equipped with a fully digital micro-processor controlled inverter system. This power source provides different operation modes according to the class of material, filler wire diameter, shielding gas and welding process selected. Table 2.9 presents the operation modes selected for the experimental work according with the characteristics of material and shielding gas chosen.

Table 2.9 – CMT and CMT-P operation mode for different welding process and consumable characteristics selected.

Operation Mode	Welding Process	Material	Filler Metal Diameter	Shielding Gas
C0908	CMT	G3Si1	1mm	18%CO ₂ 82%Ar
C1053	CMT	G3Si1	1mm	18%CO ₂ 82%Ar
C0877	CMT	CrNi 19 8	1mm	2.5%CO ₂ 97.5%Ar
C0882+P	CMT-P	CrNi 19 8	1mm	2.5%CO ₂ 97.5%Ar

These different operation modes differ in the main internal setting parameters; correspondingly the wire feed speed (WFS), the arc length correction (ALC) and the adjusting dynamics control parameter. The designation varies according to the mode selected, from hot start (CMT, mild steel) to dynamic control (CMT, duplex) and pulse control (CMT-P, duplex). The variation limits of the parameters referred are presented in the Table 2.10, below.

Table 2.10 – CMT and CMT-P setting parameters variation according with the operation mode selected.

Operation Mode	Wire Feed Speed (WFS) [m/min]	Arc Length Correction (ALC) [%]	Hot Start Time (HS) [%]	Dynamic Control (DC) [%]	Pulse Control (PC) [%]
C0908	Max 7.8 (limit)	-30 – +30	-5 – +5	-	-
C1053	Max 9.4 (limit)	-30 – +30	-5 – +5	-	-
C0877	Max 8 (limit)	-30 – +30	-	-5 – +5	-
C0882+P	Max 10 (limit)	-30 – +30	-	-	-5 – +5

This power source works in synergic mode, where the variation of WFS has a dynamic effect on arc current (I) and voltage (U). The ALC and dynamic control setting parameters offer the possibility of adjusting the waveform current and voltage, in particular in response to external variations, such as the contact tip to workpiece distance (CTWD) or the shielding gas composition. Full understanding of the effect of these parameters will be studied within experimental results. Fronius define ALC as the controlling parameter of arc length, where negative values correspond to short arc, 0 to neutral arc length and positive values to long arc length. On the other hand, the dynamic control, hot start and pulse correction have different functions assigned, depending on the operating mode being used. These settings control the short circuiting or pulse parameters associated with the metal transfer mechanism. In general, at low (negative) values the ALC determines an instantaneous

droplet transfer, at 0 it determines a soft arc, with low spatter arc and at higher (positive) values the arc is harder and stability is higher.

The equipment was designed by Fronius with a wire motion system which is included in the process control. This push pull system is integrated in the arm of the wire feeder, between the power source and the torch.

2.3.2.2. Lincoln

The Lincoln Power Wave 455/ STT power source is also designed for different operation modes, for different welding processes, materials and shielding gas composition. The chosen operation modes according with the characteristics of welding technique and consumables selected are presented in the Table 2.11, below.

Table 2.11 – RapidArc, GMAW and STT operation mode for different welding process and consumable characteristics selected.

Operation Mode	Welding Process	Material	Filler Metal Diameter	Shielding Gas
13	RapidArc	Mild steel - ¹	1mm	Ar CO ₂
34	GMAW	Duplex	1mm	Ar CO ₂
112	STT	Duplex	1mm	Ar CO ₂

The different operation modes determine changes in waveform shape, due to the position on synergic curve, according with welding technique, material and wire size and also shielding gas composition. In the Lincoln power source the main parameters that can change are WFS, trim and wavecontrol. In the overall experimental tests developed the wavecontrol was fixed at its maximum value (10) and The WFS and trim varied according with the limits defined in the Table 2.12.

Table 2.12 – RapidArc, GMAW-P and STT setting parameters variation according with the operation mode selected.

Welding Technique	Wire Feed Speed (WFS) [m/min]	Trim [%]
RapidArc	Max 18	0.5 – 1.5
GMAW-P	Max 12	0.5 – 1.5
STT	Max 8.26 (limit)	0.5 – 1.5

Lincoln defines the trim as controlling the arc length and wavecontrol controlling inductance. The trim is adjustable from 0.5 to 1.5, with nominal setting of 1. Trim values lower than 1 decrease the arc length while values greater than 1 increase the arc length. Trim also changes the peak current. The wavecontrol setting allows the operator to vary the arc characteristics from “soft” to “crisp” in most weld modes. It is adjustable from -10.0 to +10.0, with a nominal setting of 0. In pulse MIG/MAG modes the wavecontrol adjusts the pulse frequency, where the lower pulse frequency generates a wider bead and softer arc.

¹ Although material suggested is mild steel, it was also applied to the tests performed with duplex material.

The frequency is low for negative values and high for positive values. The wavecontrol setting has a direct impact on background current and heat input.

2.3.2.3. Kemppi Power Source

The Kemppi FastROOT power source is also designed with different operation modes. Two different modes were selected associated to the shielding gas chosen, as shown in Table 2.13.

Table 2.13 – FastROOT operation mode for different welding process and consumable characteristics selected.

Operation Mode	Welding Process	Material	Filler Metal Diameter	Shielding Gas
977	FastROOT	Duplex	1mm	Ar 2%CO ₂
978	FastROOT	Duplex	1mm	Ar 30%He 2%CO ₂

This process also works in a synergic mode, and the main parameters are the WFS, Base Current and Forming Pulse. As described by Kemppi, the base current parameter allows the control of background current on the waveform, and can be adjusted from -50 to +50. The Forming pulse has an important role in adjusting the welding dynamics influencing welding stability and spatter. This parameter can be adjusted from -30 to +30, and at negative values the arc is softer and the spatter is reduced, while at positive values the arc is harder for increase stability but spatter increases. The Table 2.14 summarizes the variation of these parameters applied to the experimental tests described in this chapter.

Table 2.14 – FastROOT setting parameters variation according with the operation mode selected.

Operation Mode	Wire Feed Speed (WFS) [m/min]	Base Current [%]	Forming Pulse [%]
977	Max 9 (limit)	-50 – 50	-30 – 30
978	Max 9 (limit)	-50 – 50	-30 – 30

2.3.3. Methods

The research was undertaken under the following phases:

1. Preparation of surface condition;
2. Welding conditions and experimental measurements;
3. Data analyses.

2.3.3.1. Preparation of Surface Condition

The preparation of the material (plates and pipe sections) involved cutting, removing the oxide layers using Dewalt spindle hand polisher with appropriate discs, according with the material used, and finally cleaning the surface using the solvent acetone.

2.3.3.2. Welding Conditions and Experimental Measurements

Different setting parameters were selected for the different materials and welding processes. Two different rigs were prepared for the tests carried out on bead on plate and pipe.

2.3.3.2.1. Rig for the Bead on Plates tests

These tests were undertaken in a special rig (Figure 2.11), which was prepared with remote control to operate at different travel speeds. The travel speed values were previously calibrated on the control panel for real values of speed in units of m/min. This control panel make also possible the control the welding length, and the start and end point of the welding.

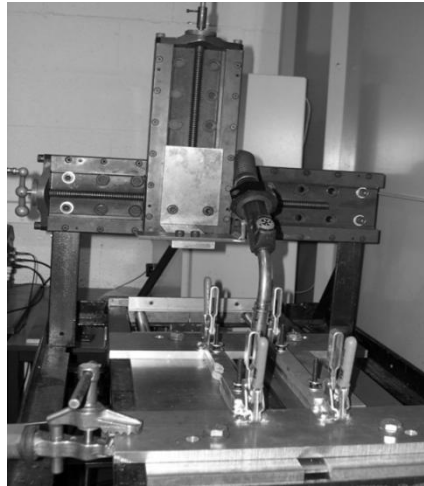


Figure 2.11 – View of the rig used for welding thin sheets.

2.3.3.2.2. Rig for the Bead on Pipe tests

The tests developed on bead on pipe were carried out using a rotator from Instrument Engineering Welding Systems (Figure 2.12).

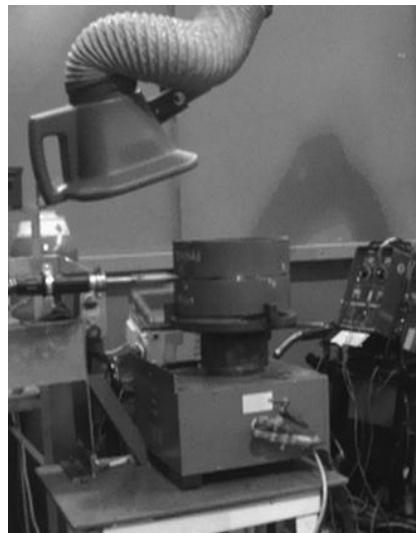


Figure 2.12 – View of the rig used for pipe welding using a rotator machine.

The pipe sections were placed vertically on the top of the rotator. The travel speed could be selected using a digital control system, which was previously calibrated through time-length measurements. The calibration curve and equation obtained for the real travel speed values are presented in the Figure 2.13.

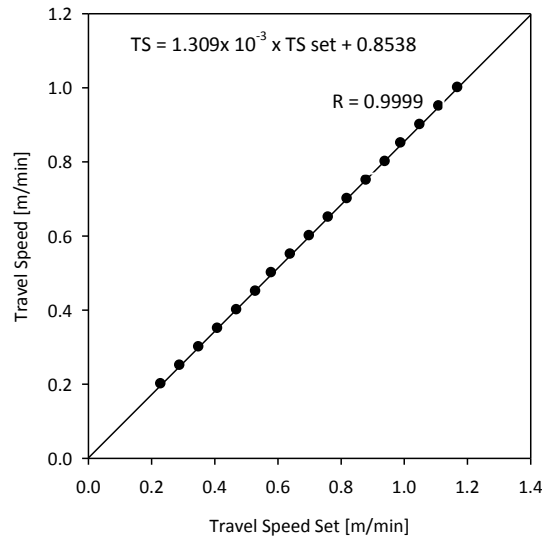


Figure 2.13 – Calibration Curve for the welding speed setting on the rotator.

2.3.3.3. Welding Processes and Conditions

The different welding processes mentioned earlier were selected using the operating modes and different setting parameters were selected within the limits previously defined. Also external parameters were selected in these tests for all the welding techniques set as follows:

- CTWD, generally kept constant at 11 mm but varied from 6 to 20 mm in some studies;
- Shielding gas composition as defined earlier;
- Welding speed, changed between 0.2 and 1.25 m/min.

In some of the tests, the study of process variations was performed with the same WFS/TS ratio in order to achieve constant molten volume. In other cases, both WFS and TS were kept constant for the study of other parameters.

The electrical analyses performed during welding were made using a Yokogawa ScopeCorder DL750 oscilloscope (Figure 2.14) with voltage probes of 1:10 ratio and Hall-effect current probes LEM PR1030. The samples rate used was 5,000 samples per second (5kHz) with 400Hz digital filter to avoid signal aliasing. Also the signal from a tachometer placed on the wire feed system was used to quantify the actual WFS. The complete weld was recorded and a sample of 5 seconds in a representative area of the waveform was taken to analyse the electrical data (the mean values of arc current, arc voltage and wire feed speed, and the average of the instantaneous value of power).



Figure 2.14 – Oscilloscope used for the current and voltage waveform and WFS signal recordings.

In addition, to the electrical measurements high speed camera recordings were made, using Phantom Miro4 camera from Vision Research. This was used to characterize the mode of transfer during the trials and also to measure the arc length associated with the welding characteristics. Previous calibrated setting made it possible to define the image resolution at 256 x 256 pixels, and sampling rate of 5000 frames per second (5KHz). These tests were carried out with the use of a back light system with 1kW halogen lamp, and a filter was used in front of the lens to provide adequate images and protect against spatter. Both high speed camera and back light system were placed at about 1m distance from the workpiece, in opposite directions (Figure 2.15).

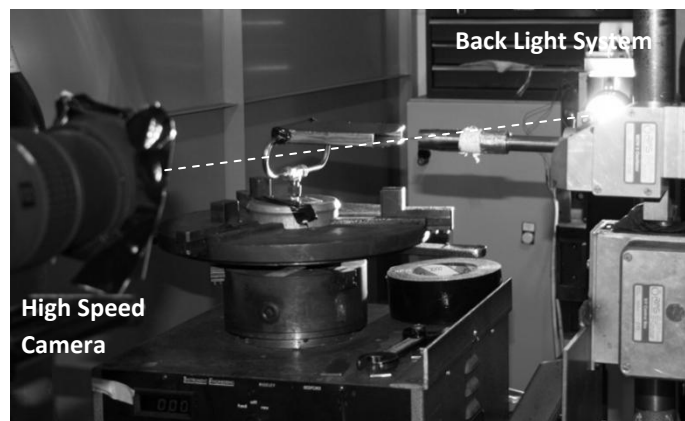


Figure 2.15 – View of high speed camera and back light system aligned in opposite directions to the welding zone (pipe specimen removed)

Figure 2.16 shows a diagram of the welding set-up used for the experiments described during this Chapter.

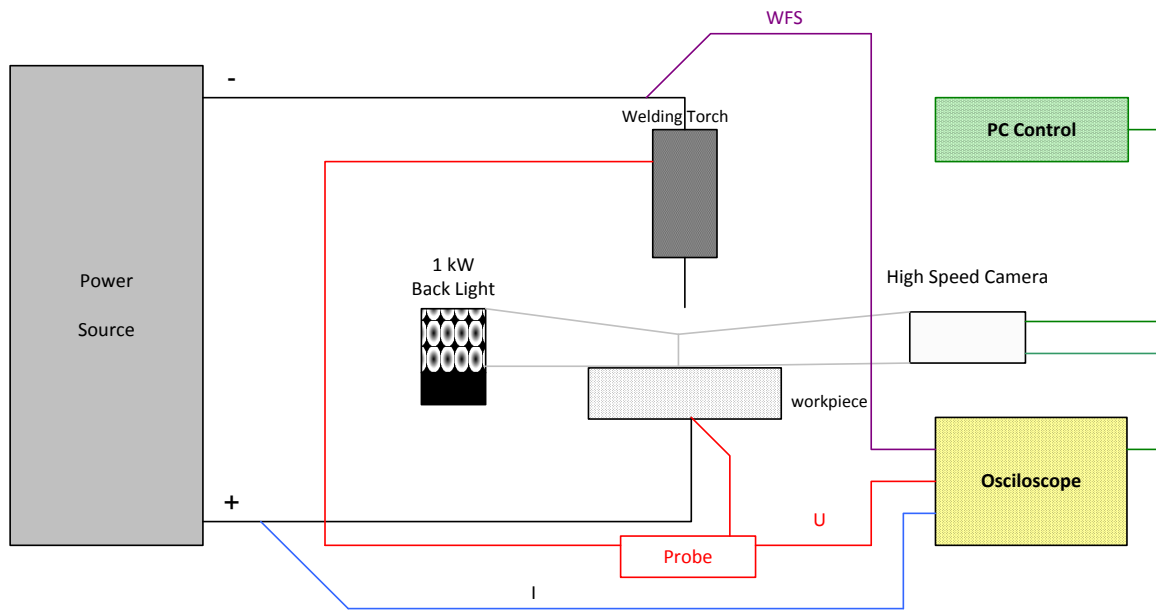


Figure 2.16 – Diagram of set-up for the experiments described in this Chapter.

2.3.3.4. Data Analyses

2.3.3.4.1. Waveform Measurements

Different analyses were performed on the data obtained from the results. The electrical data obtained from the oscilloscope were converted using Xviewer software. This software allowed the observation, measuring and selection of a zoom area range. The overall welding time and 5 seconds sample was stored for all the experiments undertaken. Arc current, voltage and wire feed speed signal were analysed using Excel. The mean values of arc current and voltage were determined. Also, the mean value of wire feed speed was calculated based on the calibration curve presented in the Figure 2.17, below.

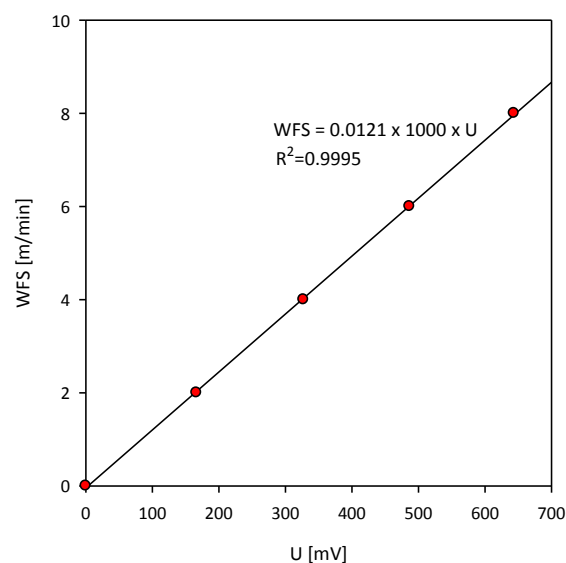


Figure 2.17 – Calibration curve for the actual WFS using voltage measurements from a tachometer.

The results obtained are probably low by 4%, hence all subsequent values should be increased by this factor.

Arc Power was calculated for instantaneous values of current and voltage, and an average of instantaneous power values was determined using equation 2.13:

$$P_{inst} = \sum_{i=1}^n \frac{I_i \cdot U_i}{n} \quad (2.13)$$

Where, P_{inst} is the instantaneous power, and I_i and U_i are the values of current and voltage measured at each instant of time.

The arc energy, defined as the ratio between the arc power (equation 2.13) and welding speed (TS), was calculated using the instantaneous power, defined in equation 2.14:

$$Arc\ Energy = \frac{P_{inst}}{TS} \quad (2.14)$$

All the specific measurements associated with the waveform, respectively peak and background current, peak and background voltage, peak time and background time were taken from an average of several measurements on the waveform.

2.3.3.4.2. Arc Length Measurements and Metal Transfer analysis

In all the experiments performed, arc length control was assessed using high speed video recording, where the 1mm wire diameter was used as calibration scale. In order to measure the arc length, WeldData software developed by Lopes (Lopes 2006) was used to measure the value of arc length at several instants of time. The errors associated with the arc length measurements were estimated to be up to 12%. This software makes also possible to evaluate the mechanisms of metal transfer associated with the different processes at different setting parameters, synchronizing the first 5000 frames of the high speed video with the arc current and voltage.

2.3.3.4.3. Bead Shape Analysis

In order to analyse bead shape characteristics, a cross section was cut and a metallographic preparation was performed. Then, measurements using image software were carried out on the macrograph, looking at penetration bead, height bead, width bead and the reinforcement and dilution areas (Figure 2.18). The errors associated with the bead shape measurements were estimated as up to 5%. However, the measurements of areas could be up to 10%. These measurements can change at a different cross sections of the weld; however, the section chosen for these measurements was selected to be representative of all welding length.

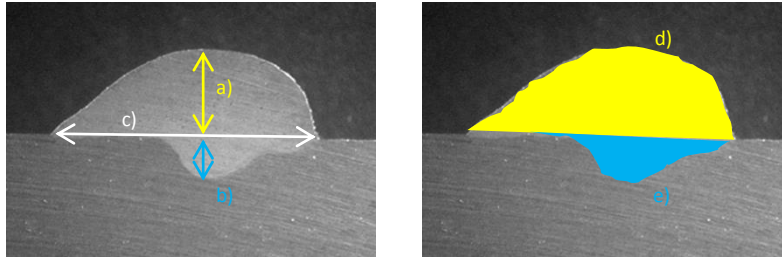


Figure 2.18 – Macrograph illustrating the bead shape measurements, respectively a) height bead; b) penetration bead; c) width bead; d) reinforcement area and e) dilution area.

Further to the measurements developed, other parameters were analysed, such as:

- The height to width ratio, also described as convexity index, from equation 2.15:

$$\text{Height to Width Ratio} = \frac{\text{Height Bead}}{\text{Width Bead}} \times 100 \quad (2.15)$$

- The dilution ratio (DR), from equation 2.16:

$$DR = \frac{\text{Dilution Area}}{\text{Total Melted Area}} \times 100 \quad (2.16)$$

- The reinforcement ratio (RR), from equation 2.17:

$$RR = \frac{\text{Reinforcement Area}}{\text{Total Melted Area}} \times 100 \quad (2.17)$$

2.4. RESULTS

2.4.1. Introduction

The research developed in this chapter was undertaken using different waveform designs, selected from Lincoln, Fronius and Kemppi power sources:

- Conventional GMAW-P (Lincoln Electric)
- STT (Lincoln Electric)
- RapidArc (Lincoln Electric)
- CMT (Fronius)
- CMT-P (Fronius)
- FastROOT (Kemppi)

Conventional GMAW-P was compared with the recently developed techniques. The waveforms presented were obtained under the following experimental conditions: WFS of 6m/min, TS of 0.38m/min, shielding gas 2.5%CO₂97.5%Ar and CTWD of 11mm. The arc length adjusting parameter was set at 1.5 for GMAW-P and RapidArc (trim), 1.0 for STT (trim) and as the nominal values (0%) for the remaining waveforms. The dynamics were set at the major limit (10) for Lincoln waveforms (wavecontrol), while nominal values (0%) were applied to the remaining waveforms. The waveforms obtained from different processes, using WFS of 6 and 8m/min, are presented in the Figures 2.19 and 2.20. The individual analysis for each waveform varying WFS is presented in Appendix VI.

The waveform shapes obtained from the welding processes and power sources selected indicate significant variations in the waveform parameters - peak and background current and voltage, peak and background times, and either short circuiting or pulse frequency (when applied). These results indicate the importance of analysis of the setting parameters in respect to the waveform characteristics and parameters, mechanism of metal transfer and arc stability control. The results obtained from the research developed in this Chapter enhance the understanding of following matters:

1. The analysis of waveform shape variations among the power sources and welding processes selected;
2. The evaluation of the effect of setting process parameters on the waveform characteristics (measured WFS, arc voltage, arc current and arc energy) and arc characteristics (arc length);
3. The analysis of the effect of setting parameters on the waveform parameters (peak current (I_p), peak time (t_p), background current (I_b), background time (t_b), peak and background voltage (U_p and U_b)), duty cycle and either short circuiting or pulse frequency;
4. The analysis of the mechanisms of metal transfer;

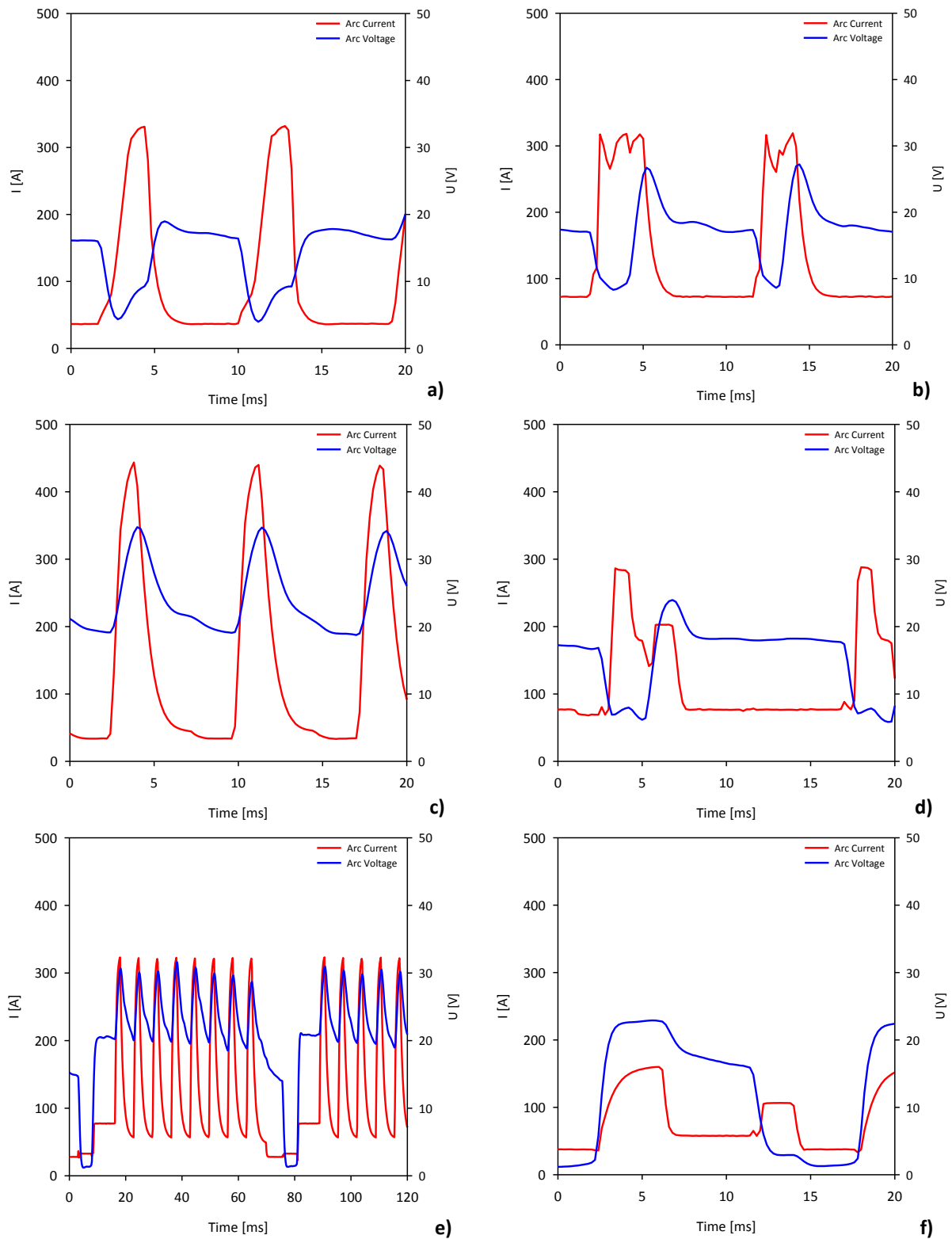


Figure 2.19 – Arc current and voltage waveforms using WFS of 6m/min for: a) GMAW-P; b) RapidArc; c) STT; d) FastROOT; e) CMT and f) CMT-P.

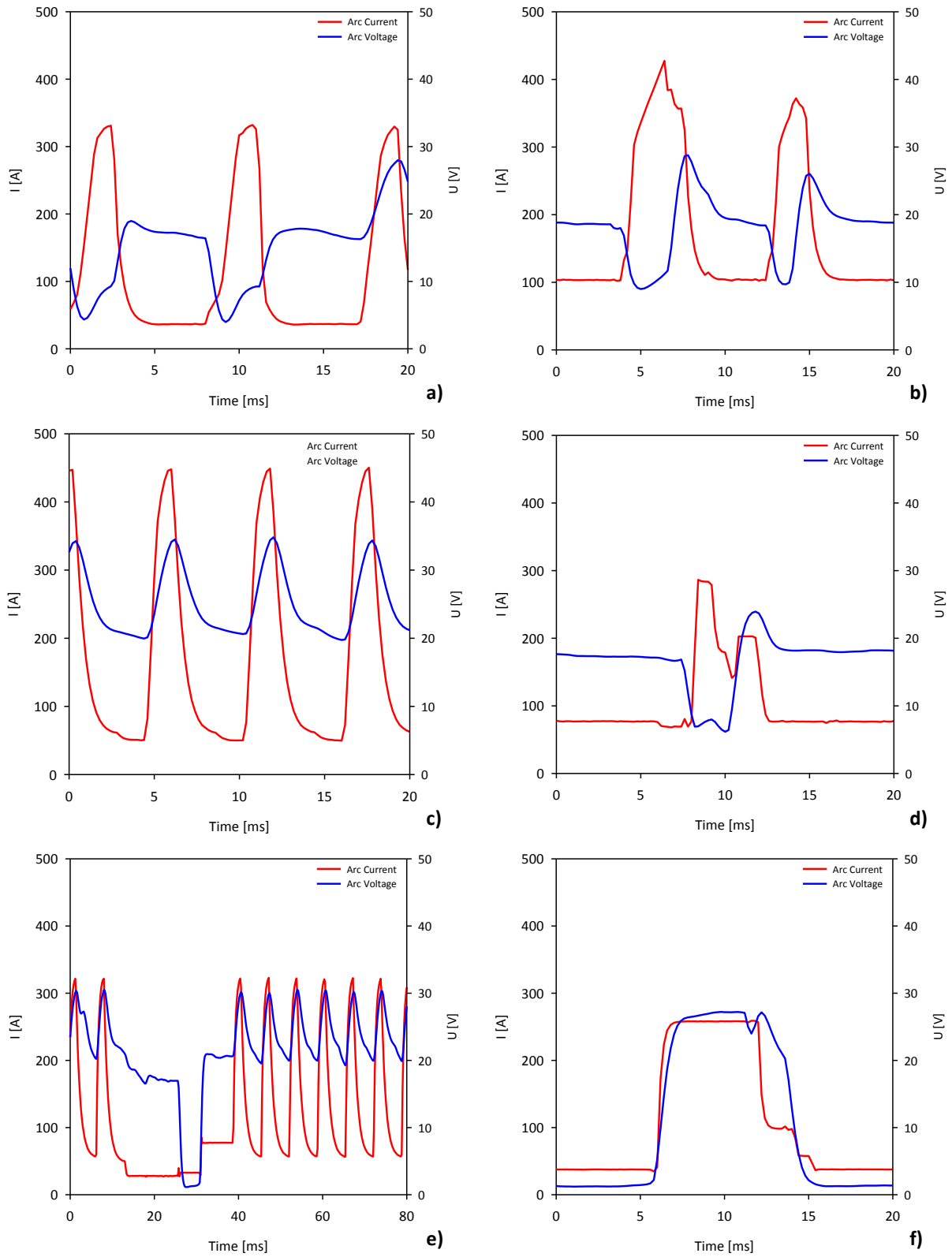


Figure 2.20 – Arc current and voltage waveforms using WFS of 8m/min for: a) GMAW-P; b) RapidArc; c) STT; d) FastROOT; e) CMT and f) CMT-P.

5. The analysis of arc stability control based on waveform signal analysis;
6. The evaluation of bead shape characteristics associated with the different waveform designs proposed (penetration, height and width bead, height to width ratio - convexity index, dilution and reinforcement ratio).

The process setting conditions applied to all waveforms are presented in Appendix II and the results obtained in the Appendices III to V. The following subsections will present the results achieved in relation to the six points introduced above.

2.4.2. Analysis of the Effect of Setting Parameters on the Arc and Waveform Characteristics

As was introduced in the Section 2.4.1, the waveforms investigated are characterized by different shape designs which lead to significant variations in the resulting waveform characteristics. The design of the arc current and voltage waveforms determine the main characteristics of arc welding, in particular, the mechanism of metal transfer, the arc stability phenomena and the resulting bead shape characteristics.

The graphical results obtained to the analysis of arc and waveform characteristics are presented in Appendix VI and the graphical results obtained for the analysis of waveform parameters are presented in Appendix VII.

The results presented in this section, unless otherwise indicated were obtained under the following experimental conditions: WFS of 6m/min, WFS/TS ratio of 16, trim of 1.5 (GMAW-P and RapidArc) or 1.0 (STT), ALC of 0% (CMT and CMT-P) and base current of 0% (FastROOT), nominal value of dynamics adjusting parameter (with exception of GMAW-P, RapidArc and STT where wavecontrol was set at 10), CTWD of 11mm and shielding gas 2.5%CO₂ 97.5%Ar.

2.4.2.1. Actual WFS

Since this work involved the comparison of several waveform systems, working in synergic mode, the wire feed speed (WFS) is considered the most significant parameter, controlling the arc current, arc voltage and cycle time. However, it has been seen that other parameters are present in the different power sources studied, which lead to significant variations on the waveform design.

The actual WFS was measured and compared with the WFS set for the different waveform designs applied. The results obtained suggest that actual WFS is significantly lower for CMT and CMT-P waveforms under the setting parameters applied (Figure 2.21).

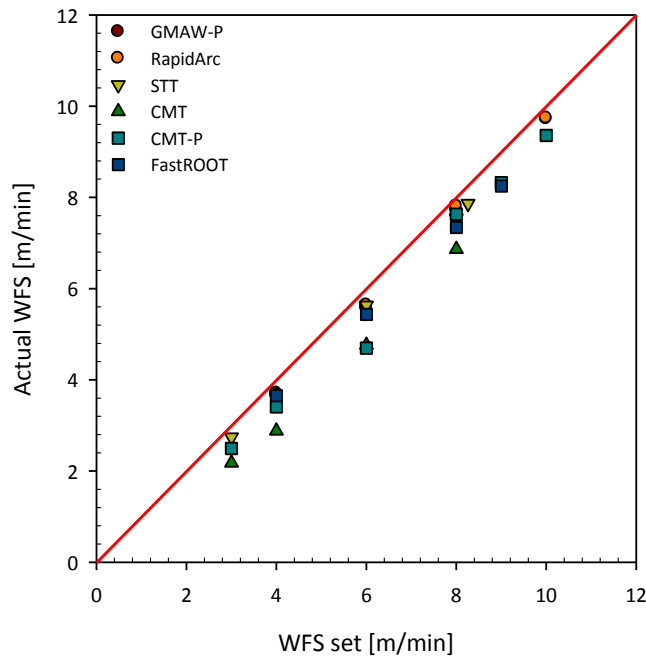


Figure 2.21 – Comparison of actual and set WFS for all welding processes considered.

The effect of adjusting arc length parameter was measured in five steps, from the lower to the upper limit, in order to compare the variation of those parameters for all waveforms. Average and RMS variation were determined and presented through the bars and correspond to the variation of one welding parameter as referenced (Figure 2.22).

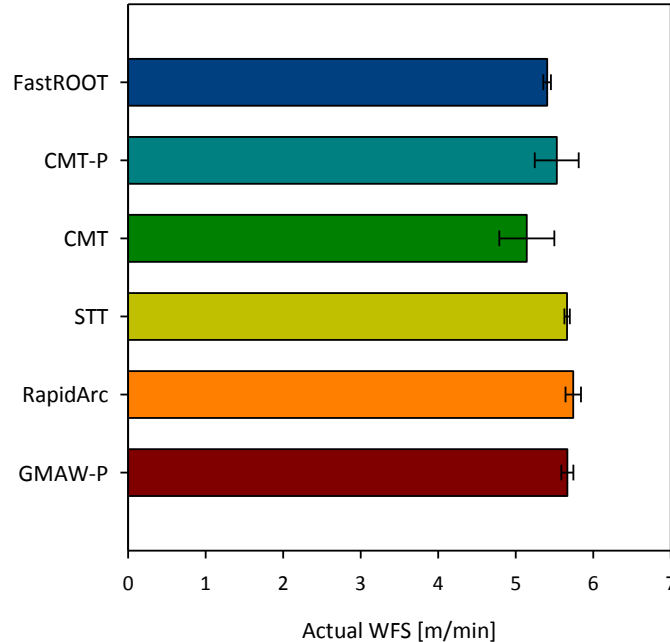


Figure 2.22 – Average and RMS variation of actual WFS (WFS set of 6m/min) for all waveforms, when adjusting arc length parameter was changed from its minor to upper limits (in five steps).

The variation of WFS associated with the arc length correction parameter suggests that no significant changes for most of the waveforms are identified. However, CMT and CMT-P showed significant variations at the welding conditions applied, and a particular reduction of WFS is noticed for CMT waveform.

The special behaviour observed for CMT and CMT-P waveforms can be explained as due to the combination of precise current control with a mechanically controlled wire feed system present in these processes. The method of wire feed speed control for CMT/CMT-P is fundamentally different to all the other processes, and this may account for the variations in WFS in CMT/CMT-P.

The analysis of the effect of CTWD on WFS was evaluated in welding of mild steel for CMT. The experimental conditions applied in these tests were: WFS of 7.8m/min, TS of 0.5m/min and shielding gas 20%CO₂ 80%Ar. As observed in the Figure 2.23, at 16mm CTWD the WFS set is similar to the actual WFS. Below this value the actual WFS decreases linearly with CTWD and above this value the actual WFS increases. These results suggest that CTWD set has a fundamental effect on WFS for CMT, as it changes linearly within the variation of this parameter. A comparison of the variation of WFS with other welding waveforms is shown in Apendix VI.

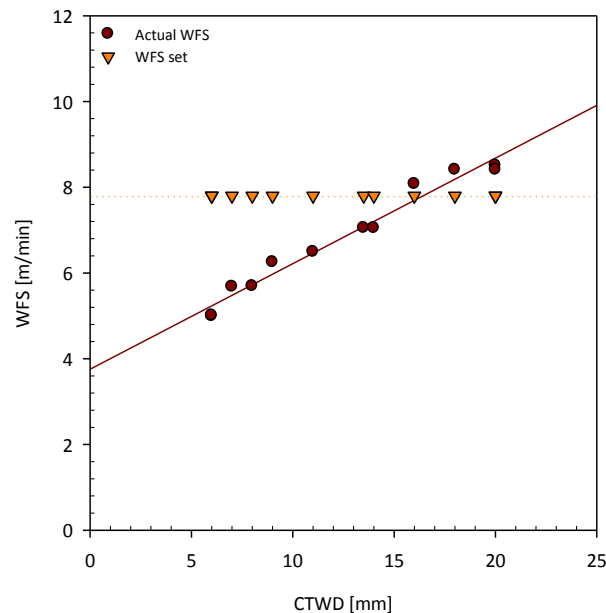


Figure 2.23 – Effect of CTWD on actual WFS, for welding of mild steel in CMT.

It was observed that STT, CMT, CMT-P and FastROOT are designed with an upper limit of WFS set. The limits identified are respectively 8.26m/min for STT, 8m/min for CMT, 10m/min for CMT-P and 9m/min for FastROOT. These upper limits are enforced by the range of conditions where the processes are applied and suit the mechanism of metal transfer and the arc stability.

2.4.2.2. Burn-Off Ratio and Arc Voltage

The arc welding process characteristics result from the variation of arc voltage and arc current waveforms. These variations have been analysed individually for each process in terms of the effect of setting process parameters. As was described earlier, all the processes studied work in synergic mode, characterized by a relationship between mean arc current and mean voltage with WFS (Norrish 1987).

2.4.2.2.1. Arc Current and Burn-Off Ratio

Burn-Off ratio is defined as the relationship between mean arc current and wire feed ratio and was characterized individually for all the waveforms in Appendix VI. A comparison between these results was performed using similar experimental conditions. These results are noteworthy showing that burn-off ratio follows a similar relationship for all the processes considered in this work (Figure 2.24).

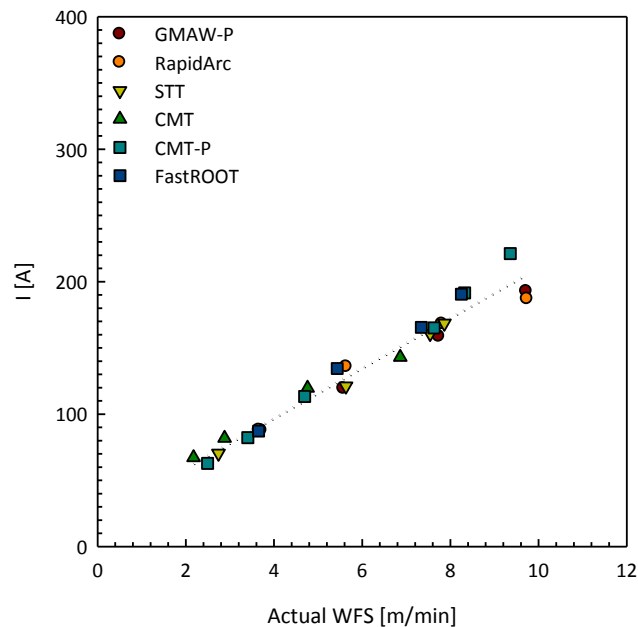


Figure 2.24 – Comparison of Burn-Off ratio for different welding waveforms.

The individual results shown in Appendix VI suggest that there may be transition region associated with the variation in the mode of metal transfer for RapidArc, CMT and CMT-P waveforms.

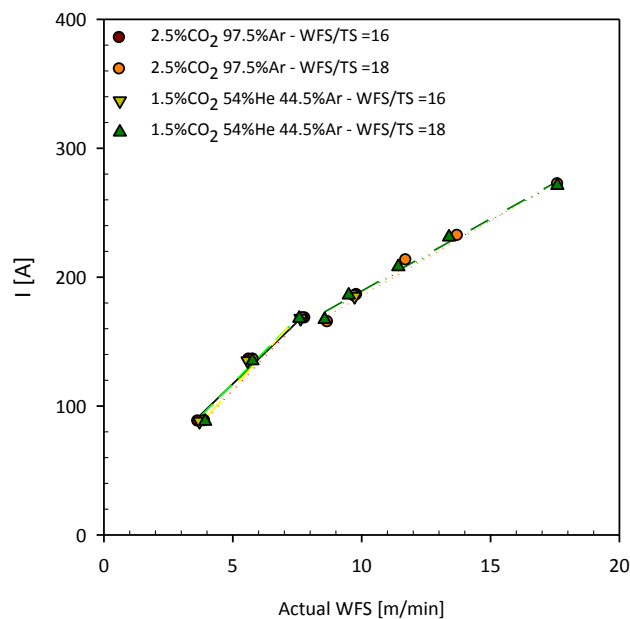


Figure 2.25 – Transition region of Burn-off ratio for RapidArc waveform.

The transition region for RapidArc is illustrated in the Figure 2.25, when WFS is changed from 4 to 18m/min (WFS), at around 170 – 180A. The transition region is observed between 8 and 9m/min (actual WFS).

Since it was established that the burn-off ratios for all processes are very similar, a detailed analyse of the variation of arc current involves the understanding of how peak and background current changes with the WFS for all these waveforms. The results of the comparison of peak and background arc current, using the similar experimental conditions is presented in Figure 2.26.

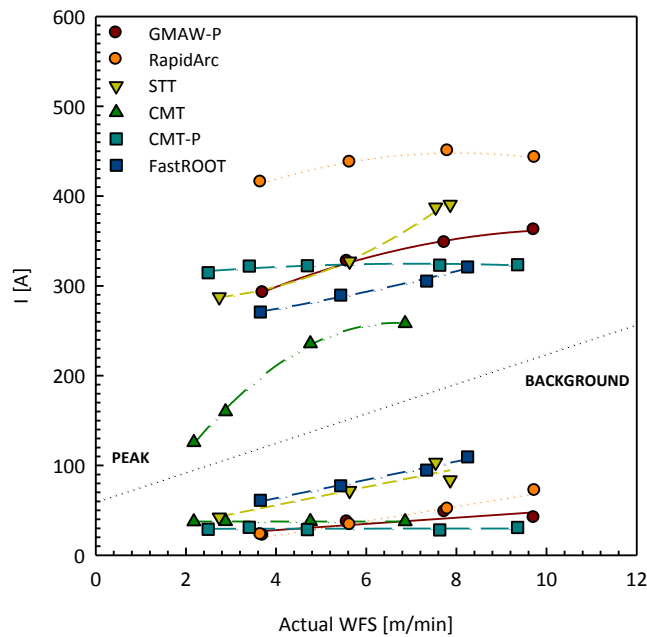


Figure 2.26 – Variation of peak and background current with actual WFS to the different waveforms.

As observed in Figure 2.26, peak and background current increase with WFS for most of the waveforms considered in this work.

Larger differences are observed in respect to the peak current, rather than the background current levels. A difference of approximately 200A is found in peak current when CMT and RapidArc waveforms are compared. These large differences are associated with the power source characteristics, and the controlling software. It is also noticed that CMT waveforms show the lowest peak current levels compared to the other processes.

Interestingly, it is observed for CMT-P that peak and background current are approximately constant at all range of WFS. The increase of mean arc current with actual WFS must therefore result from the variation of pulse and short-circuiting frequency. In fact, the short-circuiting frequency decreases with the increase of WFS, while pulse frequency becomes greater (Figure 2.27). The variation of these frequencies is due to the increase of the number of pulses per waveform cycle, and consequent increase in cycle time while short-circuiting time is almost constant.

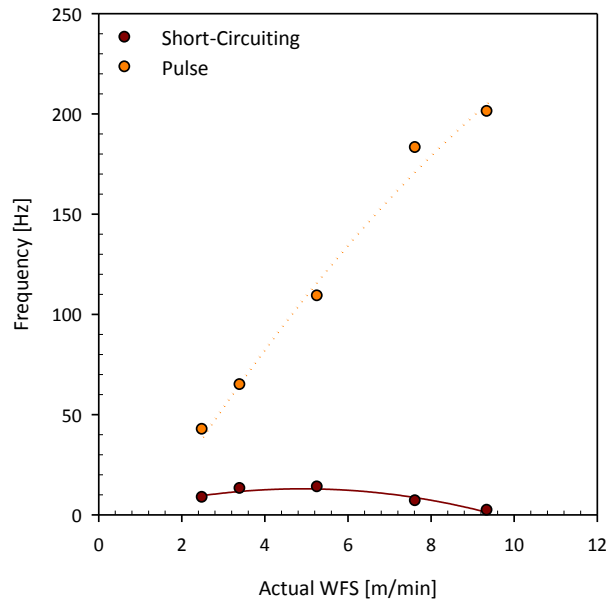


Figure 2.27 – Variation of short circuiting and pulse frequencies with WFS for CMT-P using 2.5%CO₂ 97.5%Ar.

The variation of peak and background times gives also important information about the waveform. These results are presented individually for each waveform in AppendixVII.

For GMAW-P background time is greater than peak time until 6m/min (WFS set), from where peak time becomes greater. An earlier transition is observed for RapidArc, at 4m/min (WFS set). The later transition observed for GMAW-P is probably an important signal for the uncontrolled short-circuiting phenomena verified for this process.

In short-circuiting processes background time is always greater than peak time. However, the background time decreases rapidly with the increase of WFS. For STT, the background time is 80% longer than peak time at low WFS levels (3m/min), and is only 20% longer at the maximum WFS set (8.26m/min). CMT is characterized by a longer peak time until about 7m/min (WFS set), from where the peak time becomes longer than the background time until the maximum WFS set, at 8m/min, is reached. FastROOT presents the same behaviour with an inflexion point at 8m/min (WFS set). In short-circuit waveforms, the transition point from where background time becomes smaller than peak time can be comparable to the transition of the mode of metal transfer and the small variations in burn-off ratio above identified, as observed from the metal transfer analysis.

CMT-P is characterized by longer background time, until 6m/min (WFS set), from where peak time becomes much longer, until reaching the maximum WFS set level (10m/min). This behaviour is reflected by the exponential increase in number of pulses per cycle, from 5 at 3m/min (WFS set) to 100 at 10m/min (WFS set), which results in the increase of cycle time.

Since the WFS controls the burn-off ratio of the different waveform systems investigated, working in synergic mode, it is fundamental to understand the effect of the other setting parameters in the variation of arc current. Arc length adjusting parameter, dynamics

adjusting parameter, shielding gas composition, WFS/TS ratio and CTWD were therefore analysed individually in Appendix VI.

The variation of arc length adjusting parameters was set from their lower to upper limits in five steps; average and RMS variation of those values were determined and represented in bars graph (Figure 2.28). The remaining experimental conditions applied to these tests were similar as indicated above (Section 2.4.1).

The lower values of arc current observed for CMT are due to the variations between WFS set and actual WFS discussed above. From these results significant variations of arc current with trim are observed for STT, within about 30A and about 20A for RapidArc, CMT, CMT-P and FastROOT.

Although the variation of mean arc current is not significant for GMAW-P, peak current increases by about 40A, from 280A (trim of 0.5) to 320A (trim of 1.50) (Appendix VI). For RapidArc the increase of peak current is much larger, about 100A, from 320A (trim of 0.50) to 420A (trim of 1.50) (Appendix VI).

For STT the increase of arc current with trim is not only at peak but also at background levels. This increase is similar for both background and peak terms, about 80A, respectively from 20A to 100A and from 310A to 390A (Appendix VI). The variation associated with CMT and CMT-P is due to the variation of background time which increases more significantly for CMT (Appendix VI). For FastROOT the variation observed results from the combination of the increase of background and peak current, both about 25A (respectively from 60A and 270A) and the increase of background peak time while peak time decreases (Figure 2.28).

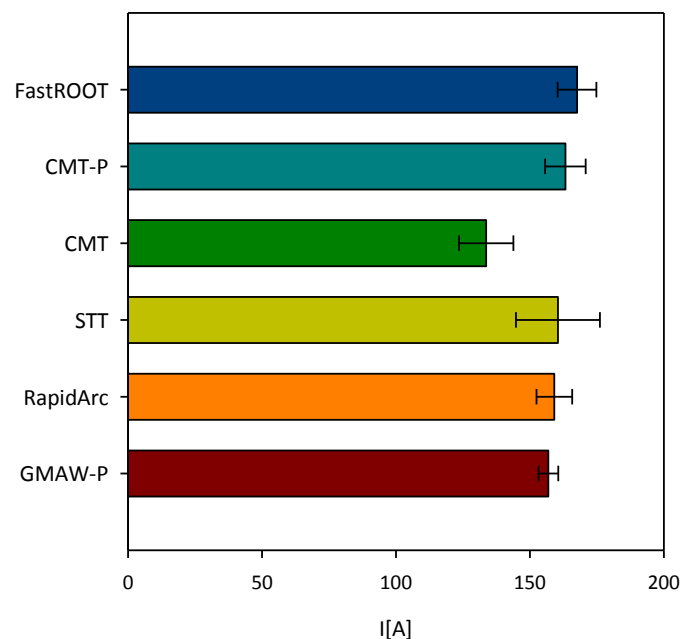


Figure 2.28 – Comparison of the average and RMS variation (bars) of mean arc current for different waveforms, obtained by changing the arc length adjusting parameter (in five steps from lower to upper limits).

The effect of the variation of CTWD on arc current was analysed from the results obtained in three steps (11, 13.5 and 16mm); average and RMS variation of those values were determined and represented in bar graph (Figure 2.29). The remaining experimental conditions applied to these tests were similar as indicated above (Section 2.4.1).

The results suggest that only GMAW-P and STT present significant variations of mean arc current. The variation observed for STT can be associated with the increase of background time resulting from the increase of CTWD (Figure 2.29).

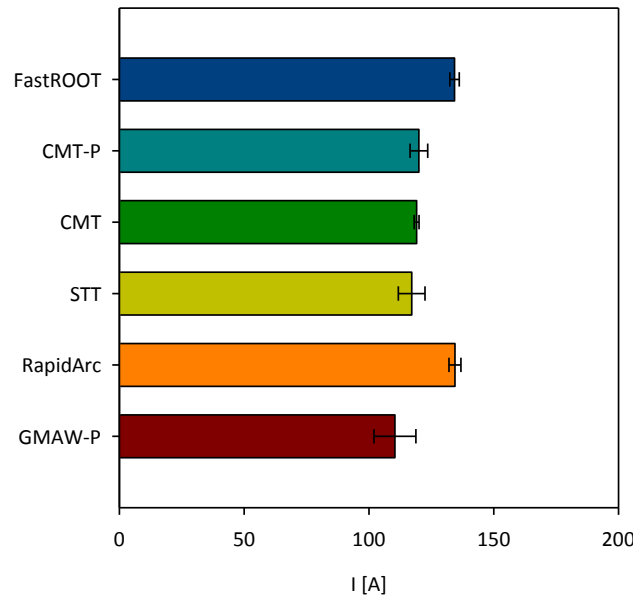


Figure 2.29 – Comparison of average and RMS variation (bars) of mean arc current for different waveforms, obtained by changing CTWD in three steps (11, 13.5 and 16mm).

The comparison of the variation of shielding gas on arc current for all waveforms does not suggest significant variations (Figure 2.30). Similar behaviour is observed to the comparison of different WFS/TS ratio (using constant WFS) (Figure 2.31).

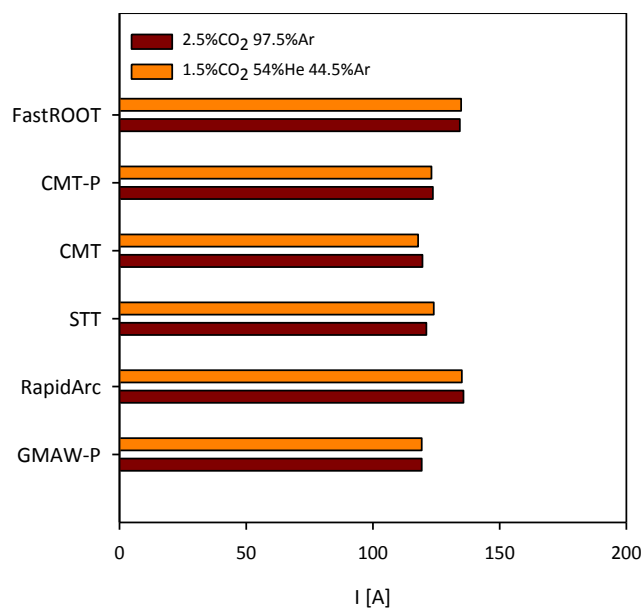


Figure 2.30 – Comparison of the variation of mean arc current with shielding gas for all waveforms (WFS set of 6m/min).

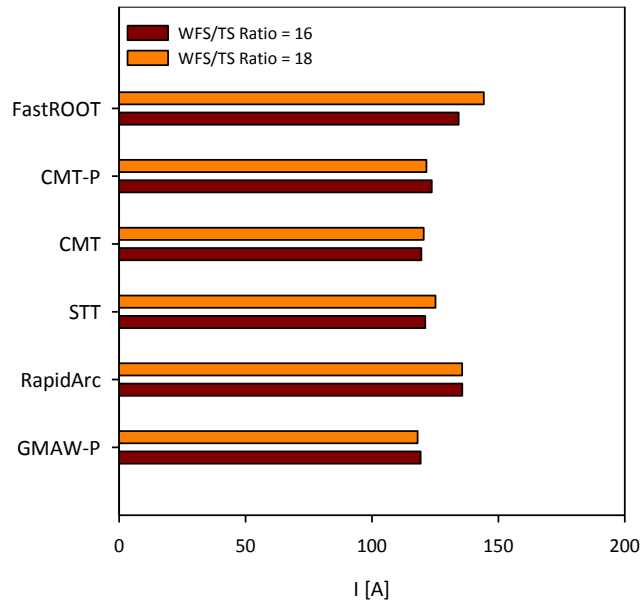


Figure 2.31 – Comparison of the variation of mean arc current with WFS/TS ratio for all waveforms (WFS set of 6m/min).

2.4.2.2.2. Arc Voltage

The synergic mode establishes also a law for the relationship between the WFS and mean arc voltage (Figure 2.32). However, in current controlled processes, the arc voltage can change considerably with arc fluctuations and process instability phenomena. These variations also depend on the power source characteristics in response to different constrictions applied, i.e. CTWD, shielding gas composition, filler wire characteristics and welding speed.

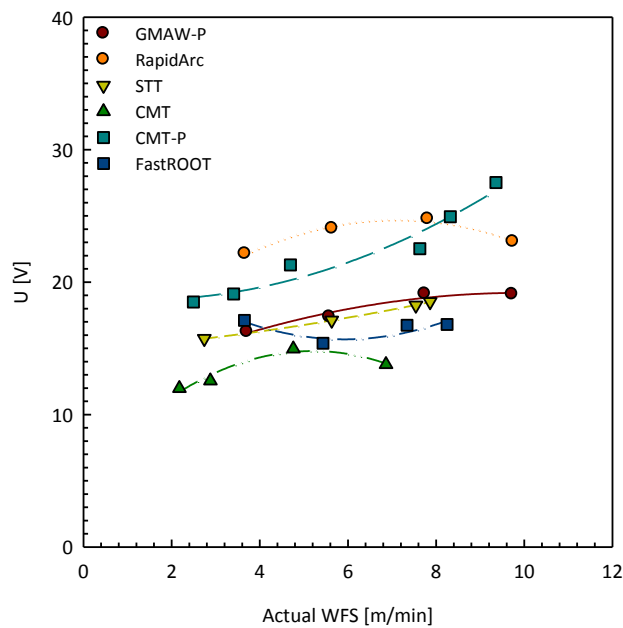


Figure 2.32 – Variation of mean arc voltage with actual WFS for all waveforms.

From the results above is observed that in general arc voltage increases with WFS for all waveforms investigated. However, in contrast to the burn-off ratio, the law for the

relationship between arc voltage and WFS differs for each waveform studied. At high WFS levels it is noticed that arc voltage decreases for GMAW-P, RapidArc and CMT waveforms. The analysis for RapidArc up to higher WFS levels suggests that after the arc voltage drop at 9m/min, the voltage is then constant (Figure 2.33).

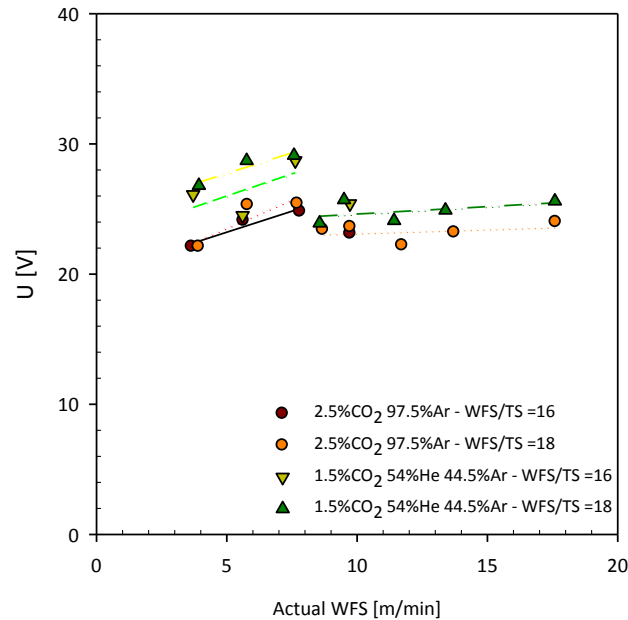


Figure 2.33 – Variation of arc voltage with actual WFS for RapidArc, using different shielding gases.

The changes observed in terms of arc voltage level for the different waveforms cause significant variations on arc energy, since the arc current is similar for all waveforms studied.

In fact, approximately 10V separates the arc voltage level between CMT and RapidArc waveforms. The waveforms characterized by pulse spray transfer mechanism (RapidArc and CMT-P) show, as expected, higher arc voltage levels. Surprisingly, the arc voltage level is slightly lower for GMAW-P, probably due to instability phenomena.

The analysis of arc voltage also involved the comparison of peak and background voltage for all waveforms investigated (Figure 2.34).

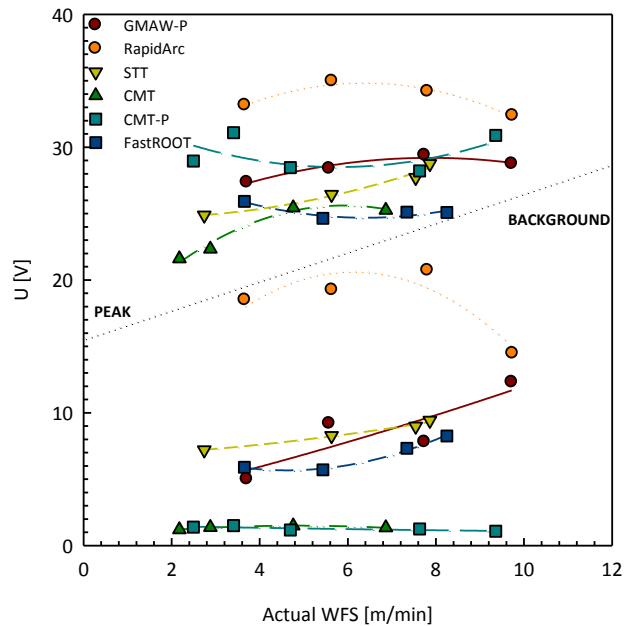


Figure 2.34 – Relationship between WFS and peak and background arc voltage for different welding waveforms.

Peak voltage level varies from about 25V (CMT) to 35V (RapidArc), while background voltage varies from about 1V (CMT and CMT-P) to about 20V (RapidArc) (Figure 2.34). The sequence of peak voltage is given from the highest to the lowest level, as follows: RapidArc -> CMT-P -> GMAW-P -> STT -> FastROOT -> CMT. The sequence for background voltage is as follow: RapidArc -> GMAW-P -> STT -> FastROOT -> CMT-P -> CMT.

The analysis of these results suggest that background voltage is higher for RapticArc, when compared with the remaining waveforms, but decreases significantly between 8 and 10m/min (actual WFS). A slightly decrease of peak voltage for FastROOT, is balanced by the slightly increase of background voltage. Background voltage is almost constant at all WFS levels for CMT and CMT-P and remains at a very low level (approximately 1V).

The variation of arc voltage with arc length adjusting parameter, dynamics adjusting parameter, shielding gas composition, WFS/TS ratio and CTWD were also investigated individually for each waveform (Appendix VII). The comparison of the results obtained was performed for all waveforms and will be discussed below.

The variation of arc length adjusting parameter was set from their lower to upper limits in five steps; average and RMS variation of these values were determined and represented in bar graphs (Figure 2.35). The remaining experimental conditions applied to these tests were similar to those indicated above (Section 2.4.1).

As observed in the Figure 2.35, the variation of arc voltage is significant for all waveforms analysed but more pronounced for RapidArc and CMT.

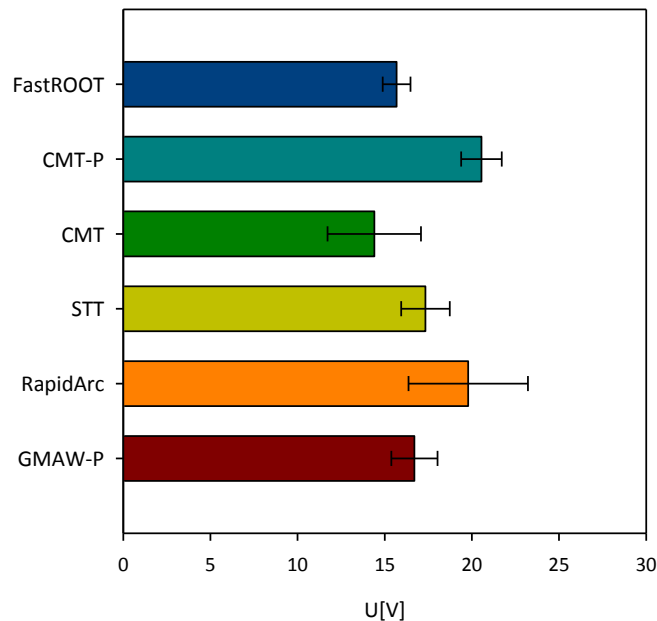


Figure 2.35 – Comparison of the average and RMS variation (bars) of mean arc voltage for different waveforms, obtained by changing the arc length adjusting parameter (in five steps from lower to upper limits).

It is noticed that the highest voltage levels are obtained for RapidArc and CMT-P, followed by GMAW-P and STT and the lowest values obtained for CMT and FastROOT.

For GMAW-P, the variation of arc voltage with trim (arc length adjusting parameter), from 0.5 to 1.5, is due to the increase of background and peak voltages, both about 3V. However, for RapidArc the increase of both background and peak voltages, corresponds to approximately 10V.

The increase of background and peak voltages for STT is not significant, but the variation observed can be associated with an increase of peak, or step, voltage frequencies. The same behaviour is associated with CMT, CMT-P and FastROOT waveforms.

The effect of the variation of CTWD on arc voltage was also analysed from the results obtained in three steps (11, 13.5 and 16mm); average and RMS variation of those values were determined and represented in bar graphs (Figure 2.36). The remaining experimental conditions applied to these tests were similar to those indicated above (Section 2.4.1.).

The variation of arc voltage with CTWD is more significant for GMAW-P, RapidArc and FastROOT waveforms. For GMAW-P, both peak and background voltage increases by approximately 5V, while for RapidArc this increase is more significant at about 10V and about 3V for FastROOT. The variation for STT is only about 1.5V for both background and peak voltage, while for CMT and CMT-P a variation lower than 5V is observed only for peak voltage.

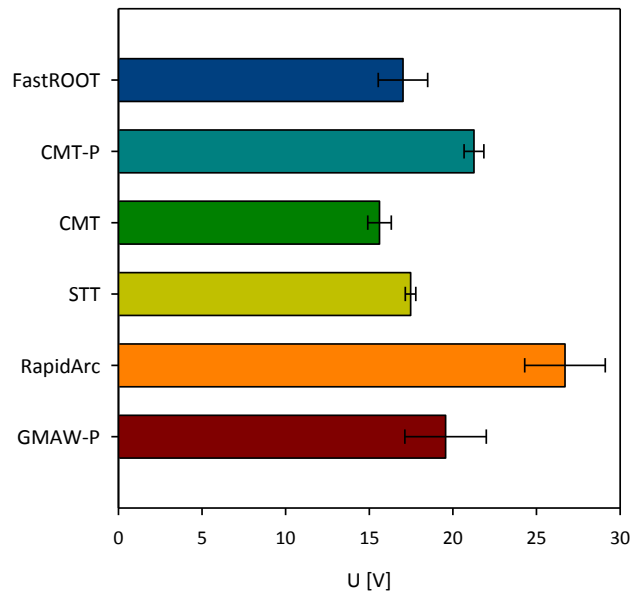


Figure 2.36 – Comparison of average and RMS variation (bars) of mean arc voltage for different waveforms, obtained by changing CTWD in three steps (11, 13.5 and 16mm).

The effect of shielding gas composition was also evaluated. The analysis of two different shielding gases demonstrates the influence of shielding gas composition on the variation of arc voltage. The shielding gas rich in helium (1.5% CO₂ 54%He 44.5%Ar) presents a significantly higher arc voltage, when compared with 2.5%CO₂ 97.5%Ar (Figure 2.37). The increase of arc voltage is determined by the physical properties of the gas mixtures, in particular the ionization potential and gas density (Hiraoka, Sakuma and Zijp 1998).

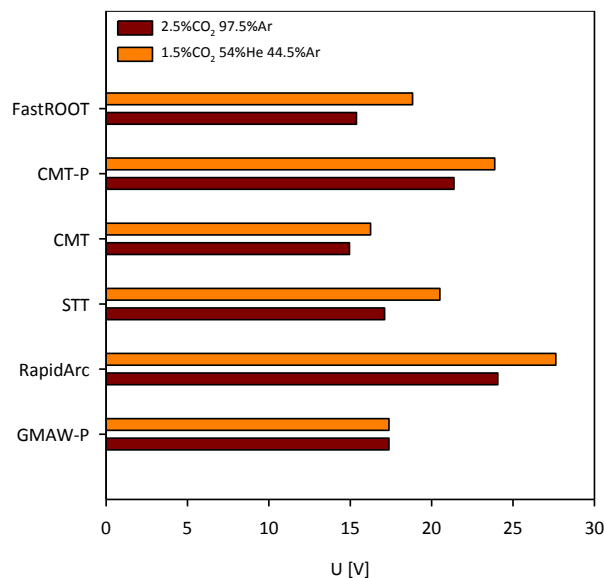


Figure 2.37 – Comparison of the variation of mean arc voltage with shielding gas for all waveforms (WFS set at 6m/min).

The comparison of the variation of different WFS/TS ratio (using constant WFS) suggests no significant changes for all waveforms investigated (Figure 2.38).

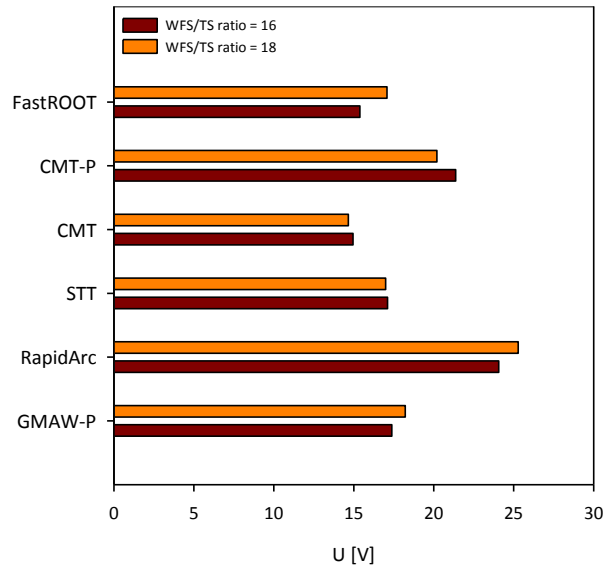


Figure 2.38 – Comparison of the variation of mean arc voltage with WFS/TS ratio for all waveforms (WFS set at 6m/min).

2.4.2.3. Arc Energy and Arc Power

A comparison of the arc energy obtained to all waveforms is shown in Figure 2.39, using similar welding conditions (Section 2.4.1).

As indicated in Figure 2.39, the arc energy varied considerably among the waveforms considered for this work. While the waveforms characterized by dip transfer (i.e. CMT, STT and FastROOT) present similar results for arc energy, the waveforms characterized by pulse spray transfer show larger differences.

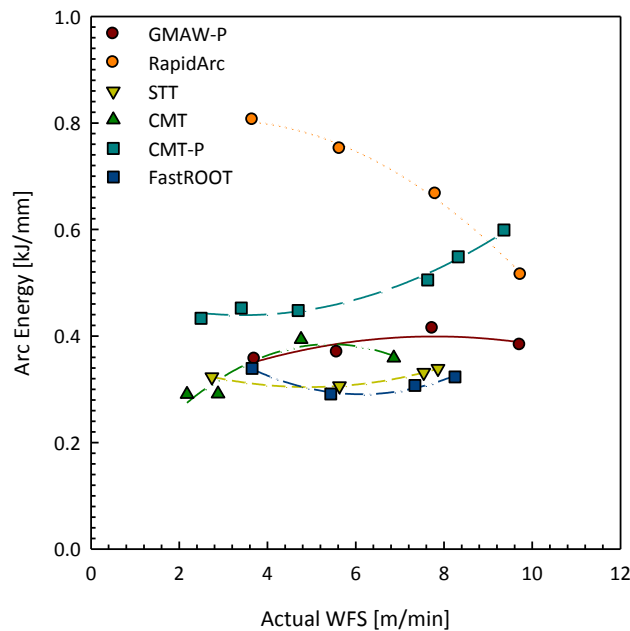


Figure 2.39 – Variation of arc energy with actual WFS for all waveforms.

The variation of arc power demonstrates that the amount of power delivered by each power source generally increases with the WFS for all waveforms (Figure 2.40). It

demonstrates that the decrease arc energy associated with RapidArc is due to the small variations on arc voltage when welding speed increases (constant WFS/TS ratios).

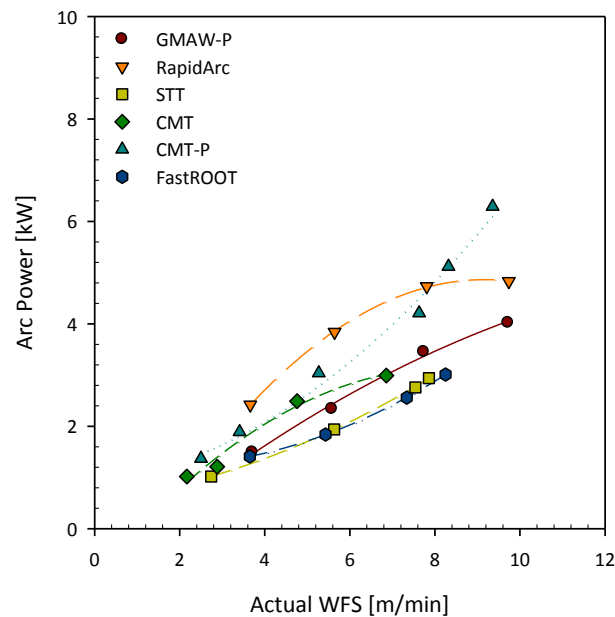


Figure 2.40 – Variation of arc power with actual WFS for all waveforms.

2.4.3. Arc Characteristics

Arc characteristics are generally characterized by the variation of arc length. Kenney et al. (1998) suggested that arc length provides a traceable view of the physics of the welding process. Although the measurement of arc length is very difficult and often results in errors, several measurements using high speed video images achieve reasonable accuracy. The variation of arc length is a response to the process setting parameter, waveform design and instability phenomena associated with the metal transfer. The comparison of the variation of arc length with WFS level for different waveforms is presented in Figure 2.41.

In general arc length slightly increases with WFS (and consequently with arc current and voltage), but a drop in arc length is observed at high WFS levels for RapidArc, GMAW-P and CMT-P, which are characterized by pulse spray transfer. This phenomenon is a consequence of the differences in the mechanism of metal transfer and will be discussed in the next section. A detailed analysis of the variation of arc length with WFS for RapidArc for higher WFS levels shows that after the transition region of metal transfer, arc length decreases progressively until reaching buried levels (Figure 2.42). It should be noticed that these results were obtained for a specific CTWD of 11mm.

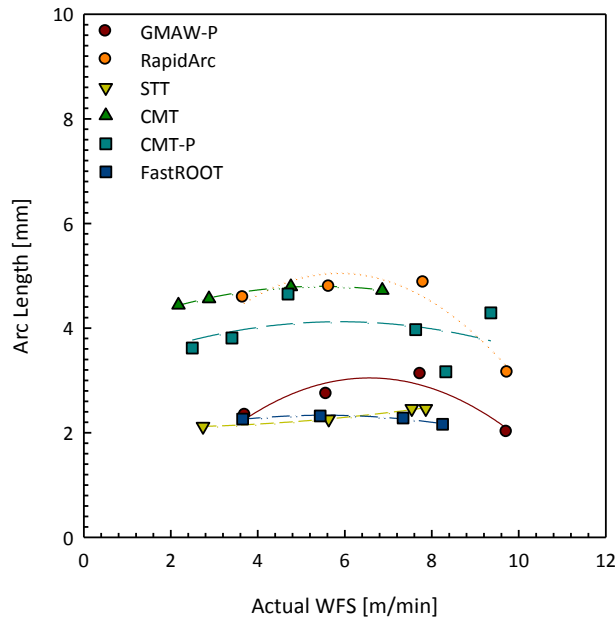


Figure 2.41 – Variation of arc length with actual WFS (measured) for all waveforms.

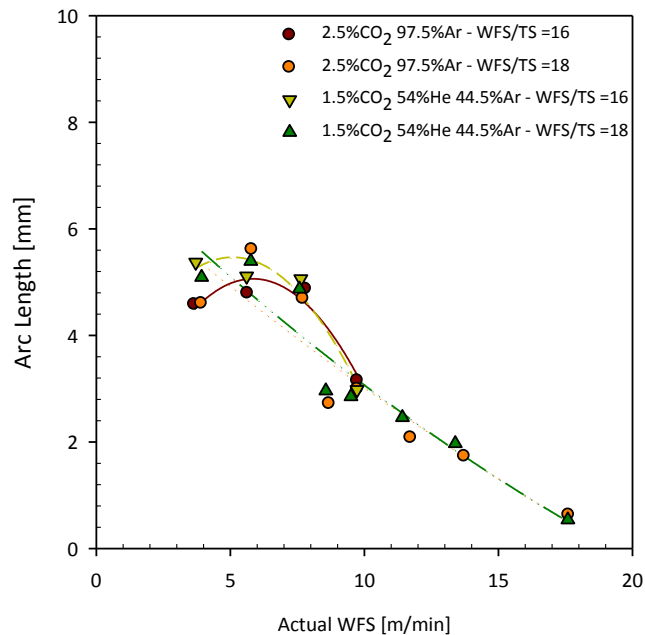


Figure 2.42 – Comparison of the variation of arc length with actual WFS (measured) for RapidArc for different shielding gases and WFS/TS ratios.

The results demonstrate that RapidArc, CMT and CMT-P present significantly high arc length values, around 4mm. GMAW-P presents values around 3mm, while for FastROOT and STT the lowest values are identified, around 2mm. As observed, the most significant variations of arc length are identified for the processes where pulse spray transfer mode is identified.

It is also noticed that, in general, short-circuiting transfer waveforms presents a much lower arc length than spray transfer waveforms. However, CMT is an exception to this observation, and the synchronization between short-circuiting transfer with high arc length levels results from the automatic wire feed speed control system, where wire feeding and retracting controls arc length.

The analysis of the effect of different setting parameters on arc length was analysed for all waveforms, respectively the arc length adjusting parameter, CTWD and shielding gas composition.

The variation of arc length with arc length adjusting parameter was compared for all waveforms using a bar graph with the average and RMS variation of several measurements, in five steps, from the lower to the upper limits (Figure 2.43). The results show that variations of arc length are more significant for RapidArc, CMT-P and GMAW-P, and these waveforms are characterized by spray transfer mechanism. For the waveforms characterized by short-circuiting, i.e. CMT, STT and FastROOT, no significant variations of arc length are observed. It is observed that the shielding gas has often a significant effect on arc length, increasing when 1.5%CO₂ 54%He 44.5%Ar is applied. This effect has been identified in the literature and result from the properties of the gas mixture, in particular the effect of the ionisation potential and density (Eagar 1981) (Kim 1989) (Modenesi 1990).

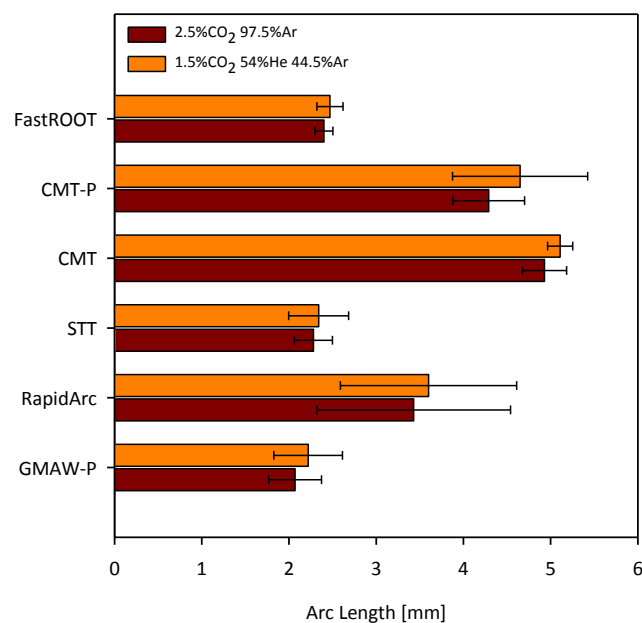


Figure 2.43 – Comparison of average and RMS variation of arc length for all waveforms, obtained by changing the arc length adjusting parameter (in five steps from the minor to upper limits) for two different shielding gases (WFS set of 6m/min).

It has been pointed out that MIG welding is conventionally operated at constant voltage to provide self-adjusting arc length. This self-adjusting results in small fluctuations in arc voltage. In this case, arc current influences the overall process characteristics, in particular the mode of metal transfer, arc stability control and fusion characteristics.

In Pulsed GMAW spray transfer is obtained by an adjustment of both peak current and time to determine at least the desirable one drop per pulse. In this case the mean arc current, obtained from all parameters together must give a burn-off ratio matching wire feed speed, where arc length can be kept approximately constant. If the pulse time or pulse current is inadequate, the arc becomes unstable with consequent variations of arc length and metal

transfer phenomena. This phenomenon will be discussed later but may account for some defects during welding.

It has been pointed out that the increase of arc length is proportional to the increase of arc voltage (American Welding Society 2007). The relationship between arc voltage and arc length was established for all waveforms considering constant wire feed speed (6m/min) and constant arc length correction (nominal values of adjusting arc length parameter). The results demonstrate that arc length in general increases with the increase of arc voltage (Figures 2.44 and 2.45).

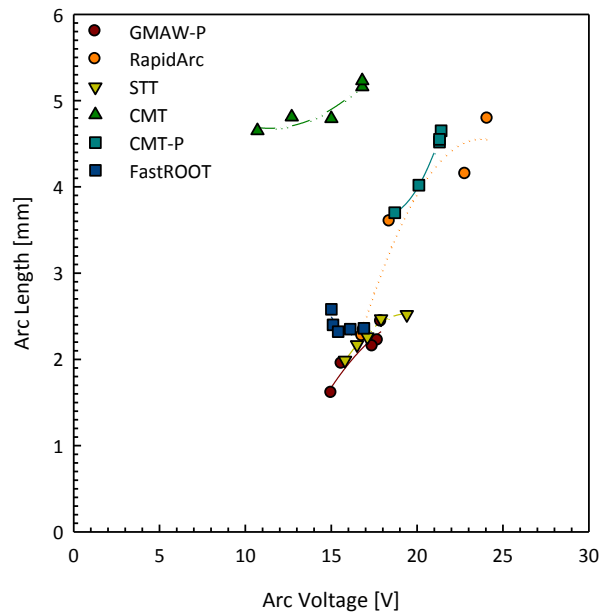


Figure 2.44 – Comparison of the variation of arc length with the arc voltage, obtained when arc length adjusting parameter was varied in five steps from the lower to upper limits (WFS set of 6m/min).

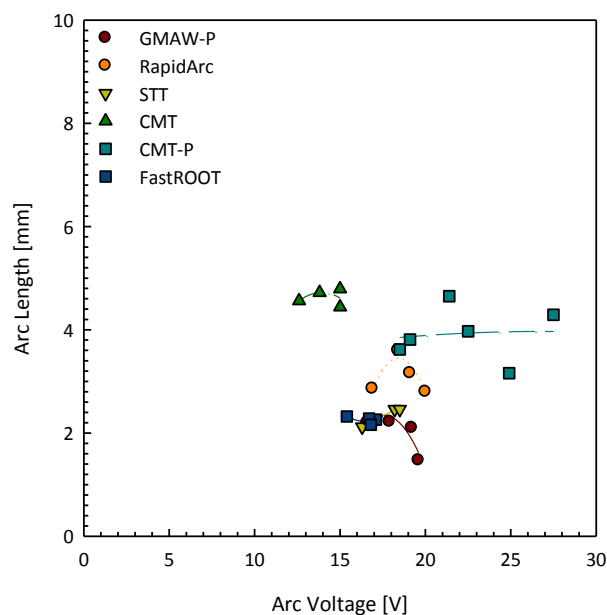


Figure 2.45 – Comparison of the variation of arc length with the arc voltage obtained when WFS set was varied from low (around 3-4m/min) to high levels (around 8-10m/min) using nominal arc length adjusting parameters for all waveforms.

The arc voltage increases with arc length adjusting parameter, but not significantly, for most of the processes evaluated (Figure 2.44). However, this behaviour is not observed for RapidArc, where the variation of trim from lower to upper limits produced a significant increase of the arc length comparable to the increase of arc voltage. Within these results it is found that the variation of arc length is generally smaller, less than 1mm for most of the waveforms. Larger variations are however verified for the RapidArc waveform, about 3mm. However, the small variations of arc length are enough to generate important variations in arc and waveform characteristics, which can account for significant changes in melting phenomena and resulting bead shape geometry.

It was shown that, in general, the increase of CTWD increases the arc length. However, this behaviour depends on the power source characteristics, waveform design and WFS level applied. The effect of CTWD on arc length was assessed for three levels (11, 13.5 and 16mm); average and RMS variation were calculated and the results presented in bar graphs (Figure 2.45). As observed from the results illustrated in the Figure 2.46, the effect of CTWD on the arc length is much significant for RapidArc and GMAW-P. However, it should be noticed that these variations are applied for 6m/min (WFS set). The variation of arc length associated with the CTWD for RapidArc suggests that this process works in controlled current (CC) mode, while the remaining processes appear to operate in controlled voltage (CV) mode, with self adjusting of stick out when CTWD is varied.

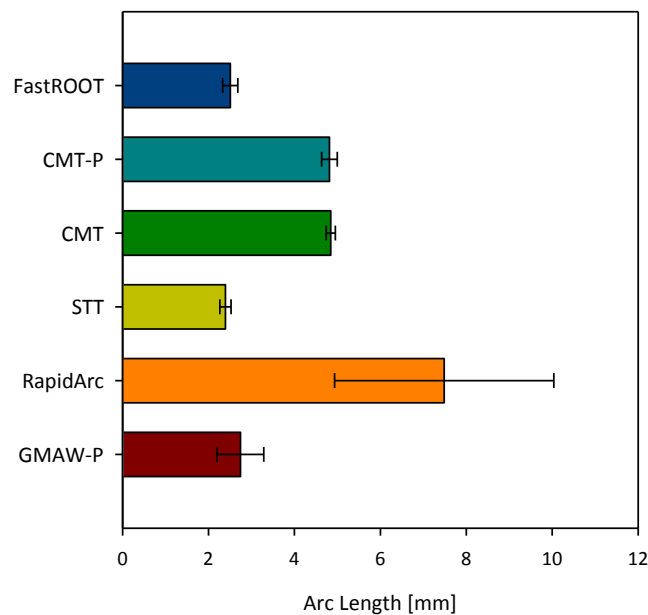


Figure 2.46 – Comparison of the average and RMS variation of arc length for all waveforms, obtained by changing CTWD (at three levels: 11, 13.5 and 16mm) (WFS set of 6m/min).

From the results presented in Appendix VI is observed that at high WFS levels, arc length varies more significantly (i.e., about 4mm difference from 11mm to 16mm CTWD when WFS set was 10m/min) with CTWD for CMT-P. In contrast, for RapidArc this variation is more significant at lower wire feed speed levels (i.e., 4mm difference between 11 and 16mm CTWD for 4 and 6m/min), rather than at high WFS (2.5mm difference for 8m/min and 1mm difference for 10m/min).

2.4.4. Analysis of Metal Transfer

The mechanism of metal transfer in arc welding depends on several factors, where the arc current and voltage waveform designs play an important role. The analyses of metal transfer were carried out using synchronized arc current and voltage waveforms with high speed video-images. In parallel to the metal transfer characterization, the arc stability phenomena associated with the transfer mechanism will be analysed. However, most detailed analyses of arc stability associated with the waveform cycle performance will be presented in the next section of this chapter (Section 2.4.5).

The effect of welding setting parameters was investigated and the experimental conditions applied (unless otherwise indicated) were presented in Section 2.4.1. The results obtained will be presented in the next subsections according to the welding process evaluated.

2.4.4.1. Characterization of the Mechanism of Metal Transfer for GMAW-P

The synchronized tests analysed for GMAW-P are summarized in the Table 2.15, below.

Table 2.15 – Summary of the welding setting process conditions analysed for GMAW-P.

Run	WFS [m/min]	WFS/TS Ratio	Trim	Shielding Gas Composition	CTWD [mm]
BG06	6	16	0.5	2.5%CO ₂ 97.5%Ar	11
BG08	6	16	1.0	2.5%CO ₂ 97.5%Ar	11
BG10	6	16	1.5	2.5%CO ₂ 97.5%Ar	11
BG15	8	16	1.5	2.5%CO ₂ 97.5%Ar	11
BG20	10	16	1.5	2.5%CO ₂ 97.5%Ar	11
BG42	6	16	1.5	1.5% CO ₂ 54%He 44.5%Ar	11
BG47	8	16	1.5	1.5% CO ₂ 54%He 44.5%Ar	11
BG52	10	16	1.5	1.5% CO ₂ 54%He 44.5%Ar	11
BG22	6	18	1.5	2.5%CO ₂ 97.5%Ar	11
BG23	8	18	1.5	2.5%CO ₂ 97.5%Ar	11
BG24	10	18	1.5	2.5%CO ₂ 97.5%Ar	11
BG26	6	16	1.5	2.5%CO ₂ 97.5%Ar	13.5
BG30	6	16	1.5	2.5%CO ₂ 97.5%Ar	16

A summary of the main observations obtained in the characterization of the metal transfer and waveform cycle performance are presented in the Table 2.16. The mechanism of metal transfer identified for GMAW-P is mainly characterized by pulse spray transfer and uncontrolled short-circuiting. The short-circuiting can occur associated with the process parameters applied and result from an unstable phenomenon. The classification of the short-circuiting level is based on the analysis of synchronized waveform and high speed images, as presented in Appendix VIII.

Table 2.16 – Summary of metal transfer and arc stability results obtained for GMAW-P.

Run	Setting Parameters (main variations)	Short-Circuiting Level	Observations
BG06	WFS 6m/min Trim 0.50	High	Arc voltage and current waveform high instability. Very short arc length. Uncontrolled short-circuiting phenomenon characterized by splashing and explosion mechanisms.
BG08	WFS 6m/min Trim 1.0	Moderate/ High	Arc current generally stable. Arc voltage instability. Short arc length. Uncontrolled short-circuiting phenomenon (to see Figure 2.47).
BG10	WFS 6m/min Trim 1.5	Moderate/ High	Similar to BG08
BG15	WFS 8.0m/min	Moderate/ High	Similar to BG10
BG20	WFS 10m/min	High	Arc length is shorter than GB15. Frequency of uncontrolled short-circuiting increases.
BG42	WFS 6m/min 1.5%CO ₂ 54%He 44.5%Ar	Moderate/ High	Similar to BG10. Higher arc voltage level.
BG47	WFS 8m/min 1.5%CO ₂ 54%He 44.5%Ar	Moderate/ High	Similar to BG15. Higher arc voltage level (to see Figure 2.48 and 2.49).
BG52	WFS 10m/min 1.5%CO ₂ 54%He 44.5%Ar	High	Similar to BG20. Higher arc voltage level.
BG22	WFS 6.0m/min WFS/TS ratio 18	Moderate	The lower welding speed, compared with BG10, results in a slight increase in arc stability phenomena.
BG23	WFS 10m/min WFS/TS ratio 18	Moderate	Similar to BG22
BG24	WFS 10m/min WFS/TS ratio 18	Moderate/ High	The lower welding speed, compared with BG20, results in a slight increase in arc stability phenomena.
BG26	CTWD 13.5mm	Low	The higher CTWD, compared with BG10, results in a decrease in short-circuiting phenomena. Higher Arc stability and transfer.
BG30	CTWD 16.0mm	Low	Almost no short-circuiting phenomena observed. Higher arc stability and transfer phenomena (to see Figure 2.50).

Short-circuiting level: High (>50%); Moderate (25-50%); Low (<25%) (The percentage is relative to the ratio of short-circuiting compared with pulse spray transfer).

According with the results obtained a representative example of the mechanism of transfer for GMAW-P is illustrated, for the test BG08, in the Figure 2.47.

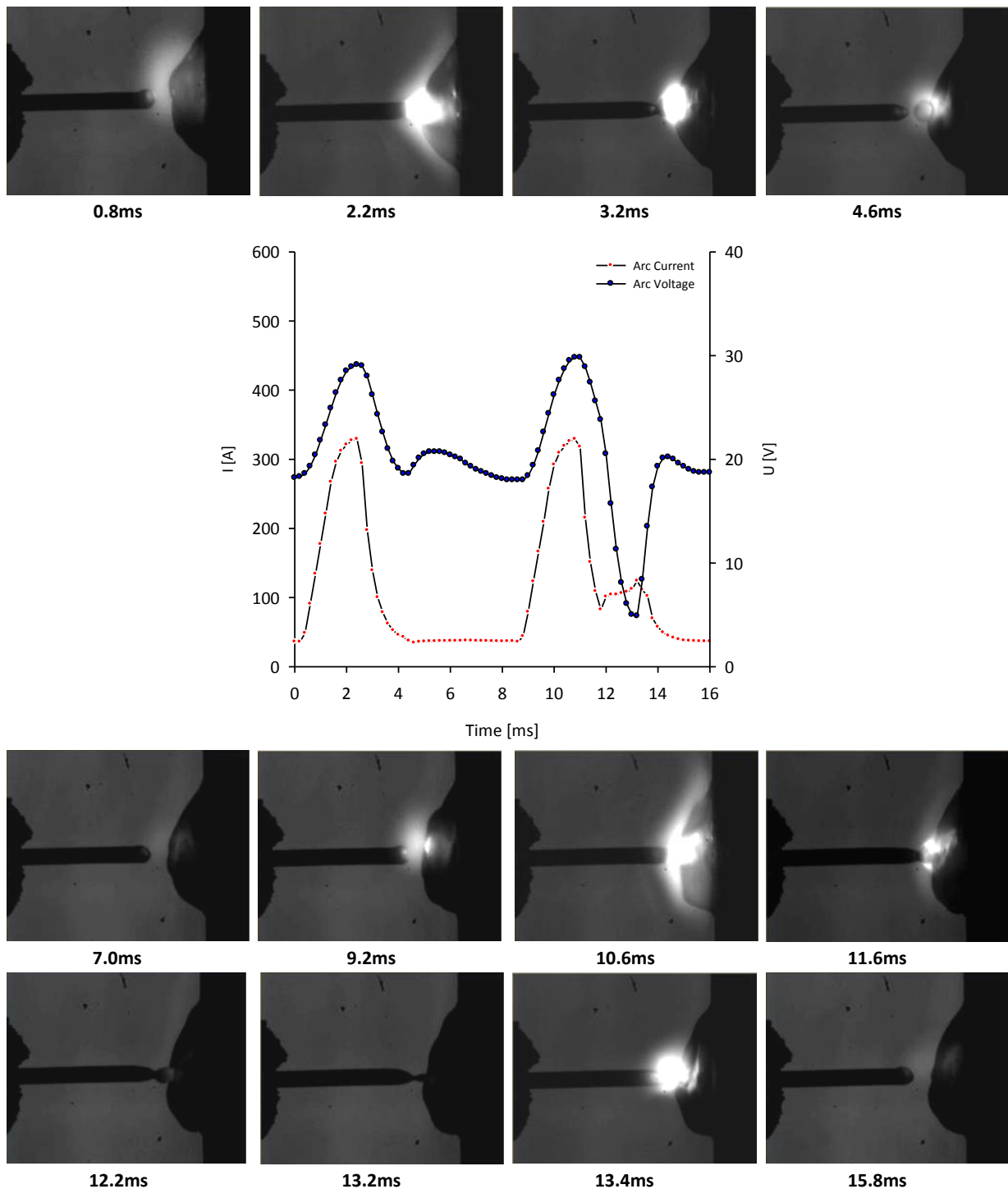


Figure 2.47 – Synchronized arc current and voltage waveforms with high speed video-images obtained from GMAW-P for test BG08.

The period of the waveform illustrated in the Figure 2.45 illustrates the two typical phenomena occurring in the mechanism of transfer of GMAW-P analysed. As observed in the Figure 2.45, the mechanism of transfer in GMAW-P can be characterized by the peak and background periods. At 2.2ms the arc energy is maximum resulting from the arc

operating at the peak current and voltage levels. From this instant of time until 4.6ms, the droplet transfer mechanism starts, with decreasing of arc current and voltage until the background levels. The droplet transfer phenomenon takes place at this instant of time, when arc current and voltage reach their minimum. At 8.6ms a new cycle started, with increase of arc current and voltage levels until their peak values. However, the voltage now falls, with a slight increase of arc current (due to the dynamics control of the power source), indicative of an uncontrolled short-circuiting transfer mechanism, associated with bridge effect, as can be observed from the images at 12.2 to 13.2ms. At 13.4ms the voltage increase again and an unstable re-ignition can be observed.

Other unstable mechanisms have been identified, as illustrated in the Figure 2.48 and 2.49, obtained from the test BG47.

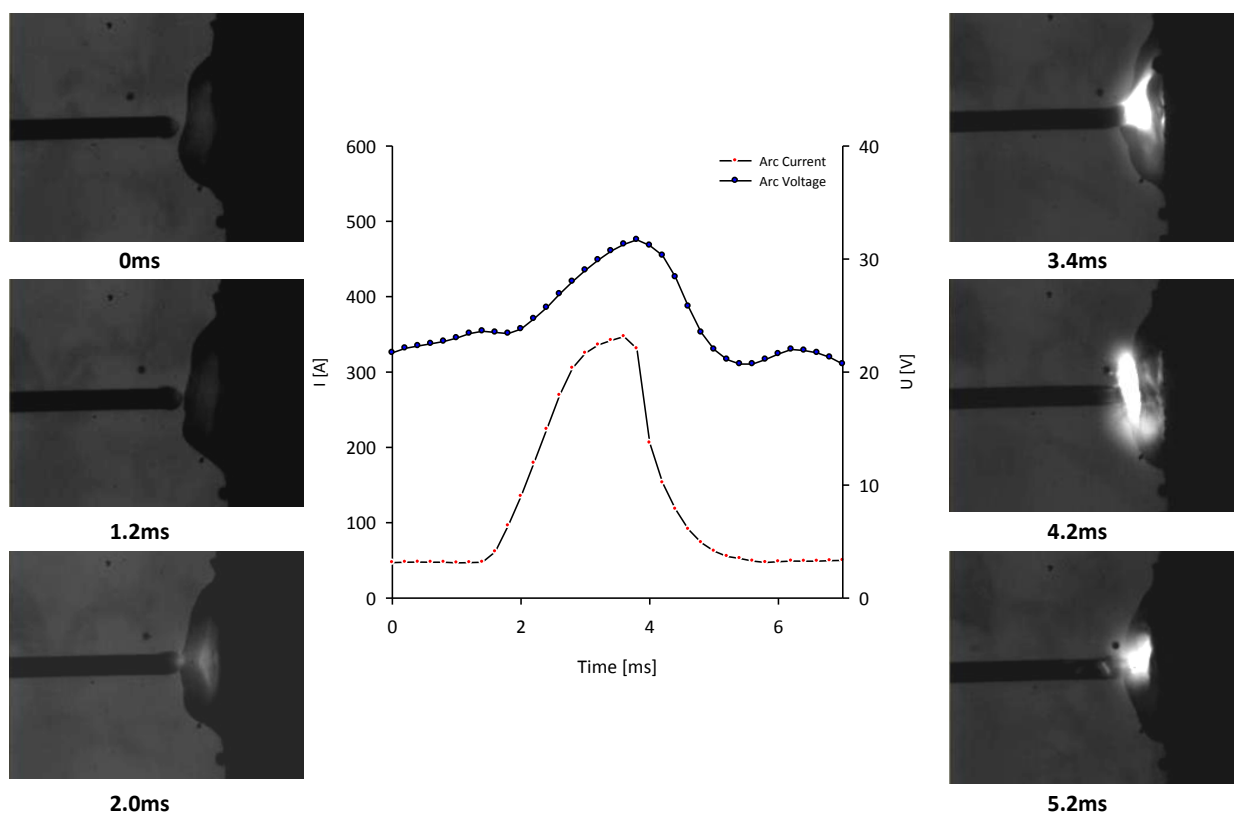


Figure 2.48 – Synchronized arc current and voltage waveforms with high speed video-images obtained for GMAW-P (test BG42).

In the Figure 2.48 instability is associated with the short arc length causing an explosion disturbance. The long tail-out effect on the arc current waveform should also be noticed.

Figure 2.49 shows another disturbance phenomena associated with the formation of a globular droplet, at very short arc length, which causes explosion and splashing behaviour during the transfer mechanism.

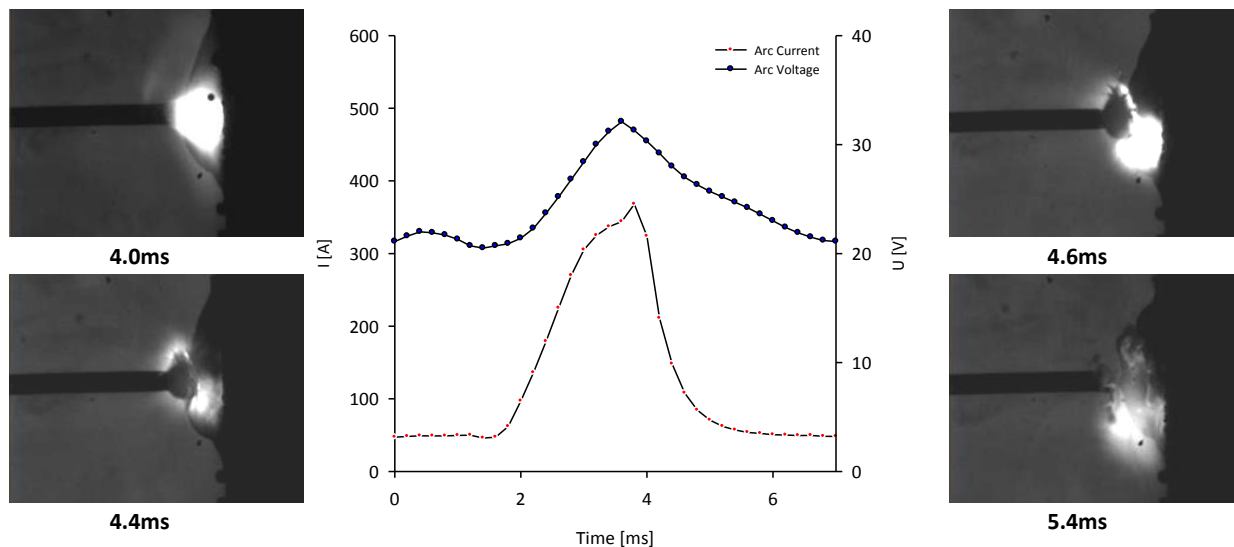


Figure 2.49 – Synchronized arc current and voltage waveforms with high speed video-images obtained for GMAW-P (test BG42).

The Figure 2.50 shows the transfer mechanism obtained for the test BG30 (CTWD of 16mm). The increase of CTWD is associated with an increase of arc length, which produces a much more stable droplet transfer mechanism, where uncontrolled short-circuiting is reduced. However, occasional unstable phenomena are still observed, characterized by arc splashing (see image at 3.6ms), which results in an increase in arc voltage at the moment of transfer.

2.4.4.2. Characterization of the Mechanism of Metal Transfer for RapidArc

A summary of the welding conditions studied for RapidArc are presented in the Table 2.17.

Table 2.17 – Summary of the welding setting process conditions analysed for RapidArc.

Run	WFS [m/min]	WFS/TS Ratio	Trim	Shielding Gas Composition	CTWD [mm]
BR06	6	16	0.5	2.5%CO ₂ 97.5%Ar	11
BR08	6	16	1.0	2.5%CO ₂ 97.5%Ar	11
BR10	6	16	1.5	2.5%CO ₂ 97.5%Ar	11
BR15	8	16	1.5	2.5%CO ₂ 97.5%Ar	11
BR20	10	16	1.5	2.5%CO ₂ 97.5%Ar	11
BR46	6	16	1.5	1.5% CO ₂ 54%He 44.5%Ar	11
BR51	8	16	1.5	1.5% CO ₂ 54%He 44.5%Ar	11
BR56	10	16	1.5	1.5% CO ₂ 54%He 44.5%Ar	11
BR22	6	18	1.5	2.5%CO ₂ 97.5%Ar	11
BR23	8	18	1.5	2.5%CO ₂ 97.5%Ar	11
BR25	10	18	1.5	2.5%CO ₂ 97.5%Ar	11
BR30	6	16	1.5	2.5%CO ₂ 97.5%Ar	13.5
BR34	6	16	1.5	2.5%CO ₂ 97.5%Ar	16

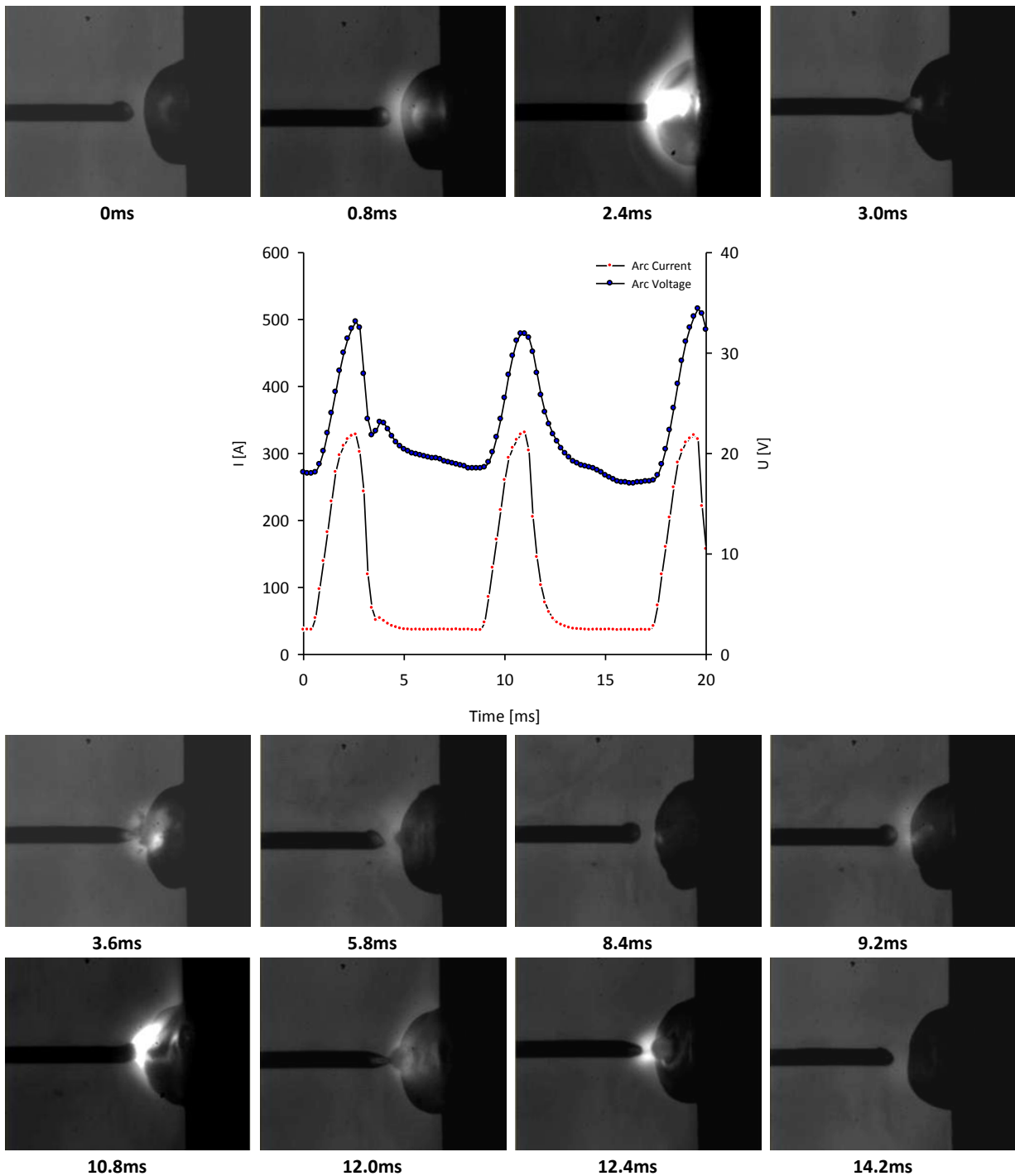


Figure 2.50 – Synchronized arc current and voltage waveforms with high speed video-images obtained to GMAW-P (BG30).

The results obtained from the analysis of the metal transfer and waveform signal for RapidArc are summarized in the Table 2.18. RapidArc is characterized by a pulse spray mechanism; therefore when short-circuiting mechanism is identified, it is due to an unstable phenomenon. The classification of the short-circuiting level is based on the analysis of synchronized waveform with high speed video-images and supported by the observation of the waveforms signal, presented in Appendix VIII.

Table 2.18 – Summary of metal transfer and arc stability results obtained for RapidArc.

Run	Setting Parameters (main variations)	Short-Circuiting Level	Observations
BR06	WFS 6m/min Trim 0.50	High	Very high instability associated with very short arc length. Uncontrolled short-circuiting phenomenon. Pulse spray transfer is not observed (to see Figure 2.52).
BR08	WFS 6m/min Trim 1.0	High	Short arc length also favourable to the arc instability phenomenon. Remains occasional short-circuiting, but arc stability is slightly better, when compared to the BR06.
BR10	WFS 6m/min Trim 1.5	-	High arc stability. Higher arc length compared with BG06 and BG08. Mechanism of transfer characterized by pulse spray (> ODPP).
BR15	WFS 8.0m/min	-	Similar to BR10
BR20	WFS 10m/min	Low/ Moderate	The instability is higher than BR10 and BR15. Shorter arc length. Pulse Spray transfer is achieved, as the background current is too high to generate short-circuiting transfer. Stubbing phenomena (explosions).
BR46	WFS 6m/min 1.5%CO ₂ 54%He 44.5%Ar	-	Similar to BR10.
BR51	WFS 8m/min 1.5%CO ₂ 54%He 44.5%Ar	-	Similar to BR15.
BR56	WFS 10m/min 1.5%CO ₂ 54%He 44.5%Ar	Low/ Moderate	Similar to BR20 (to see Figure 2.53).
BR22	WFS 6.0m/min WFS/TS ratio 18	-	Similar to BR10 (to see Figure 2.51).
BR23	WFS 10m/min WFS/TS ratio 18	-	Similar to BR23.
BR25	WFS 10m/min WFS/TS ratio 18	Low/ Moderate	Similar to BR20.
BR30	CTWD 13.5mm	-	Arc length higher than BR10. Very high arc stability. Occasional drops bigger than wire diameter size. Mechanism of transfer similar to BR10.
BR34	CTWD 16.0mm	-	Arc length is too long, but very high arc and waveform stability is kept. Before the droplet arrives to the weld pool, the arc ignition occurs.

Short-circuiting level: High (>50%); Moderate (25-50%); Low (<25%) (The percentage is relative to the ratio of short-circuiting compared with pulse spray transfer).

The metal transfer analysed for RapidArc waveforms demonstrates that the droplet transfer is characterized by pulse spray mechanism with a droplet size similar to the size of the wire diameter and followed by a small diameter drop. It is observed that at high CTWD levels the “drop spray” is sometimes followed by more than one small drop.

A representative demonstration of the mechanism observed is illustrated in Figure 2.51, obtained from the test BR22. The mechanism is characterized by a period of peak current, synchronized with the peak voltage, where the droplet is formed and arc energy is higher, followed by a decrease in the arc voltage and current, which promote the drop detachment and transfer. After the droplet is transferred to the weld pool, the arc is not completely extinguished, but is kept at low energy level, with the arc current at the background level.

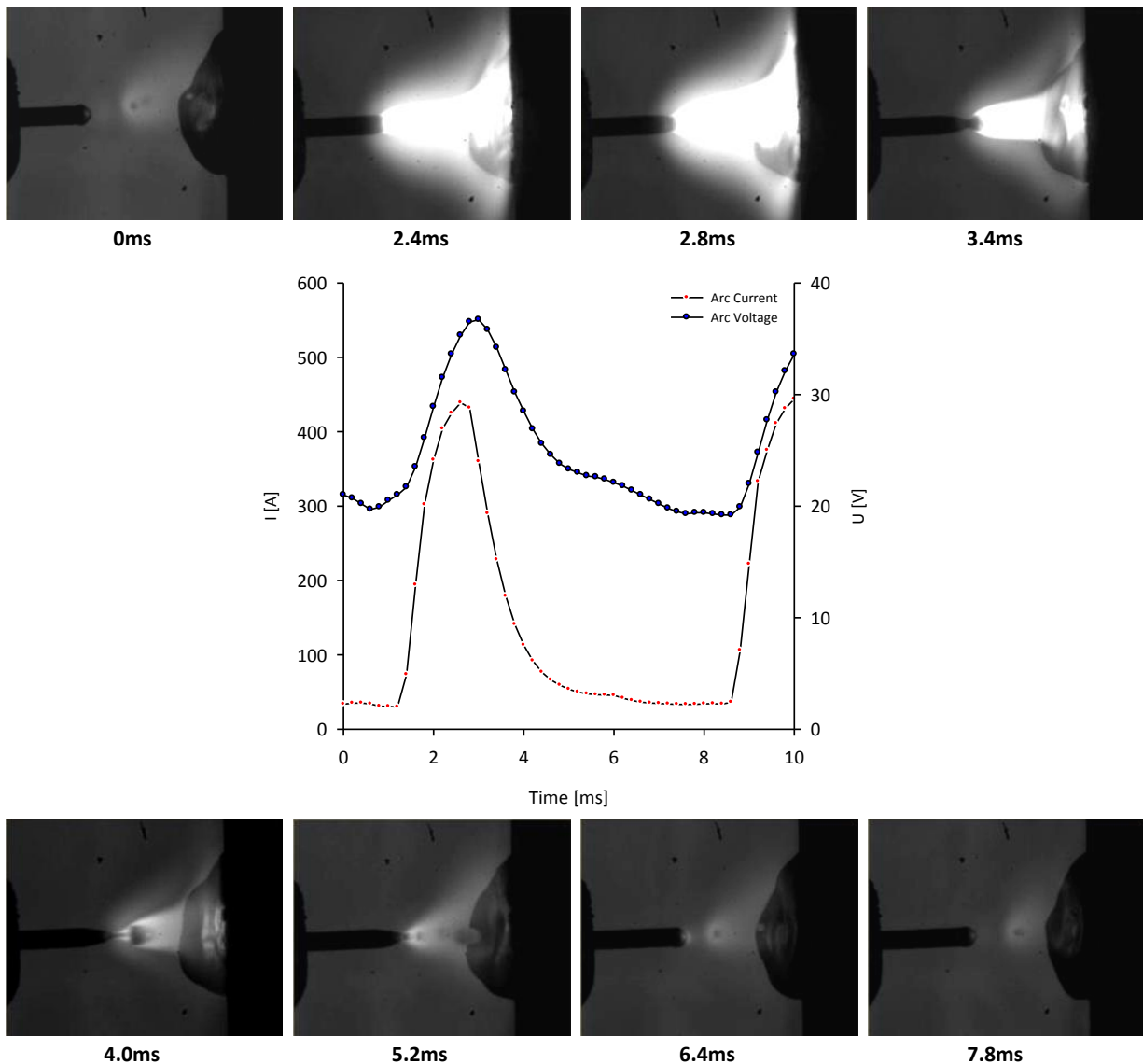


Figure 2.51 – Synchronized arc current and voltage waveforms with high speed video-images obtained for RapidArc (test BR22).

The unstable mechanisms observed for the welding setting parameters analysed are associated with:

- Arc voltage drop, when arc length is too short (trim values at low level) (Figure 2.52);
- Arc stubbing (explosions) due to the voltage slope phenomenon when high current levels were applied (when WFS of 10m/min was applied) and low arc length (Figure 2.53).

Both these two phenomena increase the probability of occurrence for unstable short-circuiting mechanisms.

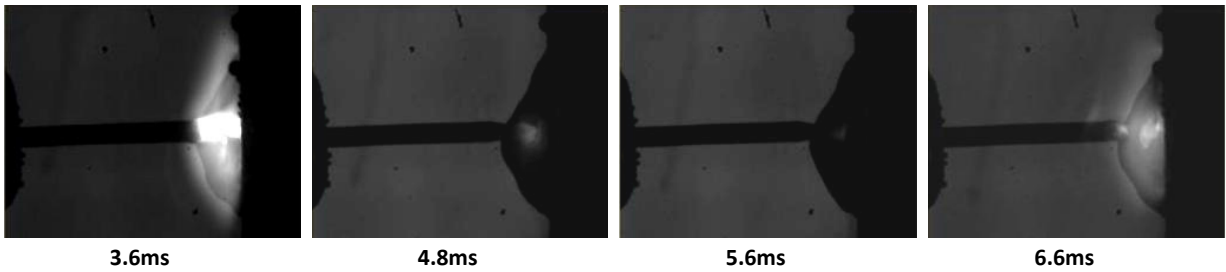
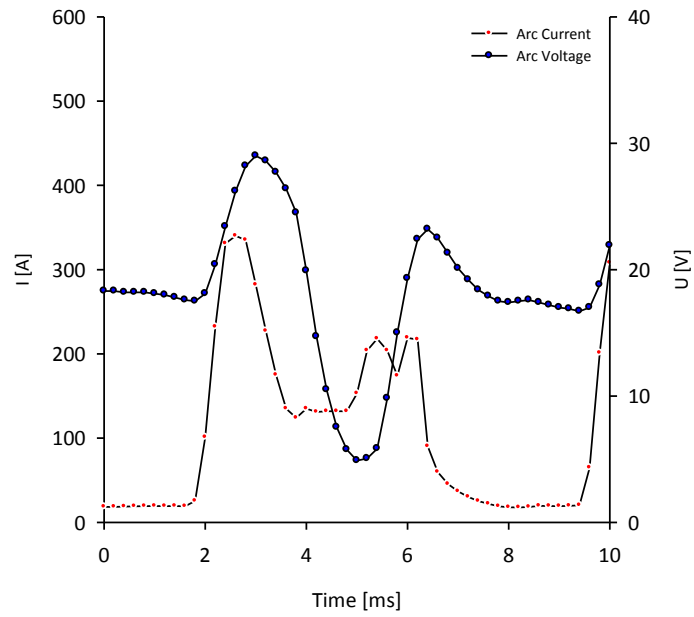
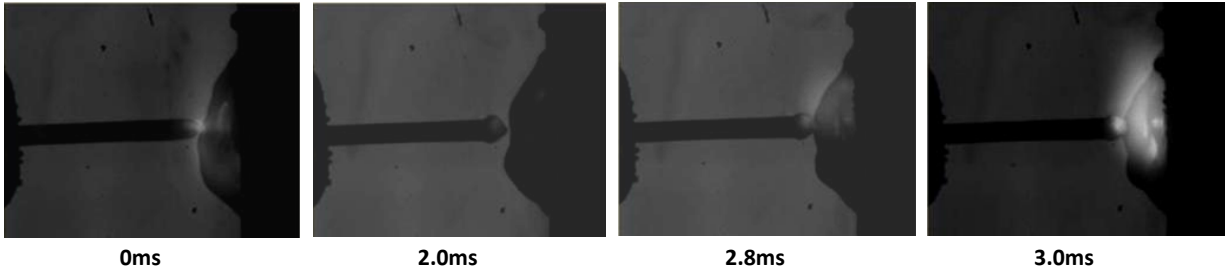


Figure 2.52 – Synchronized arc current and voltage waveforms with the high speed video-images obtained for RapidArc (BR06).

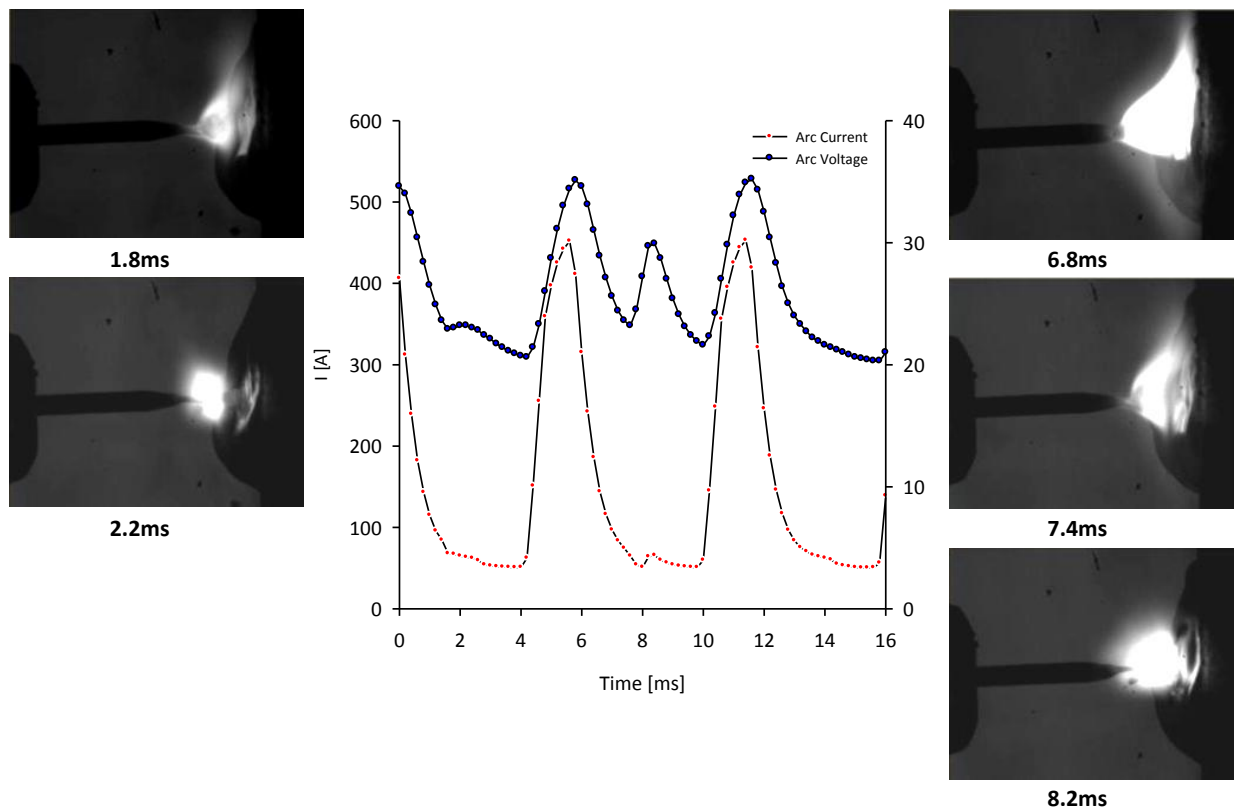


Figure 2.53 – Synchronized arc current and voltage waveforms with high speed video-images obtained for RapidArc (BR56).

2.4.4.3. Characterization of the Mechanism of Metal Transfer for STT

A summary of the welding conditions studied for STT are presented in the Table 2.19.

Table 2.19 – Summary of the welding setting process conditions analysed for STT.

Run	WFS [m/min]	WFS/TS Ratio	Trim	Shielding Gas Composition	CTWD [mm]
BS06	6	16	0.5	2.5%CO ₂ 97.5%Ar	11
BS08	6	16	1.0	2.5%CO ₂ 97.5%Ar	11
BS10	6	16	1.5	2.5%CO ₂ 97.5%Ar	11
BS13	8	16	1.0	2.5%CO ₂ 97.5%Ar	11
BS18	8.26	16	1.0	2.5%CO ₂ 97.5%Ar	11
BS40	6	16	1.0	1.5% CO ₂ 54%He 44.5%Ar	11
BS45	8	16	1.0	1.5% CO ₂ 54%He 44.5%Ar	11
BS50	8.26	16	1.0	1.5% CO ₂ 54%He 44.5%Ar	11
BS22	6	18	1.0	2.5%CO ₂ 97.5%Ar	11
BS23	8	18	1.0	2.5%CO ₂ 97.5%Ar	11
BS24	8.26	18	1.0	2.5%CO ₂ 97.5%Ar	11
BS26	6	16	1.0	2.5%CO ₂ 97.5%Ar	13.5
BS30	6	16	1.0	2.5%CO ₂ 97.5%Ar	16

The analysis of the results of the metal transfer and the waveform signal are summarized in the Table 2.20. The evaluation of waveform signal was based on the waveforms presented

in the Appendix VIII. The results obtained demonstrate that STT is characterized by a mechanism of controlled dip transfer (short-circuiting).

Table 2.20 – Summary of metal transfer and arc stability results obtained for STT.

Run	Setting Parameters (main variations)	Observations
BS06	WFS 6.0 m/min Trim 0.50	Very short arc length. Splashing (explosion effect) associated with the arc re-ignition – broken bridge. Overall instability in background times.
BS08	WFS 6.0 m/min Trim 1.0	Similar to BS06. Stability slightly higher.
BS10	WFS 6.0 m/min Trim 1.5	Mechanism of transfer is frequently alternated by globular formation. Longer arc length. Higher Instability level characterized by splashing (to see Figure 2.55).
BS13	WFS 8.0 m/min	Similar to BS08, but with higher arc instability associated with shorter arc length and high arc current level/ long background period (to see Figure 2.54).
BS18	WFS 8.26 m/min	Instability is higher than BS13. Occasional droplet transfer mechanism (with diameter size similar to the wire diameter). Short arc length level responsible by splashing disturbances.
BS40	WFS 6 m/min 1.5%CO ₂ 54%He 44.5%Ar	Similar to BS08.
BS45	WFS 8 m/min 1.5%CO ₂ 54%He 44.5%Ar	Similar to BS13
BS50	WFS 8.26 m/min 1.5%CO ₂ 54%He 44.5%Ar	Similar to BS18
BS22	WFS 6.0m/min WFS/TS ratio 18	Similar to BS08.
BS23	WFS 8.0 m/min WFS/TS ratio 18	Similar to BS13.
BS24	WFS 8.26 m/min WFS/TS ratio 18	Similar to BS18.
BS26	CTWD 13.5mm	Higher arc length than BS08 (to see Figure 2.56).
BS30	CTWD 16.0mm	Similar to BS26. Major effect associated with longer background period.

A representative demonstration of the mechanism of metal transfer observed for STT is shown in Figure 2.54, obtained from the test BS13. The mechanism is characterized by a period of short-circuiting when the voltage drops, from 5.2 to 7.2ms (about 2ms) and followed by the arc ignition, when the bridge is broken, at the peak current (7.4ms). Then, the arc is kept at a low energy stage, with the current at background level and the voltage at stable level. During this period of the droplet is formed and able to be transferred when a new cycle restarts. It is observed that the rupture of the bridge is associated with stubbing and splashing of metal, characterized by an unstable mechanism (8.0 – 8.4ms).

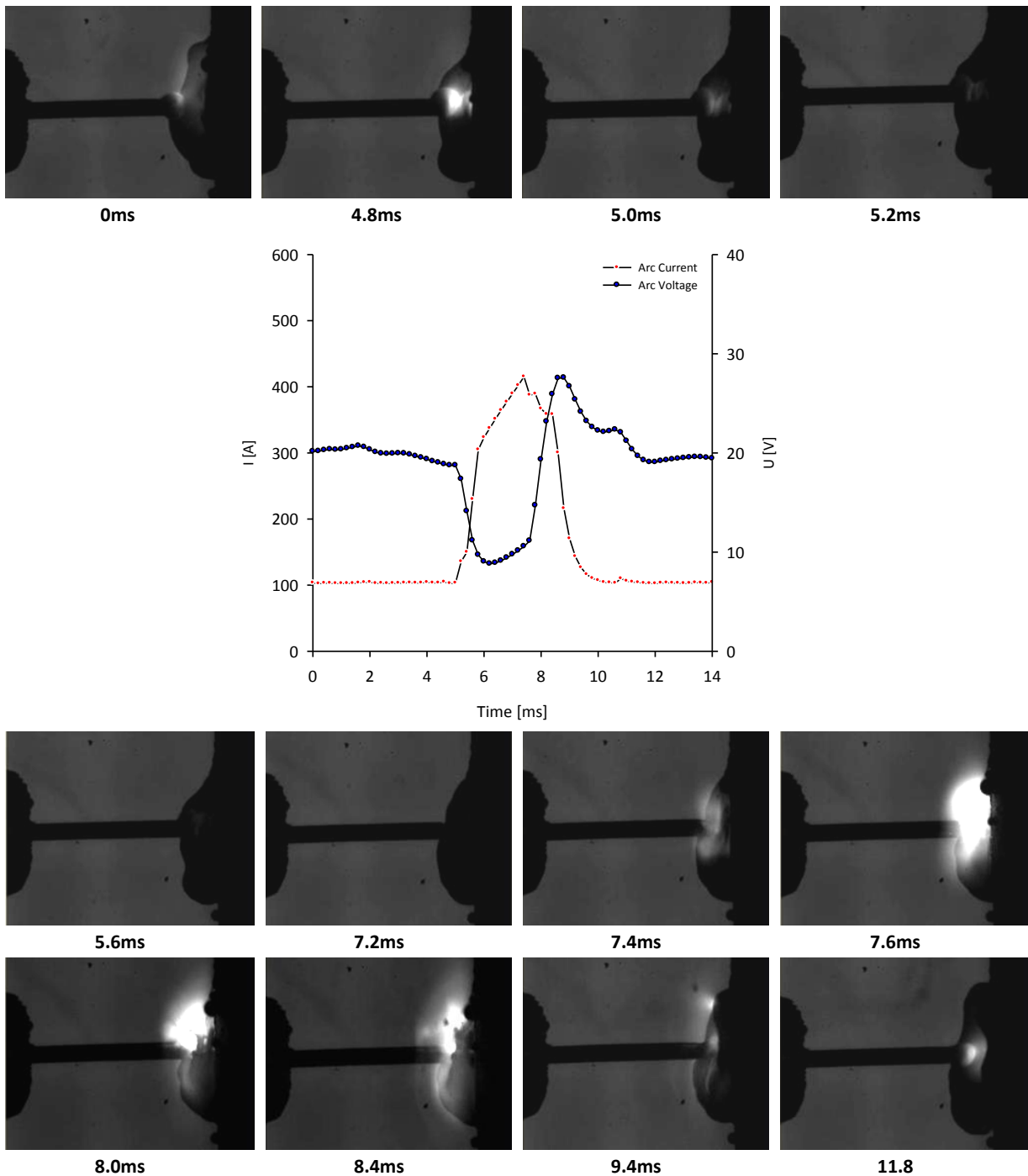


Figure 2.54 – Synchronized arc current and voltage waveforms with high speed video-images obtained for STT (BS13).

At high trim values the arc length is longer and favourable to the droplet transfer mechanism. As illustrated in Figure 2.55, for BS10, a globular transfer takes place. The similar behaviour was observed at high current levels (when high WFS values were applied) but with droplet transfer with size similar to the wire diameter size (drop spray). These phenomena result in an unstable arc behaviour promoting splashing during the metal transfer.

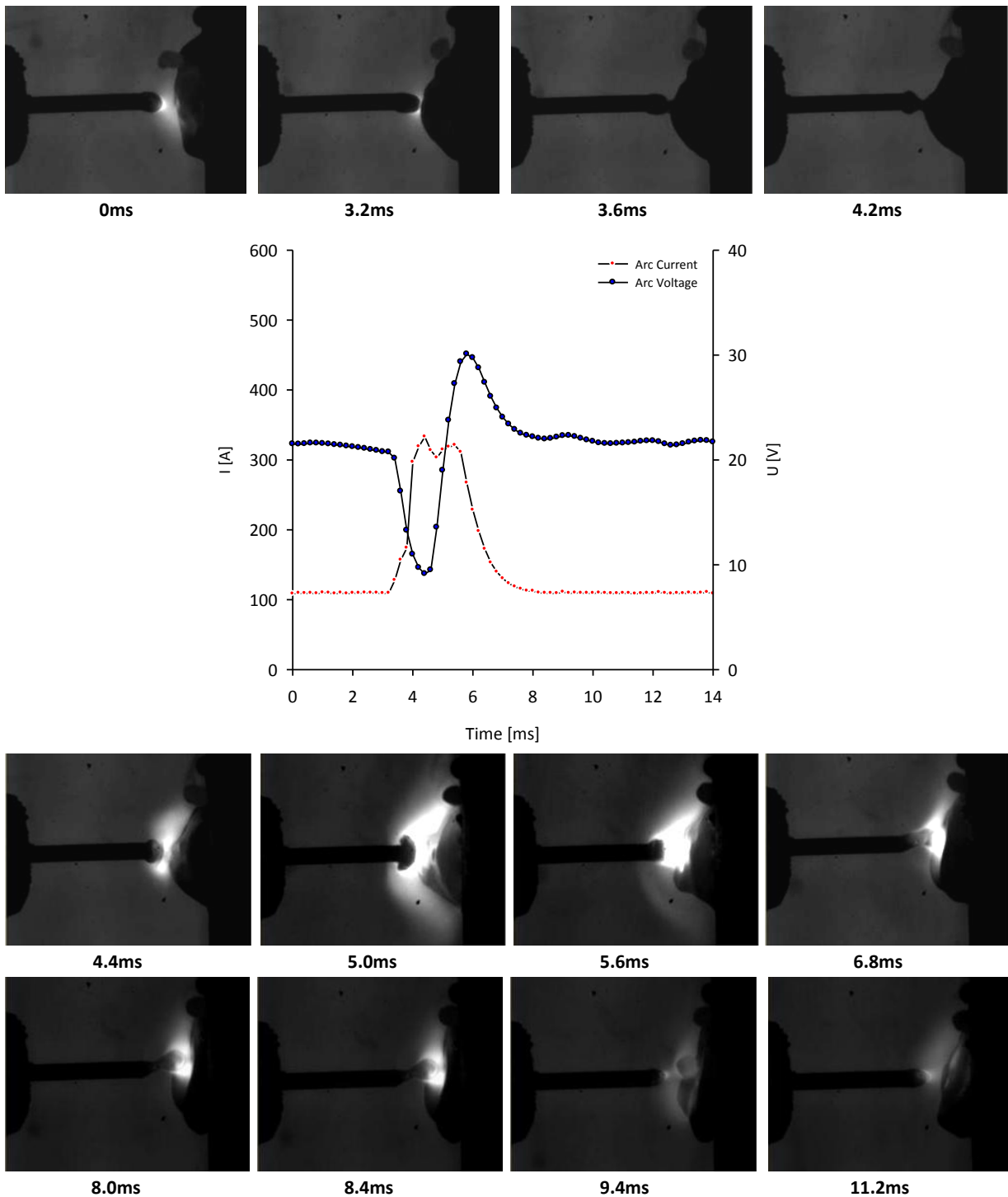


Figure 2.55 – Synchronized arc current and voltage waveforms with high speed video-images obtained for STT (BS10).

When the CTWD was increased (13.5mm and 16mm) the arc length increases and consequently there were conditions which promoted unstable droplet formation and transfer. Figure 2.56, obtained from the test BS26, illustrates this phenomenon.

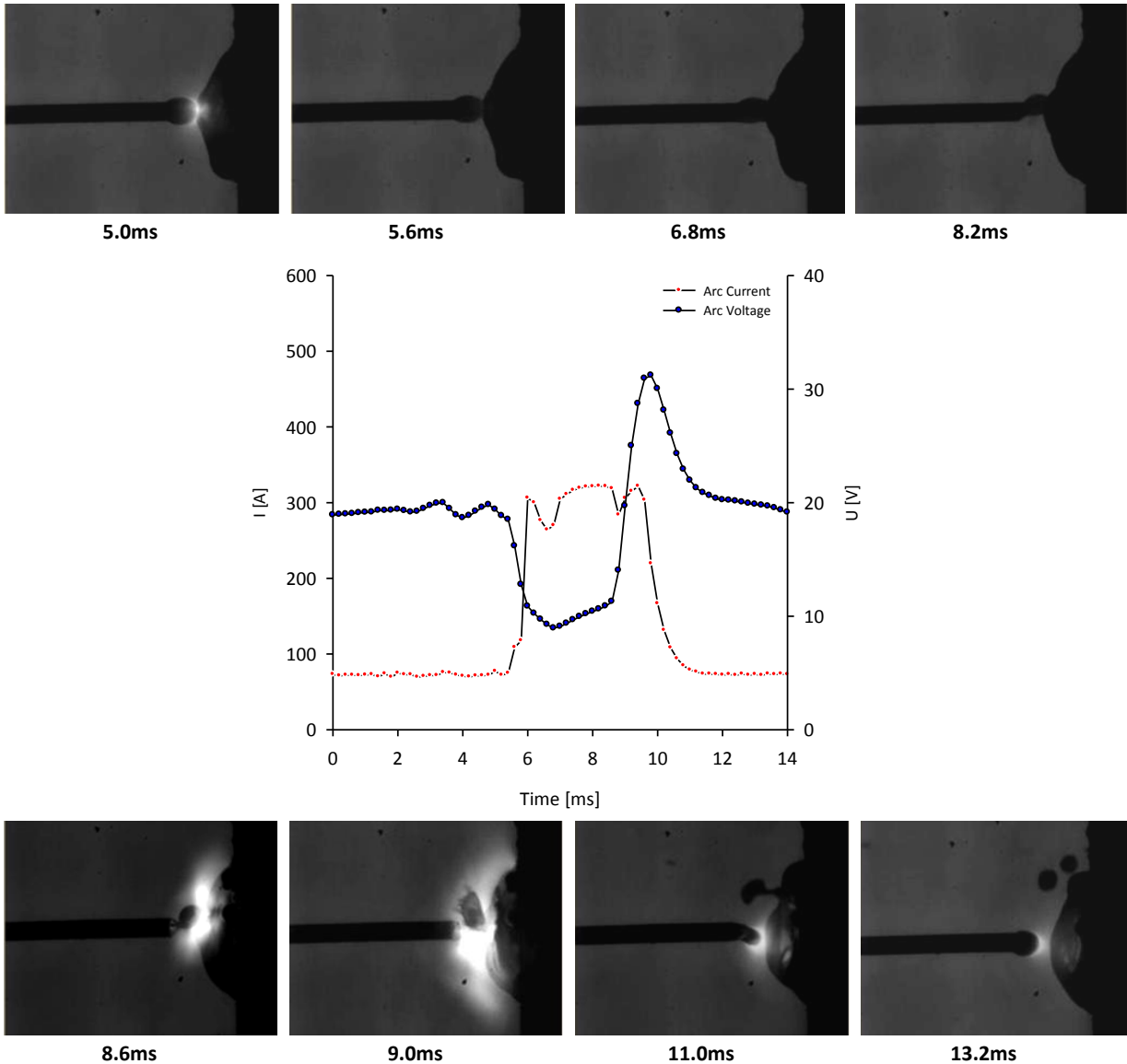


Figure 2.56 – Synchronized arc current and voltage waveforms with high speed video-images obtained for STT (BS26).

2.4.4.4. Characterization of the Mechanism of Metal Transfer for CMT

A summary of the welding conditions investigated for CMT are presented in the Table 2.21.

The analysis of the results of the metal transfer and the waveform signal make possible the observations summarized in Table 2.22. The evaluation of waveform signal was based on the waveforms presented in Appendix VIII. The results obtained demonstrate that CMT is characterized by a mechanism of controlled dip transfer (short-circuiting).

Table 2.21 – Summary of the welding setting process conditions analysed for CMT.

Run	WFS [m/min]	WFS/TS Ratio	ALC [%]	DC [%]	Shielding Gas Composition	CTWD [mm]
BC11	6	16	-30	0	2.5%CO ₂ 97.5%Ar	11
BC13	6	16	0	0	2.5%CO ₂ 97.5%Ar	11
BC15	6	16	30	0	2.5%CO ₂ 97.5%Ar	11
BC18	8	16	0	0	2.5%CO ₂ 97.5%Ar	11
BC61	6	16	0	0	1.5% CO ₂ 54%He 44.5%Ar	11
BC66	8	16	0	0	1.5% CO ₂ 54%He 44.5%Ar	11
BC39	6	18	0	0	2.5%CO ₂ 97.5%Ar	11
BC40	8	18	0	0	2.5%CO ₂ 97.5%Ar	11
BC29	6	16	0	-5	2.5%CO ₂ 97.5%Ar	11
BC32	6	16	0	5	2.5%CO ₂ 97.5%Ar	11
BC43	6	16	0	0	2.5%CO ₂ 97.5%Ar	13.5
BC47	6	16	0	0	2.5%CO ₂ 97.5%Ar	16

Table 2.22 – Summary of metal transfer and arc stability results obtained for CMT.

Run	Setting Parameters (main variations)	Observations
BC11	WFS 6m/min ALC -30%	Stable arc current and voltage waveform.
BC13	WFS 6m/min ALC 0%	Stable arc current and voltage waveform (to see Figure 2.57).
BC15	WFS 6m/min ALC 30%	Arc Instability associated with occasional droplet spray transfer mechanisms. Higher arc voltage and longer arc length. Stable waveform design (to see Figure 2.60).
BC18	WFS 8.0m/min	Arc voltage instability. Splashing and disturbances during the transfer mechanism.
BC61	WFS 6.0 m/min 1.5%CO ₂ 54%He 44.5%Ar	Similar to BC13.
BC66	WFS 8.0 m/min 1.5%CO ₂ 54%He 44.5%Ar	Similar to BC18 (to see Figures 2.58 and 2.59).
BC39	WFS 6.0 m/min WFS/TS ratio 18	Similar to BC13.
BC40	WFS 8.0 m/min WFS/TS ratio 18	Similar to BC18 (to see Figure 2.61).
BC29	DC -5%	Similar to BC13.
BC32	DC 5%	Similar to BC13.
BC43	CTWD 13.5mm	Arc length is larger, but arc stability is similar to BC13.
BC47	CTWD 16.0mm	Arc length is larger, but arc stability is similar to BC13.

As illustrated in Figure 2.57, obtained from the test BC13, the increase of arc current and voltage cause rupture of the molten bridge (2.6ms) and consequently the re-ignition of the arc takes place at the peak current (6 to 8ms). Then, the drop is formed during the period when the arc current and voltage decreases. At the background level the short-circuiting takes place (12ms), coinciding with the forward movement of the wire. The retraction of the filler wire generates a smooth broken bridge and consequently the arc re-ignition (14.8ms).

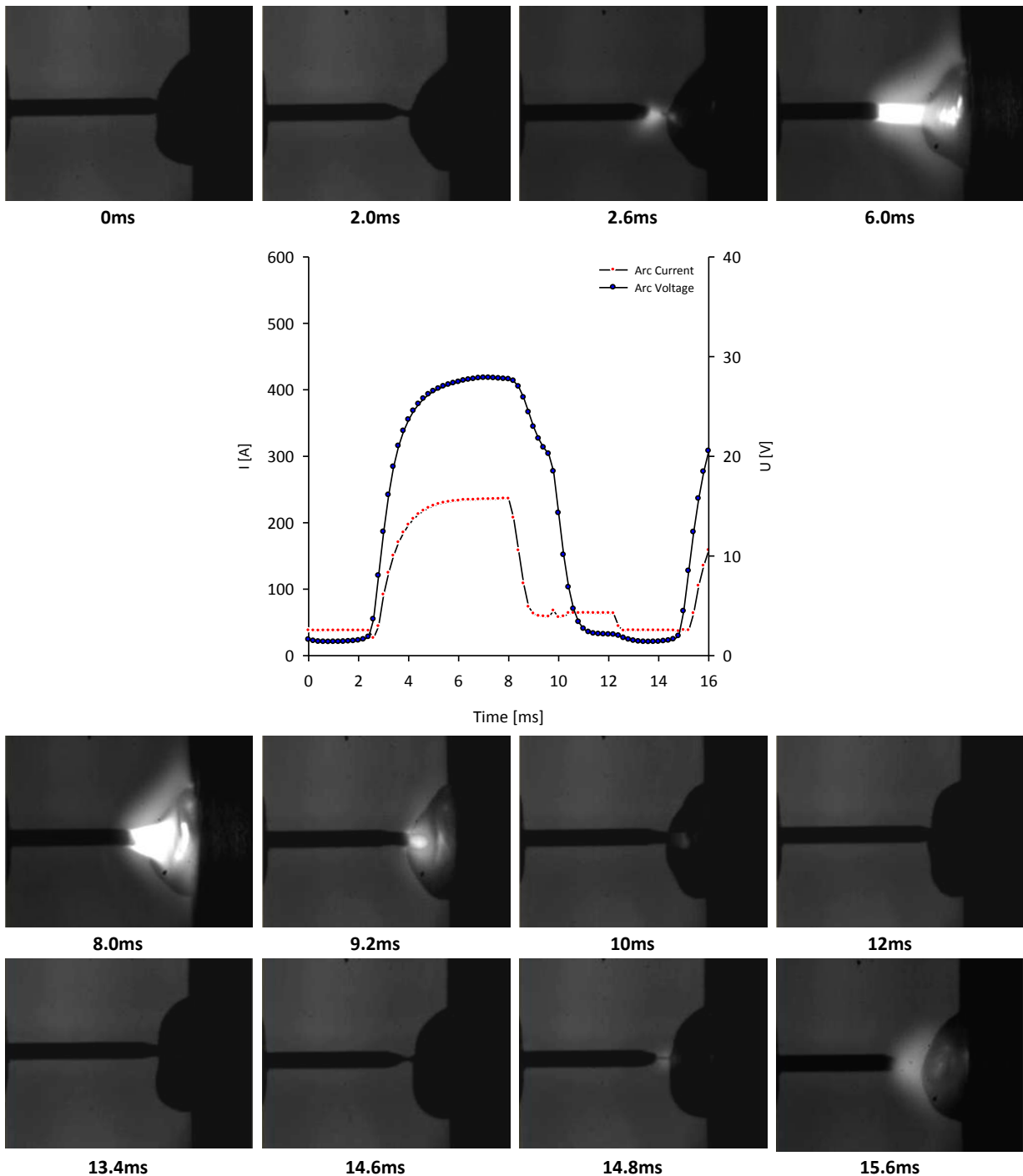


Figure 2.57 – Synchronized arc current and voltage waveforms with high speed video-images obtained for CMT (BC13).

Unstable phenomena were identified for CMT. The conditions that offered more significant disturbances were associated with the high WFS levels (8m/min) and the limits of ALC (-30 and 30%).

At high WFS levels occasional drop spray transfer was observed, instead of short-circuiting mechanism (Figure 2.58). The reason for this unstable behaviour was due to long peak duration time and high arc voltage level achieved. These conditions resulted also in splashing effect (explosions), as illustrated in Figure 2.59.

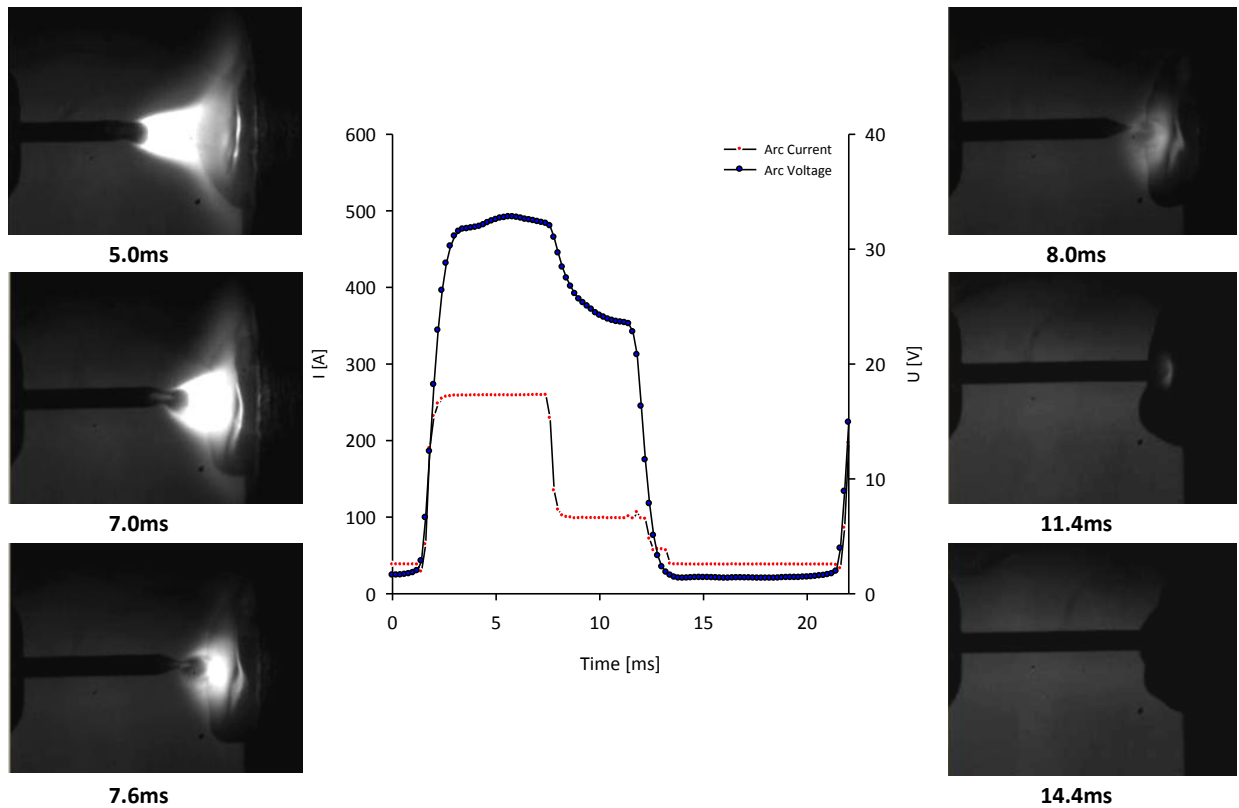


Figure 2.58 – Synchronized arc current and voltage waveforms with high speed video-images obtained for CMT (BC66).

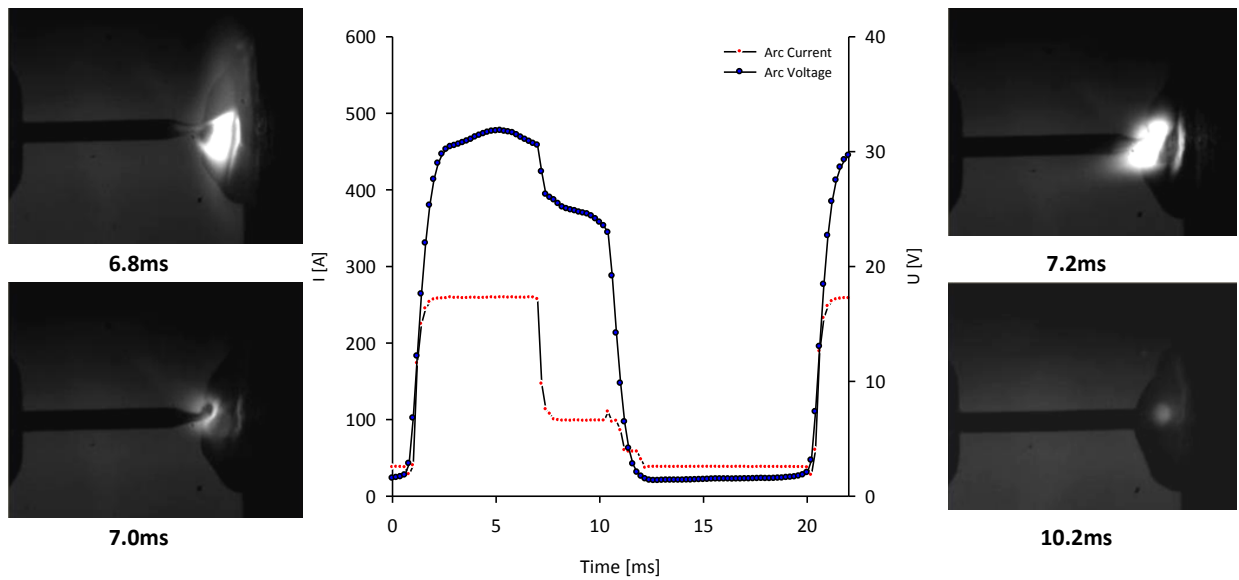


Figure 2.59 – Synchronized arc current and voltage waveforms with high speed video-images obtained for CMT (BC66).

Among the instability phenomena observed, droplet transfer during the low current period generates a change in voltage. This phenomenon was observed at high ALC values characterized by drop spray transfer and at low WFS where occasional globular transfer took place (Figures 2.60 and 2.61).

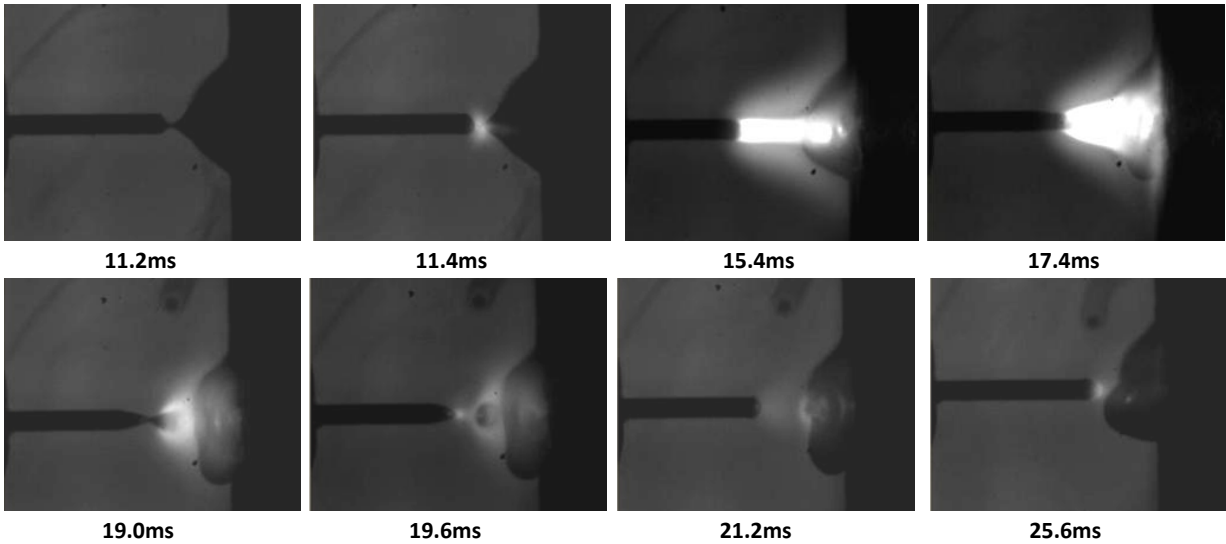
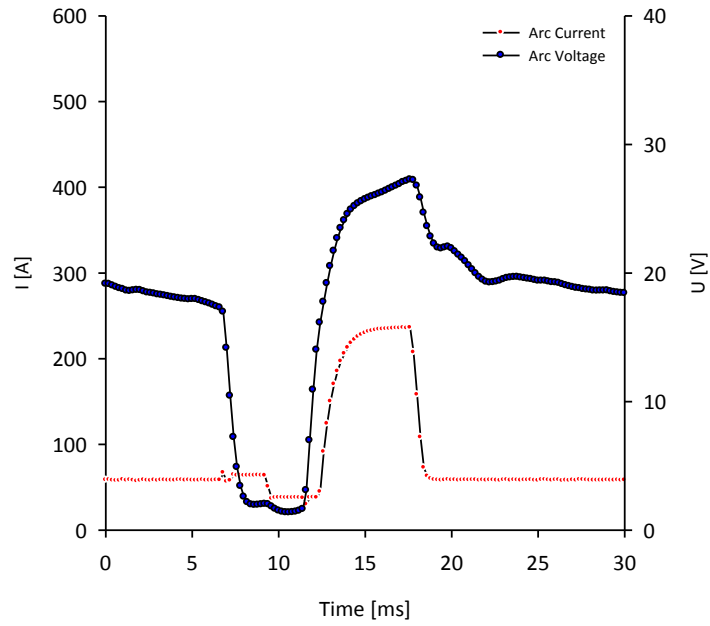
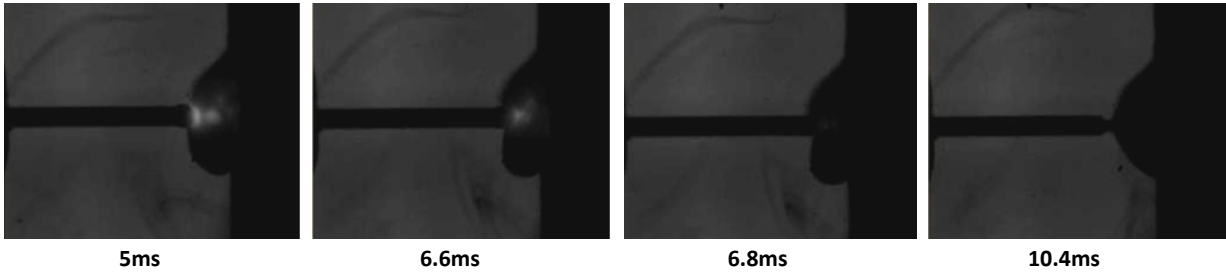


Figure 2.60 – Synchronized arc current and voltage waveforms with high speed video-images obtained for CMT (BC15).

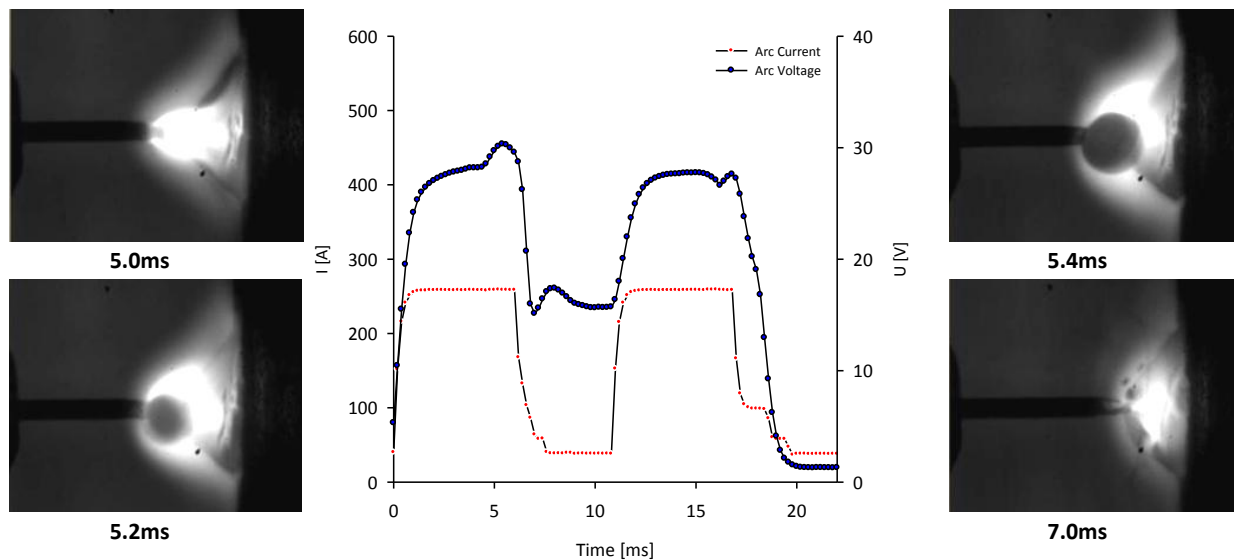


Figure 2.61 – Synchronized arc current and voltage waveforms with high speed video-images obtained for CMT (BC40).

2.4.4.5. Characterization of the Mechanism of Metal Transfer for CMT-P

A summary of the conditions investigated for CMT-P are presented in the Table 2.23.

Table 2.23 – Summary of the welding setting process conditions analysed for CMT-P.

Run	WFS [m/min]	WFS/TS Ratio	ALC [%]	PC [%]	Shielding Gas Composition	CTWD [mm]
BP11	6	16	-30	0	2.5%CO ₂ 97.5%Ar	11
BP13	6	16	0	0	2.5%CO ₂ 97.5%Ar	11
BP15	6	16	30	0	2.5%CO ₂ 97.5%Ar	11
BP18	8	16	0	0	2.5%CO ₂ 97.5%Ar	11
BP28	10	16	0	0	2.5%CO ₂ 97.5%Ar	11
BP77	6	16	0	0	1.5% CO ₂ 54%He 44.5%Ar	11
BP82	8	16	0	0	1.5% CO ₂ 54%He 44.5%Ar	11
BP87	10	16	0	0	1.5% CO ₂ 54%He 44.5%Ar	11
BP48	6	18	0	0	2.5%CO ₂ 97.5%Ar	11
BP49	8	18	0	0	2.5%CO ₂ 97.5%Ar	11
BP51	10	18	0	0	2.5%CO ₂ 97.5%Ar	11
BP35	6	16	0	-5	2.5%CO ₂ 97.5%Ar	11
BP38	6	16	0	5	2.5%CO ₂ 97.5%Ar	11
BP53	6	16	0	0	2.5%CO ₂ 97.5%Ar	13.5
BP57	6	16	0	0	2.5%CO ₂ 97.5%Ar	16

The analysis of the results of the metal transfer and waveform signal are summarized in the Table 2.24. The evaluation of waveform signal was based on the waveforms presented in Appendix VIII.

Table 2.24 – Summary of metal transfer and arc stability results obtained for CMT-P.

Run	Setting Parameters (main variations)	Observations
BP11	WFS 6m/min ALC -30%	Arc voltage instability. Shorter arc length level. Arc disturbances phenomena characterized by repulsive and streaming transfer mechanisms (to see Figures 2.63 and 2.64).
BP13	WFS 6m/min ALC 0%	Very stable arc and waveform characteristics. Controlled pulse and short-circuiting transfer mixed mode (to see Figure 2.62).
BP15	WFS 6m/min ALC 30%	Overall acceptable arc stability. Occasional instability observed immediately before the short-circuiting period.
BP18	WFS 8.0m/min	Number of pulses between short-circuiting increases. Moderate arc stability. Occasional arc splashing, in particular immediately before the short-circuiting period.
BP28	WFS 10.0m/min	Very high number of pulses between short-circuiting. Very short arc length. Very high arc instability phenomena characterized by splashing were associated with arc voltage waveform disturbance (to see Figure 2.65).
BP77	WFS 6.0 m/min 1.5%CO ₂ 54%He 44.5%Ar	Similar to BP13.
BP82	WFS 8.0 m/min 1.5%CO ₂ 54%He 44.5%Ar	Similar to BP18.
BP87	WFS 10.0 m/min 1.5%CO ₂ 54%He 44.5%Ar	Similar to BP28
BP48	WFS 6.0 m/min WFS/TS ratio 18	Similar to BP13
BP49	WFS 8.0 m/min WFS/TS ratio 18	Similar to BP18
BP51	WFS 10.0 m/min WFS/TS ratio 18	Similar to BP18
BP35	PC -5%	Similar to BP13 but occasional arc instability phenomena are observed.
BP38	PC 5%	Similar to BP13, but instability phenomena can be observed characterized by splashing effect.
BP53	CTWD 13.5mm	Similar to BP13.
BP57	CTWD 16.0mm	Similar to BP13. Drop spray followed by two or three small drops.

The metal transfer in CMT-P is characterized by a mixed mechanism consisting of a sequence of several controlled pulses followed by a short-circuiting period. The pulse mechanism is characterized by a drop spray (with diameter size similar to the filler wire diameter) followed by one or several small droplets. A representative example of the mechanism is illustrated in Figure 2.62, obtained from the test BP13. As can be observed, at the peak current the arc energy is maximum (4.8ms) followed by the current and voltage drop associated to the period of spray transfer (6.6 - 7.4 - 10ms). At that time the wire will move towards the weld pool (12.4 – 19.4ms), in parallel with a drop in arc current and voltage level, and causing the arc to extinguish (short-circuiting). After a controlled time, the current and voltage increase in parallel with the wire retracting, and resulting in a stable molten metal bridge rupture (21.8 – 22.0ms). Then, a new waveform cycle will restarts with a sequence of several controlled pulse spray transfers.

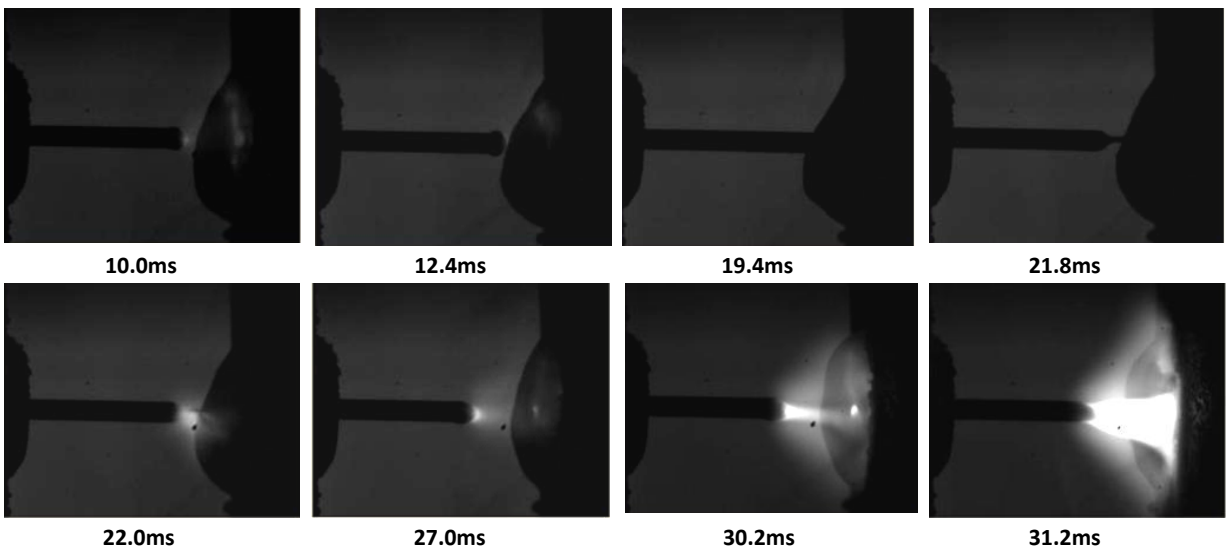
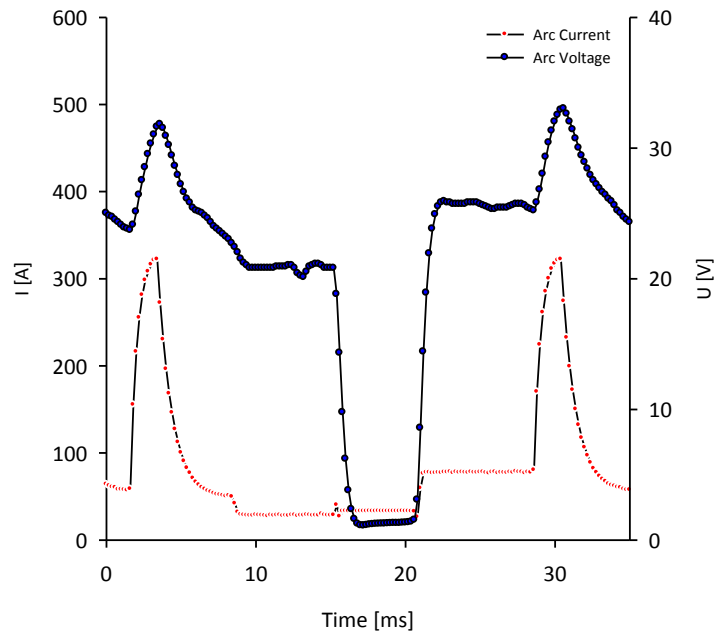
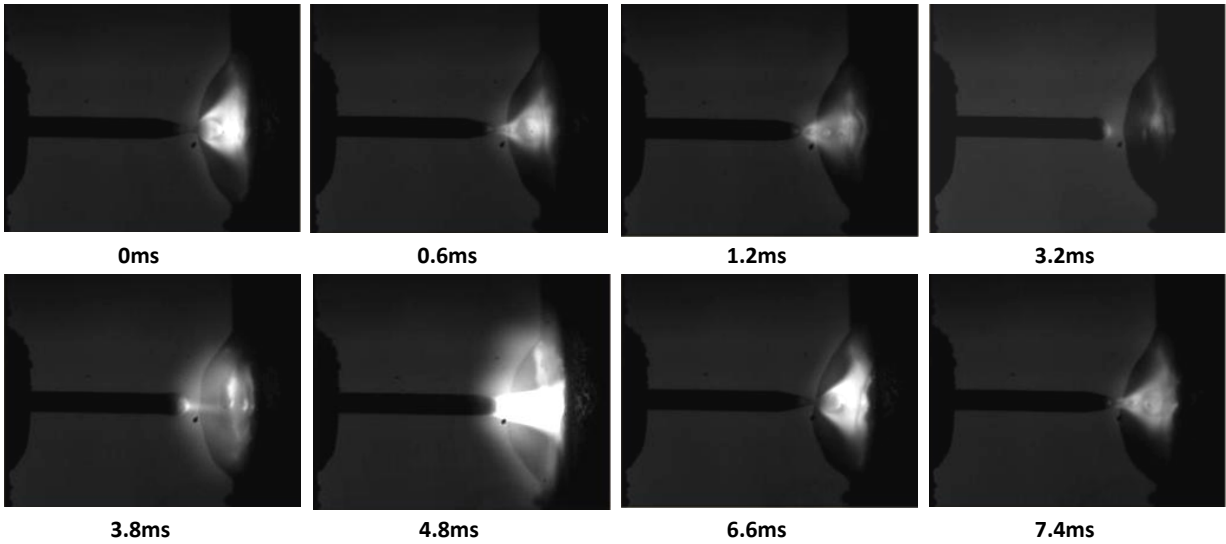


Figure 2.62 – Synchronized arc current and voltage waveforms with high speed video-images obtained for CMT-P (BP13).

Different waveform disturbances characterized by instability phenomena were observed at several setting conditions applied to CMT-P.

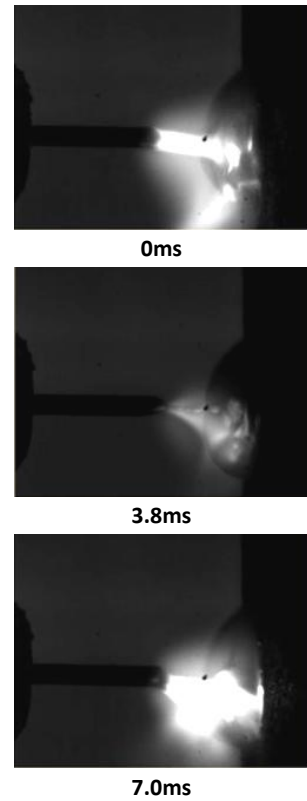
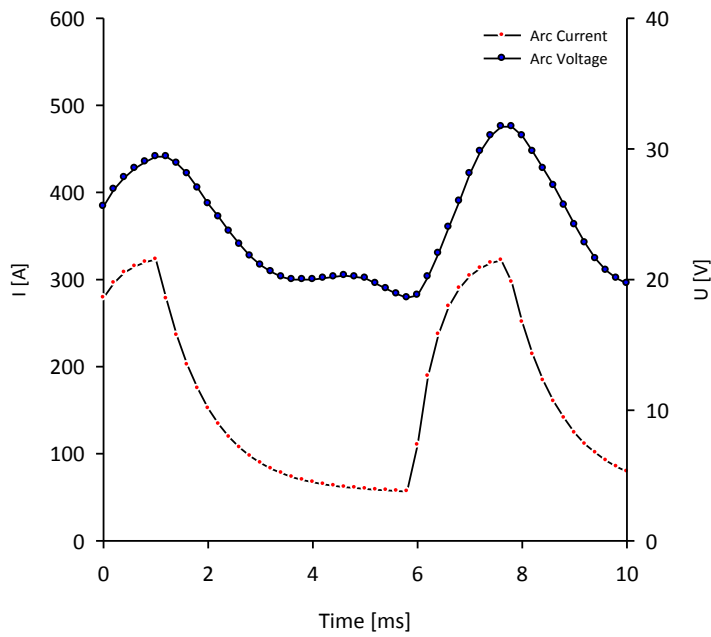


Figure 2.63 – Synchronized arc current and voltage waveforms with high speed video-images obtained for CMT-P (BP11).

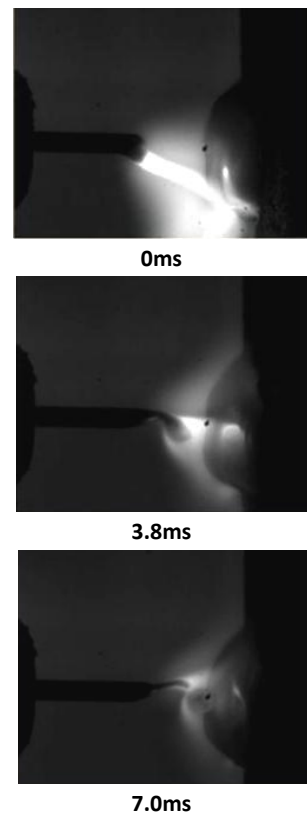
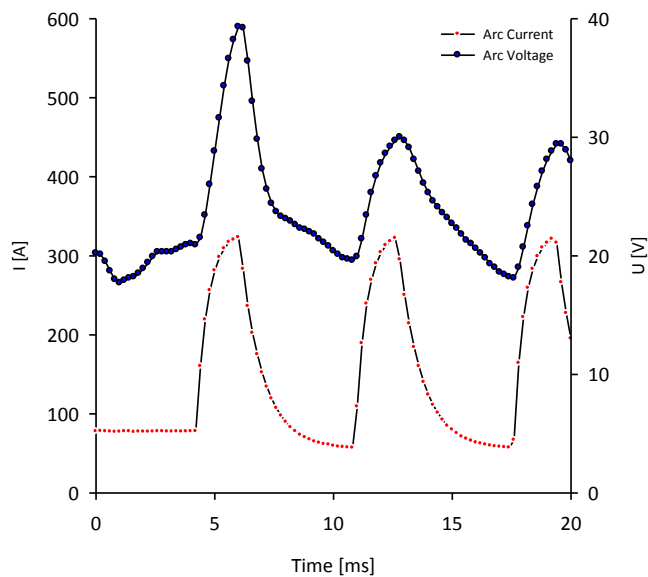


Figure 2.64 – Synchronized arc current and voltage waveforms with high speed video-images obtained for CMT-P (BP11).

Arc instability phenomena associated with voltage slope at the background stage and uncontrolled peak voltage were observed when low ALC was applied (ALC of -30%). This disturbance causes arc repulsion and streaming transfer mechanisms as is illustrated in the Figures 2.63 and 2.64.

At high WFS levels (10m/min) the instability is more frequent and characterized by splashing (explosions) phenomena associated with higher voltages during the background current period (Figure 2.65).

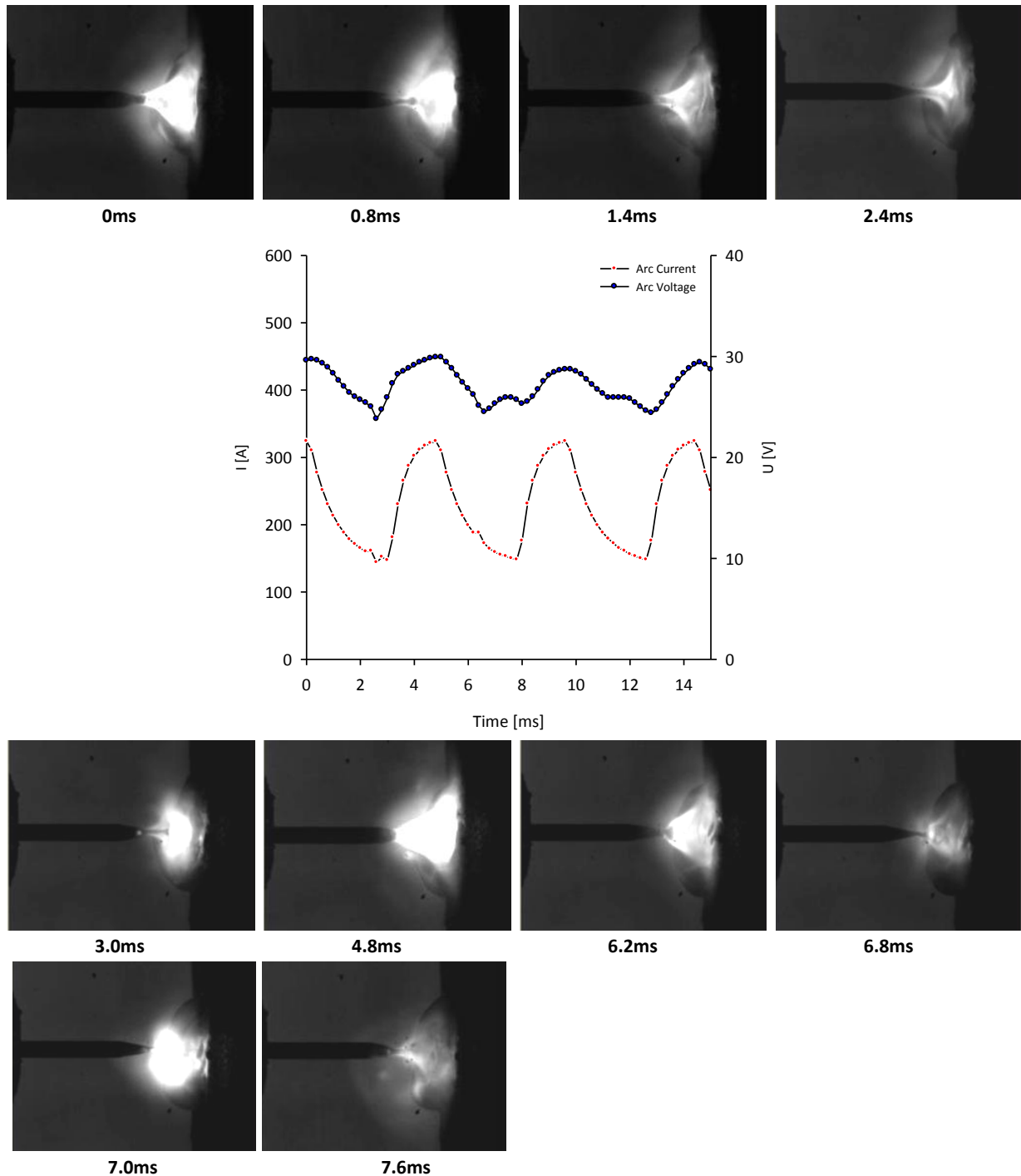


Figure 2.65 – Synchronized arc current and voltage waveforms with high speed video-images obtained for CMT-P (BP28).

2.4.4.6. Characterization of the Mechanism of Metal Transfer for FastROOT

A summary of the conditions investigated for FastROOT are presented in the Table 2.25.

Table 2.25 – Summary of the welding setting conditions analysed for FastROOT.

Run	WFS [m/min]	WFS/TS Ratio	BC [%]	FP [%]	Shielding Gas Composition	CTWD [mm]
BF06	6	16	-50	0	2.5%CO ₂ 97.5%Ar	11
BF08	6	16	0	0	2.5%CO ₂ 97.5%Ar	11
BF10	6	16	50	0	2.5%CO ₂ 97.5%Ar	11
BF18	8	16	0	0	2.5%CO ₂ 97.5%Ar	11
BF13	9	16	0	0	2.5%CO ₂ 97.5%Ar	11
BF45	6	16	0	0	1.5% CO ₂ 54%He 44.5%Ar	11
BF49	8	16	0	0	1.5% CO ₂ 54%He 44.5%Ar	11
BF53	9	16	0	0	1.5% CO ₂ 54%He 44.5%Ar	11
BF26	6	18	0	0	2.5%CO ₂ 97.5%Ar	11
BF27	8	18	0	0	2.5%CO ₂ 97.5%Ar	11
BF28	9	18	0	0	2.5%CO ₂ 97.5%Ar	11
BF21	8	16	0	-30	2.5%CO ₂ 97.5%Ar	11
BF24	8	16	0	30	2.5%CO ₂ 97.5%Ar	11
BF30	6	16	0	0	2.5%CO ₂ 97.5%Ar	13.5
BF34	6	16	0	0	2.5%CO ₂ 97.5%Ar	16

The Table 2.26 summarizes the characterization of arc stability and waveform signal analysed for the different tests evaluated. The waveform signal analyses were based on the waveforms presented in the Appendix VIII. The metal transfer for FastROOT is characterized by a controlled dip transfer mechanism (short-circuiting).

As illustrated in Figure 2.66, the voltage drop occurs in parallel with the increase of arc current, at the period where short-circuiting takes place (6.0 – 8.6ms). During this period the current rapidly decreases for a value close to the background current level. At this time the voltage and current increase rapidly and a broken bridge occurs (8.8ms). This causes arc re-ignition and current and voltage reach their peak values (10.4ms), where the arc energy intensity is higher. Then, the arc current and voltage take their background stable levels and the arc is kept at a low energy level (14.4ms), until new short-circuit occurs and the new cycle starts.

Table 2.26 – Summary of metal transfer and arc stability results obtained for FastROOT.

Run	Setting Parameters (main variations)	Observations
BF06	WFS 6m/min BC -50%	Frequent arc instability phenomena. Splashing phenomena associated with arc re-ignition (to see Figure 2.68).
BF08	WFS 6m/min BC 0%	Moderate Arc stability. Mechanism of transfer characterized by controlled short-circuiting phenomena. Slashing phenomena associated with arc re-ignition (to see Figure 2.66).
BF10	WFS 6m/min BC 50%	Similar to BF08.
BF13	WFS 8.0m/min	Similar to BF08. Arc instability increases (to see Figure 2.69).
BF18	WFS 9.0m/min	Very short arc length. High arc instability phenomena due to uncontrolled waveform design. Frequent splashing phenomena.
BF45	WFS 6.0 m/min 1.5%CO ₂ 54%He 44.5%Ar	Similar to BF08.
BF49	WFS 8.0 m/min 1.5%CO ₂ 54%He 44.5%Ar	Similar to BF13.
BF53	WFS 9.0 m/min 1.5%CO ₂ 54%He 44.5%Ar	Similar to BF18 (to see Figure 2.67).
BF26	WFS 6.0 m/min WFS/TS ratio 18	Similar to BF08.
BF27	WFS 8.0 m/min WFS/TS ratio 18	Similar to BF13.
BF28	WFS 9.0 m/min WFS/TS ratio 18	Similar to BF18.
BF21	FP -30%	Similar to BF13
BF24	FP 30%	Similar to BF13. Higher instability associated with arc splashing.
BF30	CTWD 13.5mm	Similar to BF13. Instability increases associated with higher arc length and arc splashing.
BF34	CTWD 16.0mm	Similar to BF30. Higher arc instability phenomena.

The main disturbances observed for FastROOT welding are due to either arc splashing (explosions) at the arc re-ignition time or the waveform uncontrolled phenomena. The frequency of these phenomena is higher at high WFS levels or when high Base Current and Forming Pulse parameters were at their high values.

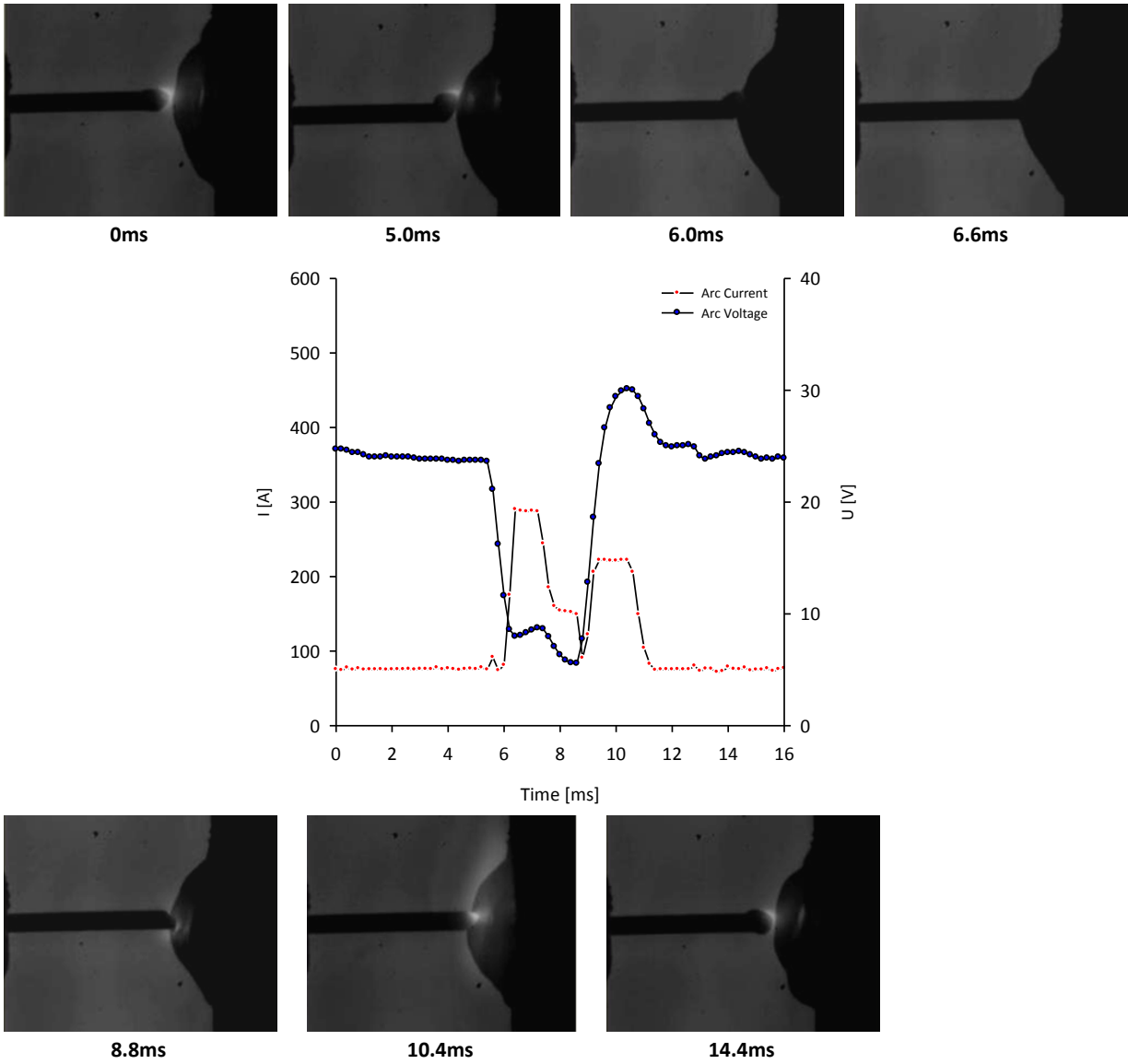


Figure 2.66 – Synchronized arc current and voltage waveforms with high speed video-images obtained for FastROOT (BF08).

The Figure 2.67 illustrates the typical phenomena of splashing from the arc re-ignition, after short-circuiting.

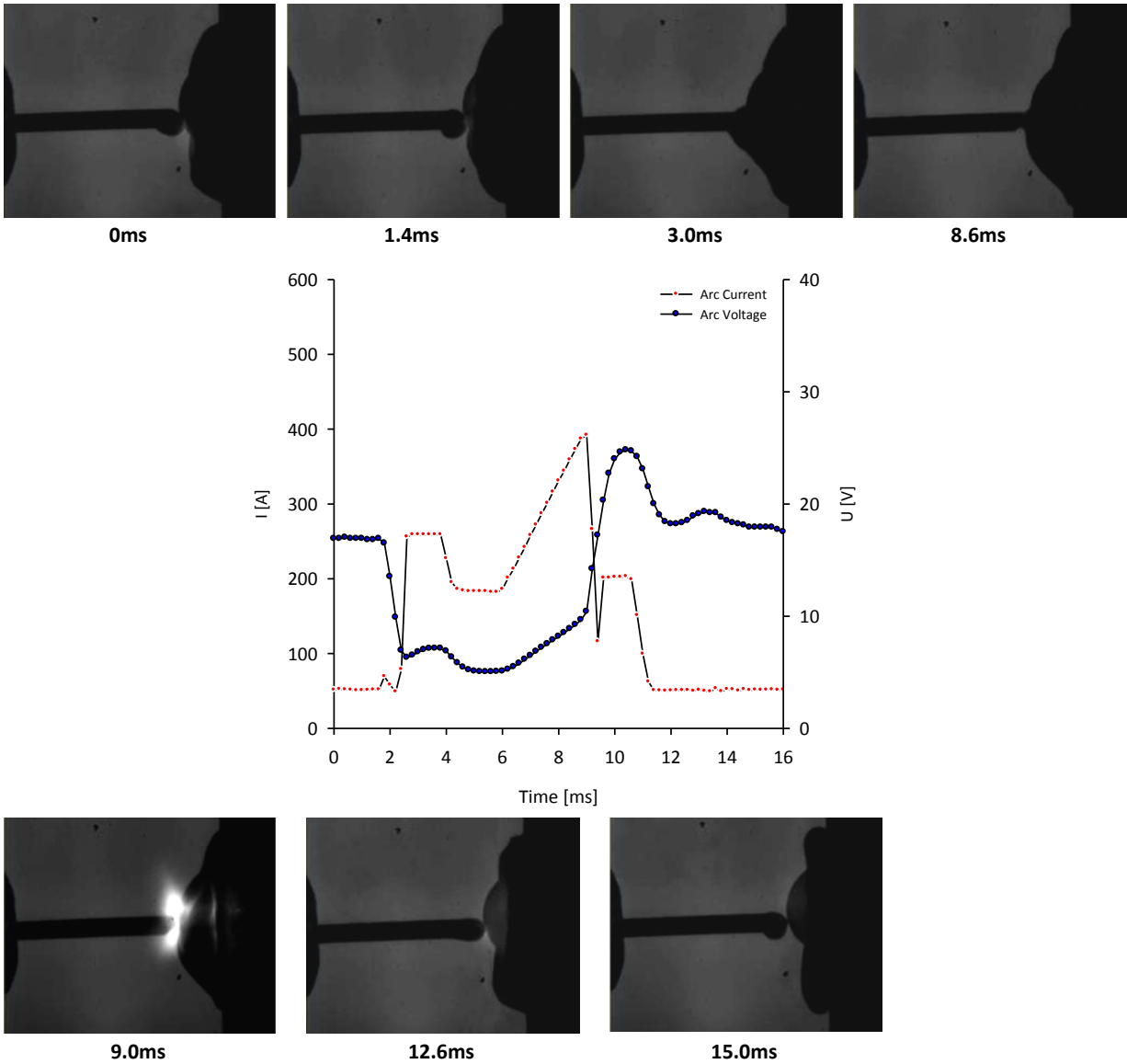


Figure 2.67 – Synchronized arc current and voltage waveforms with high speed video-images obtained for FastROOT (BF06).

The waveform uncontrolled disturbance at high WFS levels, characterized by splashing effect can be observed in the Figure 2.68. Figure 2.69 shows the instability phenomena associated with higher voltages.

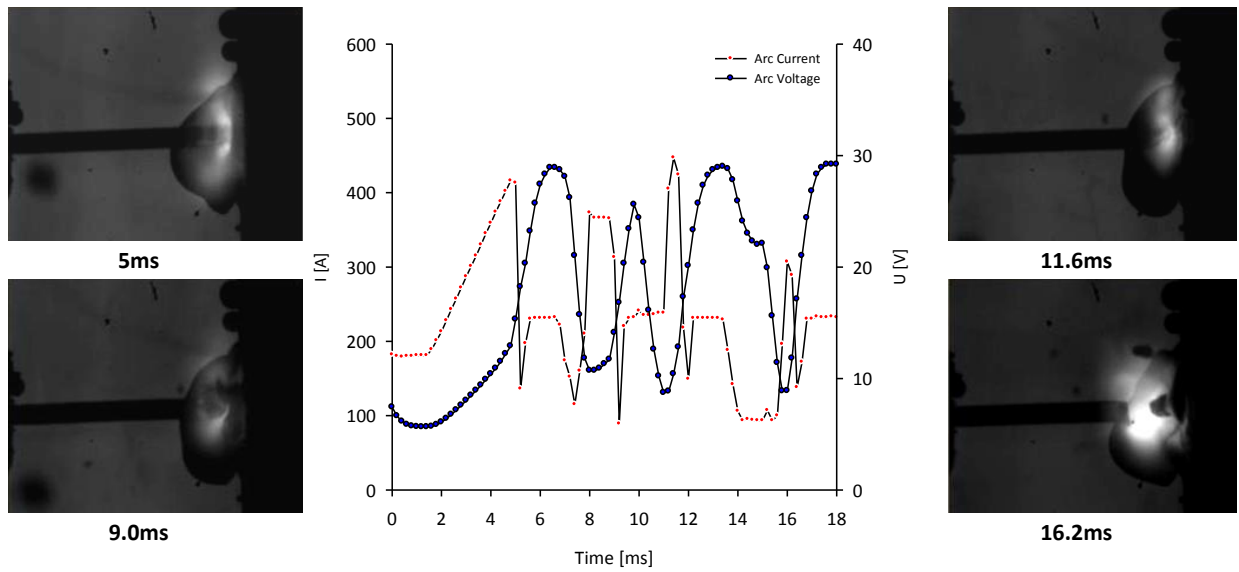


Figure 2.68 – Synchronized arc current and voltage waveforms with high speed video-images obtained for FastROOT (BF53).

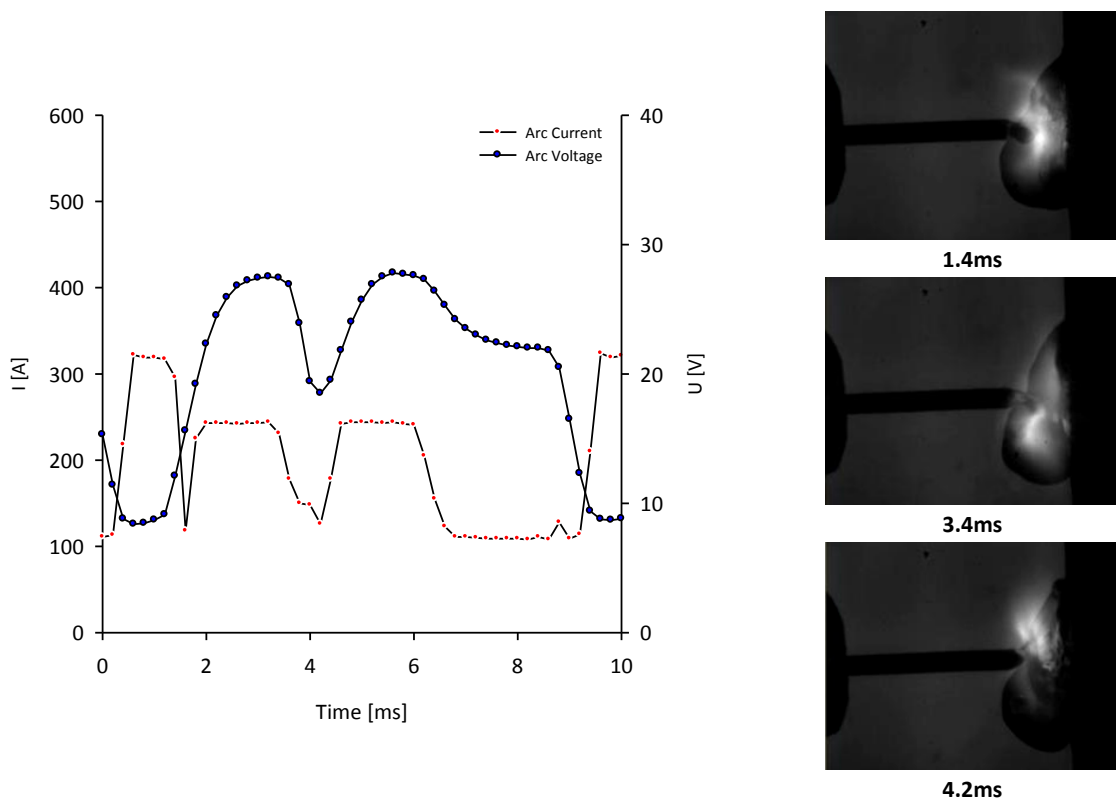


Figure 2.69 – Synchronized arc current and voltage waveforms with high speed video-images obtained for FastROOT (BF13).

2.4.5. Analysis of Arc Stability Control using Current – Voltage Diagrams

Arc stability provides a fundamental criterion to characterize welding quality. However, the analysis of arc stability in arc welding can be quite complex due to the different variations associated with arc characteristics, power source characteristics and waveform design. Different methods, from experimental to numerical techniques, have been applied to characterize the arc stability, but none has been successfully able to identify the unstable phenomena from only arc current and voltage waveform electrical data. As was observed during the previous section of this chapter, the analyses of metal transfer phenomena gave some valuable information about the unstable mechanisms. However, the method of synchronised high speed video-images with arc current and voltage waveform is difficult to apply to the overall welding length and also time consuming.

Hence in this thesis, a new method is proposed to characterize the arc stability by analysing solely the arc current and voltage waveforms. Previous work has been published to analyse the mechanism of metal transfer associated with cross plots (Scotti 2000) (Huang and Yapp 2000), but these methods have not been applied to characterize the arc stability and reach conclusions about welding performance. The method developed consists in correlating directly the arc voltage and current at each instant of time and observing the performance of waveform cycles, in “UI diagrams”.

The UI diagrams provide an alternative representation of the waveform cycle of arc voltage and current. The dots correspond to the arc current and voltage at different instants of time. As is observed in the following generic UI diagram, synchronized with the corresponding waveform (Figure 2.70), different analysis features of the waveform cycle can be more clearly seen in the U-I diagram. The distribution of dots which correspond to the pulse region is indicated in Figure 2.70, while short circuiting is indicated by a line of dots, where voltage is proportional to current, due to the resistive nature of current flow for this process. Furthermore, the dispersion of the dots provides information about the consistency or stability of the process.

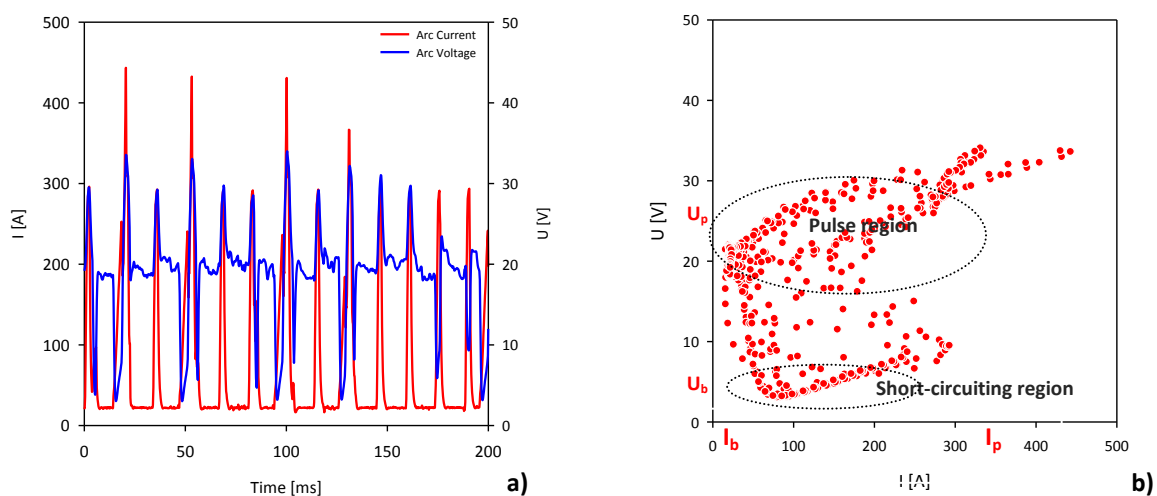


Figure 2.70 – Waveform (a) and UI Diagram (b) correspondent for a generic GMAW process.

The UI diagrams are therefore useful for characterization of arc stability and also provide important information about metal transfer phenomena. The variability of arc current and voltage waveforms is a response of the stability of the process, associated with the setting conditions applied.

The evaluation of arc stability will be presented in terms of:

- Variation of WFS at different shielding gases and WFS/TS ratio;
- Variation of arc length parameter adjustment (trim, ALC or Base Current);
- Variation of dynamics (DC, PC, FP);
- Variation of CTWD.

The experimental conditions applied to this research (unless otherwise indicated) were presented in Section 2.4.1. The following subsections will present the results obtained for the different waveform designs considered.

2.4.5.1. Characterization of Arc Stability for GMAW-P

The arc stability diagrams obtained from variation of WFS, at two different shielding gases (2.5%CO₂ 97.5%Ar and 1.5%CO₂ 54%He 44.5%Ar), are illustrated in the Figure 2.71. The distribution of the points on the waveform cycle has much less scatter at high WFS levels. It is also noticed that the variability of the cycle points is wider when 1.5%CO₂ 54%He 44.5%Ar was used. This is due to the increase of the arc voltage. For both gases a high concentration of the points at low voltage is observed (from low to high current levels) which indicates the existence of short-circuiting phenomena.

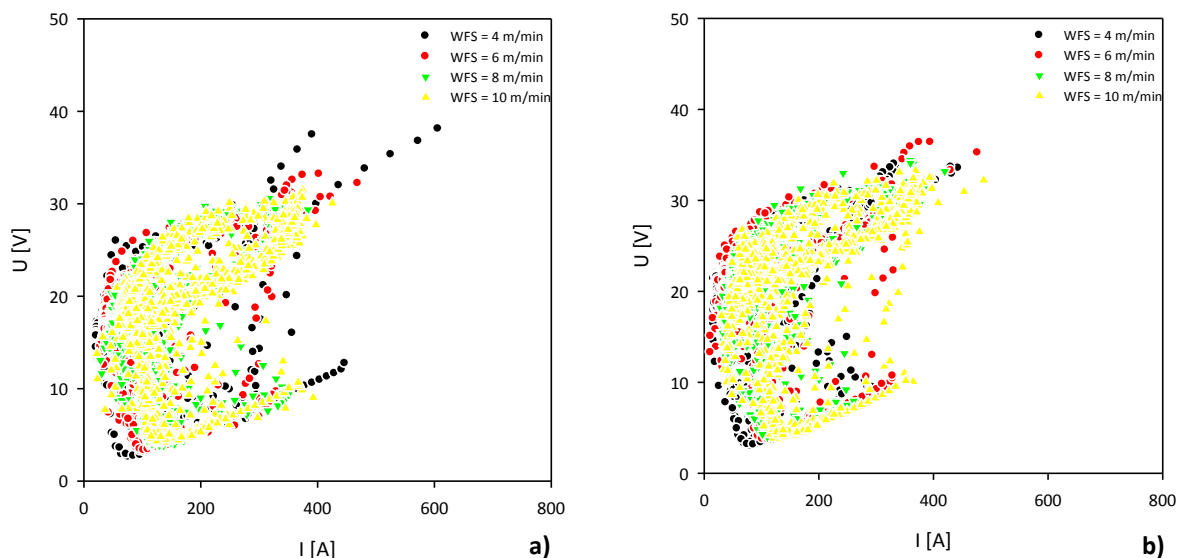


Figure 2.71 – UI diagrams of the variation with WFS for GMAW-P, using WFS/TS ratio of 16: a) 2.5%CO₂ 97.5%Ar; b) 1.5%CO₂ 54%He 44.5%Ar.

At low travel speed level (WFS/TS ratio of 18) the distribution of the points has less scatter suggesting an increase of the stability associated with the waveform cycle. The presence of short-circuiting is, however, still apparent (Figure 2.72).

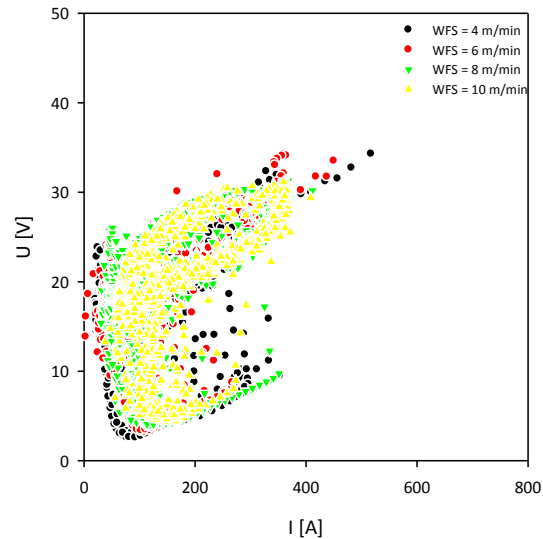


Figure 2.72 – UI diagram of the variation with WFS for GMAW-P, using WFS/TS ratio of 18.

The analysis of the effect of trim demonstrates that the variability of the points is higher at low trim levels, which suggests that higher arc stability is achieved at higher trim (Figure 2.73).

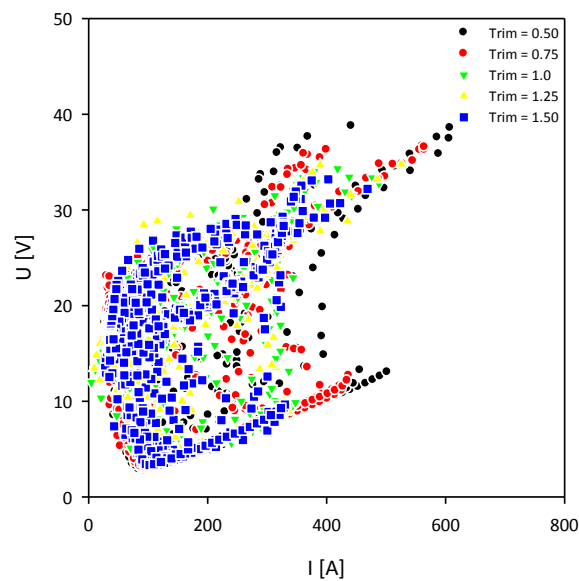


Figure 2.73 – UI diagram of the variation with trim for GMAW-P.

The effect of CTWD is the most significant among the analyses performed for GMAW-P. It is observed that at 11mm the unstable short-circuiting phenomena is significantly high, and decreases with the increasing of CTWD (Figure 2.74).

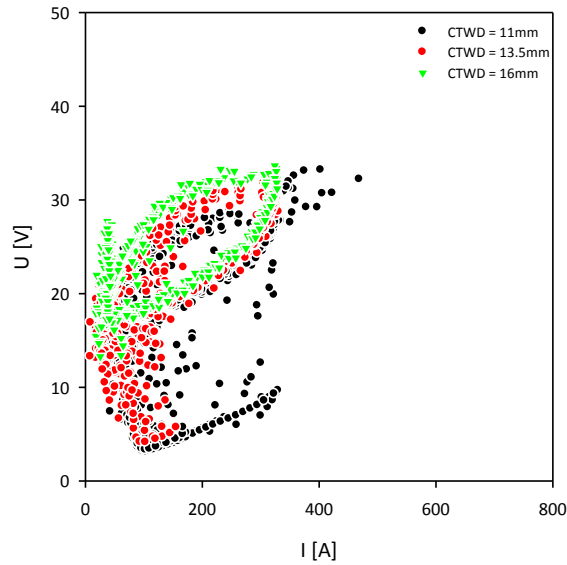


Figure 2.74 – UI diagram of the variation with CTWD for GMAW-P.

2.4.5.2. Characterization of Arc Stability for RapidArc

The effect of WFS (when WFS/TS of 16 was applied) suggests that the distribution of the points on the waveform cycle is very stable from 4 to 8m/min but an unstable phenomena at 10m/min is associated with voltage drops at low current levels. It is also observed that the variability of the points in terms of voltage is slightly higher when 1.5%CO₂ 54%He 44.5%Ar was applied (Figure 2.75).

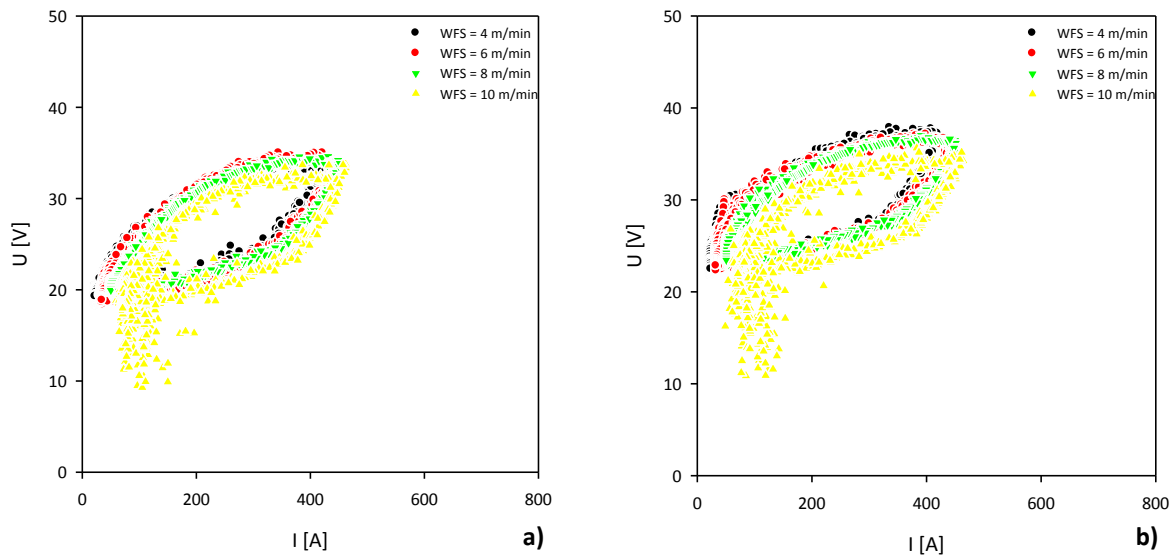


Figure 2.75 – UI diagrams of the variation with WFS for RapidArc, using WFS/TS ratio of 16: a) 2.5%CO₂ 97.5%Ar; b) 1.5%CO₂ 54%He 44.5%Ar.

Using WFS/TS ratio of 18 (lower welding speed, considering constant WFS) no significant changes can be observed, when compared with WFS/TS ratio of 16 (Figure 2.76).

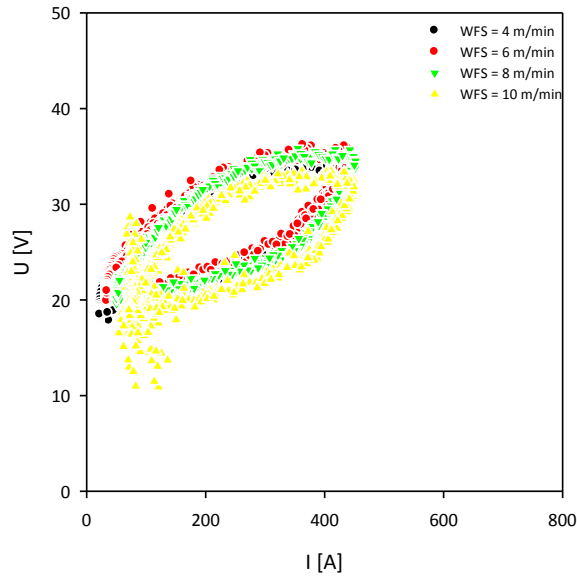


Figure 2.76 – UI diagram of the variation with WFS for RapidArc, using WFS/TS ratio of 18.

The analysis of the effect of trim demonstrates high instability phenomena from 0.5 until 1.25, and a uniform distribution of points is only reached at trim of 1.5 (Figure 2.77).

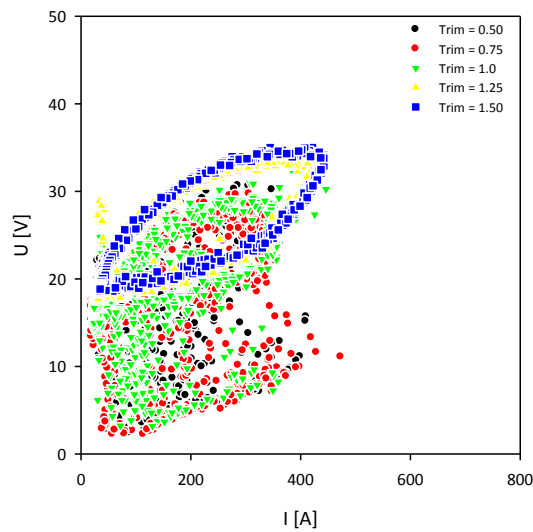


Figure 2.77 – UI diagram of the variation with trim for RapidArc.

The effect of CTWD reveals a good cycle performance for the three levels studied, but a much compact distribution of the points when 11mm was applied (Figure 2.78).

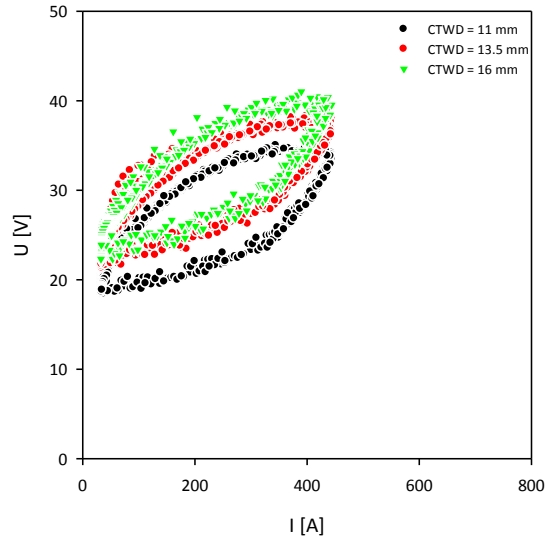


Figure 2.78 – UI diagram of the variation with CTWD for RapidArc.

2.4.5.3. Characterization of Arc Stability for STT

The effect of WFS (when WFS/TS ratio of 16 was applied) suggests that the distribution of the points is significantly unstable at high WFS levels (8 and 8.26m/min). The application of 1.5%CO₂ 54%He 44.5%Ar shows significant changes in the shape of the points distribution (current and voltage variations), when compared with 2.5%CO₂ 97.5%Ar, but no noteworthy stability variations can be observed (Figure 2.79).

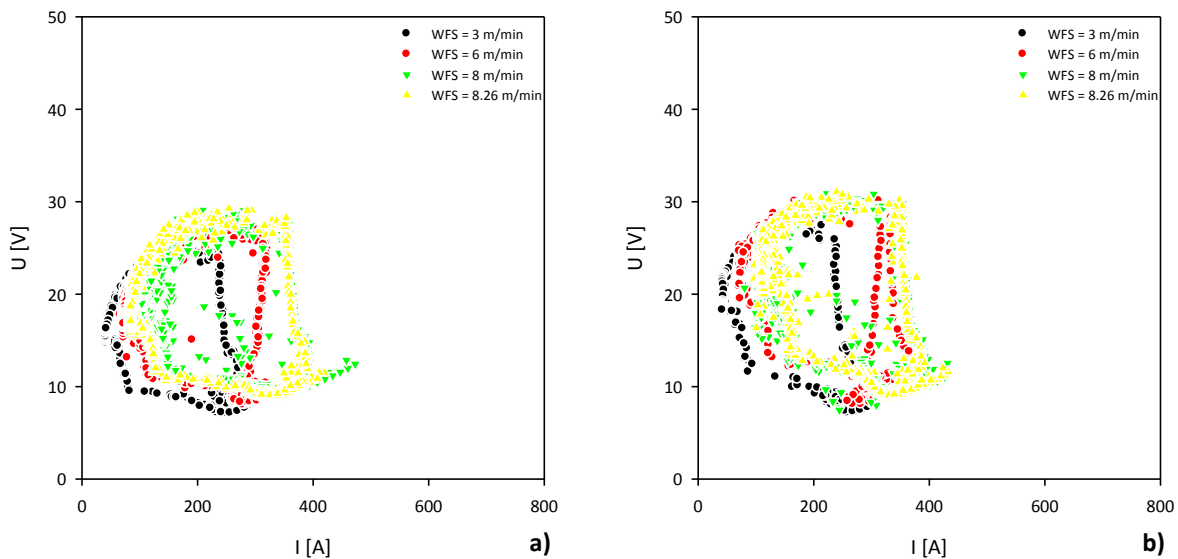


Figure 2.79 – UI diagrams of the variation with WFS for STT, using WFS/TS ratio of 16: a) 2.5%CO₂97.5%Ar; b) 1.5%CO₂ 54%He 44.5%Ar.

At lower welding speeds (when WFS/TS ratio of 18 was applied) no significant changes, are observed, when compared to the WFS/TS ratio of 16. However, the distribution of the points suggests a slightly increase of the arc stability (Figure 2.80).

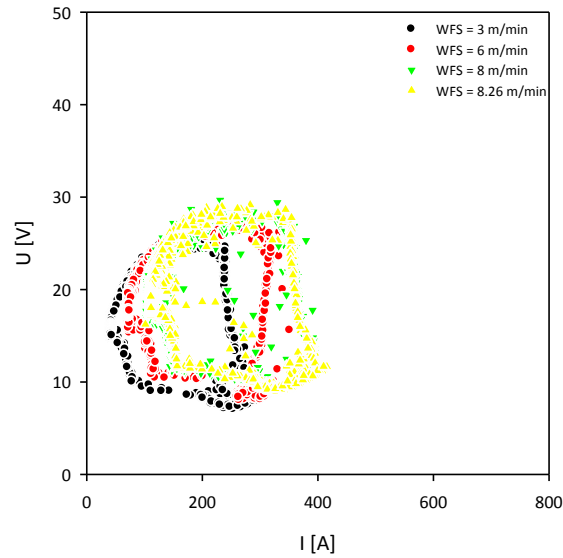


Figure 2.80 – UI diagram of the variation with WFS for STT, using WFS/TS ratio of 18.

The analysis of the effect of trim demonstrates that no significant changes are observed, but at 1.5 some instability is observed (Figure 2.81).

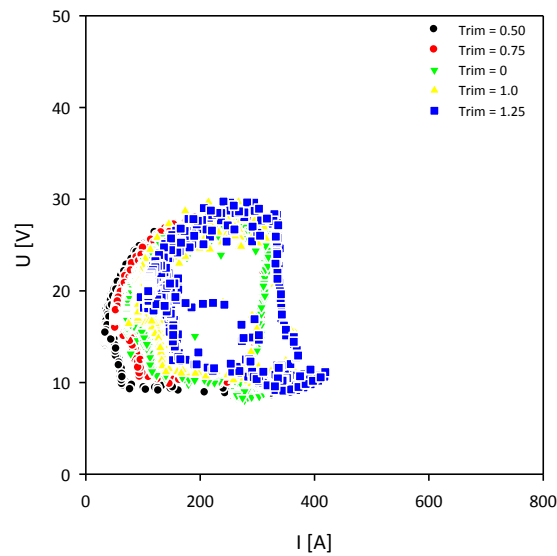


Figure 2.81 – UI diagram of the variation with trim for STT.

The effect of CTWD reveals a good cycle performance for the three levels studied, but a more condensed points distribution is observed at the highest level (16mm) (Figure 2.82).

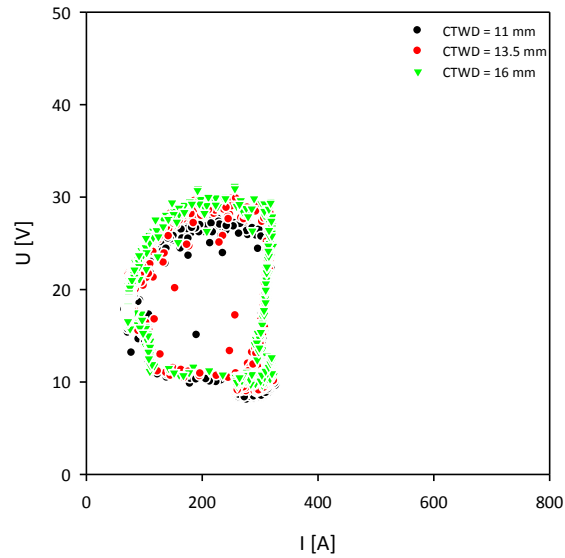


Figure 2.82 – UI diagram of the variation with CTWD for STT.

2.4.5.4. Characterization of Arc Stability for CMT

The effect of WFS (when WFS/TS ratio of 16 was applied) suggests that the instability phenomenon is higher at the highest WFS level (8m/min). This phenomenon is illustrated by a significant change in the shape of the cycle points. No significant changes are observed between both gases analysed (Figure 2.83).

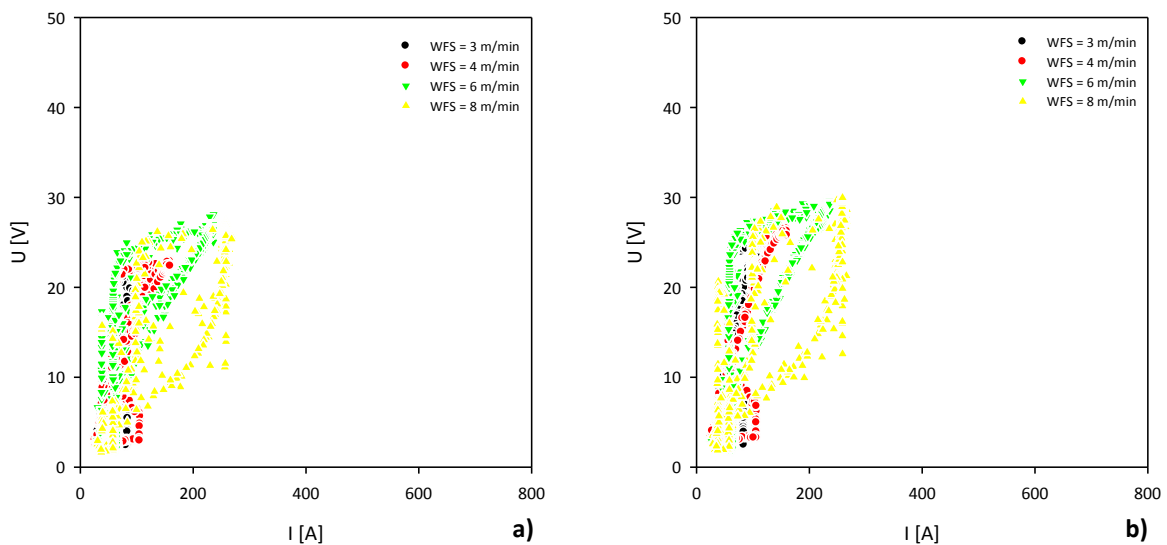


Figure 2.83 – UI diagrams of the variation with WFS for CMT, using WFS/TS ratio of 16: a) 2.5%CO₂/97.5%Ar; b) 1.5%CO₂/54%He/44.5%Ar.

The use of WFS/TS ratio of 18 (lower welding speed, considering constant WFS) suggests a slightly increase of the arc stability, compared to the WFS/TS ratio of 16 (Figure 2.84).

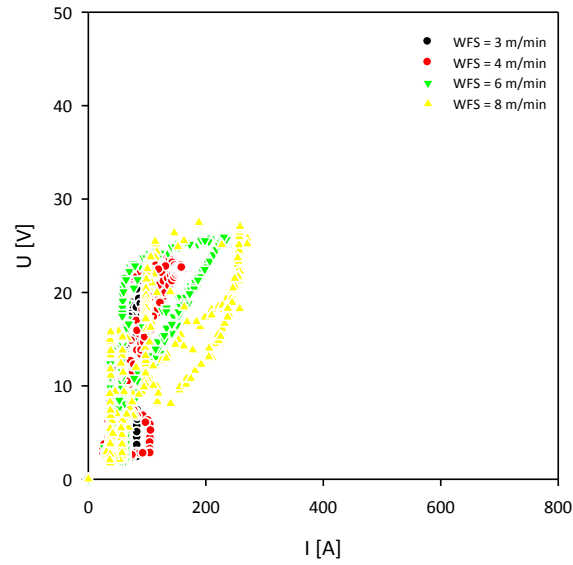


Figure 2.84 – UI diagram of the variation with WFS for CMT, using WFS/TS ratio of 18.

The analysis of the effect of ALC demonstrates that no significant changes are observed in terms of arc stability, but significant changes can be observed in shape of the cycle points (Figure 2.85).

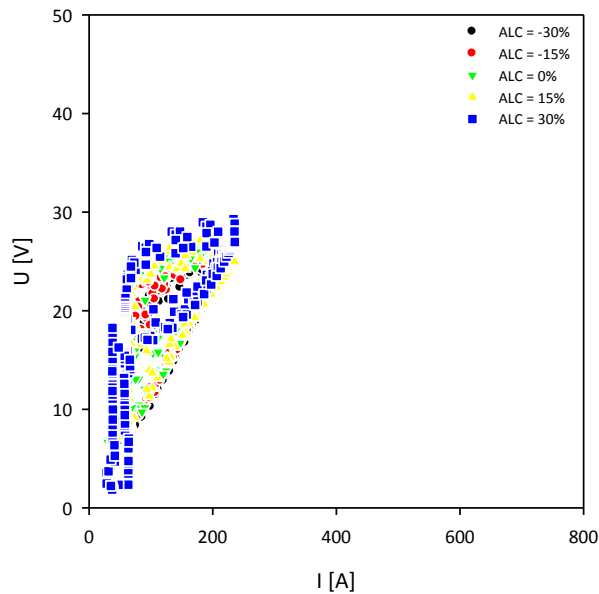


Figure 2.85 – UI diagram of the variation with ALC for CMT.

No significant variations can be observed when DC was varied (Figure 2.86).

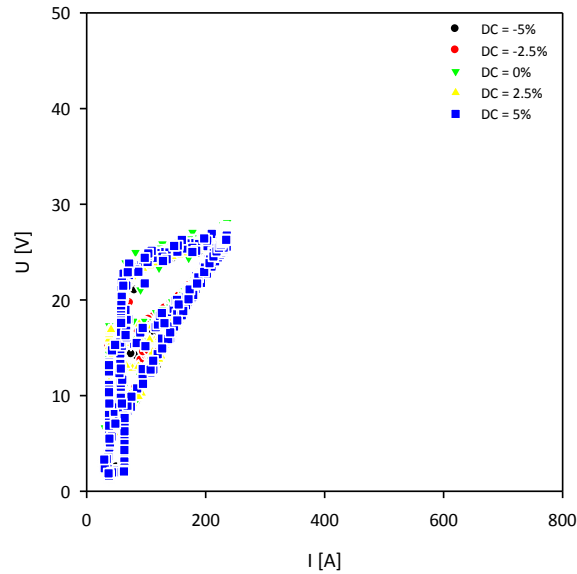


Figure 2.86 – UI diagram of the variation with DC for CMT.

No significant changes are observed for the effect of CTWD on arc stability (Figure 2.87).

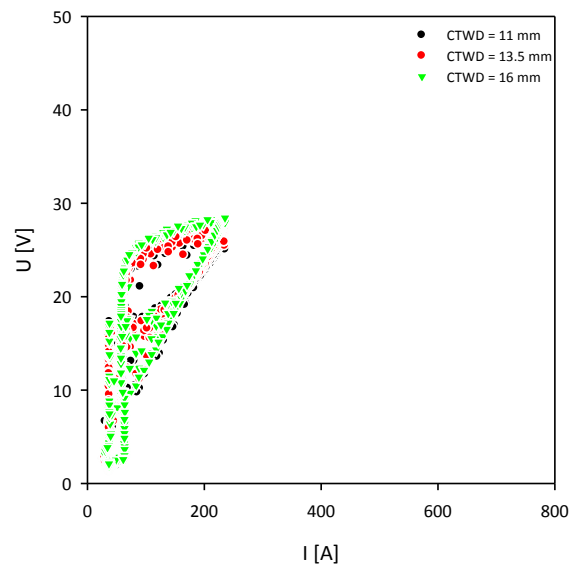


Figure 2.87 – UI diagram of the variation with CTWD for CMT.

2.4.5.5. Characterization of Arc Stability for CMT-P

The analysis of the effect of WFS (using WFS/TS ratio of 16) for both shielding gases reveal that the arc instability is more significant between 8m/min and 10m/min and more pronounced when 1.5%CO₂ 54%He 44.5%Ar was applied (Figure 2.88). The unstable phenomenon is associated with larger voltage changes, occasional at 6m/min and more often at 8m/min, and high voltage variability for 10m/min.

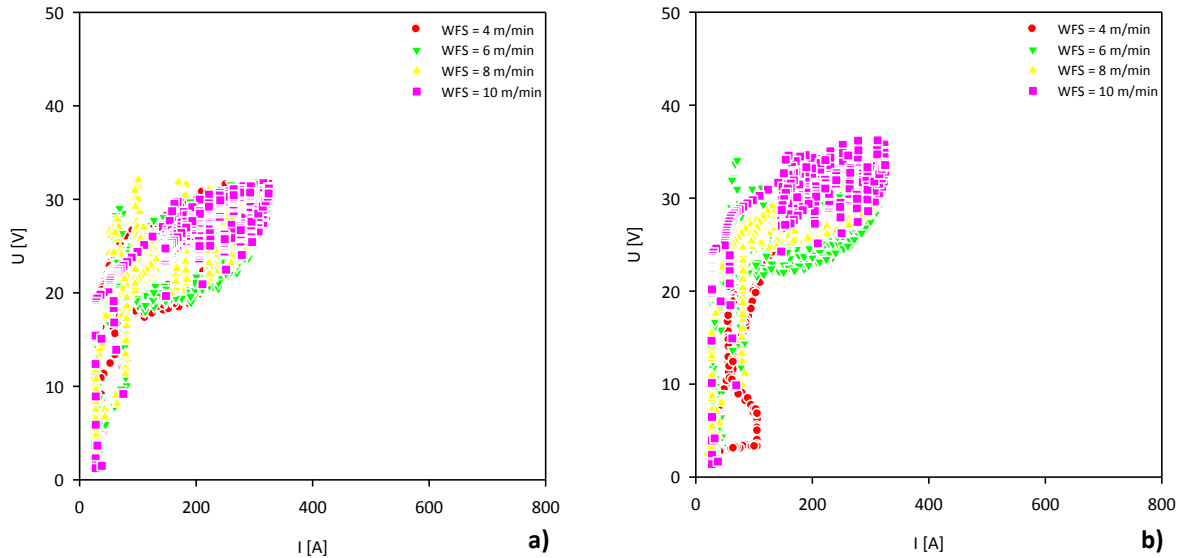


Figure 2.88 – UI diagrams of the variation with WFS for CMT-P, using WFS/TS ratio of 16: a) 2.5%CO₂97.5%Ar; b) 1.5%CO₂ 54%He 44.5%Ar.

At lower welding speeds (when WFS/TS ratio of 18 was applied) the arc instability is higher at the high WFS levels (8 and 10m/min) but similar to that observed at WFS/TS ratio of 16 for low WFS levels (4 and 6m/min) (Figure 2.89).

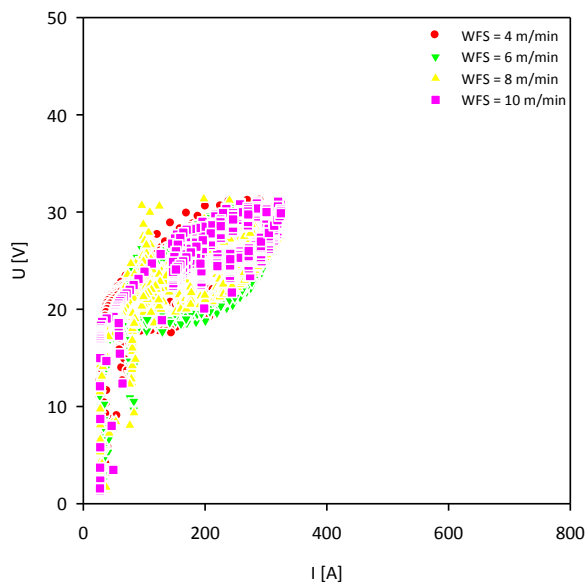


Figure 2.89 – UI diagram of the variation with WFS for CMT-P, using WFS/TS ratio of 18.

The analysis of the effect of ALC demonstrates that the stability is higher at 30%. At low ALC values (-30 and -15%) is observed very high dispersion of the cycle points, while at 0% and at 15% occasional voltage excursions can be identified (Figure 2.90).

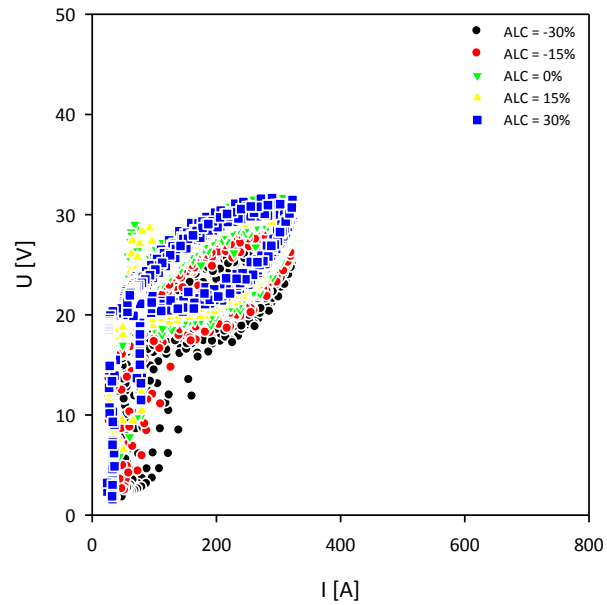


Figure 2.90 – UI diagram of the variation with ALC for CMT.

The effect of PC does not suggest a strong effect on the instability phenomena. However, at high PC level higher voltage excursions can be observed (Figure 2.91).

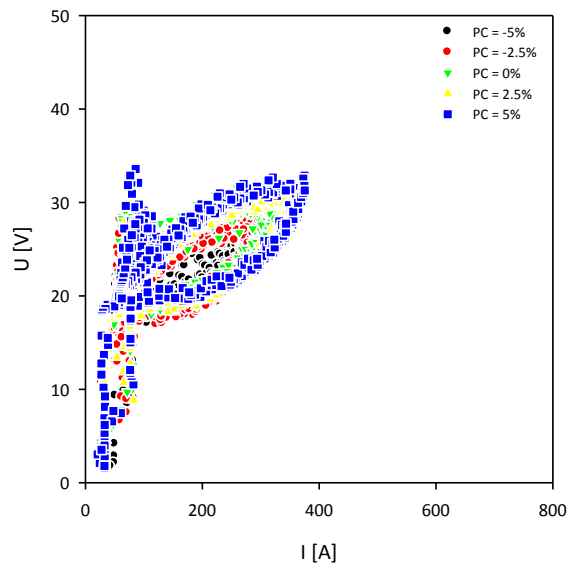


Figure 2.91 – UI diagram of the variation with PC for CMT-P.

The effect of CTWD demonstrates that in general no significant instability phenomenon can be observed. However, when the CTWD applied was 11mm an occasional voltage excursion can be identified (Figure 2.92).

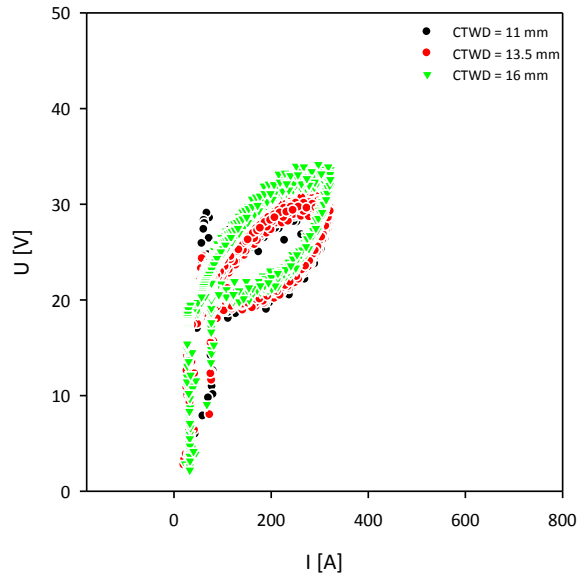


Figure 2.92 – UI diagram of the variation with CTWD for CMT-P.

2.4.5.6. Characterization of Arc Stability for FastROOT

The results obtained on the effect of WFS (using WFS/TS ratio of 16) demonstrate that no significant variations are observed between the different WFS levels evaluated. However, the application of 2.5%CO₂ 97.5%Ar suggests a much more stable distribution of the points (Figure 2.93).

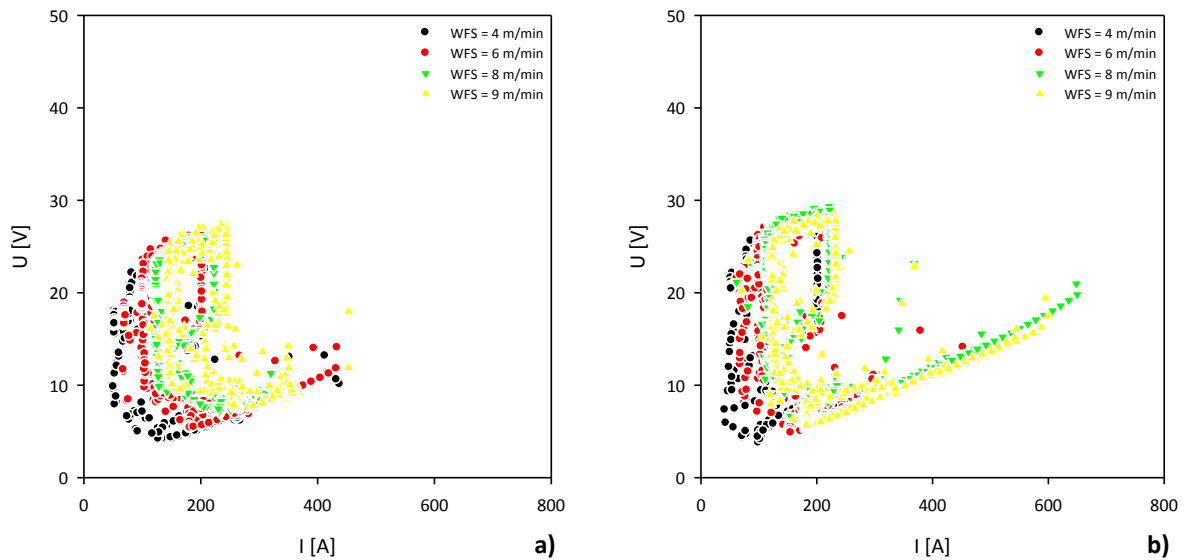


Figure 2.93 – UI diagrams of the variation with WFS for FastROOT, using WFS/TS ratio of 16: a) 2.5%CO₂ 97.5%Ar; b) 1.5%CO₂ 54%He 44.5%Ar.

At lower welding speeds (when WFS/TS ratio of 18 was applied), the diagram of stability demonstrate much higher instability in the distribution of the points (Figure 2.94).

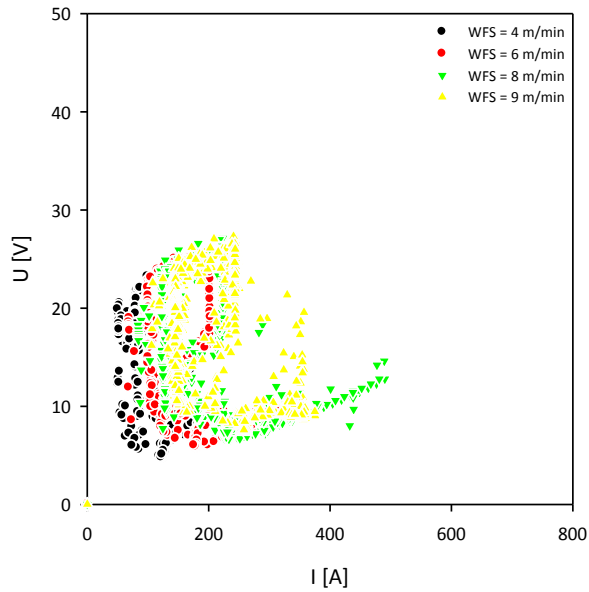


Figure 2.94 – UI diagram of the variation with WFS for FastROOT, using WFS/TS ratio of 18.

The analysis of the effect of Base Current (BC) suggests that arc stability is higher at high BC levels (25% and 50%), where the arc current does go higher than 500A (Figure 2.95).

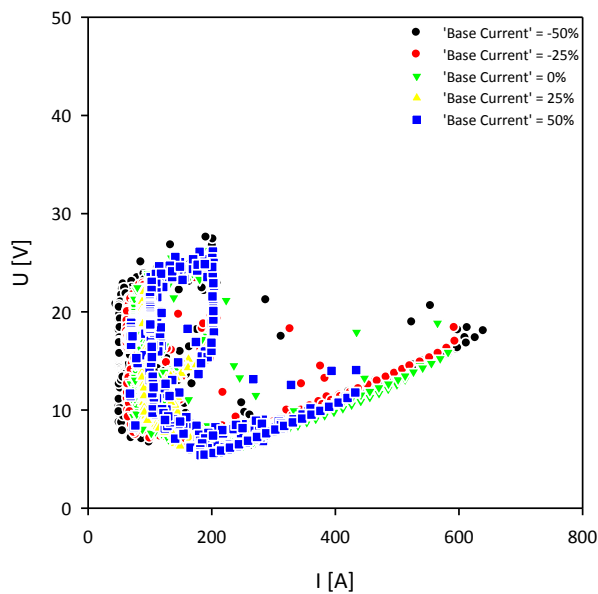


Figure 2.95 – UI diagram of the variation with Base Current for FastROOT.

The effect of Forming Pulse (FP) also suggests higher waveform cycle stability at high FP levels (between 15 and 30%), where the arc current levels are lower and points well distributed (Figure 2.96).

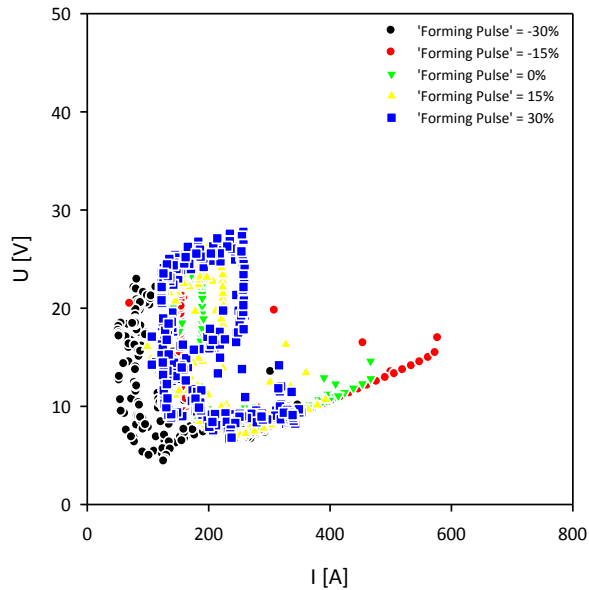


Figure 2.96 – UI diagram of the variation with Forming Pulse for FastROOT.

No significant changes are observed to the effect of CTWD in the arc stability phenomenon (Figure 2.97).

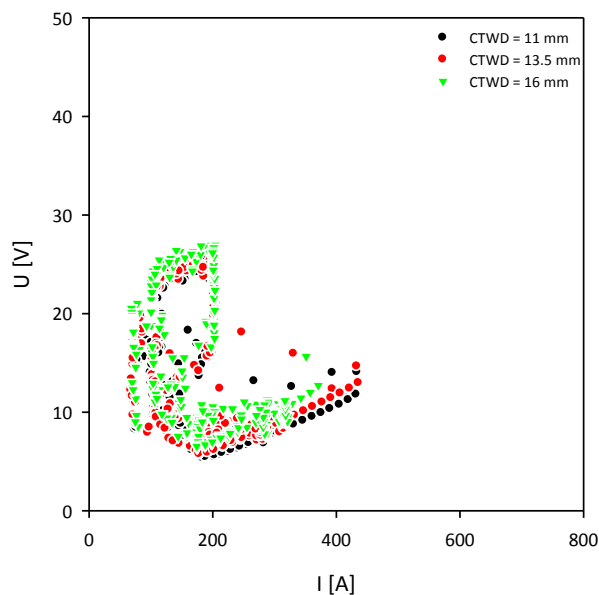


Figure 2.97 – UI diagram of the variation with CTWD for CMT-P.

2.5.6. Analysis of Bead Shape Characteristics

Different bead shape parameters were measured to analyse the fusion characteristics associated with different waveform designs and setting parameters. Among the bead shape parameters analysed depth of penetration, height and width bead, are the most important characteristics. Height to width ratio has been characterized as convexity index (Dantas e Costa 2004). Dilution ratio characterizes the molten area of base material and results in an important parameter to evaluate the fusion characteristics. The reinforcement ratio corresponds to the deposition area resulting from the wire melting. These parameters were

measured and the results of the measurements and graphical treatment are presented respectively in Appendix IX and X.

From the results obtained for all waveforms analysed, a comparison of the bead shape parameters indicated above was performed, and the results will be discussed regarding the physical phenomena and process parameters applied.

Depth of penetration is the first factor to be considered in any welding engineering application, as from this depends the success of the joining process applied. Then, other fusion characteristics that have a significant influence on welding quality are the dilution ratio and width bead. In the case of narrow groove welding, reinforcement ratio, height bead and convexity index should be always minimized to satisfy the project requirements.

2.5.6.1. Depth of Penetration

The analysis of depth of penetration as illustrated in the Figure 2.98 shows that depth of penetration in general increases when WFS was increased for all waveforms. However, above some WFS level penetration drops, as observed for RapidArc, CMT-P and CMT waveforms. This phenomenon is due to high current levels where an arc instability phenomenon has been identified, as characterized earlier. The strong variations between penetration levels have been described in the literature as affected by the peak current level. These results can be confirmed as the higher peak current levels are observed for RapidArc and CMT-P.

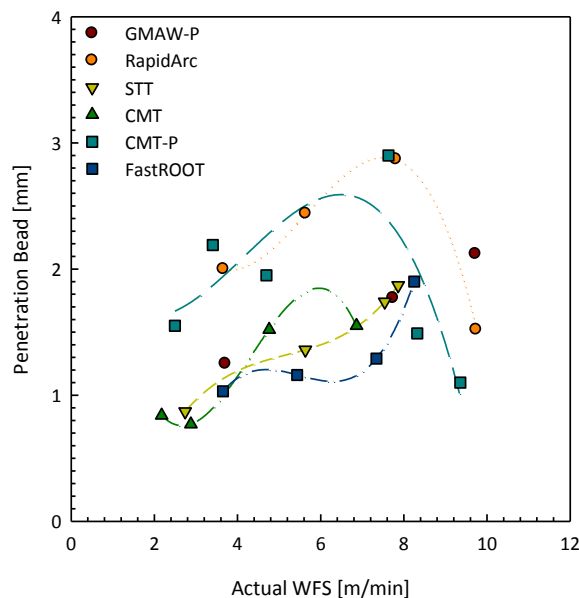


Figure 2.98 – Variation of depth of penetration with actual WFS for all waveforms.

It is observed from the results obtained that at very high currents, arc instability phenomenon takes place and a reduction of penetration bead occurs associated with the presence of undercutting.

Although the results of arc length adjusting parameter demonstrated that no significant changes happen in arc length, significant variations in depth of penetration are observed from the average and standard deviation, when this parameter is changed in five steps from the minor to the upper limits (Figure 2.99). These results are due to the significant changes in arc voltage and sometimes arc current, as illustrated earlier (Figure 2.28 and 2.35). This leads to a conclusion that arc length adjusting parameter does not change significantly the arc length, as the current is well controlled in most of these waveforms, but does contribute to significant changes in arc voltage and sometimes arc current waveforms resulting in significant changes in penetration.

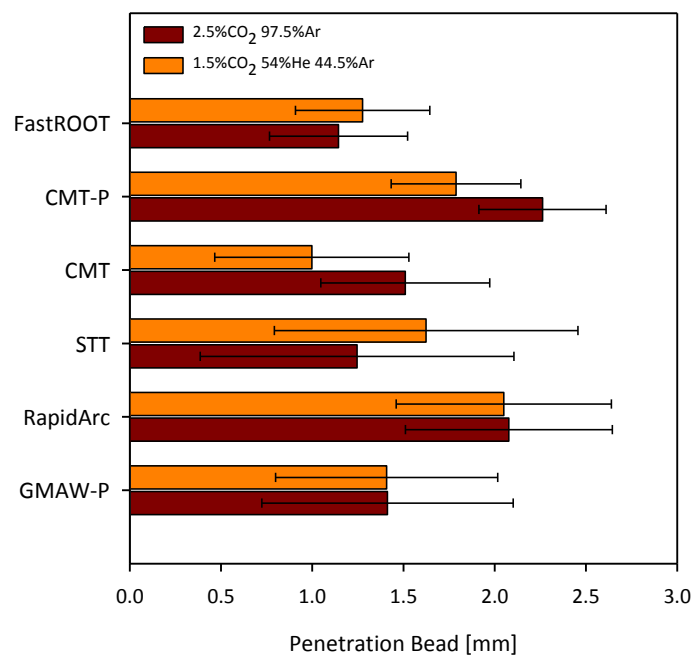


Figure 2.99 – Comparison of the average and RMS variation of depth of penetration for all waveforms, by changing arc length correction parameter (in five steps from lower to upper limits) for two shielding gas mixtures (WFS set of 6m/min).

It is observed that shielding gas composition influences differently the depth of penetration results depending on the waveform applied (Figure 2.99). Depth of penetration increases significantly when 1.5%CO₂ 54%He 44.5%Ar was applied for FastROOT and STT waveforms, compared to 2.5%CO₂ 97.5%Ar. However, the opposite is observed for CMT/ CMT-P waveforms. No effect on penetration was seen for RapidArc and GMAW-P. This led to the conclusion that shielding gas composition can affect differently the bead shape characteristics, depending on the waveform applied.

The effect of arc current on depth of penetration is shown in Figure 2.100. It is illustrated that in general depth of penetration increases with the arc current level for all waveforms. For RapidArc depth of penetration may decrease at certain WFS level, possibly due to the transition of mode of transfer.

It is observed in Figure 2.101 that in general depth of penetration increases with arc power.

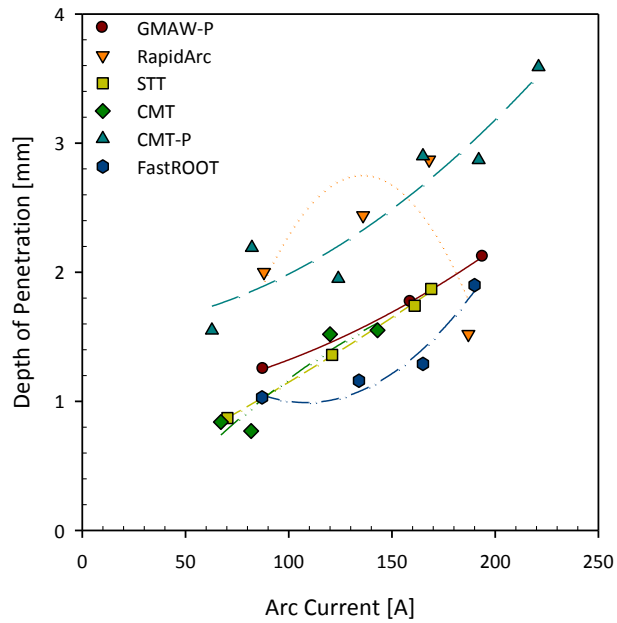


Figure 2.100 – Comparison of the effect of arc current on depth of penetration for all waveforms.

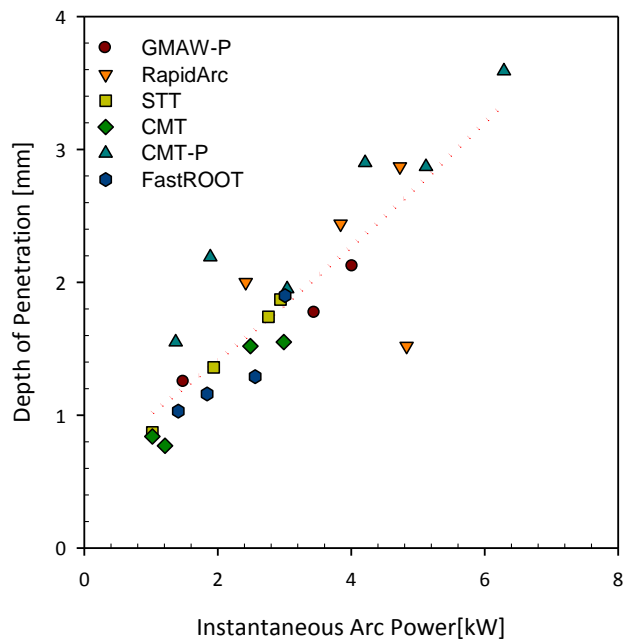


Figure 2.101 – Comparison of the effect of arc power on depth of penetration for all waveforms.

A deeper investigation was performed to understand the effect of waveform parameters on the increase of penetration. It is observed that the increase of peak current is associated with the increase of depth of penetration for most of the waveforms studied. Only CMT-P seems not to be affected by this parameter, as peak current is almost constant for the all range of WFS applied (Figure 2.102). In this case pulse frequency should play an important role in the depth penetration.

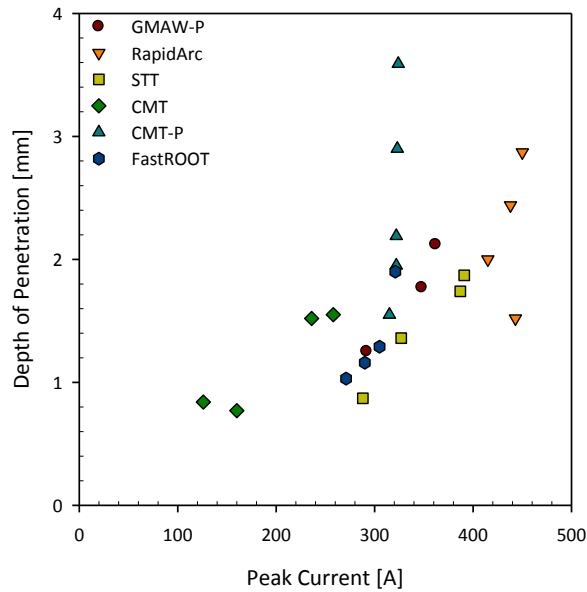


Figure 2.102 – Effect of peak current on depth of penetration for all waveforms.

2.5.6.2. Dilution Ratio and Dilution Area

The dilution ratio increases with WFS for all waveforms studied, but these variations occur differently within the different waveforms (2.103). It was observed from the macrographs obtained that at significantly high dilution ratio levels the undercutting phenomenon takes place. Furthermore, the instability conditions observed for spray transfer waveforms, at significantly high WFS levels, are also reflected by the decrease of dilution ratio.

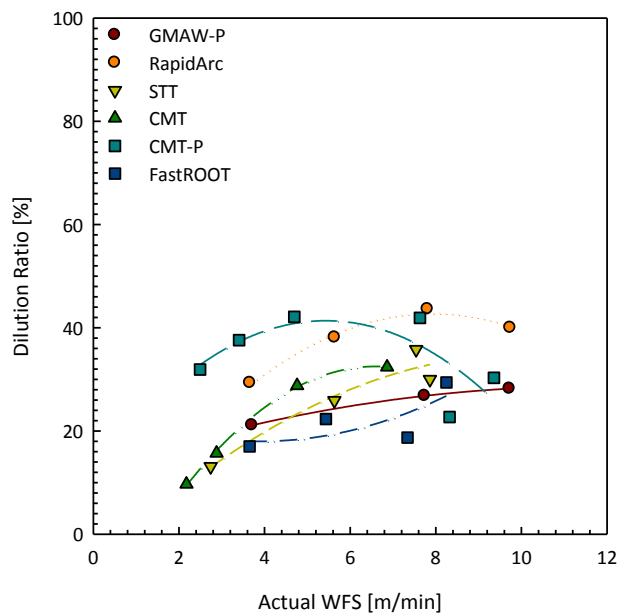


Figure 2.103 – Variation of depth of penetration with actual WFS for all waveforms.

As observed from the results of average and RMS variation for the comparison of the shielding gases when arc length adjusting parameters are varied from minor to upper limit in five steps suggest that shielding gas rich in helium creates higher dilution ratios for most of the waveforms evaluated. In fact, only Fronius waveforms are characterized by lower

dilution ratios associated with 1.5%CO₂ 54%He 44.5%Ar. This is probably due to the fact of CMT and CMT-P were optimized by Fronius to work with 2.5%CO₂ 97.5%Ar, hence the power source characteristics are able to control the physical mechanism associated to the variation of the physical properties of the gases (Figure 2.104).

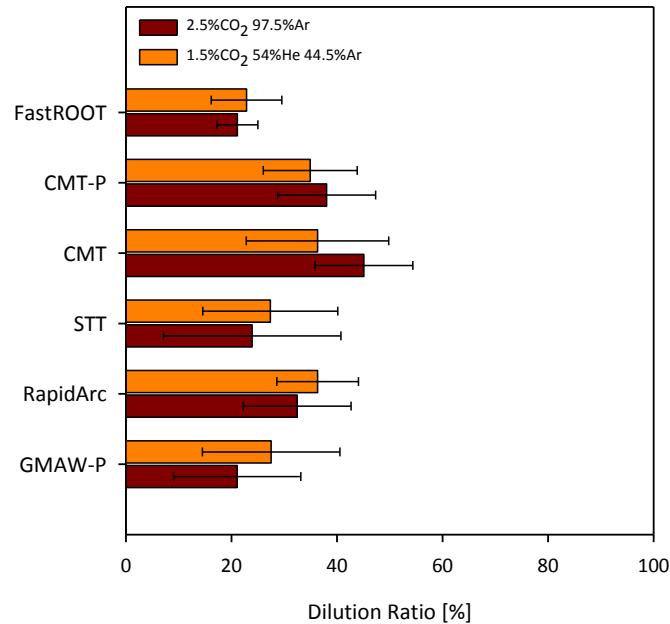


Figure 2.104 – Variation of dilution ratio with actual WFS for all waveforms.

The shielding gas composition has a similar effect for CMT and CMT-P waveforms as observed for the depth of penetration, i.e. 2.5%CO₂ 97.5%Ar is characterized by higher dilution ratios. The remaining waveforms present higher dilution ratios when 1.5%CO₂ 54%He 44.5%Ar. This led to a conclusion that Fronius waveforms (e.g. CMT and CMT-P) should be well optimized to the shielding gas suggested on the power source settings (i.e. 2.5%CO₂ 97.5%Ar).

Dilution ratio increases with the arc current level. Furthermore, it is observed for CMT that the increase of arc length correction adjusting parameter is associated with the increase of dilution ratio (Figure 2.105).

The Figures 2.106 and 2.107 shows the effects of respectively arc energy and arc current on dilution area. It is observed that in general the increase of arc current increases the dilution area for all the waveforms (Figure 2.106). Short-circuiting waveforms present lower dilution areas at the same arc current level. This led to the analysis of the effect of arc energy on the resulting dilution area (Figure 2.107).

The effect of arc power on the dilution area demonstrates that the increase of arc power is favourable to the increase of dilution area (Figure 2.107). From these analysis is observed that short-circuiting waveforms present the lower dilution areas, and CMT-P is at the highest levels.

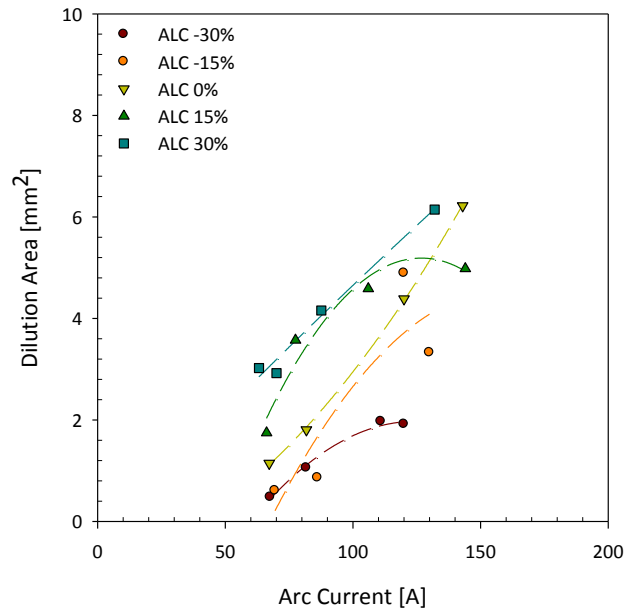


Figure 2.105 – Comparison of the variation of dilution ratio with arc current at different ALC for CMT.

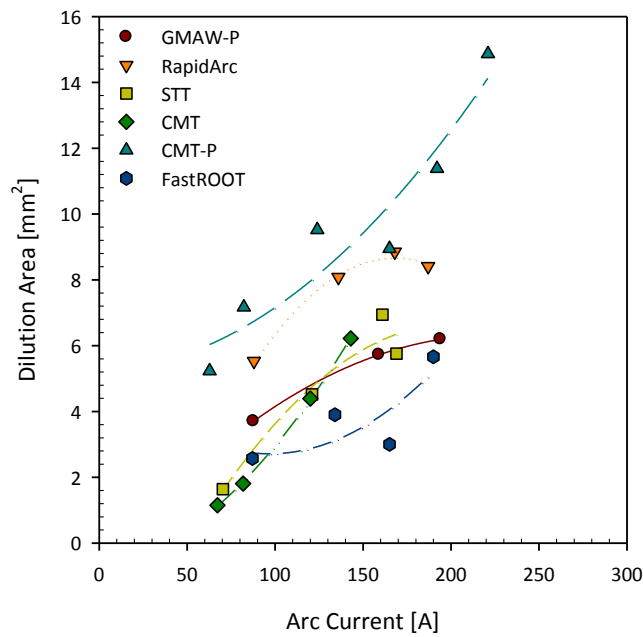


Figure 2.106 – Comparison of the variation of dilution area with arc current for all waveforms.

As observed from the Figure 2.108, with the exception of CMT-P which has constant peak current, the increase of peak current is associated with the increase of dilution area. These results led to a conclusion that the variation of dilution area for CMT-P is not affected by peak current. It is also possible to observe that similar dilution areas are achieved at different peak current levels, depending on the waveform. It may indicate that peak current even influencing the dilution phenomena, does not make it solely.

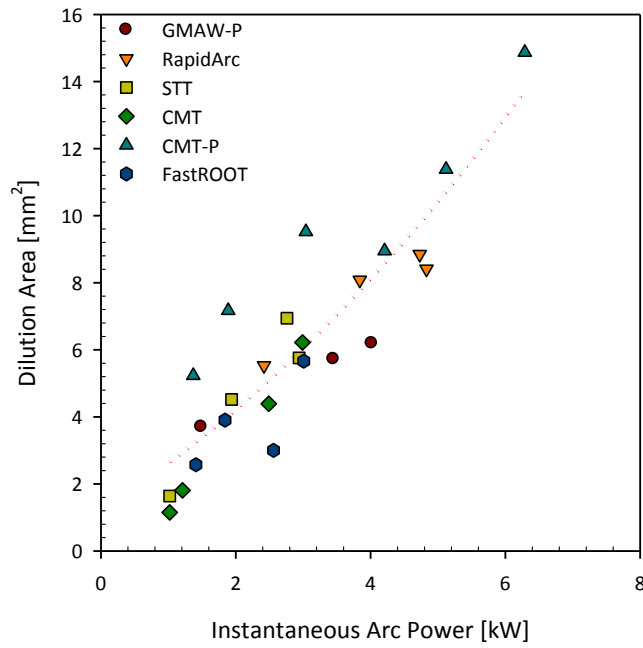


Figure 2.107 – Comparison of the variation of dilution area with arc power for all waveforms.

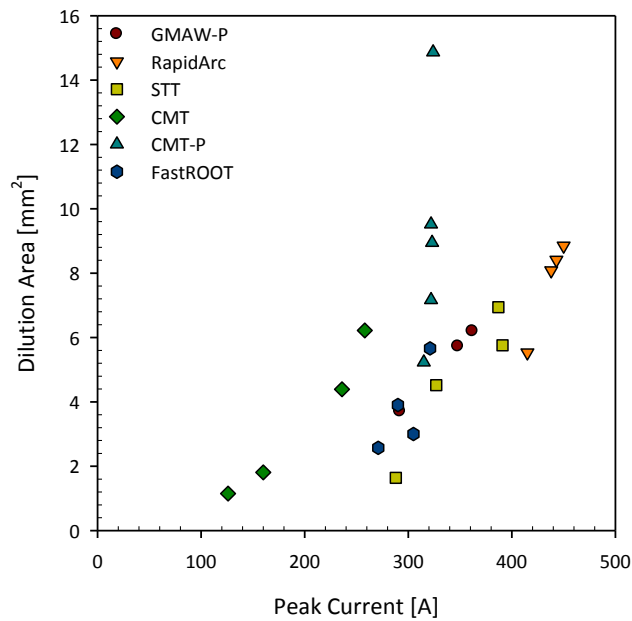


Figure 2.108 – Comparison of the variation of dilution area with peak current for all waveforms.

2.5.6.3. Width Bead Shape

The analysis of width bead shows that it generally increases with actual WFS for all waveforms evaluated. It is observed that significantly higher width beads are achieved with pulsed spray waveforms, as shown in Figure 2.109.

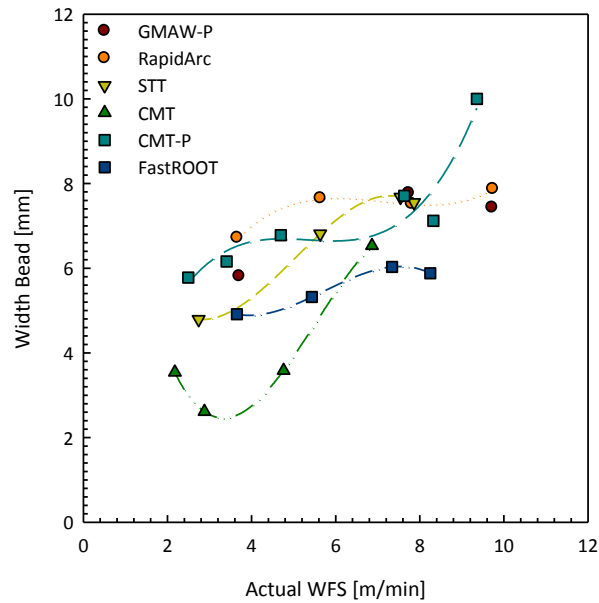


Figure 2.109 – Variation of width bead with actual WFS for all waveforms.

The variation of arc length adjusting parameter was performed in five steps from the minor to upper limits; average and RMS variation were measured and the results obtained suggest that width bead is always significantly higher when 1.5%CO₂ 54%He 44.5%Ar were applied (Figure 2.110).

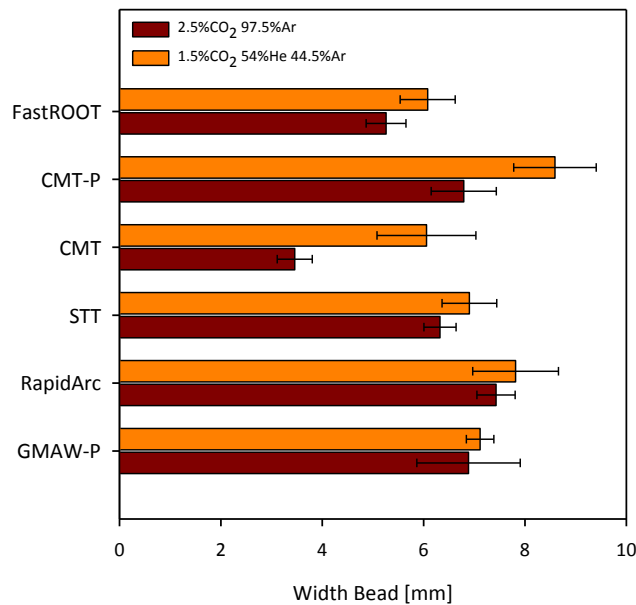


Figure 2.110 – Comparison of the average and RMS variation obtained for width bead by changing arc length adjusting parameter (in five steps from minor to upper limit) for all waveforms.

2.5.6.4. Height Bead

The analysis of the variation of height bead demonstrates that in general it does not change significantly with WFS (Figure 2.111).

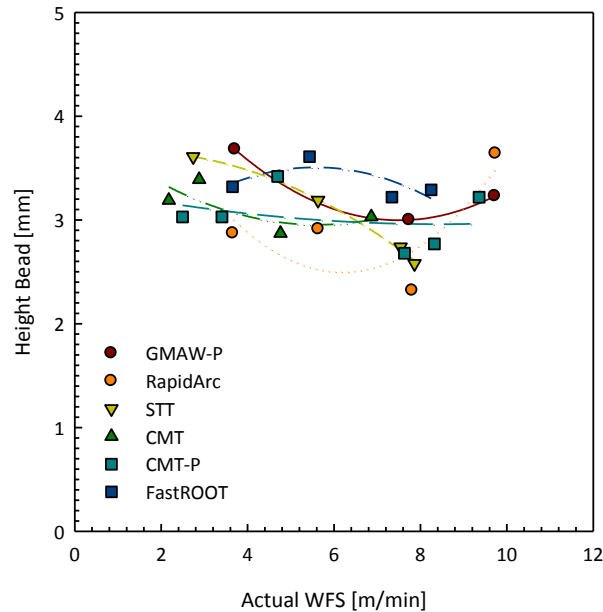


Figure 2.111 – Variation of height bead with actual WFS for all waveforms.

From the Figure 2.112 is observed that height bead seems to follow a similar law to all waveforms evaluated reaching a maximum at around 4m/min and a minimum at around 8m/min. It is still observed that the application of 2.5%CO₂ 97.5%Ar result in higher height bead shapes for all waveforms evaluated (Figure 2.112).

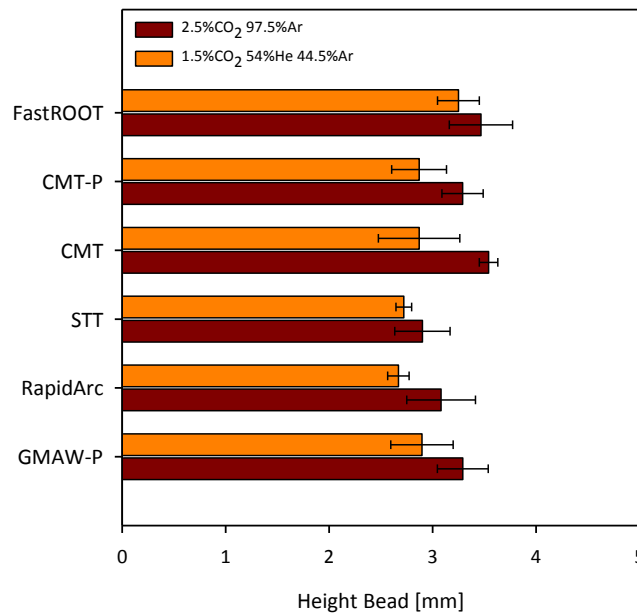


Figure 2.112 – Comparison of the variation of height bead with arc length adjusting parameter (five steps from minor to upper limit) for all waveforms.

2.5.6.5. Convexity Index

As it was characterized previously, the convexity index is characterized by the ratio between the height and width bead parameters. It is observed that in general decreases with WFS as the depth of penetration and dilution ratio increases. Convexity is generally higher for short-circuiting waveforms, as the arc energy is lower.

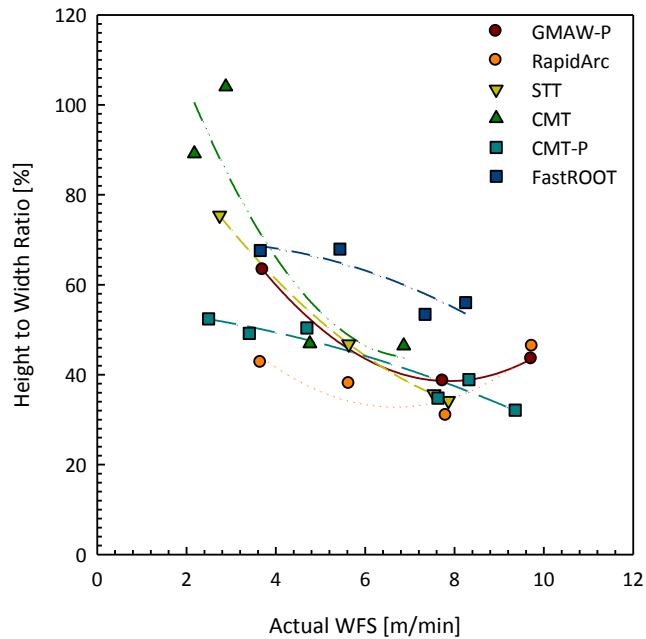


Figure 2.113 – Variation of depth of penetration with actual WFS for all waveforms.

As observed in Figure 2.113 the convexity decreases with the increase of WFS until reach a minimum in the range of 40%. It is noticed that CMT presents very high convexity at low WFS level but decreases appreciably with the increase of WFS. It is also observed that convexity index is always considerably higher when 2.5%CO₂ 97.5%Ar was applied (Figure 2.114).

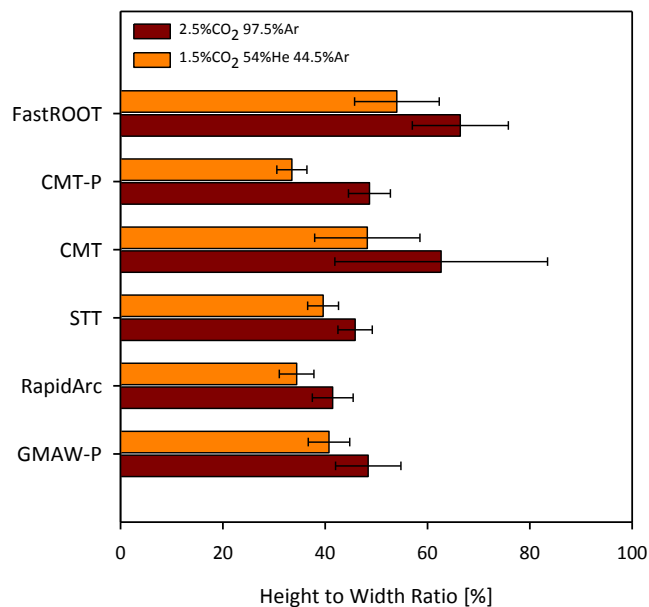


Figure 2.114 – Comparison of the average and RMS variation obtained for height to width ratio with by changing arc length adjusting parameter (in five steps from minor to upper limit) for all waveforms.

The analysis of the effect of arc energy on convexity index was also performed (Figure 2.115). It is observed that convexity index decreases with the arc energy until reach a minimum of about 30%, at 0.6kJ/mm. It is also observed from this analysis that convexity is generally higher for short-circuiting waveforms, where arc energy is considerably lower.

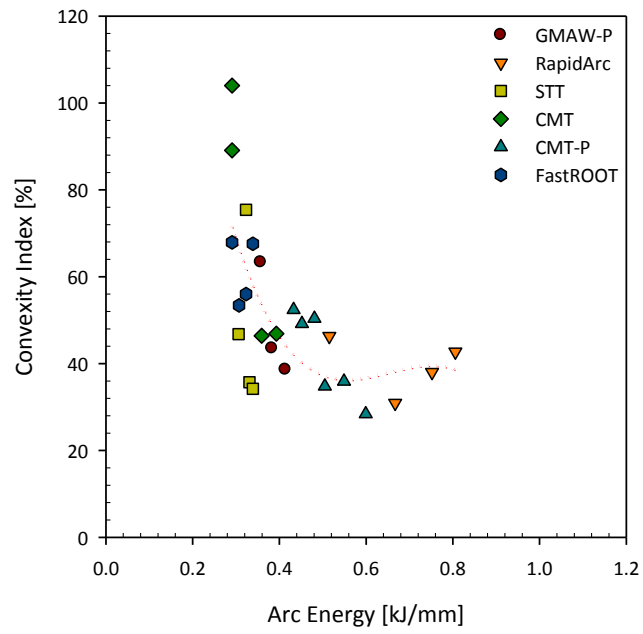


Figure 2.115 – Effect of arc energy on convexity index (height to width ratio).

2.5. DISCUSSION OF RESULTS

2.5.1. Introduction

Although during the last ten years several new gas metal arc welding (GMAW) waveforms have been developed, no significant fundamental research has been performed to evaluate the actual capabilities of these new technologies. Most of the technical information provided to the users is in marketing documents. In this perspective, several experimental tests were undertaken using those processes, in order to understand how these new technologies work and what are their main differences which are responsible to their success in the manufacturing industry.

The investigation undertaken in this Chapter included:

- The analysis of the effect of process setting parameters on the waveform design. The analysis of burn off ratio (relationship between arc current and wire feed speed) and arc voltage will be discussed;
- The characterization of the arc characteristics focused on the analysis of arc length and how arc length can vary according to the waveforms and setting parameters applied;
- The characterization of the mechanism of metal transfer – classification system and analysis of the effect of setting parameters on the transfer mechanism;
- The analysis of arc stability phenomena. It will include the examination of the factors affect that affect arc stability control during arc welding;
- The evaluation of the effect of process setting parameters and waveform design on the bead shape characteristics;
- Analysis of the arc energy generated using different waveforms and process setting parameters.

2.5.2. Waveform Design and Characteristics

Process characteristics of GMAW waveforms, using pulse spray and short-circuiting variants, have been extensively explained during the literature review and are already well established.

From the research developed in this chapter, the main differences in the design of the waveforms are now known, and may offer different shape characteristics by the way that metal is transferred and arc stability is achieved. The power source characteristics and external setting parameters have also a critical function on the arc stability phenomena and the mechanism of metal transfer.

The results obtained in the Section 2.4 shows that burn-off ratio is very similar for all the waveforms studied. This led to a conclusion that the burn-off ratio for all of the waveforms

investigated is the same, even when we work under short-circuiting or pulse spray conditions.

Arc length adjusting parameter may also affect the burn-off ratio by increasing or decreasing slightly the mean arc current. At the limit conditions of arc length correction parameter it is observed that burn-back takes place. This represents a significant observation and can be explained since arc stability conditions are only achieved around the burn-off criteria law, which is a function of the amount of the wire melted per unit of time, i.e., only depends of the size and characteristics of the filler wire. If this criterion is not established the arc stability is lost and consequently burn-back occurs.

The deeper analysis of arc current waveform still shows significant variations of peak current among all waveforms evaluated, within approximately 200A difference when CMT and RapidArc are compared. It is led to several variations on the resulting bead shape characteristics. It is also noticed that peak current does not change significantly for RapidArc and CMT-P waveforms. For CMT-P the burn-off ratio is achieved by the variation of the ratio between pulse frequency and short-circuiting frequency.

Arc current and voltage waveforms are significantly lower for short-circuiting waveforms than pulse spray waveforms, as characterized in the Section 2.4.

On the other hand, the arc voltage waveforms present more significant variations with RapidArc leading the highest peak and background values at all range of WFS. The peak current does not change considerably with WFS but background considerably drops down at about 9-10m/min, probably in consequence of unstable phenomena in the transition region of the metal transfer. This behaviour results in a significant reduction of the bead shape characteristics.

Furthermore, it is also attempted that the variation of all external parameters, e.g. CTWD, shielding gas composition, etc, affects the resulting arc voltage of this waveforms.

Although the burn-off criteria are the same, considerable variations are observed between the waveforms investigated in this work. As indicated in the Figure 2.116, using constant WFS set (6m/min), the UI diagrams shows considerable differences in the shape of the waveform cycle. The column on left shows the pulse spray waveforms (e.g. GMAW-P, CMT-P and RapidArc) while on right side is found the short-circuiting waveforms (e.g. STT, CMT and FastROOT). As can be observed it is not only the difference of arc current and voltage themselves which affect the metal transfer and arc stability phenomenon but also the way as they are synchronized and what this implies in terms of the waveform cycle characteristics.

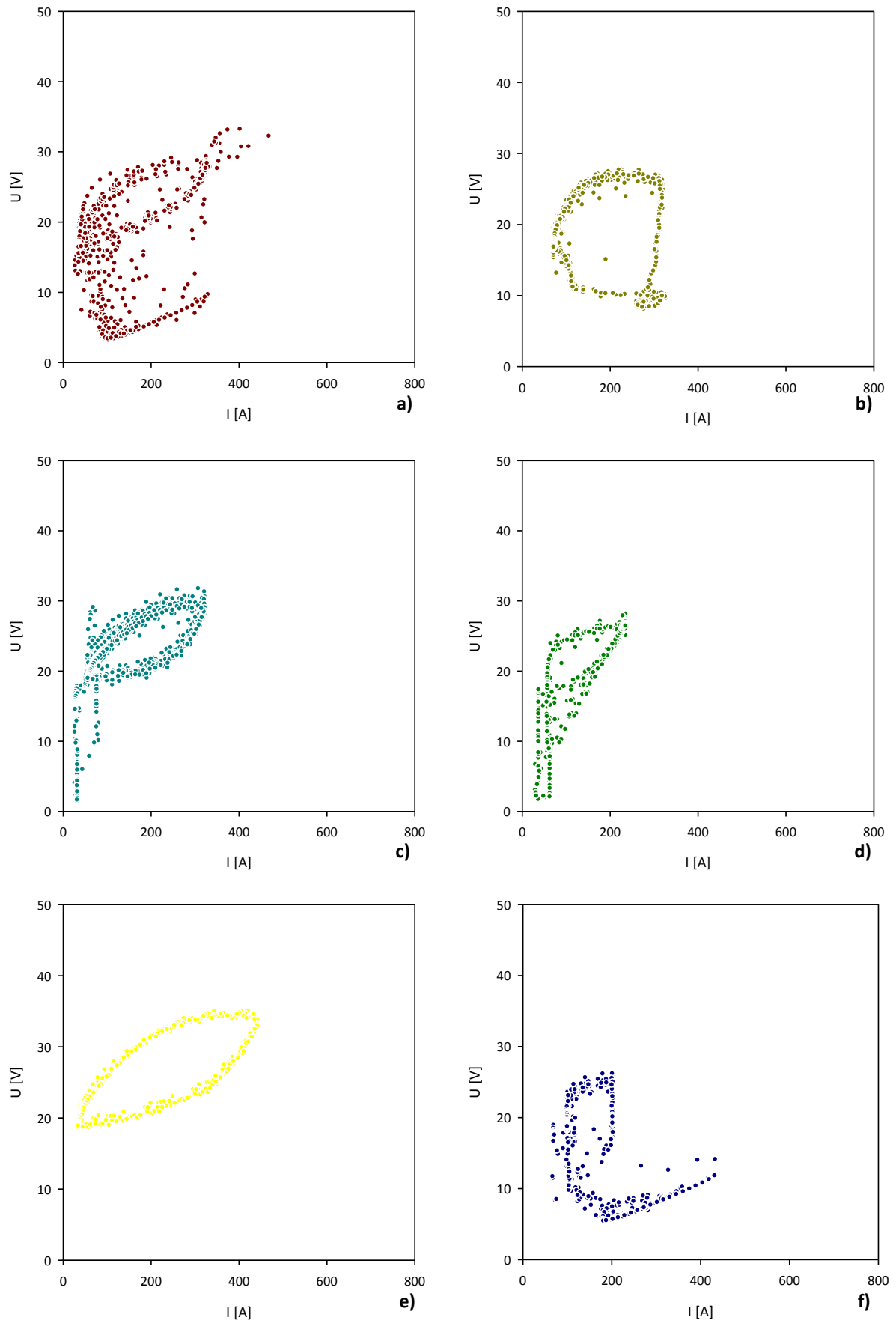


Figure 2.116 – Comparison of Stability Diagrams for all waveforms: a) GMAW-P; b) STT; c) CMT-P; d) CMT; e) RapidArc; and f) FastROOT.

Also, as observed from these diagrams, is easy to understand how the waveform reacts to the unstable arc characteristics, as the variations of cycle becomes more significant and may lead to short-circuiting associated with splashing (e.g. GMAW-P). This is the reason for highlighting the importance of UI diagrams to evaluate the waveform stability.

In these diagrams the region of short-circuiting is easily identified at low arc voltage levels. Although most short-circuiting phenomena normally occur at low arc current, as particularly observed for CMT waveform, in STT waveform it occurs at high current levels, as indicated by the concentrated points below 10V. The well defined line of points in the case of either GMAW-P or FastROOT also indicates the effect of joule heating, characterized by the resistance of wire. The peak period is given by the hysteresis and generally is established from relatively high voltage and current levels. In pulse waveforms the hysteresis represents the pulse period and process stability better as points synchronize on the passage of different cycles. This is helpful in assessing stability; much higher stability is achieved for RapidArc compared with GMAW-P at the conditions set. Both arc voltage and current get considerably higher for this waveform than the remaining waveforms evaluated.

2.5.3. Mechanism of Metal Transfer

The modes of metal transfer for arc welding processes have been extensively characterized during the literature review (Section 2.1). The recent advances in GMA welding technologies launched new challenges to understand the physical phenomenon and the transfer characteristics resulting from these new waveform designs.

Fronius launched a new concept of transfer with CMT/CMT-P waveforms, where the power source and wire feeder are automatically synchronized and can vary to promote the final arc stability. This mechanical assisted transfer process is a result of a push-pull wire feeder in the torch body assisted by a free loop in the centre of the torch hose, where the wire can advance and retract according to the power source instructions. The wire retracting and advancing system allow much higher stable arc lengths since the wire can quickly move and touch the molten pool right after the arc ignition, and retract again after transfer is completed. This results in a smooth rupture of the molten bridge during the short-circuiting period and is characterized by the reduction of splashing and spatter projection often observed in GMAW-S, with further benefits in aesthetics and bead appearance. This is in agreement with the analysis of CMT/CMT-P by (Pickin and Young 2006).

Within the CMT-P waveform, pulse transfer is synchronized with short-circuiting, increasing significantly the arc energy, and therefore promoting higher dilution ratios and depths of penetration. This is the first time a waveform has been developed as a controlled mixed mode, since previously mixed modes have been observed but under uncontrolled conditions, as a result of instability (Palani and Murugan 2006) (Scotti 2000). Although some results have been shown for welding of aluminium with CMT-P (Pickin and Young 2006), the

metal transfer mechanism has not been investigated, nor has arc stability control or process characteristics.

Some researchers (Feng, Zhang and He 2008) (Zhang, et al. 2009) (Pickin and Young 2006) have already analysed the mechanism of metal transfer for CMT waveform when applied to aluminium, but with limited information on process characteristics.

2.5.3.1. Classification of Metal Transfer

The first classification of the modes of metal transfer in arc welding with addition of filler metal was proposed in 1976 (Anon (1976)). Three categories were included in this classification, respectively short-circuiting or dip transfer, globular and spray transfer.

Several advances have been developed during the last three decades and new concepts included in this classification. Norrish (2003) extended this classification considering three main groups: natural, controlled and extended operating modes. The natural modes subdivide into the categories defined by Anon (1976) and the controlled modes into both short-circuiting and spray. Iordachescu and Quintino (2007) included a sketch of the modes of transfer into the classification for natural modes.

More recently, Ponomarev et al. (2009) proposed a new classification system based on three classes as follow: natural, controlled and combined metal transfer, but considering a more complex sub-classification scheme where contact mode and free-flight mode groups are established as the natural modes and different controlled and combined sub-categories are also considered. This proposal does not satisfy the initial idea of the classification where modes of transfer are simply classified by the way that metal is transferred, and then the advances in welding controlling systems are variants of the main modes.

Furthermore this classification does not provide a full range of controlled modes classified according with main parameters, instead of the mode of transfer as established in the natural modes, e.g. short-circuiting, spray and globular, the last ones included in the free-flight group. In addition, according with the results obtained for CMT-P the controlled metal transfer classification should include a sub-category for controlled mixed modes. The results of metal transfer classification shows that for the first time a welding process includes two different modes of controlled transfer, short-circuiting and pulse spray transfer.

STT, CMT and FastROOT should be included in the sub-category of short-circuiting controlling metal transfer, as already mentioned by some authors (Iordachescu and Quintino 2007) (Ponomarev, et al. 2009). GMAW-P and RapidArc should be included in the category of pulse spray controlled metal transfer. It was mentioned by Norrish (2003) that RapidArc should be considered in the category of extended stick out GMAW in the group of short-circuiting transfer, but in fact this process works as pulse spray transfer process.

The analysis of the all waveforms showed significant conditions where uncontrolled mixed modes were identified, but those are mainly due to the instability phenomena and result

from process setting conditions applied. These phenomena will be discussed in more detail in a further section.

Considering the Tables 2.1 and 2.2, the new classification should respect the main modes defined in the Table 2.1 and an extension should be added to the Table 2.2 in order to include the new waveforms/ processes recently developed, as illustrated in the Table 2.27, as follow.

Table 2.27 – Proposal for classification of controlled transfer modes.

Metal Transfer Mode	Commercial name
Controlled Spray Pulse transfer	Lincoln RapidArc
Controlled Short-circuiting Dip transfer	Lincoln STT, Fronius CMT, Kemppi FastROOT
Controlled mixed modes Alternated dip transfer with pulse transfer	Fronius CMT-P

2.5.3.2. Analysis of Metal Transfer

The classification of metal transfer for the waveforms evaluated were defined under the previous section, but different process settings may generate arc instability phenomena resulting in variations on the mechanism of metal transfer. The analysis of the processes parameters will be discussed from the results presented in Section 2.4.4.

An analysis of metal transfer for all waveforms investigated would indicate the following sequence according with arc stability: CMT>RapidArc>CMT-P>STT>FastROOT>GMAW-P. (Note that this sequence is only valid for the experimental conditions used in this study).

Different process parameters have produced unstable disturbances for the all waveforms considered. For high current levels, i.e. high wire feed rate, different settings of arc length adjusting parameter and CTWD, and different shielding gas composition can be associated with disturbances and process instability. However, this varies according to waveform. The disturbances observed are generally reflected by variations in arc voltage, since the arc current is well controlled for most of the waveforms under investigation.

This analysis will be performed for pulse spray transfer processes and dip transfer processes separately, since the balance of forces controlling the metal transfer mechanisms is different.

Pulse Spray Transfer

In GMAW-P the irregular behaviour observed was mainly associated with a low CTWD. Two different reasons justify the application of low CTWD, the fact that the remaining processes worked positively with this condition for bead on pipe welding tests and because low CTWD's and short arc lengths are necessary in narrow groove pipe welding to eliminate arc repulsion and deflection to the groove side (Modenesi 1990). This will be discussed in detail

in Chapter 4. However, these unstable conditions obtained with the lower CTWD set for GMAW-P limited the understanding of the effect of other parameters, such as arc current. In fact it is observed that at the CTWD applied (i.e., 11mm) the power source characteristics result in a very short arc length, increasing the arc pressure and resulting in arc splashing phenomenon. The trials carried out at higher CTWD (13.5 and 16mm) suggested a progressive decrease of the uncontrolled short-circuiting phenomena from 70% (11mm) to 20% (13.5mm) and 10%(16mm) (approximated percentages relative to the ratio of short-circuiting – droplet transfer mechanism). The analysis of the effect of trim at low trim values (below 1.0) shows that arc splashing is more frequent due to the increase of uncontrolled short-circuiting phenomena.

The uncontrolled short-circuiting observed for this process is mainly due to the voltage drop phenomena, which may result from the decrease of the electromagnetic force. This force has been considered the controlling force during the droplet detachment mechanism and its effect increases at high current levels by the effect of a high Lorentz force during a short time period (Palani and Murugan 2006). Furthermore, the decrease of arc voltage is also determined by the short arc length levels observed, which results from the balance of the forces acting in those conditions.

In contrast to what was observed for GMAW-P, for RapidArc good process stability is obtained with most of the welding conditions applied for CTWD as low as 11mm. The most significant unstable mechanisms observed for RapidArc are due to the short arc lengths observed at very high current levels (i.e. high wire feed rates) and when low trim (arc length adjusting parameter) values were set. The uncontrolled short-circuiting phenomenon was mostly identified at low trim values, while at high current levels the increase of voltage during background time generates stubbing phenomena characterized by explosions and spatter projections.

The CMT-P waveform is characterized by a controlled mixed with constant background and peak arc current, but where the number of pulses between each short-circuit increases with the wire feed rate. The results of metal transfer revealed that very good arc stability is achieved within this waveform. The main disturbances are observed at the high wire feed rates and at the limits of arc length correction and pulse control parameters. At very high currents unstable mechanisms are often observed, characterized by a high background voltage level. This may result from a very high arc pressure due to the deviation of burn-off criterion conditions. Rotation transfer is also observed and characterized by arc deflection when peak arc current is very high.

Dip Transfer

In short-circuiting transfer STT, CMT and FastROOT are characterized by a bridge effect developed between the molten wire and the weld pool. However, the wire motion system

present in CMT results in much smoother and stable control of the short-circuit promoting a clean rupture of the molten bridge.

Compared to other Lincoln waveforms analysed, i.e. GMAW-P and RapidArc, for STT welding the most stable conditions are identified within nominal trim values. In fact at very low and high trim values different disturbances were often identified, such as arc plashing, spatter and globular formations when trim is too high. This effect of globular droplet transfer is due to the significantly higher current and voltage levels identified, associated with longer arc length.

Furthermore, higher instability phenomena were found at higher current levels, at the limit of wire feed ratio allowed for this process. The increase of CTWD generated longer arc lengths and longer background periods, where short-circuiting frequency is reduced. This effect results in a considerable change of the waveform shape and droplet detachment takes place, sometimes globular and linked to splashing.

CMT is generally more stable than STT, and the waveform is much better controlled at most of the range of conditions used in this project. However, at very high arc length correction parameter arc voltage instability is linked to droplet detachment mechanism of drop spray transfer (drop size similar to wire diameter) and splashing.

At the limit of arc current levels for this process, i.e. when the wire feed rate is maximum (WFS set of 8m/min), uncontrolled mixed modes can be found, from globular, short-circuiting and drop transfer, becoming the overall transfer generally unstable.

Also when CTWD is increased from 11mm, drop spray transfer is observed within CMT. The arc length, in general considerably higher than for the remaining waveforms, becomes even higher and possibly the surface tension forces acting during dip transfer are reduced with the electromagnetic forces becoming more significant. The analysis of FastROOT transfer shows that the process is characterized by significantly higher arc instability and almost all the conditions used in this project were associated with spatter. However, some conditions worked under severe disturbances. In particular at very low base current levels (i.e. -50%) splashing is generally associated with the arc re-ignition. The instability is also significantly higher at the highest current levels (when WFS is in the range of 8-9m/min). In this case, the waveform is significantly uncontrolled, resulting in very high arc splashing. However, the arc length is always kept very short which enables the droplet detachment to occur, even at high current levels. One reason for the unstable arc conditions generated within FastROOT may due to the fact that its intended application is on open gap welding, as was pointed out by Uusitali (2007).

2.5.3.3. Droplet Detachment in Pulse Waveforms

In pulse spray transfer welding the “one droplet per pulse” (ODPP) condition has been extensively discussed in the literature (Amin 1983) (Kim 1989) (Kim and Eagar 1993 b) (Wu,

Chen and Lu 2005). These authors attempted that to ensure repeatability and controlling of GMAW-P to achieve only one droplet per pulse. Miranda et al. (2007) developed an optical sensor to recognize if less than one, one or more than droplet per pulse during GMAW-P.

The results obtained suggest that for GMAW-P the condition of one drop per pulse is generally obtained when good stability conditions were achieved. However, unstable conditions can result in a droplet diameter greater than the wire diameter, characterized by irregular globular transfer, at relatively low – medium arc currents. At high peak current levels and short pulse periods the energy is too small and the droplet transfer is characterized by large globules (Ueguri, Hara and Komura 1985).

The RapidArc waveform is characterized by more than one drop per pulse; the results suggest that a drop with size similar to the wire diameter is followed by a second small drop. At significantly high CTWD (i.e., 16mm) more than one small drop can follow the main drop. These results suggest that arc stability can be achieved with reproducible conditions when more than one droplet per pulse is achieved when this waveform is applied. This behaviour is associated with the significantly higher voltage level and has an interesting effect on bead shape characteristics. These results contradict the published data from Lincoln (Lincoln Electric 2004) (Lincoln Electric 2005), which claims that RapidArc operates at lower arc voltage levels than conventional GMAW-P. Choi et al. (1998 b) considered that when more than one droplet is transferred, higher drop transfer frequency is identified. These authors also pointed out that axial flow and radial pinch force play an important role in the detaching mechanism associated with spray and globular transfer modes. The effect of these two forces increases with arc current level, when axial flow becomes dominant. In spray transfer, the current density has also a significant effect on the free surface profile and drop size. These results are important since they are in agreement with previous work based on pinch instability theory and force balance model, and can provide some information about the forces acting during detachment mechanism in spray transfer.

2.5.4. Arc Stability Control

Arc stubbing and burn back are considered two limiting conditions in welding and result from the loss of burn-off criteria. Palani and Murugan (2006) considered that variations between wire feed ratio and burn-off ratio would compromise the stability criteria, by causing burn backs and arc stubbing characterized by the loss of the burn-off criteria and resulting in the formation of welding defects. In fact, arc stubbing was observed particularly for CMT-P welding when lower arc length correction parameter (-30% to -15%) was set at different WFS levels (9 and 10m/min). This can be considered the most severe unstable conditions which limit the application of the welding process. In general the initial stages of welding are characterized by instability which increases with arc current level and are generally characterized by spatter projections (1998 b). It has been noticed from the results obtained that this effect is lower when CMT/CMT-P and RapidArc waveforms were applied.

The instability phenomena in arc welding depends of several factors such as the welding time, arc length, shielding gas composition and power source characteristics. The instability happens when the burn-off criteria is not respected and will result in variations of waveform fluctuations and metal transfer disturbances. Furthermore consequences in the bead shape characteristics and the arc energy will be developed.

Effect of Welding Time

This effect is always observed particularly in the first instants of welding and is due to the transient start, when the plate is cold and the weld pool is being generated. This may related to the materials properties and the thermal cycle. Other factors that may contribute to this effect are the surface conditions and oxidation level. High oxide levels are thought to have a strong influence on the arc instability.

Effect of the Arc Length

The results obtained from all waveforms demonstrated that when arc length becomes shorter, unstable phenomena are observed during the metal transfer. It is known that arc length variations are much more significant in CV GMAW waveforms, as the arc length itself adjusting to ensure arc stability. However small variation in arc length associated with pulsed controlled or short-circuiting controlled waveforms can have a considerable impact which is an indication of the instability phenomena. The reduction of arc length can result from different effects such as the reduction of arc voltage, short-circuiting frequency, arc current or CTWD.

Effect of Shielding Gas Composition

The influence of shielding gas composition has also a significant effect on the arc length, arc energy and melting efficiency (Dillenbeck and Castagno 1987) (Menzel 2003). It is established that helium increases these parameters due to its higher ionization potential (Eagar 1990). Increased helium produces an increase in the arc voltage, which generates a longer arc length. Although the increase of arc length is favourable to the stability phenomena in pulse spray waveforms, for short-circuiting waveforms this reduce the stability necessary to achieve a molten bridge. Furthermore the increase of arc length is also associated with the increase of arc voltage, which determines the increase in arc energy and result in the increase of arc instability.

Effect of Power Source Characteristics

This is probably the most important factor associated with the instability phenomenon. In fact all these waveforms work in a controlled mode and follow specific characteristics developed by the different companies, which has been characterized and demonstrated during the previous sections. It is the power source characteristics that define the way the

forces act during the metal transfer, and thus create unstable welding conditions. This effect has been already pointed out by Modenesi (1990).

As observed from the waveforms, the unstable phenomena are almost always followed by the variations in the arc voltage waveform. In particular uncontrolled short-circuiting results in an unstable waveform. However, as observed for GMAW-P the unstable conditions resulting of relatively low CTWD, i.e. 11mm, are due to the very short arc lengths and probably resulting from the high arc pressures developed during the arc period. These unstable conditions are related to the power source characteristics.

2.5.5. Arc Energy

Arc energy is the electrical energy produced by the arc current and voltage waveforms. The electrical energy is transformed into thermal energy through the arc plasma formed between the torch and the workpiece. Arc energy is therefore defined as the product of welding voltage and current divided by travel speed of welding (ISO13847 2000). Commonly, arc energy has been confused with heat input, which is defined as the energy introduced into the weld region during welding (usually expressed per unit length) (PDCEN/TR14599 2005). The ratio between arc energy and heat input is defined as process efficiency and represents the percentage of heat delivered at the contact tip of the torch that is absorbed by the workpiece. The remaining heat is loss to the surroundings by conduction, convection, radiation and metal vaporization.

The study of the variations of arc energy (calculated using instantaneous arc power) demonstrates that is mainly due to the wide variations in arc voltage waveform. As indicated from the stability diagrams (Section 2.4.5) and waveform signals (Appendix VIII), arc current is well controlled in most of the waveforms evaluated. It is observed for RapidArc waveform the reduction of arc energy with the increase of WFS, using similar WFS/TS ratio (conservative volume). It may results from almost constant level obtained for the peak current and voltage parameters. Furthermore, the high arc energies obtained at low WFS levels can have consequences in material properties.

Since important variations are observed in respect to the arc energy delivered in similar welding conditions to all the waveforms tested, it is obvious that a clear understanding of the energy absorbed by the workpiece (i.e., heat input) should be obtained. This led to the conclusion that process efficiency should be investigated, to understand whether process efficiency changes between the power sources, welding waveforms or the process setting parameters.

2.5.6. Bead Shape Characteristics

The bead shape characteristics obtained on bead on pipe/ plate depends of the way that energy is transferred from the arc to the workpiece. This suggests a complex balance with variables that are not very well understood.

The analysis of melting and fusion characteristics represent a major contribution to the overall understanding of the GMAW waveforms investigated in this work. Emphasis was given on detailing the specific influences of different variables on bead shape characteristics. Among those variables, arc length adjusting parameter, CTWD and shielding gas composition were deeply evaluated.

The reinforcement area results from the melting of filler wire, while the dilution area corresponds to the area of parent material that is melted. At similar WFS/TS ratio reinforcement area should be constant, but dilution area can change. The dilution area depends on the arc energy resulting from the arc current and voltage waveforms.

From the results obtained, it is observed that dilution area increases linearly with the arc current except for CMT-P which operates at constant peak current. For CMT-P, dilution area is related to the ratio between pulse frequency and short-circuiting frequency. For the remaining waveforms dilution area is strongly affected by peak current. However, it is the arc power level that most seems to influence the resulting melting phenomena. It was observed from the results obtained for all processes that dilution area increases with arc power.

Depth of penetration is probably the most important bead shape characteristic in welding engineering. Lack of penetration is undesirable and unacceptable in most of engineering projects.

A deep investigation on the variation of depth of penetration using different GMAW waveforms was performed. It is shown from the results obtained that the depth of penetration generally increases with WFS. However, the variations on process characteristics and the mechanism of metal transfer, discussed earlier, led to significant changes in the depth of penetration obtained using different waveform designs. Pulse spray waveforms are able to achieve deeper levels of penetration than short-circuiting waveforms. Furthermore, peak current is probably the most important parameter controlling the depth of penetration but the arc power may also affects the overall penetration achieved.

It has been postulated that the fusion area in GMAW is characterized by two regions: a) central finger penetration; and b) shallower and approximately elliptic region formed possibly by heat conduction in a liquid layer (Quintino 1986) (Modenesi 1990). The arc current level influences the finger penetration, but this generally dominates in GMAW with argon rich gas shielding.

In bead on pipe welding at low travel speeds the liquid volume in the pool can be so high that it tends to flow under the arc cushioning the base metal and impairing its fusion. Quintino (1986) founded a critical travel speed for GMAW-P in the range of 1 - 3mm/s (0.06 - 0.18m/min) beyond which the penetration is greatly reduced.

The influence of arc current and arc energy on the resulting depth of penetration is similar to what has been discussed for the dilution area. It was observed from this investigation that depth of penetration is firstly controlled by the arc current, in particularly due to the peak current. However, the arc power has also a fundamental role in the depth of penetration. Different process setting parameters also suggest the variation of penetration, e.g. the arc length adjusting parameter and the shielding gas.

In fact, a linear relationship for the increase of depth of penetration with the arc length adjusting parameter was postulated. The increase of arc length adjusting parameter is generally related to the increase of depth of penetration.

From the results of bead on shape characteristics obtained is also observed that convexity decreases with the increase of arc energy. It can be pointed out that short-circuiting waveforms present higher convexity levels and lower depth of penetration and dilution area are identified. In opposite, the increase of arc energy for pulse spray waveforms can result in undercutting, as observed at high WFS levels for CMT-P and RapidArc waveforms.

The effect of shielding gas was also analysed. From the results obtained, only Fronius waveforms (i.e. CMT and CMT-P) present lower depth of penetration, when a shielding gas mixture rich in helium was applied (i.e. 1.5%CO₂ 54%He 44.5%Ar). This may result from the optimization of the waveform and the power source characteristics to the gas mixture suggested, i.e. 2.5%CO₂ 97.5%Ar.

In general the application of 2.5%CO₂ 97.5%Ar contributes to the increase of height bead and bead convexity, while the application of 1.5%CO₂ 54%He 44.5%Ar results in wider and shallower welds reducing the convexity index. However, the arc stability associated with the application of this gas is in general reduced, which lead to undesirable results in the bead shape characteristics.

2.5.7. Summary of Processes Characteristics

A summary of the main characteristics observed for the processes analysed in this thesis are present in Table 2.28.

Table 2.28 – Summary of the processes analysed.

Process	Technical Information	Results Obtained
RapidArc	<ul style="list-style-type: none"> intended for operation at low voltages; claims that conventional pulse welding uses 23-26 V, while rapid arc welding can work at 16-19V, allowing the use of high welding speeds; The increase of welding speed is associated with a reduction in the cycle time, allowing lower spatter emissions and heat input when compared with conventional MIG/MAG welding. 	<ul style="list-style-type: none"> Works at high voltages (compared with other processes); High welding speeds can be achieved; High arc stability allowing less spatter emissions; Arc energy is generally higher than other processes at low WFS and similar to other Pulse Spray processes at high WFS.
STT	<ul style="list-style-type: none"> Elimination of lack of fusion; reduction in heat input; generates less spatter and fumes; background current varies from 50 to 100A, which maintains the arc and heats the parent material; A reduction of current occurs during short-circuiting, followed by a pinch current, which promotes the detachment of the molten metal from the electrode to the weld pool. 	<ul style="list-style-type: none"> Lack of fusion was generally observed in welding of narrow groove in this project; Heat input is generally low; Arc instability associated with short-circuiting splashing is identified; At the upper limit of WFS (8.26m/min) arc instability phenomena are more significant.
CMT	<ul style="list-style-type: none"> droplet transfer is based on a mechanical oscillation of the wire; possibility of simultaneous dip transfer and pulse arc welding, with heat input lower than conventional MIG/MAG welding; The special motion system for controlling the wire speed is incorporated into the waveform control and provides control of the molten metal detachment and arc length; when the arc plasma is developed the filler wire moves to the weld pool until the wire touches the weld pool and short-circuiting takes place; The current becomes lower and the electrode is retracted enhancing the droplet detachment. 	<ul style="list-style-type: none"> Droplet transfer is promoted by a mechanical oscillation of the wire; Self-adjusting of CTWD by changing WFS; High process stability is developed by the power source characteristics and precise current control mechanism; Low heat inputs are controlled by the dynamics of the power source and waveform design; At the upper limit of WFS (8m/min) arc instability phenomena were identified.
CMT-P	<ul style="list-style-type: none"> Technical information was not found. 	<ul style="list-style-type: none"> The mechanism of metal transfer that controls this process is controlled pulse spray; Periodic short-circuiting ends the waveform cycle and short-circuiting frequency decreases with WFS; The increase of arc energy / heat input level is due to the increase of cycle time; the remaining arc current waveform does not change; At the upper limit of WFS (10m/min) arc instability phenomena were identified.
FastROOT	<ul style="list-style-type: none"> modified short arc process able to weld root pass and thin materials without spatter; allowing positional welding with required penetration beads at higher welding speeds and productivity than TIG welding; the power source is able to monitor the short circuit and control the timing of droplet transfer; The accurate control of the waveform in respect to arc current and time is able to satisfy the spatter free condition; Importance of using a root gap (between 3 and 5 mm) and torch oscillation during narrow groove root pass welding of pipes. 	<ul style="list-style-type: none"> Spatter is often observed using FastROOT, in consequence of arc instability phenomena; Positional welding was not tested in this work; At the upper limit of WFS (9m/min) arc instability phenomena are more significant; Root gap was not tested in this work, but is not often used in most applications of mechanised welding applied in pipelines.

2.6. CONCLUSIONS

- The new processes described in this thesis exhibit a quite a diverse range of waveform control strategies, implemented in software, to achieve their objective of controlled metal transfer with potential benefits to a range of applications;
- The complex interrelationships between set and measured waveform parameters have been described in detail, and their relationship to metal transfer has been clarified;
- The Burn-Off ratio, i.e. the relationship between melting rate and arc current, is similar for all waveforms characterized;
- The arc voltage waveform generally changes in consequence of external setting parameters, e.g. CTWD and shielding gas composition. This leads to significant variations of the arc energy and consequently changes in the way that metal is transferred;
- In general, arc energy and arc current play the major role in the melting phenomena, as the depth of penetration and dilution area generally increase with energy and current;
- The increase of arc energy is favourable to the reduction of convexity bead shapes, generally observed when short-circuiting waveforms were applied;
- Shielding gas composition can play a significant role in process performance and arc stability and resulting bead shape characteristics, as observed from the results obtained for 2.5%CO₂ 97.5%Ar and 1.5%CO₂ 54%He 44.5%Ar;
- UI diagrams (or cross-plots) have to be shown to provide useful information on process performance, and in particular in providing a qualitative assessment of arc stability;
- This study has indicated that very complex relationships exist between the parameters that can be set for the different process, and the resulting electrical and bead shape characteristics. This is further complicated by the fact that each process has settable parameters such as ALC where the relationship between the parameter and its effect on the process is not necessarily a clear physical relationship. However, the very detailed data presented in this Chapter should be of significant help in evaluating process performance for potential applications.

3. PROCESS EFFICIENCY AND HEAT TRANSFER CHARACTERIZATION

Scope

The mechanical properties and metallurgical characteristics in arc welding are strongly associated with heat input, and hence this is one of most important parameters in welding engineering. The “heat input” is defined as the energy absorbed by the workpiece, while the energy delivered by the welding power source at the contact tip is defined as the “arc energy”. The ratio of heat input to arc energy represents the “process efficiency”, since part of the energy delivered by the power source at the contact tip is lost by radiation, conduction and convection across the welding arc. Note that there are also losses of energy between the power source and the contact tip, mostly resistive losses in the torch cable.

This chapter is focused on the measurement and analysis of process efficiency, including a review of heat transfer phenomena. Liquid nitrogen calorimetric tests were applied to quantify the process efficiency and consequently the heat input. Experimental errors associated with the method applied will be discussed and several experimental tests were performed to analyse the effect of welding setting parameters on process efficiency for CMT and RapidArc. Finally a comparison of process efficiency obtained with several welding waveforms will be discussed.

3.1. LITERATURE REVIEW	144
3.2. RESEARCH OBJECTIVES.....	162
3.3. MATERIALS AND METHODS.....	163
3.4. RESULTS	169
3.5. DISCUSSION OF RESULTS.....	181
3.6. CONCLUSIONS.....	188

3.1. LITERATURE REVIEW

The phenomenon of heat transfer in arc welding has been investigated for many years. It was suggested by different authors (Rosenthal 1941) (Eagar and Tsai 1983) (Lancaster 1984) (Nunes 1983) (Dutta, Joshi and Franche 1994) (Vilarinho, Costa and Scotti 2005) (Pepe and Yapp 2008) that arc energy and heat input are two of the most important parameters in welding engineering. They are directly related to microstructure and material properties, since the physical transformations occurring during welding are closely associated with the amount of heat transferred to the workpiece.

Arc energy is defined as “the product of welding voltage and current divided by travel speed of welding”, and heat input is defined as “the arc energy modified by the process efficiency factor” in the ISO standard for welding of pipelines (ISO13847 2000). PD CEN/TR 14599 (2005) also defines heat input as the energy introduced into the weld region during welding (usually expressed per unit length). Process efficiency, also sometimes called welding efficiency, thermal efficiency or arc efficiency, is the ratio of heat input to arc energy.

Kenney et al. (1998) considered the heat input an important parameter to predict the microstructure and mechanical properties of weld metal region. This parameter was considered in heat flow modelling calculations. The references to the materials properties are strongly supported by other authors (Niles and Jackson 1975) (Essers and Walter 1981) (Tsai and Eagar 1984). Little and Kamtekar (1998) have analysed the effect of thermal properties and process efficiency on transient temperatures during welding.

3.1.1. Heat Flow in Arc Welding

One of the first approaches in the literature related to the heat distribution and flow during welding was a theoretical model developed by Rosenthal (1941). This author made a number of simplifying assumptions to allow solution of a theoretical model for the heat transfer during arc welding:

- As a primary approximation, the physical properties of the material would remain constant with temperature;
- The heat flow in a workpiece of long length was considered steady, or quasi-stationary;
- The heat source was regarded as a point source;
- The heat losses through the surface to atmosphere were ignored. This assumption was supported by experiments which showed that thermal conduction is much greater than heat transmission through the surface;
- The heat created by resistance heating in the filler wire, and latent heat of fusion were not considered;
- No convection in the weld pool was considered.

Using mathematical derivation and the assumptions above, Rosenthal (1941) obtained the two-dimensional state equation to describe the heat flow during welding of thin plates of infinite width:

$$T - T_0 = \frac{Q_p}{2\pi k} \exp(-\lambda vx) \frac{K_0(\lambda vr)}{g} \quad (3.1)$$

Where,

T = temperature;

T₀ = temperature of workpiece before welding;

Q_p = heat transferred from the heat source to the workpiece;

k = Thermal conductivity of the workpiece;

λ = Thermal diffusivity of the workpiece;

v = welding speed;

K₀ = Bessel function of second kind and zero order, for each value of λvr, using tables of Bessel function;

r = radius of a circle drawn around the heat source;

g = thickness of the plate

x = distance

The analytical solution obtained by Rosenthal (1941) for the three-dimensional heat flow problem, considering a semi-infinite workpiece, was defined by the Equation 3.2, as follows:

$$T - T_0 = \frac{Q_p}{2\pi k} \exp(-\lambda vx) \frac{\exp(-\lambda vR)}{R} \quad (3.2)$$

Where R was considered the radial distance from the origin, calculated from the expression $\sqrt{a^2 + b^2 + c^2}$.

Rosenthal (1941) considered that in cases where the thickness becomes small enough, the heat losses through the surface to the surrounding atmosphere should be taken into account, and for that he suggests a modification factor into the Bessel function. Some experimental analysis reported by his work (Rosenthal 1941) shows that for thicknesses of 10 mm or above heat losses might be entirely overlooked. He estimated that less than 20% of the total arc energy is consumed in heating the solid part of the electrode and heat losses associated with vaporization, radiation, etc were roughly estimated to be 15% for small electrodes, hence approximately 65% the total energy was assumed to be delivered to the workpiece.

Some of the effects analysed in his work showed that for the same welding conditions wider heat affected zones can be found for thin workpieces than for the thicker material. This implies a less pronounced gradient of temperatures. The material properties shape and structural design, arc current, welding speed and preheating were also referred to as conditions that could affect the isotherms determined by his theoretical approach.

Eagar and Tsai (1983) described the work by Christensen et al. (1965) on a dimensionless version of the Rosenthal model, applied to different materials under a wider range of heat inputs. This study indicated a good agreement with Rosenthal solution for the actual bead geometry.

Glickstein (1976) analysed ionization potential of the gases during welding to show that metal vaporization can modify the thermal and electrical properties of the arc. Temperature measurements using 100A GTAW with 2mm gap were carried out and temperatures of 11000K near the cathode and 8000K near the anode were observed. Friedman and Glickstein (1976) developed an analytical model to characterize the thermal cycle in GTAW and predict the effect of process parameters on weld bead shape and depth of penetration. In parallel, the finite element method was applied to predict the welding transient thermal cycle considering a stationary GTAW heat source to weld moderately thick plates. Good agreement between modelling results and thermocouple measurement were found by the authors, but the depth of penetration was not predicted by this model. The authors concluded that heat transfer exclusively by conduction is inadequate to characterize the depth of penetration and bead width.

The work of Essers and Walter (1981) focussed on heat transfer and penetration mechanisms with GMAW and plasma-GMAW and demonstrated that the heat associated with the transfer of metal droplets influences the total cross-sectional area of weld penetration and the impact of the drops on the liquid metal weld pool influences the depth of penetration. The analysis of the physical phenomena in GMAW (electrode positive mode) was also performed by Waszink and Van Den Heuvel (1982) in order to understand how the welding parameters affect the generation and flow of heat in the filler wire. They found out that melting rate is governed by the Joule heating and heat flow developed from the surface of the filler wire through the liquid tip, while the drop of temperature is determined by the heat generated at the surface of the filler wire. The authors analysed the heat flow mechanism considering globular and spray transfer modes, and the transition region was also considered. Oreper et al. (1983) considered that electromagnetic and surface tension forces have a major effect on the heat flow.

Nunes (1983) modified the analytical model developed by Rosenthal considering phase changes and the heat flow mechanisms in the weld pool. Although this complex model opened new perspectives for the understanding of heat flow and transfer in arc welding, the model was limited to a fixed position (i.e. without movement). Eagar and Tsai (1983) considering the solutions of Rosenthal and Christensen, and pointed out the scatter observed in Christensen's work. They showed that the point source solution did not provide any information in respect to the shape of the weld pool. Reporting the work of Linnert (1967), they mentioned the importance of including the weld pool shape in heat flow models because of the wide variations in welding behaviour associated with heat sources. The work of Eagar and Tsai (1983) was performed in order to analyse the temperature

distribution using a Gaussian travelling heat source model. This dimensionless solution included two variables to describe the heat source, the width of the heat source and the intensity or magnitude of the input energy. These two parameters were cited as varying markedly for different materials and welding processes. The study of those authors provided the first estimation of weld pool geometry based on an empirical model of heat transfer. Although this model improved previous solutions considering the transient temperature distribution, it does not accurately predict the depth of penetration, partly due to the assumption of semi-infinite thickness.

Kou and Le (1984) developed the first computer models to study the heat flow on pipe welding using autogenous GTAW. Their 3D steady-state model of the heat flow during pipe seam welding agreed well with the thermal cycles and fusion boundary measured experimentally, while a 3D transient state for girth welding agreed reasonably well, for the conditions of constant current and heat input studied.

Lancaster (1984) introduced the plot in Figure 3.1. It compares the power densities of the different welding processes considered and respective physical mechanisms occurring. This represented a clear understanding of the phenomena that are occurring during heat transfer.

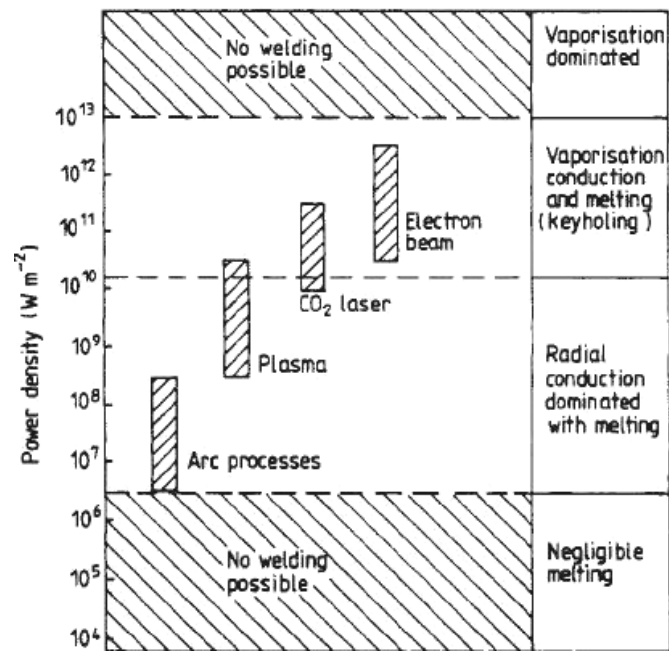


Figure 3.1 – Power density for different welding processes (Lancaster 1984).

Gilckstein and Friedman (1984) used developments in computer science to launch new approaches in the study of heat flow during welding. New models analysing both fluid flow and heat transfer mechanisms together were developed. Kou and Wang (1986) built for the first time a 3D mathematical model to describe the heat flow and convection motion in the weld pools. The model included the effect of the buoyancy, electromagnetic and surface tension forces. Finite thickness workpieces were modelled, allowing partially and fully

penetrated welds. Tsao and Wu (1988) improved the model of Kou and Wang (1986) for applications with GMAW. They added to the forces the energy exchange between the weld pool and the molten metal droplets during spray transfer. These research works were based on the heat input, and showed for the first time that is essential to know precisely the value of process efficiency for the welding process and conditions considered.

Zacharia et al. (1988 a) (1988 b) developed a 3D model where melt deformation during molten pools, particularly important in autogenous and non-autogenous GTA welding, was considered. Their simulation considered the weld pool under motion, with melting at the leading edge of the pool and weld solidification at the trailing edge. This model is a more realistic solution, when compared with the work carried on by Kou and Wang (Kou and Wang 1986).

Meanwhile, other models were developed to study the heat transfer in other welding processes, such as resistance spot welding (Han, et al. 1989) (Y.-S. E. Kim 1990).

Choo et al. (Choo, Szekely and Westhoff 1990) considered the earlier cited role of the forces interacting in the convection phenomena in the weld pools, and the shear stress exerted by the gas on the molten pool surface was also considered. They modelled high current arcs, characterized by deformed weld pools, and where interfacial regions are significantly important. Agreement with experimental results, considering flat and deformed weld pools, was found by those authors. However, when significant deformations occurred due to high heat and current flux, the model failed, suggesting that Gaussian heat flux distribution did not cover this situation. They also concluded that deformed free surfaces might result in a complex weld pool circulation outline.

Advances in the understanding of the physics beyond heat transfer have been considered by Eagar (1990) in respect to the plasma atmosphere and variations between helium and argon arcs. This author reported that the effect of helium and argon in melting and heat transfer is explained by the variation of thermal conductivity of those gases. In monatomic gases such as helium and argon, thermal conductivity is controlled by the mass diffusivity of the atoms, proportional to the inverse of square root of the atomic mass. The physical mechanisms involved were also described, such as the effect of gas mixtures on anode voltage drop, electrical current distribution, arc temperature, and radiation. Other gas mixtures can also have a significant variation in the role on thermal processes, when reactive components are present. The model developed by Kim et al. (1991) to understand the effect of electrode heat transfer in GMAW provided advances in information about the metal transfer using estimated time scales for drop formation and detachment. They analysed electron condensation on the surface of the electrode, modelling the thermal energy generated, and demonstrated that it is a major factor influencing the heat flow through the electrode.

Following the previous studies of Kim et al. (1991), Vilarinho et al. (2005) developed an experimental modelling study for the temperature and voltage drop along the electrode

during GMAW. They pointed out that those parameters can dramatically affect the prediction of process efficiency during the electrode melting and heat flow through the electrode tip. The model accounted for material properties, temperature field and voltage drop. However, when globular transfer was identified the experimental results did not agree with the model; they considered that droplet geometry between plasma and electrode should be further evaluated. It should be noted that the process efficiency is an important factor in many of the actual models available, but there is no general agreement on the process efficiency to use, and assumed values are often adopted.

Further to their previous model, Choo and Szekely (1992) researched the vaporization kinetics and surface temperature, including Langmuir vaporization and gas phase in the model developed. They found out that heat losses due to vaporization do not play a major role in limiting the temperature at the free surface of weld pools. The results suggested a thermocapilarity motion effect controls the temperature at the free surface of the weld pools. The model also pointed out that relationships between temperature and surface tension and also other parameters controlling temperature distribution at the free surface play a significant role in the behaviour of the weld pool. These authors also analyse the role of turbulence in the weld pool for GTAW (Choo and Szekely 1994). This research study demonstrated that the postulate of laminar flow in weld pool might be incorrect when penetration depth is greater than 1 mm. Following the results of their modelling, they considered that the flow in weld pools is probably turbulent or at least transitional.

A model considering the electrode extension during GMAW in short circuit mode of transfer was developed by Quinn et al. (1994). It is well established that arc stability, metal transfer mode and deposition ratio are affected by the electrode extension (or arc length) (American Welding Society 2007). Further to this study, Kim and Na (1995) analysed the effect of the contact tip to the workpiece distance (CTWD) on weld pool and shape of GMAW using 3D modelling of heat transfer and fluid flow, considering the convection forces and the effect of molten electrode drop. CTWD has a significant effect on the weld pool and shape geometry, which also depends on arc length and arc current.

The effect of thermal properties and process efficiency on the transient temperatures during welding was analysed by Little and Kamtekar (1998). The main focus of this work was on thermal conductivity and process efficiency. Thermal conductivity has a major impact on the peak temperatures obtained; higher values of this parameter create lower peak temperatures near the weld bead and higher peak temperatures in areas away from the bead. Process efficiency also can affect results, and apparently is more critical for high heat input values, where process efficiency could be smaller.

Nguyen et al. (1999) developed an analytical solution for the transient temperature field of a semi-infinite workpiece subjected to a double ellipsoidal power density travelling heat source. Experimental results well matched with the model developed in the prediction of geometrical aspects, such as the weld pool width and depth. Nguyen et al. (2004 b)

reporting the limitation of their previous model to semi-finite plates (Nguyen, Ohta, et al. 1999), and developed another analytical solution applied to finite thick plates, considering the double ellipsoidal heat source. The results published show an agreement with experimental data assessed by them, suggesting the application to thermal stress analysis, residual stress and microstructure modelling of multipass welds.

3D numerical study for the heat transfer and fluid flow in a moving GMAW process was extended by Jaidi and Dutta (2001). They launched for the first time a model combining the electrode transfer analysis with the weld pool heat transfer and fluid flow. They added that energy and momentum of the droplets have to be considered when filler metal additions are present. The authors modelled the Lorentz force field using the Maxwell equations and simulated the heat transfer and fluid flow in the weld pool using a pressure based finite volume method, where melting and solidification could be included. The model presented is also able to reveal the typical “finger penetration” sometimes present in GMAW. However, quantitative considerations are not fully accurate, and there are uncertainties associated with different welding aspects, such as process efficiency, molten droplet behaviour, surface tension coefficients, high temperature metal properties variation, etc.

A 3D string heat source model to simulate the thermal process in GMAW using a new transient solution of heat transfer was developed by Wang et al. (2005). Agreement with experimental results was obtained for GMAW.

Camilleri et al. (2004) applied infrared thermography to measure transient temperature fields generated during arc welding. Using theoretical and analytical approaches they created a finite element method to describe the variations of temperature observed within welding in different positions and time. Thermography has shown good advantages in the analysis of the temperature profile in complex and large scale plates. However, this method is limited to a thin scale plates and simple geometries, which the thermal camera can monitor.

More recently, Goncalves et al. (2006) used inverse techniques to estimate heat source, thermal efficiency and melting efficiency in GTAW. The physical model included the variation of thermal properties with temperature, phase change, and heat losses, which they considered necessary to characterize melting and process efficiency for each instant of the welding. Goyal et al. (2009) researched thermal behaviour and geometry of weld pools in pulsed GMAW using analytical modelling. Their model is able to predict penetration and width of fusion in the parent material and consequently the geometry of the weld pool. However, they consider that accuracy is $\pm 10\%$ and some limitations have been observed, which suggest that some physical aspects should be considered in order to improve precision.

The study of temperature distribution and thermal cycles associated with the heat source has been considered for a long time. Process efficiency represents a fundamental parameter

to include in the thermal models where arc energy should be corrected from the heat losses present during welding. Recently, other authors (Karkhin, et al. 2003) have developed an analytical solution based on Green's equation to understand the effect of latent heat on process efficiency. Karhin et al. (2003) considered the problem of the heat flow, including the latent heat factor, which account with the heat associated with the phase transformations during welding. Although that study did not account for different physical phenomenon defined earlier, such as the convection phenomenon, agreement was established for experimental results in the prediction of process efficiency parameter.

The science of heat flow in arc welding has been considerably discussed over the last one hundred years. Relationships between heat and fluid flow have been established and modelling is nowadays often applied to reduce time and support experimental work. However, new advances have been performed in arc welding technology in particular associated with the control of metal transfer mechanisms and the reduction of heat input. In addition, the development of thermal models to explain the heat flow, residual stresses and metallurgical features should include an accurate measurement of process efficiency, considering the heat losses during an arc welding process.

3.1.2. Heat Losses during Arc Welding

At first glance most of the studies considering the mathematical approaches have ignored or estimated heat losses occurring during arc welding (Rosenthal 1941) (Metcalf and Quigley 1975) (Waszink and Van Den Heuvel 1982)(Eagar and Tsai 1983) . In fact, it is well known that only part of the heat created by the electric arc is absorbed by the workpiece. The heat losses are associated with the followed main mechanisms: conduction, convection, radiation and vaporization. However, the precise quantification of heat losses associated with those mechanisms is very difficult due to the complex physical mechanisms occurring in the arc.

Some studies (Rosenthal 1941) (Metcalf and Quigley 1975) have demonstrated the importance of heat losses during welding and the contribution of different mechanisms. Among the measurements of heat losses associated with arc welding processes, Schauer et al. (1978) analysed the effect of cavities occurring in response to metallic vaporization using electron beam welding of aluminium alloys and steels. An infrared radiation pyrometer technique was used to detect the temperature on the surface. They evaluated the effect of alloying elements and measured temperatures in the cavity generated.

However, the quantification of heat losses during arc welding was not adequately assessed. It is difficult to obtain a full understanding about which mechanisms are present and which have more effect depending on the welding conditions and processes. Nonetheless, process efficiency represents the factor which quantifies the overall heat losses. Several methods have been applied to quantify process efficiency in arc welding processes, using analytical and experimental techniques.

3.1.3. Process Efficiency

As defined by Niles and Jackson (1975) the process efficiency is expressed as the ratio of the total energy delivered to the workpiece (per unit of length) – heat input – to the energy input generated by the power source – arc energy. Process efficiency influences the distribution of temperature and cooling rate, and therefore the heat flow models discussed above should consider the application of this factor. In this perspective, the quantification of the process efficiency is a fundamental measurement to achieve precise models for the distribution of temperature, where heat input is applied.

Different analytical methods and experimental techniques have been found in the literature to quantify process efficiency, but a wide spread of results is observed.

3.1.3.1. Analytical Methods

The theoretical and numerical models of heat flow have often been developed considering estimations of the heat losses during welding. The process efficiency was estimated from the modelling development using thermal cycle measurements.

An analytical development of the model of Rosenthal was performed by Niles and Jackson (1975) to predict the process efficiency in GTAW using thermal cycle measurements. The equation obtained by those authors (Niles and Jackson 1975) was based on conduction heat transfer and constant thermal properties were considered:

$$\frac{T-T_0}{H_i} = \frac{\exp\left[-\left(\frac{v}{2\lambda}\right)(x+r)\right]}{2\pi kr} \quad (3.3)$$

Where T is the temperature at the radius r from the point source and T₀ the room temperature and H_i is the actual heat input, i.e., the heat absorbed by the workpiece during the welding. Results obtained for process efficiency of GTAW were in the range of 31% to 64%. The authors suggested that the wide range of results was associated with the welding conditions applied.

Giedt et al. (1989) analysed the process efficiency based on temperature field measurements, obtaining results in the range of 50 to 62%. They pointed out that the solution presented by Niles and Jackson (1975) did not include the convection associated with the fluid flow, as described by Heiple and Roper (1982) or the effect of varying thermal conductivity with temperature. They also reported that other assumptions made by Niles and Jackson (1975) could explain the low values obtained for the process efficiency.

Dutta et al. (1994) used a combined experimental/ computational method to estimate process efficiencies of GTAW under quasi-steady conditions for low alloy steel. Digitized free surface images using a pulsed laser vision system were applied to obtain instantaneous measurements of the weld pool length on both sides of the electrode. Width and depth optical measurements made possible the development of three-dimensional model which was able to quantify process efficiency. The results of process efficiency determined using

that experimental/modelling approach was in the range of 62% to 85%. The authors attributed the wide variation of the results to the changes in arc current, voltage and welding speed. They also considered other factors which were fixed but may affect process efficiency, such as the arc length, electrode tip angle, shielding gas composition, flow rate and parent material.

It is clear that “process efficiency” has often been used as an adjustable parameter in order to match predictions from theoretical models with experimental measurements. Hence, there will always be significant doubt associated with the values of process efficiency determined in this way, since many other factors associated with model limitations and material properties can affect the calculated process efficiency.

3.1.3.2. Experimental Methods

A water-filled calorimeter method was used by Essers and Walter (1981) to measure the amount of heat transferred to the workpiece for GMAW. Metal strip specimens were placed in the calorimeter, almost totally immersed in water with only the upper surface just above the water level, and the water temperature variations were registered. A constant distribution of water temperature was ensured through the use of a rotating blade. Heat losses from the surface of the metal strip occurred, resulting in an error estimated at 5%.

This method was applied to quantify the process efficiency in plasma-GMAW and GMAW. Essers and Walter (1981) measured a process efficiency of 23% for non-transferred plasma (no current through the workpiece) without wire addition, 54% for transferred plasma without wire addition, 65% for plasma-GMA welding, and 71% for GMAW. They considered that although the cathode (workpiece) was the same in all cases, the anode varied between the tests performed, resulting in the differences between the results obtained. GMAW had only one anode (filler metal), while plasma-GMA had two anodes (the filler metal and non-consumable plasma).

A water calorimeter was also used by Quintino (1986) to measure the process efficiency for GMAW-P. The calorimeter tests were based on water temperature variation, before and immediately after welding, using bead on plate samples with 15mm thickness. She compared the variation of process efficiency using different welding conditions, such as mean current (100, 150 and 200A), filler wire diameter of 1.0, 1.2 and 1.6mm and two different gas mixtures (5%CO₂ 95%Ar and 1.5%CO₂ 85%He 13.5%Ar). CTWD of 20mm was kept constant in all tests performed. With those tests Quintino (1986) found that mean current does not affect significantly welding process efficiency. However, the variation of filler wire, using shielding gas 5%CO₂ 95%Ar, might have some influence with a process efficiency of 66% for 1.2mm, against 59% and 60% for 1.0mm and 1.6mm diameter wire, respectively. Trials using 1.2mm filler wire and 1.5%CO₂ 85%He 13.5%Ar gas mixture confirm the results for the other mixture, with process efficiency average values of 67%. The

results obtained by Quintino (1986) are in agreement with the previous results obtained by Essers and Walter (1981) for GMAW.

Analytical/ numerical estimations obtained by Christensen et al. (1965) (21-48%) and Niles and Jackson (1975) (35-65%) are much lower than the results obtained using a water cooler calorimeter. However, other water cooled anode measurements for GMAW are reported by Giedt et al. (1989) to have significantly higher process efficiency, in the range of 80 – 90% (Wilkinson and Milner 1960) (Tsai and Eagar 1984).

Lu and Kou (1989) used a water calorimeter to measure the process efficiency and heat input for GMAW of aluminium. The calorimeter consisted of an insulated stainless steel rectangular box. A water supply system was used by those authors to maintain a constant water flow rate. They ensured that no bubble formation due to water vaporization was achieved. Continuous water temperature measurements, using differential thermistors, were recorded and the heat absorbed was calculated using the specific heat of water (Figure 3.2).

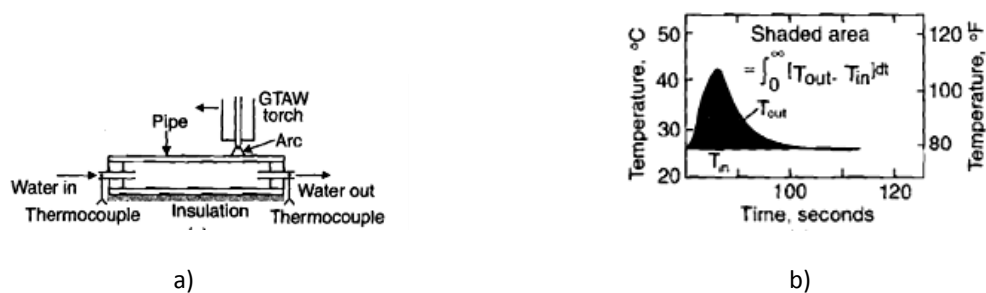


Figure 3.2 – Measurement of process efficiency in GTAW: a) Calorimeter; b) variation of water temperature as a function of time.

Process efficiency of 80% was measured, and contributions of 45% from arc radiation and convection, 23% from filler metal droplets and 12% associated to the cathode heating were estimated by the authors (Lu and Kou 1989). These results are significantly higher than the previous results obtained by Quintino (1986) and Essers and Walter (1981) for GMAW using steel. It was suggested that the material properties may justify the higher valued obtained for aluminium.

Bosworth (1991) measured the effective heat input in GMAW and GMAW-P, using a water calorimeter method. He analysed the variation of different welding conditions, such as the arc current, arc length, shielding gas mixtures in blends of argon-carbon dioxide. This author remarked for the first time that arc power calculations could have a significant effect on the results of process efficiency and suggested that the average of instantaneous power should be applied to calculate true power. An average of 85% for the process efficiency in GMAW, at wide range of burn-off rates, and 95% for short-circuiting transfer were obtained. In GMAW-P process efficiencies between 80% and 85% were observed, with the lower values obtained at high WFS. Bosworth (1991) considered that WFS has a major impact on process efficiency, and gas composition has a minor but still significant effect. It is noticed that the

results measured by this author are significantly higher when compared with earlier measurements obtained by other authors (Quintino 1986) (Essers and Walter 1981) (Lu and Kou 1989). The differences may be due to the different measurement techniques used or the method used to calculate arc power values.

A gradient layer type calorimeter was applied by Giedt et al. (1989) to measure the process efficiency. This method consists on the measurement of the temperature drop in a thin layer of the material due to the heat flow. The measurement is achieved using a thermocouple circuit placed on the inner and outer surfaces of the layer. A thermopile is formed by series of these circuits, multiplying the thermoelectric output of the system. That combination of thermopiles and gradient layers formed a heat-rate meter based on the Seebeck thermoelectric effect, and therefore it has been called a Seebeck Envelope Calorimeter (Figure 3.3.)

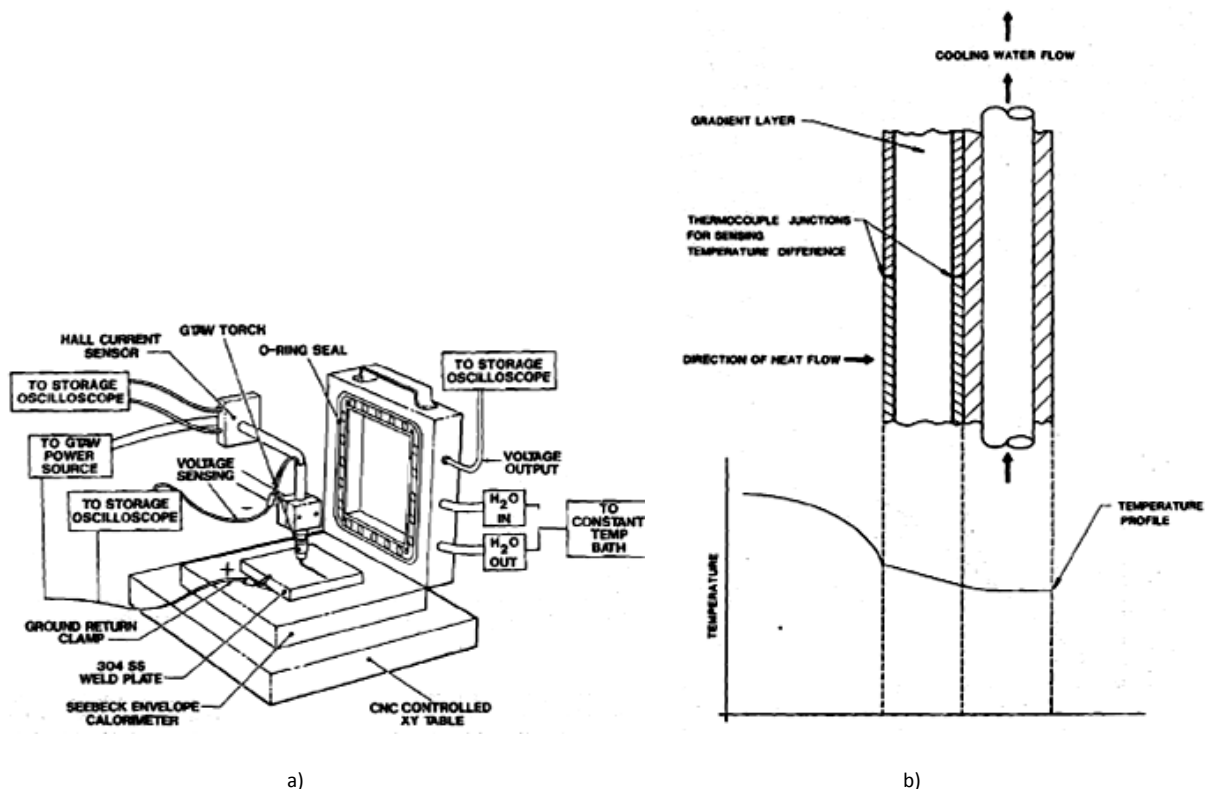


Figure 3.3 – a) Schematic sketch of Seebeck calorimeter applied to measure process efficiency; b) operating principle of a gradient layer calorimeter.

These authors (Giedt, Tallerico and Fuerschbach 1989) reported that those measurements took up to 6 hours for the workpiece normalize the temperature with the water cooler. Results of process efficiency for GTAW were in the range of 80%, even considering the variation of arc current, voltage and electrode diameter. The results of process efficiency reported did not include any correction to heat losses by radiation, convection and vaporization, but the authors estimated those to be smaller than 1%.

Fuerschbach and Knorovsky (1991) performed an intensive study using a Seebeck calorimeter on plasma arc welding and GTAW. The process efficiency results obtained by

those authors were in the range of 50 to 75% for plasma arc welding and 80% for GTAW with continuous and pulsed current conditions. Those numbers were in agreement with previous results obtained by Giedt et al. (1989) for GTAW.

Using a Seebeck envelope calorimeter, Cantin and Francis (2005) investigated the process efficiency of GTAW in aluminium (Figure 3.4). They compared the process efficiency in GTAW using AC polarity and DC with electrode positive and negative polarities. Isolating materials were applied to the specimens in order to reduce losses occurring during the welding. They investigated the effects of the variation of shielding gas composition, arc length and arc current on the power and process efficiency obtained. The results obtained for DCEN polarity, where the majority of the heat is transferred by the electrons, varied between 76% and 89%; with the highest values obtained when helium was used as a shielding gas. These results show a significant effect of the shielding gas on the process efficiency measured, and are in agreement with a similar work developed by Zijp and Den (1990) and Hiraoka et al. (1998), as reported by Cantin and Francis (2005). Using AC polarity and DCEP polarity, the power and process efficiencies could be estimated based on weighted average of EN (electrode negative) fraction under identical weld conditions. For DCEP polarity, where the electrons are supplied by the workpiece, a much colder process occurs and temperature is too low for thermionic emission to occur. In this case a cathode voltage drop takes place at the cathode as reported by Cantin and Francis (2005). Nonetheless, the process efficiency obtained is much lower with values in the range of 52 to 60%. They observed that the highest values are also associated with the highest amounts of helium. Process efficiency assessed for AC polarity varied in the range of 65 to 83%. The highest values were also obtained for the richest helium gas mixtures (75% and 100%). Arc length changes assessed in this study did not demonstrate a significant effect on the process efficiency.

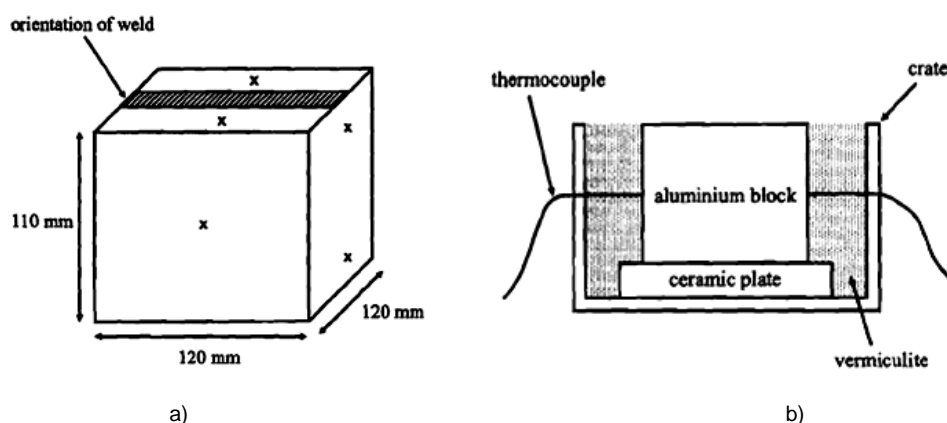


Figure 3.4 - a) aluminium specimens used in the experiments with the approximate location of thermocouples (marked by an "x"); b) schematic representation of the calorimeter.

Although water calorimeters have been extensively used in the past, they are time consuming with possible errors in the results obtained. Liquid nitrogen calorimetric tests were firstly introduced by Smartt et al. (1985) , as described by Kenney et al. (1998) and Dutta et al. (1994), who obtained process efficiencies between 71 and 84% for GMAW.

A liquid nitrogen calorimetric method was also used by Kenney et al. (1998) to analyse heat transfer in GMAW-P. They used a six litres stainless steel dewar and an electronic scale interfaced to a computer, where they measured the loss of weight associated with liquid nitrogen vaporization. Rapid transfer of welded specimens from the welding rig to the calorimeter was obtained. The results of process efficiency obtained were in the range of 69 to 82%, and with an average of 72%. They concluded that the process efficiency obtained for GMAW could not be directly related variations in pulse parameters, for either constant current or constant voltage. The technique used by those authors resulted in slightly higher values for the process efficiency compared with the tests performed using water calorimeter.

Joseph (2001) also used liquid nitrogen calorimetric tests to compare the process efficiency obtained with a wide variation of pulse parameters for GMAW-P, and compared different ways of calculating arc power. The average of the instantaneous arc power, average power (product of the average of arc current by average arc voltage), and the RMS power were considered in his study. The process efficiency obtained changed considerably using these different methods – 70.2% using instantaneous arc power calculations, 82.4% for the average power and 60.7% for RMS power.

More recently, Hsu and Soltis (2003) have undertaken an investigation on process efficiency using liquid nitrogen calorimetric tests, where STT, short-circuiting and pulsed GMAW and CV GMAW were compared. The results demonstrated that process efficiency is lower for CV spray and pulsed spray GMAW at 73%, while CV short-circuiting and STT presented higher results, respectively 85% and 86%.

Recently, Egerland (2009) have investigated the process efficiency on a narrow groove using CMT-P and GMAW-P. Although a limited number of tests have been undertaken and experimental errors were not estimated, there is an indication from this work that process efficiency is significantly higher, within approximately 10%, for applications using square groove geometry (process efficiency of 85%).

Among the work published on the analysis of process efficiency, considering both the experimental and analytical models, a wide spread of results has been observed. It is clear that material properties and welding process can play an important role on the values of process efficiency obtained. Calorimetric tests are always more reliable than calculations obtained based on assumptions and unsteady criteria defined by the analytical approaches. Nonetheless, with the new significant developments in arc welding technology and the importance of the application of process efficiency parameter in modelling studies, a more reliable study is required to determine which welding parameters affect welding process efficiency, and how it changes with waveform design.

3.1.4. Power, Arc Energy and Heat input Calculations

Interestingly, although heat transfer in arc welding and the measurement of welding thermal efficiency has been researched for many years, the importance of correct measurement of power input, arc energy and heat input has received much less attention, despite the work of Bosworth (1991) and Joseph (2001).

Power input is usually defined in arc welding, as the product of arc current and arc voltage. The arc power, created by the power source and developed by the electric arc, and can be determined using the equation 3.4, as follow:

$$P_{arc} = I \times U \quad (3.4)$$

Where P_{arc} is the power input generated by the electric arc, I the arc current and U the arc voltage for that arc.

Nonetheless, it is well known that the electric arc is generated in a complex waveform, which includes significant variations on the voltage and current during welding. Bosworth (1991) introduced for the first time an extensive study on this matter. He considered that in welding specifications where the current remains relatively constant the product of average voltage and current can be applied. However, in the case of GMAW-P, for example, current fluctuates between a peak and background value, in a regular cycle. According to Bosworth (1991) resistive and inductive effects alter the actual power in GMAW waveforms and in this case the average of instantaneous power values should be considered. More recently Joseph (2001) carried out work on the same subject, and also agreed with Bosworth's work (1991).

Considering the analysis of current and voltage, all the measurements should provide a representative picture of the waveform. Variations in pulsed waveform and the mode of metal transfer can affect the overall analysis of the results. Joseph (2001) added that the sampling frequency of measurement should provide a representative picture of the waveform; otherwise inaccuracy or aliasing can occur. In order to prevent aliasing, sample frequency should be at least twice the frequency of interest area; however, ten times is usually preferred to fully represent the waveform.

As referred in the work of Bosworth (1991) and Joseph (2001), three main ways can be applied to calculate the power input:

- Using the mean values of current and voltage, as follow:

$$P_{Av} = I_{mean} \times U_{mean} \quad (3.5)$$

Where, P_{av} corresponds to the average Power, and I_{mean} and U_{mean} the average of current and voltage which can be calculated within the equations 3.6 and 3.7, respectively:

$$I_{mean} = \frac{\sum_{i=1}^n I_i}{n} \quad (3.6)$$

$$U_{mean} = \frac{\sum_{i=1}^n U_i}{n} \quad (3.7)$$

- Using the average of the power measured at the instantaneous values of arc current and voltage, according with the equation 3.8:

$$P_{Inst} = \sum_{i=1}^n \frac{I_i \cdot U_i}{n} \quad (3.8)$$

Where, P_{Inst} is the instantaneous power, and I_i and U_i are the values of current and voltage measured on each instant of the time.

- Using a root mean square (RMS) values of current and voltage, equation 3.9:

$$P_{RMS} = I_{RMS} \cdot U_{RMS} \quad (3.9)$$

Where, P_{RMS} is the RMS Power, and I_{RMS} and U_{RMS} the average of current and voltage which can be calculated within the equations 3.10 and 3.11, respectively:

$$I_{RMS} = \sqrt{\sum_{i=1}^n \frac{I_i^2}{n}} \quad (3.10)$$

$$U_{RMS} = \sqrt{\sum_{i=1}^n \frac{U_i^2}{n}} \quad (3.11)$$

The arc energy is defined as the product of welding voltage and current (arc power) divided by travel speed of welding (normally expressed by kJ/mm), using the equation 3.12, as follow:

$$Arc\ Energy = \frac{P_{arc}}{TS} \quad (3.12)$$

Where, TS corresponds to the welding speed, or travel speed.

It should be noted that it is common to use the term “heat input” when calculating the energy absorbed by a weld, by calculating arc energy per mm, and then applying a factor to represent the process efficiency, as shown in the equation 3.13 below:

$$\eta = \frac{Heat\ Input}{Arc\ Energy} \quad (3.13)$$

Where η is the process efficiency, arc energy is the amount of energy per unit of length generated by the power source at the contact tip and determined according one of the expressions of power defined above, and heat input (H_i) is the actual amount of energy absorbed by the workpiece during welding.

Although “heat input” is widely used, sometimes it is considered with a wrong definition. Its correct application implies the use of the process efficiency factor, according to the welding process and characteristics applied, as defined by the standard (CEN/TR14599(E/F/D) 2005).

As mention earlier Joseph et al. (2001) analysed the impact of the use of the different calculation methods for the process efficiency results and conclude that the correct practice is the use of instantaneous power method. Further to this study, Nascimento et al. (2007) investigated ways to calculate electrical power and its impact on joint geometries and thermal and metallurgical predictions. Among the methods used to calculate the electrical power above considered these authors included another method defined as the instantaneous RMS power, and calculated with the equation 3.14:

$$P_{Inst\ RMS} = \sqrt{\frac{\sum_{i=1}^n (I_i \cdot U_i)^2}{n}} \quad (3.14)$$

The previous work of Bosworth (1991) mentioned a variation of 30% between results of power obtained according the three generalized methods presented above. He warned of large errors in the literature associated with the use of incorrect values; in most power supplies including analogical or digital readings of current and voltage, those values correspond to RMS, and users tend to use them in heat input calculations. Bosworth compared different ways to measure the power (as presented previously), at different power levels and when different modes of metal transfer were identified. His results suggested that instantaneous power and instantaneous RMS power can accurately be used to calculate arc power, at any mode of transfer and power level. These results have been recently supported by Melfi (2008).

3.1.5. Summary

For many years physicists and mathematicians have been investigating the phenomena of heat transfer during arc welding. Since Rosenthal approach was established, different researchers have generated more extended solutions either to describe the phenomenon of heat flow or to explore the physical-chemical mechanisms beyond.

The advancements in the computer science were essential for the development of more suitable models. However, one of the errors continuously included in those models is associated with the heat input parameter. Some authors do not account for process efficiency, or use an assumed and possibly incorrect value. This has been discussed and assessed for different arc processes and conditions; although the literature reflects wide variations between the values obtained by different authors. Different research methods have been considered, which include analytical and experimental solutions. Calorimetric techniques are most reliable, since the analytical solutions do not fully reflect the overall variables involved in the complex arc welding system.

In addition, errors were found associated with the calculation method used to determine arc power and heat input; the average of the instantaneous power is indicated as the most correct method to determine those parameters.

Finally, during last ten years new variants of GMAW have become commercialized. A fundamental research about the variation of process efficiency in these new waveform systems is now needed. Furthermore, it is essential to understand the effect of welding variables on the process efficiency and discuss the main errors associated with the experimental method applied.

3.2. RESEARCH OBJECTIVES

The main aim of the investigation developed in this chapter was to determine the process efficiency associated with different waveform designs. As has been pointed out in the literature, there is a wide spectrum of results obtained for this important parameter. In this perspective the objectives of this research were:

- To develop liquid nitrogen calorimetric tests to determine the heat absorbed by the workpiece;
- To research the different methods applied to quantify arc energy and select the most appropriate method;
- To determine process efficiency from the absorbed heat measurements using calorimetric tests;
- To analyse the errors associated with the calorimetric tests applied and propose correction factors;
- To assess how process efficiency changes with weld process parameters and waveform designs;
- To determine heat input using process efficiency values determined.

3.3. MATERIALS AND METHODS

3.3.1. Materials

Plates of mild steel EN 440 G3Si1 - S355JR with different thicknesses were used for the research developed in this chapter. The detailed characteristics of the material were already described in Chapter 2 of this thesis. A filler metal EN 10025 – S355JR with 1 mm diameter was used in this investigation. Different gas mixtures of carbon dioxide and argon blends were used in the experiments, including 8%CO₂ 92%Ar, 20%CO₂ 80%Ar and 100%CO₂.

3.3.2. Welding Processes

The main research developed in this chapter was carried out using CMT welding process. However, RapidArc was also extensively evaluated and other processes, such as STT and FastROOT waveforms were considered in terms of comparison analysis. The details of these processes have been described in Chapter 2.

3.3.3. Methods

The research developed was undertaken under the following phases:

1. Preparation of surface condition;
2. Welding conditions and experimental measurements;
3. Calorimetric tests;
4. Data analyses.

3.3.3.1. Preparation of Surface Condition

The surface preparation was carried out according to the methods described in Chapter 2.

3.3.3.2. Welding Process and Conditions

CMT welding was performed using mode 1053 of the Fronius CMT power source, as described in Chapter 2. This study was undertaken using different thicknesses, 2, 4 and 5mm. For this process the range of conditions applied to the experimental trials were from 3 to 9.4m/min of WFS, in the range from the minor to the upper limit of arc length correction (ALC) (-30% and 30%) and of hot start (HS) (-5% and 5%). CTWD was set from 6 to 20mm and the shielding gases applied were 8%CO₂92%Ar, 20%CO₂80%Ar and 100% CO₂.

The Rapid Arc waveform was applied by selecting mode 13 on Lincoln power source. The range of WFS chosen was the same as for CMT, while a trim was set between 0.5 and 1.5 to control arc length (most of the tests were carried out with a trim set at 1.5). The external parameters applied to this process were the shielding gas composition and material thickness. For the STT waveform, mode 112 of the Lincoln power source was selected, and the tests using this waveform were performed with WFS variations between 5m/min and 8m/min and the trim was kept constant at the value of 1.5.

FastROOT waveform trials were carried with the mode 903 of the Kemppi power source, using variations of wire feed speed between 6 and 7m/min with both base current and forming pulse set at 0%. The details of these welding parameters and respective meaning have already been described in Chapter 2.

The Yokagawa oscilloscope was used to record all the arc current and voltage waveforms, and WFS signal. The principle of equipment and experimental conditions applied was introduced in Chapter 2.

3.3.3.3. Validation Tests

Liquid nitrogen calorimetric tests were used to quantify the amount of energy absorbed by the weldment during welding. The heat absorbed by the sample during welding is transferred to the liquid nitrogen which will boil off. The energy associated with the phase change of liquid nitrogen can therefore be measured as the energy lost by the specimen. The calorimetric analyses are based on the loss of liquid nitrogen by weight measurements.

Liquid nitrogen has a boiling point of -196°C and a Statebourne Cryogenics dewar was used to reduce the energy loss to the environment. The cryogenic container had a capacity of 5.25 litres, internal height of 297 mm and inside diameter of 150 mm (Figure 3.5).



Figure 3.5 – Liquid nitrogen calorimetric tests: a) container during calorimetric test; b) specimens after calorimetric tests.

The loss of weight, associated to the liquid nitrogen vaporization, was measured using a Salter Brecknell B220 scale with maximum weight capacity of 30 kg and a digital readout resolution of 0.001 kg. A partially closed table was built for these experiments, with an open circle at the top to create the space for the container. In front of the scale a Logitech webcam was used to make timed recordings of the change of weight.

Preliminary tests using this calorimeter have shown that no more than about 75% of the capacity of the container should be filled with liquid nitrogen. At higher fill levels, there is an increased possibility of loss of liquid nitrogen by splashing when the sample is immersed, leading to errors in measured energy. However, the specimens tested should always remain

submerged in liquid nitrogen at the end of the test. A set of validation tests were performed to determine the rate of energy loss of liquid nitrogen from an open dewar.

Initially, the first role of experiments was carried out to evaluate the amount of liquid nitrogen lost by evaporation with time, defined as normal vaporization rate. Several trials were made in order to analyse and compare the loss of liquid nitrogen with time; three representative results are shown in the Figure 3.6 below.

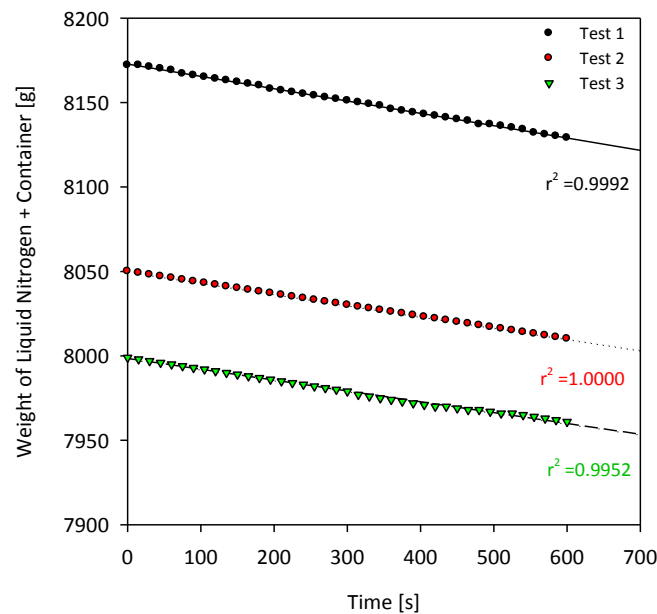


Figure 3.6 – Normal vaporization rate for liquid nitrogen with time obtained for three different trials.

It can be observed from the plot represented in the Figure 3.6, for the three experiments compared, that the loss of liquid nitrogen, in normal evaporation conditions, is about 3.8g/min. R-squared coefficients obtained range between 0.9952 and 1.000 confirm low scatter and linear loss rate.

The change of energy in the specimen is given by the specific heat, according to the equation 3.15:

$$\Delta Q = m \cdot c_p \cdot \Delta T \quad (3.15)$$

Where ΔQ is the change in energy after a temperature change of ΔT , m is the mass of the specimen and c_p is the specific heat capacity. The specific heat capacity, c_p , is the energy needed to raise the temperature of one gram of a substance by one degree Celsius. The specific heat capacity of a solid substance is a function of temperature and is taken as an average value over the temperature interval between the initial and final temperatures. The final temperature was the -196°C , corresponding to the boiling point of liquid nitrogen.

The latent heat is defined as the heat associated with the change of phase of liquid nitrogen. The heat of vaporization of the nitrogen is given by the latent heat, equation 3.16:

$$\Delta Q = \Delta m \cdot L_V \quad (3.16)$$

Where ΔQ is the quantity of energy supplied (or removed), Δm is the change of mass by vaporization and L_V is the latent heat of vaporization. The latent heat of vaporization for the liquid nitrogen is 199.5 J/g.

Since the calculation of specific heat involves the application of a specific heat capacity which varies considerably with temperature for steel this method was difficult to apply. Moreover, the specific heat capacity for the material applied to this research was not available, and estimates could also lead to calculation errors.

The loss of energy from the specimen when it is dropped inside liquid nitrogen can in principle be calculated from the energy of vaporization (boiling) of the nitrogen by phase change.

Before each experiment, the calorimeter was filled to a suitable level, as explained previously, and time/ weight of the calorimeter recordings started. Immediately after welding the specimens were placed inside the calorimeter, where loss of liquid nitrogen was recorded until the normal vaporization rate was reached. Placing the specimen inside the calorimeter increases the weight instantaneously. The weight falls rapidly as the energy is transferred, and the liquid nitrogen evaporates.

A correction must be made for the fact that the specimen is cooled to -196°C :

$$\text{Energy Absorbed} = \Delta Q_{WT-BT} - \Delta Q_{RT-BT} \quad (3.17)$$

Where ΔQ_{WT-BT} is the quantity of energy associated to the vaporization of liquid nitrogen from the welding temperature (WT) until the liquid nitrogen boiling temperature (BT) (-196°C) and ΔQ_{RT-BT} is the quantity of energy associated with the vaporization of liquid nitrogen from room temperature (RT) until -196°C .

The Figure 3.7 shows the comparison of liquid nitrogen vaporization for a normal evaporation rate, and the vaporization associated with the specimen at room temperature, and vaporization from a welded specimen. Note that the same specimen is tested both from room temperature, and after welding, so that the difference in liquid nitrogen loss from these two conditions equals the energy absorbed in the specimen from welding.

3.3.3.4. Data Analysis

The electrical data obtained from the oscilloscope were converted using Xviewer software, following the method described in Chapter 2. The arc power was calculated from the average of instantaneous power.

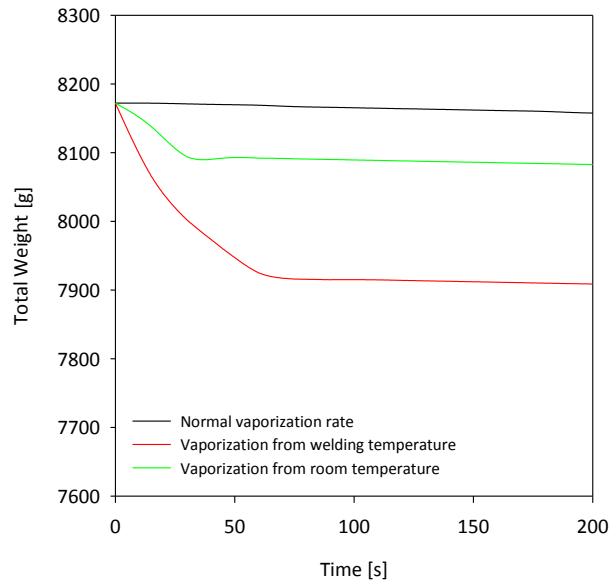


Figure 3.7 – Comparison between normal vaporization rate of liquid nitrogen with vaporization from the welding and room temperature.

In the context of the calorimetric tests, several analyses were carried out. Firstly, several measurements of weight of liquid nitrogen lost with time, for the welding and room temperature tests, were performed. The weight in the last instant before the specimen was placed into the calorimeter and the last instant before normal evaporation rate take place was applied. Then the initial weight (peak weight) considered in the calculation was the first value taken plus the mass of the specimen (assessed after welding). The difference between this value and the final value taken gives the precise variation of weight lost associated with the heat absorbed by the specimen. This procedure was performed for welding and room temperature tests.

Although experimental measurements of weight loss were carried out for the overall room temperature tests, it was observed that experimental errors could occur. Considering the same room temperature conditions and material specification, a regression line was applied to the relation between weight lost and sample mass (Figure 3.8). The application of this equation, instead of the individual experimental measurements will result in more accurate results in the estimation of heat lost for room temperature tests.

The energy during welding temperature to boiling temperature and the energy from room temperature to boiling temperature for each test was then determined using the latent heat of vaporization for liquid nitrogen. The difference between these two energies, given by the equation 3.3, previously introduced, corresponds to the real energy absorbed. Finally, the Process Efficiency could be calculated by the ratio between the energy absorbed, experimentally determined, and the arc energy supplied.

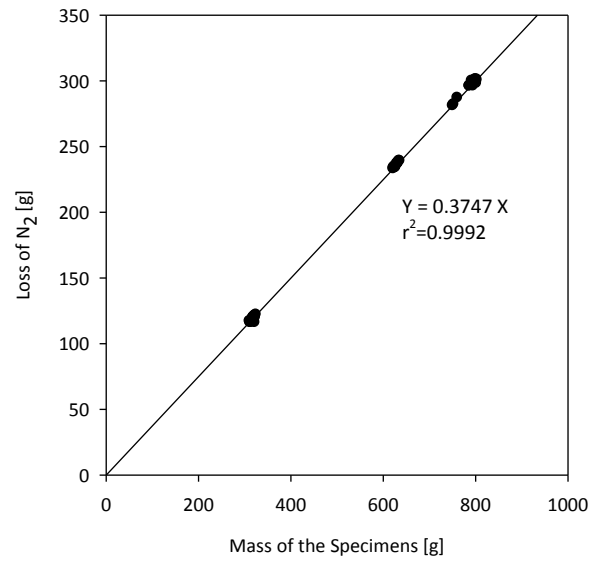


Figure 3.8 – Correlation of the mass of the specimens and the amount of liquid nitrogen lost, between room temperature and liquid nitrogen boiling temperature.

3.4. RESULTS

3.4.1. Introduction

The results obtained for the characterization of process efficiency tests using liquid nitrogen calorimetric tests are organized in three sub-sections, as follow:

- The first set of experiments correspond to the characterization of the experimental errors in relation to the calorimetric method applied;
- The second set of experiments was characterized by the analysis of different setting conditions in CMT and RapidArc waveforms. These tests were developed to understand the effect of welding process setting parameters on process efficiency;
- The final set of experiments was developed to compare the process efficiency using different GMAW waveforms, respectively CMT, RapidArc, STT and FastROOT.

Unless otherwise mentioned, the tests were carried out using experimental conditions presented in the Table 3.1, as follow:

Table 3.1 – Summary of the main experimental conditions applied.

Welding Conditions	Waveforms applied	Values
Wire Feed Speed [m/min]	All	7.8
Welding Speed [m/min]	All	0.5
CTWD [mm]	All	13.5
Arc Length Correction (ALC) [%]	CMT	0
Trim	RapidArc, STT	1.5
Base Current [%]	FastROOT	0
Hot Start (HS) [%]	CMT	0
Wave Control	RapidArc, STT	10
Forming Pulse [%]	FastROOT	0
Shielding Gas Composition	All	20%CO ₂ 80%Ar
Plates Thickness [mm]	All	2.0

3.4.2. Assessment of Experimental Errors

The first set of experimentation was performed to characterize the errors associated with the experimental method, i.e., liquid nitrogen calorimetric tests. Different sorts of conditions were analysed, as follow:

- The material of the clamping bars used during the welding tests;
- Welding length (time);
- Sample transfer movement;
- Delay (holding) time, between the welding and the beginning of the liquid nitrogen calorimetric tests.

The results for these different assessments were obtained for CMT waveform and are presented in the next subsections.

3.4.2.1. Effect of Clamping Bars

The effect of clamping bars was assessed using two different clamping systems:

- Metallic bars of aluminium;
- Insulated bars.

Three different thicknesses were assessed for these tests, respectively 2, 4 and 5mm.

The results obtained for the three thicknesses studied are plotted according with the average and RMS variation obtained to the different conditions (Figure 3.9). As observed in the Figure 3.9 the insulated bars result in a slight increase of process efficiency, more significant for 5mm thickness plates. It is also observed that calculated process efficiency increases with plate thickness.

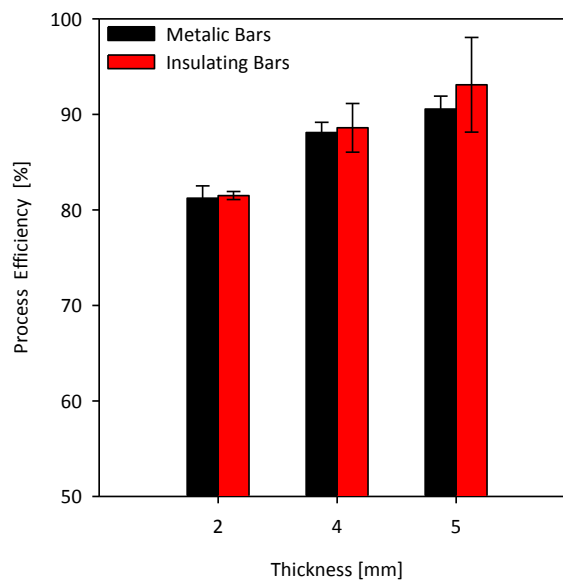


Figure 3.9 – Effect clamping bars material on process efficiency for CMT, using plates with different thicknesses.

3.4.2.2 – Effect of Welding Duration Time

The effect of welding duration time is directly dependent of the welding length at a constant welding speed. The results obtained are represented in the Figure 3.10 demonstrating that measured process efficiency decreases with the increase of welding time. The Figure 3.10 shows that about 12% of heat is lost during the first 25 seconds of welding.

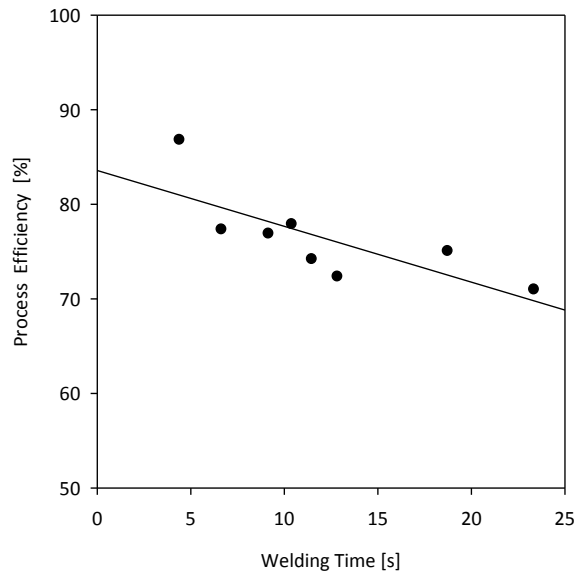


Figure 3.10 – Effect of welding duration time on process efficiency for CMT.

3.4.2.3 – Effect of Sample Transfer Movement

The movement associated with the transfer of the welded samples from the rig to the calorimeter can vary significantly between the tests performed. In order to simulate the increasing of movement ratio, a sequence of tests were undertaken based on the increasing of movements during the holding transfer time, from 0 to 16. The movements are forced convection effect obtained by oscillating the sample during the transfer time. The results are illustrated in the Figure 3.11. A slightly decrease of measured process efficiency is observed with the increase of movement during the holding transfer time.

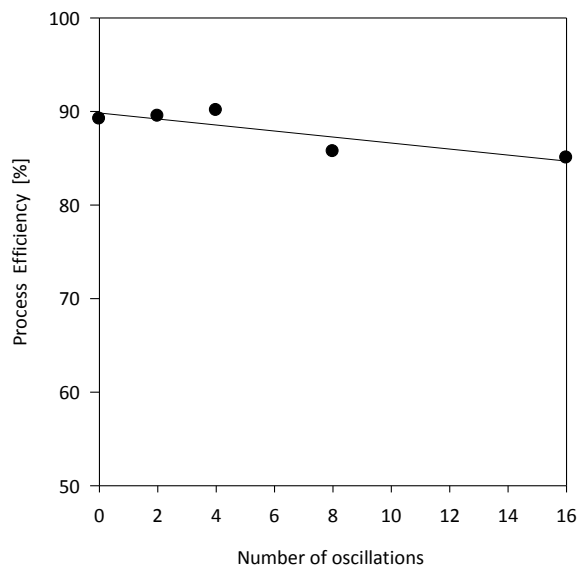


Figure 3.11 – Effect of the number of oscillations during the holding transfer time on process efficiency for CMT.

3.4.2.4 – Effect of the Delay Time

Delay time is defined as the time spent between the end of the welding and the start of the calorimetric tests, when the sample is dropped into the calorimeter. It includes the unclamping operation, holding time during the transport of the sample and drop off. It was measured that the average time spent in this operation was about 5 seconds.

Three different thicknesses were also assessed for these tests, respectively 2, 4 and 5mm. The experimental tests were performed by increasing the holding time with steps of 5 seconds.

The results are presented in Figure 3.12, where the Figure 3.12-a shows the variation of measured process efficiency, using semi-logarithmic scale, from 5 s to 900 s of delay time for 2mm thickness plates, and the Figure 3.12-b compares the variation of measured process efficiency for three different thickness plates during the first 60 seconds of delay time.

From these results is estimated about $\pm 5\%$ of scatter for tests using 2mm thickness plates and $\pm 3\%$ for tests using 4 and 5mm.

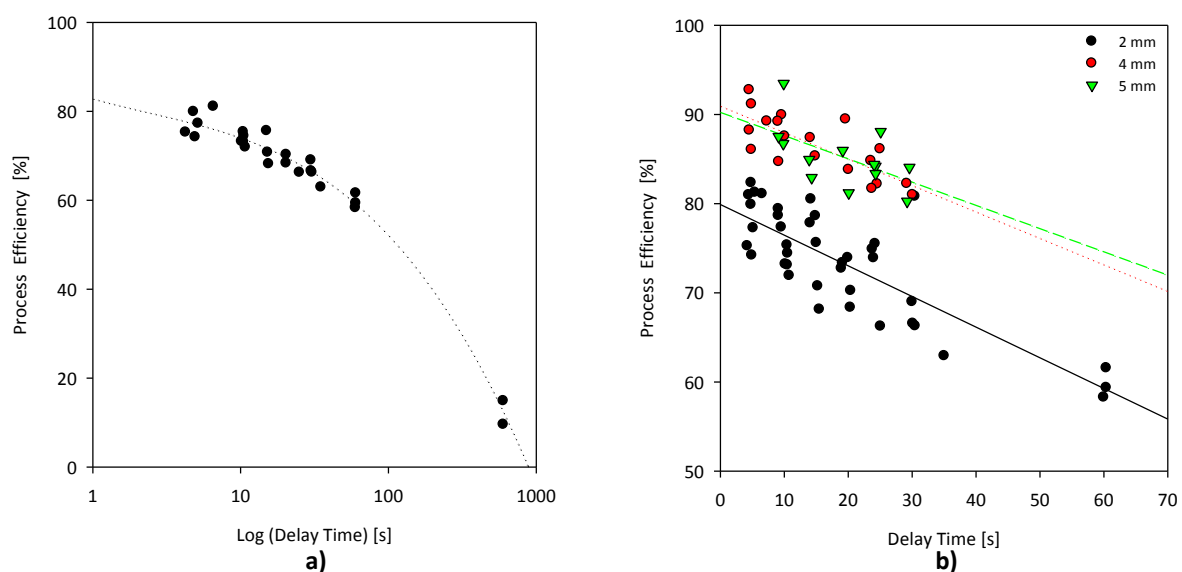


Figure 3.12 – Effect of delay time on process efficiency for CMT: a) first 900sec for 2mm thickness plates; b) first 60sec comparing plates with different thicknesses.

3.4.3. Characterization of the Effect of Welding Parameters on the Process Efficiency

The characterization of the effect of welding setting parameters on process efficiency was performed using CMT and RapidArc waveforms.

The experimental tests performed for the CMT waveform aimed to assess the following features:

- The effect of wire feed speed (WFS) and waveform characteristics (arc current, arc voltage and arc power), using constant WFS/TS ratios;

- The effect of wire feed speed at different thicknesses;
- The effect of welding speed;
- The effect of arc length correction (ALC);
- The effect of hot start (HS);
- The effect of CTWD;
- The effect of shielding gas composition, for different thickness plates.

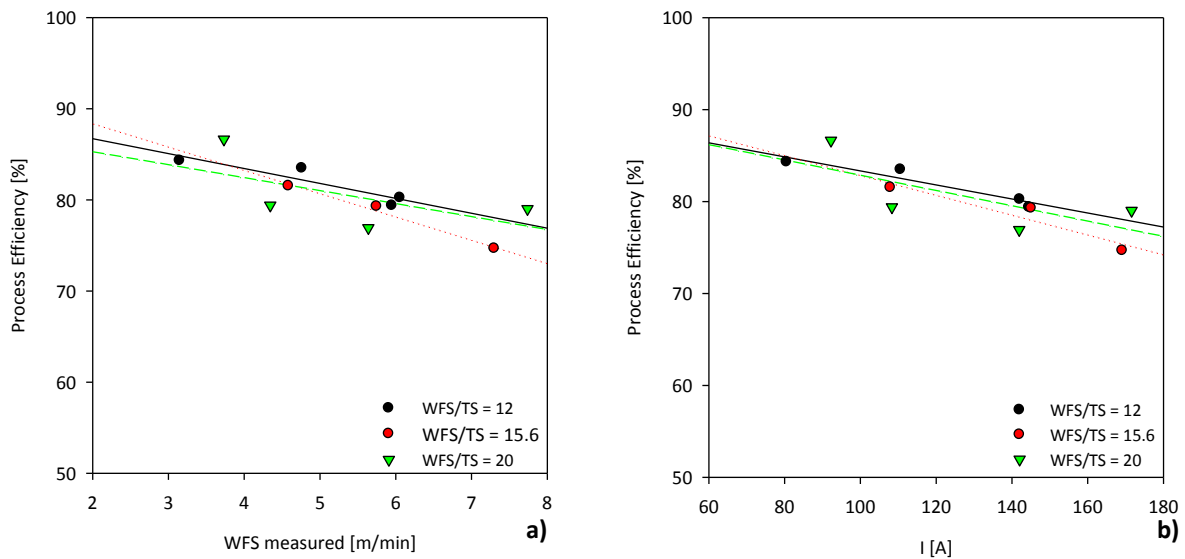
Rapid Arc waveform was also evaluated in respect to:

- The effect of wire feed speed at different thicknesses;
- The effect of trim (adjusting arc length parameter);
- The effect of shielding gas composition, for different thickness plates.

The results are presented in the following two sections according to the welding waveform applied.

3.4.3.1. Cold Metal Transfer waveform

The effect of WFS and the resulting waveform characteristics (i.e., arc current, arc voltage and arc power, calculated using instantaneous values) was assessed considering different WFS/TS ratios and thickness plates (Figure 3.13).



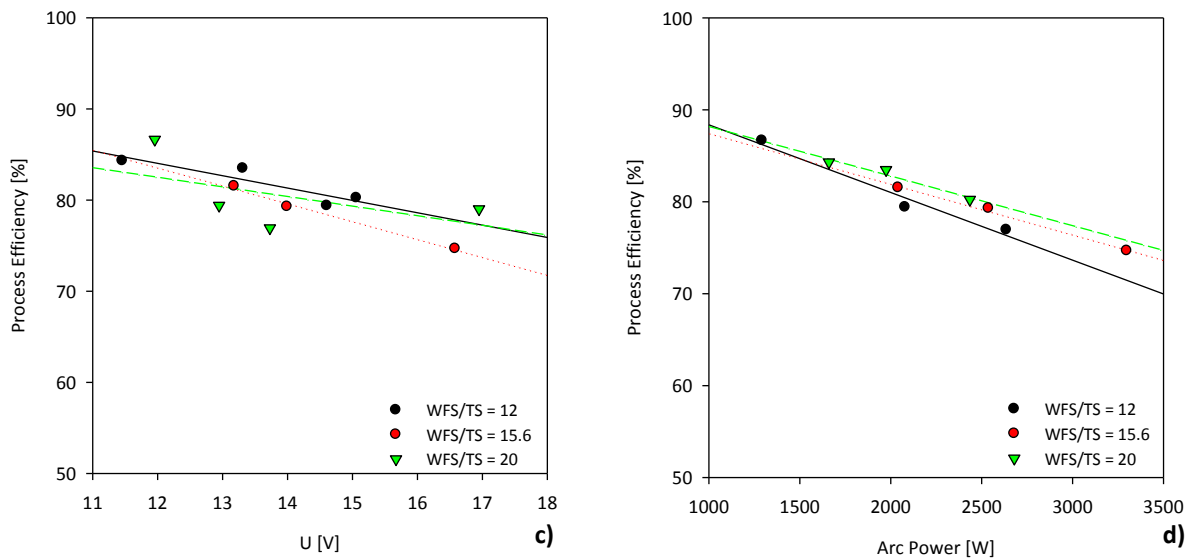


Figure 3.13 – Effect of different waveform characteristics on process efficiency for CMT, using different WFS/TS ratios and 2mm thickness plates: a) measured WFS; b) arc current; c) arc voltage and d) arc power.

The Figure 3.13 compares the process efficiency obtained for three different WFS/TS ratios, respectively 12.0, 15.6 and 20.0, using 2mm thickness plates. It is observed that process efficiency decreases with the increase of WFS and correspond waveform characteristics. No significant changes can be observed in respect to the variation of WFS/TS ratio.

The results obtained to the comparison of plates with three different thicknesses using constant WFS/TS ratio of 15.6 are presented in the Figure 3.14. It is demonstrated that measured process efficiency is considerably lower (by approximately 5 - 10%) for 2mm thickness plates, in comparison with similar higher values obtained for plates with 4 and 5mm thickness.

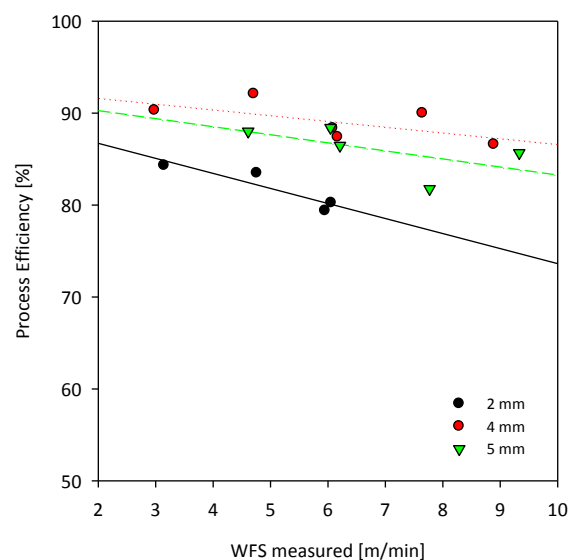


Figure 3.14 – Effect of WFS on process efficiency for CMT, using constant WFS/TS ratio of 15.6 and plates with different thicknesses.

Process efficiency was also assessed varying the welding speed using constant WFS (i.e., 7.8m/min) and three different thicknesses (2, 4 and 5mm). It is observed from Figure 3.15 that an increase of welding speed results in an increase of measured process efficiency (approximately 5% for the increase of 0.25m/min of welding speed).

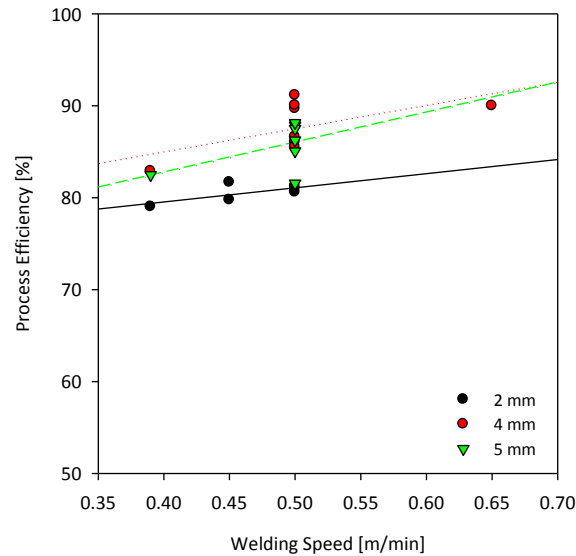


Figure 3.15 – Effect of welding speed on process efficiency for CMT, using plates with different thicknesses.

The effect of arc length correction (ALC) on process efficiency was evaluated for CMT waveform. Two different WFS levels were tested, respectively 4 and 7.8m/min (Figure 3.16). No significant effect is observed for the variation of ALC. However, higher process efficiency values are observed when lower WFS level (4.0m/min) and higher thickness plates (4mm) were applied.

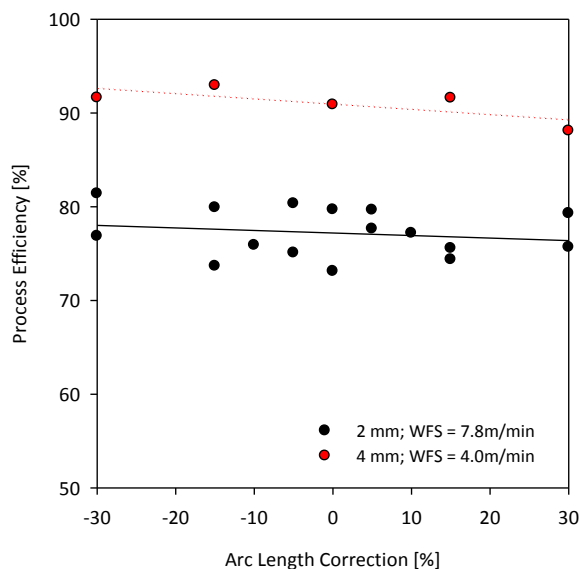


Figure 3.16 – Effect of the arc length correction (ALC) on process efficiency for CMT, at different setting conditions (thickness plates and WFS levels).

The effect of hot start (HS) setting on process efficiency was investigated for CMT waveform, using constant WFS of 4m/min and 4mm thickness plates. The results are

illustrated in the Figure 3.17 and shows that no significant changes on process efficiency are associated with hot start.

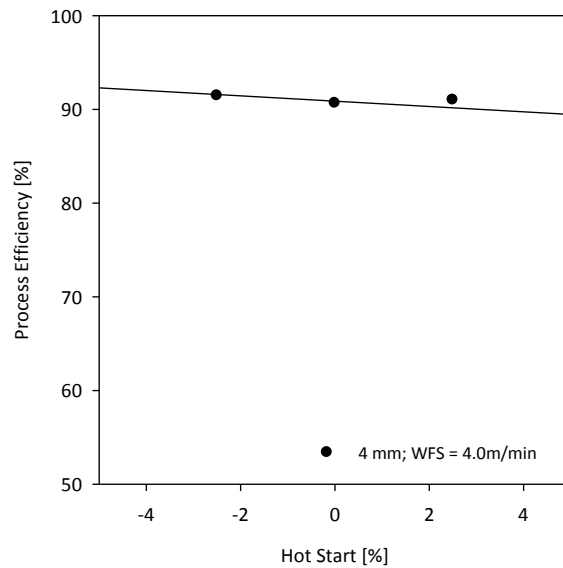


Figure 3.17 – Effect of hot start (HS) on process efficiency for CMT, using 4mm thickness plates and constant WFS (4m/min).

The effect of the CTWD on process efficiency was also evaluated from changes in CTWD from 6mm to 20mm for CMT. It is observed that process efficiency decreases rapidly between 6 and 10mm of CTWD but no significant changes are observed between 10 and 20mm CTWD (Figure 3.18).

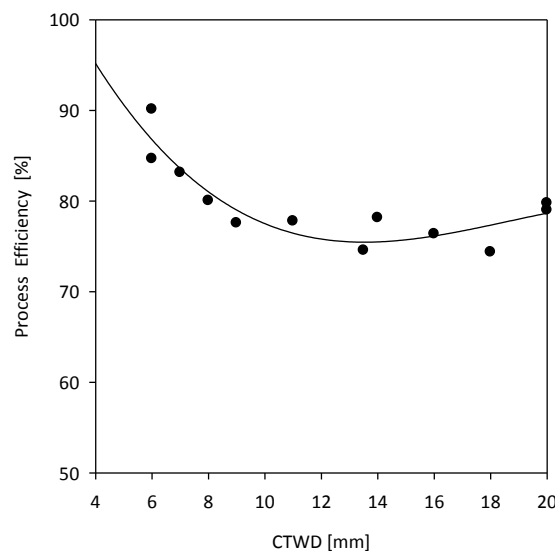


Figure 3.18 – Effect of CTWD on process efficiency for CMT.

The effect of the shielding gas composition, with different amount of carbon dioxide (i.e. 8%CO₂ 92%Ar, 20% CO₂ 80%Ar and 100%CO₂), on process efficiency was also investigated using plates with different thickness. An average and RMS variation of several tests developed with the same welding conditions were obtained and the results are presented in the Figure 3.19. About 5% lower results were achieved for the tests performed using 2mm

thickness plates, but no significant variations can be observed in result of the variation of shielding gas composition.

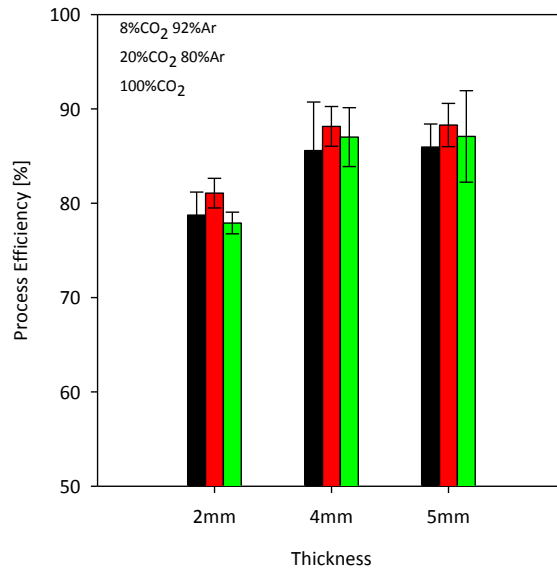


Figure 3.19 – Effect of shielding gas composition (i.e. amount of carbon dioxide) on process efficiency for CMT, using plates with different thicknesses.

3.4.3.2. RapidArc Waveform

The effect of WFS on process efficiency was also investigated for RapidArc waveform, using a constant travel speed and plates with three different thicknesses (i.e. 2, 4 and 5mm). The results are presented in the Figure 3.20. It is observed that process efficiency decreases with the increase of wire feed speed (i.e. arc current, arc voltage and arc power) and is lower for 2mm thicknesses plates.

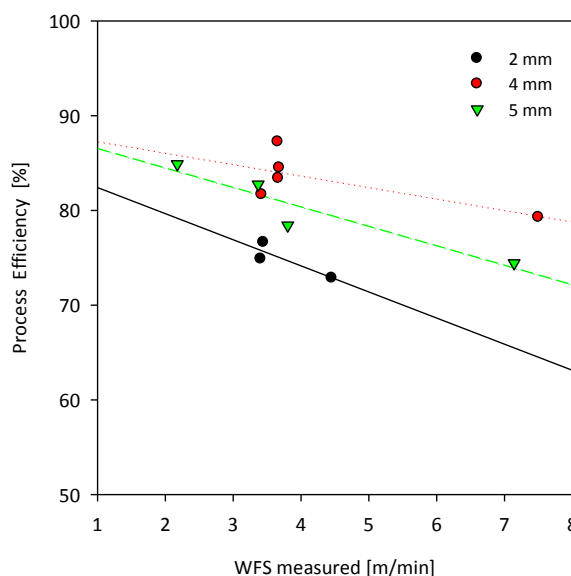


Figure 3.20 – Effect of WFS on process efficiency for RapidArc, using constant welding speed of 0.5m/min and plates with different thicknesses.

The effect of plate thickness on process efficiency was assessed for RapidArc waveform at constant WFS/TS ratio of 8. The average and RMS variation obtained for several tests are

presented in Figure 3.21. These results confirm that for 2mm thickness plates the measured process efficiency is considerably lower when compared with plates of 4 and 5mm thicknesses.

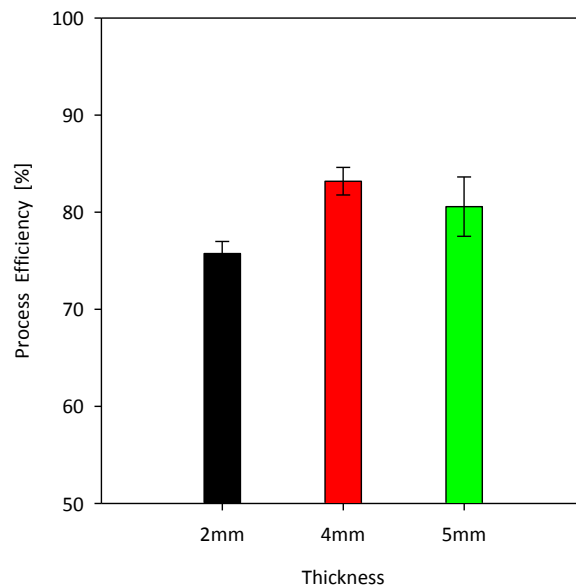


Figure 3.21 – Effect of plate thickness on the process efficiency at constant WFS/TS ratio..

The effect of the trim on process efficiency was investigated for RapidArc waveform, using WFS of 4m/min and plates with 4mm thickness. The results are illustrated in Figure 3.22; no significant effects on process efficiency are observed.

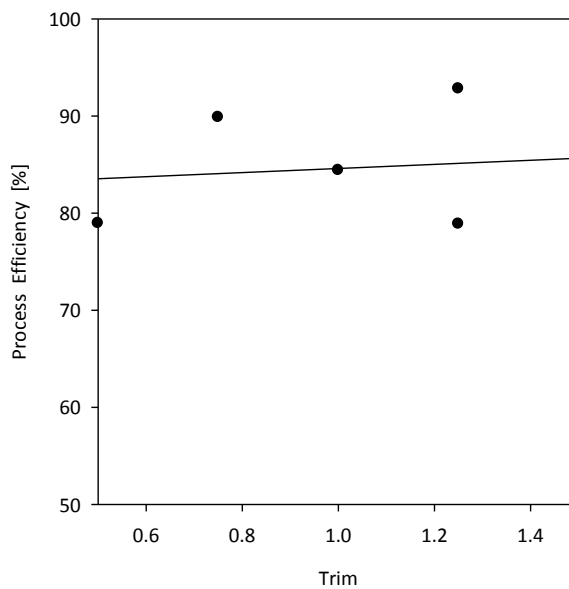


Figure 3.22 – Effect of the trim on the process efficiency.

The effect of shielding gas composition on process efficiency was also evaluated for RapidArc waveform, using 4m/min of WFS and comparing plates with different thicknesses (i.e. 2, 4 and 5mm). The average and RMS variation of several measurements with identical conditions applied suggest that no significant changes are observed for the different gases

applied, but the results for 2mm thickness plates are considerably lower when compared to the plates with 4 and 5mm thickness (Figure 3.23).

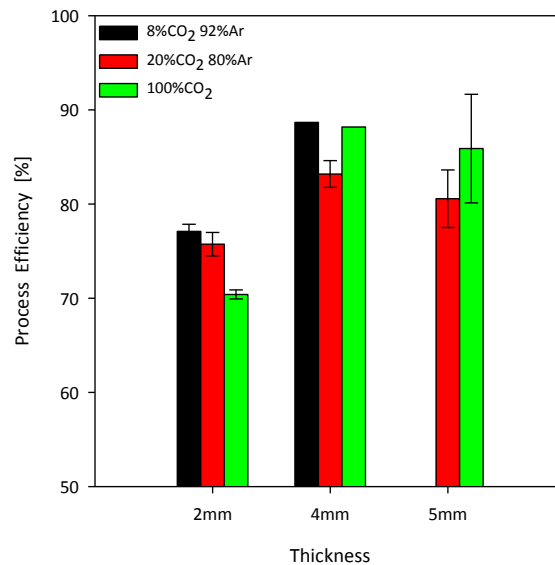


Figure 3.23 – Effect of shielding gas composition on process efficiency for RapidArc, at different thickness plates.

3.4.4. Welding Processes Comparison

The comparison of the results of process efficiency obtained to CMT and RapidArc waveforms with STT and FastROOT was performed. The experimental conditions applied to these tests are presented in the Table 3.2, below.

Table 3.2 – Summary of the welding conditions applied to the comparison on the process efficiency to CMT, RapidArc, STT and FastROOT waveforms.

Welding Conditions	Welding Waveform	Values
WFS/TS ratio	All	5 - 20
CTWD [mm]	All	13.5
Trim	RapidArc and STT	1.5
Wave control [Rapid Arc and STT	10
ALC and HS [%]	CMT	0
Hot Start [%]	CMT	0
Base Current [%]	FastROOT	0
Forming Pulse [%]	FastROOT	0
Shielding Gas	All	20%CO ₂ 80%Ar
Thickness [mm]	All	2

The results of process efficiency obtained for all the waveforms assessed using similar welding conditions are represented in the Figure 3.24.

The Figure 3.24 illustrates that measured process efficiency decreases with WFS/TS ratio (decrease of travel speed at constant WFS) for all the processes considered. It is noticed that process efficiency is significantly lower for RapidArc, when compared with the other

waveforms evaluated (about 13% lower). Short-circuiting processes result in about 90% process efficiency while RapidArc results in about 78%.

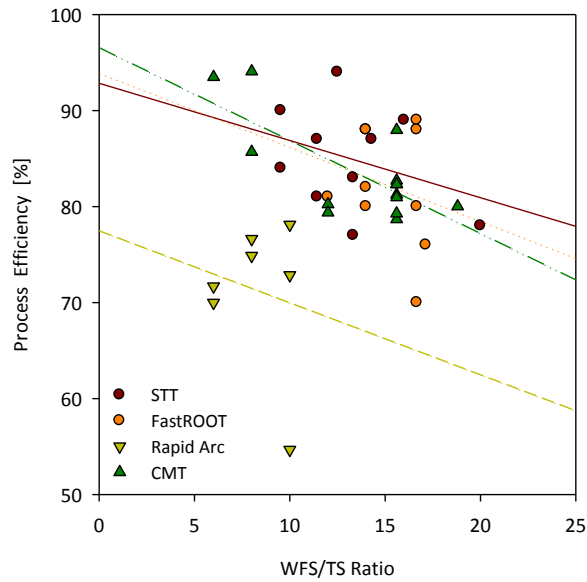


Figure 3.24 – Effect of the WFS/TS ratio on the process efficiency for different waveforms.

3.5. DISCUSSION OF RESULTS

3.5.1. Introduction

Arc energy is defined as the total energy delivered at the contact tip of the power source to the workpiece; although this does not represent the overall heat absorbed by the workpiece. The actual amount of heat introduced into the workpiece is given by the heat input which is determined by the product of arc energy and the process efficiency parameter.

During the previous chapter it was shown that different GMAW waveforms were characterized by similar burn-off ratios, but significant variations of arc energy were also identified. This phenomenon led to noteworthy changes on the melting characteristics. These changes could be affected by variations of process efficiency, associated with the waveforms and welding parameters applied.

In this respect, several studies have been performed by different authors to quantify the process efficiency and the heat input of arc welding processes. Widespread variations, in the range from 65 to 95%, were identified for GMAW waveforms in the literature. Experimental and numerical methods were applied respectively to measure and to estimate the process efficiency obtained from different welding processes and conditions. Numerical estimations do not satisfy completely the entire heat phenomena and therefore experimental measurements are most accurate for this prediction, although they also may be subject to errors.

The liquid nitrogen calorimetric tests were applied to the analysis of process efficiency under different waveforms and welding process conditions. The discussion of the results obtained will be performed in the following sub-sections considering:

- The analysis of the errors associated with the experimental method applied and the assessment of their contribution to the overall error;
- The characterization of process efficiency using CMT and RapidArc waveforms and different welding process conditions;
- The comparison of the process efficiency for several GMAW waveforms.

3.5.2. Calorimetric Test Method and Experimental Errors

The accuracy of the calorimetric method was deeply investigated in this work. Prior to the analysis of process efficiency a fundamental characterization of the contributions to the errors of measurement was attempted. The liquid nitrogen calorimetric tests aimed the measurement of the overall heat absorbed by the workpiece during welding.

A sketch of the representation of the mechanism of heat losses during welding are represented in Figure 3.25.

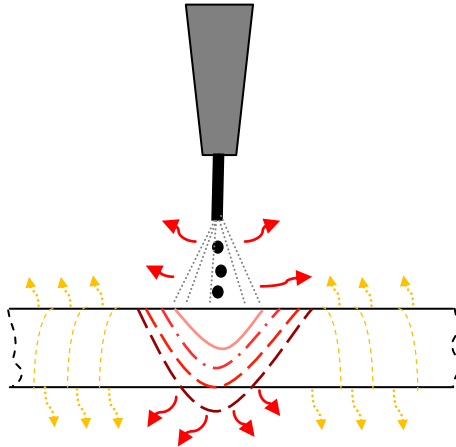


Figure 3.25 – Sketch of the heat flow in welding of thin plates, with the increase of arc energy. The red arrows represent the radiation losses during welding, while the yellow arrows represent the losses by radiation after welding.

During arc welding heat losses can occur mainly due to the convection, radiation and metal vaporization and these represent the amount of heat that is not absorbed by the workpiece. Despite the heat losses associated with the arc welding process, which represents the heat that is not absorbed by the workpiece, the yellow arrows show the heat losses that represent an experimental error in the analysis of process efficiency. This error results from heat absorbed by the workpiece that is lost before the calorimetric tests start. This is mainly due to the radiation of the heat absorbed by the workpiece that is flowing during welding through the material due to the thermal cycle. However, conduction losses can also have a small contribution. The comparison of the application of metallic and insulating bars shows that a slightly decrease of process efficiency occurs when metallic bars were applied. The results show that the difference between those two clamping bars system is as low as 0.5% (Figure 3.9). This lead to a conclusion that conduction heat losses during welding time has a very small contribution and therefore are negligible.

Thus, among the mechanisms of heat loss during welding and delay time radiation from the metal surface should be considered the most relevant.

The analysis of the effect of welding time, from 5 to 25 seconds, revealed that the process efficiency decreases by about 12% for a weld taking 25 seconds. For the general welding time defined for the overall tests, i.e. about 10 seconds long, about 3% of heat is lost, considering the Figure 3.10. On the other hand the delay time, quantified as about 5 seconds, is associated with a reduction of process efficiency of about 2%, considering the Figure 3.12.

The error associated with the transfer movement, from the rig to the calorimeter, and the loss of liquid nitrogen by ejected droplets, when the sample is dropped off inside the calorimeter were also considered. The error associated with the transfer movement was assessed by varying the movement associated with the transfer from straight (zero oscillations) to 16 oscillations (Figure 3.11). The results illustrate a small variation of process

efficiency, within less than 1%, when the transfer is produced at very high oscillations. This suggests that in that extreme case only a very small amount of heat is lost to the atmosphere by convection effect. The liquid nitrogen level was always filled to about 75% of the container to minimize ejected droplets. This leads to a conclusion that these errors are negligible.

The analysis concerning the effect of thickness also reflected that low thickness materials (2mm) present significantly higher losses of heat compared to 4 and 5mm thick plate. The heat losses result mainly from radiation effects occurring during the welding period. From these results is observed that process efficiency is about 5-10% lower when 2mm plates were applied. No significant variations were observed between the thicker plates, i.e., 4 and 5 mm. These results emphasise that for the welding conditions applied 2mm thickness is probably too low to conserve the heat absorbed during welding, before the calorimetric tests begin.

To understand the effect of thickness, it is important to understand that radiation losses increase exponentially with the increase of temperature by Stefan-Boltzmann law (Normand and Peleg 2010) (Figure 3.26). This indicates that a thinner material section will be characterized by higher radiation losses. However, as the depth of penetration increases, with the increase of WFS, the actual process efficiency can also be reduced in consequence of an increase of radiation heat losses from the bottom of the weld.

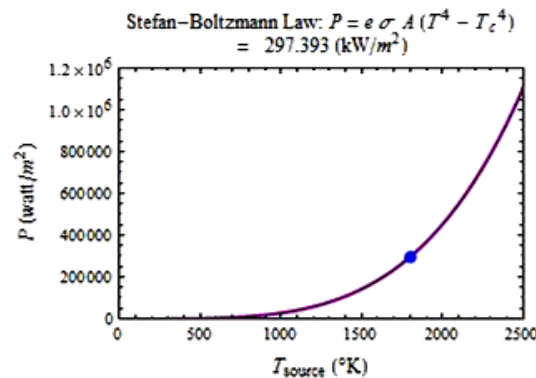


Figure 3.26 – Variation of radiation losses with the increase of temperature (Normand and Peleg 2010).

The equation applied for convective heat losses is presented as follow:

$$q = h \times A \times (T_w - T_\infty) \tag{3.18}$$

Considering 1500°C of welding temperature, and convective coefficient is 9 W/m²°C (Michaleris and DeBicari 1997), as given by Figure 3.27

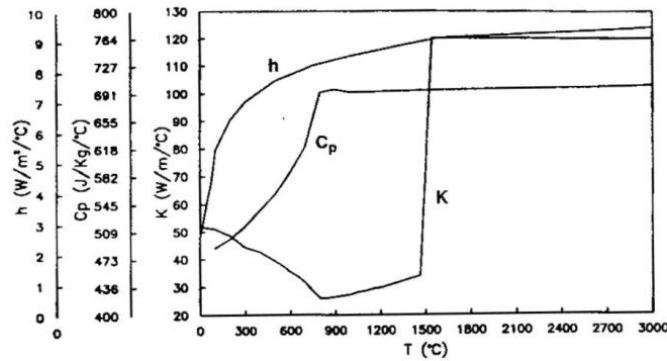


Figure 3.27 – Variation of convective coefficient (h), thermal conductivity (K) and specific heat (C_p) with temperature (Michaleris and DeBicari 1997).

Radiation losses are estimated as 100000W/m^2 and convection losses are estimated as 13500W/m^2 . Considering a section of $100\text{mm} \times 5\text{mm}$ thickness the radiation losses are estimated as 200W , compared to 27W for convection. This demonstrates that radiation is much significant than convection at this temperature level (about 10 times greater). Thus the actual process efficiency will be given by the equation 3.19, as follows:

$$\text{Actual Process Efficiency} = \text{Process efficiency} + \text{welding time error} + \text{delay time error} \quad (3.19)$$

Where the welding time error is estimated as 3% (considering 10 seconds of welding time/length) and delay time error is measured as 2% (considering 5 seconds of delay time). The sum of the two error contributions is estimated as 5%.

3.5.3. Characterization of the Effect of Setting Parameters on Process Efficiency Results

Several process setting parameters were tested and their effect on process efficiency was deeply investigated. CMT and RapidArc waveforms were assessed in detail in respect to several parameters.

As described in the previous chapter, the wire feed speed works as the main controlling parameter in the welding waveforms above cited, as a synergic mode is implemented. In this perspective the effect of WFS on process efficiency is crucial to understand how the process efficiency varies with the welding waveform (Figure 3.13 and 3.20). The results obtained shows that the increase of wire feed speed resulted in decrease of process efficiency. A variation of about 5% of process efficiency is observed between 3 and 7m/min. As identified from these results, the variation of WFS/TS ratio can be neglected. Other authors (Fuerschbach and Knorovsky 1991) (Hsu and Soltis 2003) (Bosworth 1991) have already observed a decrease of process efficiency with WFS for GMAW and GTAW. However, the effect of WFS on process efficiency has not been explained before. This increase of the heat losses due to WFS is probably a result of the increase of radiation heat losses, as the arc energy increases, and consequently the plate temperature increases (Figure 3.26). Furthermore, this generally results in a increase of depth of penetration, which emphasises the possible reduction of process efficiency in consequence of the

increase of heat losses due to radiation and convection on the bottom of the weld. This effect should be significant when low thickness materials are applied, and therefore does not represent an effective reduction of process efficiency but an increase of the experimental error.

The variations of process efficiency related to the increase of WFS can be explained by the increase of the depth of penetration and consequently the increase of losses of heat by convection and radiation on the bottom of the plates. This effect is major when 2mm thickness plates were applied. In this way, the effect of WFS should be neglected if a very thick plate were tested; it is not the effect of WFS on the process efficiency but the effect of thickness which contribute to the reduction of process efficiency through the losses occurring during welding/ holding time. This variation is illustrated for both, CMT and RapidArc, waveforms and was complemented by the visual evaluation of the specimens, where partial or full penetration was identified. This results lead to a conclusion that WFS solely does not affect process efficiency but can contribute to the increase of heat losses when full penetration is achieved accelerating the effect of convection and radiation losses in the root region. However, this phenomenon should not represent a noteworthy effect on the overall heat losses, as the main error associated with the measurement of process efficiency results from the radiation losses during welding/ delay time, particularly observed when low thickness was applied.

The variation of arc current, arc voltage and arc power is in agreement with the variation of WFS, by the law that correlates these parameters considering the synergic mode applied. Although Kenney et al. (1998) identified that process efficiency is inversely related to arc energy, this probably results from the variation of WFS and consequently the arc current and voltage, prior to the obtained arc energy, and thus depends on the measurement technique applied.

The variation of arc length correction (ALC) and hot start (HS) for CMT and trim for RapidArc demonstrated that none of these parameters affect process efficiency (Figure 3.16, 3.17 and 3.22). No previous studies were identified in the literature in respect to these parameters.

Apart of the welding parameters controlled by the power source, other external parameters were also considered, in particular CTWD and shielding gas composition (Figure 3.18, 3.19 and 3.23).

The results of the effect of CTWD for CMT suggested that this parameter has a significant contribution on the increase of process efficiency when CTWD is lower than 11mm. Nevertheless, a deep analyse on the effect of CTWD on WFS for CMT suggest that WFS varies significantly within this parameter. The results presented in chapter 2 indicated that when CTWD is lower than 16mm, WFS decrease significantly with the decrease of CTWD, while above 16mm the WFS increases. At higher values, the WFS increases but this increase is not significant to represent a variation in the process efficiency assessed.

This behaviour observed for CMT results from the control system of the power source that is able to change the actual WFS in order to compensate the variations of CTWD. These changes in WFS, in particular at very low WFS levels, have a particular influence on the heat transfer phenomena, as the melting rate at very low WFS is reduced and the effects of heat losses during the delay time are also reduced or even eliminated, giving a better approximation of the process efficiency for CMT, in the range of 90%, as observed in the Figure 3.16. However, from 11mm of CTWD, process efficiency becomes constant at approximately 80%; this can be explained by the fact of the maximum losses associated with relationship between thickness and the WFS level is achieved at this point. It is also according to the full penetration level achieved from this point.

The results obtained to the variation of shielding gas composition suggested that the increase of the amount of carbon dioxide, from 8%, to 20% and 100%, is not significantly important (Figure 3.19 and 2.23). These results are in agreement with the work of Bosworth (1991).

3.5.4. Characterization of Process Efficiency using Different Waveform Systems

The comparison of the results of process efficiency, under similar WFS/TS ratios, for different waveforms suggested that CMT, STT and FastROOT waveforms present significantly higher process efficiency than RapidArc. The process efficiency obtained for RapidArc was, in average, 78%, while CMT, STT and FastROOT demonstrated process efficiency as high as 90%. The scatter obtained for the measurement of process efficiency was about $\pm 3\%$ (considering 4 and 5mm thickness plates).

RapidArc is characterized by a mechanism of pulse spray transfer while the remaining processes are regarded as short-circuiting. This is the main difference that may justify the variation of about 10% difference on the process efficiency obtained. This leads to a better understanding of how the metal transfer mechanism influences the process efficiency. Hsu and Soltis (2003) have already described the effect of the mechanism of metal transfer on the process efficiency. They found out that process efficiency is about 85% for short-circuiting GMAW, in particular STT (e.g. 86%), while about 73% was established for pulsed GMAW. These results are in agreement with those obtained in this study.

Previously, Quintino (1986) obtained process efficiencies in the range of 62-72% for GMAW-P. Other authors (Kenney, Miller and Smartt 1998) (Joseph 2001) achieved results in agreement with Quintino (1986), 73% and 70% respectively but slightly below the values obtained in this study. The work of Bosworth (1991) indicated process efficiencies from 75% to 80% for pulsed welding, while non pulsed GMAW was assessed in the range of 85 to 95%. The results published by Bosworth (1991) are in agreement with the results obtained in this work. Bosworth (1991) found out that the arc energy was lower for the pulsed welding than non pulsed GMAW, with the exception of short-circuiting GMAW.

The lower arc energy in pulsed GMAW is actually explained by the waveform design. Pulse waveform is characterized by high energy level delivered during the pulse period, enough to achieve the one drop per pulse stability criteria, and reduced in the period between pulses (background time). In the case of short-circuiting the current works always at significantly lower level resulting in lower arc energy.

This significant variation between these two groups of MIG/MAG welding processes should be related to the amount of energy loss by radiation during the background period in GMAW-P/ RapidArc, while in short-circuiting processes this period represents the direct transfer of metal and energy to the weld pool, with less potential to guarantee the heat losses.

The results obtained are according to the physical mechanisms described in the literature, as introduced in the section of the literature review. In fact, the higher values of process efficiency associated with short-circuiting transfer are supported by the fact that heat transfer is promoted by the metal transfer under bridging effect. This mechanism of transfer is more efficient than spray transfer where the heat is partially transferred by the drop fly effect. Furthermore, the lower energy developed under the dip transfer conditions is favourable to its higher efficiency. This has been explained already by several authors (Dean, Norrish and Cook 2006) (Tsao and Wu 1988).

3.6. CONCLUSIONS

- Process Efficiencies were successfully quantified for several welding waveforms and setting process characteristics;
- Errors have a significant effect on the actual process efficiency obtained. Higher temperatures lead to higher errors due to the losses occurring during welding, in particular due to radiation phenomena occurring during welding and delay time;
- The experiments performed with 2mm thickness led to 5 – 10% error due to greater radiation losses associated with full depths of penetration;
- The WFS has a similar effect to the small thickness plates applied (i.e. 2mm); At high WFS level, even when higher thickness (i.e. 4 and 5mm) were undertaken, the plate temperature increases and consequently depth of penetration also increases resulting in higher heat losses;
- CTWD may have an effect on the resulting process efficiency; At low CTWD levels, arc length is shorter and heat absorption may increase;
- None of the remaining process setting parameters evaluated, i.e. arc length adjusting parameter, dynamics adjusting parameter, shielding gas composition, affects significantly process efficiency;
- No significant differences are observed between the short-circuiting processes, measured as $90\pm 3\%$;
- Measured efficiency for pulse spray was $78\pm 3\%$ attributed to higher heat losses to the open arc processes, compared to lower losses obtained in short-circuiting processes;
- The global results obtained using this method demonstrate that some errors may occur, but it is a very easy and quick test to analyse the process efficiency of welding processes.

Finally, the aim of this research work was to compare the short-circuiting waveforms and it was possible to conclude that no variations were found between the waveforms investigated.

4. CHARACTERIZATION OF NARROW GROOVE PIPE WELDING

SCOPE

Narrow groove welding is considered for many engineering applications when thick materials have to be joined. Although narrow groove welding has been studied for a long time the arc behaviour changes considerably compared with bead on pipe tests analysed in Chapter 2. This has critical consequences in terms of the resulting bead shape characteristics, in particular in terms of welding defects.

In this chapter the waveforms studied in Chapter 2 will be analysed with respect to the bead shape characteristics resulting from narrow groove pipe welding using a “J” groove design with 1.5mm root face. The waveforms will be compared in terms of several responses using statistical modelling when wire feed speed and travel speed change. Productivity performance will be evaluated by the variation of welding speed. The characterization of defects, in particular lack of penetration, will be studied to evaluate the performance of these waveforms when applied to a narrow groove.

4.1. LITERATURE REVIEW	192
4.2. AIMS AND OBJECTIVES	199
4.3. MATERIALS AND METHODS.....	200
4.4. RESULTS.....	205
4.5. DISCUSSION OF RESULTS	221
4.6. CONCLUSIONS	226

4.1. LITERATURE REVIEW

4.1.1. Introduction

During the previous chapters the process characteristics in relation to the metal transfer mechanism and arc stability associated with different waveform designs were investigated. The arc energy and heat input were also evaluated to generate full understanding of how process efficiency changes with waveform design and process characteristics. Furthermore, the bead shape characteristics were evaluated using constant volume (WFS/TS ratio). This work has provided a detailed explanation of how heat input and weld bead shape change when different waveform designs are applied.

One of the most important applications of arc welding is the construction of pipelines. The welding of pipelines typically involves a narrow groove preparation. It is well known that the behaviour of the electric arc in a narrow groove is different from welding on bead on pipes/plates or butt welds; the groove geometry affects the arc characteristics and stability. This is the main reason for fundamental research using the waveform designs considered previously applied to the narrow groove welding of CRA pipes.

The main aspects of the research developed in this chapter have been already discussed in the literature review of Chapter 2. However, in this chapter we will focus on narrow groove welding and weld bead shape quality aspects, including the formation of defects and the process parameters which can affect their generation.

4.1.2. Narrow Groove Welding

Narrow groove welding application is characterized by a multiple pass technique to join thick materials with almost parallel side walls (Kang and Na 2003) (Halmoy, Olsen and Samuelsen 1983) (American Welding Society 2007). Different bevel configurations have been proposed depending on the application and welding processes applied. Narrow groove welding is preferred to conventional “V” grooves due to the reduction in deposited material, welding speed applied to fill the groove, and overall costs.

Narrow groove welding has been extensively applied to the welding of pipelines. Different methods have been applied in this area, depending on material properties, thickness and application. In construction of pipelines for subsea applications, welding is generally used from the exterior of the pipe, but there are situations where internal TIG welding is applied for the root pass.

The major problem associated with narrow groove welding is the susceptibility to welding defects, particularly undercutting and side wall lack of fusion. Extensive research work in this subject has been reviewed by Mondenesi (1990).

More recently, Lopes (2006) applied an arc-sensing technique to narrow groove welding. In fact different controlling systems have been developed to improve weld bead deposition in

narrow groove welding using oscillation techniques. However, these techniques are not suitable for all applications, and in some cases the oscillation parameters (frequency and width) are difficult to optimize and significantly reduce welding speed (American Welding Society 2007).

4.1.3. Weld Bead Quality

Weld bead quality is one of most important requirements in welding engineering. The weld bead quality depends on arc process and parameters, i.e. power source, waveform design, parameter control, and shielding gas composition (Oshima, Xiang and Yamane 2004). These parameters have a fundamental effect on arc welding stability and control, which determine the final quality of the welds and the presence or absence of welding imperfections and defects. In order to evaluate the final quality required in welding construction there are international standards recognized by different organizations and commissions which classify the acceptance criteria requirements. These standards define general quality criteria required according with the application. In respect to construction of pipelines the following European and International standards characterize weld quality requirements:

- BS EN 12732:2000 – “Gas supply systems. Welding steel pipe work. Functional requirements” (BS-EN12732 2000);
- ISO 13847:2000 – “Petroleum and natural gas industries -- Pipeline transportation systems -- Welding of pipelines” (ISO13847 2000);
- BS EN 14163:2001 – “Petroleum and natural gas industries. Pipeline transportation systems. Welding of pipelines” (BS-EN14163 2001).

These standards mention requirements concerning the welding of root pass, in the following aspects:

- External profile;
- Internal profile;
- Root concavity;
- Undercutting;
- Inadequate root penetration;
- Incomplete (lack of) of root penetration.

A summary of the main aspects found in these standards regarding the points above is presented in the Table 4.1, below.

Table 4.1 – Summary of welding acceptance criteria defined in BS EN 12732:2000, ISO 13847:2000(E) and EN 14163:2001(E).

	BS EN 12732:2000	ISO 13847:2000 (E)	EN 14163:2001 (E)
General weld profile	-	Should have a substantially uniform smooth around the entire circumference with a smooth transition to the base material	
External Profile	should be uniform and no more than 3 mm in height	External reinforcement should not exceed specified values (3mm height) (pp. 27, 35)	
Internal Profile	root bead or any concavity should merge smoothly into the adjacent surface but at no point should the weld be thinner than the pipe thickness	Internal reinforcement and concavity should not exceed specified values (3mm height)	
Root Concavity	maximum length 25% of weld circumference and maximum depth 1.5mm or 0.1xT (if less)	Maximum length 25% of the total length	
Undercut (root)	maximum length 25mm in 300mm or 8% of the circumference (if less) and maximum depth of 1mm or 0.1xT (if less)	Should not be deeper than 1mm or 10% of the pipe wall thickness whichever is smaller Should have a maximum length of 50mm (in 300mm) or should not exceed 15% of wall length	
Inadequate root penetration	maximum length of 25 mm (in 300mm) or 8% of circumference (if less)	Should not exceed 25 mm of length (in 300mm) or 8% of weld length (if less)	
Incomplete (lack of) root fusion	maximum length of 25mm (in 300mm) or 8% of circumference (if less)	Length of an individual indication should not exceed 25mm (in 300mm) or 8% of weld length (if less)	

The standards mentioned above suggest the main non destructive tests considered to identify and classify those criteria requirements.

Waveform signals have been investigated to predict the existence of welding defects. Quinn et al. (1999) used the arc sensing method to identify and analyse welding defects through the waveform signal.

The effect of arc current, arc voltage, electrode polarity and diameter and travel speed on bead shape geometry and quality have been investigated, particularly in terms of penetration and deposition rate. Kim et al. (2003) developed an experimental and modelling study to analyse the effect of arc current, voltage, travel speed and welding angle on bead on plate CO₂ GMAW, where the impact on penetration bead was demonstrated. Other authors (Suban and Tusek 2001) (Muchuhara and Yikegami 2006) reported the influence of shielding gas mixture on the bead shape geometry and quality. Luksa (2006) analysed the welding imperfections associated with arc instability in short circuiting GMAW. The results achieved by this author demonstrate that is possible to detect imperfections related to gas shielding or electrode extension (i.e. arc length).

4.1.4. Weld Imperfections and Defects in Arc Welding

Welding processes are susceptible to weld bead defects and imperfections. The difference between defect and imperfection is associated with the size, frequency and continuity of the indication observed. When it compromises the structural integrity of the weld, it is considered a defect; in other cases it is called an imperfection. It has been concluded that porosity, excessive convexity, inclusions, cracking, undercutting, humping and incomplete fusion are the main imperfections in arc welding. The origin of these imperfections is mainly dependent on welding processes and arc parameters chosen, but also can be associated with the material selection or shielding gas composition.

Productivity in welding engineering is responsible for determining costs and strongly depends on travel speed, welding current and filler wire diameter. However, increasing arc current and travel speed increases the susceptibility to welding defects. Some of these defects can cause a limitation in welding processes conditions, in particular at high travel speeds and arc current levels, where the melting rate is higher. The main defects identified in arc welding processes will now be discussed and characterized.

4.1.5. Characterization of Imperfections and Defects in Arc Welding

The increase of productivity in arc welding has a very high potential in costs saving for manufacturing industry worldwide. However, increases in welding productivity result in increasing susceptibility to the formation of imperfections and defects. In fact, welding speed and high current levels have been found to be the most critical factors in initiation of imperfections (Mendez and Eagar 2000). Mendez and Eagar (2000) (2003) reported that humping, undercutting and tunnel porosity determine a limit in productivity, according with

the waveform design applied. In the next subsections the most critical imperfections and defects associated with arc welding will be discussed.

4.1.5.1. Incomplete Fusion

Incomplete fusion is observed when parent material and weld metal are not completely joined and can also occur between passes in multiple pass welding, often associated with excessive convexity on the previous welding pass. This often results in lack of penetration, more commonly observed when the short-circuiting mode is applied (Hobart Institute of Welding Technology 1997). The common causes of incomplete fusion are following described:

- Excessive travel speed which promotes an excessively convex bead or does not allow an adequate penetration;
- Low arc current;
- Poor joint preparation;
- Large electrode size.

4.1.5.2. Porosity

Porosity is commonly associated with the effect of gas during the solidification process and general classified as a cavity-type discontinuity (Hobart Institute of Welding Technology 1997). The main causes of this defect in arc welding are:

- Inadequate shielding gas flow rate;
- Presence of oxides or other contaminants in the parent metal;
- Incorrect welding parameters;
- Excessive welding current and/or voltage;
- Excessive welding speed, causing weld pool freezing before gases go away;
- Impurities on weld metal or parent material, such as sulphur or phosphorous.

4.1.5.3. Excessive Convexity

Excessive convexity has a major impact in the weld area and consequently a stress concentration effect. The main cause for this is associated with insufficient welding current or incorrect welding technique. In multiple pass welding, it can cause the generation of inter pass defects, such as, undercutting and lack of fusion (Hobart Institute of Welding Technology 1997).

4.1.5.4. Cracking

Cracking has been extensively discussed in the literature, and it is one of most dramatic welding imperfections (Hobart Institute of Welding Technology 1997).

4.1.5.5. Undercutting

Undercutting is a defect commonly observed in arc welding and characterized by a deep depression of the material produced at the solid – liquid interface (Hobart Institute of Welding Technology 1997). Some authors (Mendez and Eagar 2003) (Gratzket, et al. 1992) also associated this phenomenon with travel speed at relatively low currents (100-250A). It has also been associated with the chemical composition of the material, in particular with the sulphur content.

This defect is also commonly observed in fillet welding or narrow groove welding and is due to one or several of the following main effects:

- Excessive welding current and/ or arc voltage;
- Excessive travel speeds;
- Incorrect electrode angles, especially on vertical and horizontal welds;
- Inadequate wire feed rate;

The following corrective actions are usually proposed:

- Use of lower travel speeds;
- Reduction in arc voltage and/ or wire feed speed;
- Increasing the arc pressure effect.

Mendez and Eagar (2003) reported that the undercutting mechanism is associated with the Marangoni forces in the presence of high sulphur content. They considered that Marangoni forces acting at the rear of the weld pool create a thin liquid layer that solidifies prematurely. This will prevent the wetting characteristics in that region and so undercutting is formed. Furthermore, these authors reported that reduction of travel speed will reduce recirculation flow effects in the weld pool and decrease the susceptibility to undercutting formation.

4.1.5.6. Humping

This defect is commonly identified at high travel speeds, characterized by a periodic irregular surface shape causing solid protuberances. Humping is determined by a large depression of the weld pool and is formed at high currents and travel speeds (Mendez and Eagar 2000) (2003) (Mendez, Niece and Eagar November 1999) (Gratzket, et al. 1992) (Soderstrom and Mendez 2006) (Scotti, Larsen and Norrish 1991).

It has been observed that tunnelling, split bead and parallel humping are sometimes associated with humping. Tunnelling is characterized by an unfilled open space at the root, while the split bead occurs by separation of two parallel seams with an open space in the middle. Finally, the parallel humping is a specific case of split bead, where the parallel seams are humped.

Two different morphologies for humping have been recently reviewed, the gouging region morphology (GRM) and beaded cylinder morphology (BCM) (Soderstrom and Mendez 2006).

The humping phenomenon is due to a strong background momentum of the droplet metal, where the travel speed is the key factor. However, it can be avoid with changing of shielding gas composition and welding position. Other authors (Gratzket, et al. 1992) reported the existence of critical travel speed for the start of this phenomenon. They also considered that at currents between 250 and 450A isolated humping occurs but above this current level at lower travel speeds humping comes together with undercutting. This behaviour was observed both with argon and helium shielding gases, but with an increase of the critical travel speed. It was also reported that increasing of pulse frequency results in a decrease in the critical travel speed.

Scotti et al. (1991) reported that humping occurs more severely at extreme conditions as they verified in vertical position narrow groove welding.

4.1.6. Summary

It is recognized that welding of narrow groove behaviour differently than on bead on pipe/plate. It has been attempted that arc length should be very short to guarantee arc stability control inside of the groove.

Unstable phenomena occurring during welding are the main cause of defects and undesirable shape characteristics. Acceptance criteria for welding of pipelines have been also characterized in relation to root runs through several standards.

The main defects controlling the tolerance of welding have been characterized. Lack of penetration and side wall fusion, undercutting and humping are probably the most critical defects and are mainly due to the welding process setting conditions applied.

4.2. AIMS AND OBJECTIVES

The main aim of the research developed during this stage was to understand the effect of the waveforms evaluated and characterized during Chapter 2 when applied to the root runs on Narrow Groove Welding (NGW) of CRA pipes.

In this perspective, different objectives were established, which are described as follow:

- To identify the main issues in welding of CRA pipes, in particular related to the groove preparation and design, purging gas protection of root surface, and welding position;
- To analyse of the response of different waveforms in respect to the bead shape characteristics, such as: depth of penetration, height bead ratio and root and top width;
- The fundamental determination of the region of desirability based on industrial quality criteria established;
- The evaluation of productivity issues obtained using the different waveform designs based on the desirability maps established;
- To analyse the welding defects associated with different waveforms and welding process parameters (WFS and WFS/TS ratio).

4.3. MATERIALS AND METHODS

4.3.1. Materials

The material used in this stage was the 13% Chrome supermartensitic stainless steel. The research was developed using pipe sections of this material, which have been already characterized in terms of dimensions, properties and chemical composition in Chapter 2 of this thesis. The filler metal applied to this study was a superduplex stainless steel AWS A5.9: ER220 (EN 12071: G22 9 3NL), 1 mm wire diameter, also already mentioned in Chapter 2. The gases used previously have also been applied to this research, correspondingly the 2.5%CO₂ 97.5%Ar and 1.5%CO₂ 54%He 44.5%Ar.

4.3.2. Welding Processes

The welding processes applied to the research developed in this chapter were described in Chapter 2, respectively, conventional GMAW-P, RapidArc and STT, using Lincoln Power Wave 455/ STT power source, the CMT and CMT-P, using the Fronius TransPulsSynergic 5000 CMT power source, and the FastROOT, using the Kemppi FastROOT power source.

4.3.3. Methods

The research work was undertaken with the following main phases:

1. Pipe bevel preparation and surface cleaning;
2. Welding tests and experimental measurements;
3. Data analyses.

4.3.3.1. Pipe Bevel Preparation and Surface Cleaning

The research developed during this stage was undertaken using narrow groove welding on CRA pipes. A preliminary study of the bevel preparation was carried out using different designs traditionally applied to pipeline construction. One of the most important points in the design of the groove was the root face. A 2mm root face was used initially, but preliminary tests demonstrated that it would be an advantage to reduce this to 1.5mm. The bevel design varied from a standard “V” configuration (Figure 4.1), a modified “V” (Figure 4.2), and a “J” configuration (Figure 4.3).

The decision about the choice of groove preparation was made comparing the following parameters: (a) depth of penetration; (b) height bead shape; (c) welding defects. The results obtained showed that the more desirable solutions could be obtained using the “J” configuration.

It is important to state that the groove preparation has a fundamental role in the bead shape and quality obtained and the study carried out was a strategic analysis to understand which of the groove configurations offered a better depth of penetration with a general

height bead quality on welding of the root pass. It was not the objective to research the effect of groove configuration on bead shape and quality features.

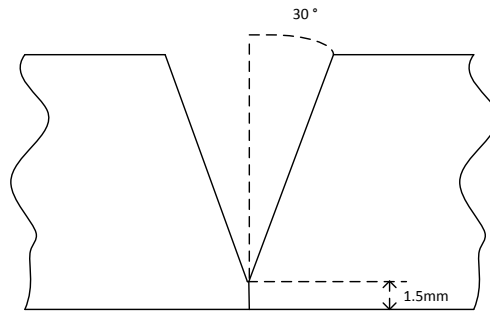


Figure 4.1 – Groove design based on “V” configuration with a bevel angle of 30 degrees and 1.5mm root face.

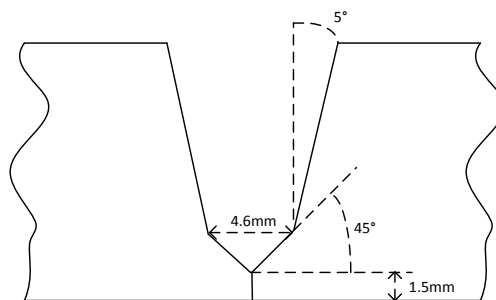


Figure 4.2 – Groove design based on modified “V” configuration with 1.5mm root face.

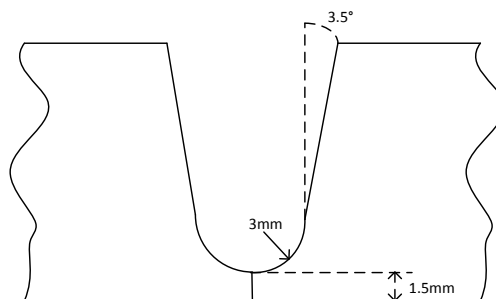


Figure 4.3 – Groove design based on “J” configuration with 1.5mm root face.

After the machining of the selected bevel configuration, two pipe sections were aligned and three TIG spots were welded to ensure the alignment of the pipes during welding tests. Further to this the surface was cleaned using acetone, immediately before welding.

4.3.3.2. Welding Tests and Experimental Measurements

The research was undertaken using the rotator machine with speed control, which was described in Chapter 2. For the current study, the experimental work was developed using a constant CTWD. This distance was chosen to allow a direct comparison between the processes. A preliminary research study demonstrated that 11mm would be the most favourable for arc stability and depth of penetration.

In Chapter 2 a constant volume method was applied by keeping the WFS/TS ratio fixed. The research for this chapter also involves the analysis of productivity, where welding speed (TS) and WFS will change. However, different constant WFS/TS ratios were used for each WFS applied.

Furthermore, the processes were evaluated with two shielding gases, as also evaluated in Chapter 2. The remaining process parameters, such as the arc length correction/ trim and other dynamic controls associated with different power sources were kept constant.

The research developed during this stage was performed in order to establish the plots for each gas and waveform design where lack of penetration and penetration could be achieved, using different binomial settings of WFS and WFS/TS ratios. This is necessary to determine the area of the setting parameters which offer successful conditions for the narrow groove geometry selected. Then, other parameters can be evaluated to analyse the quality issues, such as, the height bead shape, and the root and top width.

The oscilloscope was applied to ensure the recording of current, voltage and WFS waveform during the overall tests carried out using a sample rate of 5,000 samples per second (5kHz). The main details of the equipment and conditions applied were described previously during Chapter 2. The high speed camera was also synchronized with the oscilloscope signal to enable the analysis of metal transfer mechanisms and arc length control.

A critical aspect related to the welding of the CRA root pass is the purging gas protection of the root surface. In this perspective, different purging gas devices were developed and studied in order to achieve a bright, non oxidized surface.

The first device developed was built to be adjacent to the root surface and was formed by a metallic box with a crossing pipe inside, which was formed with equidistant holes. Inside the metallic box wire wool was used to disperse the shielding gas coming from the holes. This was intended to achieve a quasi-uniform distribution of the gas on the root surface and prevent oxygen contamination (Figure 4.4)

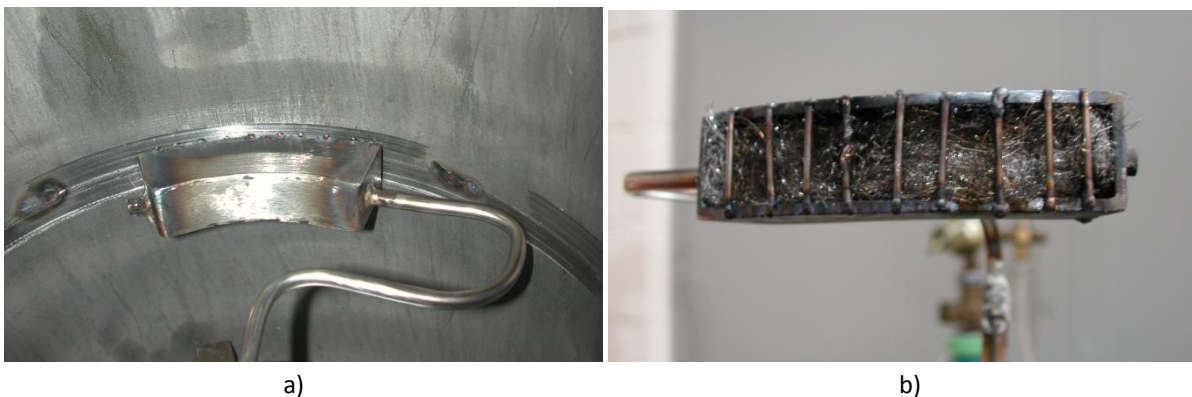


Figure 4.4 – Adjacent purging gas device applied to the root protection: a) detail of the application; b) detail of the first device developed with wire wool.

The application of this solution resulted in a non uniform surface with variations in oxide colouration. Furthermore, in cases of deep penetration or burn through the device was melted and welded along the internal pipe section. The wire wool was then changed to a sintered material to achieve uniform distribution of the gas. Although this worked better, complete uniformity was not achieved. Another solution was to apply a layer of fibre glass material and a surface with wire mesh (Figure 4.5-a), where similar results of non uniformity were obtained. The same problems, associated with high current welding and deep penetration, were observed. Thus, a different device was developed without any material but with increase of the number of internal pipes and holes to spread the gas (Figure 4.5-b). The burn-through problems were eliminated with this solution but wider problems of shielding quality were observed.

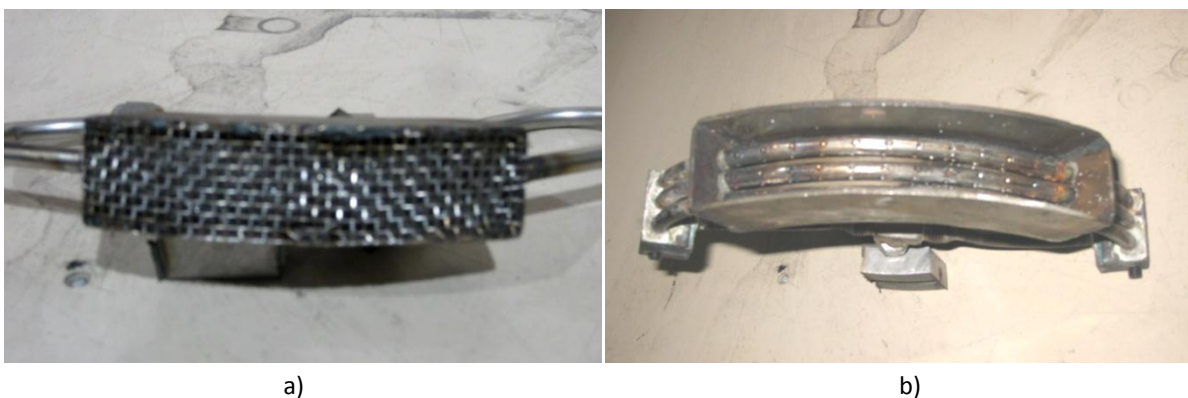


Figure 4.5 – Adjacent purging gas devices applied to the root protection: a) device with fibre glass and wire mesh on the surface; b) device without any material but built with three internal pipes.

One of the problems associated with the previous devices was related to the gas flow. It is thought that the high pressure resulted in turbulent flow, causing non uniform protection on the root surface. This resulted in the development of a different purging gas device able to achieve a laminar gas flow. This device (Figure 4.6) was developed with a 10cm length and with 1cm height, with an internal pipe built with holes and a thin layer of wire mesh adjacent to the pipe and closed with a wire mesh net. The application of this device to the shielding protection resulted in a high quality shielding protection where uniform non oxidized roots were achieved.

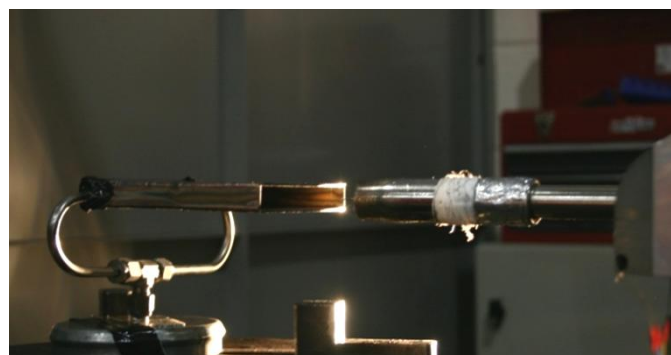


Figure 4.6 – Final solution of purging gas device applied to the root protection achieving laminar gas flow.

4.3.3.3. Data Analyses

In order to analyse bead shape characteristics, a cross section was cut and a metallographic preparation was performed. The macrosection obtained was photographed and bead shape measurements carried out using image software. The main parameters measured and respective criteria can be observed in the Figure 4.7. Different situations have been considered for the measurements performed. Specifically, lack of penetration was established as a negative value, while height ratio was obtained from the quotient between height low (HL) by height high (HH).

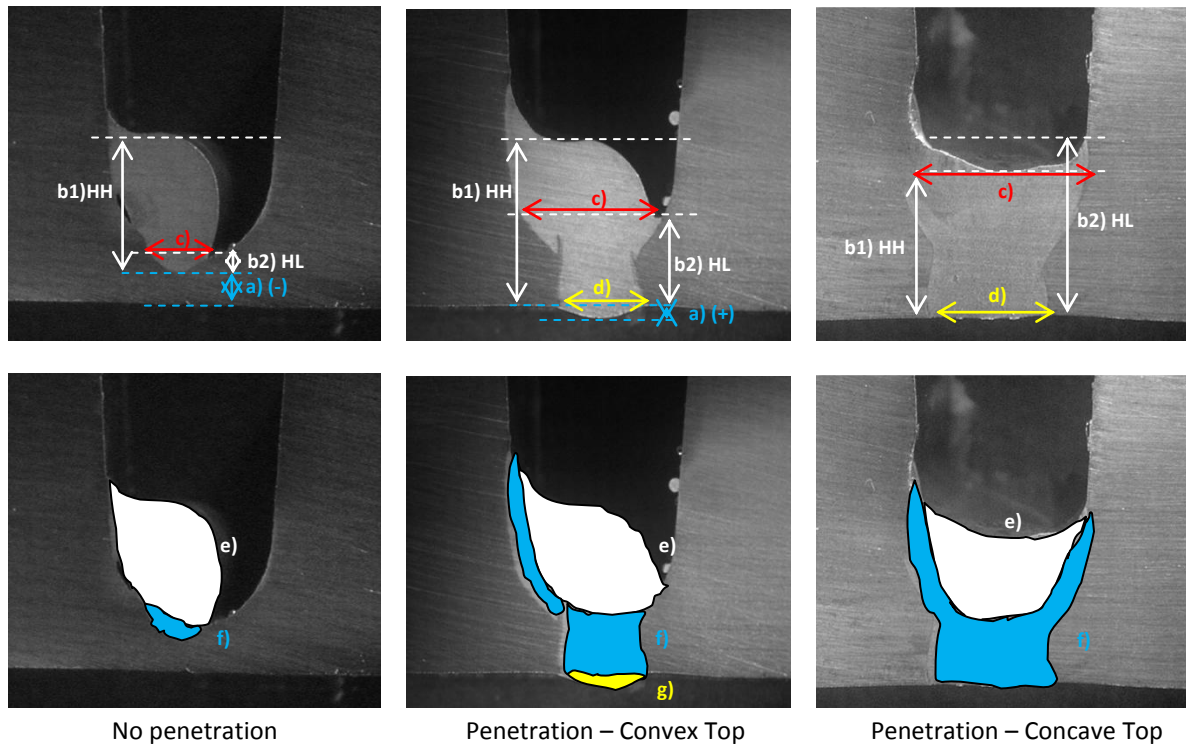


Figure 4.7 – Bead shape measurements at different situations considering the following measures: a) depth of penetration; b1) High height bead (HH); b2) low height bead (HL); c) Top width bead; d) root width bead; e) reinforcement area; f) dilution area; and g) root area.

4.4. RESULTS

4.4.1. Introduction

The analyses undertaken during this chapter were focused on the characterization of bead shape characteristics, when the welding was developed inside a narrow groove. The results of the measurements obtained according with Figure 4.4, indicated above, are presented in Appendix VIII. From the analysis of these results complex relationships were found; this led to the development of statistical modelling, to understand the effect of several bead shape characteristics in the overall quality performance of the shape geometry obtained inside the groove with a design accurately machined. Design Expert software was applied to these analyses.

This work was organized into three different phases, as follow:

1. The characterization of bead shape characteristics using different waveforms and shielding gas mixtures. This includes the application of statistical modelling as indicated above;
2. The construction of penetration/ lack of penetration maps to evaluate the range of conditions of WFS and WFS/TS ratio favourable to satisfy the minimum penetration level using different waveforms and shielding gas mixtures;
3. The analysis of defects obtained in the region of penetration of the maps obtained in the point 2, for each waveform under investigation.

4.4.2. Analysis of Bead Shape Analysis

The analysis of the bead shape characteristics on welding of narrow groove pipes is a key factor to understand how these different waveforms perform at similar conditions, inside the narrow groove. The analyses developed tried to understand the double effect of the variation of WFS and WFS/TS ratio. In this way, contour graphs were applied to this analysis. In order to obtain these plots statistical modelling was applied to the experimental data obtained. The modelling was undertaken using Design Expert 7.1.5 (DOE) for all the waveforms considered in Chapter 2 for two different shielding gas mixtures, i.e., 2.5%CO₂ 97.5%Ar and 1.5%CO₂ 54%He 44.5%Ar. The design was chosen to enable analysis of historical data.

Considering the welding of narrow groove pipes with the groove design established, as introduced in the section 4.3, the responses evaluated in this work were, as follow:

- **Depth of penetration (DP)** is analysed in respect to the root surface; below the root surface penetration is marked as a positive value and above the lack of penetration is marked as a negative value;
- **Height Ratio (HR)** corresponds to the ratio between lower (H_L) and higher (H_H) height bead; when $H_L < H_H$ the height ratio will be in the range of $0 < HR < 1$ and this

means that convexity or asymmetric top bead shapes are achieved, when $H_L=H_H$ flat bead shapes are observed and this means that $HR=1$; when $H_L>H_H$ the height ratio will be $HR>1$ and concave bead shapes will be observed.

- **Root Width (RW)** represents the width bead measured at the root surface of the pipe. It means that when lack of penetration is observed the RW will be 0 and the more significant the dilution, the higher will be RW;
- **Top Width (TW)** corresponds to the width bead measured at the H_L , where full side wall penetration is achieved at both sides of the groove;

The experimental data obtained according to the procedures identified in the section 4.4.2 are presented in Appendix XI.

4.4.2.1. Bead Shape Characteristics Statistical Models

The models were built based on three process variables, WFS, WFS/TS ratio and shielding gas mixtures, respectively. The shielding gas mixtures were defined as a categorical variable (A = 2.5%CO₂ 97.5%Ar and B = 1.5%CO₂ 54%He 44.5%Ar) and the first two as numerical variables, defined in the range of conditions established according with the power source.

The statistical modelling analysis using DOE included several statistical parameters which together evaluate the validation of the models for each response, individually. A valid model is firstly characterized as “significant”. The statistical parameters analysed using this software are described below (Design Expert Software 2006):

- **Prob > F (p-value)** analyses if the model terms are significant when is lower than 0.05 or not significant when $\text{Prob} > F > 0.10$;
- **Model F-value** compares the model variance with the residual variance. When those two variances are similar the ratio will be approximated to 1; this means that the probability of any of the factors have a significant effect on the model response is reduced;
- **Lack of Fit** is measured through **F-value** and **Prob > F (p-value)**. The higher the F-value will be, the greater the probability that the data does not fit the model. Strong lack of fit is undesirable and characterized by $p\text{-value} < 0.05$ while not significant lack of fit is characterized by $p\text{-value} > 0.1$;
- **Adj. R-Squared** characterizes the variation around mean and adjusted by the model terms of the model. This parameter decreases with the increase of not significant terms in the model;
- **Pred. R-squared** measures the variation of new data obtained from the model.

In general, Adj. R-Squared and Pred. R-Squared should match within 0.20

- **Adeq. Precision** represents the signal noise and should be greater than 4.

The model should represent accurately the process variation according with the setting process conditions changed. The model equations obtained from the DOE software were developed by ANOVA (analysis of variance) and are reported in Appendix XII in actual factors for both shielding gases applied to this study. The model responses analysed, as reported above were correspondingly the depth of penetration, the height ratio, the top width and the root width.

The models are primarily defined by a manual function (e.g. Linear, 2F1, Quadratic or Cubic). When statistical requirements are not satisfied a modified model can be applied using backward, forward or stepwise elimination. Furthermore the Box-Cox (e.g. $\ln(\text{Residuals})$ vs. λ) plot indicates if the mathematical function should be transformed into a more complex equation that better fits the data, reducing the noise or the blocking effects associated with the data. The statistical information obtained from the equation models for the different responses and waveforms are presented in the Tables 4.2 to 4.7.

For GMAW-P a backward elimination using alpha of 0.10 was applied for the Height Ratio (HR) model to better fit the statistical requirements, as suggested by DOE software.

In RapidArc a negative “Pred R-Squared” obtained for the depth of penetration model means that the overall mean is a better predictor of this response than the current model. However, the remaining statistical parameters indicate that the model is significant and therefore it will be considered as obtained. The model obtained for Height Ratio was transformed into a Natural log model with λ 0 and constant (k) 0.

For STT the Height Ratio model was transformed to a Power function model with λ -1.54 and constant 0, as suggested by the DOE software. Also for STT, the Root width model was transformed to a base 10 log function model with λ 0 and constant 0.0494.

The Height Ratio model obtained for CMT was transformed into a Square Root function with λ 0.5 and constant (k) 0.

The model of depth of penetration obtained for CMT-P was transformed into a power function with λ of 2.13 and constant (k) of 1.32, and the model for Height Ratio into an Inverse function with λ of -1 and constant (k) of 0.

Finally, for FastROOT the Height Ratio model was transformed to a power model with λ of 2.57 and constant (k) of 0 and the Root width model was transformed to a square root model with λ of 0.5 and constant (k) of 0.0438.

Table 4.2 – Results of statistical analyses obtained from DOE software for the different model responses for GMAW-P.

Response	Type of model	Pred. R-Squared	Adj. R-Squared	F-value	Model	Adeq. Precision	F-value	Lack of Fit	Std. Dev.
					P-value			P-value	
Depth of Penetration	Surface Cubic	0.6659	0.8562	17.67	< 0.0001 (significant)	20.413	2.10	0.2477 (not significant)	0.23
Height Ratio	Modified (Backward)	0.0247	0.1394	2.70	0.0449 (significant)	6.711	1.30	0.44473 (not significant)	0.07
Root Width	Quadratic	0.7886	0.8725	36.93	< 0.0001 (significant)	20.725	12.62	0.0119 (significant)	0.48
Top Width	2F1	0.5690	0.6463	13.79	< 0.0001 (significant)	14.961	2.03	0.2586 (not significant)	0.29

Table 4.3 – Results of statistical analyses obtained from DOE software for the different model responses for RapidArc.

Response	Type of model	Pred. R-Squared	Adj. R-Squared	F-value	Model	Adeq. Precision	F-value	Lack of Fit	Std. Dev.
					P-value			P-value	
Depth of Penetration	Surface Cubic	-0.1756	0.5343	3.98	0.0013 (significant)	7.529	1.69	0.3271 (not significant)	0.17
Height Ratio	2F1 (Natural log)	0.3085	0.4264	5.83	0.0003 (significant)	9.462	0.54	0.8516 (not significant)	0.40
Root Width	Surface Cubic	0.8434	0.9268	33.94	< 0.0001 (significant)	23.035	0.88	0.6345 (not significant)	0.45
Top Width	2F1	0.4987	0.5881	10.28	< 0.0001 (significant)	13.425	0.38	0.9432 (not significant)	0.75

Table 4.4 – Results of statistical analyses obtained from DOE software for the different model responses for STT.

Response	Type of model	Pred. R-Squared	Adj. R-Squared	F-value	Model P-value	Adeq. Precision	F-value	Lack of Fit P-value	Std. Dev.
Depth of Penetration	2F1	0.0681	0.2452	2.84	0.0274 (significant)	7.184	0.89	0.6163 (not significant)	0.78
Height Ratio	Linear (Power)	0.0228	0.2137	2.54	0.0432 (significant)	5.598	0.59	0.8279 (not significant)	0.32
Root Width	2F1 (Base 10 log)	0.1945	0.4241	4.13	0.0027 (significant)	8.872	0.53	0.8681 (not significant)	0.61
Top Width	2F1	0.3884	0.5389	7.62	< 0.0001 (significant)	9.628	1.88	0.2215 (not significant)	0.21

Table 4.5 – Results of statistical analyses obtained from DOE software for the different model responses for CMT.

Response	Type of model	Pred. R-Squared	Adj. R-Squared	F-value	Model P-value	Adeq. Precision	F-value	Lack of Fit P-value	Std. Dev.
Depth of Penetration	Quadratic	0.5635	0.8609	18.79	< 0.0001 (significant)	16.783	-	-	0.22
Height Ratio	2F1 (Square root)	0.7728	0.8715	26.99	< 0.0001 (significant)	18.831	-	-	0.053
Root Width	2F1	0.7454	0.8536	23.35	< 0.0001 (significant)	18.310	-	-	0.40
Top Width	Linear	0.5009	0.6354	14.36	< 0.0001 (significant)	14.188	-	-	0.46

Table 4.6 - Results of statistical analyses obtained from DOE software for the different model responses for CMT-P.

Response	Type of model	Pred. R-Squared	Adj. R-Squared	Model F-value	Model P-value	Adeq. Precision	Lack of Fit F-value	Lack of Fit P-value	Std. Dev.
Depth of Penetration	Linear (Power)	0.1032	0.2138	4.26	0.0119 (significant)	6.953	-	-	0.79
Height Ratio	Linear (Inverse)	0.0106	0.0015	5.35	0.0041 (significant)	8.297	-	-	0.74
Root Width	Quadratic	0.6697	0.7765	16.64	< 0.0001 (significant)	12.565	-	-	0.65
Top Width	Linear	0.6839	0.7245	32.56	< 0.0001 (significant)	17.599	-	-	0.82

Table 4.7 - Results of statistical analyses obtained from DOE software for the different model responses for FastROOT.

Response	Type of model	Pred. R-squared	Adj. R-squared	Model F-value	Model P-value	Adeq. Precision	Lack of Fit F-value	Lack of Fit P-value	Std. Dev.
Depth of Penetration	Linear	0.5279	0.5972	16.81	< 0.0001 (significant)	13.464	35.41	0.1322 (not significant)	0.41
Height Ratio	Linear (Power)	0.1611	0.2926	5.41	0.0044 (significant)	7.482	1.85	0.5316 (not significant)	0.14
Root Width	Linear (Square Root)	0.5720	0.6224	18.58	< 0.0001 (significant)	15.855	-	-	0.41
Top Width	Linear	0.0841	0.2280	4.15	0.0145 (significant)	6.442	0.44	0.8570 (not significant)	0.64

Even with function transformations, a few non satisfactory models were obtained in these analyses. This may (or may not) be resolved by the increasing the range of experiments over the limit conditions. However, it should be noticed that arc welding processes are complex system of interacting variables and responses, which emphasises that is very difficult to satisfy all responses at once.

4.4.2.2. Modelling Validation

The model validation could be performed by matching the actual values, obtained from experimental (historical) data, with the predictions obtained from the model. Furthermore new experimental tests could be undertaken to evaluate if under different conditions the models will or will not fit. However, the comparison between actual and predicted values is already considered very good information to understand the accuracy of the model equation. These analyses were evaluated for the response of depth of penetration as an example and the graphs obtained are presented in Appendix XIII. This results show that in general actual and predicted values are in reasonable agreement. Exceptions are mainly observed for CMT-P and STT where at lower process setting conditions (WFS and WFS/TS ratio) there are some considerable variations. This is an indication of model validity.

4.4.2.3. Modelling Results

From the models obtained several relationships can be established to understand the variation of critical responses with the binomial WFS – WFS/TS ratio, at different shielding gas compositions. The results from bead shape characteristics were characterized in two different ways, i.e.:

- The analysis of individual responses; and
- The optimization of responses through the established acceptance quality criteria, defined according to the information from standards and technical information provided from industrial contractors.

Firstly a comparison of the different waveforms studied was taken at same shielding gas condition for the different responses, using contour plots with similar colour scales. The results are presented in Appendix XIV. It is observed that the shielding gas has a considerably effect on the on the results of all responses analysed. In general, the 1.5%CO₂ 54%He 44.5%Ar is associated with an increase in depth of penetration and width bead.

Among the welding waveforms studied, it is observed that the probability that depth of penetration is positive (actual penetration) increases with WFS level and decreases with welding speed (TS). However, it is also observed that the range of positive depth of penetration is more favourable for RapidArc, GMAW-P and CMT-P waveforms. At high welding speeds RapidArc and CMT-P generate fully penetrated roots with a concave top bead, due to the high arc energy – peak current levels.

The analysis of Height ratio shows that very poor results are obtained in terms of asymmetry/ convexity for CMT, STT and FastROOT waveform. Very good results were observed with RapidArc regarding concave top beads (Height ratio > 1).

The root width and top width increases with the increasing melting rate, and are generally higher at high WFS levels.

The desirability analyses were performed based on an acceptance criteria established according to the standards and industrial acceptance requirements. Tables 4.8 and 4.9 show the criteria established. The diagrams of the criteria are presented in Appendix XV.

Table 4.8 – Desirability criteria defined for the models optimization.

Responses	Goal	Importance
Depth of Penetration (DP)	maximize	+++++
Height Ratio (HR)	maximize	++++
Root Width (RW)	maximize	+++
Top Width (TW)	maximize	+++
WFS/TS Ratio	minimize	+

Table 4.9 – Desirability Limits set for different Waveforms.

Responses	GMAW-P	RapidArc	STT	CMT	CMT-P	FastROOT
DP	-0.15 – 0.65	-0.15 – 0.65	-0.15 – 0.65	-0.15 – 0.65	1.40 – 4.24	-0.15 – 0.65
HR	0.80 – 0.93	-0.22 – 0.43	0.56 – 44.3	0.75 – 0.90	1.25 – 3.62	0.56 – 0.70
WFS/TS	8 – 27	6 – 24	12 – 30	12 – 24	6 – 22	12 – 24

Only the responses Root Width (RW) and Top Width (TW) are maximized. In the particular case of RW the aim is to be higher than zero. Special attention was given to the process WFS limits.

According to the desirability criteria different solutions were obtained from the combination of model responses. The graphical analysis obtained for these criteria is presented for all waveforms and two shielding gas mixtures in Appendix XVI. The solutions obtained and respectively desirability are presented in the Tables 4.10 to 4.15, below. No solutions were found for CMT waveform according to the desirability criteria established. However, if the height ratio criteria increase from 0.800 to 0.750, the following solutions can be found (Table 4.13).

Table 4.10 – Solutions obtained for GMAW-P according to the desirability criteria established.

	WFS	WFS/TS	Gas ²	DP	HR	RW	TW	Desirability
1	5.48	25.81	B	0.65	0.843	2.43	5.89	0.543
2	10	12.50	B	0.41	0.812	2.00	5.23	0.348
3	10	12.34	B	0.39	0.812	1.94	5.22	0.348
4	4.79	26.87	A	0.45	0.807	0.75	6.19	0.231

² Gas A: 2.5%CO₂ 97.5%Ar; Gas B: 1.5%CO₂ 54%He 44.5%Ar.

Table 4.11 – Solutions obtained for RapidArc according to the desirability criteria established.

	WFS	WFS/TS	Gas ²	DP	Ln(HR)	RW	TW	Desirability
1	4	23.44	B	1.62	0.210	9.41	7.17	0.726
2	4	23.32	B	1.60	0.189	9.32	7.12	0.725
3	10	23.22	B	0.43	-0.049	7.68	6.54	0.521
4	9.90	11.30	B	0.13	0.144	3.54	5.66	0.516
5	10	9.74	A	0.07	-0.120	2.48	5.07	0.319
6	10	9.63	A	0.06	-0.114	2.43	5.07	0.318
7	10	10.02	A	0.09	-0.137	2.59	5.09	0.316
8	4	23.96	A	2.11	-0.200	12.9	5.96	0.284

Table 4.12 – Solutions obtained for STT according to the desirability criteria established.

	WFS	WFS/TS	Gas ²	DP	Ln(HR)	RW	TW	Desirability
1	8.12	18.48	B	0.32	1.32	0.13	5.47	0.322
2	8.13	12.00	A	0.72	1.41	0.63	5.58	0.136

Table 4.13 – Solutions obtained for CMT according to the desirability criteria established.

	WFS	WFS/TS	Gas ²	DP	Ln(HR)	RW	TW	Desirability
1	8.00	23.78	B	0.85	0.870	3.26	5.56	0.335
2	8.00	23.84	B	0.86	0.870	3.27	5.56	0.333

Table 4.14 – Solutions obtained for CMT-P according to the desirability criteria established.

	WFS	WFS/TS	Gas ²	$(DP+1.32)^{2.13}$	1/HR	RW	TW	Desirability
1	10	18.52	B	1.58	0.939	3.26	6.59	0.819
2	10	18.61	B	1.59	0.933	3.27	6.61	0.819
3	10	18.40	B	1.58	0.947	3.23	6.56	0.819
4	10	18.50	A	1.90	1.172	3.53	6.44	0.800
5	10	18.40	A	1.89	1.179	3.51	6.42	0.800
6	10	18.65	A	1.90	1.162	3.56	6.48	0.800
7	10	18.29	A	1.88	1.186	3.48	6.40	0.800
8	9.98	17.83	A	1.87	1.221	3.38	6.27	0.798

Table 4.15 – Solutions obtained for FastROOT according to the desirability criteria established.

	WFS	WFS/TS	Gas ²	DP	$(HR)^{2.57}$	Sqrt(RW+0.04)	TW	Desirability
1	9	22.82	B	1.52	0.650	2.531	6.38	0.764
2	9	22.89	B	1.53	0.651	2.543	6.36	0.764
3	9	22.72	B	1.51	0.648	2.515	6.34	0.764
4	9	22.94	B	1.54	0.652	2.551	6.37	0.764
5	9	23.35	B	1.60	0.659	2.618	6.41	0.756

These solutions obtained from the modelling optimization analyses cannot be indicated as actual solutions, since they have not been tested experimentally, but represent an indication about the welding process setting conditions that could be applied to satisfy the criteria established within the desirability level indicated in the tables above. It should also be noticed that they are only valid for the criteria conditions established. However, it gives important information about possible welding conditions that satisfy the requirements of the standards and industrial acceptance criteria.

4.4.3. Analysis of Penetration Maps

There is in fact one significant part of the analyses of quality that will be presented in the next section. Since the penetration, or lack of it, is considered the most critical condition to satisfy for the acceptance criteria defined by the standards and the contractors, it will be analysed separately in this section.

According to the data obtained from the research work it is possible to build the curves that separate the region of penetration and lack of penetration for each waveform and shielding gas mixture (2.5%CO₂ 97.5%Ar or 1.5%CO₂ 54%He 44.5%Ar) applied (Figure 4.8). This makes it possible to determine values of WFS and WFS/TS ratio (metal volume) to obtain penetration. However, this does not represent necessarily the region of acceptance, since even when penetration is achieved, welding defects can be identified, in particular concerning the top region of the welding pass.

It is observed that for all waveforms the application of 1.5%CO₂ 54%He 44.5%Ar increases the range of penetration suggesting that the application of this shielding gas can produce higher productivity levels. The processes where it is possible to work at lower WFS/TS ratios, respectively CMT-P and RapidArc may correspond to the processes where higher productivity can be achieved, since at same WFS level the decrease of WFS/TS ratio is proportional to the increase of welding speed (TS).

4.4.4. Analysis of Defects

The first critical condition of welding is to achieve a full root penetration. Nevertheless, to ensure desirable weld bead quality an agreement between full penetration and sound weld should be obtained. A sound weld is achieved when no defects are observed. In this analysis the top width and height bead parameters are significantly important to understand to presence or absence of defects. An asymmetric top width generally is accompanied by a side lack of penetration or undercutting phenomena. Also side lack of fusion occurs frequently and is considered an actual cause of defects. This analysis will be performed individually for each waveform evaluated to understand which main problems are associated with the waveform when applied to the welding of narrow groove pipes. The range of conditions applied will be indicated and the defects identified. The analysis of defects was based on the macrostructures obtained from the several welding tests performed in narrow groove.

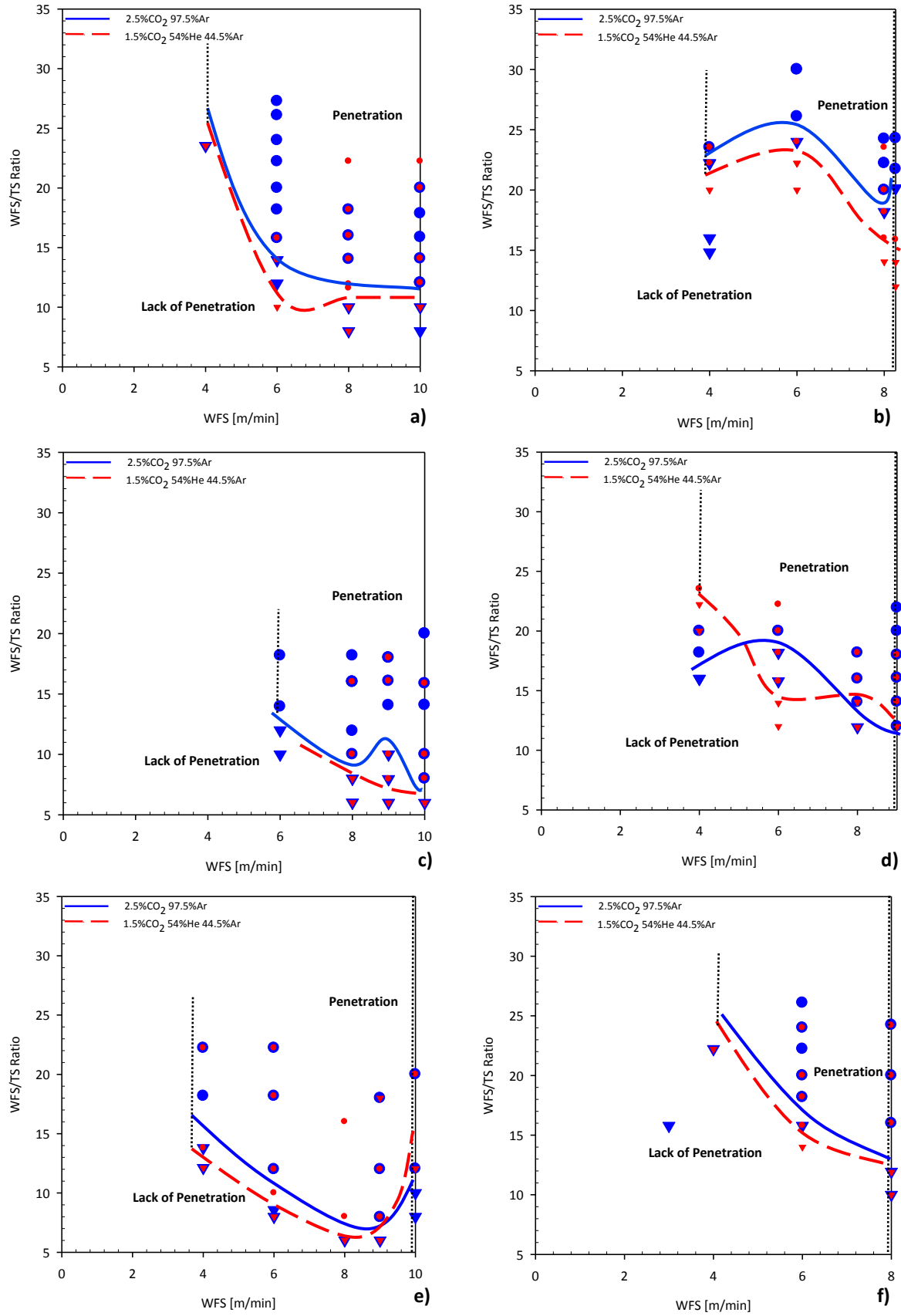


Figure 4.8 – Penetration/ Lack of Penetration maps obtained by the variation of WFS and WFS/TS ratios for different waveforms: a) GMAW-P; b) STT; c) RapidArc; d) FastROOT; e) CMT-P and f) CMT. The circle represents penetration and the triangle lack of penetration.

4.4.4.1. Characterization of defects for GMAW-P

An example of the defects observed for GMAW-P, under the welding conditions applied, are illustrated bellow:

- Lack of side wall fusion (Figure 4.9 – a);
- Porosities (Figure 4.9 – b);
- Lack of penetration (Figure 4.9 – c);
- Excessive depth of penetration (Figure 4.9);
- Asymmetric convex top bead (Figure 4.9).

Although the asymmetric convex top bead cannot be defined as a defect, it is undesirable will offer conditions for most of the weld beads obtained for GMAW-P were characterized by a convex top, which can be associated with defects in the following welding passes.

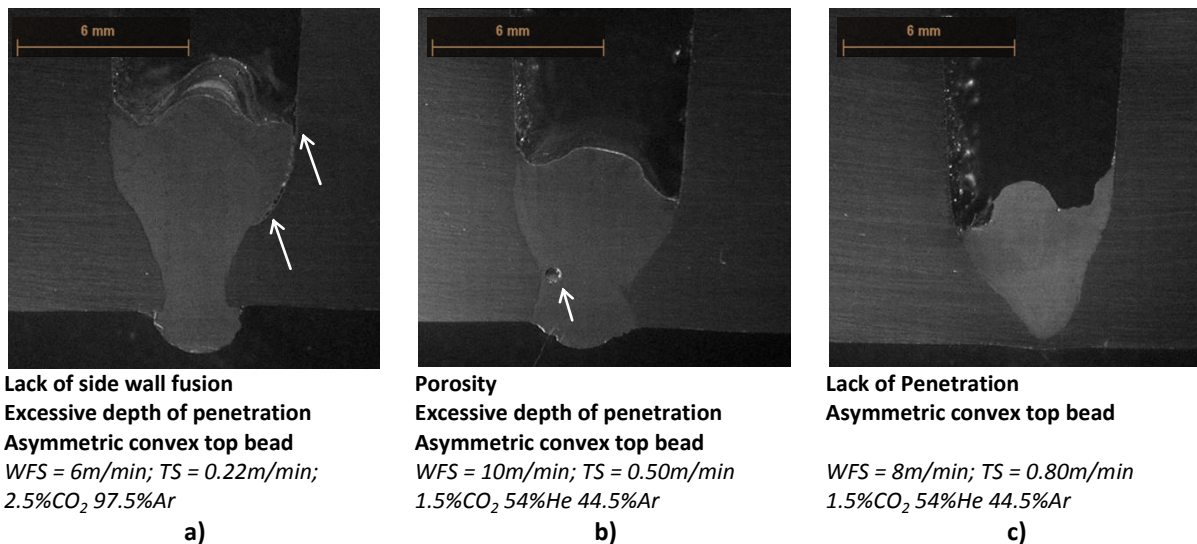


Figure 4.9 – Macrostructures illustrating defects on welding of narrow groove pipe using GMAW-P.

4.4.4.2. Characterization of defects for RapidArc

The defects observed for RapidArc waveform, under the welding conditions applied, are described as follow:

- Lack of side wall fusion (Figure 4.10-a, b, c, e);
- Lack of penetration; (Figure 4.10-b, e))
- Undercutting (Figure 4.10-d);
- Convex and asymmetric top beads (Figure 4.10-b, c, e)
- Concave root beads (Figure 4.10-f)

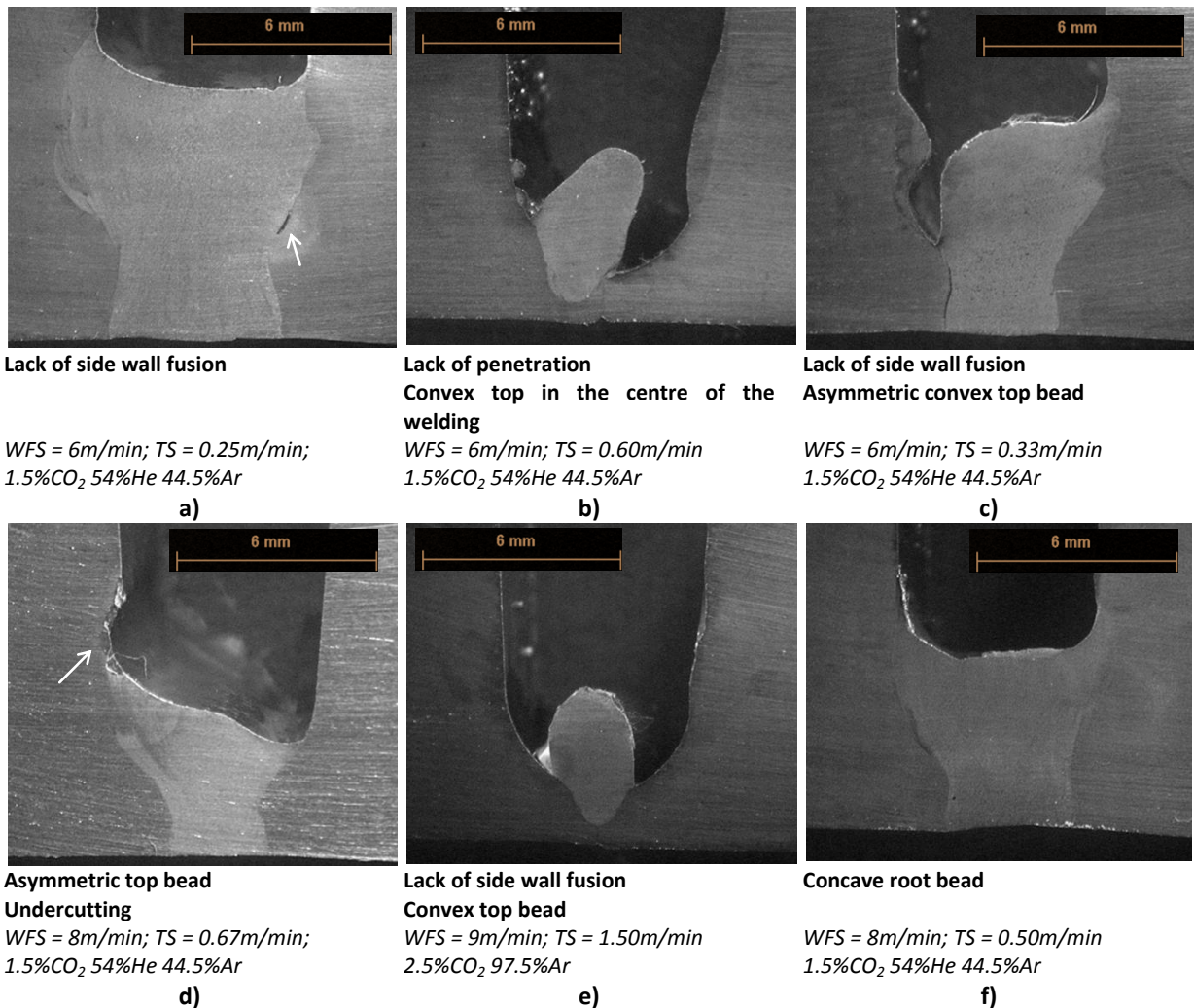


Figure 4.10 – Macrostructures illustrating defects on welding of narrow groove pipe using GMAW-P.

4.4.4.3. Characterization of defects for STT

Most of the welds obtained for STT were characterized by lack of side wall fusion (Figure 4.11)

Convex asymmetric top are also often identified in the macrosections obtained for this waveform (Figure 4.11).

Among other defects, lack and excess of penetration were also identified (Figure 4.11).

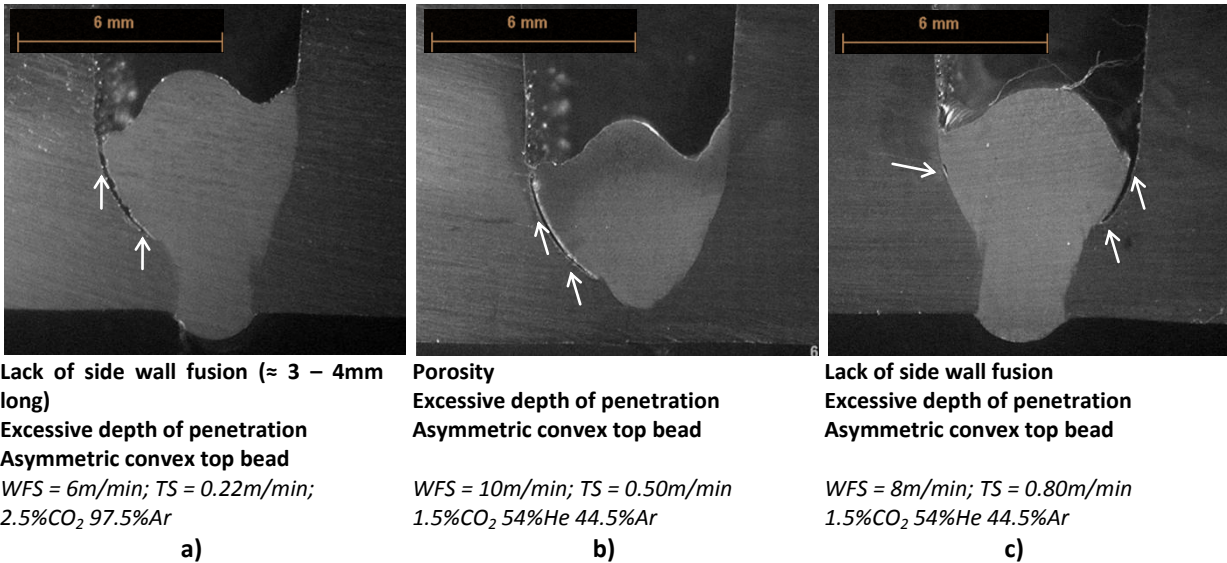


Figure 4.11 – Macrostructures illustrating defects on welding of narrow groove pipe using STT.

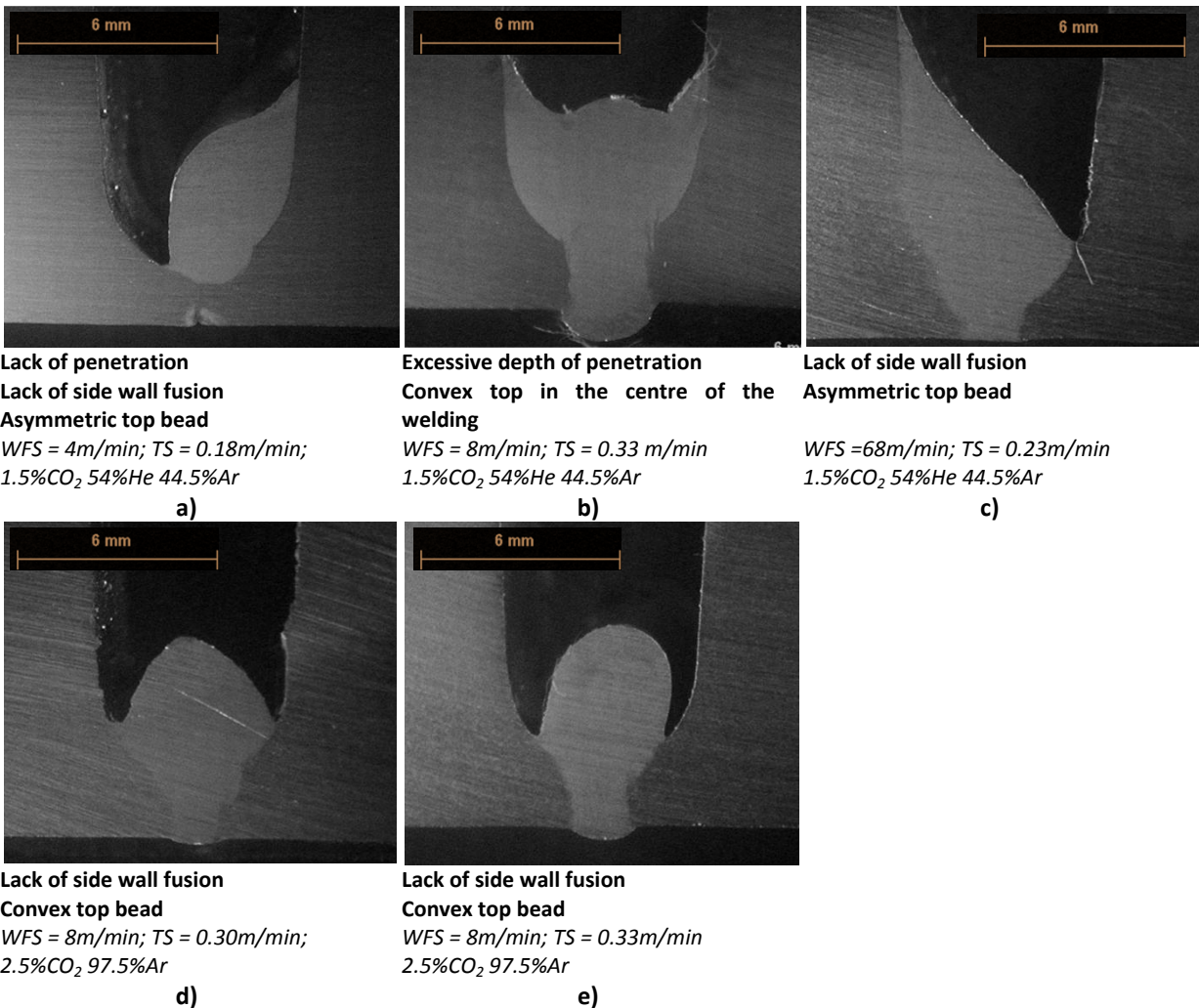


Figure 4.12 – Macrostructures illustrating defects on welding of narrow groove pipe using CMT.

4.4.4.4. Characterization of defects for CMT

It is observed that most of the defects identified for CMT waveform are associated with the height bead shape. Under the welding conditions applied were identified:

- Lack of penetration (Figure 4.12 – a);
- Asymmetric top bead (Figure 4.12 – a, c);
- convex top beads (Figure 4.12 – b, d, e);
- Side wall lack of fusion (Figure 4.12 – a, c, d, e);
- Excess of penetration (Figure 4.12- a).

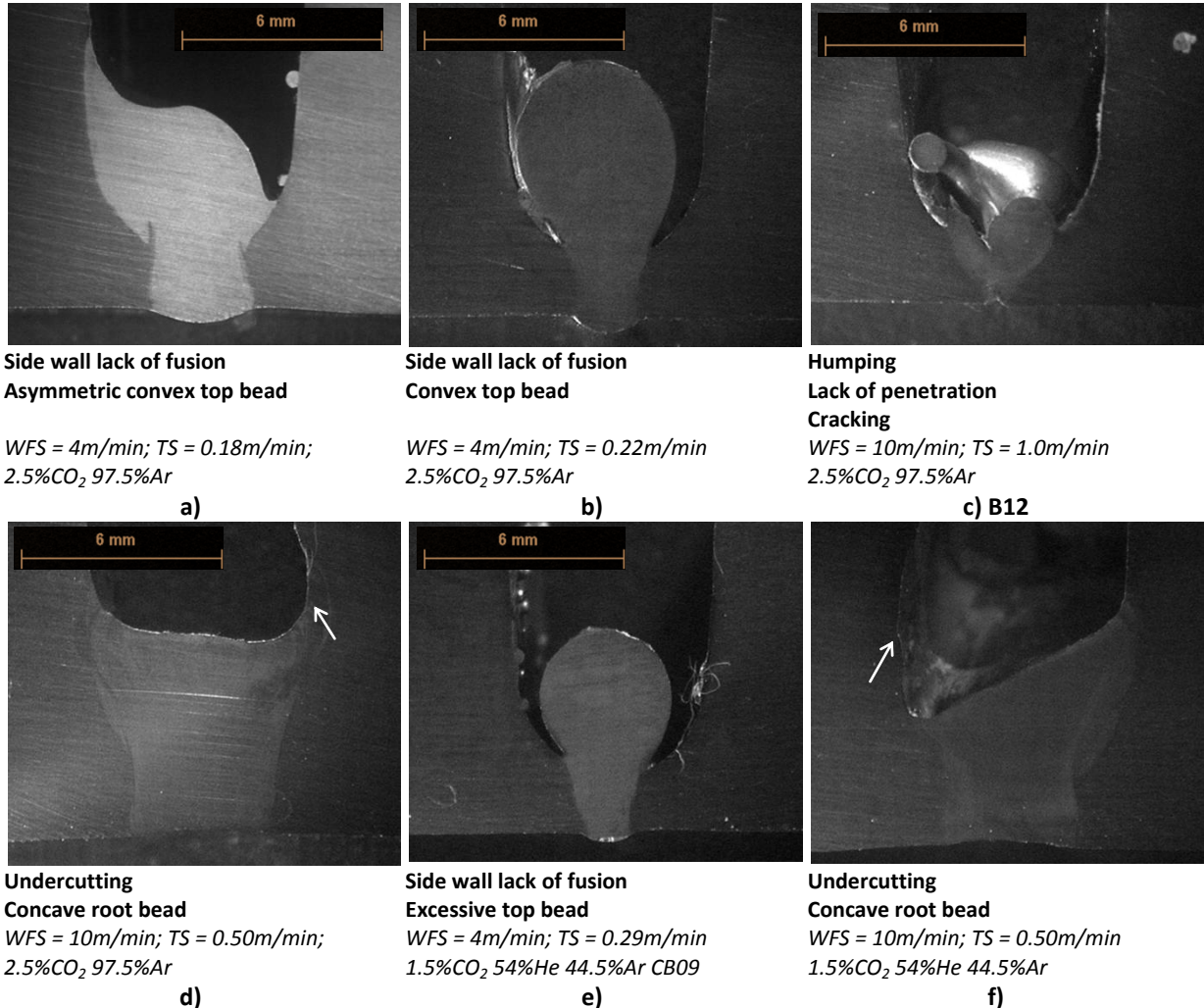


Figure 4.13 – Macrostructures illustrating defects on welding of narrow groove pipe using CMT-P.

4.4.4.5. Characterization of defects for CMT-P

The main defects observed for CMT are associated with either convexity top beads or undercutting, especially at high WFS/ high welding speed conditions.

Among the defects observed the macrosections presented in the Figure 4.13 shows:

- Lack of side wall fusion (Figure 4.13 – a, b, e);
- Lack of penetration (Figure 4.13 – c);
- Undercutting (Figure 4.13 – d, f);
- Humping (Figure 4.13 – c);
- Cracking (Figure 4.13 – c);

- Convex top beads (Figure 4.13 – b, e);
- Concave root beads (Figure 4.13 – d, f);
- Asymmetric top bead (Figure 4.13 – a).

4.4.4.6. Characterization of defects for FastROOT

The defects observed for FastROOT waveforms are listed below:

- Lack of penetration (Figure 4.14 - c);
- Lack of side wall fusion (Figure 4.14 –a, b, c, d, e);
- Convex top beads (Figure 4.14 –a, b, c, d);
- Asymmetric top beads (Figure 4.14 – a, b, c);
- Porosities (Figure 4.14 - c);
- Metallurgical defects (Figure 4.14 - a);
- Excessive depth of penetration (Figure 4.14 -e);

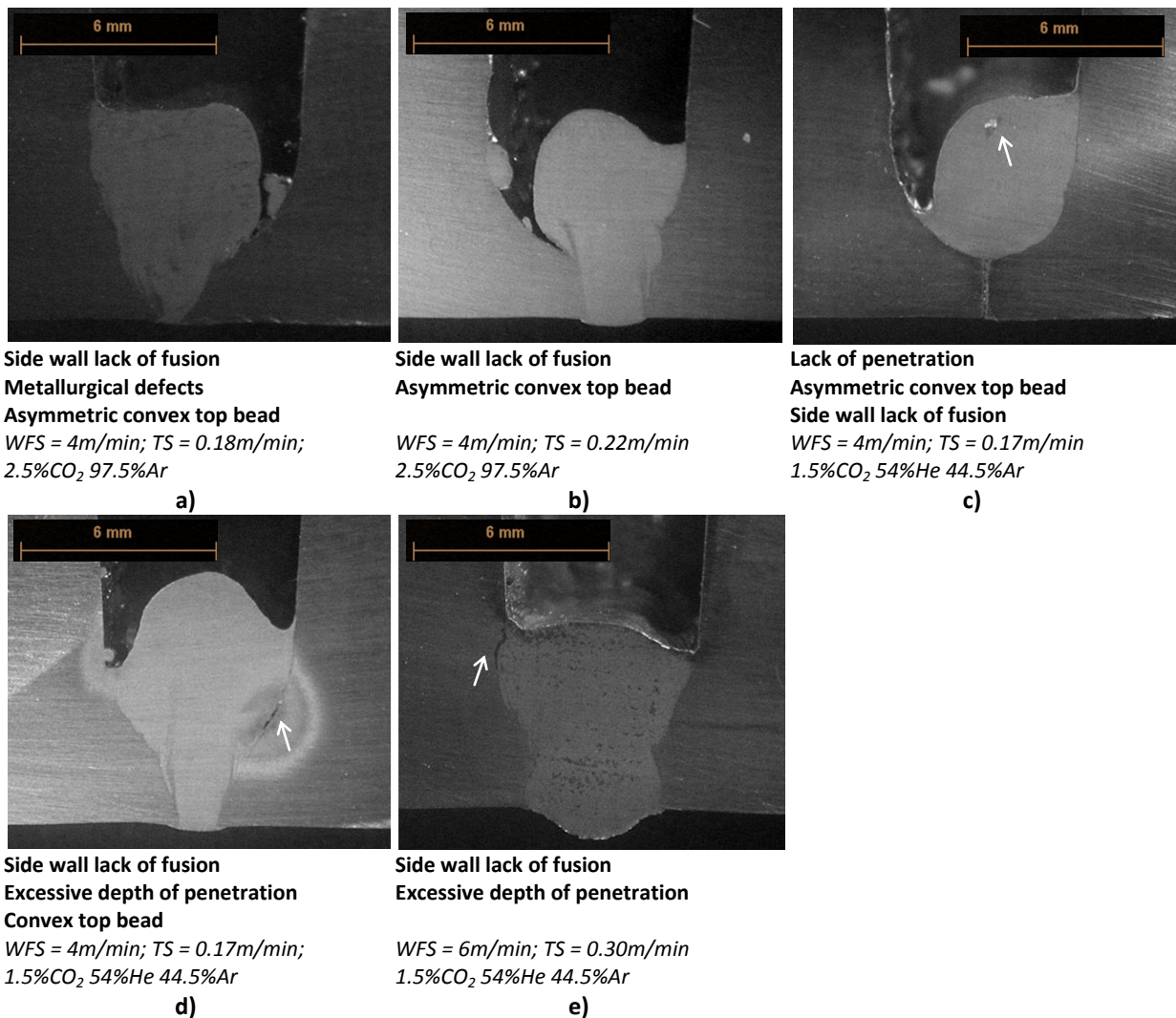


Figure 4.14 – Macrostructures illustrating defects on welding of narrow groove pipe using CMT-P.

4.5. DISCUSSION OF RESULTS

4.5.1. Introduction

The bead shape characteristics obtained in welding of narrow groove pipes were intensively characterized by the variation of setting parameters, correspondingly the WFS, the WFS/TS ratio and the shielding gas mixture. The remaining process setting conditions were kept constant according to the know-how developed from Chapter 2.

Particular attention should be given to the application of 11mm of CTWD; that was due to the fact of the welding in narrow groove should be performed at low arc length levels to better control the arc stability phenomena, and consequently the resulting bead shape performance.

The same waveforms investigated during Chapter 2 using 13%Chrome supermartensitic stainless steel were now analysed for the application of welding of root pipes. The tests were carried out using a “J” groove design with 1.5mm of root face.

The main topics of the discussion for the analyses performed in this Chapter were, as follow:

- To understand how the bead shape characteristics vary in narrow groove welding for different waveforms and conditions;
- To predict which waveforms better satisfy acceptance criteria defined through the standards and industrial requirements;
- To analyse the productivity obtained using different waveforms by keeping or improving the standard welding quality level;
- To evaluate the defects obtained for the different waveforms and at which conditions they may take place;
- To determine about which waveform(s) better fit the requirements for welding of root pipes.

4.5.2. Depth of Penetration

The first requirement in welding of root runs is to achieve full penetration beads. It is well known that for a given waveform the depth of penetration is mainly controlled by the WFS and welding speed (TS). It was this postulate that led to the investigation undertaken in this chapter, in order to determine the range of welding conditions that result in penetration/lack of penetration.

Depth of penetration increases with WFS and decreases with welding speed (TS), as observed from all analyses performed. For a given groove design, there is a limit of welding speed (TS) that can be applied to achieve full penetration at a determined WFS. For this reason instead of analysing the WFS vs. TS, a comparison of WFS with WFS/TS ratio it was applied instead.

Since a maximum limit of WFS is defined by the power sources for all short-circuiting waveforms (i.e., STT, CMT and FastROOT) and CMT-P, it can be concluded that it is possible to determine the highest welding speed that we are able to achieve with any GMAW waveform. As seen in Chapter 2, these limit conditions are result of the stable conditions limit for the mode of transfer established by the power sources.

In this perspective several tests were undertaken to determine the limit conditions from relatively low WFS to their limit. However, since the limit WFS conditions of RapidArc and GMAW-P are significantly higher, 10m/min was set as the maximum WFS applied (similar to CMT-P).

From the tests undertaken is observed that is very difficult to work at WFS below 6m/min, since the WFS/TS ratio necessary to achieve full penetration is too high, and the welding speed is reduced to very low value, i.e. below 0.20m/min. Considering the industrial target of about 0.25m/min and the limitation of the rotator applied to this experiments (i.e., around 0.17-0.18m/min) it became difficult to apply such low conditions.

Figure 4.8 and the maps for the depth of penetration achieved by the modelling analyses (to see appendix XIV) show that the range of WFS/TS ratio applied increases in this sequence: STT < FastROOT < CMT < GMAW-P < CMT-P < RapidArc. It should be noticed that this sequence correspond to a general overview of the results obtained, and some variations can occur in specific conditions. It also does not account to the actual depth of penetration, but only consider the categorical analysis of full penetration/ lack of penetration. However these results are explained by the arc energy delivered by the processes and therefore the capacity for achieving full penetration at much higher welding speeds.

Although all the waveforms work with stable arc conditions, not all satisfy the fundamental requirement of achieving full penetration root runs. Significantly higher welding speeds can be achieved using RapidArc and CMT-P waveforms with full penetration root conditions.

It is observed that using CMT-P and RapidArc travel speeds in the order of 1 – 1.25m/min can satisfy the full penetration root runs, when WFS applied was 9 – 10m/min. However, it is noticed that the application of the maximum WFS level (i.e. 10m/min) for CMT-P are characterized by high arc instability phenomena which is reflected by a decrease of the range of full penetration conditions (Figure 4.14). In other words, the WFS/TS ratio for full penetration is reduced from 8 (9m/min of WFS) to 12 (10m/min of WFS). This led to a reduction of the welding speed from 1.13m/min (9m/min of WFS) to 0.83m/min (10m/min of WFS). This behaviour observed for CMT-P are due to conditions applied (e.g. in particular the WFS) which are already beyond the stability limit of the process.

Finally, should be noticed that the application of 1.5%CO₂ 54%He 44.5%Ar shielding gas mixture led to an overall increase of the range of welding speed conditions (WFS/TS ratios) applied. This suggests that productivity may be increased by changing the shielding gas

mixture. This is probably due to the higher ionisation potential for helium compared to argon, resulting in higher arc energy delivered by the power source and consequently improving the melting phenomena.

4.5.3. Height Bead Shape

Although satisfactory penetration beads can be controlled by the WFS/TS ratio applied, i.e. the binomial WFS and welding speed (TS), other requirements should be accomplished, such as the weld top condition. A convex top is unfavourable to the hot pass (next welding pass).

The analysis of convexity/ concavity/ flat top are fundamental to understanding the probability of generating defects in the second (hot) pass, such as lack of side wall fusion or porosity. A height ratio parameter was developed to analyse if the top is concave, flat or convex, and in the last case to evaluate asymmetry. Two height levels were measured in all welds obtained, and the ratio between the low and high height gives a closer idea about this top effect.

It is recognized that height ratios in the range of 0 to 1 correspond to convex / asymmetric top beads, while height ratio of 1 correspond to flat beads and above 1 concave bead shapes are obtained. This parameter was analysed through the statistical modelling undertaken to evaluate the overall variation of top bead shape for all waveforms and for the two shielding gases applied.

In general, even when full penetration is achieved, very peaky top beads are observed for all the waveforms obtained working in short-circuiting transfer mode, i.e. STT, CMT and FastROOT. This is characterized by height ratios below 1 with high convexity and asymmetric bead shapes.

In average the height ratio obtained for GMAW-P is 0.75, what means that convexity bead shapes are generally obtained using this waveform. The convexity level is lower compared to that obtained for short-circuiting waveforms (average height ratio below 0.60), which may be due to the increase of arc energy resulting in improved melting phenomena.

The top bead shapes obtained for RapidArc and CMT-P waveforms are significantly better and flat and concave beads (height ratios ≥ 1) can be observed in certain conditions, possibly due to the increase of arc energy and waveform stability control of these welding modes. This lead to an improving of the melting characteristics which is favourable for obtaining high quality welds, even when the conditions of work are set to high welding speed levels (i.e. high productivity).

However, although the melting characteristics are improved at high WFS levels and high welding speeds, undercutting can limit the quality of the welds obtained. This was observed when 1.5%CO₂ 54%He 44.5% was applied and has been already described by several authors (Gratzket, et al. 1992) (Mendez and Eagar 2000) (Mendez and Eagar 2003). There are also

some indications that suggest the occurrence of humping phenomena, when high WFS and very high welding speeds were applied.

4.5.4. Width Bead Shape

The width bead shape is considered an important weld characteristic, in particular in welding of a narrow groove, where side wall fusion should be achieved. Two width measurements were applied to analyse this parameter, at the root surface (when 0 indicates that lack of penetration was obtained) and at the lower height level at which full side wall penetration was achieved.

Similar conclusions are taken from these analyses, i.e. the arc current (given by the WFS applied) and overall arc energy obtained from the process characteristics controls the side wall fusion, and hence the width bead obtained. For short-circuiting waveforms (e.g. STT, CMT and FastROOT) width is generally poor, while for pulse spray waveforms much wider width beads are obtained. It was particularly observed that the weld beads obtained for STT are often characterized by side wall lack of fusion in this study.

Width bead requirements are almost always achieved using pulse spray waveforms. However, when current level is low or welding speed is too high a narrow root width is obtained. This behaviour can be improved by reducing the welding speed applied.

It is noticed that using CMT-P and RapidArc waveforms at very low WFS/TS ratios (high WFS and very high welding speeds) concave fully penetrated roots are obtained. This may be considered a limitation for the application of welding, depending of the acceptance requirements established, under the conditions used in this study

4.5.5. Welding Quality and Desirability Conditions

From the results obtained using statistical modelling is observed that no short-circuiting waveforms satisfy entirely the quality criteria established for the welding of 13%Chrome supermartensitic stainless steel pipes, in the range of conditions used in this study Several issues can be identified that may (or may not) result in this conclusion:

- The design of the groove is not optimum for these waveforms;
- The root face is too thick to satisfy the fusion characteristics achieved within these waveforms;
- The arc energy delivered at the contact tip of the torch and the peak current are not high enough to obtain optimum melting conditions.
- The short circuit processes have not been individually optimised for this application, with several parameters and joint conditions set at standard conditions to facilitate comparison of the processes

However, in certain conditions is possible to satisfy partially the requirements, and some solutions were obtained from the modelling results.

In general, the waveforms working in pulse spray transfer mode satisfy more closely the acceptance criteria for bead shape characteristics. This is also shown by the statistical modelling solutions obtained for these waveforms.

The convex/ asymmetric top beads compromise the application of GMAW-P for most of the conditions applied, but some good quality conditions can be found as observed from the modelling results for this waveform. An example of a good welding condition for GMAW is presented in the Figure 4.15, below. Fully penetration and flat top bead are obtained and no defects were observed.

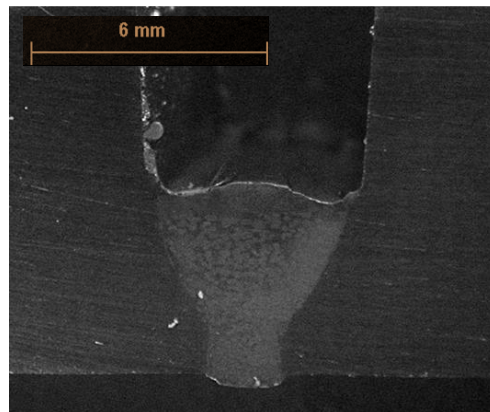


Figure 4.15 – Weld bead obtained for GMAW-P using WFS = 10m/min; TS = 0.83m/min; and 1.5%CO₂54%He44.5%Ar.

Although undercutting and humping should not be neglected, in particularly using welding speeds above 1m/min or for 1.5%CO₂ 54%He 44.5%Ar, sound welds are easily obtained using RapidArc and CMT-P waveforms (Figure 4.16). This led to a conclusion that these two welding processes show considerable promise for welding of pipe root runs in 13% Chrome stainless steel).

Nevertheless, the variations observed for the effect of shielding gas mixture on the bead shape characteristics should also be better understood through a deep investigation on the variation of shielding gas composition at a constant setting process conditions.

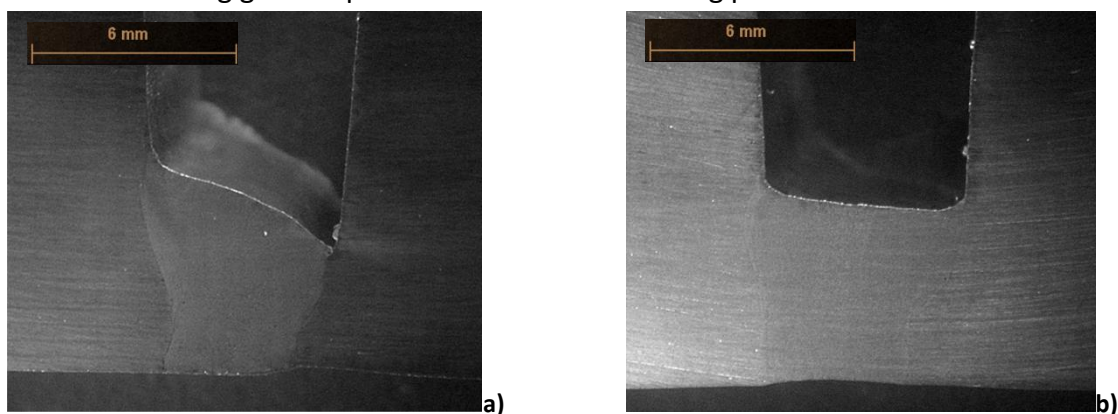


Figure 4.16 – Weld bead obtained for RapidArc using WFS = 9m/min and TS = 0.50m/min: a) 2.5%CO₂ 97.5%Ar; b) 1.5%CO₂54%He44.5%Ar.

4.6. CONCLUSIONS

The main conclusions that can be drawn from this Chapter are, as follow:

- It is shown from the results presented in this chapter that is possible to increase the welding speed from the common 0.25m/min, to at least 1m/min.
- The waveforms working in pulse spray transfer mode demonstrate highest quality in respect to the bead shape characteristics for the weld preparation used in this study. In particular, adequate depth of penetration was difficult to achieve using waveforms working in dip transfer mode;
- Although it is possible to obtain positive depth of penetration using conventional GMAW-P, asymmetric convex top beads are often produced, which are likely to generate defects in subsequent passes;
- The typical defects observed in short-circuiting waveforms are side wall lack of fusion, asymmetric convex top beads and excessive depth of penetration;
- Under some conditions it is possible to get adequate quality at low welding speed using short-circuiting waveforms;
- In pulse spray processes, at high welding speeds/ wire feed speeds undercutting is the most unfavourable defect observed. The results demonstrate that this phenomenon is more critical when 1.5%CO₂ 54%He 44.5%Ar shielding gas mixture is used;
- The processes which showed most promise in this study for combining high quality with high productivity levels were RapidArc and CMT-P;
- Under some conditions it is possible to get adequate quality at low welding speed using short-circuiting waveforms.

5. EFFECT OF SHIELDING GAS MIXTURES ON WELD BEAD SHAPE CHARACTERISTICS

SCOPE

It has been seen that in arc welding the shielding gas mixture has a fundamental effect not only on the protection and heat conduction phenomena but also on the resulting bead shape characteristics.

Using statistical modelling, mixtures design was performed to analyse the effect of shielding gas composition on the bead shape characteristics for CMT-P and RapidArc waveforms. The results obtained and the main conclusions of this research will be presented in this chapter.

5.1. LITERATURE REVIEW	230
5.2. AIMS AND OBJECTIVES	239
5.3. MATERIALS AND METHODS.....	240
5.4. RESULTS.....	246
5.5. DISCUSSION OF RESULTS	251
5.6. CONCLUSIONS	256

5.1. LITERATURE REVIEW

5.1.1. Introduction

The fundamental knowledge established during the previous Chapter in narrow groove welding of CRA pipes indicated that only some of the waveforms studied appeared to have a high potential for application to the welding of root pass at high productivity level based on the experimental conditions applied, i.e. narrow groove design, CTWD, shielding gas composition. It was also apparent that shielding gas composition has a fundamental impact on weld bead shape characteristics and arc stability. It may also be possible to improve productivity and weld bead quality through optimization of the shielding gas composition.

Thus, the research developed in this Chapter will be focused on the evaluation of the effect of shielding gas composition on bead shape and quality using RapidArc and CMT-P welding processes.

No literature was found regarding the effect of the shielding gas composition on weld bead quality for the welding processes considered. However, shielding gas properties will be reviewed, together with the impact of gas properties on other waveform systems.

Finally, the effect of purging gas protection and oxygen on root bead quality will also be reviewed.

5.1.2. Effect of Shielding Gas in Arc Welding

Among the main characteristics of promoting the arc plasma ignition and arc stability, the shielding gas has other important features as follows (Menzel 2003) (Hilton and Norrish 1988) (Matz 2005):

- Protection of oxidation and cleanness;
- Metal transfer mechanism;
- Surface tension effects on weld pool;
- Bead shape geometry and quality;
- Metallurgical and mechanical properties;
- Energy distribution;
- Environmental impact, associated with fumes emissions, gases and dust formation;
- Melting rate and welding productivity.

Direct Current (DC) arc welding is characterized by ionized gases conducting high intensity electrical current. The arc plasma that maintains a complex balance between the heat generated (arc energy) and the heat transferred to the weldment (heat input) and lost to the surrounding atmosphere. The energy distribution in the arc strongly depends of the balance between the pressure due to the thermal expansion of the arc plasma and the pressure of the electromagnetic constriction associated with the ionic conduction. If this

balance is broken an unstable arc will be created, which can produce significant variations in arc current and possibly arc extinction (Eagar 1978).

5.1.3. Characteristics of Common Gases

The choice of shielding gas used in GMAW strongly depends on material properties and the gas (or mixture of gases) characteristics. In the following subsections the main characteristics and properties of common shielding gases used in GMAW will be presented.

5.1.3.1. Argon

Argon is an inert gas with high density, in comparison to air, offering good shielding efficiency. Its low ionisation potential provides very good arc stability with spatter reduction, and it also results in lower voltage, resulting in lower arc energy. Other characteristics associated with the use of argon are smaller penetration beads, less undercutting, high reinforcement level and poor bead appearance. Due to these characteristics argon is commonly used together with small to high amounts of an active gas, such as oxygen or carbon dioxide, which have the capability to improve the ionisation potential with advantages for bead penetration (Hilton and Norrish 1988).

5.1.3.2. Helium

It is also an inert gas, with a lower density, relative to the atmospheric air, which can be a disadvantage, together with high cost. Helium has a high ionisation potential (24.6eV), which results in higher arc voltages, when compared with argon, and so higher heat inputs. The application of this gas results in weld bead shape characterized by low depth-to-width ratio, good fusion characteristics and low reinforcement levels. These characteristics can be beneficial for high travel speeds (Hilton and Norrish 1988). Furthermore, the combination of helium with carbon dioxide has been reported to achieve significant increase in penetration (Dillenbeck and Castagno 1987). However, the use of helium is associated with more significant arc length variations, and difficulty in arc ignition (Menzel 2003).

5.1.3.3. Carbon Dioxide

Carbon dioxide is a reactive gas at high temperature, since it dissociates to carbon monoxide and oxygen; at very high temperatures the oxygen can still ionize. Although carbon monoxide restricts partially the effectiveness of oxygen, the atmosphere created is very oxidizing (high oxidising potential). The most common mechanism of metal transfer observed with this gas is short-circuiting transfer, but globular and repelled can also be observed with highly unstable characteristics (Hilton and Norrish 1988). Carbon dioxide in GMAW increases depth of penetration beads without undercutting, but with high spatter levels (Dillenbeck and Castagno 1987). As a pure gas carbon dioxide is only applied for GMAW of steels, but mixtures with argon and/ or helium offer in general much higher stability and still with good penetration levels. However, it can be applied to high-alloy steels in relatively small amounts (in general lower than 5%) (Menzel 2003).

5.1.3.4. Oxygen

It is also a reactive gas and used as a component of a gas mixture in many of the commercial gases available, with higher oxidation potential than CO₂. Oxygen has a fundamental action on surface tension and arc rooting of weld metal and filler wire droplets, and small additions of this gas can be important when free-flight metal transfer is applied. Furthermore, its ionisation potential, similar to argon, allows very good arc stability with low spatter. This gas also can significantly improve bead shape appearance, in particular to reduce the reinforcement. Moreover, oxygen promotes wetting and reduces the susceptibility to undercutting (Menzel 2003).

5.1.3.5. Nitrogen

Nitrogen is also a reactive gas commonly used in small amount as a shielding gas on superaustenitic and superduplex stainless steels. Due to the presence of about 0.5% of nitrogen content in these materials, the use of nitrogen in the shielding has a major benefit in improving mechanical properties and resistance to pitting corrosion. However, in absence of this element porosity is commonly observed. This gas has been also applied for root shielding protection, together with 10% of hydrogen, due to good reducing properties (Menzel 2003).

5.1.3.6. Hydrogen

Hydrogen is considered as a reducing gas, normally used in small amounts in GMAW, allowing the reduction of oxide surface films. It has a relatively low ionisation potential (13.59eV) but a very high thermal conductivity which requires high voltages levels. The increase in arc energy results in increase of weld pool fluidity and depth of penetration. However, in some materials, such as ferritic steels or martensitic stainless steels, the use of this gas may result in hydrogen embrittlement and crack formation (Menzel 2003).

5.1.4. Physical-Chemical Properties of the Gases

The properties of the shielding gas individually and the shielding gas mixture, when more than one gas is applied, determines the whole characteristics of the arc plasma and therefore the welding performance and weld bead shape. The main physical-chemical properties will be discussed for the most common used gases.

5.1.4.1. Density and Ionisation Potential

Table 5.1 presents the density and ionisation potential for the most common gases used in arc welding.

Table 5.1 – Gas density and ionisation potential for the most common gases (Menzel 2003).

Properties	Argon (Ar)	Helium (He)	Oxygen (O ₂)	Carbon Dioxide (CO ₂)	Nitrogen (N ₂)	Hydrogen (H ₂)
Gas density (kg/m ³)	1.784	0.1784	1.326	1.977	1.161	0.083
Ionisation potential (eV)	15.75	24.58	13.61	14.4	14.54	13.59

The gas density, relative to the atmospheric air, affects the shielding efficiency in the weld pool. Thus, the higher densities associated with argon and carbon dioxide provides excellent shielding efficiency. In contrast hydrogen and helium provide poorer shielding efficiency characteristics, since they are respectively 20 and 10 times less dense than argon. This characteristic may result in turbulent flow at the end of the nozzle due to thermal effects (Menzel 2003). However, as was pointed out by Menzel (2003), the low density of helium can be beneficial for root shielding protection.

The electric arc characteristics, ignition and arc stability, are strongly affected by the ionization potential which determines in MIG/MAG welding the capacity for the molten metal vapour to ionize. Thus, the low ionization potential of argon generates a stable and soft arc, while the high ionisation potential of helium is associated with a lower arc stability and more difficult ignition (Suban and Tusek 2001) (Menzel 2003).

5.1.4.2. Electrical and Thermal Conductivity

The electrical and thermal conductivity of the gases are strongly affected by temperature, as can be observed in the Figure 5.1 (Menzel 2003) (Suban and Tusek 2001).

Electrical conductivity does not change significantly with the shielding gas but increases exponentially with the increase of temperature, due to the dissociation and ionization at high temperatures.

The thermal conductivity is high for hydrogen, carbon dioxide and helium. Therefore, the use of high amounts of these gases is associated with high melting rates. The thermal conductivity of a gas affects the temperature of the arc plasma with consequent variation of arc and weld pool shape and resulting in a change of the weld bead size.

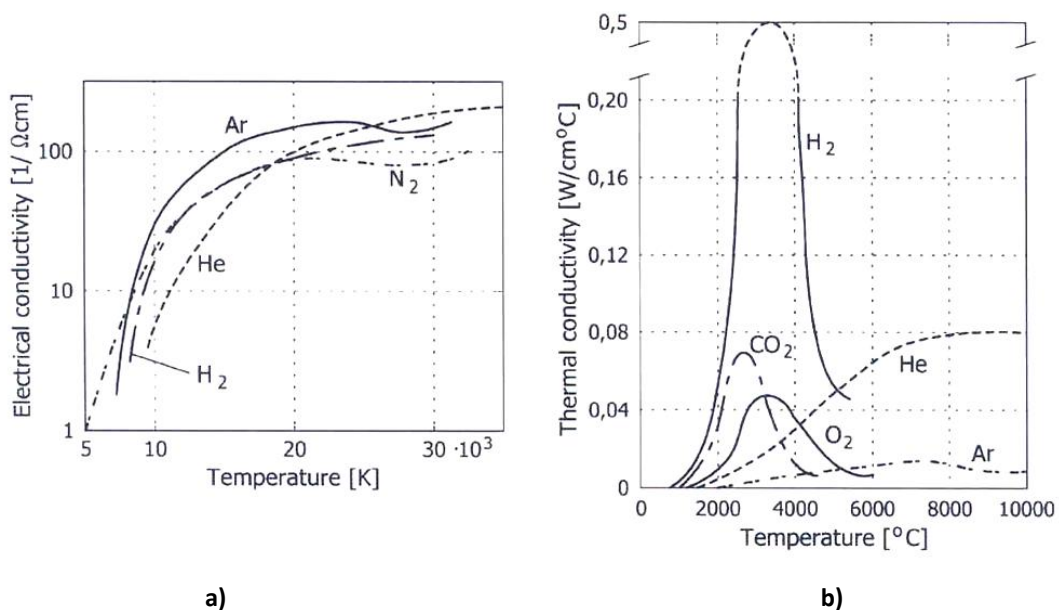


Figure 5.1 – Electric (a) and Thermal (b) Conductivity of gases at pressure of 1 atm (Suban and Tusek 2001).

5.1.4.3. Metallurgical and Mechanical Properties

Since shielding gas composition has a major effect on weld bead shape and quality, the metallurgical features and mechanical properties will also be affected. In particular, shielding gas will have an effect on metallurgical phenomena and formation of weld defects, which will strongly affect the resulting mechanical properties. Menzel (2003) reported that in welding of carbon and low-alloy steels the reduction of oxygen and carbon dioxide in gas composition causes a reduction in oxide formation and fine grain microstructures that influence impact strength. On the other hand, the increasing of oxygen and carbon dioxide leads to an increasing of burn-off the alloying elements, which can cause an increase of brittleness and the tensile strength reduction. It is clear that active gases have an important effect on overall metallurgical features and mechanical properties.

5.1.5. Effect of Shielding Gas Mixtures on Process Characteristics

Argon was used initially as a shielding gas for GMAW, but the introduction of carbon dioxide became very important to GMAW of steels, allowing the increase of welding speeds, depth of penetration and desirable mechanical properties with a lower cost compared to the inert gases.

The shielding gas composition has a major effect on the arc physics characteristics. The addition of small amounts of helium increases thermal conductivity and ionization potential, which generates higher arc voltage (Hiraoka, Sakuma and Zijp 1998). Hiraoka et al. (1998) considered that the reason for this phenomenon is due to increase of the voltage in the cathode region, remaining partially constant in the arc column and anode region. These investigators explained that this results in higher heat input to the weldment, but heat losses decrease with increasing helium content, which is associated with increases in process efficiency. It has been suggested that the presence of helium in the shielding gas makes the welding process more sensitive to variations of the arc length (Modenesi 1990). The increasing of arc length was also reported to affect process efficiency results, resulting in a decrease of this parameter. Furthermore, Suban and Tusek (2001) considered that the increase in arc voltage was responsible for an increase in depth of penetration.

The effect of argon and helium as a shielding gas has been extensively studied by Jonsson et al. (1995). Pure argon presents a significantly low ionisation potential and an average thermal conductivity, while helium is characterized by a very high ionization potential but is a good conductor of thermal energy. Helium has been particularly used together with argon and small amounts of active gases (carbon dioxide and/or oxygen) in welding of stainless steels. The physical-chemical characteristics of this gas, particularly its ionization energy make it possible to achieve higher travel speeds, and in narrow groove welding better side wall penetration.

The effect of shielding gases on melting rate for arc welding have been discussed in the literature (Hiraoka, Sakuma and Zijp 1998) (Suban and Tusek 2001) (Tusek and Suban 2000).

The use of helium as a shielding gas in GMAW has been associated with higher melting rates and heat transfer rates than argon (Hiraoka, Sakuma and Zijp 1998). The explanation of these phenomena was firstly associated with the higher ionisation potential of helium. However, Eagar (1990) and Kim (1989) have studied the phenomena of heat and metal transfer responsible for this characteristic and considered thermal conductivity to be the key factor for this mechanism. In their study, they observed that only about 20% of the total energy is transferred to the weld pool from the arc plasma; the remaining 80% derives from the arc current. This phenomenon was also observed in polyatomic gases, such as hydrogen, where reactive conductivity generates a higher melting rate. Tusek and Suban (2000) analysed the effect of hydrogen in TIG and MIG welding; they demonstrated that the increase of hydrogen content increases melting rate and melting efficiency in both MIG and TIG processes, but with higher impact on TIG welding.

Moran and Yapp (1998) have studied the effect of different shielding gases and arc parameters on the bead shape and size for GMAW in mild steel. They found that increasing arc length causes an increasing of bead width, while decreasing argon content is associated with higher penetration levels. These authors also pointed out that increasing of arc length is sustained by increasing arc voltage, which is associated with the shielding gas composition, in particular with the increase of amount of carbon dioxide.

Dillenbeck and Castagno (1987) investigated the bead characteristics associated with different shielding gas in GMAW of steel. These authors (Dillenbeck and Castagno 1987) pointed out the following main aspects:

- The increase of helium amount helps to stabilize the arc and increase the heat input, with significant increase in bead width;
- The atmospheric contamination was only observed when no shielding was used;
- Spatter projections are strongly affected by the increasing of CO₂ amount. However, helium can have an important effect on controlling spatter;
- For higher amounts of carbon dioxide, the penetration will be much higher and the bead appearance worse.

The effect of shielding gas on welding of stainless steel has been extensively reviewed by Hilton and Norrish (1988). The application of shielding gases for GMAW of stainless steels was firstly based on argon/ oxygen mixtures with oxygen content between 1 and 5%. However, these gas mixtures were associated with surface oxides and slag islands. Furthermore, a distinctive finger type penetration and associated porosity due to the rapid cooling rates were indentified. In contrast, the application of Ar 5%CO₂ was beneficial in terms of surface appearance, but with an increase in weld metal carbon levels up to 0.04%.

More recently, mixtures of He/Ar/CO₂/O₂ have been considered in dip transfer welding, where good fusion propertied allow good depth of penetration with low reinforcement and good surface appearance. It has been reported that the increase of helium amount

increases dip frequency and arc voltage (and hence arc energy). Gas mixtures of Ar/He/CO₂/O₂ have also been applied to spray and pulse spray transfer modes. In these cases, low amounts of helium can provide a shorter and stable arc, solving the deflection issues associated with Ar/CO₂ mixtures. Furthermore, it is pointed out that good fusion characteristics and penetration can be obtained (Hilton and Norrish 1988).

Jonsson et al. (1995) studied the effect of oxygen in GMAW and concluded that additions of oxygen content up to 5% affect, but not significantly, the characteristics of the arc column with an impact on mass flow, momentum flux, electric potential and temperature. The authors still pointed out that the effects of oxygen are greater on the anode and cathode regions.

5.1.6. Gas Flow Control

Gas flow control has a major influence in the generation of desirable arc characteristics. The application of high gas flow causes turbulence which promotes the mixture of air with the shielding gas stream. The presence of atmospheric air can cause spatter and internal porosity (Hilton and Norrish 1988) (Uttrachu 2006). Hilton and Norrish (1988) observed that acceptable flow rates for GMAW are in the range of 14 to 16 L/min, and can increase to 16 to 18 L/min if very high currents (above 350A) are applied due to the increase of stick out and thermal turbulence. The correct determination of flow rate should be consistent with gas density of the gas mixture used. The low density of helium requires an increase of overall flow rate, when this gas is used. Uttrachu (2006) described a relationship between the size of the nozzle and gas flow, where the maximum flow associated with laminar flow is 15L/min for a 12 mm diameter nozzle and 23L/min for a 16 mm diameter nozzle.

5.1.7. Effect of Oxygen in Arc Welding

The effect of small amounts of oxygen can dramatically affect arc characteristics in GMAW. Oxygen potential (OP) defines the oxidizing effect of the shielding gas. The OP affects fume emission, fluidity of the weld pool, oxides and slag formation, and mechanical properties such as toughness and strength of the weld metal (Costa, Starling and Modenesi 2009) (Stenbacka and Persson 1989). The presence of oxygen in the weld metal is mainly associated with the shielding gas composition, but also affected by the filler wire and parent material compositions. Stenbacka and Persson (1989) reported that increasing of current reduces the oxygen content, and increasing voltage increases oxygen content. Furthermore, the same authors reported that the welding speed has a minor effect, while positive polarity causes higher oxygen content compared to negative polarity.

Different studies have been undertaken to understand the effect of different gases on the level of oxygen content and losses of alloying elements. Stenbacka and Persson (1989) concluded that reduction in oxygen and carbon dioxide percentages in the gas mixture will reduce oxygen content levels, causing a reduction in the amount and size of oxide inclusions, which can have a major effect on toughness. However, a minimum oxygen

content level is required for steels, since oxide inclusions promote the growth of acicular ferrite, which is associated with high toughness.

The oxygen is a surface active element in stainless steel alloys. The presence of oxygen during GMAW can have two main effects, the oxygen layer formation and/ or influence on surface tension gradients of molten metal. Experimental measurements show the strong effect of oxygen on weld pool, increasing its length, width, volume and section (Hansen 1994).

5.1.7.2. Purging Gas Protection and Oxidation

Oxidation is one of most critical phenomena affecting mechanical properties and corrosion resistance in stainless steel during welding. The heated surface of this class of materials reacts with atmospheric oxygen forming an oxide layer. At temperatures above 200-300 °C this layer shows discoloration due to the increase of its thickness (Hansen 1994). Thus, temperature and oxygen concentration are the critical parameters responsible for surface oxidation.

Different oxidation colour maps have been developed to explain and control the surface oxidation levels in stainless steel and titanium alloys (Hansen 1994) (EWI ; Navy Joining Center 2000-2001). These research programmes have analysed the effect of the oxygen content in oxidation through observation of coloration changes in the metal surface. The application of purging gas devices in welding of these materials is particularly important to achieve a non oxidized shiny surface. As can be observed in the Figure 5.2 and Table 5.2, amounts of oxygen greater than 15-32ppm are enough to promote the beginning of oxidation mechanism during arc welding.

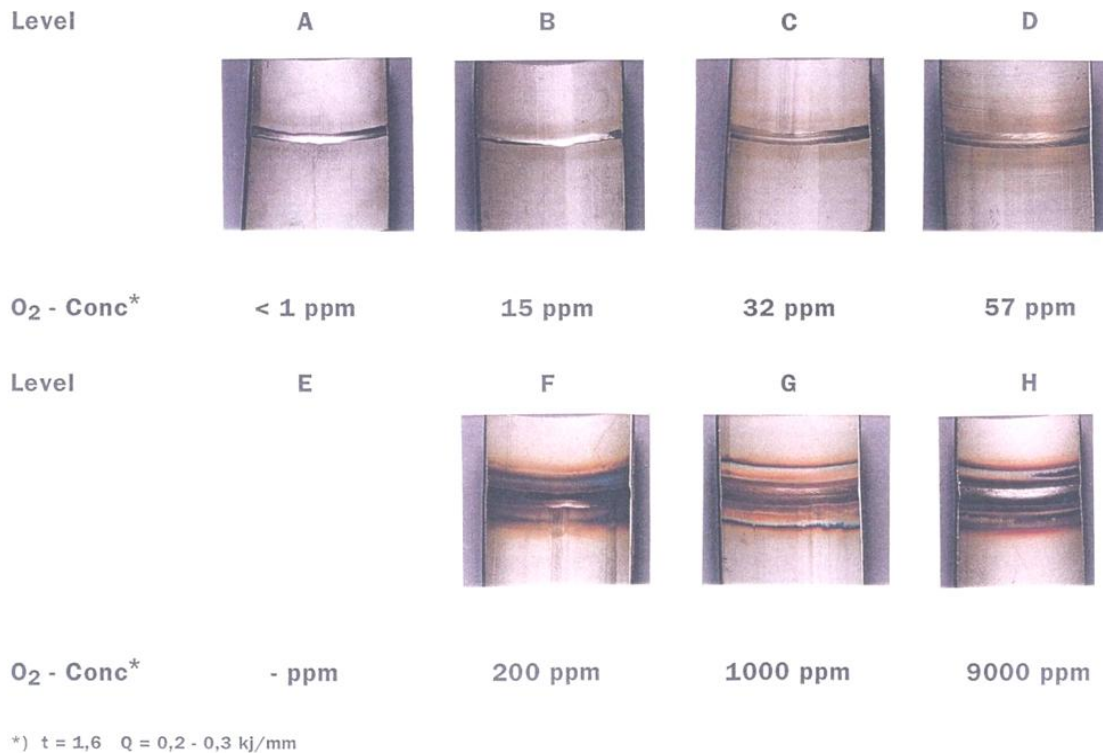


Figure 5.2 – Map of oxidation based on coloration and oxygen content measurement on austenitic stainless steel, using argon as a purging gas (Hansen 1994).

Table 5.2 – Oxidation classification levels associated with the colour observed.

Classification Levels	
A	No visible heat tint, (discolouring)
B	Shades of grey
C	Light yellow
D	Significant yellow
E	Light blue
F	Strong blue to purple
G	Brown and blue areas, dull grey weld metal
H	Brown and blue zones, a significantly thicker oxide, scaling on weld metal

5.1.8. Summary

The physical-chemical properties of the main gases applied as shielding gas mixtures for GMAW have been discussed in this Chapter.

Many publications have been found regarding the analysis of shielding gas mixtures. However, the characteristics of the shielding gas mixture may change considerably when are applied under different conditions, e.g. material or welding waveform.

It is also pointed out the critical importance of shielding gas protection, in special when stainless steel or titanium alloys are applied.

5.2. AIMS AND OBJECTIVES

The main aim of the research developed in this chapter is to evaluate the effect of shielding gas composition on weld bead shape and quality. In this perspective, two different arc current and voltage waveforms will be applied, respectively RapidArc and CMT-P welding. In fact, these two processes have demonstrated high potential for root pass of CRA pipe welding, at high welding speeds. Thus, different objectives can be detailed described:

- To understand the effect of shielding gas mixtures of carbon dioxide, argon and helium on arc length for RapidArc and CMT-P waveforms;
- To perform a design of experiments using the software Design-Expert 7.1.5;
- To evaluate the response of the weld bead shape through the application of different shielding gas mixtures, correspondingly the depth of penetration bead, height ratio, top and root width bead and undercutting;
- Evaluate the susceptibility to the formation of defects associated with different shielding gas compositions and welding waveforms (e.g. undercutting).
- To assess productivity issues and optimum solutions for root pass CRA pipe welding, in relation to arc current and voltage waveforms and shielding gas composition.

5.3. MATERIALS AND METHODS

5.3.1. Materials

The research was developed under the same material and filler metal applied in the previous Chapter. Although the commercial shielding gases used in previous Chapters have been also applied here (2.5%CO₂ 97.5%Ar and 1.5%CO₂ 54%He 44.5%), the overall shielding gas mixtures have been developed using the pure shielding gases argon, helium and carbon dioxide using a gas mixer. The purging gas applied to the root protection was pure argon.

5.3.2. Welding Processes

This study was developed using RapidArc and CMT-P welding processes.

5.3.3. Methods

The methods were developed under the following phases, which will be described during the next sections:

1. Pipe preparation and surface cleaning;
2. Welding tests and experimental measurements;
3. Data analysis.

5.3.3.1. Pipe Preparation and Surface Cleaning

The pipe preparation was developed using the “J” bevel geometry followed by attachment of two pipe sections and surface cleaning immediately before welding, as previously described in Chapter 4.

5.3.3.2. Welding Tests and Experimental Measurements

The general welding conditions applied to the research developed in this Chapter are summarized in the Table 5.3.

Table 5.3 – Summary of welding conditions applied to the research developed in Chapter 5.

Welding Process	WFS set [m/min]	TS [m/min]	WFS/TS ratio	CTWD [mm]	Pulse Control [-5 – 5]	Wave Control [-10 – 10]
RapidArc	9	0.5	18	11	-	10
CMT-P	9	0.5	18	11	0	-

Trim changes were applied to RapidArc welding in order to evaluate the variation of arc length within each of the gases applied. The variation was carried out between 1 and 1.5, in the range of 0.5 to 1.5. The same principle was undertaken in CMT-P through the variation of ALC between 0 and 30%, in the range of -30% to 30%.

The research was performed using a Design of Experiments (DOE) method, implemented using the software Design Expert 7.1.5. The main attributes initially were the range of gas concentration as shown in Table 5.4.

Table 5.4 – Range of gas composition applied to the research developed in Chapter 5.

Limits	Carbon Dioxide [%]	Helium [%]	Argon [%]
Maximum	1	99	99
Minimum	5	0	0

The responses which were evaluated were the depth of penetration, height ratio, top and root width bead and undercutting. The shielding gas mixtures suggested by mixtures design undertaken using DOE software are shown in Table 5.5.

Table 5.5 – Shielding gas mixtures suggested by DOE software using a mixtures design.

Run	Component A: CO ₂ [%]	Component B: He [%]	Component C: Ar [%]
1	1	0	99
2	1	14	85
3	1	31	68
4	1	56	43
5	1	70	29
6	1.5	20.5	78
7	1.5	39.5	59
8	3	8	89
9	3	34	63
10	5	7	88
11	5	45	50
12	5	62	33

These mixtures were compared to the commercial gases applied in the previous Chapters, respectively 2.5%CO₂ 97.5%Ar and 1.5%CO₂ 54%He 44.5%Ar.

These shielding gas mixtures were assessed at different trim/ ALC parameters in order to evaluate the variation of arc length and establish a constant arc length.

These experimental tests were executed using a gas analyser, Unit Instruments, Inc. PRC-3000 equipped with a portable, self-contained system which is able to measure, display and automatically control the flow of multiple gases. This gas analyser was designed for three different channels prepared for specific gases, helium, argon and carbon dioxide, respectively. Each gas channel has a band of limits for which the percentage of shielding gas to apply should be adjusted according with the gas flow selected. The lowest limit corresponds to the channel of carbon dioxide which has a capacity defined between 0.2L/min (2%) and 10L/min (100%). The channels corresponding to the argon and helium support a maximum capacity of 40L/min (100%). The step variation on the display of the gas analyser is 1% and could vary from 2% to 100%.

In this perspective and considering the smallest amount of gas defined as the 1%CO₂99%Ar, it was determined that the flow level for the gas would remain constant at 20L/min, considering the narrow scale for the CO₂ channel. Table 5.6 shows the percentage of each

gas component, obtained (actual) and displayed (set), as well as the corresponding gas flow for each gas considering the flow level defined above.

Table 5.6 – Shielding gas composition as actual (obtained) and set on gas analyser and respective flow level for each of component gases applied.

Shielding Gas	Component A: CO ₂			Component B: He			Component C: Ar		
	Actual [%]	Actual [L/min]	Set [%]	Actual [%]	Actual [L/min]	Set [%]	Actual [%]	Actual [L/min]	Set [%]
1%CO ₂ 99%Ar	1	0.2	2	-	-	-	99	19.8	50
1%CO ₂ 14%He85%Ar	1	0.2	2	14	2.8	7	85	17	43
1%CO ₂ 31%He68%Ar	1	0.2	2	31	6.2	16	68	13.6	34
1%CO ₂ 56%He43%Ar	1	0.2	2	56	11.2	28	43	8.6	21
1%CO ₂ 70%He29%Ar	1	0.2	2	70	14	35	29	5.8	14
1.5%CO ₂ 20.5%He78%Ar	1.5	0.3	3	20.5	4.1	10	78	15.6	39
1.5%CO ₂ 39.5%He59%Ar	1.5	0.3	3	39.5	7.9	20	59	11.8	29
3%CO ₂ 8%He89%Ar	3	0.6	6	8	1.6	4	89	17.8	44
3%CO ₂ 34%He63%Ar	3	0.6	6	34	6.8	17	63	12.6	31
5%CO ₂ 7%He88%Ar	5	1	10	7	1.4	3	88	17.6	44
5%CO ₂ 45%He50%Ar	5	1	10	45	9	23	50	10	25
5%CO ₂ 62%He33%Ar	5	1	10	62	12.4	31	33	6.6	16
2.5%CO ₂ 97.5%Ar	2.5	0.5	5	-	-	-	97.5	19.5	49
1.5%CO ₂ 54%He44.5%Ar	1.5	0.3	3	44	8.8	22	44.5	8.9	22

As can also be observed in the Table 5.6, the two commercial gases have also been evaluated in order to compare the results obtained using gas analyser and commercial mixtures.

Previous to performing the experimental tests, a set of calibrations were made to check the accuracy of the gas analyser and respective mixtures obtained. This calibration tests were developed using a gas meter, at the end of the gas analyser and at the end of torch. A flow level of 15L/min was applied.

The first set of tests was performed at the outlet of the gas analyser, using single channels. These first tests had the objective of evaluating the flow level read at the flow meter when different percentages of gas were applied. The respective regression lines have been applied for each of the gases as a reference for single readings. These results are illustrated in the Figure 5.3.

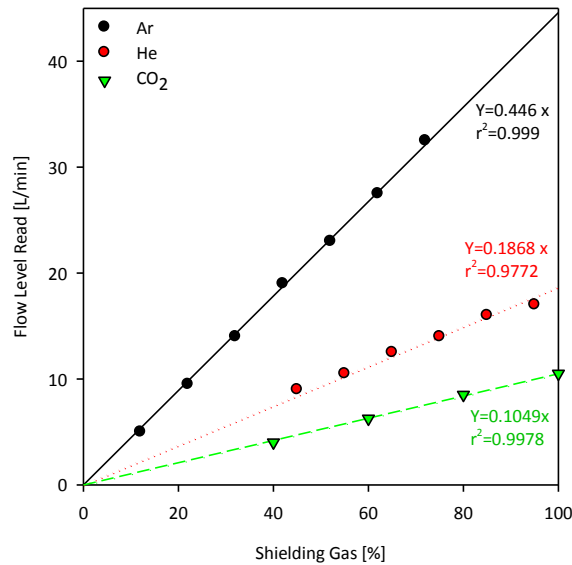


Figure 5.3 – Flow level read measurements obtained for each gas at different shielding rates on the outlet of the gas analyser.

A range of gas mixtures, with two and three components, with respective reading values and expected values, based on the regression equations obtained above, were compared. The results are shown in Table 5.7.

These results show a negative error for all the tests performed, which corresponds to the expected values lower than read values. In general the errors associated are not very significant, but rise with the increasing of helium percentage, may be due to its low density, compared with argon and carbon dioxide.

Table 5.7 – Expected and Read Values at the outlet of the gas analyser for different gas mixtures, and respective error.

Run	Channel Inputs [%]			Expected Values			Read Value	Error
	CO ₂	Ar	He	CO ₂	Ar	He		
A	100	25	0	10.49	11.15	21.6	22	-0.4
B	100	22	0	10.49	9.81	20.3	20.5	-0.2
C	50	22	0	5.25	9.81	15.1	15.5	-0.4
D	0	22	35		9.81	6.5	16.4	-2.7
E	0	22	55		9.81	10.27	20.1	-2.9
F	16	16	30	1.678	7.14	5.6	14.4	-0.6

Several tests have also been performed in the end of the torch using just single channels and measuring the flow level of the gas using a universal flow meter. The flow level was measured with reference to the metal indicator. The results obtained and respective regression lines are illustrated in the Figure 5.4.

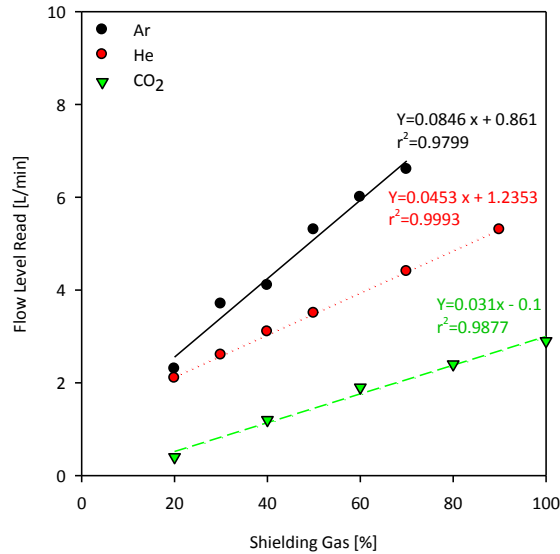


Figure 5.4 – Flow level read measurements obtained for each gas at different shielding rates on the welding torch.

Gas mixture measurements were also assessed at the end of the torch and the results are presented in the Table 5.8. It is possible to observe the expected values, based on the calculation carried out using the regression equations based on single measurements, the read values at the metal reference of the flow meter and the error between both results.

The results obtained show that different situations with positive and negative error difference were obtained, which means that the variation corresponds a systematic error. In general the error obtained is very low. These results indicate very high confidence in the application of the gas analyser to the study the effect of shielding gas mixtures on weld bead shape quality.

Table 5.8 – Expected and Read Values at the welding torch for different gas mixtures, and respective error.

Run	Channel Inputs [%]			Expected Values				Read Value	Error
	CO ₂	Ar	He	CO ₂	Ar	He	Mixture		
A	0	20	55	2.549	3.727	6.3	5.9	0.4	
B	0	20	35	2.549	2.821	5.4	5.1	0.3	
C	0	20	0	2.549		2.5	2.7	-0.2	
D	40	20	0	1.14	2.549		3.6	0.1	
E	50	0	20	1.45		2.141	3.5	0.1	
F	30	16	16	0.83	2.211	1.960	4.7	0.3	

For the application of the gas analyser several seconds of pre-flow were always applied to ensure that the gas composition required at the welding torch is achieved.

During all the experimental tests carried out in this Chapter, current and voltage waveform and WFS signal were recorded throughout of the oscilloscope. The characteristics of the equipment and experimental conditions applied were described during Chapter 2. The high speed camera was also applied to the experimental tests to determine the arc length.

5.3.3.3. Data Analyses

5.3.3.3.1. *Waveform Measurements*

The waveforms recorded were converted using Xviewer software as described in Chapter 2. These results ensure the analysis of arc energy and heat input, together with the instantaneous arc power and process efficiency resulting from the Chapter 3 analysis.

5.3.3.3.2. *Arc Length Measurements*

In all the experiments performed, arc length control was assessed using high speed video recording throughout of the software WeldData, as described in Chapter 2 of this thesis.

5.3.3.3.3. *Bead Shape Analysis*

Bead shape characteristics were evaluated through a cross section, which was cut and prepared metallographically. The macrosection obtained was photographed and the bead shape measurements were evaluated using image software. The main parameters measured correspond to the depth of penetration, low and high height bead, top and root width. Undercutting was also determined when it was identified. The measurements were executed according with the criteria previously defined in Chapter 4.

5.4. RESULTS

5.4.1. Introduction

The results obtained during this Chapter were aimed at the characterization of the effect of shielding gas mixtures on the bead shape characteristics obtained in narrow groove welding, using RapidArc and CMT-P waveforms. The quality of the root surface obtained from the purging shielding device developed was also evaluated.

The variation of three components mixture generates a very complex analysis; this led to the application of design of experiments software in order to perform statistical modelling by simplifying the range of conditions tested.

The analysis of the variation of arc length with arc length correction parameter (trim or ALC) and respective comparison for shielding gas mixtures defined by the design of experiments will be shown. Further to this, and applying a normalized arc length level, the mixture designs will be obtained for both waveforms and desirability optimization analysis will be performed based on defined criteria.

5.4.2. Root Shielding Quality

As introduced in Chapter 4 (Section 4.3) different shielding gas devices were developed during this investigation to achieve a good purging shielding condition. The root quality was analysed by comparing the root shield coloration with photos from the literature, which have related the amount of oxygen present to the coloration obtained for stainless steel (Hansen 1994). In this way it is possible predict the oxidation level by the coloration obtained. A comparison between a good shielding quality, obtained using pure argon spread out from the final purging shielding device developed, with one without purging protection is observed in the Figure 5.9.

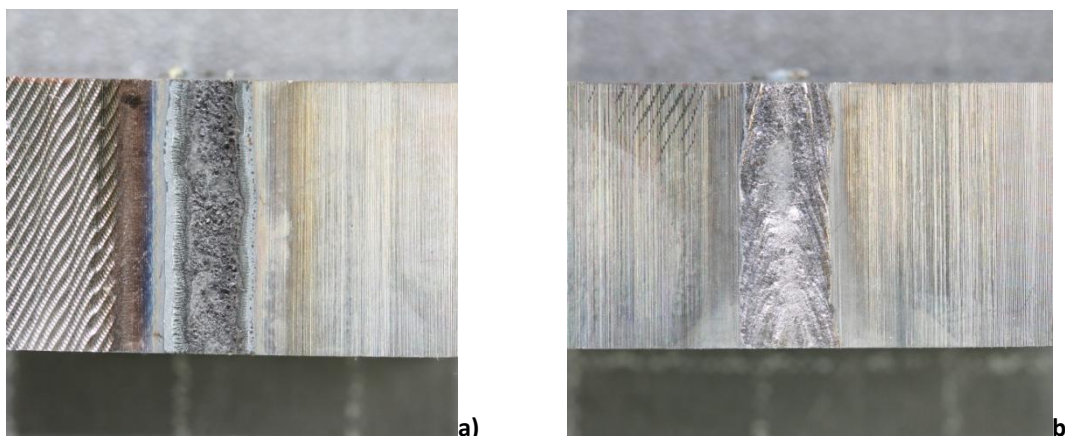


Table 5.9 – Visual illustration of a section of weld root surface: a) without purging shielding protection; b) with purging shielding protection using pure Argon.

5.4.3. Analysis of Arc Length

Several welding tests using the shielding gas mixtures defined previously (to see Section 5.3) were undertaken by varying the arc length adjusting parameter (trim/ ALC) for RapidArc and CMT-P waveforms. The results obtained for these measurements are presented in Appendix XVIII. The average and RMS variation of the variation of arc length obtained for each mixture with the variation of arc length correction parameter are also presented in Appendix XVIII.

The results of the variation of arc length by changing the arc length correction parameter (trim/ ALC) for different shielding gas compositions are illustrated in the Figure 5.5 and 5.6, respectively for RapidArc and CMT-P. According to these results an arc length of about 3.5mm was established for RapidArc while for CMT the arc length was in the range of 4 – 4.5mm.

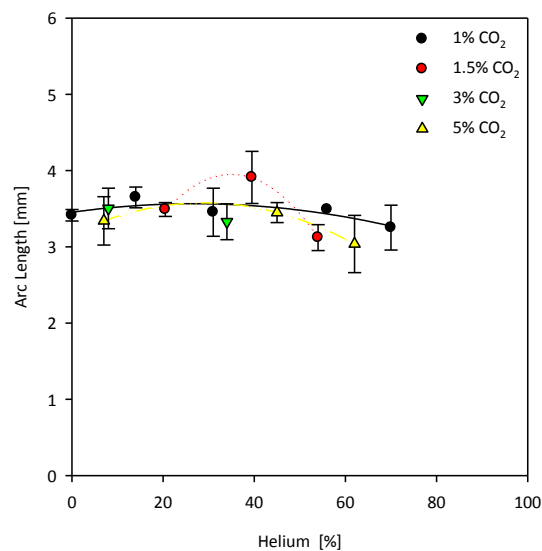


Figure 5.5 – Variation of arc length for different shielding gas mixtures for RapidArc. The bars represent the RMS variation when trim was changed.

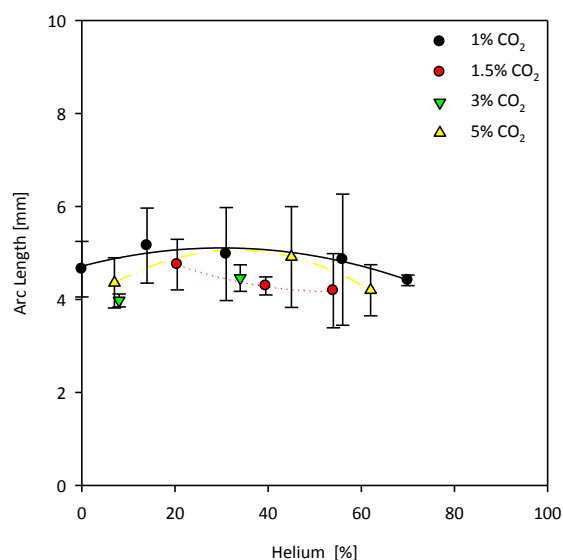


Figure 5.6 – Variation of arc length for different shielding gas mixtures for CMT-P. The bars represent the RMS variation when arc length correction was changed.

5.4.4. Modelling Analysis

The analysis of the effect of shielding gas mixtures on bead shape characteristics were developed through the Design Expert 7.1.5 using a mixtures design. The responses applied to this study were, as follow:

- Depth of penetration;
- Height Ratio (already defined in Section 2.4.4);
- Root Width;
- Top Width; and
- Undercutting

The results obtained to these measurements are presented in Appendix XVIII. It should be noticed that undercutting was not identified at the experimental conditions applied for RapidArc waveform. Thus, undercutting was not considered as a response for the statistical modelling developed for RapidArc.

From these results the design was run for both waveforms considered, and the model equations obtained are presented in Appendix XIX. The results of the statistical parameters obtained from the analysis of variance (ANOVA) are presented in the Tables 5.10 and 5.11, below.

In RapidArc waveform the model obtained for top width was considered not significant. This was perhaps due to the variations obtained to the top width are not significantly different among the shielding gas mixtures studied. Although other mix orders were tried, no better results were obtained. The negative “Pred R-Squared” also found to this model means that the overall mean should be a better prediction than the actual model applied.

For CMT-P waveform the equation of quadratic order applied to Height Ratio was transformed into a power function with lambda -2.11 and constant (k) of 0. In addition, a not significant model was also obtained to the root width for CMT-P waveform.

Considering the overall analysis achieved from the statistical modelling, optimization was performed based on desirability criteria. The diagrams of the desirability criteria obtained for RapidArc and CMT-P are presented in Appendix XX.

The desirability analyses were performed based on an acceptance criteria established according to the standards and industrial acceptance requirements. The Table 5.12 shows the goal and importance established for each response considered. The responses that showed not significant model p-value were rejected to the optimization.

Table 5.10 – Results of statistical analyses obtained from DOE software for the different model responses of mixtures design for RapidArc.

Response	Type of model	Pred.	Adj.	Model		Adeq.	Lack of Fit		Std. Dev.
		R-Squared	R-Squared	F-value	P-value	Precision	F-value	P-value	
Depth of Penetration	Quadratic	0.4523	0.6122	7.63	0.0008 (significant)	8.036	1.58	0.2665 (not significant)	0.12
Height Ratio	Linear	0.0816	0.2482	4.47	0.0257 (significant)	5.553	0.85	0.6067 (not significant)	0.098
Root Width	Linear	0.1177	0.2514	4.53	0.0247 (significant)	6.756	0.85	0.6063 (significant)	0.51
Top Width	Special Cubic	-1.7973	0.1331	1.54	0.2329 (not significant)	4.201	1.09	0.4469 (not significant)	0.25

Table 5.11 – Results of statistical analyses obtained from DOE software for the different model responses of mixtures design for CMT-P.

Response	Type of model	Pred.	Adj.	Model		Adeq.	Lack of Fit		Std. Dev.
		R-Squared	R-Squared	F-value	P-value	Precision	F-value	P-value	
Depth of Penetration	Linear	0.4346	0.5289	16.16	< 0.0001 (significant)	11.119	0.87	0.5860 (not significant)	0.064
Height Ratio	Quadratic (Power)	0.6198	0.6921	13.14	< 0.0001 (significant)	11.770	1.11	0.4100 (not significant)	0.36
Root Width	Quadratic	-0.1667	0.1526	1.97	0.1228 (not significant)	4.163	2.79	0.0445 (significant)	0.30
Top Width	Linear	0.4374	0.5116	15.14	< 0.0001 (significant)	11.271	1.12	0.4130 (not significant)	0.27
Undercutting	Linear	0.5031	0.5750	19.26	< 0.0001 (significant)	10.236	1.52	0.2278 (not significant)	0.20

Table 5.12 – Desirability criteria defined for the model optimization for RapidArc and CMT-P.

Responses	Goal	Importance
Depth of Penetration (DP)	maximize	+++++
Height Ratio (HR)	maximize	+++ (or ++++ when undercutting is not applied)
Root Width (RW) <i>(when applied)</i>	maximize	+++
Top Width (TW) <i>(when applied)</i>	maximize	++ (or +++ when undercutting is not applied)
Undercutting (U) <i>(when applied)</i>	minimize	++++

The solutions obtained for RapidArc and CMT-P from the optimization of the mixture designs are presented in the Table 5.13, below.

Table 5.13 – Solutions obtained for the optimization of the designs analysed for RapidArc and CMT-P waveforms.

Waveform	Shielding Gas (%)			DP (mm)	HR	RW (mm)	TW (mm)	U (mm)	Desirability
	CO ₂	He	Ar						
RapidArc	1.94	43.39	54.67	0.30	0.835	5.05	-	-	0.589
CMT-P	2.77	0	97.23	0.03	1.020	-	6.41	0.24	0.635
CMT-P	1.00	0	99.00	-0.04	0.950	-	6.19	0.21	0.574

5.5. DISCUSSION OF RESULTS

5.5.1. Introduction

It was observed from the results obtained during Chapter 4 that shielding gas composition may affect the resulting bead shape characteristics, in particular the depth of penetration. This led to a fundamental research to characterize the effect of shielding gas composition on the resulting bead shape characteristics.

Initially, the characterization of the root surface quality was attempted based on application of a purging gas device developed during this research to achieve a surface with oxidation free. A comparison between the root runs obtained experimentally with photograms from the literature (Hansen 1994) demonstrates that less than 15ppm of oxygen was achieved.

The analysis of the effect of shielding gas composition on bead shape characteristics was performed for RapidArc and CMT-P waveforms using statistical modelling. Several gas mixtures were indicated by the software to be tested and the experimental results obtained were analysed and optimized according to an established criteria. The tests were carried out at a relatively similar arc length.

The discussion of the results obtained will be undertaken based on the results of the modelling analysis and respective desirable solutions obtained.

5.5.2. Effect of Arc Length

It is well known that arc length varies considerably with the shielding gas composition. This variation has been mainly associated with the physical properties of the gases (Hiraoka, Sakuma and Zijp 1998) (Modenesi 1990) (Liratzis 2007). The analysis of arc length for several experimental tests by changing the arc length adjusting parameter have shown 1mm difference for RapidArc and 2mm difference for CMT-P. According to the results of arc length obtained for both waveforms the value of arc length considered in the analysis was approximately 3.5mm for RapidArc and 4 - 4.5mm for CMT-P.

It should be noticed that trim/ ALC were not set below the nominal value (i.e. nominal value trim = 1 and ALC = 0%), since below this burn-through take place at the welding conditions applied (WFS = 9m/min; TS = 0.50m/min). At certain shielding gas mixtures burn-through also occurred above the nominal value, in particular when the amount of helium increased significantly. This behaviour was observed for both waveforms investigated (i.e. RapidArc and CMT-P). This led to a conclusion that welding speed can be increased if sound welds are obtained, or the groove design could be changed by increasing the thickness of the root face.

5.5.3. Analysis of the Modelling Responses

The analysis of bead shape characteristics using similar arc length level was performed through the Design Expert software. The critical parameters defined for this analysis were the depth of penetration, the height ratio (i.e. measure of the top convexity/ asymmetry), the width bead (on top and root surface) and the undercutting.

Although the results obtained for RapidArc show that undercutting does not happen for any of the shielding as mixtures evaluated, CMT-P is characterized by undercutting in most of the shielding gas mixtures analysed. As is observed from the Figure 5.7, at the process setting conditions established (i.e. WFS set = 9m/min; TS = 0.50m/min; CTWD = 11mm), the undercutting increases with the amount of helium in the shielding gas. It is not possible draw a final conclusion about the effect of carbon dioxide, but there is an indication that undercutting also increases with the amount of this gas component.

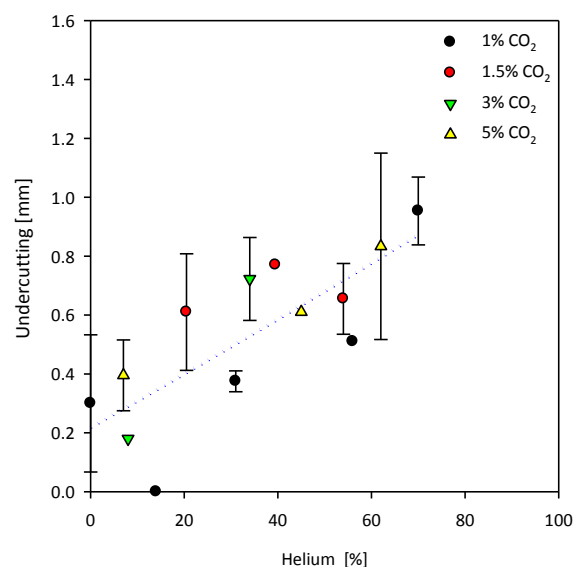


Figure 5.7 – Effect of shielding gas mixtures on undercutting for CMT-P.

The variation of bead shape characteristics due to the shielding gas composition is illustrated in the Figure 5.8 and 5.9, respectively for RapdiArc and CMT-P.

The depth of penetration was measured in respect to the root surface. Below root surface positive depth of penetration is achieved, while above root surface (when both lack of penetration or concave root bead takes place) negative depth of penetration is obtained.

The results obtained demonstrate that helium does not have a significant effect on the overall shape characteristics. It may improve the depth of penetration but increases the convexity of the top bead for RapidArc. In contrast, depth of penetration may reduced by the increasing the amount of helium for CMT-P. This is probably due to the high arc energy delivered to the workpiece which is able to promote very high dilution ratios and consequently generate a fully penetrated concave root bead.

In addition, the width bead is not changing significantly with the variation of the shielding gas mixtures. For higher amounts of helium the width may increase but not significantly. This is a similar behaviour observed for both waveforms, i.e. RapidArc and CMT-P.

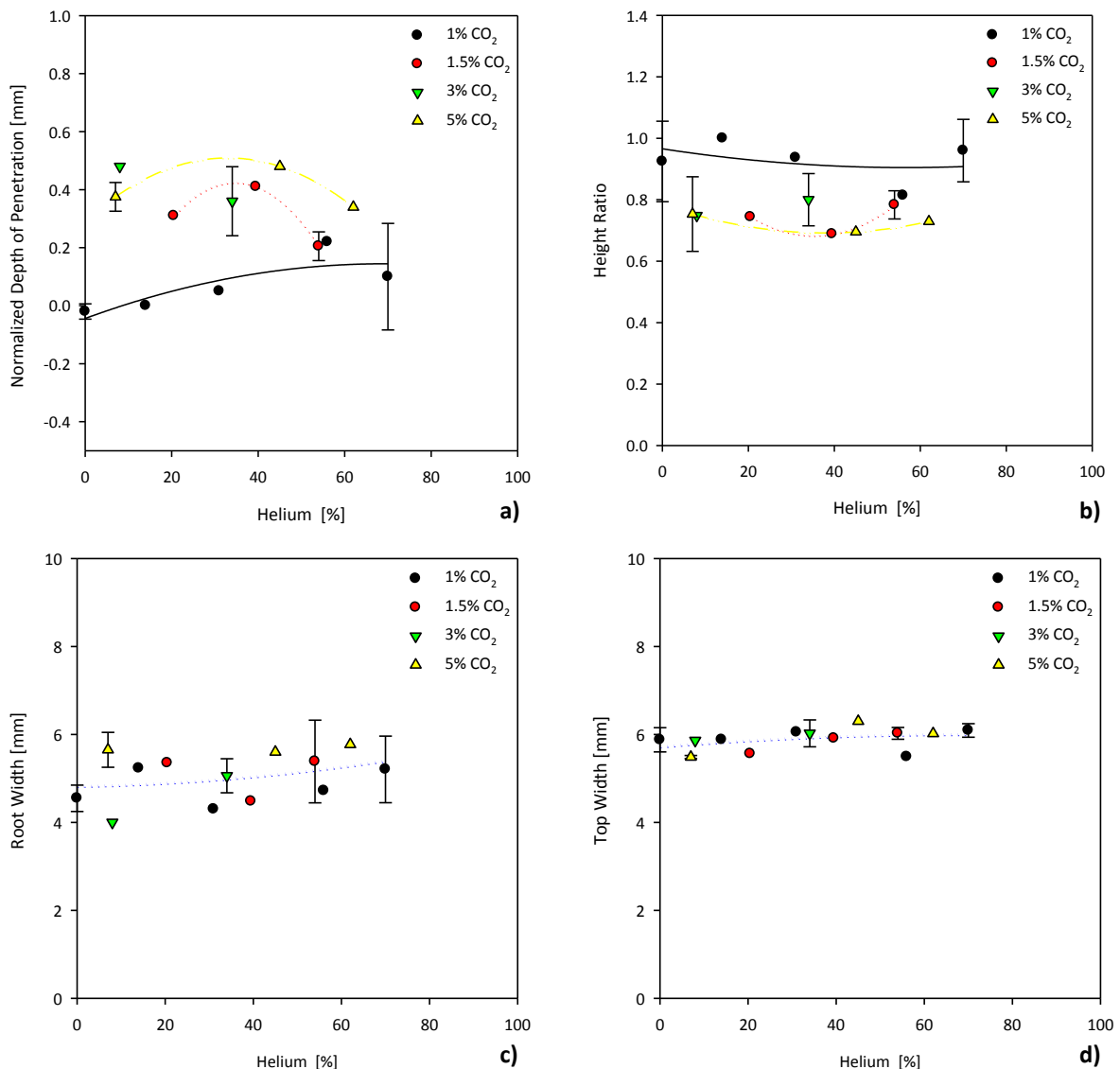


Figure 5.8 – Effect of shielding gas mixtures on bead shape characteristics for RapidArc: a) Depth of penetration; b) height ratio; c) root width and d) top width.

The increase of the amount of carbon dioxide increases significantly the depth of penetration, for both waveforms. This behaviour has been observed already in the literature and is due to the physical properties of the carbon dioxide (Dillenbeck and Castagno 1987) (Suban and Tusek 2001). However, the increase of the amount of carbon dioxide is a disadvantage for the top bead performance, by increasing its convexity and asymmetry level.

Width bead is not affected by the variation of the amount of carbon dioxide in the shielding gas mixture.

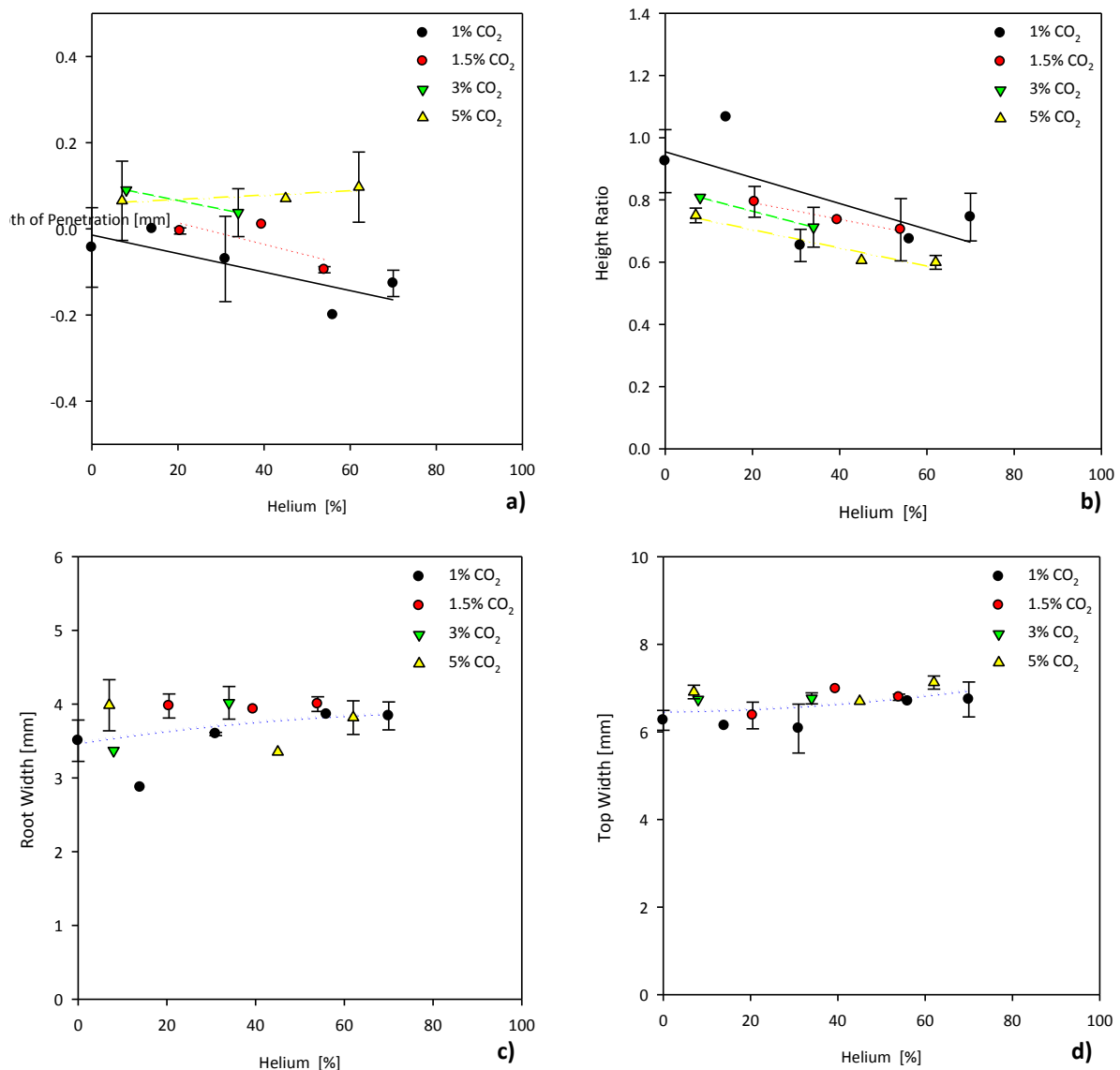


Figure 5.9 – Effect of shielding gas mixtures on bead shape characteristics for CMT-P: a) Depth of penetration; b) height ratio; c) root width and d) top width.

5.5.4. Analysis of Desirability and Optimum Solutions

The desirability plots obtained from the optimization of mixtures design for RapidArc and CMT-P are presented in the Figure 5.10. The desirability criteria were established in order to achieve high quality root runs and two different solutions were obtained for the waveforms investigated.

For RapidArc the application of 2%CO₂ 43%He 55%Ar is suggested, which quite close to the commercial gas mixture applied in this investigation, i.e. 1.5%CO₂ 54%He 44.5%Ar.

In respect to CMT-P a surprising optimum solution is comparable to the shielding gas mixture suggested by the power source, i.e. 2.5%CO₂ 97.5%Ar. It leads to a conclusion that Fronius may have chosen this shielding gas by the optimisation of the bead shape performance for the waveform design applied to supermartensitic stainless steel alloy.

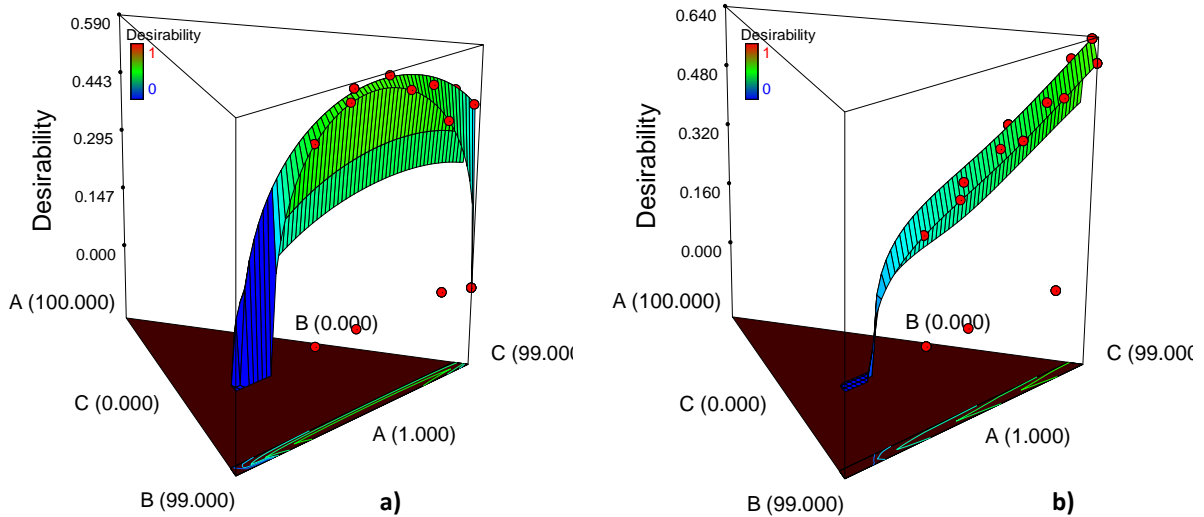


Figure 5.10 – Desirability obtained to the effect of shielding gas mixture on bead shape characteristics a) RapidArc; b) CMT-P. A = CO₂; B = He and C = Ar.

5.6. CONCLUSIONS

The main conclusions obtained from the study of the effect of shielding gas mixtures on welding of corrosion resistant alloys (CRA) narrow groove pipes are, as follow:

- The purging shielding gas device developed was able to eliminate completely the oxidation of root runs and obtain a shiny root surface;
- The shielding gas mixture has a fundamental effect on the depth of penetration and play an important role on the top bead quality;
- The shielding gas mixture can also be optimised to achieve higher productivity levels, as by increasing the amount of carbon dioxide the depth of penetration is generally increased. However the top becomes convex and asymmetry also takes place;
- The increase of helium increases the overall arc energy but does not have a significant effect for both waveforms in improving bead shape characteristics. Furthermore, at certain conditions arc instability phenomena can overcome the partial benefits and result in undesirable bead shape conditions;
- It was observed that at the setting conditions defined, CMT-P presents for almost all range of shielding gases an undesirable undercutting defect;
- The solutions obtained from the statistical modelling the shielding gas composition that best fits the bead shape requirements for CMT-P is similar to the shielding gas suggested by the power source, i.e. 2.5%CO₂ 97.5%Ar;
- The desirability analysis obtained from the optimisation of the mixture design to RapidArc suggest the application of 2%CO₂ 43%He 55%Ar, which is similar to the 1.5%CO₂ 54%He 44.5%Ar, also used in this work.

6. CONCLUSIONS AND PERSPECTIVES FOR FURTHER WORK

Scope

The main conclusions of the thesis and the perspectives for further work will be drawn during this chapter. The fundamental achievements and benefits of the work developed will be presented in the conclusions. Then, some suggestions for further work following the results obtained will be also presented.

6.1. CONCLUSIONS	258
6.2. PERSPECTIVES FOR FURTHER WORK	260

6.1. CONCLUSIONS

Controlled short-circuiting, pulse spray and controlled mixed mode gas metal arc welding processes have been characterized in depth in this thesis, considering different GMAW waveforms recently developed. The main conclusions of this thesis are as follow:

- The new processes described in this thesis exhibit a quite a diverse range of waveform control strategies, implemented in software, to achieve their objective of controlled metal transfer with potential benefits to a range of applications;
- Detailed study shows that waveforms are not always as shown in manufactures literature;
- The complex interrelationships between set and measured waveform parameters have been described in detail, and their relationship to metal transfer has been clarified;
- The Burn-Off ratio, i.e. the relationship between melting rate and arc current, is similar for all waveforms characterized;
- The arc voltage waveform generally changes in consequence of external setting parameters, e.g. CTWD and shielding gas composition. This leads to significant variations of the arc energy and consequently changes in the way that metal is transferred;
- In general, arc energy and arc current play the major role in the melting phenomena, as the depth of penetration and dilution area generally increase with energy and current. Short-circuiting waveforms in general led to lower depth of penetration and dilution areas and higher convexity top beads compared to pulse spray waveforms;
- Shielding gas composition can play a significant role in process performance and arc stability and resulting bead shape characteristics, as observed from the results obtained for 2.5%CO₂ 97.5%Ar and 1.5%CO₂ 54%He 44.5%Ar;
- UI diagrams (or cross-plots) have to shown to provide useful information on process performance, and in particular in providing a qualitative assessment of arc stability;
- A new metal transfer classification has been proposed to include CMT-P as a controlled mixed mode; i.e. short-circuiting and pulse spray transfer;
- The investigation on process efficiency indicated that significant radiation (and convection) losses can take place during the measurement of process efficiency, leading to errors in calculated process efficiency. Typically, up to 3% of energy may be lost during welding, and 2% during specimen transfer, for the liquid nitrogen

calorimeter method used in this thesis. These losses will also be higher as wire feed speed is increased;

- The results obtained show that all the short-circuiting waveforms analysed (i.e. CMT, STT and FastROOT) had a similar process efficiency of $90\pm 3\%$, while pulse spray waveforms (GMAW-P, CMT-P and RapidArc) are characterized by lower process efficiency, approximately $78\pm 3\%$;
- The global results obtained using this method demonstrate that some errors may occur, but it is a very easy and quick test to analyse the process efficiency of welding processes;
- For the CRA pipe materials and weld preparations used in this study, CMT-P and RapidArc are able to satisfy the acceptance criteria for welding of root runs. It was observed that even when penetration is achieved, short-circuiting waveforms are characterized by high convexity levels. (Note that these results are only valid under the experimental conditions set, in particular the geometry of groove design established).
- By using the selected process and optimised welding conditions, it was possible to achieve high quality root runs in CRA pipes at welding speeds up to 1m/min, i.e. four times higher productivity than is actually achieved in industry with RapidArc and CMT-P;
- The shielding gas device developed in this work achieved 15ppm oxygen, with no oxidation of the weld root, and assisting significantly in obtaining high weld quality
- The shielding gas composition has significant effect on bead shape characteristics and arc stability phenomena. The detailed study on the effect of shield gas composition for RapidArc and CMT-P welding of weld roots in supermartensitic stainless steel led to the interesting conclusion that the optimum shielding gases were those actually used in industry: 2.5%CO₂ 97.5%Ar for CMT-P and 2%CO₂ 43%He 55%Ar for RapidArc.

6.2. PERSPECTIVES FOR FURTHER WORK

- Although important conclusions and scientific know-how has been established at first time with the research developed in this thesis, process setting parameters should be evaluated in more detail for all waveforms;
- Other applications should be considered for the short-circuiting waveforms, where lower depths of penetration are applied (e.g. laser arc hybrid welding);
- The study of process efficiency should be further developed, in particular considering other applications (e.g. narrow groove welding) and welding processes;
- Positioning welding and welding gap could be applied to test possible benefits, especially for FastROOT waveform, since the technical information suggest some benefits can be taken when root gap is applied;
- In narrow groove welding oscillation should be considered for waveforms where convexity is significant, even recognizing the reduction of depth of penetration. Another groove designs could also be investigated in more detail;
- The benefits of the application of a shielding gases rich in helium should be understood regarding the increase of penetration;
- Mechanical properties, fatigue and corrosion performance should be performed to perform a complete evaluation of CRA pipe root welding;
- The performance of root runs on welding of narrow groove CRA pipes should be compared with the application of multi-wire GTAW system and conduction laser welding.

7. REFERENCES

Allum, C. "Metal Transfer in Arc Welding as a Varicose Instability: I. Varicose Instabilities in a Current-carrying Liquid Cylinder with Surface Charge." (*J. Physics D: Applied Physics*) 18 (1985 a): 1431-1446.

Allum, C. "Metal Transfer in Arc Welding as a Varicose Instability: II. Development of Model for Arc Welding." *Journal of Physics. D: Applied Physics* 18 (1985 b): 1447-1468.

Allum, C. "MIG Welding - Time for a Reassessment." *Metal Construction*, June 1983: 347-353.

American Welding Society. *Welding Handbook - Welding Processes Part 1*. Edited by 9th Edition. Vol. 2. USA, 2007.

Amin, M. "Pulse Current Parameters for Arc Stability and Controlled Metal Transfer in Arc Welding." *Metal Construction*, May 1983: 272-278.

Amin, M. "Synergic Pulse MIG Welding." *Metal Construction*, June 1981: 349-353.

Amson, J. "An Analysis of the Gas-Shielded Consumable Metal Arc Welding System." *British Welding Journal* 41, no. 4 (1962): 232-249.

Anon. "Classification of Metal Transfer." *IIW Doc. XII-636-76*. 1976.

Arif, N., J. Lee, and C. Yoo. "Modelling of Globular Transfer Considering Momentum Flux in GMAW." *Journal of Physics D: Applied Physics* 41, no. 19 (October 2008).

Blackman, S. "Developments Forecast to Reduce Pipeline Construction Costs." *Welding and Metal Fabrication* (Welding and Metal Fabrication) 69, no. 8 (2001): 7-10.

Blackman, S., and D. Dorling. "High Speed Tandem GMAW for Pipeline Welding." *International Pipeline Conference*. Calgary, Alberta, Canada: Proceeding of IPC, 2002.

Bless, S. "Drop Transfer in Short-Circuit Welding." *Journal of Physics. D: Applied Physics* 7 (1974): 526-539.

Bosworth, M. "Effective Heat Input in Pulsed Current Gas Metal Arc Welding with Solid Wire Electrodes." *Welding Journal* 70, no. 5 (1991): 111s-117s.

Bregagnollo, Moreno. "Evolution Continues in Welding, Beveling and Laying of Offshore Pipelines." *Pipeline & Gas Journal*, February 2005: 45-46.

Bruckner, J. "Cold Metal Transfer has a Future Joining Steel to Aluminium." *Welding Journal*, June 2005: 38-40.

BS-EN12732. Gas Supply Systems. Welding Steel Pipework. Functional Requirements. 2000.

BS-EN14163. Petroleum and Natural Gas Industries . Pipeline Transportation Systems. Welding of Pipelines. 2001.

Camilleri, D., T. Gray, and T. Comlekci. "Use of Thermography to Calibrate Fusion Welding Procedures in Virtual Fabrication Applications." *InfraMation* . 2004.

Cantin, G., and J. Francis. "Arc Power and Efficiency in Gas Tungsten Arc Welding of Aluminium." *Science and Technology of Welding and Joining* 10, no. 2 (2005): 200-210.

CEN/TR14599(E/F/D). Terms and Definitions for Welding Purposes in Relation with EN1972. 2005.

Choi, S., C. Yoo, and Y.-S. Kim. "Dynamic Simulation of Metal Transfer in GMAW Part 1: Globular and Spray Transfer Modes." *Welding Journal* 77, no. 1 (1998 b): 38s-44s.

Choi, S., S. Ko, C. Yoo, and T.-S. Kim. "Dynamic Simulation of Metal Transfer in GMAW - Part 2: Short-Circuit Transfer Mode." *Welding Journal* 77, no. 1 (January 1998 a): 45s-51s.

Choo, R., and J. Szekely. "The Possible Role of Turbulence in GTA Weld Pool Behavior." *Welding Journal* 73, no. 2 (February 1994): 25s-31s.

Choo, R., and J. Szekely. "Vaporization Kinetics and Surface Temperature in a Mutually Coupled Spot Gas Tungsten Arc Weld and Weld Pool." *Welding Journal* 71, no. 3 (March 1992 b): 77s-93s.

Choo, T., J. Szekely, and R. Westhoff. "Modeling of High-Current Arcs with Emphasis on Free Surface Phenomena in the Weld Pool." *Welding Journal* 69, no. 9 (September 1990): 346s-361s.

Christensen, N., and V. and Gjermundsen, K. Davies. "The Distribution of Temperature in Arc Welding." *British Welding Journal* 12, no. 2 (1965): 54-75.

Chu, Y., S. Hu, W. Hou, P. Wang, and S. Marin. "Signature Analysis for Quality Monitoring in Short-Circuit GMAW." *Welding Journal*, 2004: 336s-343s.

Clark, D., C. Buhrmaster, and H. Smartt. *2nd Int. Conf. on Trends in Welding Research*. Gatlinburg, US: ASM International, 1989. 371-375.

Collard, J. "Adaptative Pulsed GMAW Control: The Digipulse System." *Welding Journal*, November 1988: 35-38.

Cornot-Ganolphe, Sylvie, Olivier Appert, Marie-Francoise Chabrelie Ralf Dickel, and Alexandre Rojey. "The Challenges of Further Cost Reductions for New Supply Options (Pipeline, LNG, GTL)." *22nd World Gas Conference* . Tokyo, 2003.

Costa, M., C. Starling, and P. Modenesi. "Low Oxidation Potential Shielding Gas Instability in GMA Welding." *Science and Technology of Welding and Joining* 14 (2009): 42-51.

Cumino, G., A. Poli, T. Ono, S. Hashizume, K. Yamazaki, and L. Scoppio. "Supermartensitic 13% Cr Large Diameter Seamless Pipes: Mechanical, Corrosion and Weldability Properties." *Lat. Am. Appl. Res.* 32, no. 3 (July 2002): 215-219.

Dantas, M, and S. Costa. "Uma Contribuição ao Estudo da Influência dos Parâmetros de Pulso na Qualidade da Solda em um Processo MIG-MAG Pulsado através da Técnica DOE." *XXIV Encontro Nacional de Engenharia de Produção*. Florianópolis, SC, Brasil: (In Portuguese Language), 2004. 561-568.

Dean, G., J Norrish, and C. Cook. "Effective Heat Input in Dip Transfer Gas Metal Arc Welding." *Welding Research Supplement*, 2006: 39-48.

DeRuntz, Bruce. "Assessing the Benefits of Surface Tension Transfer for Welding Industry." *Journal of Industrial Technology* 19, no. 4 (2003).

Design Expert Software. Version 7 user's guide, Minneapolis, MI: Stat-Ease Inc., 2006.

Dillenbeck, V., and L. Castagno. "The Effects of Various Shielding Gases and Associated Mixtures in GMA Welding of Mild Steel." *Welding Journal*, September 1987: 45-49.

DragonLNG. *DragonLNG - Energy for Wales*. 2008. <http://www.dragonlng.co.uk/whyislngneededin.cfm> (accessed May 127, 2009).

Dutta, P., Y. Joshi, and C. Franche. "Determination of Gss Tungsten Arc Welding Efficiencies." *Experimental Thermal and Fluid Science* 9 (1994): 80-89.

Eagar, T. "Oxygen and Nitrogen Contamination." *Proc. of Weldments: Physical Metallurgy and Failure Phenomena*. Bolton Landing, Lake George, US, 1978.

—. "Physics of Arc Welding." *Conference of Physiscs in the Steel Industry*. Bethlehem: AIP/AISI, 1981.

—. "The Physics of Arc Welding Processes." *Advanced Joining Technologies*. Chapman and Hall, London, UK: T.H. North, ed., 1990.

Eagar, T., and N.-S. Tsai. "Temperature Fields Produced by Travelling Distributed Heat Sources." *Welding Journal* 62, no. 12 (December 1983): 346s-355s.

Egerland, S. *Investigations on the Influence of Joint Geometry on the Efficiency of Gas Shielded Metal Arc Welding by Using Solid State Calorimetry*. Design Project, Msc Course, Cranfield University, 2009.

Essers, W., and R. Walter. "Heat Transfer and Penetration Mechanisms with GMAW and Plasma-GMA Welding." *Welding Journal* 60, no. 2 (February 1981): 37s-42s.

EWI ; Navy Joining Center. *Titanium Weld Color Inspection Kit -Part 1: Technology Guide*. Technical Report, Ohio, US: EWI, 2000-2001.

Feng, J., H. Zhang, and P. He. "The CMT Short-circuiting Metal Transfer Process and its Use in Thin Aluminium Sheets Welding." *Materials and Design* 30, no. 5 (2008): 1850-1852.

Friedman, E. "Analysis of Weld Ouddle Distortion and its Effect on Penetration." *Welding Journal* 56, no. 6 (1978): 161s-166s.

Friedman, E., and S. Glickstein. "An Investigation of the Thermal Response of Stationary Gas Tungsten Arc Welds." *Welding Journal* 55, no. 12 (December 1976): 408s-420s.

Fronius. *CMT: Cold Metal Transfer*. Technical Report, Austria: Fronius International GmbH, 2005.

Fuerschbach, W., and G. Knorovsky. "A Study of Melting Efficiency in Plasma Arc and Gas Tungsten Arc Welding." *Welding Journal* 70, no. 1 (January 1991): 287s-297s.

Fulmer, B. *Rapid Arc - Welding Guidelines*. Technical Report by Application Engineering, Cleveland OH, USA: The Lincoln Electric Company, 2004.

Giedt, W., L. Tallerico, and P. Fuerschbach. "GTA Welding Efficiency: Calorimetric and Temperature Field Measurements." *Welding Journal* 68, no. 1 (January 1989): 28s-32s.

Glickstein, S. "Temperature Measurements in a Free Burning Arc." *Welding Journal* 55, no. 8 (August 1976): 222s-229s.

Glickstein, S., and E. Friedman. "Weld Modeling Applications." *Welding Journal* 63, no. 9 (September 1984): 38-42.

Goncalves, C., L. Vilarinho, A. Scotti, and G. Guimaraes. "Estimation of Heat Source and Thermal Efficiency in GTAW Proces by Using Inverse Techniques." *Journal of Materials Processing Technology* 172 (2006): 42-51.

Gower, Stephen, and Mark Howard. "Changing Economics of Gas Transportation." *22nd World Gas Conference*. Tokyo, 2003.

Goyal, V., P. Ghosh, and J. Saini. "Analytical Studies on Thermal Behaviour and Geometry of Weld Pool in Pulsed Current Gas Metal Arc Welding." *Journal of Materials Processing Technology* 209 (2009): 1318-1336.

Gratzket, U., P. Kapadiat, J. Dowdent, and J. Simons, G. Krooss. "Theoretical Approach of the Humping Phenomenon in Welding Processes." *J. Phys. D: Appl. Phys.* 25 (1992): 1640-1647.

Greene, W. "An Analysis of Transfer in Gas-Shielded Welding Arcs." *Trans. AIEE Part. 2* 79, no. 7 (1960): 194-203.

Haidar, J., and J. Lowke. "Predictions of Metal Droplet Formation in Arc Welding." *Journal of Physics. D: Applied Phisics* 29 (1996): 2951-2960.

Halmoy, E., H. Olsen, and S. Samuelsen. "Adaptively Controlled MIG Narrow Gap Welding." *Developments and Innovations for Improved Welding Production - 1st International Conference*. Birmingham, UK, 1983. 13-15.

Han, Z., J. Orozco, J. Indacpchea, and C. Chen. "Resistance Spot Welding: A Heat Transfer Study." *Welding Journal* 68, no. 9 (September 1989): 363s-371s.

Hansen, J. *Reference Colour Charts - for Purity of Purging Gas in Stainless Steel Tubes*. Technical Report 94.34, Copenhagen: Force Institute, 1994.

Hazlett, T., and G. Gordon. "Studies of Welding Arcs Using Various Atmospheres and Power Supplies." *Welding Journal* 36 (1957): 382s-386s.

Heald, P., R. Madigan, T. Siewert, and S. Liu. "Mapping the Droplet Transfer Modes for an ER100S-1 GMAW Electrode." *Welding Journal* 73, no. 2 (1994): 38s-44s.

Heiple, C., and J. Roper. "Mechanism for Minor Element Effect on GTA Fusion Zone Geometry." *Welding Journal* 61, no. 4 (April 1982): 97s-102s.

Hermans, M., and G. Ouden. "Process Behaviour and Stability in Short-Circuit Gas Metal Arc Welding." *Welding Journal* 78, no. 4 (1999): 137s-141s.

Hilton, D., and J. Norrish. "Shielding Gases for Arc Welding." *Welding and Metal Fabrication*, May/June 1988: 189-196.

Himmelbauer, Karin. "The CMT Process - A Revolution in Welding Technology." *IIW Assembly - Comission XII*. Prague: IIW Doc. XII-1845-05, 2005.

Hiraoka, K., N. Sakuma, and J. Zijp. "Energy Balance in Argon-Helium Mix Gas Tungsten (TIG) Arc - Study of Characteristics of Gass Tungsten Arc Shielded by Mixed Gases (3rd Report)." *Welding International* 12, no. 5 (1998): 372-379.

Hobart Institute of Welding Technology. "What's Ailing that Weld?" *Welding Journal* 76, no. 8 (August 1997): 45-48.

Hsu, C., and P. Soltis. "Heat Input Comparision of STT vs Short-Circuiting and Pulsed GMAW vs CV Processes." *6th International Trends in Welding Research Conference Proceedings*. Pine Mountain, GA: ASM International, 2003.

Huang, T., and D. Yapp. "Synchronised Data Acquisition and Video Imaging of Metal Transfer in Gas Metal Arc Welding." *International Conference on Advances in Welding Technology (ICAWT) - Gas Metal Arc Welding for 21st Century*. Orlando, FL, USA, 2000.

Hudson, Mark. *Welding of X100 Pipeline*. PhD Thesis, Bedfordshire: Cranfield University, 2004.

International Energy Agency. *Resources to Reserves - Oil & Gas Technologies for the Energy Markets of the Future*. Technical Report, France: OECD/ IEA, 2005.

Iordachescu, D., and L. Quintino. "Steps toward a New Classification of Metal Transfer in Gas Metal Arc Welding." *Journal of Materials Processing Technology* 202, no. 1-3 (2007): 391-397.

Ishchenko, Y. "Relationships Governing Droplet Transfer During a Short Circuit." *Welding International* 7, no. 8 (1993): 627-631.

ISO13847. *Petroleum and Natural Gas Industries - Pipeline Transportation Systems - Welding of Pipelines*. 2000.

Jaidi, J., and P. Dutta. "Modeling of Transport Phenomena in a Gas Metal Arc Welding Process." *Numerical Heat Transfer, Part A* 40 (2001): 543-562.

Johnson, J., H. Smartt, N. Carson, and M. Waddoups. *3rd Int. Conf. on Trends in Welding Research*. Gatlinburg, US: ASM International, 1992. 987-991.

Jones, L., P. Mendez, D. Weiss, and T. Eagar. "Dynamic Behavior of Gas Metal Arc Welding." *9th Annual Conference on Iron and Steel Technology*. Pohang, Korea, 1997.

Jones, L., T. Eagar, and J. Lang. "The Temporal Nature of Forces Acting on Metal Drops in Gas Metal Arc Welding." *14th Symposium on Energy Engineering Sciences*. Argonne, IL, USA: Argonne National Laboratory, 1996.

Jonsson, P., A. Murphy, and J. Szekely. "The Influence of Oxygen Additions on Argon-Shielded Gas Metal Arc Welding Processes." *Welding Journal* 74, no. 2 (1995): 48s-58s.

Jonsson, P., T. Eagar, and J. Szekely. "Heat and Metal Transfer in Gas Metal Arc Welding Using Argon and Helium." *Metallurgical and Materials Transactions B* 26B (April 1995): 383-395.

Joseph, A. *Assessing the Effects of GMAW-P Parameters on Arc Power and Weld Heat Input*. MSc Thesis, OH, USA: The Ohio State University, 2001.

Kang, Y., and S. Na. "Characteristics of Welding and Arc Signal in Narrow Groove [narrow gap] Gas Metal Arc Welding using Electromagnetic Arc Oscillation." *Welding Journal* 82, no. 5 (2003).

Karkhin, V., A. Llin, V. Plochikhine, and A. Prikhodovsky. "Effect of Latent Heat on Thermal Efficiency of Base Metal fusing." *IIW Doc. XII -1739-03*. St. Petersburg, Russia: IIW, 2003. 318-327.

Kenney, K., K. Miller, and H. Smartt. "Heat Transfer in Pulsed Gas Metal Arc Welding." *Trends in Welding Research - 5th International Conference*. Pine Mountain, Georgia, USA: AWS, 1998. 357-361.

—. "Heat Transfer in Pulsed Gas Metal Arc Welding." *Trends in Welding Research*. Pine Mountain, Georgia, USA: AWS, 1998.

Kim b, Y.-S., D. McEligot, and T. Eagar. "Analyses of Electrode Heat Transfer in Gas Metal Arc Welding." *Welding Journal* 70, no. 1 (January 1991): 20s-31s.

Kim, I. S., J. Son, I. G. Kim, J. Y. Kim, and O. S. Kim. "A Study on Relationship between Process Variables and Bead Penetration for Robotic Carbon Dioxide Arc Welding." *Journal of Materials Processing Technology* 136 (2003): 139-145.

Kim, J.-W., and S.-J. Na. "A Study on the Effect of Contact Tube-to-Workpiece Distance on Weld Pool Shape in Gas Metal Arc Welding." *Welding Journal* 74, no. 5 (May 1995): 141s-152s.

Kim, Y., and T. Eagar. "Modeling of Metal Transfer in Gas Metal Arc Welding." *Edison Welding Institute Annual North American Research Seminar*. Columbus, OH, USA, 1988.

Kim, Y.-S. *Metal Transfer in Gas Metal Arc Welding*. PhD Thesis, Massachusetts Institute of Technology, 1989.

Kim, Y.-S., Eagar, T. "Temperature Distribution and Energy Balance in the Electrode during GMAW." *Recent Trends in Welding Science and Technology*. OH, USA: AWS, 1990. 13-18.

Kim, Y.-S., McEligot D., and T. Eagar. "Analyses of Electrode Heat Transfer in Gas Metal Arc Welding." *Welding Journal* 70, no. 1 (January 1991): 20s-31s.

Kim, Y-S., and T. Eagar. "Analysis of Metal Transfer in Gas Metal Arc Welding." *Welding Journal*, June 1993 a: 269s-278s.

Kim, Y-S., and T. Eagar. "Metal Transfer in Pulsed Current Gas Metal Arc Welding." *Welding Journal* 72, no. 7 (1993 b): 279s-287s.

Kostrivas, A. *Orbital Welding of Mild Steel Pipelines with Twin Wire GMAW Process*. MSc Thesis, Bedfordshire: Cranfield University, 1995.

Kou b, S., and Y. Le. "Heat Flow during Autogenous GTA Welding of Pipes." *Metallurgical Transactions A* 15A, no. 6 (June 1984): 1165-1171.

Kou, S., and Y. Wang. "Weld Pool Convection and Its Effect." *Welding Journal* 65, no. 3 (March 1986): 63s-70s.

Kvaale, Per Egil, and Stein Olsen. "Experience with Supermartensitic Stainless Steels in Flowline Applications." *Stainless Steel World Conference*. 1999.

- Lancaster, J. "The Physics of Welding." *Phys. Technol.* 15 (1984): 73-79.
- Lauro, A., and M. Mandina. "Welding and Weldability of the Super-austenitic and Super-martensitic Stainless Steels." *Welding International* 17, no. 9 (2003): 710-720.
- Lesnewich, A. "Control of Melting Rate and Metal Transfer in Gas Shielding Metal-Arc Welding Part I - Control of Electrode Melting Rate." (*Welding Journal*) 37, no. 8 (1958): 343s-353s.
- Lesnewich, A. "Control of Melting Rate and Metal Transfer in Gas-Shielded Metal Arc Welding Parte II - Control of Metal Transfer." (*Welding Journal*) 37, no. 9 (1958 b): 418s-425s.
- Lin, M., and T. Eagar. "Influence of Arc Pressure on Weld Pool Geometry." *Welding Journal*, June 1985: 163s-169s.
- Lin, M., and T. Eagar. "Influence of Surface Depression and Convection on Arc Weld Pool Geometry." *Transport Phenomena in Materials Processing, ASME* 10, no. 11 (November 1983): 63-69.
- Lincoln Electric. *Rapid Arc - High Speed GMA Welding*. Technical Report, The Lincoln Electric Company, 2005.
- Lincoln Electric. "Rapid Arc - Welding Guidelines." Technical Report, 2004.
- Lincoln Electric. *Surface Tension Transfer (STT)*. Technical Report, The Lincoln Electric Company, 2006.
- Linnert, G. "Weldability of Austenitic Stainless Steel." *ASTM STP 418*, 1967.
- Liratzis, Theocharis. *Tandem Gas Metal Arc Pipeline Welding*. PhD Thesis, Bedfordshire: Cranfield University, 2007.
- Little, G., and A. Kamtekar. "The Effect of Thermal Properties and Weld Efficiency on Transient Temperatures during Welding." *Computers and Structures* 68 (1998): 157-165.
- Lopes, A. *Arc-Based Sensing in Narrow Groove Pipe Welding*. PhD Thesis, Cranfield, Bedfordshire, UK: Cranfield University, 2006.
- Lu, J., and S. Kou. "Power Inputs in Gas Metal Arc Welding of Aluminum - Part 2." *Welding Journal* 68, no. 11 (November 1989): 452s-456s.
- Lucas, W., and M. Amin. *Metal Construction* 7 (February 1975): 77-83.
- Lucas, W., D. Iordachescu, and V. Ponomarev. "Classification of Metal Transfer Modes in GMAW." *IIW Doc. No XII-1859-05*. Prague, 2005.

Luksa, K. "Influence of Weld Imperfection on Short Circuit GMA Welding Arc Stability." *Journal of Materials Processing Technology* 175 (2006): 285-290.

Ma, J. *Metal Transfer in MIG Welding*. PhD Thesis, Bedfordshire, U.K.: Cranfield Institute of Technology, 1982.

Matz, C. "Shielding Gas: Commodity or Valuable Tool?" *IIW Annual Assembly*. Prague: IIW , 2005. 409-412.

—. "Shielding Gas: Commodity or Valuable Tool?" *57th Annual Assembly of IIW*. Osaka, Japan, 2004. 409-412.

Melfi, T. "What's New with AWS, API, NACE and ASME Specs." *IIW Sub-Commission XI-E "Transmission Pipelines"*. Hammerfest, Norway: IIW XI-E-1037-08, 2008.

Mendez, P., and T. Eagar. "Estimation of the Characteristic Properties of the Weld Pool during High Productivity Arc Welding." *Mathematical Modelling of Weld Phenomena - 5th Edition*. Institute of Materials, London, UK, 2000.

Mendez, P., and T. Eagar. "Penetration and Defect Formation in High-Current Arc Welding." *Welding Journal* 82, no. 10 (October 2003): 296s-306s.

Mendez, P., K. Niece, and T. Eagar. "Humping Formation in High Current GTA Welding." *International Conference on Joining of Advanced and Speciality Materials II*. Cincinnati, OH, USA, November 1999.

Mendez, P., N. Jenkins, and T. Eagar. "Effect of Electrode Droplet Size on Evaporation and Fume Generation in GMAW." *Proceedings of the GMAW for the 21st Century Conference*. Orlando, FL, USA, 2000.

Menzel, M. "The Influence of Individual Components of an Industrial Gas Mixture on the Welding Process and the Properties of Welded Joints." *Welding International* 17, no. 4 (2003): 262-264.

Metcalfe, J., and B. Quigley. "Heat Transfer in Plasma-Arc Welding." *Welding Journal* 54, no. 1 (January 1975): 99s-103s.

Michaleris, P., and A. DeBiccari. "Prediction of Welding Distortion." *Welding Journal*, April 1997: 172s-181s.

Michie, K. *Twin-wire GMAW of Pipeline Girth Welds*. PhD Thesis, Bedfordshire: Cranfield University, 1998.

Miranda, A. B. *Submerged Arc Welding of Weldable 13% Cr Steel for Pipelines*. MSc Thesis, Bedfordshire: Cranfield University, 1996.

Miranda, H., A. Scotti, and V. Ferraresi. "Identification and Control of Metal Transfer in Pulsed GMAW using Optical Sensor." *Science and Technology of Welding Joining* 12, no. 3 (2007): 249-257.

Modenesi, P. *Statistical Modelling of the Narrow Gap Gas Metal Arc Welding Process*. PhD Thesis, Cranfield, Bedfordshire, UK: Cranfield University, 1990.

Modenesi, P., and J. Nixon. *Welding Journal* 73, no. 9 (1994): 218s-224s.

Modenesi, P., C. Starling, and R. Reis. "Wire Melting Phenomena in Gas Metal Arc Welding." *Science and Technology of Welding and Joining* 10, no. 5 (2005): 610-616.

Mohamed, A. H. *Laser root welding and Tandem GMAW on X100 steel*. MSc Thesis, Bedfordshire: Cranfield University, 2005.

Moran, S., and D. Yapp. "The Effect of Welding Parameters on Weld Bead Shape and Size in GMAW." *AWS Annual Convention*. St. Louis, Missouri, USA: AWS, 1998.

Muchuhara, and Yikegami. "A Survey of Possible Welding Defects in Steel Sheets Caused by Shielding Gases in GMAW and Laser Welding." *Welding International* 20, no. 7 (2006): 521-524.

Murray, P., and A. Scotti. "Depth Penetration in Gas Metal Arc Welding." *Science and Technology of Welding and Joining* 4, no. 2 (1999): 112-117.

Nascimento, A., M. Batista, V. Nascimento, and A. Scotti. "Avaliacao dos Metodos de Calculo de Potencia Electrica em Soldagem a Arco e as suas Consequencias sobre as Previsoes Geometricas, Termicas e Metalurgicas da Junta." *Soldagem e Inspeccao* 12, no. 2 (April/June 2007): 97-106.

Nemchinsky, V. "Size and Shape of the Liquid Droplet at the Molten Tip of an Arc Electrode." *Journal of Physics. D: Applied Physics* 27 (1994): 1433-1442.

Nguyen, N., A. Ohta, K. Matsuoka, N. Suzuki, and Y. Maeda. "Analytical Solutions for Transient Temperature of Semi-Infinite Body Subjected to 3D Moving Heat Sources." *Welding Journal* 78, no. 8 (August 1999): 265s-274s.

Nguyen, N., Y.-W., Simpson, S. Mai, and A. Ohta. "Analytical Approximate Solution for Double Ellipsoidal Heat Source in Finite Thick Plate." *Welding Journal* 83, no. 3 (March 2004 b): 82s-93s.

Niles, R., and C. Jackson. "Weld Thermal Efficiency of the GTAW Process." *Welding Journal* 54, no. 1 (January 1975): 25s-32s.

Normand, M., and M. Peleg. "Stefan-Boltzmann Law" from *The Wolfram Demonstrations Project*. 2010. <http://demonstrations.wolfram.com/StefanBoltzmannLaw/> (accessed 2010).

Norrish, J. "A Review of Metal Transfer Classification in Arc Welding." *IIW Doc. No. XII-1769-03*. Bucharest, 2003.

Norrish, J. "What id Synergic MIG?" *Welding and Metal Fabrication*, July 1987: 227-232.

Nunes, JR. "An Extended Rosenthal Weld Model." *Welding Journal* 62, no. 6 (June 1983): 165s-170s.

Oreper, G., T. Eagar, and J. Szekely. "Convection in Arc Weld Pools." *Welding Journal* 62, no. 11 (November 1983): 307s-312s.

Oshima, K., S. Xiang, and S. Yamane. "Effect of Power Source Characteristic on Carbon Dioxide Short Circuiting Arc Welding." *IIW Doc. XII-1793-04*. 2004.

Palani, P., and N. Murugan. "Selection of Parameters of Pulsed Current Gas Metal Arc Welding." *Journal of Materials Processing Technology* 172 (2006): 1-10.

PDCEN/TR14599. Terms and Definitions for Welding Pruposes in relation with EN 1792. Ed. British Standards. 2005.

Pepe, N., and D. Yapp. "Measurement of Process Efficiency for a Range of MIG/MAG Welding Processes." *Computers in Welding*. Cranfield, UK: TWI, 2008.

Perdure, Jeanne. "The evolution of offshore facilities." *E&P*, April 2003.

Pickin, C., and K. Young. "Evaluation of Cold Metal Transfer (CMT) Process for Welding Aluminium Alloy." *Science and Technology of Welding and Joining* 11, no. 4 (2006).

Poloskov, S., Y. Ishchenko, V. Lebedev, and O. Getskin. "Special Features of Controlled Heat and Mass Transfer in Consumable Electrode Welding with Short-circuiting of the Arc Gap." *Welding International* 16, no. 12 (2002): 959-965.

Ponomarev, V., A. Scotti, J. Norrish, and W. Lucas. "Metal Transfer Modes in MIG/MAG (GMAW) Welding: Contributions to a New IIW Classification." *IIW Doc. XII-1960-09*. 2009.

Praveen, P., P. Yarlagadda, and M. Kang. "Advancements in Pulse Gas Metal Arc Weling." *Journal of Materials Processing Technology*, 2005: 1113-1119.

Quinn, T., C. Smith, C. McCowan, E. Bachowiak, and R. Madigan. "Arc Sensing for Defects in Constant-Voltage Gas Metal Arc Wedling." *Welding Journal*, September 1999: 322s-328s.

Quinn, T., R. Madigan, and T. Siewert. "An Electrode Extension Model for Gas Metal Arc Welding." *Welding Journal* 73, no. 10 (October 1994): 241s-248s.

Quintino, L. *Fusion Characteristics in Pulsed GMAW of Mild Steel*. PhD Thesis, Cranfield, Bedfordshire, UK: Cranfield University, 1986.

Quintino, L. *Fusion Characteristics in Pulsed-GMAW of Mild Steel*. PhD Thesis, Cranfield, Bedfordshire, UK: Cranfield University, 1986.

Quintino, L., and C. Allum. "Pulsed GMAW: Interactions between Processes Parameters - Part I." *Welding and Metal Fabrication* 52, no. 2 (March 1984 a): 85-89.

Quintino, L., and C. Allum. "Pulsed GMAW: Interactions between Processes Parameters - Part II." *Welding and Metal Fabrication* 52, no. 3 (April 1984 b): 126-129.

Rajasekaran, S., and S. Kulkarni. "Droplet Detachment and Plate Fusion Characteristics in Pulsed Current Gas Metal Arc Welding." *Welding Journal* 77, no. 6 (June 1998): 254s-269s.

Reutzel, E., C. Einerson, J. Johson, H. Smartt, T. Harmer, and L. Moore. *4th Int. Conf. on Trends in Welding Research*. Gatlinburg, US: ASM International, 1995. 377-384.

Rosenthal, D. "Mathematical Theory of Heat Distribution During Welding and Cutting." *Welding Journal* 20, no. 5 (1941): 220s-234s.

Sagirov, D. "Mechanised Welding with a Short Arc." *Welding International* 20, no. 7 (2006): 577-578.

Schauer, D., W. Giedt, and S. Shintaku. "Electron Beam Welding Cavity Temperature Distributions in Pure Metals and Alloys." *Welding Journal* 57, no. 5 (May 1978): 127s-133s.

Scotti, A. "Mapping Transfer Modes for Stainless Steel Gas Metal Arc Welding." *Science and Technology of Welding and Joining* 5, no. 4 (2000): 227-234.

Scotti, A., and C. Rodrigues. "A Methodology for Determining Kinematic and Dynamic Characteristics of a Transferring Droplet Aiming Modeling Validation of MIG/MAG Welding." *17th International Conference - Computer Technology in Welding and Engineering*. Cranfield, UK: TWI, 2008.

Scotti, A., and V. Ponomarev. *Soldagem MIG/MAG*. Sao Paulo, Brasil: Artliber Editora Lda, 2008.

Scotti, A., U. Larsen, and J. Norrish. "Bead Instability of Mechanized P-MIG Welding in Vertical-up Position." *Proc. Int. Conf. Joining of Materials JOM-5*. Denmark, 1991. 127-134.

Smartt, H. B., J. A. Stewart, and C. J. Einerson. "Heat Transfer in Gas Tungsten Arc Welding." *Proc. ASM Int. Welding Congress*. ASM, 1985.

Smati, Z. "Automatic Pulsed MIG Welding." *Metal Construction*, January 1986: 38R-44R.

Smith, A. *CO₂ Welding of Steel*. Cambridge, U.K.: The Welding Institute, 1966, 21-25.

Soderstrom, E., and P. Mendez. "Humping Mechanisms Present in High Speed Welding." *Science Technology of Welding and Joining* 11, no. 5 (2006): 572-579.

Stava, Elliott, and Peter Nicholson. "New Technology Speeds Oil Sands Pipe Welding." *Pipeline & Gas Journal* 228, no. 12 (December 2001): 37-39.

Stenbacka, N., and K.-A. Persson. "Shielding Gases for Gas Metal Arc Welding." *Welding Journal*, November 1989: 41-47.

Suban, M., and J. Tusek. "Dependence of Melting Rate in MIG/MAG Welding on the Type of Shielding Gas Used." *Journal of Materials Processing Technology* 119 (2001): 185-192.

Subramaniam, S., D. White, D. Scholl, and W. Weber. "In situ Optical Measurement of Liquid Drop Surface Tension in Gas Metal Arc Welding." *Journal of Physics D; Applied Physics* 31 (1998): 1963-1967.

Subramaniam, S., D. White, J. Jones, and D. Lyons. "Experimental Approach to Selection of Pulsing Parameters in Pulsed GMAW." *Welding Journal* 78, no. 5 (May 1999): 166s-172s.

Tsai, N.-S., and T. Eagar. "Changes of Weld Pool Shape by Variations in the Distribution of Heat Source in Arc Welding." *Modelling of Casting and Welding Processes II*. New York, USA: AIME, 1984. 317-328.

Tsao, K., and C. Wu. "Fluid Flow and Heat Transfer in GMA Weld Pools." *Welding Journal* 67, no. 3 (March 1988): 70s-75s.

Tusek, J., and M. Suban. "Experimental Research of the Effect of Hydrogen in Argon as a Shielding Gas in Arc Welding of High Alloy Stainless Steel." *International Journal of Hydrogen Energy* 25 (2000): 369-376.

Tusek, J., F. Markej, J. Barbic, and B. Jez. "Influence of Type of Welded Joint on Welding Efficiency." *Science and Technology of Welding and Joining* 8, no. 3 (2003): 157-164.

Ueguri, S., K. Hara, and H. Komura. "Study of Metal Transfer in Pulsed GMA Welding." *Welding Journal*, August 1985: 242s-250s.

Uttrachu, G. "Gas Waste and Weld Start Quality Issues in Common GMAW Shielding Gas Delivery Systems and Suggested Solution." *IIW*. 2006.

Uusitalo, Jyri. "Modified Short Arc Process - A New Way of Welding Root Passes." *60th Annual Assembly and International Conference*. Dubrovnik & Cavatat, Croatia: Proceedings of the IIW, 2007. 283-289.

Vilarinho, L., A. Costa, and A. Scotti. "A Contribution to Numerical and Experimental Determination of Electrode Temperature and Voltage Drop during GMAW." *Soldagem e Inspeccao* 10, no. 2 (April/June 2005): 92-99.

Vilarinho, L., and A. Scotti. "An Alternate Algorithm for Sinergic Pulsed GMAW of Aluminium." *Aust. Welding Journal* 45 (2000): 36-44.

Wang, H., J. Sun, Y. Wei, and Y. Zheng. "Simulation of GMAW Thermal Process bases on String Heat Source Model." *Science and Technology of Welding and Joining* 10, no. 5 (2005): 511-520.

Waszink, J., and G. Van Den Heuvel. "Heat Generation and Heat Flow in the Filler Metal in GMA Welding." *Welding Journal* 61, no. 8 (August 1982): 269s-282s.

Waszink, J., and L. Graat. "Experimental Investigation of the Forces Acting on a Drop of Weld Metal." *Welding Journal* 62, no. 4 (1983): 109s-116s.

Watkins, A., H. Smartt, and J. Johnson. *3rd Int. Conf. on Trends in Welding Research*. Gatlinburg, US: ASM International, 1992. 993-997.

Wilkinson, J. B., and D. R. Milner. "Heat Transfer from Arcs." *British Welding Journal* 7, no. 2 (1960): 115-128.

Wu, C., M. Chen, and Y. Lu. "Effect of Current Waveforms on Metal Transfer in Pulsed Gas Metal Arc Welding." *Measurement Science and Technology* 16 (2005): 2459-2465.

Wu, Y., and R. Kovacevic. "Mechanically Assisted Droplet Transfer Process in Gas Metal Arc Welding." *Proc Instn Mech Engrs Part B: J. Engineering Manufacture* 216 (2002): 555-564.

Yapp, D., and S. Blackman. "Recent Developments in High Productivity Pipeline Welding." *II Brazillian Manufacturing Congress*. Uberlandia, Brazil, 2003.

Yero, Suleiman. *Welding of Pipelines incorporating the Pressure Balanced Joint™ for J- Lay*. MSc Thesis, Bedfordshire: Cranfield University, 2006.

Yukio, Miyata, Kimura Mitsuo, Tomoya, and Koseki. *Martensitic Stainless Steel Pipe for Linepipe*. Thecnical Report, JFE, 2006.

Zacharia, T., H. Eraslan, and D. Aidun. "Modeling of Autogenous Welding." *Welding Journal* 67, no. 3 (1988 b): 53s-62s.

Zacharia, T., H. Eraslan, and D. Aidun. "Modeling of Non-Autogenous Welding." *Welding Journal* 67, no. 1 (January 1988 a): 18s-27s.

Zhang, H., J. Feng, P. He, B. Zhang, J. Chen, and L. Wang. "The Arc Characteristics and Metal Transfer Behaviour of Cold Metal Transfer and its Use in Joining Aluminium to Zinc-coated Steel." *Materials Science and Engineering A* 499, no. 1-2 (January 2009): 111-113.

Zijp, J. P., and G. Den Ouden. *Proc. Int. Conf. "Advances in Joining and Cutting Processes"*. Harrogate, UK: The Institutue of Welding , 1990. 24-32.

APPENDICES

I. PIPE MATERIAL CHEMICAL ANALYSIS CERTIFICATE

Materials Testing

Bodycote Testing Ltd, Coventry Laboratory, 14 High Marsh, Coventry, Northants, NN11 4EB
 Tel: 01327 700000, Fax: 01327 700001

www.bodycote.com
 www.mt.bodycote.com

Test Certificate

Cranfield University
 Welding Eng Research Centre
 Building 46
 Cranfield University
 Cranfield
 MK43 0AL

REF No D604540 : Issue 1
 Ord No 709708
 Date Tested 07/12/06
 Date Reported 07/12/06

Attn: John Savill

Item _____ - Steel sample Ref: A


Specification - Carbon Steel - No Product Specification Details Available

Chemical Analysis - See Below													
	C [X]	Si [X]	Mn [X]	P [X]	S [X]	Cr [X]	Mo [X]	Ni [X]	Al [X]	Cu [X]	Nb [X]	Comments	
001:	0.010	0.29	0.40	0.013	<0.003	12.1	2.53	6.78	0.03	0.05	<0.01	N11	
	Pb [X]	V [X]	N [X]										Comments
001:	<0.01	0.03	0.006										N11

Certificate Comments

Chemical analysis carried out by a UKAS accredited laboratory
 (No. 0239). Report No. X605755 refers.
 ----- End of Text -----

Tested by Bodycote Chemistry


T. L. SMITH
 AIMMM 1256
 OPERATIONS MANAGER
 For and on authority of
 Bodycote Testing Ltd

This certificate should not be reproduced other than in full, without the written approval of Bodycote Testing Ltd.
 These results pertain only to the sample(s) tested as supplied by the client unless otherwise indicated.
 Unless stated otherwise, testing will have been conducted to the version of any specification quoted, current at the date of test.
 The contents of this report are governed by the terms and conditions overlaid.

Page 1 of 1

II. SETTING PROCESS PARAMETERS APPLIED TO THE BEAD ON PIPE TESTS

The setting process parameters applied to the individual experimental trials are described as follow:

- Wire Feed Speed (WFS);
- Welding Speed (TS);
- WFS/TS Ratio;
- Adjusting Arc Length Parameter (Trim for GMAW-P, RapidArc and STT, Arc Length Correction (ALC) form CMT and CMT-P and Base Current (BC) for FastROOT);
- Adjusting Dynamics Parameter (WaveControl for for GMAW-P, RapidArc and STT, Dynamics Control (DC) for CMT, Pulse Control (PC) for CMT-P and Forming Pulse (FP) for FastROOT);
- Contact Tip to Workpiece Distance (CTWD);
- Shielding Gas composition.

The setting process parameters are presented in different tables according to the waveform and shielding gases applied. The reference was applied with two letters followed by a number. The first letter corresponds to the welding application (i.e., bead on pipe), designated by B, and followed by the initial of the waveform process (e.g. G for GMAW-P, with exception for CMT-P, where “P” was applied).

Table II.1 – Setting parameters applied for GMAW-P, using 2.5%CO₂ 97.5%Ar.

Run	WFS [m/min]	TS [m/min]	WFS/TS Ratio	Trim	Wave Control	Shielding Gas	CTWD [mm]
BG01	4	0.25	16	0.50	10	2.5%CO ₂ 97.5%Ar	11
BG02	4	0.25	16	0.75	10	2.5%CO ₂ 97.5%Ar	11
BG03	4	0.25	16	1.00	10	2.5%CO ₂ 97.5%Ar	11
BG04	4	0.25	16	1.25	10	2.5%CO ₂ 97.5%Ar	11
BG05	4	0.25	16	1.50	10	2.5%CO ₂ 97.5%Ar	11
BG06	6	0.38	16	0.50	10	2.5%CO ₂ 97.5%Ar	11
BG07	6	0.38	16	0.75	10	2.5%CO ₂ 97.5%Ar	11
BG08	6	0.38	16	1.00	10	2.5%CO ₂ 97.5%Ar	11
BG09	6	0.38	16	1.25	10	2.5%CO ₂ 97.5%Ar	11
BG10	6	0.38	16	1.50	10	2.5%CO ₂ 97.5%Ar	11
BG11	8	0.50	16	0.50	10	2.5%CO ₂ 97.5%Ar	11
BG12	8	0.50	16	0.75	10	2.5%CO ₂ 97.5%Ar	11
BG13	8	0.50	16	1.00	10	2.5%CO ₂ 97.5%Ar	11
BG14	8	0.50	16	1.25	10	2.5%CO ₂ 97.5%Ar	11
BG15	8	0.50	16	1.50	10	2.5%CO ₂ 97.5%Ar	11
BG16	10	0.63	16	0.50	10	2.5%CO ₂ 97.5%Ar	11
BG17	10	0.63	16	0.75	10	2.5%CO ₂ 97.5%Ar	11
BG18	10	0.63	16	1.00	10	2.5%CO ₂ 97.5%Ar	11
BG19	10	0.63	16	1.25	10	2.5%CO ₂ 97.5%Ar	11
BG20	10	0.63	16	1.50	10	2.5%CO ₂ 97.5%Ar	11
BG21	4	0.22	18	1.5	10	2.5%CO ₂ 97.5%Ar	11
BG22	6	0.33	18	1.5	10	2.5%CO ₂ 97.5%Ar	11
BG23	8	0.44	18	1.5	10	2.5%CO ₂ 97.5%Ar	11
BG24	10	0.56	18	1.5	10	2.5%CO ₂ 97.5%Ar	11
BG25	4	0.25	16	1.5	10	2.5%CO ₂ 97.5%Ar	13.5
BG26	6	0.38	16	1.5	10	2.5%CO ₂ 97.5%Ar	13.5
BG27	8	0.50	16	1.5	10	2.5%CO ₂ 97.5%Ar	13.5
BG28	10	0.63	16	1.5	10	2.5%CO ₂ 97.5%Ar	13.5
BG29	4	0.25	16	1.5	10	2.5%CO ₂ 97.5%Ar	16
BG30	6	0.38	16	1.5	10	2.5%CO ₂ 97.5%Ar	16
BG31	8	0.50	16	1.5	10	2.5%CO ₂ 97.5%Ar	16
BG32	10	0.63	16	1.5	10	2.5%CO ₂ 97.5%Ar	16

Table II.2 – Setting parameters applied for GMAW-P, using 1.5%CO₂ 54%He 44.5%Ar.

Run	WFS [m/min]	TS [m/min]	WFS/TS Ratio	Trim	Wavecontrol	Shielding Gas	CTWD [mm]
BG33	4	0.25	16	0.50	10	1.5%CO ₂ 54%He 44.5%Ar	11
BG34	4	0.25	16	0.75	10	1.5%CO ₂ 54%He 44.5%Ar	11
BG35	4	0.25	16	1.00	10	1.5%CO ₂ 54%He 44.5%Ar	11
BG36	4	0.25	16	1.25	10	1.5%CO ₂ 54%He 44.5%Ar	11
BG37	4	0.25	16	1.50	10	1.5%CO ₂ 54%He 44.5%Ar	11
BG38	6	0.38	16	0.50	10	1.5%CO ₂ 54%He 44.5%Ar	11
BG39	6	0.38	16	0.75	10	1.5%CO ₂ 54%He 44.5%Ar	11
BG40	6	0.38	16	1.00	10	1.5%CO ₂ 54%He 44.5%Ar	11
BG41	6	0.38	16	1.25	10	1.5%CO ₂ 54%He 44.5%Ar	11
BG42	6	0.38	16	1.50	10	1.5%CO ₂ 54%He 44.5%Ar	11
BG43	8	0.50	16	0.50	10	1.5%CO ₂ 54%He 44.5%Ar	11
BG44	8	0.50	16	0.75	10	1.5%CO ₂ 54%He 44.5%Ar	11
BG45	8	0.50	16	1.00	10	1.5%CO ₂ 54%He 44.5%Ar	11
BG46	8	0.50	16	1.25	10	1.5%CO ₂ 54%He 44.5%Ar	11
BG47	8	0.50	16	1.50	10	1.5%CO ₂ 54%He 44.5%Ar	11
BG48	10	0.63	16	0.50	10	1.5%CO ₂ 54%He 44.5%Ar	11
BG49	10	0.63	16	0.75	10	1.5%CO ₂ 54%He 44.5%Ar	11
BG50	10	0.63	16	1.00	10	1.5%CO ₂ 54%He 44.5%Ar	11
BG51	10	0.63	16	1.25	10	1.5%CO ₂ 54%He 44.5%Ar	11
BG52	10	0.63	16	1.50	10	1.5%CO ₂ 54%He 44.5%Ar	11
BG53	4	0.22	18	1.5	10	1.5%CO ₂ 54%He 44.5%Ar	11
BG54	6	0.33	18	1.5	10	1.5%CO ₂ 54%He 44.5%Ar	11
BG55	8	0.44	18	1.5	10	1.5%CO ₂ 54%He 44.5%Ar	11
BG56	10	0.56	18	1.5	10	1.5%CO ₂ 54%He 44.5%Ar	11
BG57	4	0.25	16	1.5	10	1.5%CO ₂ 54%He 44.5%Ar	13.5
BG58	6	0.38	16	1.5	10	1.5%CO ₂ 54%He 44.5%Ar	13.5
BG59	8	0.50	16	1.5	10	1.5%CO ₂ 54%He 44.5%Ar	13.5
BG60	10	0.63	16	1.5	10	1.5%CO ₂ 54%He 44.5%Ar	13.5
BG61	4	0.25	16	1.5	10	1.5%CO ₂ 54%He 44.5%Ar	16
BG62	6	0.38	16	1.5	10	1.5%CO ₂ 54%He 44.5%Ar	16
BG63	8	0.50	16	1.5	10	1.5%CO ₂ 54%He 44.5%Ar	16
BG64	10	0.63	16	1.5	10	1.5%CO ₂ 54%He 44.5%Ar	16

Table II.3 – Setting parameters applied for RapidArc, using 2.5%CO₂ 97.5%Ar.

Run	WFS [m/min]	TS [m/min]	WFS/TS Ratio	Trim	Wave Control	Shielding Gas	CTWD [mm]
BR01	4	0.25	16	0.50	10	2.5%CO ₂ 97.5%Ar	11
BR02	4	0.25	16	0.75	10	2.5%CO ₂ 97.5%Ar	11
BR03	4	0.25	16	1.00	10	2.5%CO ₂ 97.5%Ar	11
BR04	4	0.25	16	1.25	10	2.5%CO ₂ 97.5%Ar	11
BR05	4	0.25	16	1.50	10	2.5%CO ₂ 97.5%Ar	11
BR06	6	0.38	16	0.50	10	2.5%CO ₂ 97.5%Ar	11
BR07	6	0.38	16	0.75	10	2.5%CO ₂ 97.5%Ar	11
BR08	6	0.38	16	1.00	10	2.5%CO ₂ 97.5%Ar	11
BR09	6	0.38	16	1.25	10	2.5%CO ₂ 97.5%Ar	11
BR10	6	0.38	16	1.50	10	2.5%CO ₂ 97.5%Ar	11
BR11	8	0.50	16	0.50	10	2.5%CO ₂ 97.5%Ar	11
BR12	8	0.50	16	0.75	10	2.5%CO ₂ 97.5%Ar	11
BR13	8	0.50	16	1.00	10	2.5%CO ₂ 97.5%Ar	11
BR14	8	0.50	16	1.25	10	2.5%CO ₂ 97.5%Ar	11
BR15	8	0.50	16	1.50	10	2.5%CO ₂ 97.5%Ar	11
BR16	10	0.63	16	0.50	10	2.5%CO ₂ 97.5%Ar	11
BR17	10	0.63	16	0.75	10	2.5%CO ₂ 97.5%Ar	11
BR18	10	0.63	16	1.00	10	2.5%CO ₂ 97.5%Ar	11
BR19	10	0.63	16	1.25	10	2.5%CO ₂ 97.5%Ar	11
BR20	10	0.63	16	1.50	10	2.5%CO ₂ 97.5%Ar	11
BR21	4	0.22	18	1.5	10	2.5%CO ₂ 97.5%Ar	11
BR22	6	0.33	18	1.5	10	2.5%CO ₂ 97.5%Ar	11
BR23	8	0.44	18	1.5	10	2.5%CO ₂ 97.5%Ar	11
BR24	9	0.50	18	1.5	10	2.5%CO ₂ 97.5%Ar	11
BR25	10	0.56	18	1.5	10	2.5%CO ₂ 97.5%Ar	11
BR26	12	0.67	18	1.5	10	2.5%CO ₂ 97.5%Ar	11
BR27	14	0.78	18	1.5	10	2.5%CO ₂ 97.5%Ar	11
BR28	18	1.00	18	1.5	10	2.5%CO ₂ 97.5%Ar	11
BR29	4	0.22	16	1.5	10	2.5%CO ₂ 97.5%Ar	13.5
BR30	6	0.33	16	1.5	10	2.5%CO ₂ 97.5%Ar	13.5
BR31	8	0.50	16	1.5	10	2.5%CO ₂ 97.5%Ar	13.5
BR32	10	0.63	16	1.5	10	2.5%CO ₂ 97.5%Ar	13.5
BR33	4	0.22	16	1.5	10	2.5%CO ₂ 97.5%Ar	16
BR34	6	0.33	16	1.5	10	2.5%CO ₂ 97.5%Ar	16
BR35	8	0.50	16	1.5	10	2.5%CO ₂ 97.5%Ar	16
BR36	10	0.63	16	1.5	10	2.5%CO ₂ 97.5%Ar	16

Table II.4 – Setting parameters applied for RapidArc, using 1.5%CO₂ 54%He 44.5%Ar.

Run	WFS [m/min]	TS [m/min]	WFS/TS Ratio	Trim	Wave Control	Shielding Gas	CTWD [mm]
BR37	4	0.25	16	0.50	10	1.5%CO ₂ 54%He 44.5%Ar	11
BR38	4	0.25	16	0.75	10	1.5%CO ₂ 54%He 44.5%Ar	11
BR39	4	0.25	16	1.00	10	1.5%CO ₂ 54%He 44.5%Ar	11
BR40	4	0.25	16	1.25	10	1.5%CO ₂ 54%He 44.5%Ar	11
BR41	4	0.25	16	1.50	10	1.5%CO ₂ 54%He 44.5%Ar	11
BR42	6	0.38	16	0.50	10	1.5%CO ₂ 54%He 44.5%Ar	11
BR43	6	0.38	16	0.75	10	1.5%CO ₂ 54%He 44.5%Ar	11
BR44	6	0.38	16	1.00	10	1.5%CO ₂ 54%He 44.5%Ar	11
BR45	6	0.38	16	1.25	10	1.5%CO ₂ 54%He 44.5%Ar	11
BR46	6	0.38	16	1.50	10	1.5%CO ₂ 54%He 44.5%Ar	11
BR47	8	0.50	16	0.50	10	1.5%CO ₂ 54%He 44.5%Ar	11
BR48	8	0.50	16	0.75	10	1.5%CO ₂ 54%He 44.5%Ar	11
BR49	8	0.50	16	1.00	10	1.5%CO ₂ 54%He 44.5%Ar	11
BR50	8	0.50	16	1.25	10	1.5%CO ₂ 54%He 44.5%Ar	11
BR51	8	0.50	16	1.50	10	1.5%CO ₂ 54%He 44.5%Ar	11
BR52	10	0.63	16	0.50	10	1.5%CO ₂ 54%He 44.5%Ar	11
BR53	10	0.63	16	0.75	10	1.5%CO ₂ 54%He 44.5%Ar	11
BR54	10	0.63	16	1.00	10	1.5%CO ₂ 54%He 44.5%Ar	11
BR55	10	0.63	16	1.25	10	1.5%CO ₂ 54%He 44.5%Ar	11
BR56	10	0.63	16	1.50	10	1.5%CO ₂ 54%He 44.5%Ar	11
BR57	4	0.22	18	1.5	10	1.5%CO ₂ 54%He 44.5%Ar	11
BR58	6	0.33	18	1.5	10	1.5%CO ₂ 54%He 44.5%Ar	11
BR59	8	0.44	18	1.5	10	1.5%CO ₂ 54%He 44.5%Ar	11
BR60	9	0.50	18	1.5	10	1.5%CO ₂ 54%He 44.5%Ar	11
BR61	10	0.56	18	1.5	10	1.5%CO ₂ 54%He 44.5%Ar	11
BR62	12	0.67	18	1.5	10	1.5%CO ₂ 54%He 44.5%Ar	11
BR63	14	0.78	18	1.5	10	1.5%CO ₂ 54%He 44.5%Ar	11
BR64	18	1.00	18	1.5	10	1.5%CO ₂ 54%He 44.5%Ar	11
BR65	4	0.22	16	1.5	10	1.5%CO ₂ 54%He 44.5%Ar	13.5
BR66	6	0.33	16	1.5	10	1.5%CO ₂ 54%He 44.5%Ar	13.5
BR67	8	0.50	16	1.5	10	1.5%CO ₂ 54%He 44.5%Ar	13.5
BR68	10	0.63	16	1.5	10	1.5%CO ₂ 54%He 44.5%Ar	13.5
BR69	4	0.22	16	1.5	10	1.5%CO ₂ 54%He 44.5%Ar	16
BR70	6	0.33	16	1.5	10	1.5%CO ₂ 54%He 44.5%Ar	16
BR71	8	0.50	16	1.5	10	1.5%CO ₂ 54%He 44.5%Ar	16
BR72	10	0.63	16	1.5	10	1.5%CO ₂ 54%He 44.5%Ar	16

Table II.5 – Setting parameters applied for STT, using 2.5%CO₂ 97.5%Ar.

Run	WFS [m/min]	TS [m/min]	WFS/TS Ratio	Trim	Wavecontrol	Shielding Gas	CTWD [mm]
BS01	3	0.19	16	0.50	10	2.5%CO ₂ 97.5%Ar	11
BS02	3	0.19	16	0.75	10	2.5%CO ₂ 97.5%Ar	11
BS03	3	0.19	16	1.00	10	2.5%CO ₂ 97.5%Ar	11
BS04	3	0.19	16	1.25	10	2.5%CO ₂ 97.5%Ar	11
BS05	3	0.19	16	1.50	10	2.5%CO ₂ 97.5%Ar	11
BS06	6	0.38	16	0.50	10	2.5%CO ₂ 97.5%Ar	11
BS07	6	0.38	16	0.75	10	2.5%CO ₂ 97.5%Ar	11
BS08	6	0.38	16	1.00	10	2.5%CO ₂ 97.5%Ar	11
BS09	6	0.38	16	1.25	10	2.5%CO ₂ 97.5%Ar	11
BS10	6	0.38	16	1.50	10	2.5%CO ₂ 97.5%Ar	11
BS11	8	0.50	16	0.50	10	2.5%CO ₂ 97.5%Ar	11
BS12	8	0.50	16	0.75	10	2.5%CO ₂ 97.5%Ar	11
BS13	8	0.50	16	1.00	10	2.5%CO ₂ 97.5%Ar	11
BS14	8	0.50	16	1.25	10	2.5%CO ₂ 97.5%Ar	11
BS15	8	0.50	16	1.50	10	2.5%CO ₂ 97.5%Ar	11
BS16	8.26	0.52	16	0.50	10	2.5%CO ₂ 97.5%Ar	11
BS17	8.26	0.52	16	0.75	10	2.5%CO ₂ 97.5%Ar	11
BS18	8.26	0.52	16	1.00	10	2.5%CO ₂ 97.5%Ar	11
BS19	8.26	0.52	16	1.25	10	2.5%CO ₂ 97.5%Ar	11
BS20	8.26	0.52	16	1.50	10	2.5%CO ₂ 97.5%Ar	11
BS21	3	0.17	18	1	10	2.5%CO ₂ 97.5%Ar	11
BS22	6	0.33	18	1	10	2.5%CO ₂ 97.5%Ar	11
BS23	8	0.44	18	1	10	2.5%CO ₂ 97.5%Ar	11
BS24	8.26	0.46	18	1	10	2.5%CO ₂ 97.5%Ar	11
BS25	3	0.19	16	1	10	2.5%CO ₂ 97.5%Ar	13.5
BS26	6	0.38	16	1	10	2.5%CO ₂ 97.5%Ar	13.5
BS27	8	0.50	16	1	10	2.5%CO ₂ 97.5%Ar	13.5
BS28	8.26	0.52	16	1	10	2.5%CO ₂ 97.5%Ar	13.5
BS29	3	0.19	16	1	10	2.5%CO ₂ 97.5%Ar	16
BS30	6	0.38	16	1	10	2.5%CO ₂ 97.5%Ar	16
BS31	8	0.50	16	1	10	2.5%CO ₂ 97.5%Ar	16
BS32	8.26	0.52	16	1	10	2.5%CO ₂ 97.5%Ar	16

Table II.6 – Setting parameters applied for STT, using 1.5%CO₂ 54%He 44.5%Ar.

Run	WFS [m/min]	TS [m/min]	WFS/TS Ratio	Trim	Wavecontrol	Shielding Gas	CTWD [mm]
BS33	3	0.19	16	0.50	10	1.5%CO ₂ 54%He 44.5%Ar	11
BS34	3	0.19	16	0.75	10	1.5%CO ₂ 54%He 44.5%Ar	11
BS35	3	0.19	16	1.00	10	1.5%CO ₂ 54%He 44.5%Ar	11
BS36	3	0.19	16	1.25	10	1.5%CO ₂ 54%He 44.5%Ar	11
BS37	3	0.19	16	1.50	10	1.5%CO ₂ 54%He 44.5%Ar	11
BS38	6	0.38	16	0.50	10	1.5%CO ₂ 54%He 44.5%Ar	11
BS39	6	0.38	16	0.75	10	1.5%CO ₂ 54%He 44.5%Ar	11
BS40	6	0.38	16	1.00	10	1.5%CO ₂ 54%He 44.5%Ar	11
BS41	6	0.38	16	1.25	10	1.5%CO ₂ 54%He 44.5%Ar	11
BS42	6	0.38	16	1.50	10	1.5%CO ₂ 54%He 44.5%Ar	11
BS43	8	0.50	16	0.50	10	1.5%CO ₂ 54%He 44.5%Ar	11
BS44	8	0.50	16	0.75	10	1.5%CO ₂ 54%He 44.5%Ar	11
BS45	8	0.50	16	1.00	10	1.5%CO ₂ 54%He 44.5%Ar	11
BS46	8	0.50	16	1.25	10	1.5%CO ₂ 54%He 44.5%Ar	11
BS47	8	0.50	16	1.50	10	1.5%CO ₂ 54%He 44.5%Ar	11
BS48	8.26	0.52	16	0.50	10	1.5%CO ₂ 54%He 44.5%Ar	11
BS49	8.26	0.52	16	0.75	10	1.5%CO ₂ 54%He 44.5%Ar	11
BS50	8.26	0.52	16	1.00	10	1.5%CO ₂ 54%He 44.5%Ar	11
BS51	8.26	0.52	16	1.25	10	1.5%CO ₂ 54%He 44.5%Ar	11
BS52	8.26	0.52	16	1.50	10	1.5%CO ₂ 54%He 44.5%Ar	11
BS53	3	0.17	18	1	10	1.5%CO ₂ 54%He 44.5%Ar	11
BS54	6	0.33	18	1	10	1.5%CO ₂ 54%He 44.5%Ar	11
BS55	8	0.44	18	1	10	1.5%CO ₂ 54%He 44.5%Ar	11
BS56	8.26	0.46	18	1	10	1.5%CO ₂ 54%He 44.5%Ar	11
BS57	3	0.19	16	1	10	1.5%CO ₂ 54%He 44.5%Ar	13.5
BS58	6	0.38	16	1	10	1.5%CO ₂ 54%He 44.5%Ar	13.5
BS59	8	0.50	16	1	10	1.5%CO ₂ 54%He 44.5%Ar	13.5
BS60	8.26	0.52	16	1	10	1.5%CO ₂ 54%He 44.5%Ar	13.5
BS61	3	0.19	16	1	10	1.5%CO ₂ 54%He 44.5%Ar	16
BS62	6	0.38	16	1	10	1.5%CO ₂ 54%He 44.5%Ar	16
BS63	8	0.50	16	1	10	1.5%CO ₂ 54%He 44.5%Ar	16
BS64	8.26	0.52	16	1	10	1.5%CO ₂ 54%He 44.5%Ar	16

Table II.7 – Setting parameters applied for CMT, using 2.5%CO₂ 97.5%Ar.

Run	WFS [m/min]	TS [m/min]	WFS/TS Ratio	ALC [%]	DC [%]	Shielding Gas	CTWD [mm]
BC01	3	0.19	16	-30	0	2.5%CO ₂ 97.5%Ar	11
BC02	3	0.19	16	-15	0	2.5%CO ₂ 97.5%Ar	11
BC03	3	0.19	16	0	0	2.5%CO ₂ 97.5%Ar	11
BC04	3	0.19	16	15	0	2.5%CO ₂ 97.5%Ar	11
BC05	3	0.19	16	30	0	2.5%CO ₂ 97.5%Ar	11
BC06	4	0.25	16	-30	0	2.5%CO ₂ 97.5%Ar	11
BC07	4	0.25	16	-15	0	2.5%CO ₂ 97.5%Ar	11
BC08	4	0.25	16	0	0	2.5%CO ₂ 97.5%Ar	11
BC09	4	0.25	16	15	0	2.5%CO ₂ 97.5%Ar	11
BC10	4	0.25	16	30	0	2.5%CO ₂ 97.5%Ar	11
BC11	6	0.38	16	-30	0	2.5%CO ₂ 97.5%Ar	11
BC12	6	0.38	16	-15	0	2.5%CO ₂ 97.5%Ar	11
BC13	6	0.38	16	0	0	2.5%CO ₂ 97.5%Ar	11
BC14	6	0.38	16	15	0	2.5%CO ₂ 97.5%Ar	11
BC15	6	0.38	16	30	0	2.5%CO ₂ 97.5%Ar	11
BC16	8	0.50	16	-30	0	2.5%CO ₂ 97.5%Ar	11
BC17	8	0.50	16	-15	0	2.5%CO ₂ 97.5%Ar	11
BC18	8	0.50	16	0	0	2.5%CO ₂ 97.5%Ar	11
BC19	8	0.50	16	15	0	2.5%CO ₂ 97.5%Ar	11
BC20	8	0.50	16	30	0	2.5%CO ₂ 97.5%Ar	11
BC21	3	0.19	16	0	-5	2.5%CO ₂ 97.5%Ar	11
BC22	3	0.19	16	0	-2.5	2.5%CO ₂ 97.5%Ar	11
BC23	3	0.19	16	0	2.5	2.5%CO ₂ 97.5%Ar	11
BC24	3	0.19	16	0	5	2.5%CO ₂ 97.5%Ar	11
BC25	4	0.25	16	0	-5	2.5%CO ₂ 97.5%Ar	11
BC26	4	0.25	16	0	-2.5	2.5%CO ₂ 97.5%Ar	11
BC27	4	0.25	16	0	2.5	2.5%CO ₂ 97.5%Ar	11
BC28	4	0.25	16	0	5	2.5%CO ₂ 97.5%Ar	11
BC29	6	0.38	16	0	-5	2.5%CO ₂ 97.5%Ar	11
BC30	6	0.38	16	0	-2.5	2.5%CO ₂ 97.5%Ar	11
BC31	6	0.38	16	0	2.5	2.5%CO ₂ 97.5%Ar	11
BC32	6	0.38	16	0	5	2.5%CO ₂ 97.5%Ar	11
BC33	8	0.50	16	0	-5	2.5%CO ₂ 97.5%Ar	11
BC34	8	0.50	16	0	-2.5	2.5%CO ₂ 97.5%Ar	11
BC35	8	0.50	16	0	2.5	2.5%CO ₂ 97.5%Ar	11
BC36	8	0.50	16	0	5	2.5%CO ₂ 97.5%Ar	11
BC37	3	0.17	18	0	0	2.5%CO ₂ 97.5%Ar	11
BC38	4	0.22	18	0	0	2.5%CO ₂ 97.5%Ar	11
BC39	6	0.33	18	0	0	2.5%CO ₂ 97.5%Ar	11
BC40	8	0.44	18	0	0	2.5%CO ₂ 97.5%Ar	11
BC41	3	0.19	16	0	0	2.5%CO ₂ 97.5%Ar	13.5
BC42	4	0.25	16	0	0	2.5%CO ₂ 97.5%Ar	13.5
BC43	6	0.38	16	0	0	2.5%CO ₂ 97.5%Ar	13.5
BC44	8	0.50	16	0	0	2.5%CO ₂ 97.5%Ar	13.5
BC45	3	0.19	16	0	0	2.5%CO ₂ 97.5%Ar	16
BC46	4	0.25	16	0	0	2.5%CO ₂ 97.5%Ar	16
BC47	6	0.38	16	0	0	2.5%CO ₂ 97.5%Ar	16
BC48	8	0.50	16	0	0	2.5%CO ₂ 97.5%Ar	16

Table II.8 – Setting parameters applied for CMT, using 1.5%CO₂, 54%He 44.5%Ar.

Run	WFS [m/min]	TS [m/min]	WFS/TS Ratio	ALC [%]	DC [%]	Shielding Gas	CTWD [mm]
BC49	3	0.19	16	-30	0	1.5%CO ₂ 54%He 44.5%Ar	11
BC50	3	0.19	16	-15	0	1.5%CO ₂ 54%He 44.5%Ar	11
BC51	3	0.19	16	0	0	1.5%CO ₂ 54%He 44.5%Ar	11
BC52	3	0.19	16	15	0	1.5%CO ₂ 54%He 44.5%Ar	11
BC53	3	0.19	16	30	0	1.5%CO ₂ 54%He 44.5%Ar	11
BC54	4	0.25	16	-30	0	1.5%CO ₂ 54%He 44.5%Ar	11
BC55	4	0.25	16	-15	0	1.5%CO ₂ 54%He 44.5%Ar	11
BC56	4	0.25	16	0	0	1.5%CO ₂ 54%He 44.5%Ar	11
BC57	4	0.25	16	15	0	1.5%CO ₂ 54%He 44.5%Ar	11
BC58	4	0.25	16	30	0	1.5%CO ₂ 54%He 44.5%Ar	11
BC59	6	0.38	16	-30	0	1.5%CO ₂ 54%He 44.5%Ar	11
BC60	6	0.38	16	-15	0	1.5%CO ₂ 54%He 44.5%Ar	11
BC61	6	0.38	16	0	0	1.5%CO ₂ 54%He 44.5%Ar	11
BC62	6	0.38	16	15	0	1.5%CO ₂ 54%He 44.5%Ar	11
BC63	6	0.38	16	30	0	1.5%CO ₂ 54%He 44.5%Ar	11
BC64	8	0.50	16	-30	0	1.5%CO ₂ 54%He 44.5%Ar	11
BC65	8	0.50	16	-15	0	1.5%CO ₂ 54%He 44.5%Ar	11
BC66	8	0.50	16	0	0	1.5%CO ₂ 54%He 44.5%Ar	11
BC67	8	0.50	16	15	0	1.5%CO ₂ 54%He 44.5%Ar	11
BC68	8	0.50	16	30	0	1.5%CO ₂ 54%He 44.5%Ar	11
BC69	3	0.19	16	0	-5	1.5%CO ₂ 54%He 44.5%Ar	11
BC70	3	0.19	16	0	-2.5	1.5%CO ₂ 54%He 44.5%Ar	11
BC71	3	0.19	16	0	2.5	1.5%CO ₂ 54%He 44.5%Ar	11
BC72	3	0.19	16	0	5	1.5%CO ₂ 54%He 44.5%Ar	11
BC73	4	0.25	16	0	-5	1.5%CO ₂ 54%He 44.5%Ar	11
BC74	4	0.25	16	0	-2.5	1.5%CO ₂ 54%He 44.5%Ar	11
BC75	4	0.25	16	0	2.5	1.5%CO ₂ 54%He 44.5%Ar	11
BC76	4	0.25	16	0	5	1.5%CO ₂ 54%He 44.5%Ar	11
BC77	6	0.38	16	0	-5	1.5%CO ₂ 54%He 44.5%Ar	11
BC78	6	0.38	16	0	-2.5	1.5%CO ₂ 54%He 44.5%Ar	11
BC79	6	0.38	16	0	2.5	1.5%CO ₂ 54%He 44.5%Ar	11
BC80	6	0.38	16	0	5	1.5%CO ₂ 54%He 44.5%Ar	11
BC81	8	0.50	16	0	-5	1.5%CO ₂ 54%He 44.5%Ar	11
BC82	8	0.50	16	0	-2.5	1.5%CO ₂ 54%He 44.5%Ar	11
BC83	8	0.50	16	0	2.5	1.5%CO ₂ 54%He 44.5%Ar	11
BC84	8	0.50	16	0	5	1.5%CO ₂ 54%He 44.5%Ar	11
BC85	3	0.17	18	0	0	1.5%CO ₂ 54%He 44.5%Ar	11
BC86	4	0.22	18	0	0	1.5%CO ₂ 54%He 44.5%Ar	11
BC87	6	0.33	18	0	0	1.5%CO ₂ 54%He 44.5%Ar	11
BC88	8	0.44	18	0	0	1.5%CO ₂ 54%He 44.5%Ar	11
BC89	3	0.19	16	0	0	1.5%CO ₂ 54%He 44.5%Ar	13.5
BC90	4	0.25	16	0	0	1.5%CO ₂ 54%He 44.5%Ar	13.5
BC91	6	0.38	16	0	0	1.5%CO ₂ 54%He 44.5%Ar	13.5
BC92	8	0.50	16	0	0	1.5%CO ₂ 54%He 44.5%Ar	13.5
BC93	3	0.19	16	0	0	1.5%CO ₂ 54%He 44.5%Ar	16
BC94	4	0.25	16	0	0	1.5%CO ₂ 54%He 44.5%Ar	16
BC95	6	0.38	16	0	0	1.5%CO ₂ 54%He 44.5%Ar	16
BC96	8	0.50	16	0	0	1.5%CO ₂ 54%He 44.5%Ar	16

Table II.9 – Setting parameters applied for CMT, using 2.5%CO₂ 97.5%Ar.

Run	WFS [m/min]	TS [m/min]	WFS/TS Ratio	ALC [%]	PC [%]	Shielding Gas	CTWD [mm]
BP01	3	0.19	16	-30	0	2.5%CO ₂ 97.5%Ar	11
BP02	3	0.19	16	-15	0	2.5%CO ₂ 97.5%Ar	11
BP03	3	0.19	16	0	0	2.5%CO ₂ 97.5%Ar	11
BP04	3	0.19	16	15	0	2.5%CO ₂ 97.5%Ar	11
BP05	3	0.19	16	30	0	2.5%CO ₂ 97.5%Ar	11
BP06	4	0.25	16	-30	0	2.5%CO ₂ 97.5%Ar	11
BP07	4	0.25	16	-15	0	2.5%CO ₂ 97.5%Ar	11
BP08	4	0.25	16	0	0	2.5%CO ₂ 97.5%Ar	11
BP09	4	0.25	16	15	0	2.5%CO ₂ 97.5%Ar	11
BP10	4	0.25	16	30	0	2.5%CO ₂ 97.5%Ar	11
BP11	6	0.38	16	-30	0	2.5%CO ₂ 97.5%Ar	11
BP12	6	0.38	16	-15	0	2.5%CO ₂ 97.5%Ar	11
BP13	6	0.38	16	0	0	2.5%CO ₂ 97.5%Ar	11
BP14	6	0.38	16	15	0	2.5%CO ₂ 97.5%Ar	11
BP15	6	0.38	16	30	0	2.5%CO ₂ 97.5%Ar	11
BP16	8	0.50	16	-30	0	2.5%CO ₂ 97.5%Ar	11
BP17	8	0.50	16	-15	0	2.5%CO ₂ 97.5%Ar	11
BP18	8	0.50	16	0	0	2.5%CO ₂ 97.5%Ar	11
BP19	8	0.50	16	15	0	2.5%CO ₂ 97.5%Ar	11
BP20	8	0.50	16	30	0	2.5%CO ₂ 97.5%Ar	11
BP21	9	0.56	16	-30	0	2.5%CO ₂ 97.5%Ar	11
BP22	9	0.56	16	-15	0	2.5%CO ₂ 97.5%Ar	11
BP23	9	0.56	16	0	0	2.5%CO ₂ 97.5%Ar	11
BP24	9	0.56	16	15	0	2.5%CO ₂ 97.5%Ar	11
BP25	9	0.56	16	30	0	2.5%CO ₂ 97.5%Ar	11
BP26	10	0.63	16	-30	0	2.5%CO ₂ 97.5%Ar	11
BP27	10	0.63	16	-15	0	2.5%CO ₂ 97.5%Ar	11
BP28	10	0.63	16	0	0	2.5%CO ₂ 97.5%Ar	11
BP29	10	0.63	16	15	0	2.5%CO ₂ 97.5%Ar	11
BP30	10	0.63	16	30	0	2.5%CO ₂ 97.5%Ar	11
BP31	4	0.25	16	0	-5	2.5%CO ₂ 97.5%Ar	11
BP32	4	0.25	16	0	-2.5	2.5%CO ₂ 97.5%Ar	11
BP33	4	0.25	16	0	2.5	2.5%CO ₂ 97.5%Ar	11
BP34	4	0.25	16	0	5	2.5%CO ₂ 97.5%Ar	11
BP35	6	0.38	16	0	-5	2.5%CO ₂ 97.5%Ar	11
BP36	6	0.38	16	0	-2.5	2.5%CO ₂ 97.5%Ar	11
BP37	6	0.38	16	0	2.5	2.5%CO ₂ 97.5%Ar	11
BP38	6	0.38	16	0	5	2.5%CO ₂ 97.5%Ar	11
BP39	8	0.50	16	0	-5	2.5%CO ₂ 97.5%Ar	11
BP40	8	0.50	16	0	-2.5	2.5%CO ₂ 97.5%Ar	11
BP41	8	0.50	16	0	2.5	2.5%CO ₂ 97.5%Ar	11
BP42	8	0.50	16	0	5	2.5%CO ₂ 97.5%Ar	11
BP43	10	0.63	16	0	-5	2.5%CO ₂ 97.5%Ar	11
BP44	10	0.63	16	0	-2.5	2.5%CO ₂ 97.5%Ar	11
BP45	10	0.63	16	0	2.5	2.5%CO ₂ 97.5%Ar	11
BP46	10	0.63	16	0	5	2.5%CO ₂ 97.5%Ar	11
BP47	4	0.22	18	0	0	2.5%CO ₂ 97.5%Ar	11
BP48	6	0.33	18	0	0	2.5%CO ₂ 97.5%Ar	11
BP49	8	0.44	18	0	0	2.5%CO ₂ 97.5%Ar	11
BP50	9	0.50	18	0	0	2.5%CO ₂ 97.5%Ar	11
BP51	10	0.56	18	0	0	2.5%CO ₂ 97.5%Ar	11
BP52	4	0.25	16	0	0	2.5%CO ₂ 97.5%Ar	13.5
BP53	6	0.38	16	0	0	2.5%CO ₂ 97.5%Ar	13.5
BP54	8	0.50	16	0	0	2.5%CO ₂ 97.5%Ar	13.5
BP55	10	0.63	16	0	0	2.5%CO ₂ 97.5%Ar	13.5
BP56	4	0.25	16	0	0	2.5%CO ₂ 97.5%Ar	16
BP57	6	0.38	16	0	0	2.5%CO ₂ 97.5%Ar	16
BP58	8	0.50	16	0	0	2.5%CO ₂ 97.5%Ar	16
BP59	10	0.63	16	0	0	2.5%CO ₂ 97.5%Ar	16

Table II.10 – Setting parameters applied for CMT-P, using 1.5%CO₂ 54%He 44.5%Ar.

Run	WFS [m/min]	TS [m/min]	WFS/TS Ratio	ALC [%]	PC [%]	Shielding Gas	CTWD [mm]
BP60	3	0.19	16	-30	0	1.5%CO ₂ 54%He 44.5%Ar	11
BP61	3	0.19	16	-15	0	1.5%CO ₂ 54%He 44.5%Ar	11
BP62	3	0.19	16	0	0	1.5%CO ₂ 54%He 44.5%Ar	11
BP63	3	0.19	16	15	0	1.5%CO ₂ 54%He 44.5%Ar	11
BP64	3	0.19	16	30	0	1.5%CO ₂ 54%He 44.5%Ar	11
BP65	4	0.25	16	-30	0	1.5%CO ₂ 54%He 44.5%Ar	11
BP66	4	0.25	16	-15	0	1.5%CO ₂ 54%He 44.5%Ar	11
BP67	4	0.25	16	0	0	1.5%CO ₂ 54%He 44.5%Ar	11
BP68	4	0.25	16	15	0	1.5%CO ₂ 54%He 44.5%Ar	11
BP69	4	0.25	16	30	0	1.5%CO ₂ 54%He 44.5%Ar	11
BP70	6	0.38	16	-30	0	1.5%CO ₂ 54%He 44.5%Ar	11
BP71	6	0.38	16	-15	0	1.5%CO ₂ 54%He 44.5%Ar	11
BP72	6	0.38	16	0	0	1.5%CO ₂ 54%He 44.5%Ar	11
BP73	6	0.38	16	15	0	1.5%CO ₂ 54%He 44.5%Ar	11
BP74	6	0.38	16	30	0	1.5%CO ₂ 54%He 44.5%Ar	11
BP75	8	0.50	16	-30	0	1.5%CO ₂ 54%He 44.5%Ar	11
BP76	8	0.50	16	-15	0	1.5%CO ₂ 54%He 44.5%Ar	11
BP77	8	0.50	16	0	0	1.5%CO ₂ 54%He 44.5%Ar	11
BP78	8	0.50	16	15	0	1.5%CO ₂ 54%He 44.5%Ar	11
BP79	8	0.50	16	30	0	1.5%CO ₂ 54%He 44.5%Ar	11
BP80	9	0.56	16	-30	0	1.5%CO ₂ 54%He 44.5%Ar	11
BP81	9	0.56	16	-15	0	1.5%CO ₂ 54%He 44.5%Ar	11
BP82	9	0.56	16	0	0	1.5%CO ₂ 54%He 44.5%Ar	11
BP83	9	0.56	16	15	0	1.5%CO ₂ 54%He 44.5%Ar	11
BP84	9	0.56	16	30	0	1.5%CO ₂ 54%He 44.5%Ar	11
BP85	10	0.63	16	-30	0	1.5%CO ₂ 54%He 44.5%Ar	11
BP86	10	0.63	16	-15	0	1.5%CO ₂ 54%He 44.5%Ar	11
BP87	10	0.63	16	0	0	1.5%CO ₂ 54%He 44.5%Ar	11
BP88	10	0.63	16	15	0	1.5%CO ₂ 54%He 44.5%Ar	11
BP89	10	0.63	16	30	0	1.5%CO ₂ 54%He 44.5%Ar	11
BP90	4	0.25	16	0	-5	1.5%CO ₂ 54%He 44.5%Ar	11
BP91	4	0.25	16	0	-2.5	1.5%CO ₂ 54%He 44.5%Ar	11
BP92	4	0.25	16	0	2.5	1.5%CO ₂ 54%He 44.5%Ar	11
BP93	4	0.25	16	0	5	1.5%CO ₂ 54%He 44.5%Ar	11
BP94	6	0.38	16	0	-5	1.5%CO ₂ 54%He 44.5%Ar	11
BP95	6	0.38	16	0	-2.5	1.5%CO ₂ 54%He 44.5%Ar	11
BP96	6	0.38	16	0	2.5	1.5%CO ₂ 54%He 44.5%Ar	11
BP97	6	0.38	16	0	5	1.5%CO ₂ 54%He 44.5%Ar	11
BP98	8	0.50	16	0	-5	1.5%CO ₂ 54%He 44.5%Ar	11
BP99	8	0.50	16	0	-2.5	1.5%CO ₂ 54%He 44.5%Ar	11
BP100	8	0.50	16	0	2.5	1.5%CO ₂ 54%He 44.5%Ar	11
BP101	8	0.50	16	0	5	1.5%CO ₂ 54%He 44.5%Ar	11
BP102	10	0.63	16	0	-5	1.5%CO ₂ 54%He 44.5%Ar	11
BP103	10	0.63	16	0	-2.5	1.5%CO ₂ 54%He 44.5%Ar	11
BP104	10	0.63	16	0	2.5	1.5%CO ₂ 54%He 44.5%Ar	11
BP105	10	0.63	16	0	5	1.5%CO ₂ 54%He 44.5%Ar	11
BP106	4	0.22	18	0	0	1.5%CO ₂ 54%He 44.5%Ar	11
BP107	6	0.33	18	0	0	1.5%CO ₂ 54%He 44.5%Ar	11
BP108	8	0.44	18	0	0	1.5%CO ₂ 54%He 44.5%Ar	11
BP109	9	0.50	18	0	0	1.5%CO ₂ 54%He 44.5%Ar	11
BP110	10	0.56	18	0	0	1.5%CO ₂ 54%He 44.5%Ar	11
BP111	4	0.25	16	0	0	1.5%CO ₂ 54%He 44.5%Ar	13.5
BP112	6	0.38	16	0	0	1.5%CO ₂ 54%He 44.5%Ar	13.5
BP113	8	0.50	16	0	0	1.5%CO ₂ 54%He 44.5%Ar	13.5
BP114	10	0.63	16	0	0	1.5%CO ₂ 54%He 44.5%Ar	13.5
BP115	4	0.25	16	0	0	1.5%CO ₂ 54%He 44.5%Ar	16
BP116	6	0.38	16	0	0	1.5%CO ₂ 54%He 44.5%Ar	16
BP117	8	0.50	16	0	0	1.5%CO ₂ 54%He 44.5%Ar	16
BP118	10	0.63	16	0	0	1.5%CO ₂ 54%He 44.5%Ar	16

Table II.11 – Setting parameters applied for FastROOT, using 2.5%CO₂ 97.5%Ar.

Run	WFS [m/min]	TS [m/min]	WFS/TS Ratio	BC [%]	FP [%]	Shielding Gas	CTWD [mm]
BF01	4	0.25	16	-50	0	2.5%CO ₂ 97.5%Ar	11
BF02	4	0.25	16	-25	0	2.5%CO ₂ 97.5%Ar	11
BF03	4	0.25	16	0	0	2.5%CO ₂ 97.5%Ar	11
BF04	4	0.25	16	25	0	2.5%CO ₂ 97.5%Ar	11
BF05	4	0.25	16	50	0	2.5%CO ₂ 97.5%Ar	11
BF06	6	0.38	16	-50	0	2.5%CO ₂ 97.5%Ar	11
BF07	6	0.38	16	-25	0	2.5%CO ₂ 97.5%Ar	11
BF08	6	0.38	16	0	0	2.5%CO ₂ 97.5%Ar	11
BF09	6	0.38	16	25	0	2.5%CO ₂ 97.5%Ar	11
BF10	6	0.38	16	50	0	2.5%CO ₂ 97.5%Ar	11
BF11	8	0.50	16	-50	0	2.5%CO ₂ 97.5%Ar	11
BF12	8	0.50	16	-25	0	2.5%CO ₂ 97.5%Ar	11
BF13	8	0.50	16	0	0	2.5%CO ₂ 97.5%Ar	11
BF14	8	0.50	16	25	0	2.5%CO ₂ 97.5%Ar	11
BF15	8	0.50	16	50	0	2.5%CO ₂ 97.5%Ar	11
BF16	9	0.56	16	-50	0	2.5%CO ₂ 97.5%Ar	11
BF17	9	0.56	16	-25	0	2.5%CO ₂ 97.5%Ar	11
BF18	9	0.56	16	0	0	2.5%CO ₂ 97.5%Ar	11
BF19	9	0.56	16	25	0	2.5%CO ₂ 97.5%Ar	11
BF20	9	0.56	16	50	0	2.5%CO ₂ 97.5%Ar	11
BF21	8	0.50	16	0	-30	2.5%CO ₂ 97.5%Ar	11
BF22	8	0.50	16	0	-15	2.5%CO ₂ 97.5%Ar	11
BF23	8	0.50	16	0	15	2.5%CO ₂ 97.5%Ar	11
BF24	8	0.50	16	0	30	2.5%CO ₂ 97.5%Ar	11
BF25	4	0.22	18	0	0	2.5%CO ₂ 97.5%Ar	11
BF26	6	0.33	18	0	0	2.5%CO ₂ 97.5%Ar	11
BF27	8	0.44	18	0	0	2.5%CO ₂ 97.5%Ar	11
BF28	9	0.50	18	0	0	2.5%CO ₂ 97.5%Ar	11
BF29	4	0.25	16	0	0	2.5%CO ₂ 97.5%Ar	13.5
BF30	6	0.38	16	0	0	2.5%CO ₂ 97.5%Ar	13.5
BF31	8	0.50	16	0	0	2.5%CO ₂ 97.5%Ar	13.5
BF32	9	0.56	16	0	0	2.5%CO ₂ 97.5%Ar	13.5
BF33	4	0.25	16	0	0	2.5%CO ₂ 97.5%Ar	16
BF34	6	0.38	16	0	0	2.5%CO ₂ 97.5%Ar	16
BF35	8	0.50	16	0	0	2.5%CO ₂ 97.5%Ar	16
BF36	9	0.56	16	0	0	2.5%CO ₂ 97.5%Ar	16

Table II.12 – Setting parameters applied for FastROOT, using 1.5%CO₂ 54%He 44.5%Ar.

Run	WFS [m/min]	TS [m/min]	WFS/TS Ratio	BC [%]	FP [%]	Shielding Gas	CTWD [mm]
BF37	4	0.25	16	-50	0	1.5%CO ₂ 54%He 44.5%Ar	11
BF38	4	0.25	16	-25	0	1.5%CO ₂ 54%He 44.5%Ar	11
BF39	4	0.25	16	0	0	1.5%CO ₂ 54%He 44.5%Ar	11
BF40	4	0.25	16	25	0	1.5%CO ₂ 54%He 44.5%Ar	11
BF41	4	0.25	16	50	0	1.5%CO ₂ 54%He 44.5%Ar	11
BF42	6	0.38	16	-50	0	1.5%CO ₂ 54%He 44.5%Ar	11
BF43	6	0.38	16	-25	0	1.5%CO ₂ 54%He 44.5%Ar	11
BF44	6	0.38	16	0	0	1.5%CO ₂ 54%He 44.5%Ar	11
BF45	6	0.38	16	25	0	1.5%CO ₂ 54%He 44.5%Ar	11
BF46	6	0.38	16	50	0	1.5%CO ₂ 54%He 44.5%Ar	11
BF47	8	0.50	16	-50	0	1.5%CO ₂ 54%He 44.5%Ar	11
BF48	8	0.50	16	-25	0	1.5%CO ₂ 54%He 44.5%Ar	11
BF49	8	0.50	16	0	0	1.5%CO ₂ 54%He 44.5%Ar	11
BF50	8	0.50	16	25	0	1.5%CO ₂ 54%He 44.5%Ar	11
BF51	8	0.50	16	50	0	1.5%CO ₂ 54%He 44.5%Ar	11
BF52	9	0.56	16	-50	0	1.5%CO ₂ 54%He 44.5%Ar	11
BF53	9	0.56	16	-25	0	1.5%CO ₂ 54%He 44.5%Ar	11
BF54	9	0.56	16	0	0	1.5%CO ₂ 54%He 44.5%Ar	11
BF55	9	0.56	16	25	0	1.5%CO ₂ 54%He 44.5%Ar	11
BF56	9	0.56	16	50	0	1.5%CO ₂ 54%He 44.5%Ar	11
BF57	8	0.50	16	50	-30	1.5%CO ₂ 54%He 44.5%Ar	11
BF58	8	0.50	16	50	-15	1.5%CO ₂ 54%He 44.5%Ar	11
BF59	8	0.50	16	50	15	1.5%CO ₂ 54%He 44.5%Ar	11
BF60	8	0.50	16	50	30	1.5%CO ₂ 54%He 44.5%Ar	11
BF61	4	0.22	18	50	0	1.5%CO ₂ 54%He 44.5%Ar	11
BF62	6	0.33	18	50	0	1.5%CO ₂ 54%He 44.5%Ar	11
BF63	8	0.44	18	50	0	1.5%CO ₂ 54%He 44.5%Ar	11
BF64	9	0.50	18	50	0	1.5%CO ₂ 54%He 44.5%Ar	11
BF65	4	0.25	16	0	0	1.5%CO ₂ 54%He 44.5%Ar	13
BF66	6	0.38	16	0	0	1.5%CO ₂ 54%He 44.5%Ar	13
BF67	8	0.50	16	0	0	1.5%CO ₂ 54%He 44.5%Ar	13
BF68	9	0.56	16	0	0	1.5%CO ₂ 54%He 44.5%Ar	13
BF69	4	0.25	16	0	0	1.5%CO ₂ 54%He 44.5%Ar	16
BF70	6	0.38	16	0	0	1.5%CO ₂ 54%He 44.5%Ar	16
BF71	8	0.50	16	0	0	1.5%CO ₂ 54%He 44.5%Ar	16
BF72	9	0.56	16	0	0	1.5%CO ₂ 54%He 44.5%Ar	16

III. ARC LENGTH MEASUREMENTS FOR THE BEAD ON PIPE TESTS

The tables presented in this section show the arc length measurements obtained for all the welding tests performed. Average, standard deviation, minimum and maximum were measured for the tests performed using same WFS and different arc length adjusting parameter for all the waveforms and at different shielding gases. The values of arc length were determined by the average of several individual measurements obtained from high speed videos recorded for all these tests.

Table III.1 – Arc length measurements obtained for GMAW-P, using 2.5%CO₂ 97.5%Ar.

Run	Arc Length [mm]	Average	Standard Deviation	Minimum	Maximum
BG01	2.08				
BG02	2.12				
BG03	2.20	2.20	0.108	2.08	2.34
BG04	2.28				
BG05	2.34				
BG06	1.61				
BG07	1.95				
BG08	2.22	2.07	0.303	1.61	2.44
BG09	2.44				
BG10	2.15				
BG11	-				
BG12	1.46				
BG13	1.47	2.16	0.803	1.46	3.12
BG14	2.60				
BG15	3.12				
BG16	1.72				
BG17	1.97				
BG18	2.10	2.29	0.764	1.72	3.63
BG19	2.01				
BG20	3.63				
BG21	2.29	-	-	-	-
BG22	2.57	-	-	-	-
BG23	2.85	-	-	-	-
BG24	2.25	-	-	-	-
BG25	2.44	-	-	-	-
BG26	2.86	-	-	-	-
BG27	3.25	-	-	-	-
BG28	2.72	-	-	-	-
BG29	2.49	-	-	-	-
BG30	3.22	-	-	-	-
BG31	4.40	-	-	-	-
BG32	3.80	-	-	-	-

Table III.2 – Arc length measurements obtained for GMAW-P, using 1.5%CO₂, 54%He 44.5%Ar.

Run	Arc Length [mm]	Average	Standard Deviation	Minimum	Maximum
BG33	1.91				
BG34	1.95				
BG35	1.93	1.96	0.0566	1.91	2.05
BG36	1.98				
BG37	2.05				
BG38	1.84				
BG39	1.77				
BG40	2.44	2.22	0.394	1.77	2.66
BG41	2.39				
BG42	2.66				
BG43	1.49				
BG44	1.77				
BG45	2.51	2.28	0.618	1.49	2.91
BG46	2.72				
BG47	2.91				
BG48	1.96				
BG49	2.05				
BG50	2.24	2.29	0.304	1.96	2.67
BG51	2.53				
BG52	2.67				
BG53	2.14	-	-	-	-
BG54	2.66	-	-	-	-
BG55	2.88	-	-	-	-
BG56	2.68	-	-	-	-
BG57	2.76	-	-	-	-
BG58	2.71	-	-	-	-
BG59	2.95	-	-	-	-
BG60	2.88	-	-	-	-
BG61	2.95	-	-	-	-
BG62	3.08	-	-	-	-
BG63	3.68	-	-	-	-
BG64	3.47	-	-	-	-

Table III.3 – Arc length measurements obtained for RapidArc, using 2.5%CO₂, 97.5%Ar.

Run	Arc Length [mm]	Average	Standard Deviation	Minimum	Maximum
BR01	-				
BR02	2.66				
BR03	2.86	3.37	0.865	2.66	4.58
BR04	3.39				
BR05	4.58				
BR06	2.34				
BR07	2.27				
BR08	3.60	3.43	1.11	2.27	4.79
BR09	4.15				
BR10	4.79				
BR11	2.77				
BR12	2.60				
BR13	3.16	3.52	0.979	2.60	4.87
BR14	4.21				
BR15	4.87				
BR16	2.05				
BR17	1.57				
BR18	2.80	2.54	0.694	1.57	3.15
BR19	3.10				
BR20	3.15				
BR21	4.60	-	-	-	-
BR22	5.61	-	-	-	-
BR23	4.69	-	-	-	-
BR24	2.72	-	-	-	-
BR25	2.99	-	-	-	-
BR26	2.08	-	-	-	-
BR27	1.73	-	-	-	-
BR28	0.63	-	-	-	-
BR29	6.94	-	-	-	-
BR30	7.81	-	-	-	-
BR31	5.70	-	-	-	-
BR32	3.57	-	-	-	-
BR33	8.92	-	-	-	-
BR34	9.86	-	-	-	-
BR35	7.07	-	-	-	-
BR36	4.14	-	-	-	-

Table III.4 – Arc length measurements obtained for RapidArc, using 1.5%CO₂, 54%He 44.5%Ar.

Run	Arc Length [mm]	Average	Standard Deviation	Minimum	Maximum
BR37	2.64				
BR38	2.67				
BR39	2.76	3.33	1.16	2.64	5.37
BR40	3.22				
BR41	5.37				
BR42	2.62				
BR43	2.93				
BR44	3.22	3.60	1.01	2.62	5.11
BR45	4.12				
BR46	5.11				
BR47	2.77				
BR48	2.93				
BR49	2.99	3.63	1.03	2.77	5.06
BR50	4.40				
BR51	5.06				
BR52	1.43				
BR53	1.63				
BR54	1.85	2.08	0.649	1.43	2.98
BR55	2.53				
BR56	2.98				
BR57	5.09	-	-	-	-
BR58	5.39	-	-	-	-
BR59	4.87	-	-	-	-
BR60	2.96	-	-	-	-
BR61	2.85	-	-	-	-
BR62	2.46	-	-	-	-
BR63	1.97	-	-	-	-
BR64	0.54	-	-	-	-
BR65	7.12	-	-	-	-
BR66	7.99	-	-	-	-
BR67	6.41	-	-	-	-
BR68	3.82	-	-	-	-
BR69	7.74	-	-	-	-
BR70	8.53	-	-	-	-
BR71	7.21	-	-	-	-
BR72	5.43	-	-	-	-

Table III.5 – Arc length measurements obtained for STT, using 2.5%CO₂, 97.5%Ar

Run	Arc Length [mm]	Average	Standard Deviation	Minimum	Maximum
BS01	1.74				
BS02	2.07				
BS03	2.12	2.20	0.357	1.74	2.68
BS04	2.41				
BS05	2.68				
BS06	1.99				
BS07	2.17				
BS08	2.26	2.28	0.218	1.99	2.52
BS09	2.52				
BS10	2.47				
BS11	1.91				
BS12	2.09				
BS13	2.46	2.35	0.338	1.91	2.74
BS14	2.53				
BS15	2.74				
BS16	1.96				
BS17	2.21				
BS18	2.46	2.41	0.328	1.96	2.79
BS19	2.61				
BS20	2.79				
BS21	2.20	-	-	-	-
BS22	2.22	-	-	-	-
BS23	2.41	-	-	-	-
BS24	2.38	-	-	-	-
BS25	2.36	-	-	-	-
BS26	2.40	-	-	-	-
BS27	2.69	-	-	-	-
BS28	2.86	-	-	-	-
BS29	2.48	-	-	-	-
BS30	2.52	-	-	-	-
BS31	2.71	-	-	-	-
BS32	2.82	-	-	-	-

Table III.6 – Arc length measurements obtained for STT, using 1.5%CO₂, 54%He 44.5%Ar.

Run	Arc Length [mm]	Average	Standard Deviation	Minimum	Maximum
BS33	1.88				
BS34	2.12				
BS35	2.32	2.30	0.318	1.88	2.72
BS36	2.44				
BS37	2.72				
BS38	2.00				
BS39	2.05				
BS40	2.38	2.34	0.313	2.00	2.75
BS41	2.50				
BS42	2.75				
BS43	1.88				
BS44	2.05				
BS45	2.50	2.37	0.387	1.88	2.78
BS46	2.64				
BS47	2.78				
BS48	1.79				
BS49	2.30				
BS50	2.55	2.38	0.361	1.79	2.67
BS51	2.61				
BS52	2.67				
BS53	2.52	-	-	-	-
BS54	2.33	-	-	-	-
BS55	2.48	-	-	-	-
BS56	2.47	-	-	-	-
BS57	2.80	-	-	-	-
BS58	2.47	-	-	-	-
BS59	2.60	-	-	-	-
BS60	2.81	-	-	-	-
BS61	2.58	-	-	-	-
BS62	2.66	-	-	-	-
BS63	2.75	-	-	-	-
BS64	2.91	-	-	-	-

Table III.7 – Arc length measurements obtained for CMT, using 2.5%CO₂ 97.5%Ar.

Run	Arc Length [mm]	Average	Standard Deviation	Minimum	Maximum
BC01	4.14				
BC02	4.20				
BC03	4.44	4.48	0.362	4.14	5.05
BC04	4.55				
BC05	5.05				
BC06	4.27				
BC07	4.30				
BC08	4.56	4.60	0.374	4.27	5.19
BC09	4.70				
BC10	5.19				
BC11	4.65				
BC12	4.81				
BC13	4.79	4.93	0.253	4.65	5.23
BC14	5.16				
BC15	5.23				
BC16	5.16				
BC17	5.27				
BC18	4.72	4.89	0.305	4.60	5.27
BC19	4.69				
BC20	4.60				
BC21	4.54	-	-	-	-
BC22	4.45	-	-	-	-
BC23	4.86	-	-	-	-
BC24	4.58	-	-	-	-
BC25	4.70	-	-	-	-
BC26	4.67	-	-	-	-
BC27	4.65	-	-	-	-
BC28	4.62	-	-	-	-
BC29	5.20	-	-	-	-
BC30	5.33	-	-	-	-
BC31	5.22	-	-	-	-
BC32	5.06	-	-	-	-
BC33	4.20	-	-	-	-
BC34	4.89	-	-	-	-
BC35	4.81	-	-	-	-
BC36	5.03	-	-	-	-
BC37	4.62	-	-	-	-
BC38	4.66	-	-	-	-
BC39	4.71	-	-	-	-
BC40	4.76	-	-	-	-
BC41	4.65	-	-	-	-
BC42	4.76	-	-	-	-
BC43	4.88	-	-	-	-
BC44	4.97	-	-	-	-
BC45	4.80	-	-	-	-
BC46	4.91	-	-	-	-
BC47	4.97	-	-	-	-
BC48	5.08	-	-	-	-

Table III.8 – Arc length measurements obtained for CMT, using 1.5%CO₂, 54%He 44.5%Ar.

Run	Arc Length [mm]	Average	Standard Deviation	Minimum	Maximum
BC49	4.30				
BC50	4.44				
BC51	4.50	4.62	0.330	4.30	5.15
BC52	4.70				
BC53	5.15				
BC54	4.20				
BC55	4.33				
BC56	4.58	4.61	0.404	4.20	5.24
BC57	4.71				
BC58	5.24				
BC59	4.95				
BC60	5.04				
BC61	5.06	5.11	0.144	4.95	5.31
BC62	5.21				
BC63	5.31				
BC64	5.14				
BC65	5.36				
BC66	5.05	5.05	0.238	4.70	5.36
BC67	4.70				
BC68	5.02				
BC69	4.56	-	-	-	-
BC70	4.69	-	-	-	-
BC71	4.75	-	-	-	-
BC72	4.60	-	-	-	-
BC73	5.12	-	-	-	-
BC74	4.78	-	-	-	-
BC75	5.26	-	-	-	-
BC76	4.82	-	-	-	-
BC77	5.49	-	-	-	-
BC78	5.54	-	-	-	-
BC79	5.71	-	-	-	-
BC80	5.51	-	-	-	-
BC81	5.05	-	-	-	-
BC82	5.20	-	-	-	-
BC83	5.01	-	-	-	-
BC84	5.06	-	-	-	-
BC85	4.53	-	-	-	-
BC86	4.43	-	-	-	-
BC87	4.83	-	-	-	-
BC88	4.88	-	-	-	-
BC89	4.70	-	-	-	-
BC90	4.86	-	-	-	-
BC91	5.19	-	-	-	-
BC92	5.38	-	-	-	-
BC93	4.82	-	-	-	-
BC94	4.98	-	-	-	-
BC95	5.26	-	-	-	-
BC96	5.45	-	-	-	-

Table III.9 – Arc length measurements obtained for CMT-P, using 2.5%CO₂ 97.5%Ar.

Run	Arc Length [mm]	Average	Standard Deviation	Minimum	Maximum
BP01	3.26				
BP02	3.41				
BP03	3.62	3.55	0.215	3.26	3.80
BP04	3.80				
BP05	3.67				
BP06	3.82				
BP07	3.87				
BP08	3.81	4.00	0.255	3.81	4.40
BP09	4.40				
BP10	4.12				
BP11	3.70				
BP12	4.02				
BP13	4.65	4.29	0.411	3.70	4.65
BP14	4.52				
BP15	4.55				
BP16	2.81				
BP17	3.73				
BP18	3.97	3.87	0.677	2.81	4.63
BP19	4.20				
BP20	4.63				
BP21	unstable	-	-	-	-
BP22	3.06				
BP23	3.16	4.11	1.16	3.06	5.34
BP24	4.86				
BP25	5.34				
BP26	unstable	-	-	-	-
BP27	unstable	-	-	-	-
BP28	4.29				
BP29	7.58	6.66	2.07	4.29	8.12
BP30	8.12				
BP31	3.70	-	-	-	-
BP32	3.61	-	-	-	-
BP33	4.75	-	-	-	-
BP34	4.72	-	-	-	-
BP35	3.57	-	-	-	-
BP36	3.90	-	-	-	-
BP37	4.17	-	-	-	-
BP38	4.70	-	-	-	-
BP39	3.70	-	-	-	-
BP40	3.81	-	-	-	-
BP41	4.43	-	-	-	-
BP42	4.73	-	-	-	-
BP43	unstable	-	-	-	-
BP44	2.40	-	-	-	-
BP45	4.88	-	-	-	-
BP46	6.38	-	-	-	-
BP47	3.79	-	-	-	-
BP48	4.80	-	-	-	-
BP49	3.89	-	-	-	-
BP50	3.30	-	-	-	-
BP51	4.16	-	-	-	-
BP52	3.94	-	-	-	-
BP53	4.97	-	-	-	-
BP54	4.24	-	-	-	-
BP55	5.63	-	-	-	-
BP56	4.88	-	-	-	-
BP57	5.01	-	-	-	-
BP58	4.72	-	-	-	-
BP59	7.74	-	-	-	-

Table III.10 – Arc length measurements obtained for CMT-P, using 1.5%CO₂, 54%He 44.5%Ar.

Run	Arc Length [mm]	Average	Standard Deviation	Minimum	Maximum
BP60	3.75				
BP61	4.19				
BP62	3.97	4.22	0.430	3.75	4.89
BP63	4.31				
BP64	4.89				
BP65	3.75				
BP66	4.18				
BP67	4.27	4.42	0.580	3.75	5.31
BP68	4.58				
BP69	5.31				
BP70	3.65				
BP71	4.30				
BP72	4.59	4.65	0.775	3.65	5.72
BP73	5.01				
BP74	5.72				
BP75	3.01				
BP76	4.47				
BP77	4.81	4.49	0.870	3.01	5.17
BP78	5.17				
BP79	5.01				
BP80	unstable	-	-	-	-
BP81	3.81				
BP82	3.84	4.58	0.877	3.81	5.50
BP83	5.15				
BP84	5.50				
BP85	unstable	-	-	-	-
BP86	2.68				
BP87	4.83				
BP88	7.94	5.92	2.65	2.68	8.22
BP89	8.22				
BP90	4.50	-	-	-	-
BP91	4.02	-	-	-	-
BP92	5.06	-	-	-	-
BP93	4.80	-	-	-	-
BP94	4.43	-	-	-	-
BP95	4.80	-	-	-	-
BP96	4.99	-	-	-	-
BP97	5.03	-	-	-	-
BP98	3.54	-	-	-	-
BP99	4.50	-	-	-	-
BP100	5.02	-	-	-	-
BP101	5.19	-	-	-	-
BP102	unstable	-	-	-	-
BP103	3.46	-	-	-	-
BP104	6.22	-	-	-	-
BP105	7.73	-	-	-	-
BP106	4.49	-	-	-	-
BP107	4.71	-	-	-	-
BP108	4.90	-	-	-	-
BP109	3.76	-	-	-	-
BP110	4.65	-	-	-	-
BP111	5.00	-	-	-	-
BP112	4.84	-	-	-	-
BP113	4.98	-	-	-	-
BP114	6.85	-	-	-	-
BP115	5.40	-	-	-	-
BP116	5.42	-	-	-	-
BP117	5.51	-	-	-	-
BP118	9.10	-	-	-	-

Table III.11 – Arc length measurements obtained for FastROOT, using 2.5%CO₂ 97.5%Ar.

Run	Arc Length [mm]	Average	Standard Deviation	Minimum	Maximum
BF01	2.59				
BF02	2.34				
BF03	2.26	2.45	0.176	2.26	2.68
BF04	2.40				
BF05	2.68				
BF06	2.40				
BF07	2.58				
BF08	2.32	2.40	0.103	2.32	2.58
BF09	2.35				
BF10	2.36				
BF11	2.30				
BF12	2.22				
BF13	2.28	2.31	0.071	2.22	2.39
BF14	2.39				
BF15	2.38				
BF16	2.13				
BF17	2.00				
BF18	2.16	2.15	0.104	2.00	2.29
BF19	2.29				
BF20	2.19				
BF21	2.16	-	-	-	-
BF22	2.31	-	-	-	-
BF23	2.26	-	-	-	-
BF24	2.19	-	-	-	-
BF25	2.22	-	-	-	-
BF26	2.26	-	-	-	-
BF27	2.17	-	-	-	-
BF28	2.20	-	-	-	-
BF29	2.67	-	-	-	-
BF30	2.53	-	-	-	-
BF31	2.38	-	-	-	-
BF32	2.40	-	-	-	-
BF33	2.71	-	-	-	-
BF34	2.67	-	-	-	-
BF35	2.46	-	-	-	-
BF36	2.64	-	-	-	-

Table III.12 – Arc length measurements obtained for FastROOT, using 1.5%CO₂ 54%He 44.5%Ar.

Run	Arc Length [mm]	Average	Standard Deviation	Minimum	Maximum
BF37	2.67				
BF38	2.47				
BF39	2.55	2.50	0.182	2.20	2.67
BF40	2.60				
BF41	2.20				
BF42	2.35				
BF43	2.59				
BF44	2.49	2.47	0.150	2.29	2.64
BF45	2.64				
BF46	2.29				
BF47	2.24				
BF48	2.60				
BF49	2.20	2.41	0.180	2.20	2.60
BF50	2.48				
BF51	2.53				
BF52	2.40				
BF53	2.48				
BF54	2.36	2.36	0.149	2.11	2.48
BF55	2.11				
BF56	2.47				
BF57	2.23	-	-	-	-
BF58	2.07	-	-	-	-
BF59	2.47	-	-	-	-
BF60	2.53	-	-	-	-
BF61	2.19	-	-	-	-
BF62	2.39	-	-	-	-
BF63	2.47	-	-	-	-
BF64	2.48	-	-	-	-
BF65	2.68	-	-	-	-
BF66	3.21	-	-	-	-
BF67	2.76	-	-	-	-
BF68	2.50	-	-	-	-
BF69	3.18	-	-	-	-
BF70	3.28	-	-	-	-
BF71	2.88	-	-	-	-
BF72	2.79	-	-	-	-

IV. RESULTS OF WAVEFORM CHARACTERISTICS FOR THE BEAD ON PIPE TESTS

The waveform characteristics were defined as the main characteristics obtained from the waveform, and will be described as follow:

- Actual Wire Feed Speed (WFS_{measured});
- Mean Arc Current (I_{mean});
- RMS Arc Current (I_{RMS});
- Mean Arc Voltage (U_{mean});
- RMS Arc Voltage (U_{RMS});
- Average of Instantaneous Arc Power (P_{inst});
- Arc Energy (AE).

The mathematical expressions used to calculate these parameters were already introduced during the dissertation.

Table IV.1 – Waveform characteristics obtained for GMAW-P, using 2.5%CO₂ 97.5%Ar.

Run	WFS set [m/min]	WFS measured [m/min]	U_{mean} [V]	I_{mean} [A]	U_{RMS} [V]	I_{RMS} [A]	P_{inst} [kW]	Arc Energy [kJ/mm]
BG01	4	3.69	14.9	86.7	16.1	135	1.34	0.320
BG02	4	3.74	15.6	78.6	16.6	126	1.30	0.312
BG03	4	3.70	16.6	81.3	18.3	123	1.45	0.349
BG04	4	3.66	16.0	81.6	17.0	125	1.46	0.350
BG05	4	3.71	16.3	87.7	17.6	132	1.49	0.357
BG06	6	5.54	15.0	118	16.2	173	1.81	0.285
BG07	6	5.55	15.6	123	17.0	170	2.06	0.326
BG08	6	5.61	17.7	123	18.7	162	2.46	0.388
BG09	6	5.60	17.9	120	18.8	159	2.42	0.382
BG10	6	5.58	17.4	119	18.5	159	2.34	0.370
BG11	8	7.64	15.4	150	17.2	198	2.47	0.297
BG12	8	7.70	16.2	158	17.6	201	2.67	0.321
BG13	8	7.75	19.6	159	20.7	195	3.53	0.424
BG14	8	7.81	18.6	158	19.9	190	3.40	0.408
BG15	8	7.74	19.1	159	20.3	192	3.45	0.414
BG16	10	9.72	16.3	184	17.7	236	2.73	0.260
BG17	10	9.75	18.1	180	19.5	225	3.15	0.300
BG18	10	9.74	19.2	189	20.6	219	4.06	0.386
BG19	10	9.78	18.4	192	19.9	219	3.97	0.378
BG20	10	9.72	19.1	194	20.4	224	4.02	0.383
BG21	4	3.87	16.1	84.5	17.1	128	1.49	0.406
BG22	6	5.65	18.2	118	19.8	155	2.46	0.446
BG23	8	7.74	20.0	152	21.0	186	3.50	0.478
BG24	10	9.73	19.6	186	21.0	214	4.14	0.443
BG25	4	3.92	16.1	79.3	17.0	120	1.39	0.333
BG26	6	5.69	19.1	109	19.9	151	2.42	0.382
BG27	8	7.62	21.8	146	22.6	184	3.66	0.439
BG28	10	9.73	20.7	175	21.9	207	4.19	0.399
BG29	4	3.90	17.3	71.0	18.1	111	1.44	0.346
BG30	6	5.73	22.2	103	22.8	144	2.71	0.428
BG31	8	7.64	25.3	142	25.8	180	4.04	0.485
BG32	10	9.57	25.5	169	26.0	202	4.75	0.453

Table IV.2 – Waveform characteristics obtained for GMAW-P, using 1.5%CO₂, 54%He 44.5%Ar.

Run	WFS set [m/min]	WFS measured [m/min]	U_{mean} [V]	I_{mean} [A]	U_{RMS} [V]	I_{RMS} [A]	P_{inst} [kW]	Arc Energy [kJ/mm]
BG33	4	3.87	16.7	81.0	18.1	127	1.32	0.316
BG34	4	3.85	17.6	81.8	18.9	131	1.42	0.341
BG35	4	3.76	19.0	79.3	20.1	121	1.58	0.379
BG36	4	3.75	19.0	77.5	20.1	117	1.60	0.385
BG37	4	3.74	19.1	75.3	20.0	119	1.53	0.367
BG38	6	5.59	17.3	120	19.0	167	1.84	0.291
BG39	6	5.58	17.4	115	19.0	159	1.97	0.311
BG40	6	5.67	20.3	118	21.4	157	2.61	0.413
BG41	6	5.66	20.8	117	21.7	157	2.65	0.418
BG42	6	5.60	21.1	115	22.1	154	2.69	0.424
BG43	8	7.65	17.5	153	19.5	199	2.67	0.321
BG44	8	7.60	17.4	151	19.2	196	2.59	0.311
BG45	8	7.64	21.7	154	22.8	188	3.73	0.447
BG46	8	7.64	22.2	153	23.3	188	3.85	0.462
BG47	8	7.61	22.1	156	23.3	190	3.87	0.465
BG48	10	9.65	16.4	182	18.4	220	2.81	0.268
BG49	10	9.74	17.7	183	19.6	219	3.25	0.310
BG50	10	9.75	21.4	183	22.6	212	4.31	0.411
BG51	10	9.78	21.7	185	22.9	215	4.37	0.416
BG52	10	9.80	21.8	186	23.0	215	4.38	0.417
BG53	4	3.90	18.8	79.4	19.8	120	1.53	0.417
BG54	6	5.71	20.7	117	21.6	156	2.59	0.471
BG55	8	7.75	22.1	153	23.1	188	3.76	0.512
BG56	10	9.75	21.0	190	22.3	219	4.31	0.462
BG57	4	3.88	19.8	74.1	20.6	114	1.60	0.383
BG58	6	5.74	21.8	114	22.7	153	2.78	0.439
BG59	8	7.74	24.5	145	25.1	183	3.98	0.477
BG60	10	9.70	23.4	176	24.6	207	4.65	0.443
BG61	4	3.89	19.5	73.3	20.4	112	1.53	0.367
BG62	6	5.69	23.5	103	24.0	144	2.83	0.447
BG63	8	7.74	27.2	142	27.5	180	4.26	0.511
BG64	10	9.72	27.4	169	27.8	202	5.03	0.479

Table IV.3 – Waveform characteristics obtained for Rapid Arc, using 2.5%CO₂ 97.5%Ar.

Run	WFS set [m/min]	WFS measured [m/min]	U_{mean} [V]	I_{mean} [A]	U_{RMS} [V]	I_{RMS} [A]	P_{inst} [kW]	Arc Energy [kJ/mm]
BR01	4	3.87	19.4	77.0	20.2	123	1.59	0.593
BR02	4	3.72	15.9	81.9	16.7	128	1.45	0.514
BR03	4	3.67	16.9	75.9	17.5	123	1.56	0.516
BR04	4	3.74	20.4	82.9	20.9	141	2.14	0.705
BR05	4	3.66	22.1	88.0	22.6	149	2.42	0.806
BR06	6	5.48	16.9	119	17.9	160	2.20	0.452
BR07	6	5.58	16.8	118	17.8	162	2.16	0.456
BR08	6	5.71	18.4	117	19.2	161	2.48	0.487
BR09	6	5.65	22.8	126	23.3	181	3.39	0.667
BR10	6	5.64	24.1	136	24.6	194	3.84	0.752
BR11	8	7.70	17.6	154	19.0	190	2.96	0.434
BR12	8	7.74	17.4	152	18.7	191	2.86	0.428
BR13	8	7.77	19.1	157	20.2	193	3.35	0.466
BR14	8	7.80	24.1	164	24.6	215	4.51	0.636
BR15	8	7.81	24.8	168	25.2	220	4.73	0.667
BR16	10	9.73	17.6	181	19.1	212	3.42	0.386
BR17	10	9.78	17.6	184	19.2	212	3.49	0.387
BR18	10	9.76	20.0	183	21.1	216	4.03	0.434
BR19	10	9.82	22.6	186	23.3	227	4.72	0.503
BR20	10	9.74	23.1	187	23.6	229	4.83	0.515
BR21	4	3.92	22.1	88.2	22.6	149	2.43	0.916
BR22	6	5.80	25.3	136	25.7	194	3.99	0.907
BR23	8	7.71	25.4	168	25.8	220	4.85	0.776
BR24	9	8.69	23.4	165	23.9	211	4.35	0.604
BR25	10	9.74	23.6	185	24.1	227	4.84	0.585
BR26	12	11.73	22.2	213	23.2	247	5.27	0.513
BR27	14	13.73	23.2	232	24.0	264	5.89	0.488
BR28	18	17.62	24.0	272	24.7	306	7.17	0.454
BR29	4	3.93	24.7	87.9	25.1	149	2.66	0.897
BR30	6	5.84	27.3	136	27.7	194	4.29	0.850
BR31	8	7.77	27.8	168	28.2	220	5.25	0.746
BR32	10	9.74	26.7	182	27.1	225	5.37	0.582
BR33	4	3.91	26.5	84.5	26.9	144	2.74	0.928
BR34	6	5.75	28.8	132	29.2	189	4.39	0.871
BR35	8	7.72	30.3	168	30.7	220	5.68	0.811
BR36	10	9.72	29.2	182	29.6	225	5.80	0.633

Table IV.4 – Waveform characteristics obtained for RapidArc, using 1.5%CO₂, 54%He 44.5%Ar.

Run	WFS set [m/min]	WFS measured [m/min]	U_{mean} [V]	I_{mean} [A]	U_{RMS} [V]	I_{RMS} [A]	P_{inst} [kW]	Arc Energy [kJ/mm]
BR37	4	-	-	-	-	-	-	-
BR38	4	3.85	20.0	74.7	20.7	125	1.57	0.620
BR39	4	3.79	20.8	72.4	21.4	120	1.61	0.617
BR40	4	3.78	23.1	80.0	23.5	131	2.15	0.738
BR41	4	3.71	26.1	88.1	26.4	149	2.74	0.943
BR42	6	5.60	19.6	116	20.7	154	2.35	0.502
BR43	6	5.60	19.8	120	20.9	158	2.46	0.520
BR44	6	5.59	20.4	117	21.4	156	2.50	0.526
BR45	6	5.61	24.5	120	24.9	175	3.41	0.687
BR46	6	5.58	27.6	135	28.0	193	4.26	0.855
BR47	8	7.67	20.0	149	21.3	187	3.03	0.476
BR48	8	7.64	20.2	147	21.5	183	3.09	0.473
BR49	8	7.63	20.9	154	22.2	190	3.43	0.507
BR50	8	7.62	25.3	158	25.6	208	4.44	0.638
BR51	8	7.63	28.7	168	29.0	220	5.28	0.765
BR52	10	9.77	19.9	178	21.5	209	3.66	0.429
BR53	10	9.78	20.1	177	21.7	208	3.70	0.430
BR54	10	9.77	21.5	179	23.0	209	4.09	0.459
BR55	10	9.75	25.0	183	25.5	224	5.05	0.544
BR56	10	9.73	25.4	185	25.9	227	5.20	0.562
BR57	4	3.93	26.8	88.1	27.1	149	2.78	1.100
BR58	6	5.76	28.7	135	29.0	193	4.38	1.020
BR59	8	7.58	29.1	168	29.4	221	5.39	0.885
BR60	9	8.56	23.9	167	24.3	212	4.43	0.618
BR61	10	9.50	25.7	186	26.1	228	5.24	0.638
BR62	12	11.42	24.1	208	24.9	244	5.51	0.544
BR63	14	13.39	24.9	231	25.7	264	6.23	0.521
BR64	18	17.59	25.6	271	26.4	305	7.60	0.483
BR65	4	3.92	28.9	86.5	29.2	147	2.90	1.027
BR66	6	5.73	31.1	132	31.4	189	4.57	0.938
BR67	8	7.57	31.3	168	31.5	220	5.73	0.834
BR68	10	9.45	29.2	183	29.5	225	5.75	0.632
BR69	4	3.84	29.8	82.8	30.0	140	2.82	1.012
BR70	6	5.57	31.9	123	32.2	178	4.37	0.903
BR71	8	7.43	33.1	156	33.4	206	5.63	0.825
BR72	10	9.61	32.4	183	32.6	226	6.32	0.701

Table IV.5 – Waveform characteristics obtained for STT, using 2.5%CO₂ 97.5%Ar.

Run	WFS set [m/min]	WFS measured [m/min]	U_{mean} [V]	I_{mean} [A]	U_{RMS} [V]	I_{RMS} [A]	P_{inst} [kW]	Arc Energy [kJ/mm]
BS01	3	2.88	15.4	58.0	15.7	98.7	0.807	0.255
BS02	3	2.84	15.7	63.6	16.0	97.4	0.909	0.287
BS03	3	2.74	15.7	70.3	16.0	97.8	1.02	0.323
BS04	3	2.83	16.3	73.3	16.5	94.4	1.11	0.351
BS05	3	2.79	17.5	72.8	17.6	83.9	1.23	0.389
BS06	6	5.56	15.8	104	16.4	152	1.54	0.243
BS07	6	5.58	16.5	115	17.0	154	1.75	0.277
BS08	6	5.63	17.1	121	17.6	150	1.94	0.306
BS09	6	5.64	19.4	143	19.7	161	2.66	0.419
BS10	6	5.65	17.9	137	18.3	164	2.33	0.368
BS11	8	7.55	15.5	140	16.2	186	2.02	0.243
BS12	8	7.54	16.9	150	17.5	186	2.39	0.286
BS13	8	7.54	18.2	161	18.7	189	2.76	0.331
BS14	8	7.55	19.5	174	19.9	192	3.21	0.386
BS15	8	7.54	21.4	177	21.7	187	3.67	0.440
BS16	8.26	7.93	15.9	148	16.7	190	2.17	0.250
BS17	8.26	7.85	17.6	152	18.1	187	2.51	0.290
BS18	8.26	7.86	18.5	169	19.0	193	2.94	0.339
BS19	8.26	7.81	19.8	180	20.2	196	3.36	0.387
BS20	8.26	7.78	21.5	185	21.9	192	3.88	0.447
BS21	3	2.95	15.5	70.7	15.8	98.7	1.03	0.362
BS22	6	5.71	17.0	125	17.5	155	1.99	0.362
BS23	8	7.74	18.0	157	18.4	184	2.69	0.366
BS24	8.26	7.91	18.2	167	18.7	192	2.87	0.375
BS25	3	2.88	16.6	65.9	16.8	91.6	1.01	0.320
BS26	6	5.66	17.7	119	18.1	148	2.00	0.316
BS27	8	7.68	18.9	154	19.4	180	2.77	0.332
BS28	8.26	7.95	18.7	159	19.1	182	2.83	0.327
BS29	3	2.94	16.1	63.8	16.3	87.7	0.973	0.307
BS30	6	5.70	17.6	111	18.0	138	1.89	0.298
BS31	8	7.73	19.2	145	19.6	168	2.66	0.319
BS32	8.26	8.02	19.7	151	20.1	173	2.85	0.329

Table IV.6 – Waveform characteristics obtained for STT, using 1.5%CO₂, 54%He 44.5%Ar.

Run	WFS set [m/min]	WFS measured [m/min]	U_{mean} [V]	I_{mean} [A]	U_{RMS} [V]	I_{RMS} [A]	P_{inst} [kW]	Arc Energy [kJ/mm]
BS33	3	2.93	17.9	59.0	18.3	101	0.880	0.278
BS34	3	2.87	17.9	66.3	18.3	101	1.02	0.323
BS35	3	2.82	18.8	68.9	19.1	96.3	1.15	0.365
BS36	3	2.83	21.9	78.5	22.3	103	1.51	0.476
BS37	3	2.86	22.4	71.2	22.6	81	1.53	0.482
BS38	6	5.57	18.4	106	19.0	154	1.66	0.262
BS39	6	5.62	19.1	117	19.8	156	1.94	0.306
BS40	6	5.55	20.5	124	21.0	159	2.29	0.361
BS41	6	5.61	22.1	135	22.6	162	2.75	0.433
BS42	6	5.61	23.6	140	24.0	158	3.08	0.486
BS43	8	7.79	18.3	140	19.1	185	2.19	0.263
BS44	8	7.81	20.0	149	20.7	188	2.69	0.323
BS45	8	7.78	21.2	165	21.9	193	3.17	0.381
BS46	8	7.74	22.4	174	23.0	193	3.61	0.434
BS47	8	7.82	25.4	177	25.8	186	4.32	0.518
BS48	8.26	8.08	18.1	148	19.0	193	2.32	0.267
BS49	8.26	8.11	20.3	151	21.0	186	2.76	0.318
BS50	8.26	8.08	21.3	168	22.0	192	3.28	0.378
BS51	8.26	8.06	23.9	178	24.6	195	3.92	0.452
BS52	8.26	8.07	25.3	186	25.7	193	4.52	0.521
BS53	3	2.91	19.2	68.7	19.6	95.5	1.17	0.413
BS54	6	5.68	20.8	121	21.3	154	2.27	0.412
BS55	8	7.56	21.7	155	22.2	182	3.09	0.421
BS56	8.26	7.80	21.3	161	21.9	185	3.13	0.409
BS57	3	2.95	22.2	70.9	22.6	100	1.34	0.424
BS58	6	5.70	21.3	121	21.9	151	2.31	0.365
BS59	8	7.72	22.2	153	22.7	180	3.10	0.372
BS60	8.26	8.03	22.3	157	22.9	180	3.22	0.372
BS61	3	2.94	19.8	62.8	20.1	85.6	1.14	0.359
BS62	6	5.69	21.1	112	21.5	139	2.16	0.342
BS63	8	7.71	22.1	145	22.6	168	3.00	0.360
BS64	8.26	7.90	23.0	151	23.5	172	3.25	0.375

Table IV.7 – Waveform characteristics obtained for CMT, using 2.5%CO₂, 97.5%Ar.

Run	WFS set [m/min]	WFS measured [m/min]	U _{mean} [V]	I _{mean} [A]	U _{RMS} [V]	I _{RMS} [A]	P _{inst} [kW]	Arc Energy [kJ/mm]
BC01	3	2.52	9.51	67.7	12.3	73.9	0.798	0.252
BC02	3	2.50	10.4	69.5	13.1	75.2	0.861	0.272
BC03	3	2.17	12.0	67.2	14.4	72.4	0.920	0.291
BC04	3	2.23	14.6	66.2	16.3	70.4	1.02	0.324
BC05	3	2.11	16.7	63.2	17.6	66.0	1.07	0.339
BC06	4	2.99	10.1	81.8	13.3	93.2	1.10	0.263
BC07	4	3.21	11.0	86.2	13.7	96.7	1.18	0.282
BC08	4	2.88	12.6	81.8	15.0	91.8	1.21	0.291
BC09	4	2.66	15.0	77.5	16.6	86.3	1.26	0.302
BC10	4	2.35	17.0	70.1	17.9	76.8	1.23	0.295
BC11	6	4.86	10.7	111	15.0	139	2.04	0.322
BC12	6	5.27	12.7	120	16.8	146	2.41	0.380
BC13	6	4.76	15.0	120	18.1	145	2.49	0.393
BC14	6	4.21	16.8	106	18.9	131	2.26	0.356
BC15	6	3.34	16.8	87.6	18.3	109	1.78	0.281
BC16	8	5.34	10.0	120	14.8	157	2.27	0.273
BC17	8	6.37	11.4	130	16.0	166	2.60	0.312
BC18	8	6.86	13.8	143	17.4	176	2.99	0.359
BC19	8	6.38	16.7	144	19.3	173	3.20	0.385
BC20	8	5.48	18.0	132	19.8	154	2.90	0.348
BC21	3	2.28	12.3	67.7	14.7	72.9	0.947	0.299
BC22	3	2.29	11.9	68.1	14.3	73.3	0.924	0.292
BC23	3	2.22	12.3	67.8	14.7	73.0	0.951	0.300
BC24	3	2.20	12.0	68.3	14.5	73.6	0.940	0.297
BC25	4	2.91	12.6	82.7	15.1	92.7	1.23	0.295
BC26	4	2.82	12.6	82.5	15.1	92.5	1.23	0.294
BC27	4	2.90	12.7	82.9	15.1	92.8	1.23	0.295
BC28	4	2.99	12.9	82.0	15.4	91.9	1.25	0.299
BC29	6	4.84	14.8	120	17.9	145	2.48	0.392
BC30	6	4.66	14.5	119	17.9	145	2.47	0.391
BC31	6	4.64	14.6	119	17.9	145	2.47	0.390
BC32	6	4.65	14.9	121	18.2	146	2.54	0.401
BC33	8	6.49	13.5	144	17.4	177	3.01	0.361
BC34	8	6.78	13.5	142	17.4	175	2.97	0.357
BC35	8	7.05	14.5	148	17.9	181	3.15	0.378
BC36	8	7.23	14.4	145	18.0	178	3.11	0.374
BC37	3	2.35	12.3	68.5	14.6	73.7	0.951	0.336
BC38	4	2.89	12.4	81.9	15.0	91.9	1.21	0.329
BC39	6	4.73	14.7	120	18.0	146	2.49	0.453
BC40	8	7.02	14.2	143	17.8	176	3.05	0.417
BC41	3	2.44	12.3	67.2	14.7	72.3	0.939	0.297
BC42	4	3.27	13.0	82.6	15.4	92.6	1.26	0.303
BC43	6	5.21	15.5	120	18.6	145	2.56	0.405
BC44	8	7.60	15.0	142	18.6	175	3.17	0.381
BC45	3	2.66	12.7	67.5	15.1	72.6	0.974	0.308
BC46	4	3.39	13.3	81.5	15.7	91.4	1.27	0.305
BC47	6	5.46	16.4	118	19.5	143	2.65	0.419
BC48	8	8.37	15.6	142	19.4	174	3.30	0.396

Table IV.8 – Waveform characteristics obtained for CMT, using 1.5%CO₂, 54%He 44.5%Ar.

Run	WFS set [m/min]	WFS measured [m/min]	U _{mean} [V]	I _{mean} [A]	U _{RMS} [V]	I _{RMS} [A]	P _{inst} [kW]	Arc Energy [kJ/mm]
BC49	3	2.33	11.3	66.9	14.9	73.1	0.939	0.296
BC50	3	2.35	12.5	68.2	15.8	74.0	1.02	0.321
BC51	3	2.33	14.3	68.5	17.2	73.7	1.11	0.350
BC52	3	2.25	16.3	66.2	18.5	70.4	1.16	0.366
BC53	3	2.22	19.9	63.1	21.0	65.9	1.27	0.402
BC54	4	2.83	11.5	78.9	15.4	90.3	1.21	0.290
BC55	4	2.91	12.8	81.2	16.4	92.0	1.31	0.315
BC56	4	2.93	14.9	81.1	18.0	91.2	1.42	0.340
BC57	4	2.68	17.6	77.4	19.8	86.2	1.47	0.352
BC58	4	2.44	21.3	69.1	22.3	75.6	1.49	0.358
BC59	6	4.47	12.1	103	17.2	132	2.18	0.345
BC60	6	5.26	14.0	116	18.8	143	2.59	0.410
BC61	6	4.90	16.3	118	20.3	144	2.75	0.435
BC62	6	4.48	18.4	107	21.4	132	2.53	0.399
BC63	6	3.36	20.4	89.0	22.1	111	2.11	0.334
BC64	8	5.66	11.5	118	17.0	156	2.60	0.312
BC65	8	6.26	13.3	129	18.2	165	2.94	0.353
BC66	8	7.06	15.8	138	20.0	171	3.30	0.396
BC67	8	6.55	19.0	143	22.4	172	3.66	0.439
BC68	8	5.43	19.7	129	21.9	151	3.10	0.372
BC69	3	2.24	15.2	68.5	18.6	73.7	1.18	0.374
BC70	3	2.18	15.3	68.9	18.6	74.1	1.19	0.377
BC71	3	2.06	15.0	68.2	18.3	73.4	1.16	0.367
BC72	3	2.20	14.8	68.8	17.9	74.1	1.15	0.364
BC73	4	2.74	15.5	81.6	18.9	91.7	1.48	0.355
BC74	4	2.85	15.1	82.0	18.3	92.0	1.45	0.347
BC75	4	2.90	15.0	81.4	18.2	91.4	1.43	0.342
BC76	4	2.84	14.8	81.4	18.0	91.5	1.42	0.341
BC77	6	4.76	15.8	116	19.9	142	2.67	0.421
BC78	6	4.54	15.6	116	19.8	142	2.67	0.421
BC79	6	4.85	16.3	118	20.4	144	2.76	0.436
BC80	6	5.02	16.2	117	20.1	143	2.70	0.427
BC81	8	6.96	16.3	141	20.4	174	3.43	0.412
BC82	8	7.00	16.6	144	20.7	177	3.55	0.426
BC83	8	6.79	16.3	143	20.5	176	3.51	0.421
BC84	8	6.54	15.7	140	20.1	174	3.39	0.407
BC85	3	2.19	15.2	67.3	18.6	72.5	1.16	0.411
BC86	4	2.68	15.6	80.3	19.1	90.3	1.46	0.399
BC87	6	4.82	16.2	118	20.3	144	2.75	0.500
BC88	8	6.73	16.9	138	21.1	171	3.46	0.472
BC89	3	2.32	15.6	67.3	19.1	72.5	1.20	0.379
BC90	4	2.99	15.9	81.8	19.1	91.8	1.51	0.363
BC91	6	5.25	17.0	117	21.1	143	2.83	0.447
BC92	8	7.28	17.1	137	21.3	170	3.48	0.418
BC93	3	2.40	16.1	67.1	19.5	72.2	1.22	0.386
BC94	4	3.23	16.5	81.0	19.8	91.0	1.55	0.373
BC95	6	5.70	17.6	116	21.7	141	2.88	0.456
BC96	8	7.85	17.1	132	21.6	165	3.42	0.410

Table IV.9 – Waveform characteristics obtained for CMT-P, using 2.5%CO₂ 97.5%Ar.

Run	WFS set [m/min]	WFS measured [m/min]	U _{mean} [V]	I _{mean} [A]	U _{RMS} [V]	I _{RMS} [A]	P _{inst} [kW]	Arc Energy [kJ/mm]
BP01	3	2.75	18.2	63.4	18.8	97.6	1.37	0.431
BP02	3	2.66	18.3	62.8	19.0	96.1	1.37	0.432
BP03	3	2.50	18.5	62.8	19.1	96.0	1.37	0.433
BP04	3	2.55	18.8	62.7	19.3	96.0	1.39	0.438
BP05	3	2.38	18.5	61.1	19.2	94.0	1.34	0.424
BP06	4	3.68	19.1	85.2	20.0	120	1.94	0.466
BP07	4	-	-	-	-	-	-	-
BP08	4	3.41	19.1	82.2	20.0	117	1.88	0.452
BP09	4	3.42	19.6	80.3	20.5	115	1.89	0.454
BP10	4	3.27	19.4	78.0	20.3	112	1.82	0.437
BP11	6	5.81	18.7	127	19.9	158	2.78	0.439
BP12	6	5.55	20.1	125	21.1	156	2.92	0.460
BP13	6	5.27	21.4	124	22.3	155	3.04	0.481
BP14	6	4.91	21.3	122	22.2	154	2.99	0.472
BP15	6	4.70	21.3	113	22.3	147	2.84	0.448
BP16	8	8.10	18.3	170	20.3	195	3.64	0.437
BP17	8	8.11	22.2	170	23.3	195	4.26	0.512
BP18	8	7.63	22.5	165	23.5	192	4.21	0.505
BP19	8	7.02	22.7	158	23.7	187	4.09	0.491
BP20	8	6.69	23.2	153	24.1	183	4.06	0.487
BP21	9	8.63	15.3	186	18.4	207	3.25	0.348
BP22	9	9.01	22.1	191	23.2	211	4.63	0.496
BP23	9	8.32	24.9	192	25.5	211	5.12	0.549
BP24	9	7.67	25.2	183	26.0	205	5.05	0.541
BP25	9	7.07	25.9	180	26.6	204	5.08	0.545
BP26	10	10.43	5.6	198	5.9	213	1.23	0.117
BP27	10	10.30	23.7	222	24.1	233	5.45	0.519
BP28	10	9.36	27.5	221	27.8	233	6.29	0.599
BP29	10	8.34	29.5	218	29.8	231	6.65	0.633
BP30	10	7.00	28.7	217	29.0	230	6.46	0.615
BP31	4	2.93	18.9	72.7	19.6	97.2	1.57	0.376
BP32	4	3.18	18.9	77.1	19.7	107	1.70	0.409
BP33	4	3.77	18.9	86.7	19.9	127	2.02	0.485
BP34	4	4.07	19.8	96.2	20.7	143	2.36	0.566
BP35	6	4.18	19.4	106	20.3	128	2.32	0.366
BP36	6	4.74	19.8	115	20.7	141	2.59	0.408
BP37	6	5.62	20.5	129	21.6	166	3.12	0.493
BP38	6	6.09	21.3	136	22.4	179	3.48	0.550
BP39	8	6.26	20.8	144	21.8	162	3.35	0.402
BP40	8	6.94	20.8	157	21.7	178	3.64	0.437
BP41	8	8.03	23.4	171	24.5	204	4.60	0.552
BP42	8	8.49	24.3	187	25.3	223	5.19	0.622
BP43	10	7.17	12.7	183	16.4	192	2.50	0.238
BP44	10	9.29	25.1	208	25.3	217	5.36	0.511
BP45	10	9.43	28.0	234	28.4	249	6.84	0.652
BP46	10	9.60	29.7	247	30.1	265	7.71	0.734
BP47	4	3.61	19.0	82.2	19.9	117	1.87	0.510
BP48	6	5.22	20.2	122	21.2	154	2.86	0.520
BP49	8	7.55	22.1	164	23.1	191	4.11	0.561
BP50	9	8.40	24.5	191	25.1	211	5.03	0.603
BP51	10	9.32	26.2	221	26.4	232	5.98	0.640
BP52	4	3.69	18.9	80.9	19.8	115	1.85	0.444
BP53	6	5.49	20.6	120	21.6	152	2.89	0.456
BP54	8	8.00	22.8	161	23.8	189	4.20	0.504
BP55	10	9.38	28.7	219	29.0	232	6.52	0.621
BP56	4	4.05	19.6	79.4	20.5	114	1.89	0.453
BP57	6	5.83	21.8	117	22.9	150	3.01	0.476
BP58	8	8.34	24.2	160	25.2	189	4.42	0.531
BP59	10	9.61	30.7	216	31.1	230	6.91	0.658

Table IV.10 – Waveform characteristics obtained for CMT-P, using 1.5%CO₂, 54%He 44.5%Ar.

Run	WFS set [m/min]	WFS measured [m/min]	U _{mean} [V]	I _{mean} [A]	U _{RMS} [V]	I _{RMS} [A]	P _{inst} [kW]	Arc Energy [kJ/mm]
BP60	3	2.67	23.3	63.5	24.0	97.7	1.64	0.518
BP61	3	2.73	23.9	64.1	24.5	97.6	1.70	0.537
BP62	3	2.53	23.7	62.9	24.3	96.2	1.66	0.525
BP63	3	2.48	24.0	63.1	24.5	97.5	1.68	0.531
BP64	3	2.44	24.0	61.7	24.7	94.0	1.64	0.518
BP65	4	3.61	23.1	85.5	24.0	121	2.23	0.536
BP66	4	3.54	23.3	85.3	24.2	120	2.26	0.542
BP67	4	3.39	23.6	83.2	24.4	119	2.24	0.537
BP68	4	3.21	23.8	81.0	24.7	116	2.19	0.526
BP69	4	3.16	24.3	80.9	25.2	116	2.23	0.536
BP70	6	6.14	22.1	125	23.7	157	3.23	0.510
BP71	6	5.87	23.6	125	24.6	156	3.33	0.527
BP72	6	5.54	23.9	123	24.8	155	3.32	0.524
BP73	6	5.25	24.7	120	25.6	153	3.35	0.528
BP74	6	5.13	25.3	115	26.2	148	3.30	0.521
BP75	8	8.78	22.0	172	23.9	197	4.30	0.516
BP76	8	8.37	24.3	169	25.5	195	4.60	0.552
BP77	8	7.76	25.7	164	26.7	192	4.70	0.564
BP78	8	7.35	26.7	161	27.5	189	4.73	0.568
BP79	8	6.91	26.4	155	27.3	185	4.55	0.546
BP80	9	8.91	16.6	187	19.8	208	3.49	0.375
BP81	9	9.49	27.2	193	27.7	212	5.57	0.597
BP82	9	8.80	27.5	190	28.1	210	5.58	0.598
BP83	9	7.94	28.4	184	29.0	207	5.60	0.600
BP84	9	7.25	28.5	180	29.1	203	5.50	0.589
BP85	10	9.00	11.9	207	16.1	221	2.71	0.258
BP86	10	10.90	28.5	221	28.8	233	6.48	0.618
BP87	10	9.70	30.3	220	30.6	232	6.87	0.654
BP88	10	8.45	32.9	216	33.3	230	7.36	0.701
BP89	10	7.13	32.8	216	33.1	230	7.29	0.695
BP90	4	3.15	24.3	72.2	25.1	96.5	1.92	0.461
BP91	4	3.33	23.2	78.2	24.1	108	2.04	0.491
BP92	4	3.73	25.3	90.5	26.1	131	2.60	0.624
BP93	4	4.10	25.5	92.6	26.4	138	2.75	0.660
BP94	6	4.53	23.7	107	25.0	129	2.79	0.440
BP95	6	4.85	24.1	114	25.1	141	3.05	0.482
BP96	6	5.72	26.3	133	27.2	170	3.94	0.623
BP97	6	5.88	26.3	134	27.5	177	4.08	0.644
BP98	8	6.03	23.0	147	24.6	164	3.68	0.442
BP99	8	7.00	25.0	155	25.9	177	4.25	0.510
BP100	8	7.90	28.0	173	29.2	205	5.44	0.653
BP101	8	8.34	28.8	190	29.8	225	6.13	0.736
BP102	10	8.10	5.0	175	5.9	184	0.93	0.088
BP103	10	9.35	28.9	208	29.1	217	6.14	0.585
BP104	10	9.68	31.6	234	31.9	249	7.66	0.730
BP105	10	9.71	32.0	248	32.5	266	8.29	0.789
BP106	4	3.59	24.4	82.7	25.3	117	2.27	0.620
BP107	6	5.37	25.1	122	26.1	154	3.45	0.627
BP108	8	7.48	26.9	165	27.9	192	4.90	0.668
BP109	9	8.32	29.0	191	29.5	211	5.87	0.704
BP110	10	9.41	31.3	221	31.5	232	7.09	0.760
BP111	4	3.89	24.0	83.5	24.9	119	2.31	0.554
BP112	6	5.54	26.1	123	27.1	155	3.61	0.571
BP113	8	7.74	27.3	161	28.3	189	4.90	0.588
BP114	10	9.47	33.2	218	33.5	231	7.46	0.711
BP115	4	3.93	25.7	81.3	26.7	116	2.40	0.577
BP116	6	5.87	26.8	116	27.9	149	3.56	0.562
BP117	8	8.23	29.3	162	30.3	189	5.27	0.632
BP118	10	9.78	36.3	216	36.7	230	8.11	0.773

Table IV.11 – Waveform characteristics obtained for FastROOT, using 2.5%CO₂ 97.5%Ar.

Run	WFS set [m/min]	WFS measured [m/min]	U_{mean} [V]	I_{mean} [A]	U_{RMS} [V]	I_{RMS} [A]	P_{inst} [kW]	Arc Energy [kJ/mm]
BF01	4	3.76	15.2	89.4	16.0	119	1.22	0.292
BF02	4	3.70	16.8	84.0	17.4	105	1.33	0.320
BF03	4	3.65	17.1	87.1	17.6	104	1.41	0.339
BF04	4	3.74	16.8	102	17.5	121	1.58	0.379
BF05	4	3.58	16.5	105	17.3	121	1.60	0.383
BF06	6	5.42	15.1	127	15.8	173	1.75	0.276
BF07	6	5.44	15.0	136	16.0	164	1.82	0.288
BF08	6	5.43	15.4	134	16.2	158	1.84	0.291
BF09	6	5.39	16.1	137	16.9	157	1.99	0.315
BF10	6	5.36	16.9	141	17.6	155	2.19	0.346
BF11	8	7.19	15.5	157	16.4	195	2.25	0.270
BF12	8	7.24	15.7	167	16.8	190	2.41	0.289
BF13	8	7.34	16.7	165	17.7	187	2.56	0.307
BF14	8	7.30	16.6	173	17.5	190	2.66	0.320
BF15	8	7.30	17.7	175	18.6	188	2.90	0.348
BF16	9	8.30	16.2	183	17.3	212	2.80	0.300
BF17	9	8.27	16.0	187	17.0	211	2.81	0.301
BF18	9	8.25	16.8	190	17.9	206	3.01	0.323
BF19	9	8.25	17.7	189	18.5	205	3.19	0.342
BF20	9	8.28	19.1	190	19.7	202	3.49	0.374
BF21	8	7.26	16.4	179	17.3	197	2.59	0.311
BF22	8	7.28	16.9	175	17.7	188	2.70	0.324
BF23	8	7.37	18.7	177	19.4	191	3.21	0.385
BF24	8	7.31	19.6	172	20.2	189	3.35	0.402
BF25	4	3.77	17.7	106	18.4	121	1.75	0.478
BF26	6	5.55	17.1	144	17.9	161	2.25	0.410
BF27	8	7.37	17.3	179	18.1	192	2.90	0.396
BF28	9	8.27	18.9	195	19.6	207	3.55	0.427
BF29	4	3.78	17.5	95.3	18.0	111	1.57	0.376
BF30	6	5.35	17.4	136	18.1	149	2.22	0.351
BF31	8	7.23	18.6	168	19.2	181	2.97	0.357
BF32	9	8.17	19.9	182	20.5	193	3.50	0.376
BF33	4	3.70	18.3	95.5	18.9	110	1.64	0.395
BF34	6	5.44	18.3	132	19.0	146	2.25	0.356
BF35	8	7.22	18.8	157	19.5	171	2.79	0.335
BF36	9	8.23	19.8	170	20.4	181	3.23	0.346

Table IV.12 – Waveform characteristics obtained for FastROOT, using 1.5%CO₂ 54%He 44.5%Ar.

Run	WFS set [m/min]	WFS measured [m/min]	U _{mean} [V]	I _{mean} [A]	U _{RMS} [V]	I _{RMS} [A]	P _{inst} [kW]	Arc Energy [kJ/mm]
BF37	4	3.82	17.8	87.8	18.8	117	1.33	0.319
BF38	4	3.72	17.5	96.8	18.6	124	1.46	0.350
BF39	4	3.67	19.2	96.8	20.2	119	1.64	0.394
BF40	4	3.72	21.0	96.5	22.1	114	1.82	0.437
BF41	4	3.67	21.5	105	22.9	122	1.99	0.479
BF42	6	5.50	16.8	136	18.4	167	1.90	0.300
BF43	6	5.46	17.6	136	19.0	169	2.06	0.324
BF44	6	5.52	18.8	135	20.2	159	2.21	0.349
BF45	6	5.51	19.4	141	20.9	161	2.37	0.375
BF46	6	5.49	20.1	150	21.7	170	2.64	0.417
BF47	8	7.15	17.3	168	19.2	204	2.39	0.286
BF48	8	7.29	17.4	171	19.2	204	2.50	0.300
BF49	8	7.38	18.2	156	19.3	188	2.53	0.303
BF50	8	7.44	18.6	166	20.0	186	2.78	0.334
BF51	8	7.31	19.0	169	20.3	185	2.95	0.354
BF52	9	8.32	17.2	168	18.6	208	2.55	0.273
BF53	9	8.34	17.6	171	18.9	207	2.69	0.288
BF54	9	8.36	17.1	184	18.5	211	2.83	0.304
BF55	9	8.44	18.0	180	19.3	207	2.90	0.310
BF56	9	8.47	18.2	187	19.5	210	3.10	0.332
BF57	8	7.46	17.6	170	18.8	194	2.61	0.314
BF58	8	7.38	18.3	169	19.6	188	2.75	0.330
BF59	8	7.44	19.3	171	20.4	189	3.07	0.369
BF60	8	7.38	20.6	169	21.8	188	3.34	0.401
BF61	4	3.85	23.3	102	24.7	118	2.14	0.583
BF62	6	5.57	20.5	142	22.0	159	2.60	0.473
BF63	8	7.36	18.8	172	20.2	189	2.92	0.398
BF64	9	8.29	18.5	185	20.0	204	3.12	0.375
BF65	4	3.85	22.9	97.6	24.2	114	1.99	0.478
BF66	6	5.40	20.6	128	21.7	145	2.40	0.379
BF67	8	7.34	19.3	163	20.3	180	2.91	0.349
BF68	9	8.23	19.6	177	20.9	192	3.25	0.348
BF69	4	3.71	23.8	90.2	24.7	105	1.97	0.473
BF70	6	5.48	20.7	121	21.5	139	2.32	0.367
BF71	8	7.31	20.8	154	21.8	168	2.98	0.358
BF72	9	8.21	20.9	168	21.9	182	3.34	0.358

V. WAVEFORM PARAMETERS FOR THE BEAD ON PIPE TESTS

The waveform parameters were defined as the all the parameters obtained from the analysis of the waveforms. They will be described as follow:

- Peak Current (I_p) – Average of peak current values at stable conditions;
- Peak Voltage (U_p) – Average of peak voltage values at stable conditions;
- Background Current (I_b);
- Step Voltage (when applied) (U_{step});
- Background Voltage (U_b);
- Short Circuiting Current (I_{sc});
- Short Circuiting Voltage (U_{sc});
- Peak time (t_p);
- Background time (t_b);
- Cycle time (t_{cycle});
- Number of pulses per cycle (only applied to CMT-P);
- Duty cycle (D.C.);
- Short-circuiting Frequency (f_{sc});
- Pulse Frequency (f_p).

Table V.1 – Waveform parameters obtained for GMAW-P.

Run	WFS [m/min]	WFS/TS Ratio	Trim	Gas	CTWD [mm]	I _p [A]	U _p [V]	I _b [A]	U _{step} [V]	U _b [V]	t _p [ms]	t _b [ms]	t _{cycle} [ms]	Duty Cycle [%]	F _p [Hz]
BG05	4	16	1.50	A	11	292	27.4	22.0	16.6	5.00	5.75	11.3	17.0	33.8	58.8
BG06	6	16	0.50	A	11	269	23.8	27.9	14.7	4.46	6.50	4.50	11.0	59.1	90.9
BG07	6	16	0.75	A	11	276	26.1	30.7	17.1	5.58	4.50	7.00	11.5	39.1	87.0
BG08	6	16	1.00	A	11	328	28.5	36.5	16.8	7.40	5.50	3.00	8.5	64.7	118
BG09	6	16	1.25	A	11	329	28.4	36.7	17.1	8.93	5.00	3.50	8.5	58.8	118
BG10	6	16	1.50	A	11	327	28.4	37.1	17.2	9.20	4.75	4.25	9.0	52.8	111
BG15	8	16	1.50	A	11	348	29.4	48.3	17.3	7.80	5.50	1.50	7.0	78.6	143
BG20	10	16	1.50	A	11	362	28.8	41.8	17.1	12.3	3.75	1.50	5.3	71.4	190
BG21	4	18	1.50	A	11	293	26.2	21.8	16.7	5.19	3.60	9.60	13.2	27.3	75.8
BG22	6	18	1.50	A	11	328	29.0	36.7	16.8	11.1	5.50	3.50	9.0	61.1	111
BG23	8	18	1.50	A	11	347	29.3	48.2	16.4	9.64	4.25	1.50	5.8	73.9	174
BG24	10	18	1.50	A	11	361	30.4	61.6	16.1	11.1	4.25	0.75	5.0	85.0	200
BG26	6	16	1.50	A	13.5	327	31.8	36.6	17.3	8.54	4.50	4.00	8.5	52.9	118
BG30	6	16	1.50	A	16	327	32.3	36.5	17.7	14.8	4.25	4.00	8.3	51.5	121
BG33	4	16	1.50	B	11	294	30.4	22.2	20.4	7.79	5.25	9.25	14.5	36.2	69.0
BG38	6	16	1.50	B	11	328	31.4	36.7	22.5	7.47	5.75	3.00	8.8	65.7	114
BG43	8	16	1.50	B	11	349	31.5	31.9	20.0	11.2	4.25	2.25	6.5	65.4	154
BG48	10	16	1.50	B	11	360	30.5	38.4	21.5	15.3	3.50	1.75	5.3	66.7	190

Gas A: 2.5%CO₂ 97.5%Ar; Gas B: 1.5%CO₂ 54%He 44.5%Ar.

Table V.2 – Waveform parameters obtained for RapidArc.

Run	WFS [m/min]	WFS/TS Ratio	Trim	Gas	CTWD [mm]	I _p [A]	U _p [V]	I _b [A]	U _b [V]	t _p [ms]	t _b [ms]	t _{cycle} [ms]	Duty Cycle [%]	F _p [Hz]
BR05	4	16	1.50	A	11	415	33.2	22.8	18.5	5.50	5.50	11.0	50.0	90.9
BR06	6	16	0.50	A	11	349	27.3	19.0	8.2	5.50	2.00	7.50	73.3	133
BR07	6	16	0.75	A	11	346	25.3	18.8	11.8	5.25	2.00	7.25	72.4	138
BR08	6	16	1.00	A	11	357	28.4	23.7	10.8	5.50	1.75	7.25	75.9	138
BR09	6	16	1.25	A	11	419	33.0	31.7	18.5	5.75	2.00	7.75	74.2	129
BR10	6	16	1.50	A	11	438	35.0	33.9	19.3	5.50	2.00	7.50	73.3	133
BR15	8	16	1.50	A	11	450	34.2	51.3	20.7	4.75	1.00	5.75	82.6	174
BR20	10	16	1.50	A	11	443	32.4	71.8	14.5	3.75	1.25	5.00	75.0	200
BR21	4	18	1.50	A	11	419	33.6	22.5	18.7	5.25	5.75	11.0	47.7	90.9
BR22	6	18	1.50	A	11	442	35.5	33.8	21.6	5.50	2.00	7.50	73.3	133
BR23	8	18	1.50	A	11	450	34.9	50.7	21.2	4.50	1.50	6.00	75.0	167
BR25	10	18	1.50	A	11	446	32.1	70.8	16.6	3.50	1.50	5.00	70.0	200
BR30	6	16	1.50	A	13.5	442	37.0	33.6	23.3	5.50	1.75	7.25	75.9	138
BR34	6	16	1.50	A	16	441	40.4	33.3	24.1	5.50	2.00	7.50	73.3	133
BR37	4	16	1.50	B	11	418	36.3	22.8	22.4	5.25	5.50	10.8	48.8	93.0
BR42	6	16	1.50	B	11	444	37.6	33.2	22.5	5.25	2.25	7.50	70.0	133
BR47	8	16	1.50	B	11	447	36.4	52.2	25.0	4.50	1.50	6.00	75.0	167
BR52	10	16	1.50	B	11	444	33.9	72.0	16.3	4.00	1.00	5.00	80.0	200

Gas A: 2.5%CO₂ 97.5%Ar; Gas B: 1.5%CO₂ 54%He 44.5%Ar

Table V.3 – Waveform parameters obtained for STT.

Run	WFS [m/min]	WFS/TS Ratio	Trim	Gas	CTWD [mm]	I _p [A]	U _p [V]	I _b [A]	U _{step} [V]	U _b [V]	t _p [ms]	t _b [ms]	t _{cycle} [ms]	Duty Cycle [%]	F _{sc} [Hz]
BS03	3	16	1.00	A	11	288	24.9	42.3	16.2	7.2	5.00	22.5	27.5	18.2	36.4
BS06	6	16	0.50	A	11	321	26.8	34.6	15.6	8.34	5.25	8.25	13.5	38.9	74.1
BS07	6	16	0.75	A	11	327	27.3	52.9	16.1	8.35	4.50	5.25	9.75	46.2	103
BS08	6	16	1.00	A	11	327	26.4	72.0	17.3	8.26	5.25	8.00	13.3	39.6	75.5
BS09	6	16	1.25	A	11	378	27.8	91.2	17.6	9.04	5.00	11.5	16.5	30.3	60.6
BS10	6	16	1.50	A	11	395	29.3	110	19.5	9.31	6.00	10.5	16.5	36.4	60.6
BS13	8	16	1.00	A	11	387	27.7	103	18.4	8.98	5.00	10.5	15.5	32.3	64.5
BS18	8.26	16	1.00	A	11	391	28.7	83.7	18.1	9.42	4.50	5.50	10.0	45.0	100
BS21	3	18	1.00	A	11	294	24.7	41.5	15.4	7.65	6.00	12.8	18.8	32.0	53.3
BS22	6	18	1.00	A	11	319	27.5	72.5	16.9	8.73	5.25	8.00	13.3	39.6	75.5
BS23	8	18	1.00	A	11	387	27.1	103	18.3	9.44	4.50	8.25	12.8	35.3	78.4
BS25	8.26	18	1.00	A	11	393	25.3	111	18.5	9.23	5.00	9.00	14.0	35.7	71.4
BS26	6	16	1.00	A	13.5	324	27.9	71.7	17.0	9.25	4.75	10.5	15.3	31.2	65.6
BS30	6	16	1.00	A	16	321	29.8	72.1	17.7	9.63	6.00	12.0	18.0	33.3	55.6
BS35	3	16	1.00	B	11	285	26.7	41.8	19.0	7.89	5.00	22.0	27.0	18.5	37.0
BS40	6	16	1.00	B	11	317	28.3	71.5	20.2	8.32	5.00	10.5	15.5	32.3	64.5
BS45	8	16	1.00	B	11	376	29.6	104	21.2	9.27	4.50	7.00	11.5	39.1	87.0
BS50	8.26	16	1.00	B	11	387	30.2	111	22.7	8.72	4.50	6.50	11.0	40.9	90.9

Gas A: 2.5%CO₂ 97.5%Ar; Gas B: 1.5%CO₂ 54%He 44.5%Ar

Table V.4 – Waveform parameters obtained for CMT.

Run	WFS [m/min]	WFS/TS Ratio	ALC [%]	DC [%]	Gas	CTWD [mm]	I _p [A]	U _p [V]	I _b [A]	U _b [V]	t _p [ms]	t _b [ms]	t _{cycle} [ms]	Duty Cycle [%]	F _{sc} [Hz]
BC03	3	16	0	0	A	11	126	21.6	37.3	1.20	4.00	11.0	15.0	26.7	66.7
BC08	4	16	0	0	A	11	160	22.3	37.7	1.37	6.00	12.0	18.0	33.3	55.6
BC11	6	16	-30	0	A	11	235	27.8	37.8	1.41	6.60	12.0	18.6	35.5	53.8
BC12	6	16	-15	0	A	11	235	26.3	37.6	1.43	6.25	5.75	12.0	52.1	83.3
BC13	6	16	0	0	A	11	236	25.4	37.6	1.49	6.40	6.40	12.8	50.0	78.1
BC14	6	16	15	0	A	11	236	26.5	37.5	1.33	6.00	12.5	18.5	32.4	54.1
BC15	6	16	30	0	A	11	234	28.0	37.1	1.66	6.00	22.0	28.0	21.4	35.7
BC18	8	16	0	0	A	11	258	25.3	37.4	1.34	7.00	6.00	13.0	53.9	76.9
BC29	6	16	0	-5.0	A	11	236	27.1	37.5	1.41	7.00	7.00	14.0	50.0	71.4
BC30	6	16	0	-2.5	A	11	235	27.0	37.3	1.26	6.80	6.00	12.8	53.1	78.1
BC31	6	16	0	2.5	A	11	235	26.0	37.5	1.47	8.00	7.50	15.5	51.6	64.5
BC32	6	16	0	5.0	A	11	235	27.3	37.6	1.36	8.25	7.20	15.5	53.4	64.7
BC37	3	18	0	0	A	11	126	21.4	37.5	1.38	3.60	10.4	14.0	25.7	71.4
BC38	4	18	0	0	A	11	160	22.5	37.4	1.22	4.60	10.0	14.6	31.5	68.5
BC39	6	18	0	0	A	11	235	26.4	37.5	1.03	6.40	7.20	13.6	47.1	73.5
BC40	8	18	0	0	A	11	257	25.2	37.3	1.48	9.00	5.00	14.0	64.3	71.4
BC43	6	16	0	0	A	13.5	126	24.5	37.8	1.38	4.00	11.0	15.0	26.7	66.7
BC46	6	16	0	0	A	16	234	26.9	37.4	1.66	6.00	6.50	12.5	48.0	80.0
BC51	3	16	0	0	B	11	234	28.8	37.3	1.56	6.00	7.00	13.0	46.2	76.9
BC56	4	16	0	0	B	11	160	26.5	37.3	1.44	6.00	12.5	18.5	32.4	54.1
BC61	6	16	0	0	B	11	236	28.4	37.3	1.32	6.80	6.40	13.2	51.5	75.8
BC66	8	16	0	0	B	11	259	29.8	37.6	1.46	7.00	12.0	19.0	36.8	52.6

Gas A: 2.5%CO₂ 97.5%Ar; Gas B: 1.5%CO₂ 54%He 44.5%Ar

Table V.5 – Waveform parameters obtained for CMT-P.

Run	WFS [m/min]	WFS/ TS Ratio	ALC [%]	PC [%]	Gas	CTWD [mm]	I _p [A]	U _p [V]	I _b [A]	U _b [V]	I _{sc} [A]	U _{sc} [V]	N _{p/sc}	t _p [ms]	t _b [ms]	t _{sc} [ms]	t _{cycle} [ms]	Duty Cycle [%]	F _p [Hz]	F _{sc} [Hz]
BP03	3	16	0	0	A	11	315	29.0	22.7	16.2	37.5	1.39	5	30.0	78.5	9.50	118.0	25.4	42.4	8.47
BP08	4	16	0	0	A	11	322	31.1	30.9	17.1	37.7	1.50	5	35.0	37.3	5.00	77.3	45.3	64.7	12.9
BP11	6	16	-30	0	A	11	322	29.1	56.8	18.3	32.8	1.30	8	48.0	18.5	5.50	72.0	66.7	111	13.9
BP12	6	16	-15	0	A	11	321	27.5	57.6	18.6	32.9	1.27	8	48.0	18.0	6.00	72.0	66.7	111	13.9
BP13	6	16	0	0	A	11	322	28.5	59.9	19.0	32.7	1.17	8	46.1	22.0	5.00	73.1	63.0	109	13.7
BP14	6	16	15	0	A	11	321	29.5	56.8	19.0	32.8	1.21	8	48.0	23.2	5.00	76.2	63.0	105	13.1
BP15	6	16	30	0	A	11	323	30.6	57.0	20.7	32.7	1.34	8	46.8	28.5	5.00	80.3	58.3	100	12.5
BP18	8	16	0	0	A	11	323	28.2	113.9	22.8	27.7	1.25	27	130	12.5	5.50	148	87.8	183	6.78
BP28	10	16	0	0	A	11	324	30.9	148.0	24.8	27.5	1.08	100	470	22.0	5.50	498	94.5	201	2.01
BP35	6	16	0	-5.0	A	11	269	24.9	56.6	17.4	32.9	1.23	8	42.0	17.1	5.00	64.1	65.5	125	15.6
BP36	6	16	0	-2.5	A	11	295	27.2	56.5	18.0	32.8	1.30	8	46.0	19.8	5.25	71.0	64.8	113	14.1
BP37	6	16	0	2.5	A	11	348	29.7	57.3	18.8	32.9	1.31	8	48.0	23.4	5.00	76.4	62.8	105	13.1
BP38	6	16	0	5.0	A	11	375	31.2	57.2	19.2	32.8	1.21	8	48.8	25.8	4.90	79.5	61.4	101	12.6
BP47	3	18	0	0	A	11	322	29.1	31.0	16.9	37.8	1.46	5	35.0	38.3	4.00	77.3	45.3	64.7	12.9
BP48	4	18	0	0	A	11	323	28.0	56.7	18.6	33.0	1.30	8	44.8	23.0	5.00	72.8	61.5	110	13.7
BP49	6	18	0	0	A	11	322	29.3	96.4	22.4	27.7	1.05	14	65.8	12.0	6.00	83.8	78.5	167	11.9
BP51	8	18	0	0	A	11	324	29.3	114.0	21.6	27.5	1.22	27	128	13.4	6.00	148	86.9	183	6.77
BP53	6	16	0	0	A	13.5	324	29.4	148.4	22.6	27.5	1.07	100	450	53.0	6.00	509	88.4	196	1.96
BP57	6	16	0	0	A	16	323	30.3	56.4	18.9	32.6	1.33	8	46.4	22.1	5.50	74.0	62.7	108	13.5
BP62	3	16	0	0	B	11	322	32.4	56.7	20.3	32.8	1.55	8	46.4	25.4	5.50	77.3	60.1	104	12.9
BP67	4	16	0	0	B	11	311	30.2	28.1	20.4	37.6	1.44	5	32.5	80.3	5.00	118	27.6	42.5	8.5
BP72	6	16	0	0	B	11	322	31.6	31.5	21.8	37.8	1.44	5	34.6	38.0	4.80	77.4	44.8	64.6	12.9
BP77	8	16	0	0	B	11	322	30.2	57.1	21.8	32.9	1.25	8	47.0	20.5	5.38	72.9	64.5	110	13.7
BP87	10	16	0	0	B	11	325	31.9	95.3	25.7	27.8	1.24	14	67.2	13.6	5.50	86.3	77.9	162	11.6

Gas A: 2.5%CO₂ 97.5%Ar; Gas B: 1.5%CO₂ 54%He 44.5%Ar

Table V.6 – Waveform parameters obtained for FastROOT.

Run	WFS [m/min]	WFS/TS Ratio	BC [%]	FP [%]	Gas	CTWD [mm]	I _p [A]	U _p [V]	I _b [A]	U _{step} [V]	U _b [V]	t _p [ms]	t _b [ms]	t _{cycle} [ms]	Duty Cycle [%]	F _{sc} [Hz]
BF03	4	16	0	0	A	11	271	25.9	61.1	18.8	5.89	4.80	9.80	14.6	32.9	68.5
BF06	6	16	-50	0	A	11	262	24.3	51.4	16.7	6.17	5.50	5.50	11.0	50.0	90.9
BF07	6	16	-25	0	A	11	280	24.2	64.5	16.9	5.92	6.50	7.50	14.0	46.4	71.4
BF08	6	16	0	0	A	11	290	24.6	77.2	18.3	5.69	5.00	6.25	11.3	44.4	88.9
BF09	6	16	25	0	A	11	301	23.9	88.0	18.2	6.85	5.00	10.0	15.0	33.3	66.7
BF10	6	16	50	0	A	11	311	23.3	101	18.7	5.84	4.50	9.50	14.0	32.1	71.4
BF13	8	16	0	0	A	11	305	25.1	94.8	17.9	7.33	5.50	4.50	10.0	55.0	100
BF18	9	16	0	0	A	11	321	25.1	110	18.5	8.24	5.00	1.75	6.75	74.1	148
BF21	8	16	0	-30	A	11	339	22.1	123	19.5	7.08	3.25	4.00	7.25	44.8	138
BF22	8	16	0	-15	A	11	337	23.5	122	19.7	8.6	4.50	3.50	8.00	56.3	125
BF23	8	16	0	15	A	11	336	26.9	123	18.7	9.05	4.00	5.25	9.25	43.2	108
BF24	8	16	0	30	A	11	337	28.4	123	20.5	8.35	4.50	5.00	9.50	47.4	105
BF25	4	18	0	0	A	11	295	24.2	80.2	18.4	5.56	5.00	11.0	16.0	31.3	62.5
BF26	6	18	0	0	A	11	314	24.7	101	20.2	7.04	5.00	8.00	13.0	38.5	76.9
BF27	8	18	0	0	A	11	336	25.5	123	21.4	7.95	5.00	7.00	12.0	41.7	83.3
BF28	9	18	0	0	A	11	353	26.4	145	19.7	9.21	4.50	3.00	7.50	60.0	133
BF30	6	16	0	0	A	13.5	313	25.3	101	19.1	6.47	4.75	11.0	15.8	30.2	63.5
BF34	6	16	0	0	A	16	317	26.1	101	19.7	7.98	5.00	10.5	15.5	32.3	64.5
BF39	4	16	0	0	B	11	275	27.5	60.4	22.8	3.91	6.00	13.0	19.0	31.6	52.6
BF44	6	16	0	0	B	11	296	27.8	76.1	20.9	6.25	5.75	10.0	15.8	36.5	63.5
BF49	8	16	0	0	B	11	297	27.6	86.2	21.2	8.08	5.50	8.50	14.0	39.3	71.4
BF54	9	16	0	0	B	11	310	27.6	96.0	22.2	6.13	6.25	4.00	10.3	61.0	97.6

Gas A: 2.5%CO₂ 97.5%Ar; Gas B: 1.5%CO₂ 54%He 44.5%Ar

VI. GRAPHICAL ANALYSIS OF THE EFFECT OF PROCESS SETTING PARAMETERS ON WAVEFORM AND ARC CHARACTERISTICS

The effect of several process setting parameters on waveform and arc characteristics was analysed for all waveforms: WFS, adjusting arc length parameters (trim, ALC, BC), adjusting dynamics parameters (wavecontrol, DC, PC, FP), CTWD, shielding gas composition and the volume of filler metal deposited (WFS/TS ratio). The tests performed are identified according to the conditions presented in Appendix II. The arc characteristics were determined by the measurement of arc length (Appendix III). The waveform characteristics were defined in terms of measured WFS, average arc current, arc voltage and arc energy (Appendix IV).

The experimental conditions applied to the welding tests performed, unless otherwise indicated, were: WFS of 6m/min; WFS/TS of 16, trim of 1.5 (GMAW-P and RapidArc) or 1.0 (STT), ALC of 0% (CMT, CMT-P), Base Current of 0% (FastROOT), nominal value (0%) for dynamic control parameter (exception for GMAW-P, RapidArc and STT, where wavecontrol was set at 10), CTWD of 11mm and 2.5%CO₂ 97.5%Ar.

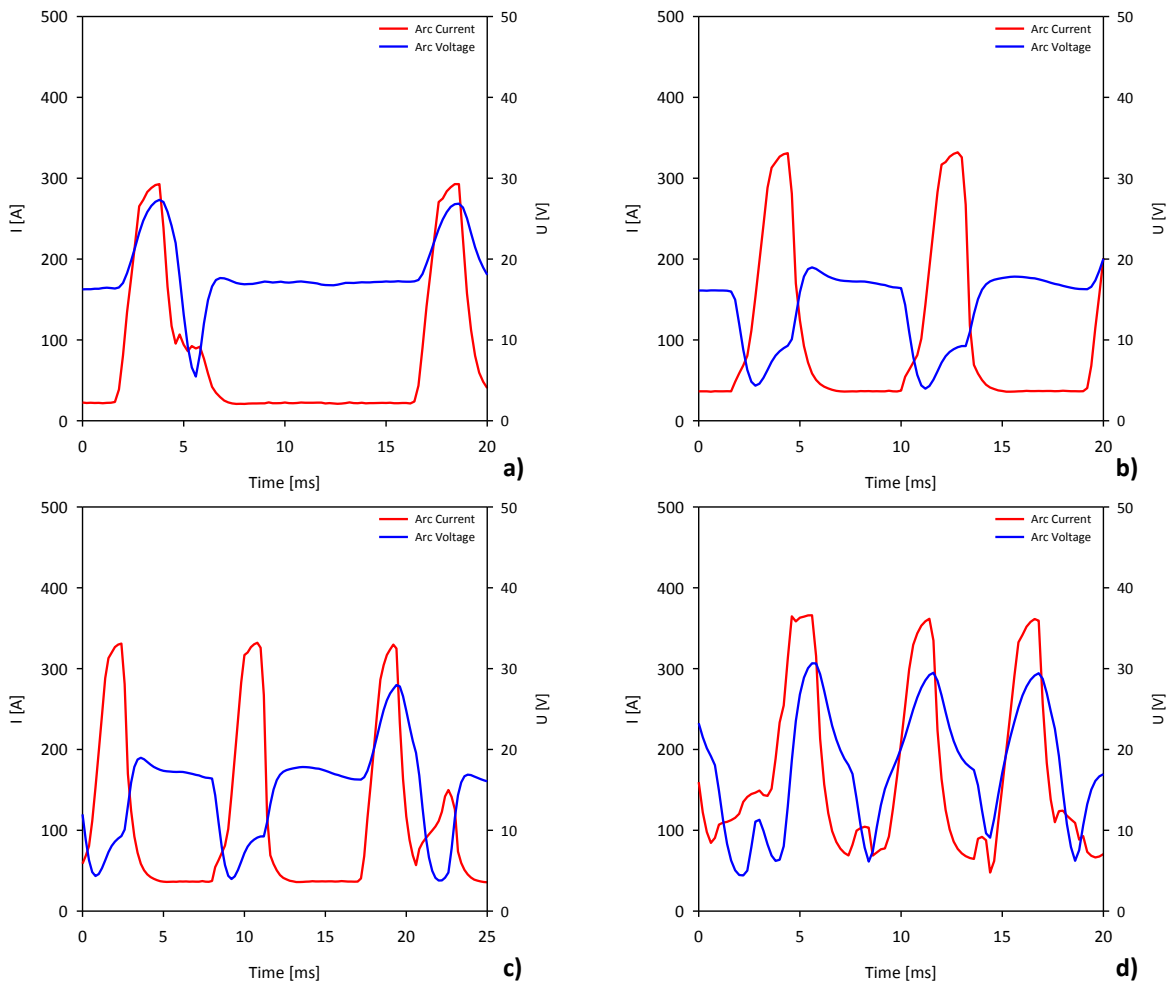


Figure VI.1 – GMAW-P Waveforms obtained for different WFS levels: a) 4m/min; b) 6m/min; c) 8m/min and d) 10m/min.

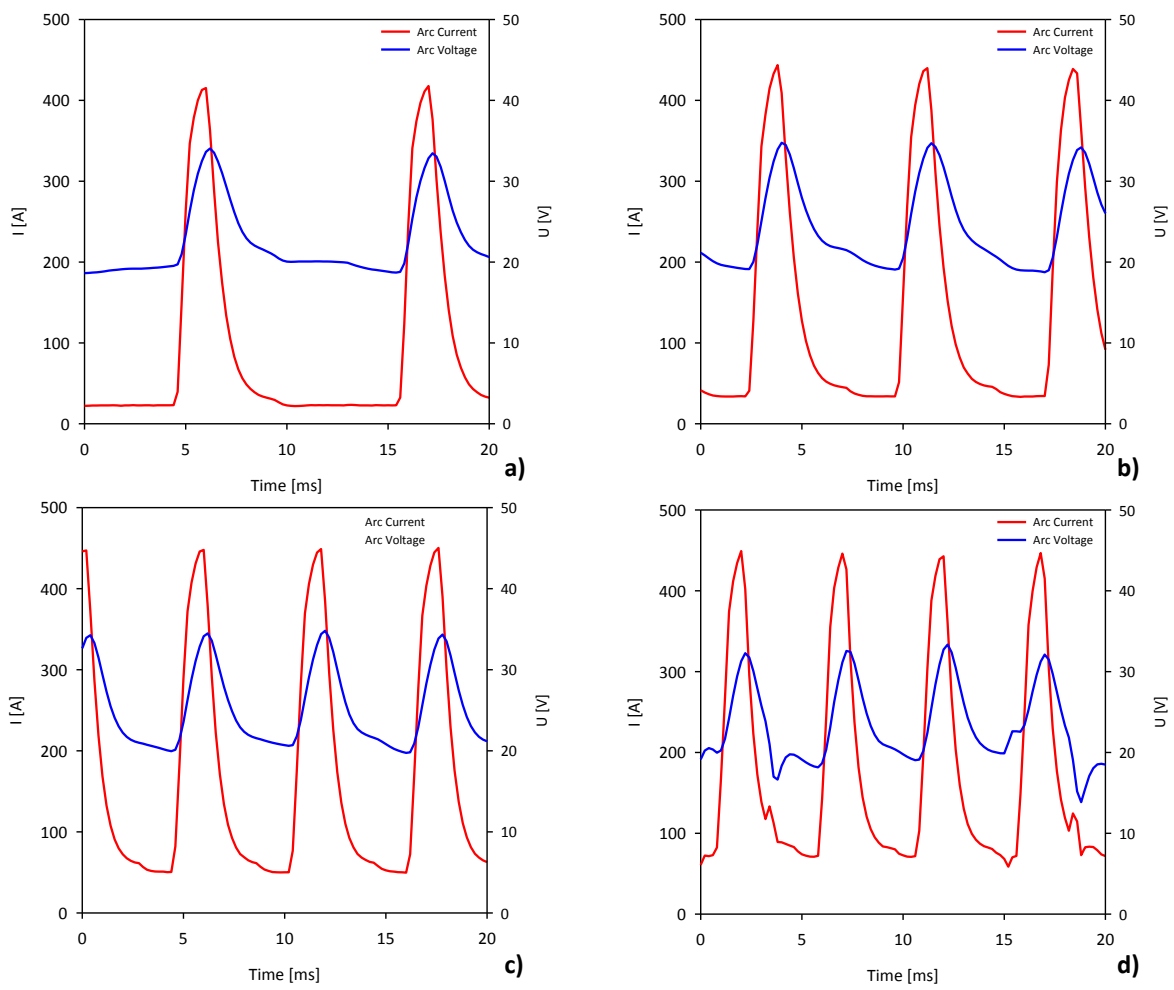


Figure VI.2 – RapidArc Waveforms obtained for different WFS levels: a) 4m/min; b) 6m/min; c) 8m/min and d) 10m/min.

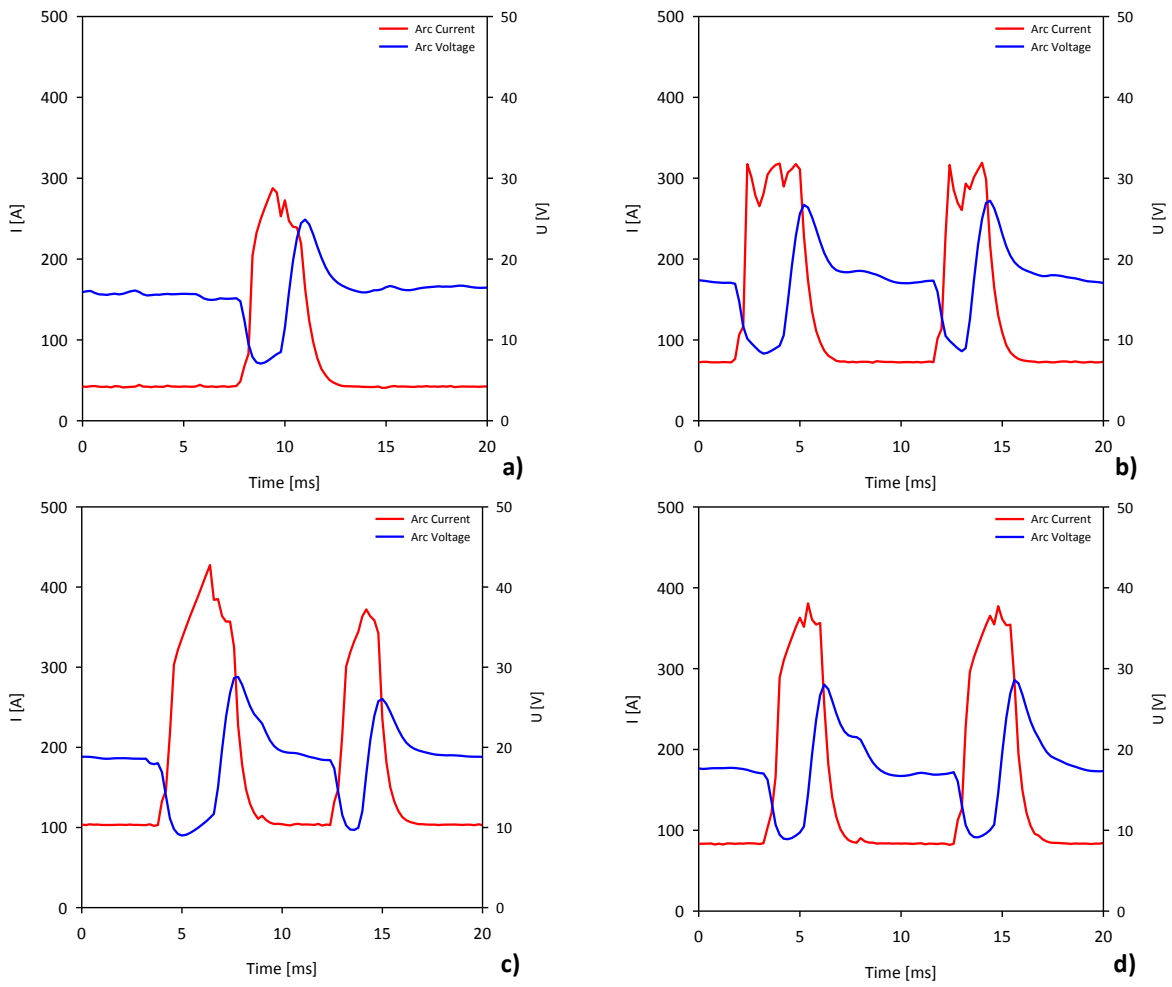


Figure VI.3 – STT Waveforms obtained for different WFS levels: a) 3m/min; b) 6m/min; c) 8m/min and d) 8.26m/min.

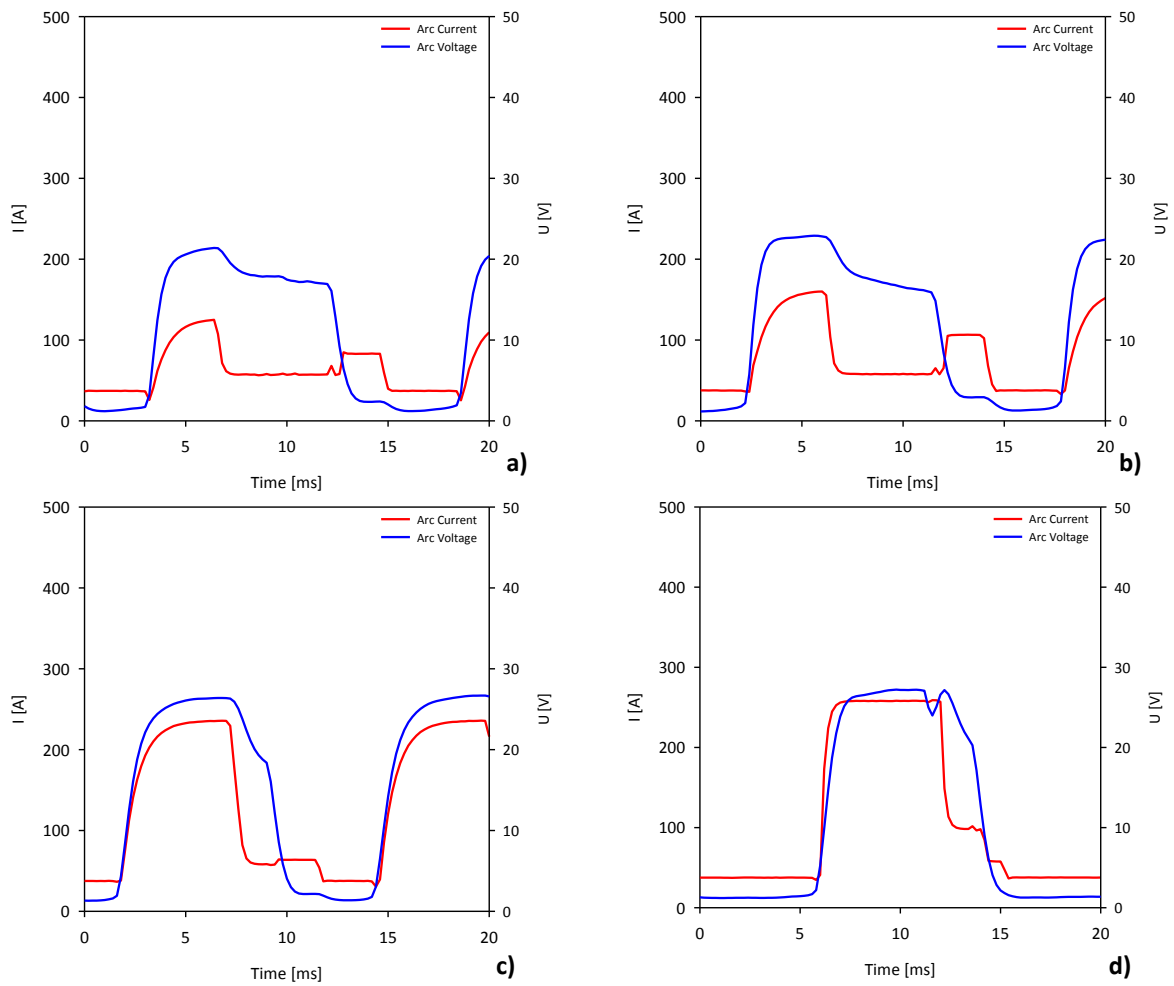


Figure VI.4 – CMT Waveforms obtained for different WFS levels: a) 3m/min; b) 4m/min; c) 6m/min and d) 8m/min.

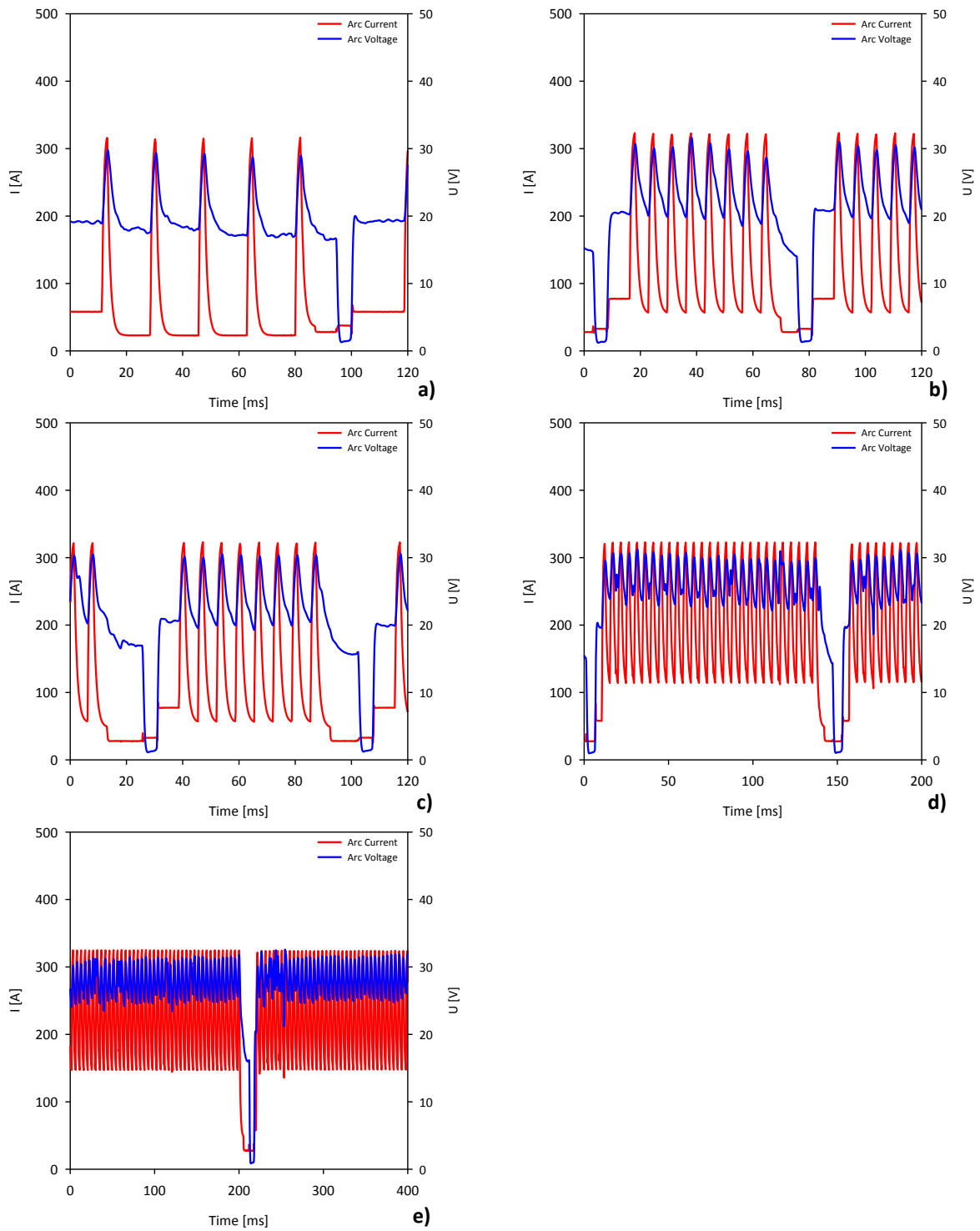


Figure VI.5 – CMT-P Waveforms obtained for different WFS levels: a) 3m/min; b) 6m/min; c) 8m/min, d) 9m/min and e) 10m/min.

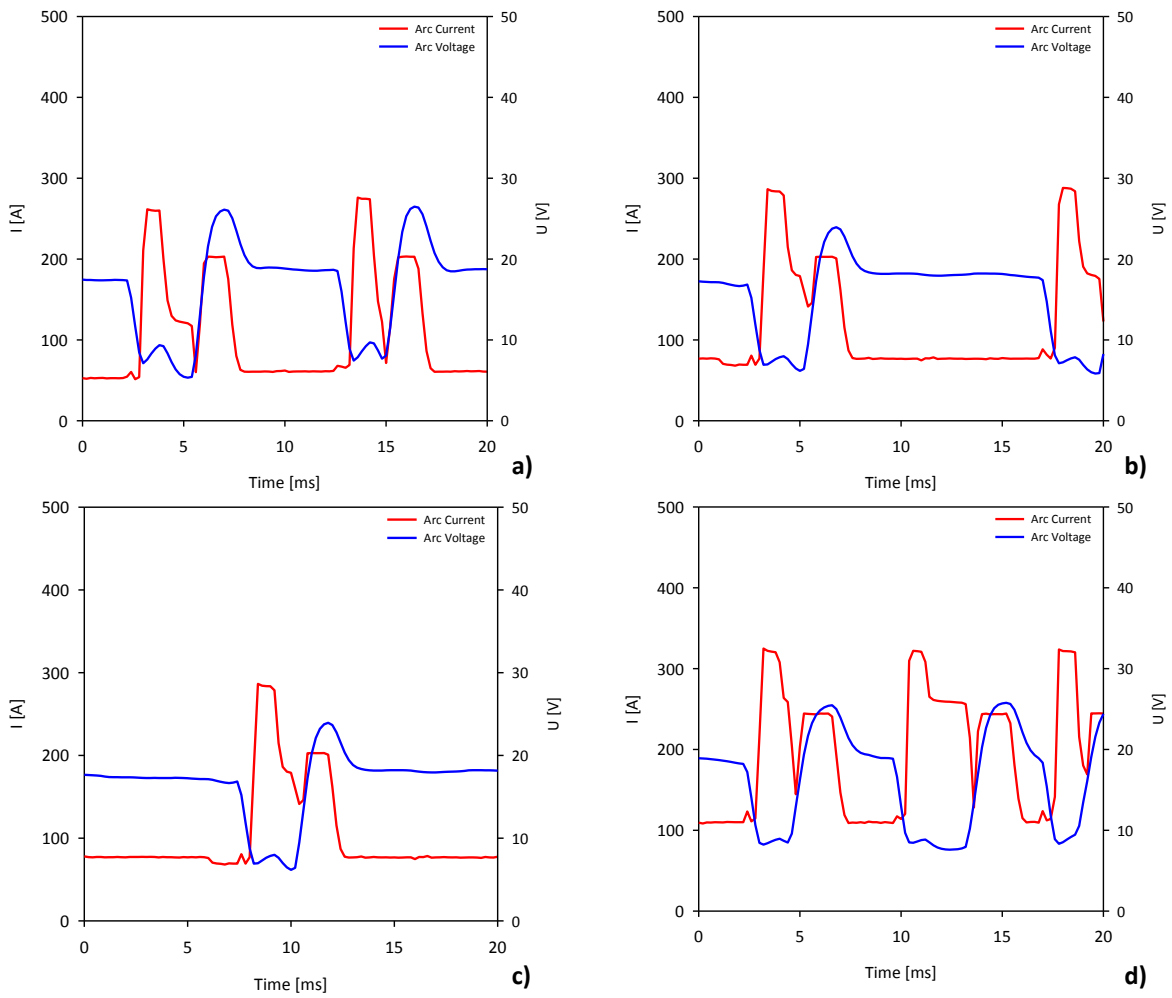


Figure VI.6 – FastROOT Waveforms obtained for different WFS levels: a) 4m/min; b) 6m/min; c) 8m/min and d) 9m/min.

VI.1. Characterization of Waveform Characteristics and Arc Length for GMAW-P

The effect of WFS on the arc length and waveform characteristics was evaluated for GMAW-P and the results obtained are presented in the Figure VI.7 and VI.8.

The effect of trim (arc length adjusting parameter) varying the setting from 0.5 (minor limit) to 1.5 (major limit) at different WFS levels are shown in Figures VI.9 and VI.10. This plot is represented by the average (line) and standard deviation (bars) from the five measurements obtained from 0.5 to 1.5. The effects of trim changes from 0.5 to 1.5 at a constant WFS of 6m/min are shown in Figures VI.11 and VI.12.

The effect of CTWD was analysed and the results are illustrated in the Figures VI.13 and VI.14.

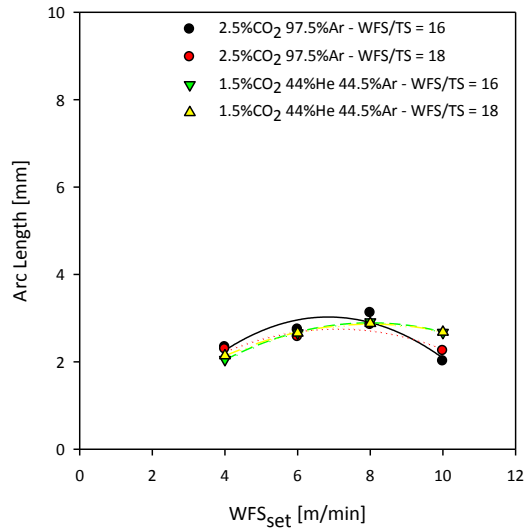


Figure VI.7 – Effect of WFS on arc length for GMAW-P, at different WFS/TS ratios and shielding gases.

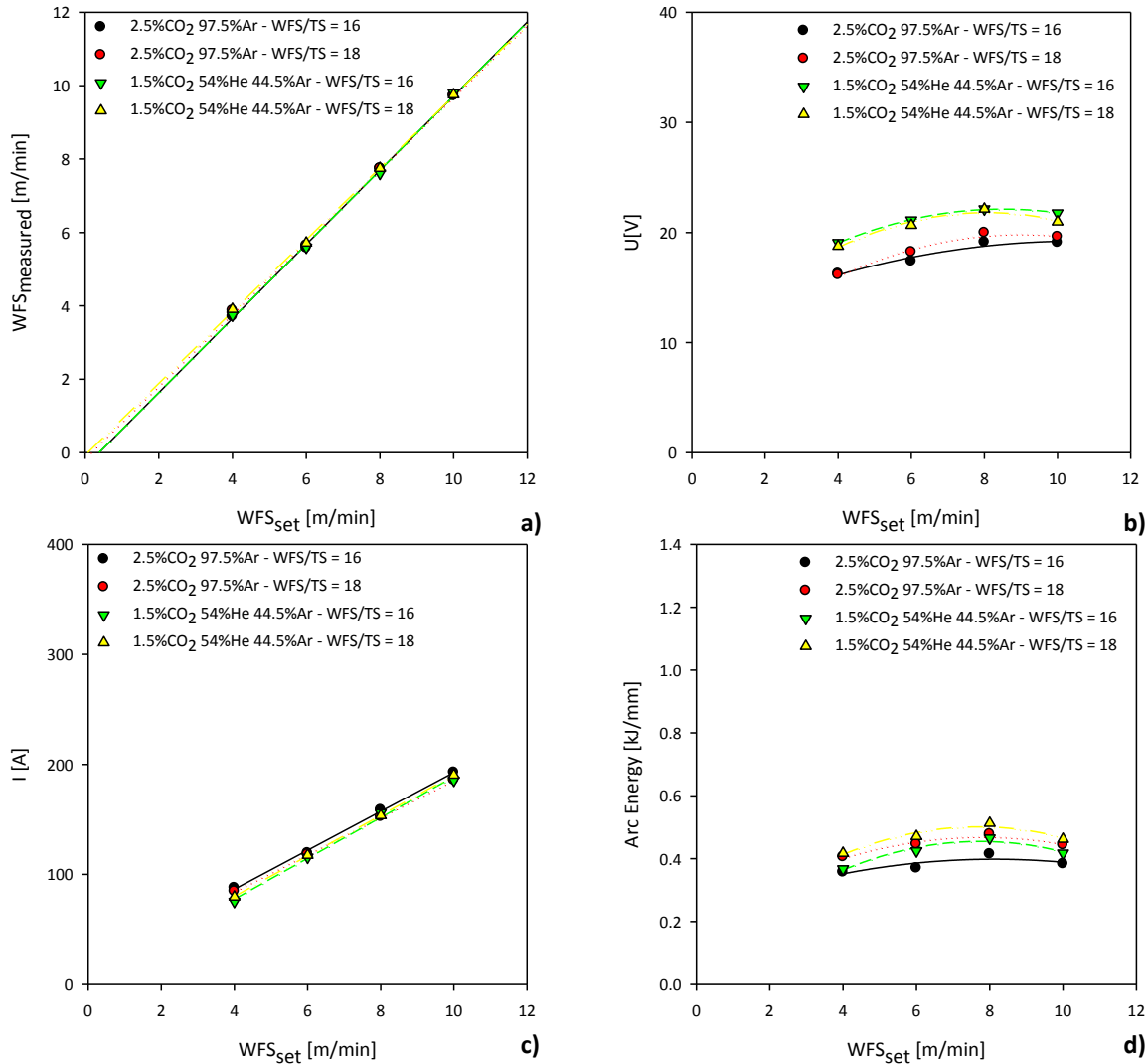


Figure VI.8 – Effect of WFS on waveform characteristics for GMAW-P, at different WFS/TS ratios and shielding gases: a) measured WFS; b) arc voltage; c) arc current; d) arc energy.

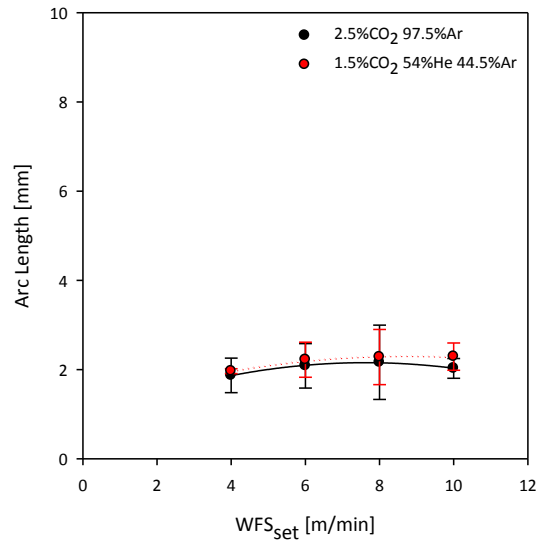


Figure VI.9 – Effect of the variation of trim on arc length for GMAW-P, at different WFS levels and shielding gases.

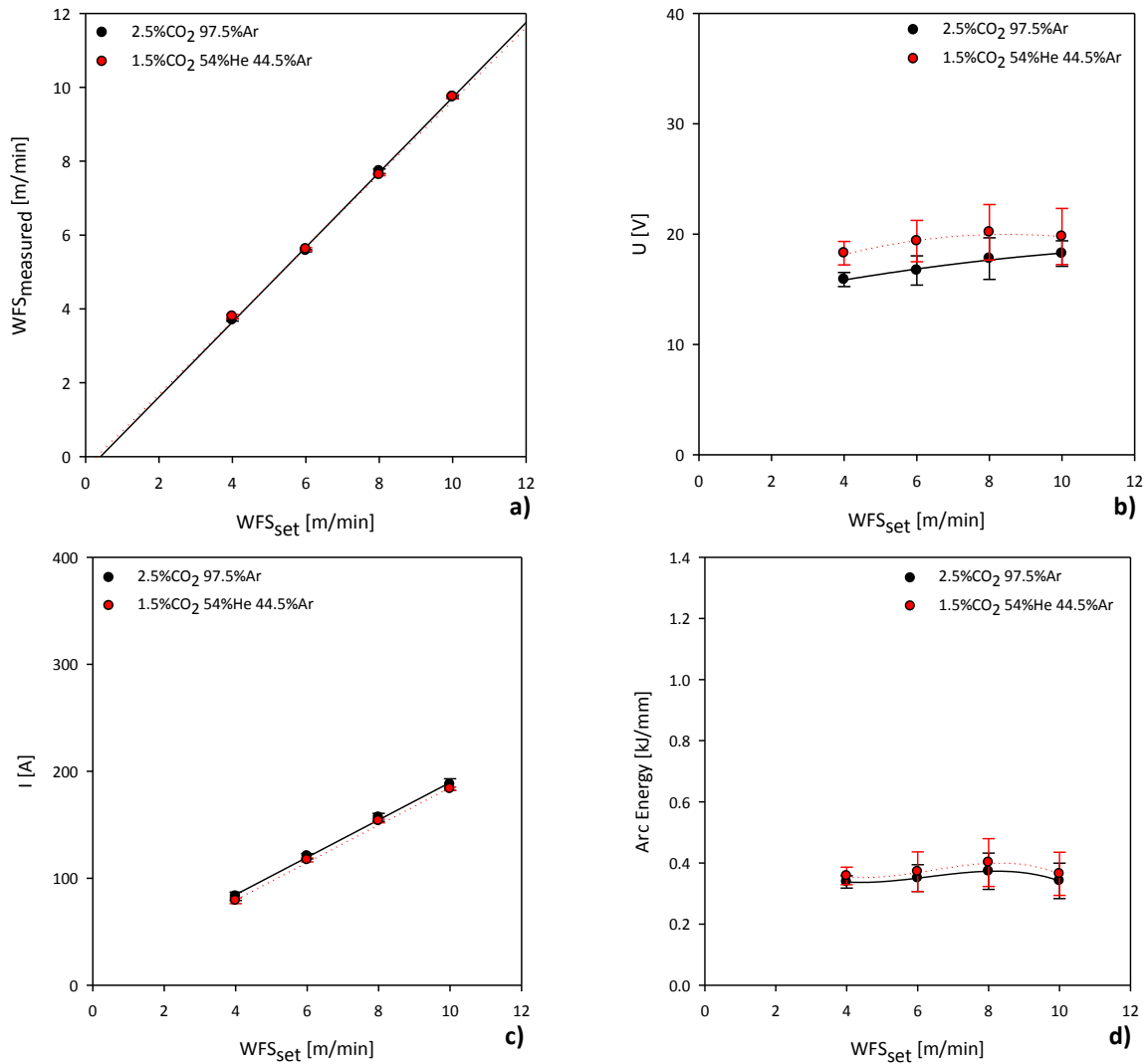


Figure VI.10 - Effect of the variation of trim on waveform characteristics to RapidArc, at different WFS levels and shielding gases: a) measured WFS; b) arc voltage; c) arc current; d) arc energy.

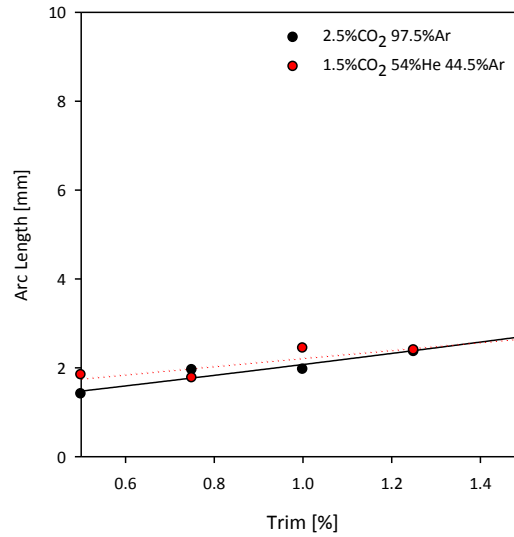


Figure VI.11 – Effect of trim on arc length for GMAW-P, at different shielding gases.

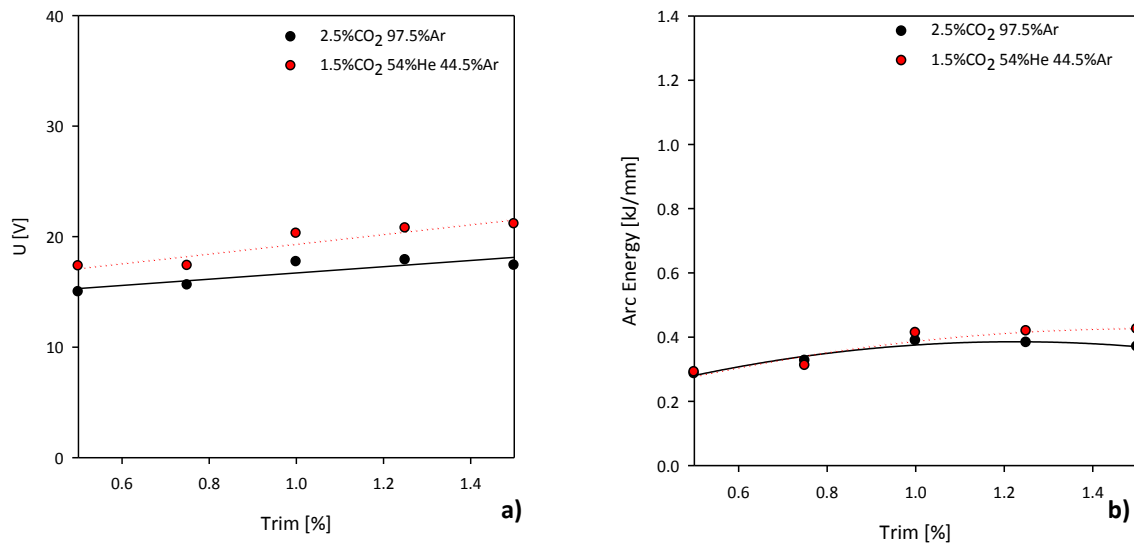


Figure VI.12 – Effect of trim on arc voltage (a) and arc energy (b) for GMAW-P, at different shielding gases.

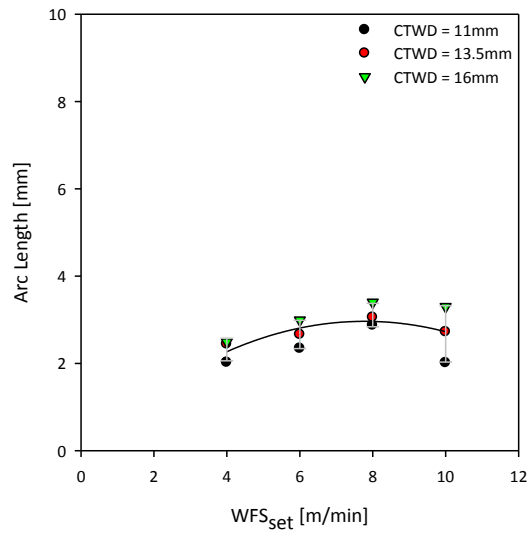


Figure VI.13 – Effect of the variation of CTWD on arc length for GMAW-P at different WFS levels.

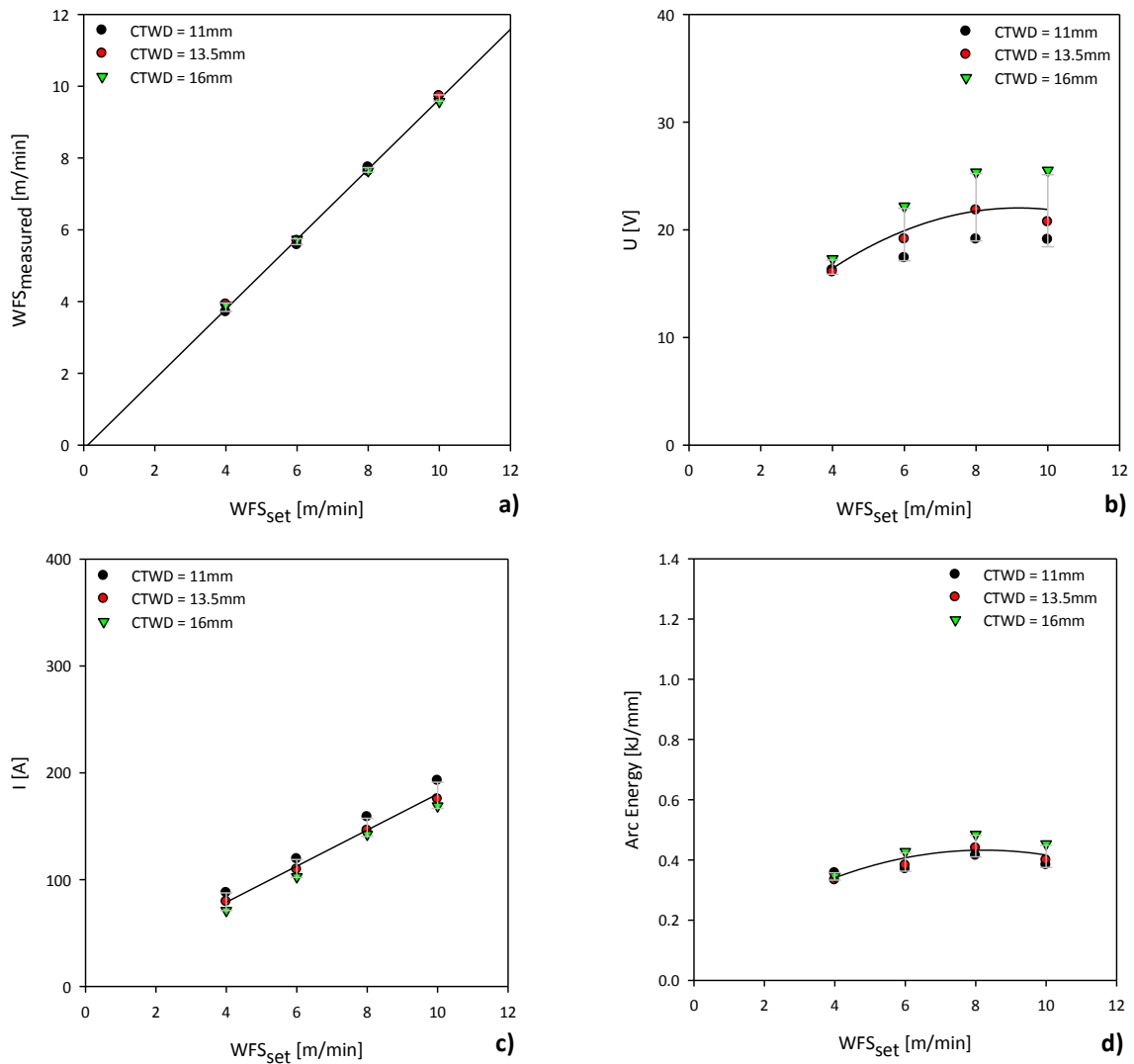


Figure VI.14 – Effect of the variation of CTWD on waveform characteristics for GMAW-P, at different WFS levels: a) measured WFS; b) arc voltage; c) arc current; d) arc energy.

VI.2. Characterization of Waveform Characteristics and Arc Length for RapidArc

The effect of WFS on the arc length and waveform characteristics was also studied for RapidArc, applying a wider range of WFS, when WFS/TS ratio of 18 was chosen. The results are presented in the Figures VI.15 and VI.16.

The effect of trim was also assessed for RapidArc in the same way as was performed to GMAW-P, by changing the trim setting from 0.5 to 1.5 in five steps. The results are illustrated in the Figures VI.17 to VI.20.

The effect of CTWD was also assessed for RapidArc at different WFS levels. The results are illustrated in the Figures VI.21 and VI.22.

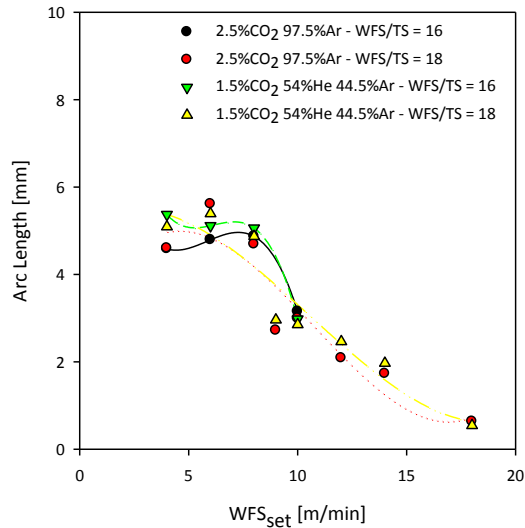


Figure VI.15 – Effect of WFS on arc length for RapidArc, at different WFS/TS ratios and shielding gases.

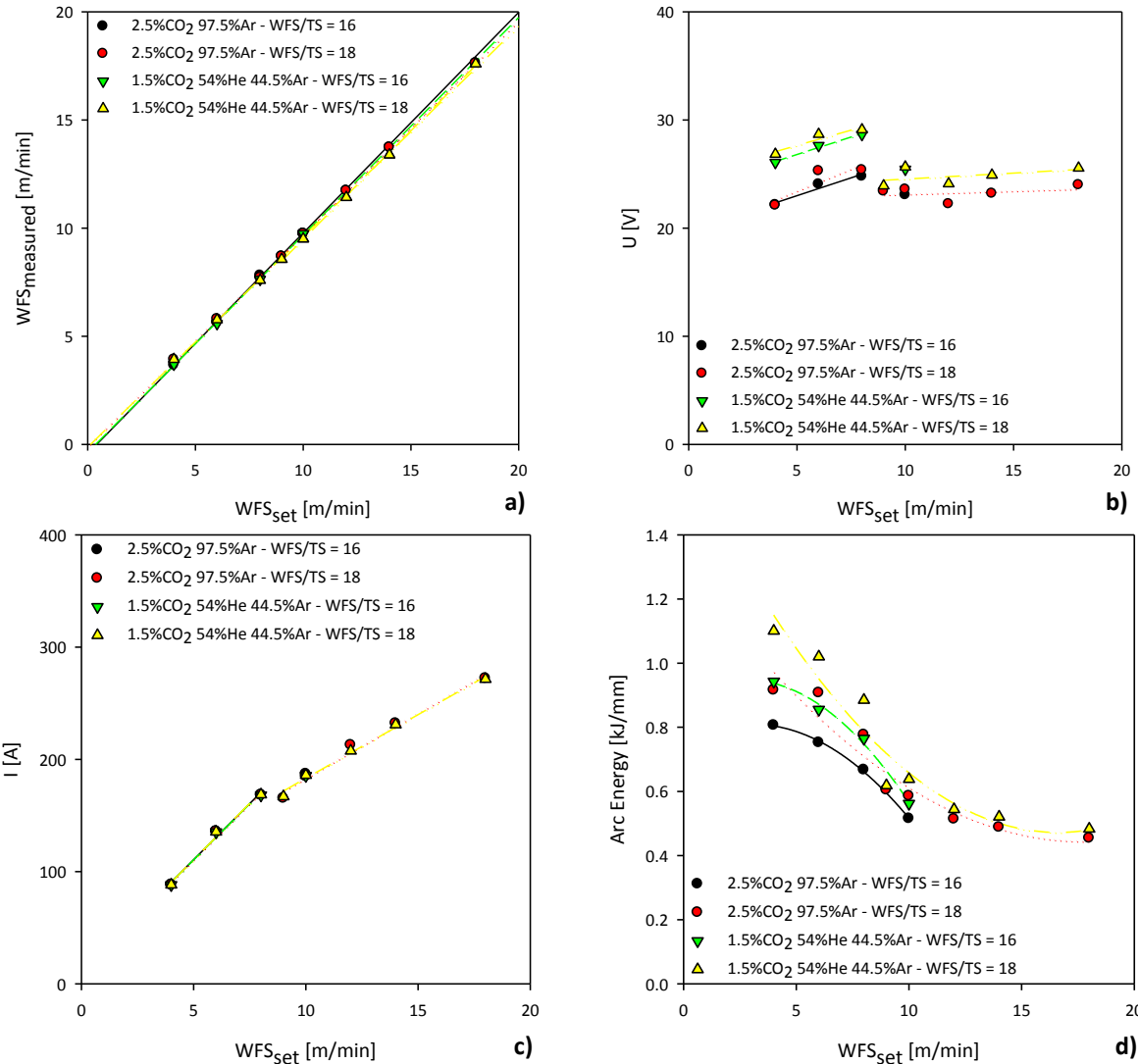


Figure VI.16 – Effect of WFS on waveform characteristics for RapidArc, at different WFS/TS ratios and shielding gases: a) measured WFS; b) arc voltage; c) arc current; d) arc energy.

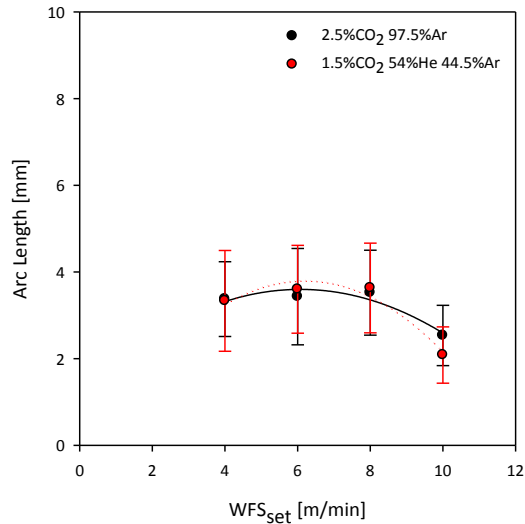


Figure VI.17 – Effect of the variation of trim on arc length for RapidArc, at different WFS levels and shielding gases.

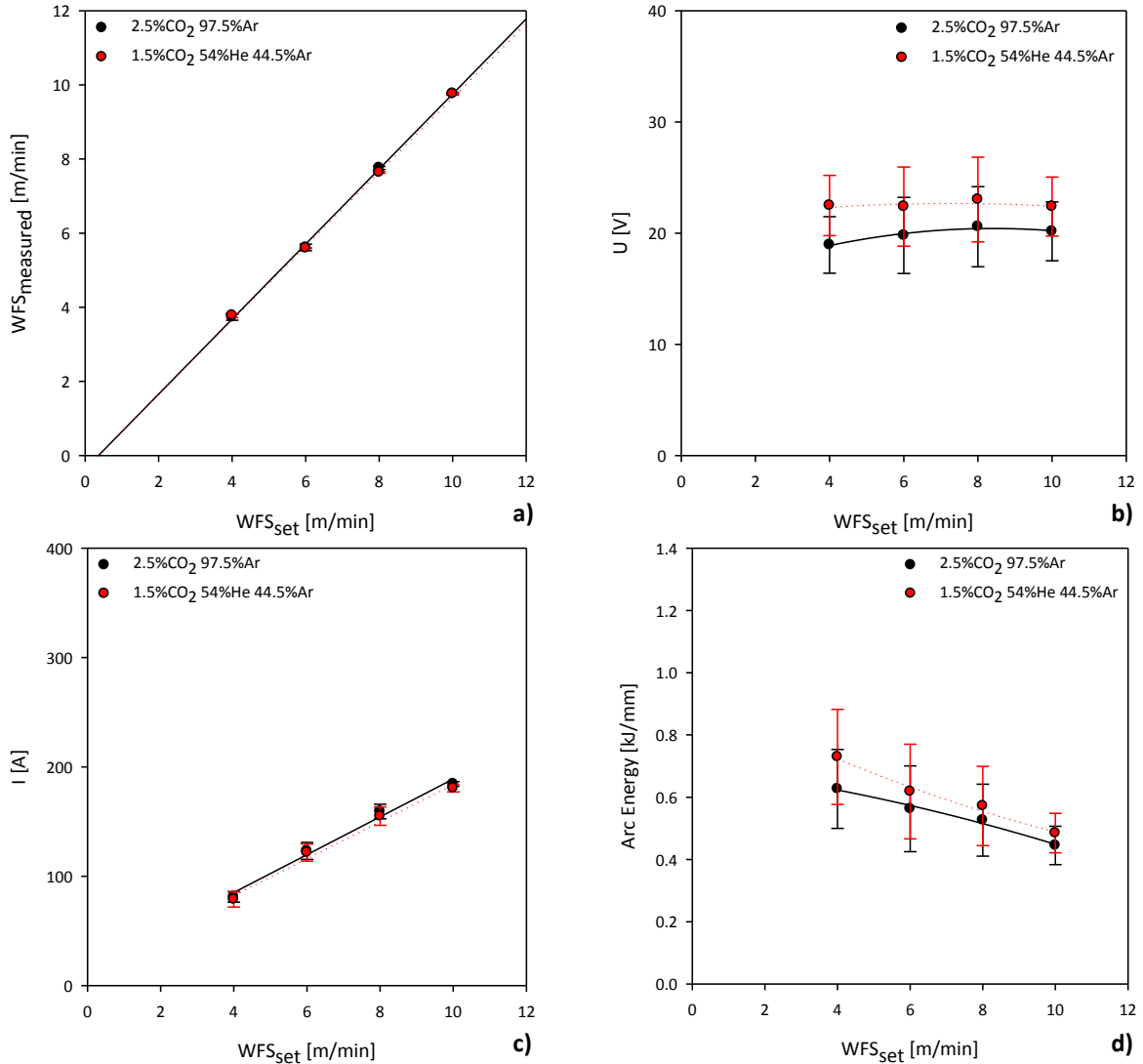


Figure VI.18 – Effect of the variation of trim on waveform characteristics to RapidArc, at different WFS levels and shielding gases: a) measured WFS; b) arc voltage; c) arc current; d) arc energy.

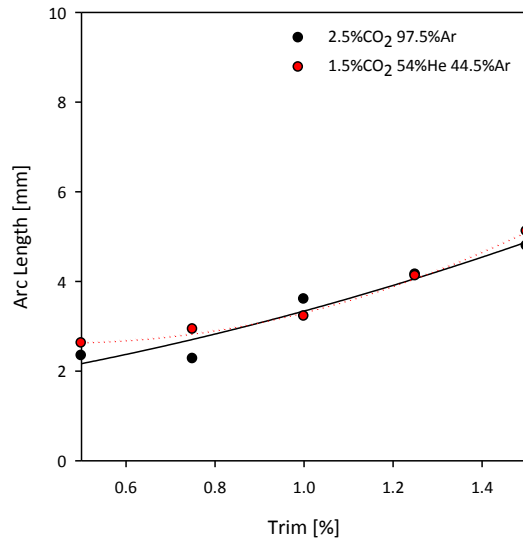


Figure VI.19 – Effect of trim on the arc length for RapidArc, at different shielding gases.

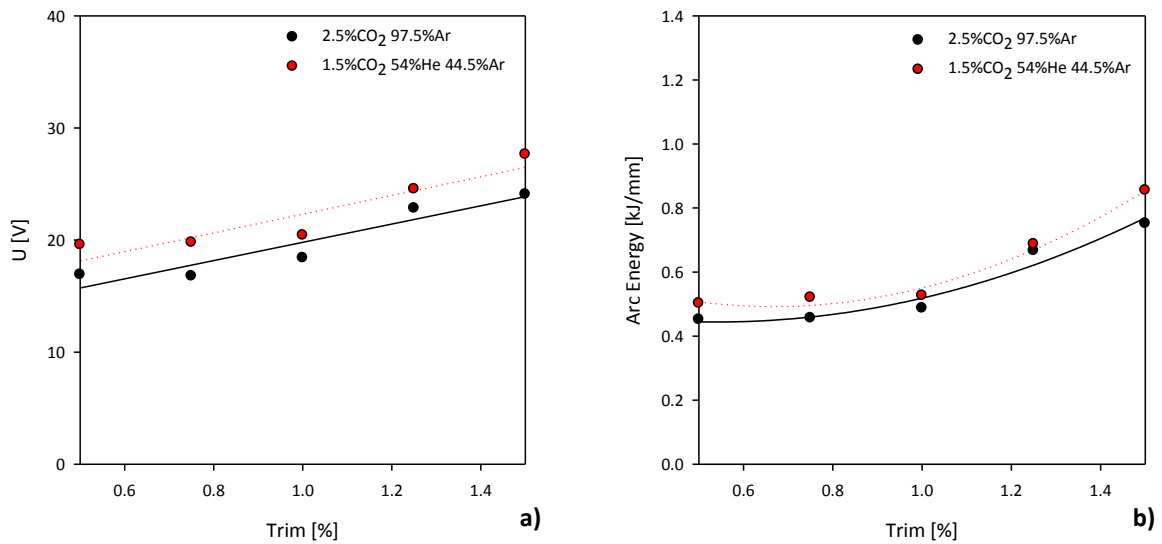


Figure VI.20 – Effect of trim on the arc voltage (a) and arc energy (b) for RapidArc, at different shielding gases.

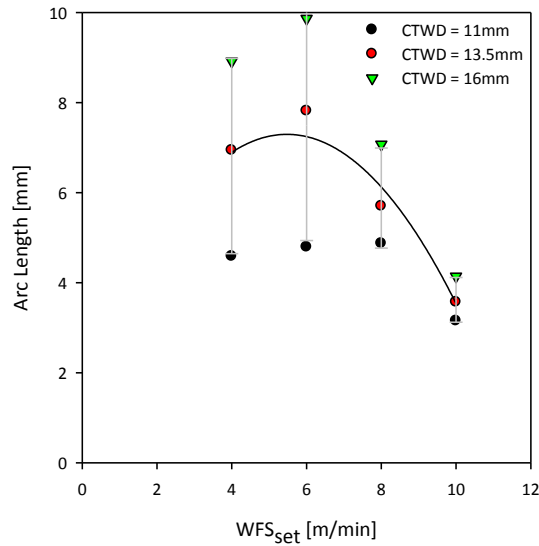


Figure VI.21 – Effect of the variation of CTWD on arc length for RapidArc, at different WFS levels.

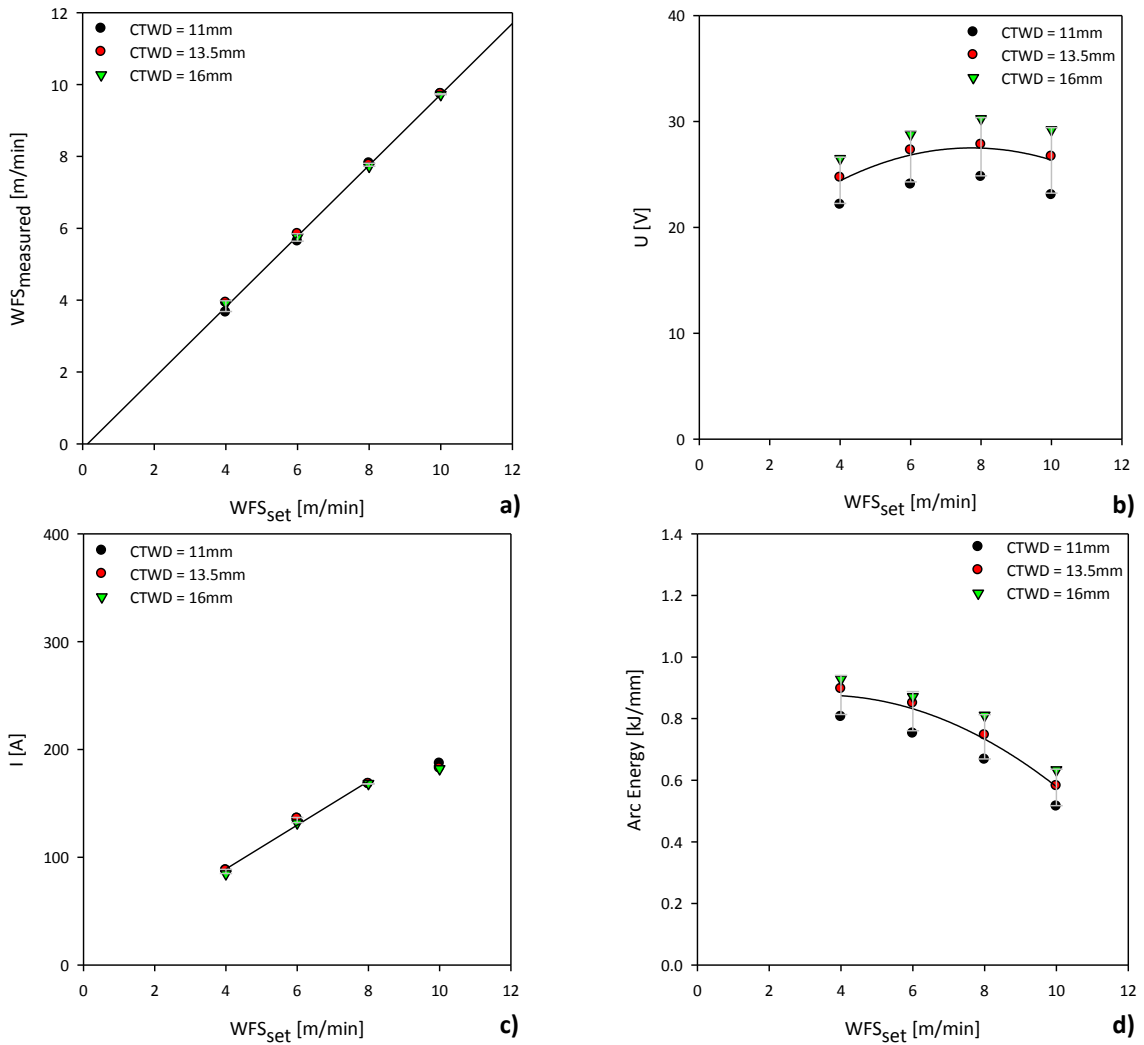


Figure VI.22 – Effect of the variation of CTWD on waveform characteristics for RapidArc, at different WFS levels: a) measured WFS; b) arc voltage; c) arc current; d) arc energy.

VI.3. Characterization of Waveform Characteristics and Arc Length for STT

The effect of WFS on the arc length and waveform characteristics was also studied for STT; the results are presented in the Figure VI.22 and VI.23.

The effect of trim was also assessed for STT at constant WFS (6m/min) (Figures VI.24 to VI.27)

The results of the variation of CTWD are illustrated in the Figure VI.28 and VI.29.

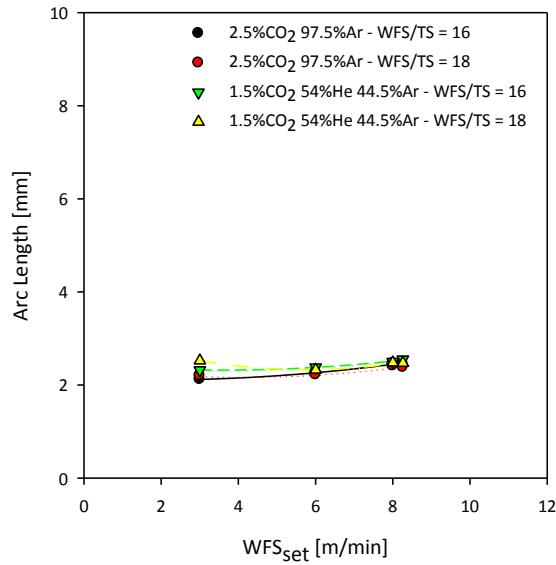


Figure VI.23– Effect of WFS on arc length for STT, at different WFS/TS ratios and shielding gases.

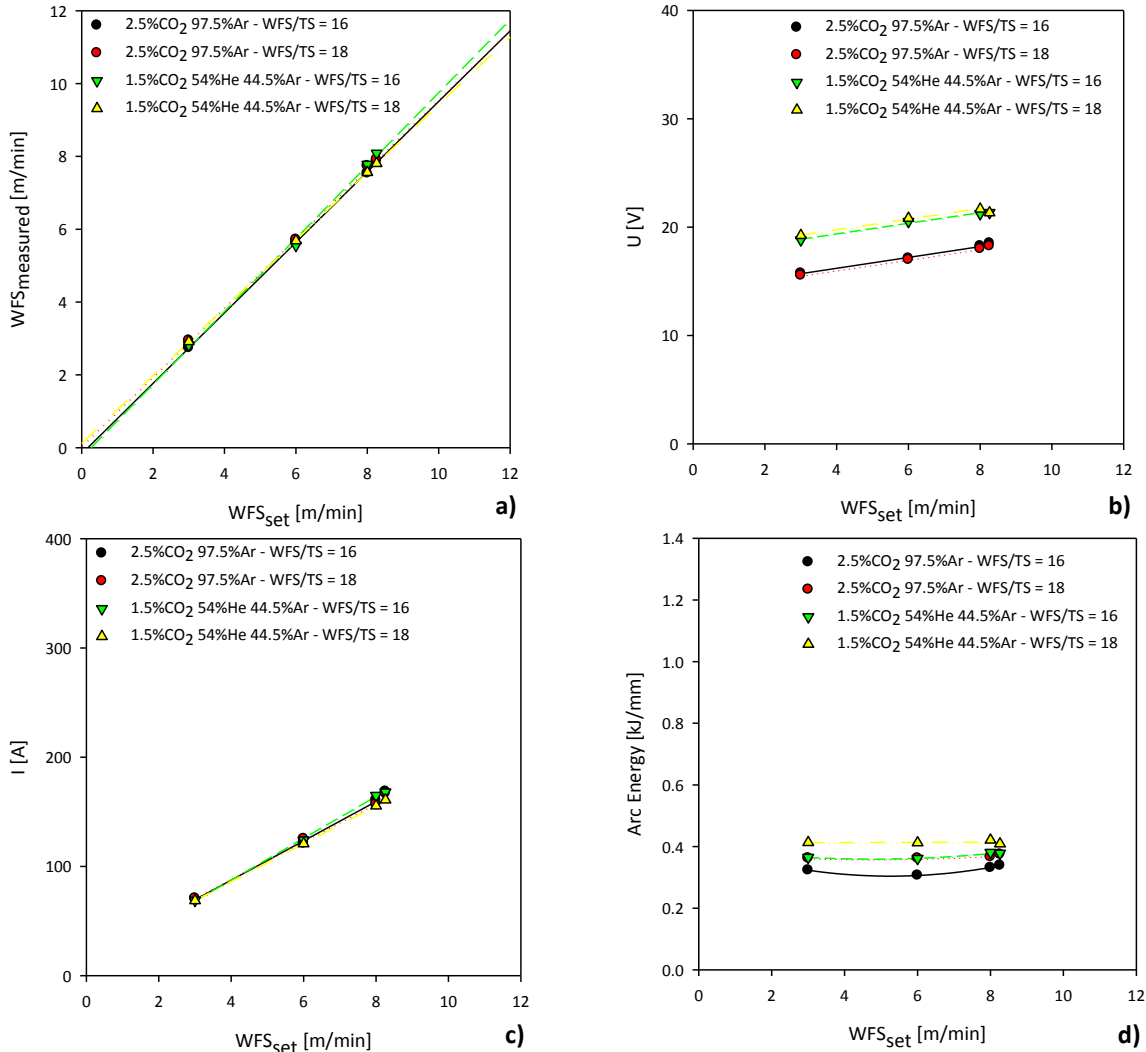


Figure VI.24 – Effect of WFS on waveform characteristics for STT, at different WFS/TS ratios and shielding gases: a) measured WFS; b) arc voltage; c) arc current; d) arc energy.

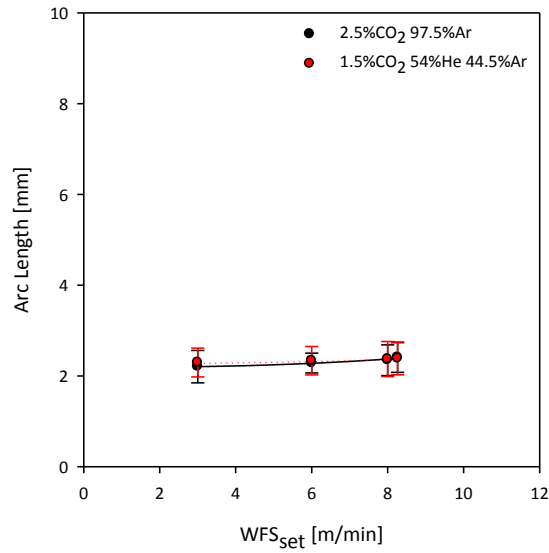


Figure VI.25 – Effect of the variation of trim on arc length for STT, at different WFS levels and shielding gases.

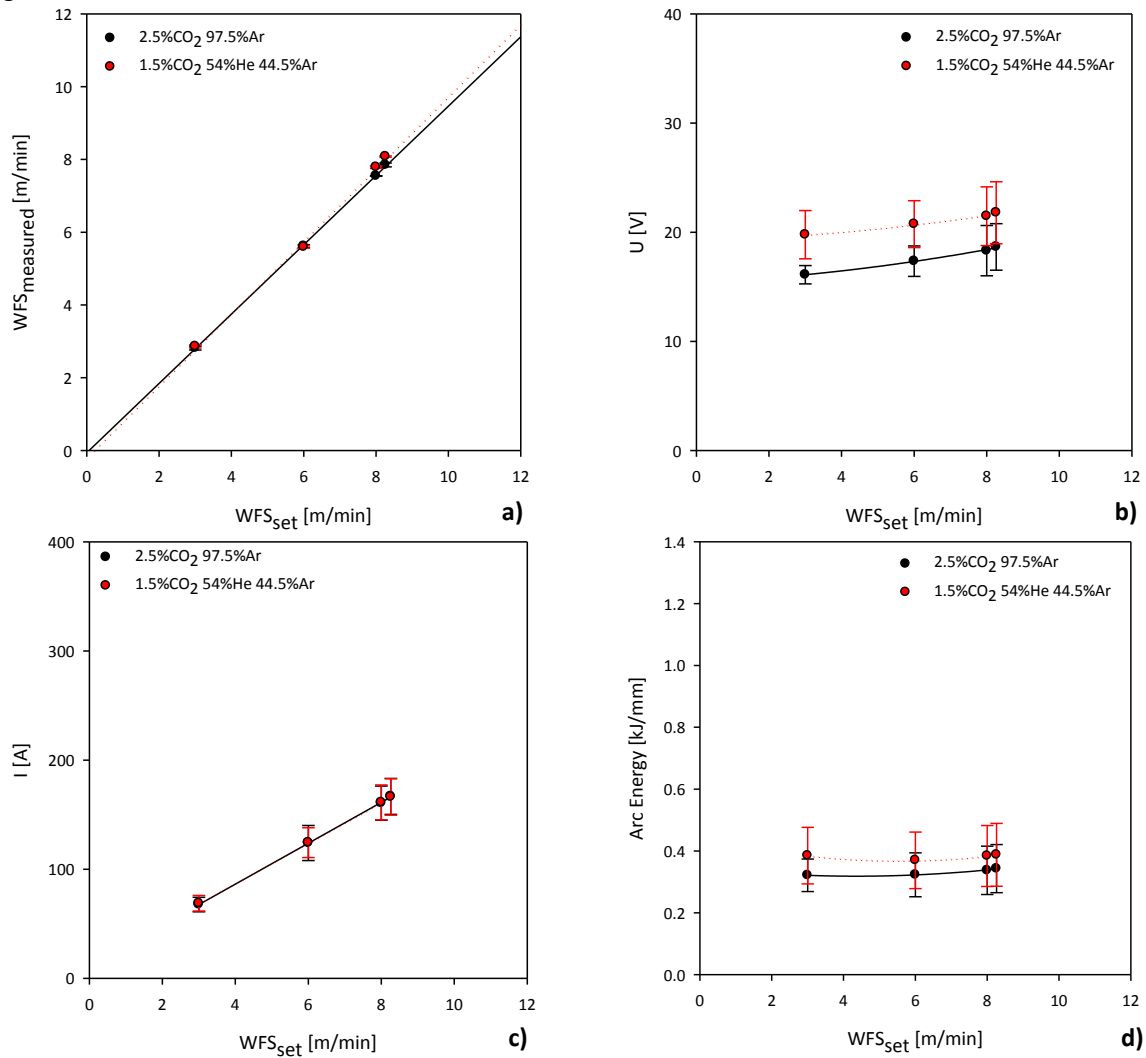


Figure VI.26 – Effect of the variation of trim on waveform characteristics for STT, at different WFS levels and shielding gases: a) measured WFS; b) arc voltage; c) arc current; d) arc energy.

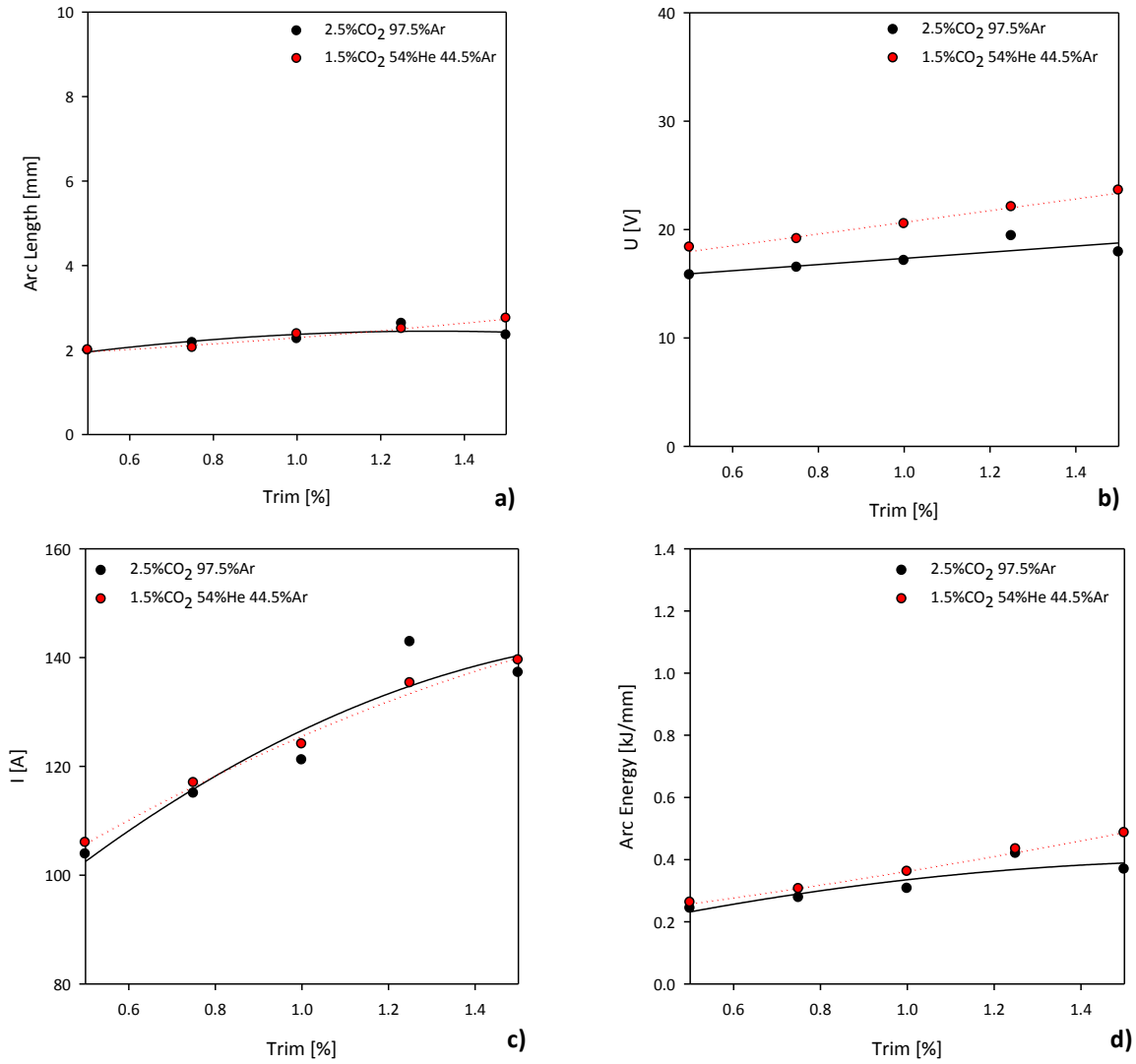


Figure VI.27 – Effect of trim on waveform characteristics for STT, at different shielding gases: a) arc length; b) measured WFS; c) arc voltage; d) arc current and d) arc energy.

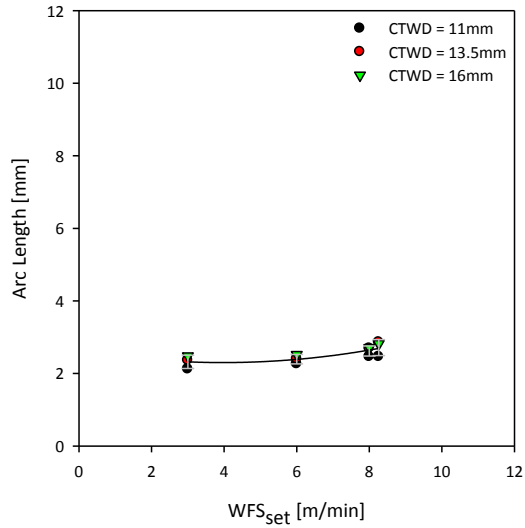


Figure VI.28 – Effect of the variation of CTWD on waveform characteristics for STT, at different WFS levels.

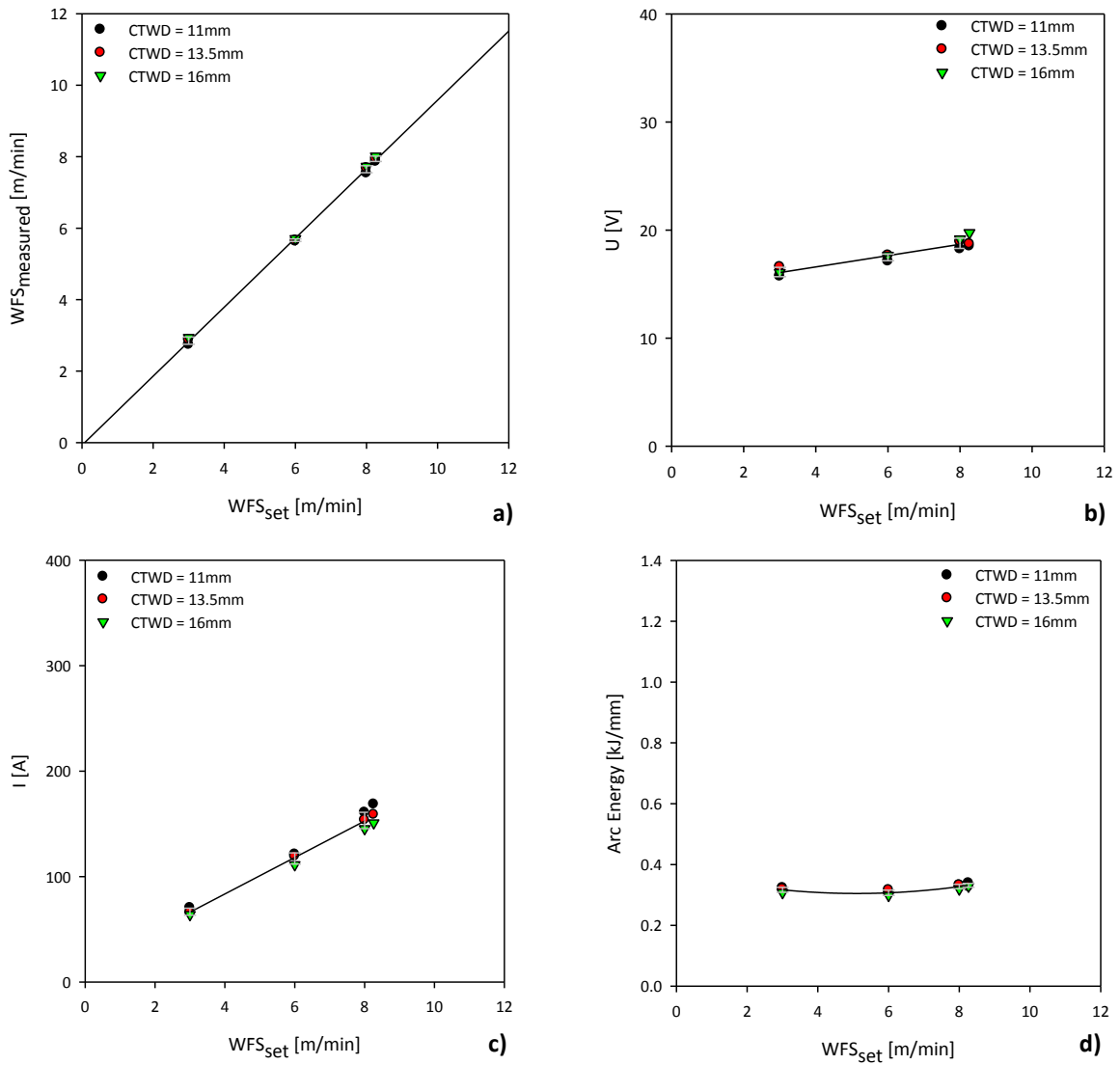


Figure VI.29 – Effect of variation of CTWD on waveform characteristics for STT, at different WFS levels: a) measured WFS; b) arc voltage; c) arc current; d) arc energy.

VI.4. Characterization of Waveform Characteristics and Arc Length for CMT

The effect of setting parameters on the arc length and waveform characteristics to CMT was evaluated using 13% chrome supermartensitic steel and mild steel. The results will be presented in two different subsections, according with the CMT mode applied. The arc length was not monitored for the tests performed using mild steel.

VI.4.1. 13% Chrome Supermartensitic Stainless Steel

The effect of WFS was evaluated and the results obtained are presented in the Figure VI.30 and VI.31

The effect of ALC was assessed in terms of its variability at different WFS levels and its variation at constant WFS, as illustrated from the Figure VI.32 to VI.38.

The effect of Dynamic Control (DC) was also assessed in terms of its variability. The results obtained are illustrated in the Figure VI.39 and VI.40.

The effect of CTWD was also evaluated and the results are presented in the Figure VI.41 and VI.42

VI.4.2. Mild Steel

The tests performed to CMT welding using mild steel were undertaken with the following constant experimental conditions (unless anything else is mentioned): WFS of 7.8m/min, TS of 0.5m/min, ALC and HS of 0%, CTWD of 13.5mm and shielding gas 20%CO₂80%Ar.

The results of the effect of WFS are presented in the Figure VI.43.

The effect of ALC on welding parameters was assessed by varying the setting from -30 to +30, using constant WFS for mild steel (Figure VI.44).

The “Hot Start” (HS) parameter was evaluated for CMT using mild steel (Figure VI.45).

The effect of CTWD evaluated to CMT using mild steel is illustrated in Figure VI.46.

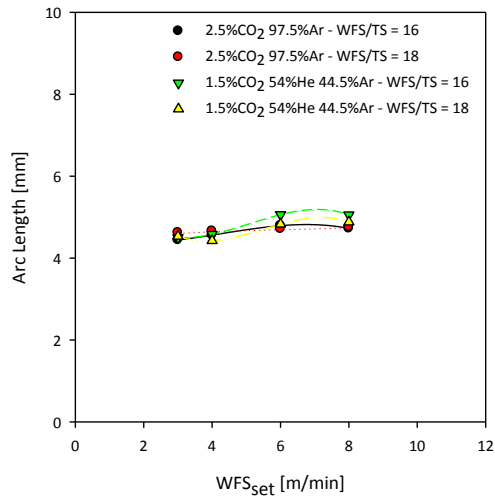


Figure VI.30 – Effect of WFS on arc length for CMT, at different WFS/TS ratios and shielding gases.

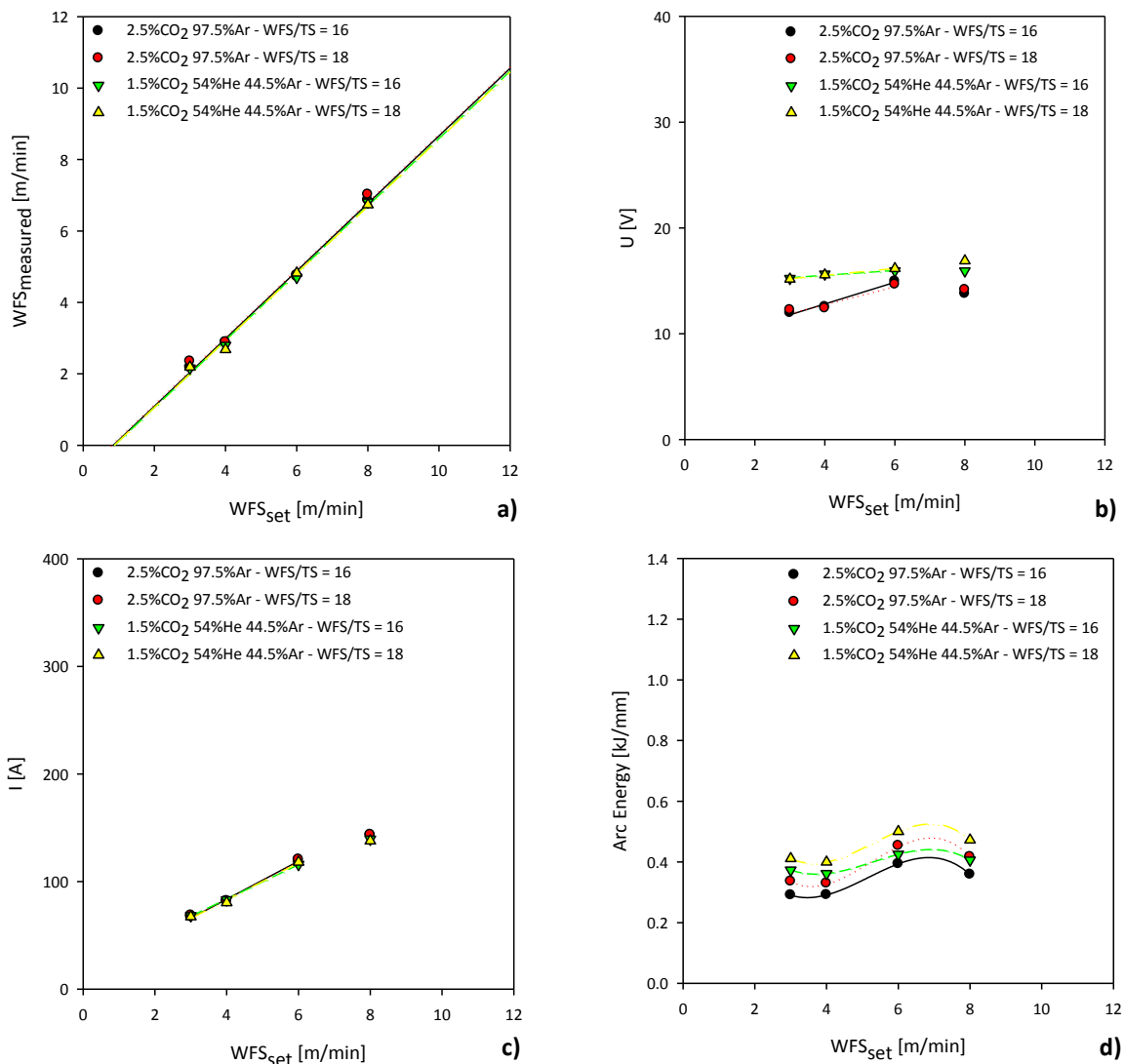


Figure VI.31 – Effect of WFS on waveform characteristics to CMT, at different WFS/TS ratios and shielding gases: a) measured WFS; b) arc voltage; c) arc current; d) arc energy.

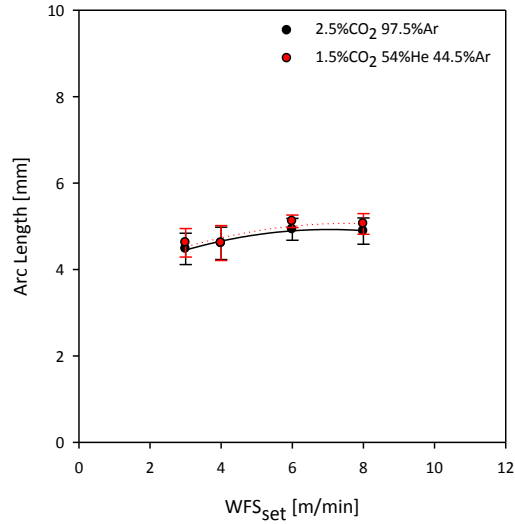


Figure VI.32 – Effect of the variation of ALC on arc length to CMT, at different WFS levels and shielding gases.

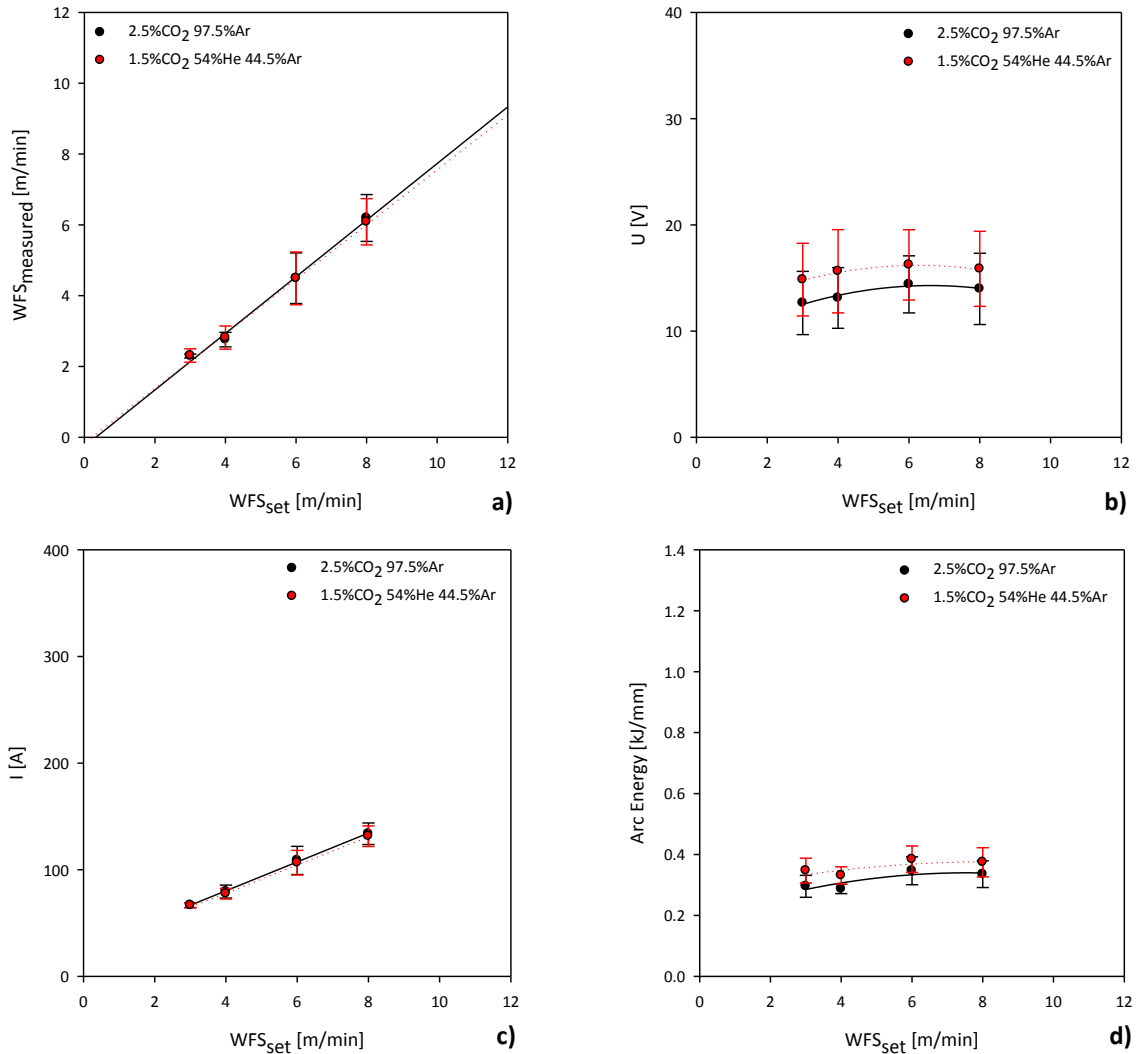


Figure VI.33 – Effect of the variation of ALC on waveform characteristics for CMT, at different WFS levels and shielding gases: a) measured WFS; b) arc voltage; c) arc current; d) arc energy.

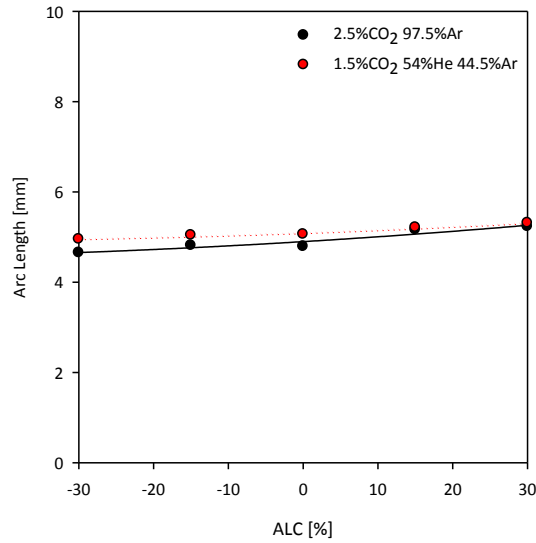


Figure VI.34 – Effect of ALC on arc length to CMT, at different shielding gases.

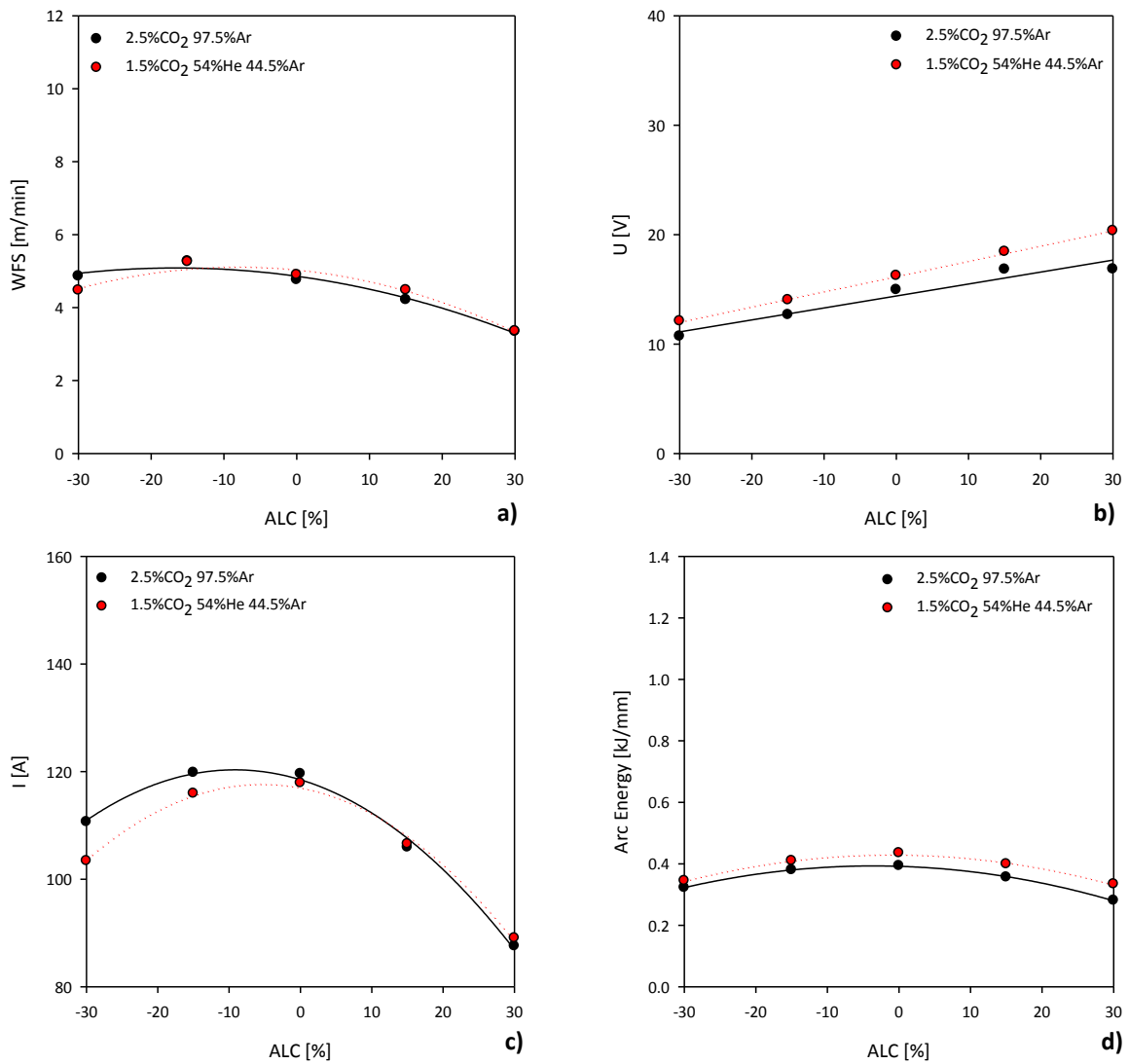


Figure VI.35 – Effect of ALC on waveform characteristics for CMT, at different shielding gases: a) measured WFS; b) arc voltage; c) arc current and d) arc energy.

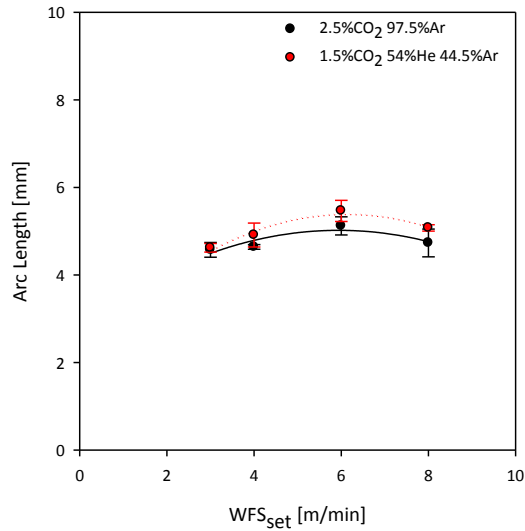


Figure VI.36 – Effect of the variation of DC on arc length to CMT, at different WFS levels and shielding gases.

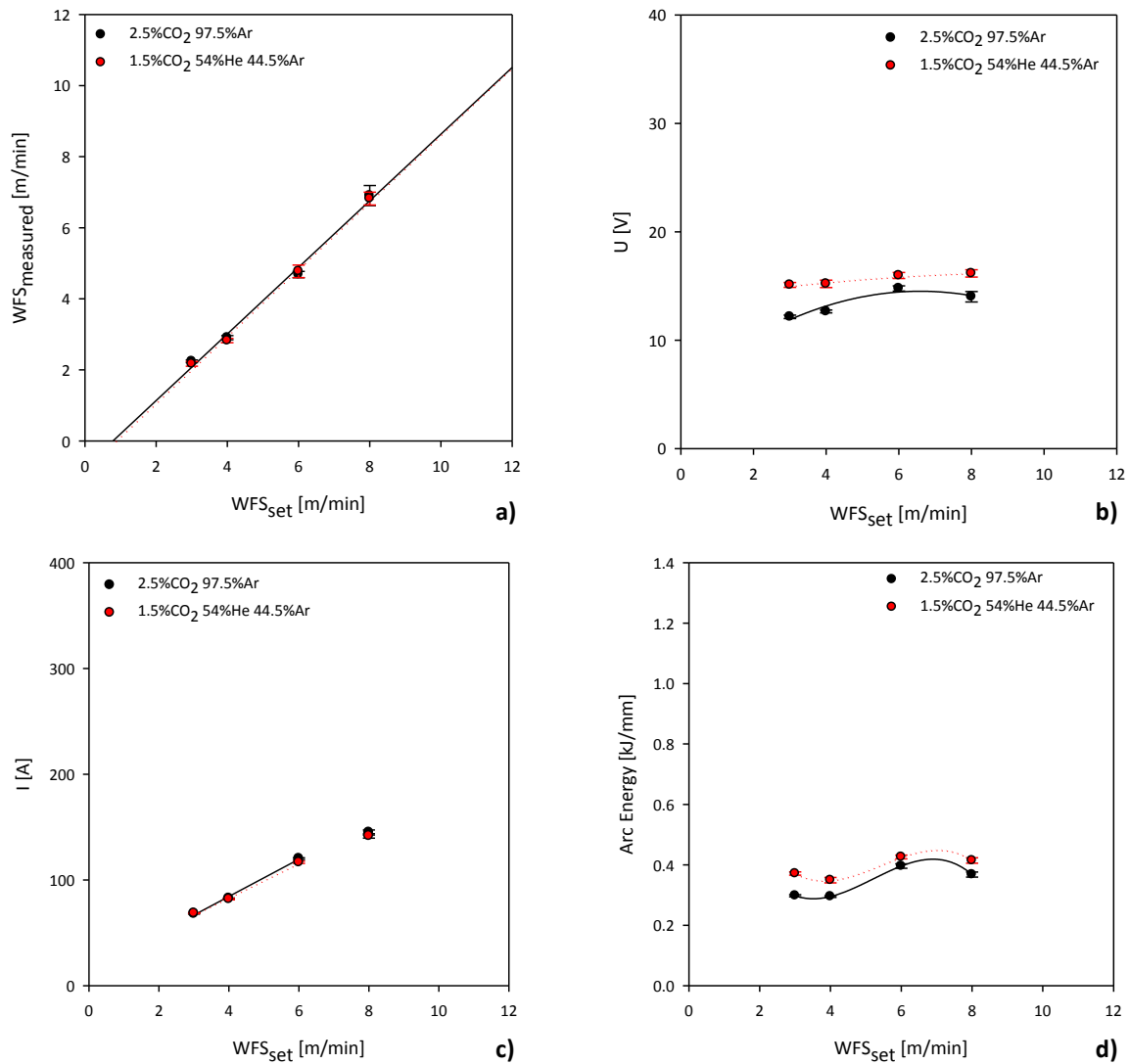


Figure VI.37 – Effect of the variation of DC on waveform characteristics for CMT, at different WFS levels and shielding gases: a) measured WFS; b) arc voltage; c) arc current; d) arc energy.

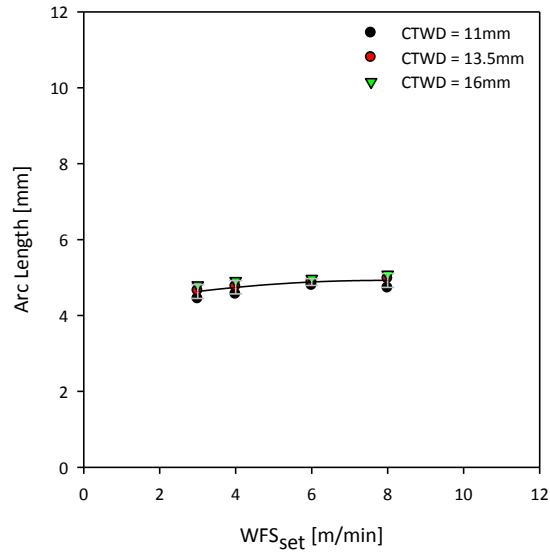


Figure VI.38 – Effect of the variation of CTWD on arc length to CMT, at different WFS levels.

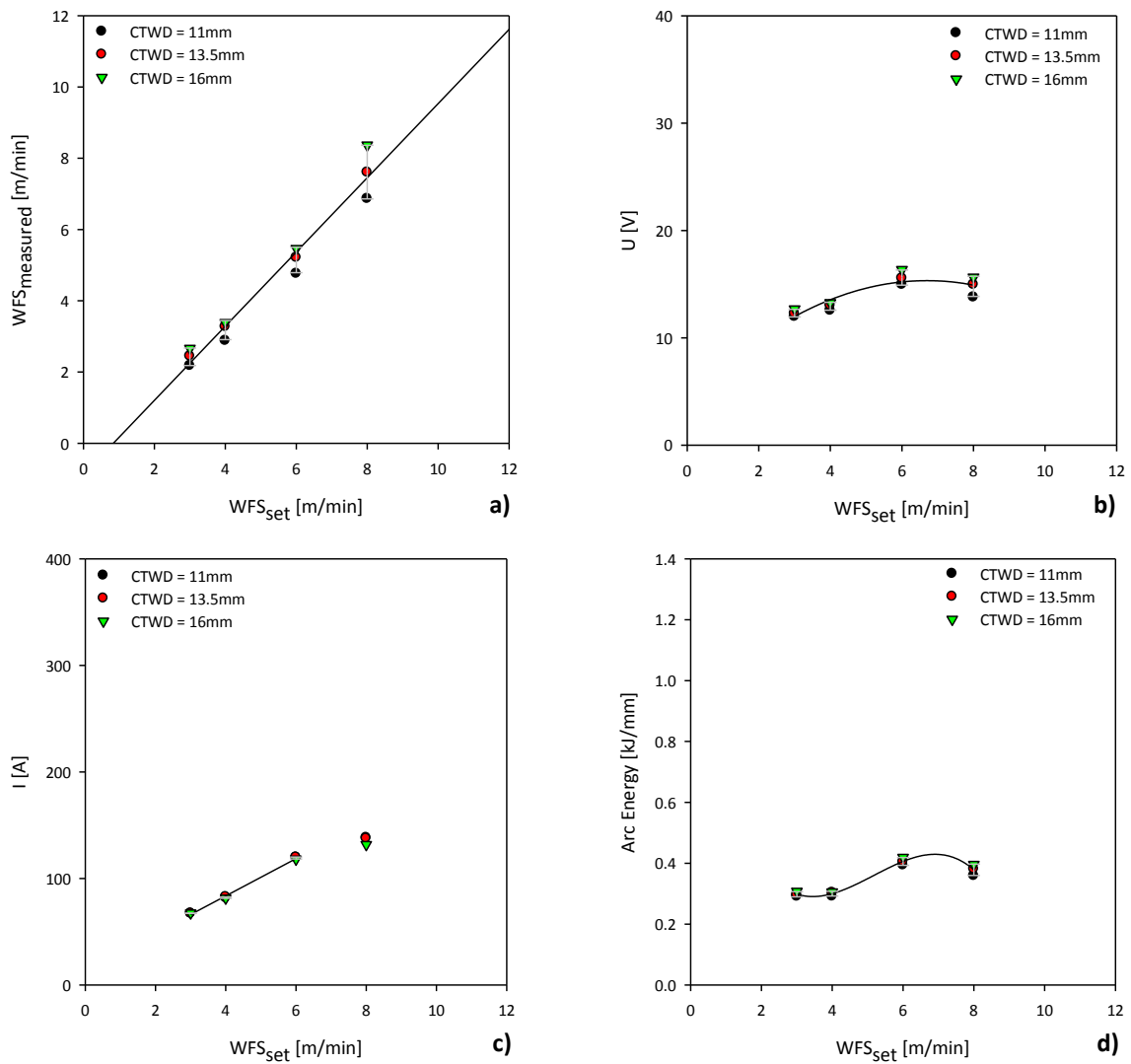


Figure VI.39 – Effect of the variation of CTWD on waveform characteristics for CMT, at different WFS levels: a) measured WFS; b) arc voltage; c) arc current; d) arc energy.

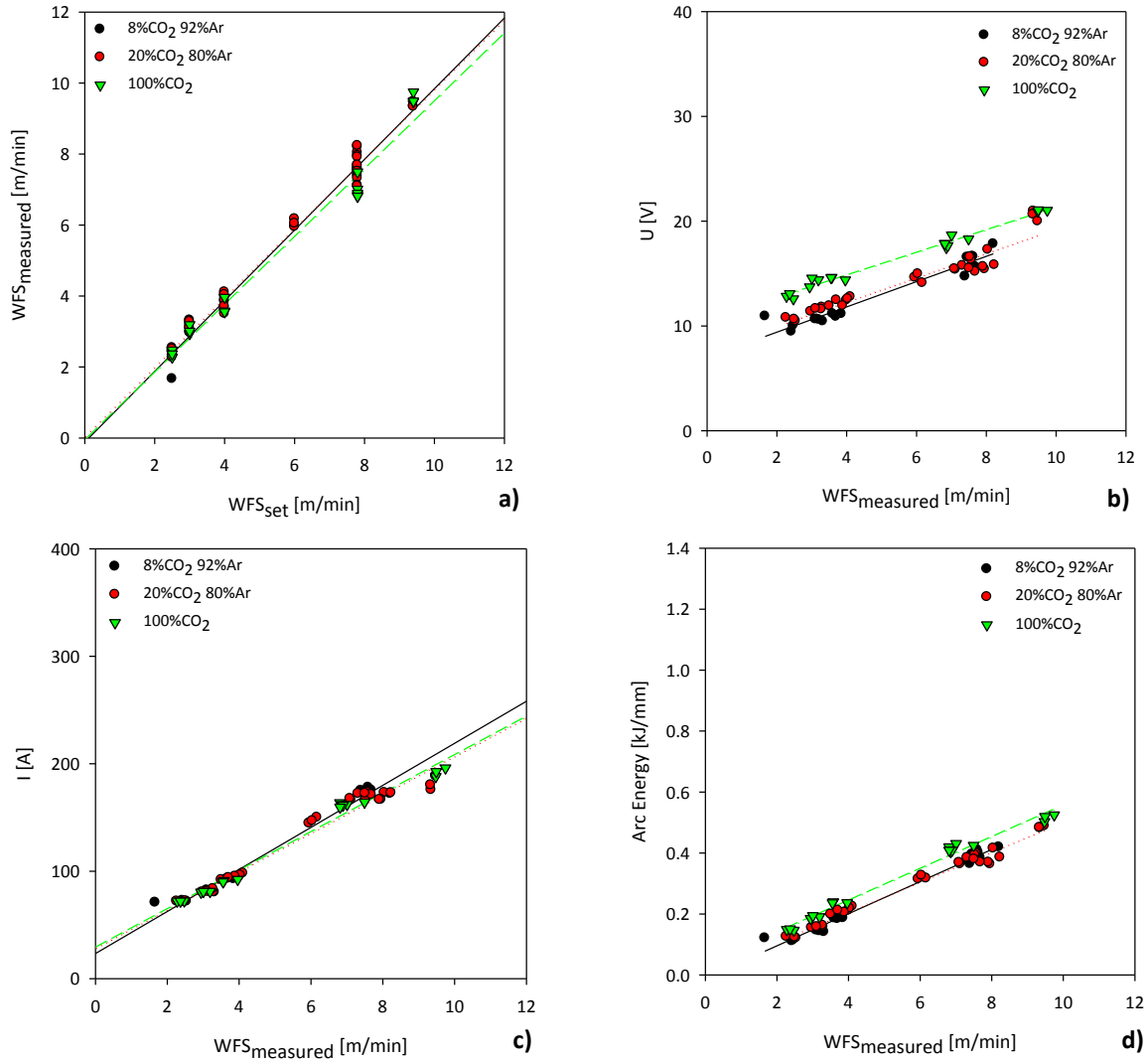


Figure VI.40 – Effect of WFS on waveform characteristics to CMT, at different shielding gases using mild steel: a) measured WFS; b) arc voltage; c) arc current; d) arc energy.

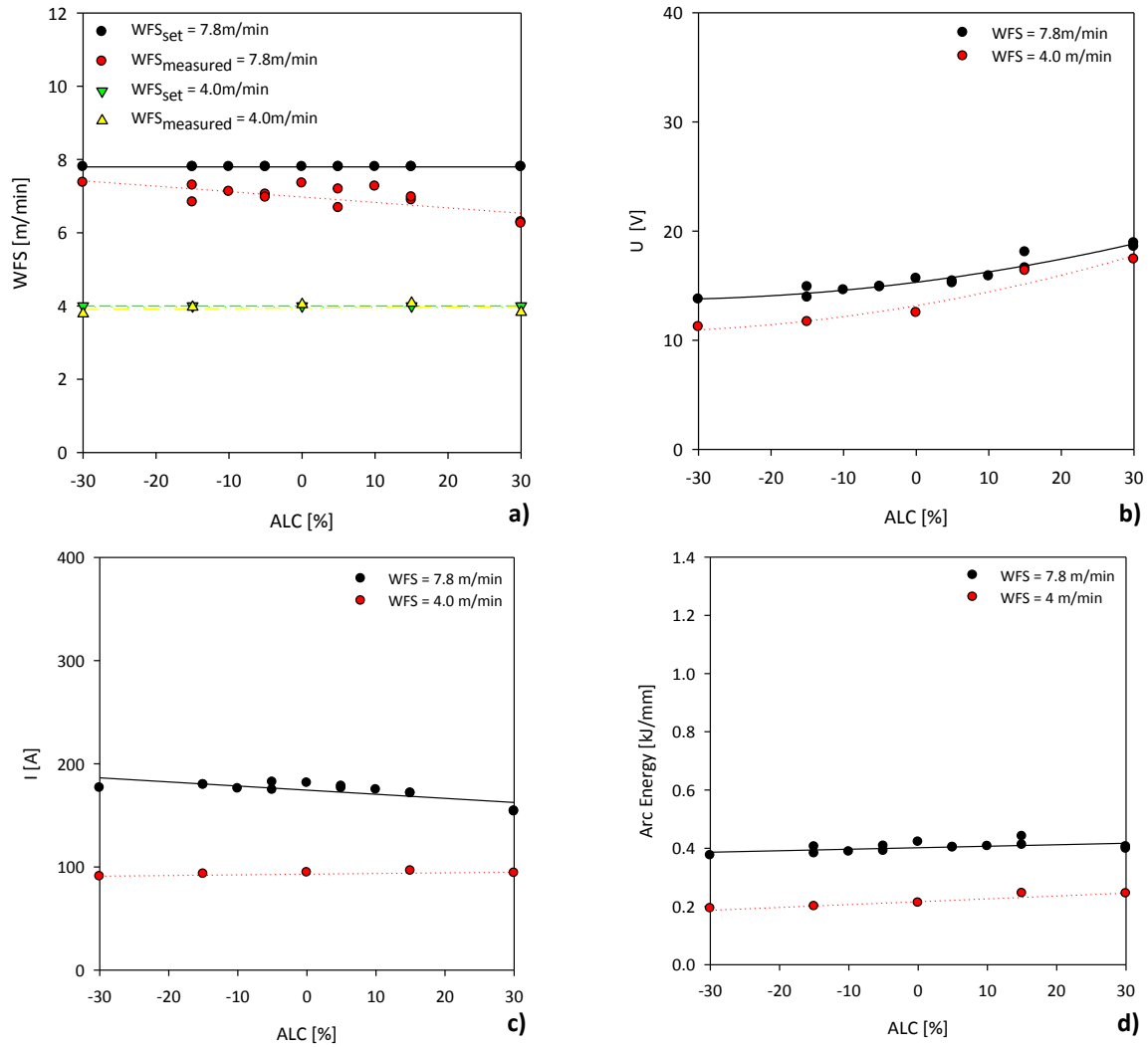


Figure VI.41 – Effect of ALC on waveform characteristics for CMT, at different WFS levels using mild steel: a) measured WFS; b) arc voltage; c) arc current and d) arc energy.

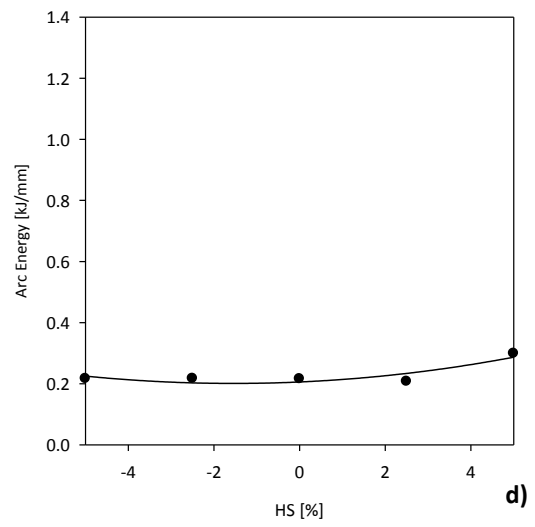
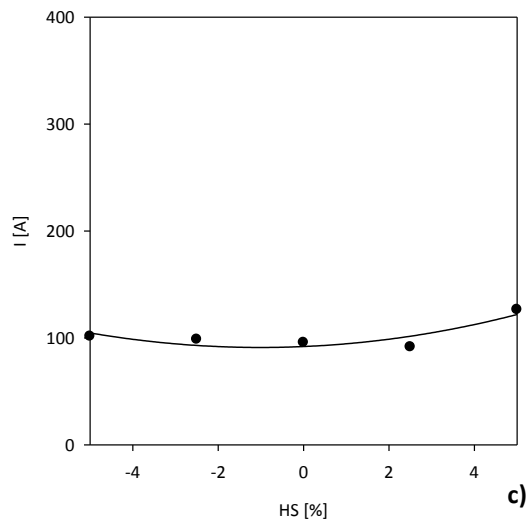
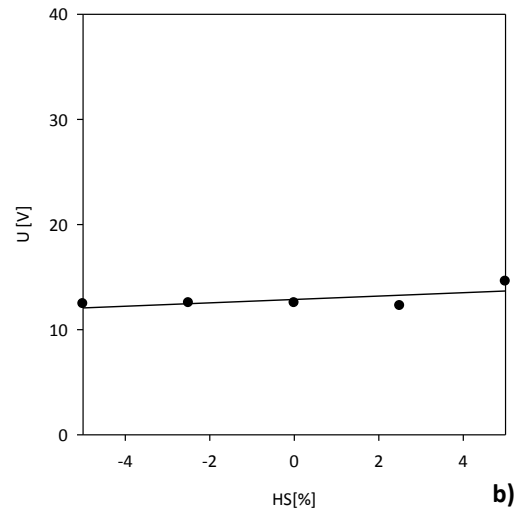
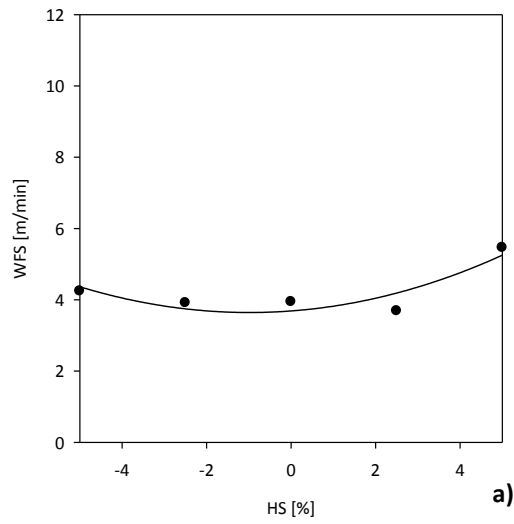
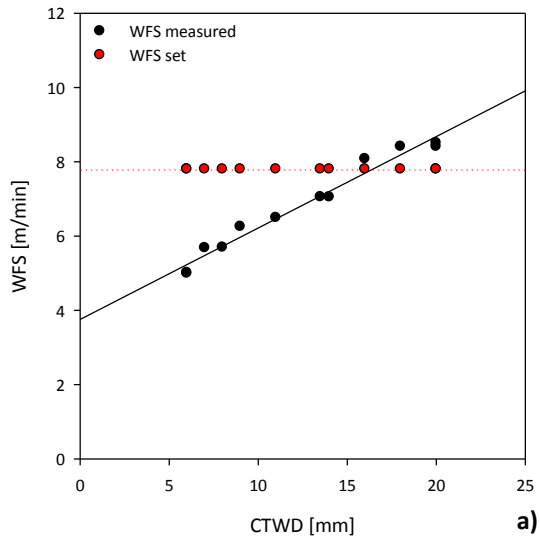
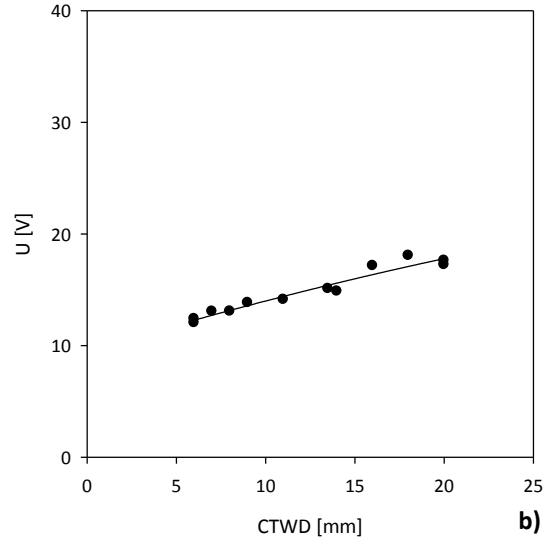


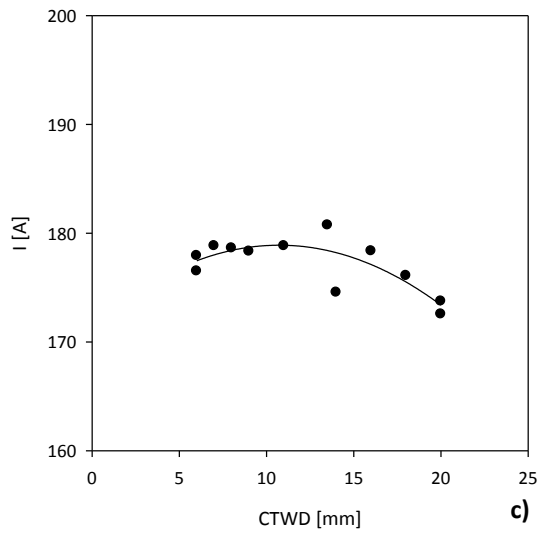
Figure VI.42 – Effect of HS on waveform characteristics to CMT using mild steel: a) measured WFS; b) arc voltage; c) arc current and d) arc energy.



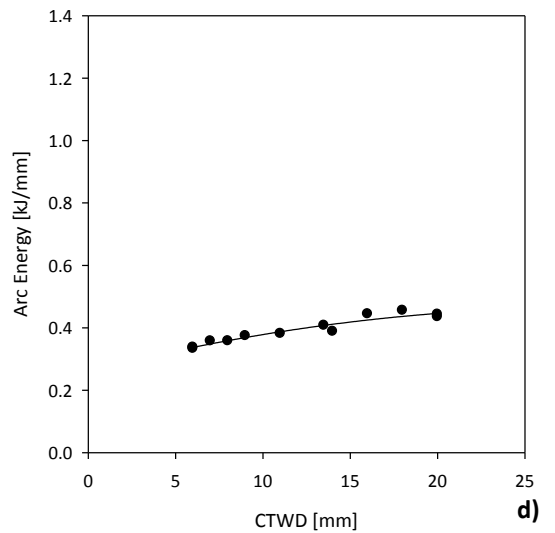
a)



b)



c)



d)

Figure VI.43 – Effect of CTWD on waveform characteristics to CMT, using mild steel: a) measured WFS; b) arc voltage; c) arc current; d) arc energy.

VI.5. Characterization of Waveform Characteristics and Arc Length for CMT-P

The effect WFS was also evaluated for CMT-P and the results are illustrated in the Figures VI.44 and VI.45.

The effect of ALC on welding parameters was also assessed for different WFS levels and at constant WFS (6m/min). The results are presented from the Figure VI.46 to VI.49

Pulse Control (PC) was also evaluated by varying the setting from -5 to +5 for different WFS levels and constant WFS (6m/min). The results are presented from the Figure VI.50 to VI.53

The results of the effect of CTWD are illustrated in the Figures VI.54 and IV.55.

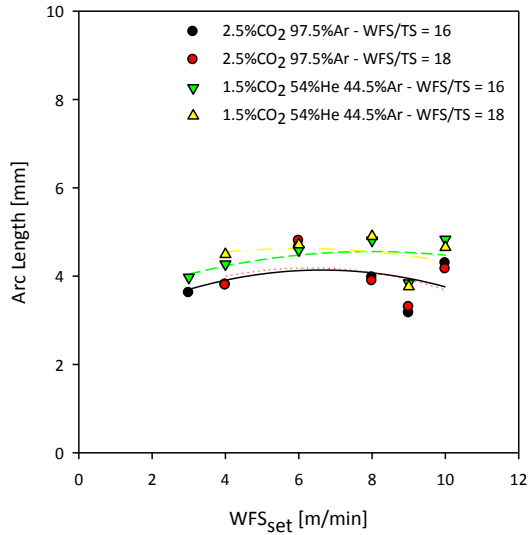


Figure VI.44 – Effect of WFS on arc length for CMT-P, at different WFS/TS ratios and shielding gases.

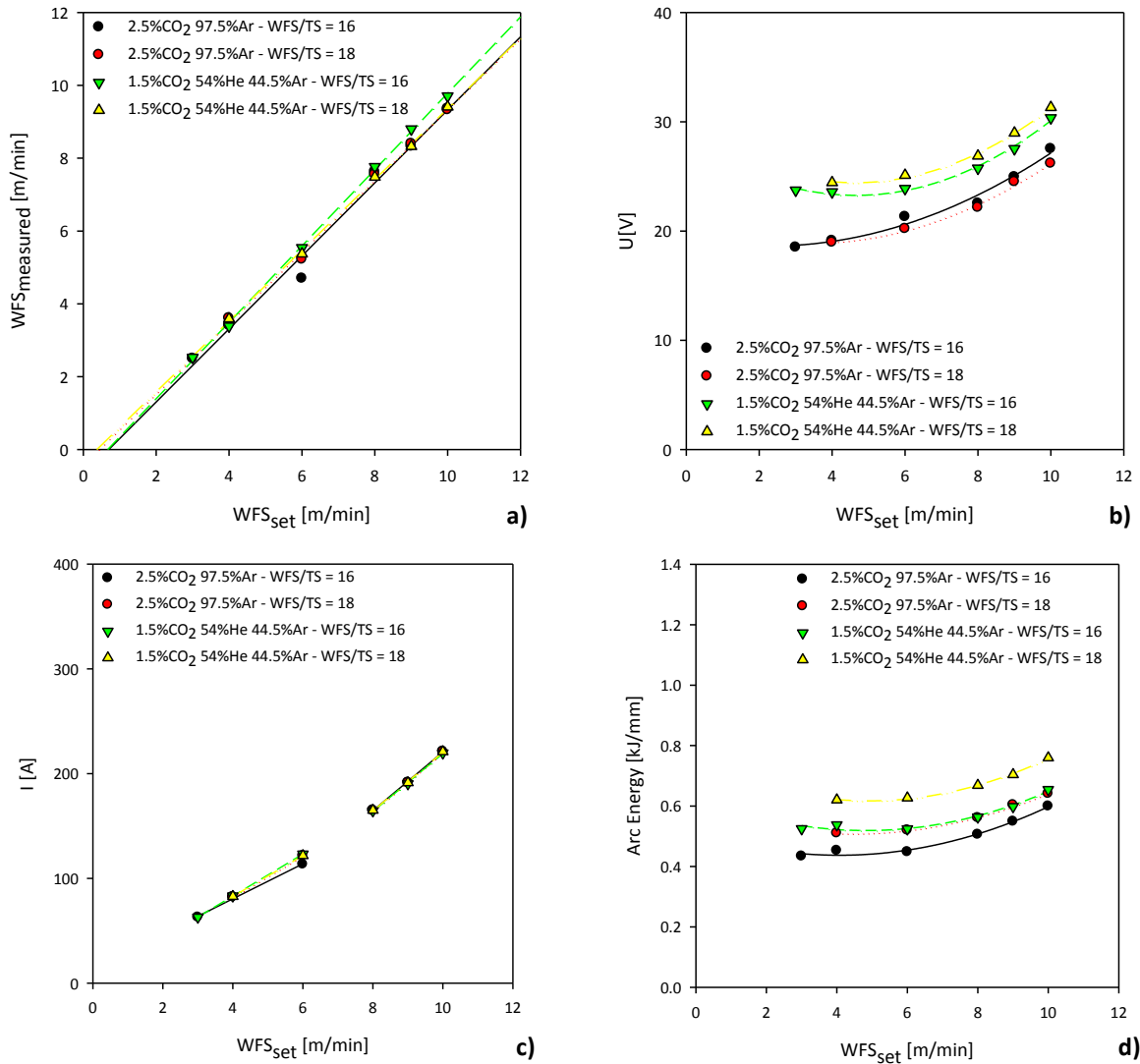


Figure VI.45 – Effect of WFS on waveform characteristics for CMT-P, at different WFS/TS ratios and shielding gases: a) measured WFS; b) arc voltage; c) arc current; d) arc energy.

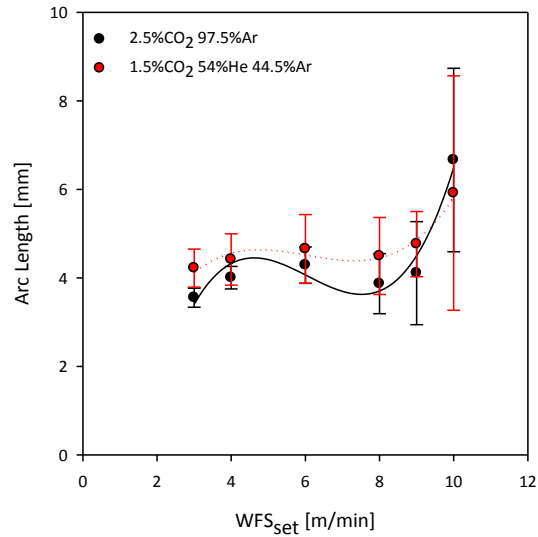


Figure VI.46 – Effect of the variation of ALC on arc length for CMT-P, at different WFS levels and shielding gases.

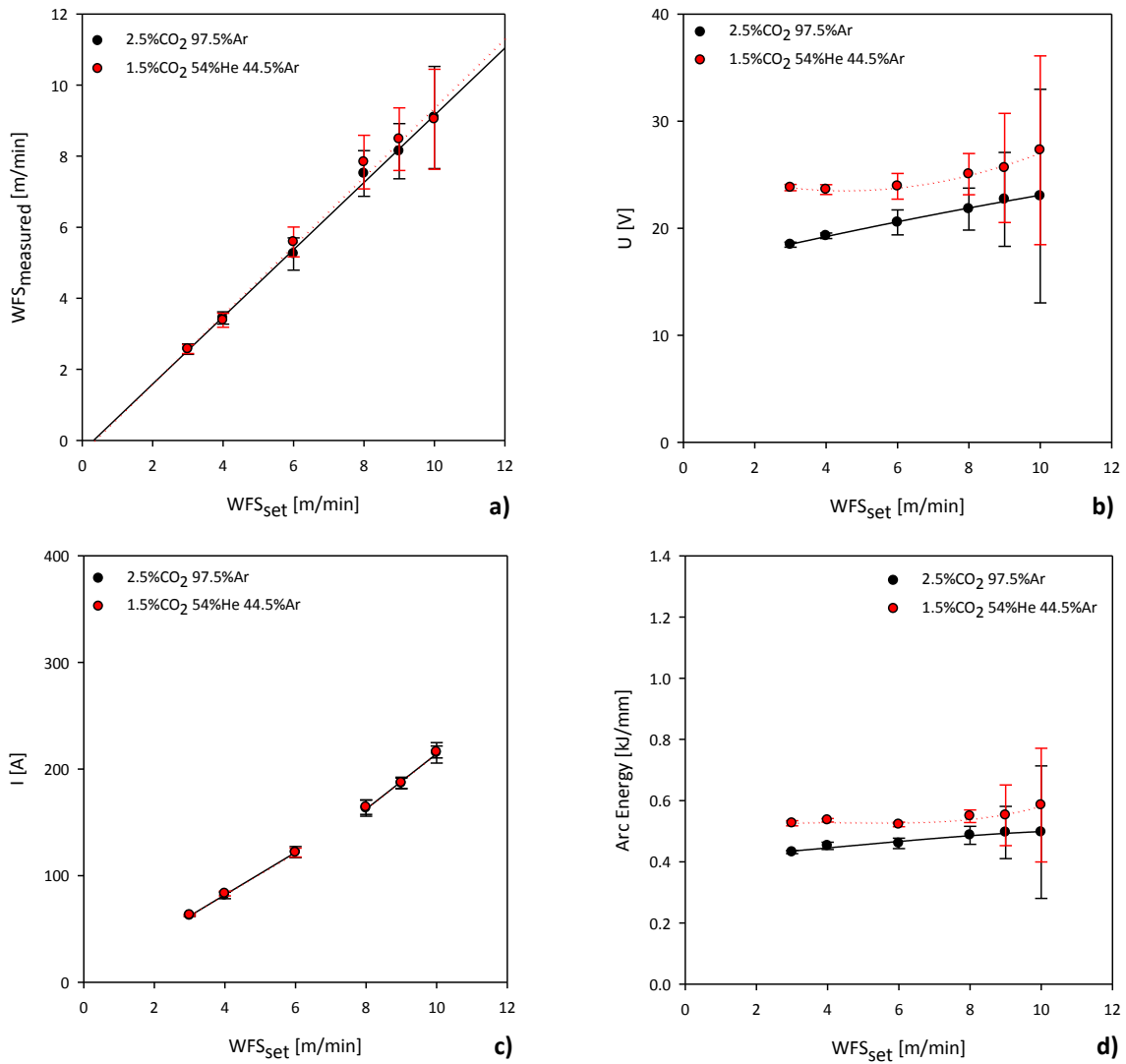


Figure VI.47 – Effect of the variation of ALC on waveform characteristics for CMT-P, at different WFS levels and shielding gases: a) WFS measured; b) arc voltage; c) arc current; d) arc energy.

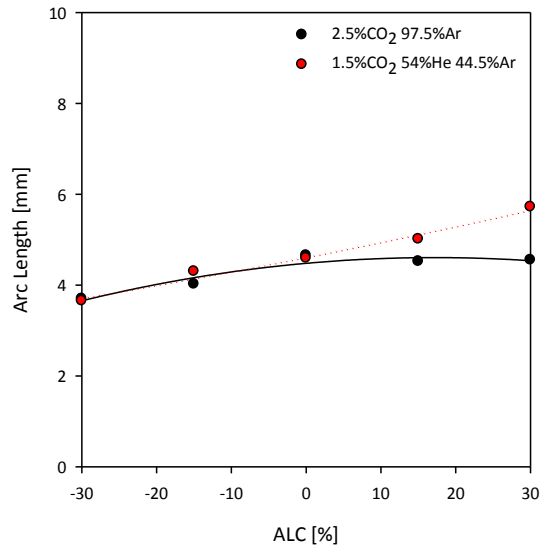


Figure VI.48 – Effect of ALC on arc length for CMT-P, at different shielding gases.

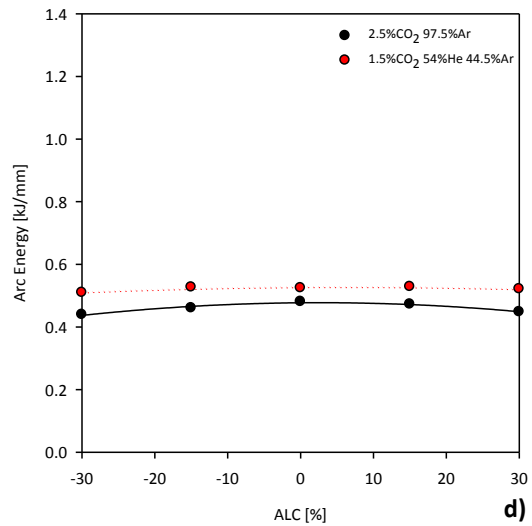
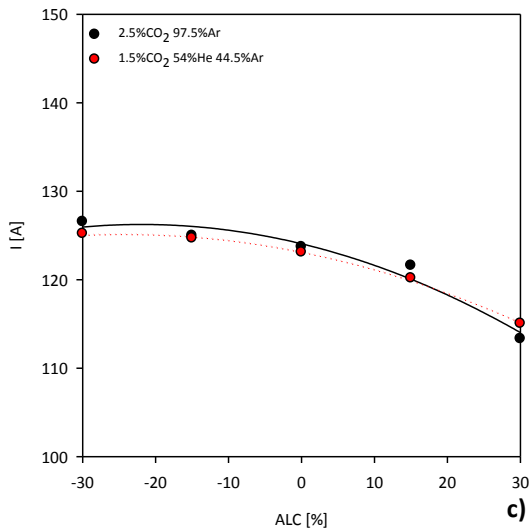
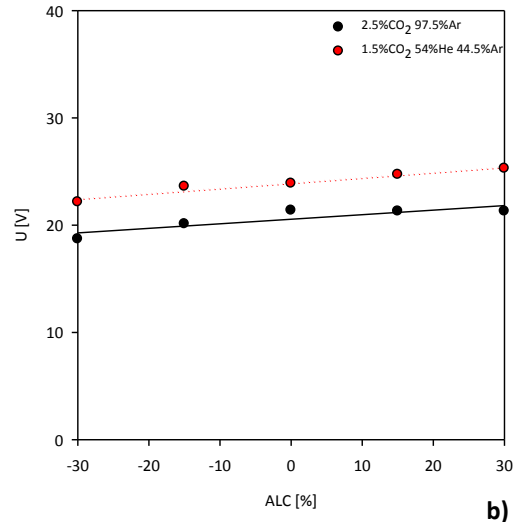
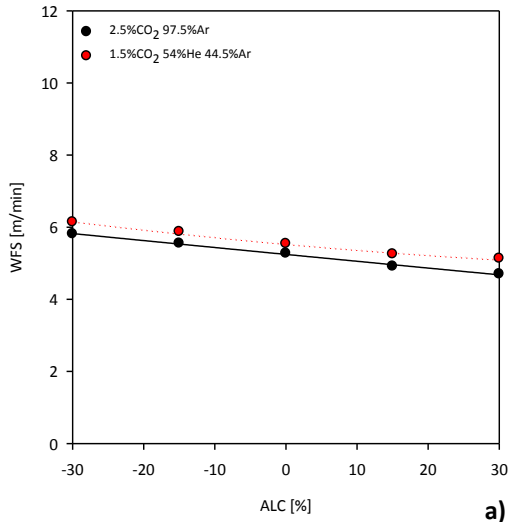


Figure VI.49 – Effect of ALC on waveform characteristics for CMT-P, at different shielding gases: a) measured WFS; b) arc voltage; c) arc current and d) arc energy.

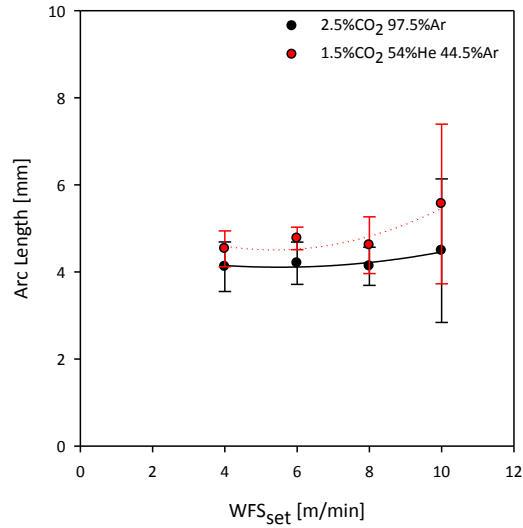


Figure VI.50 – Effect of the variation of PC on arc length to CMT-P, at different WFS levels and shielding gases.

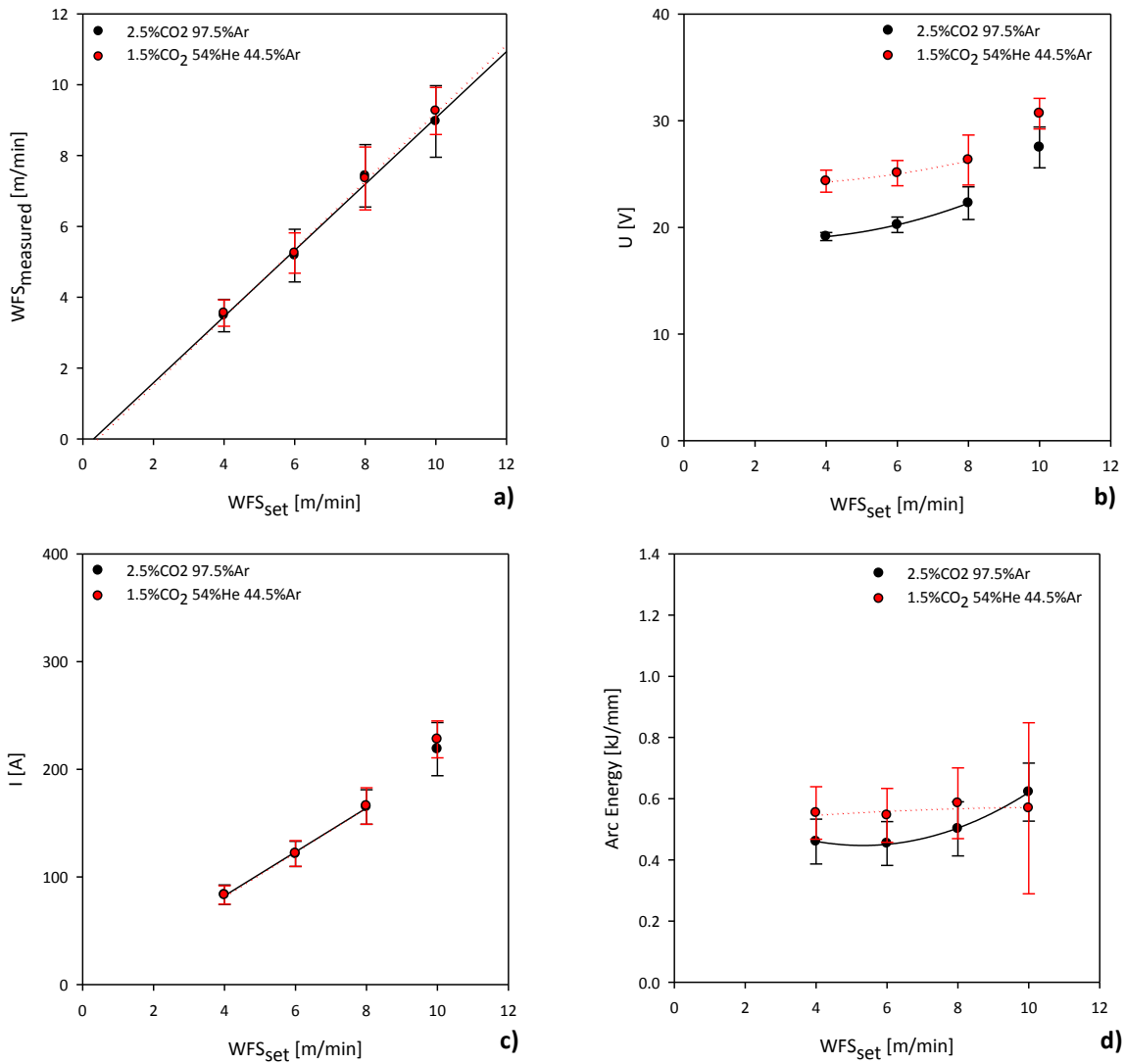


Figure VI.51 – Effect of the variation of PC on waveform characteristics for CMT-P, at different WFS levels and shielding gases: a) measured WFS; b) arc voltage; c) arc current; d) arc energy.

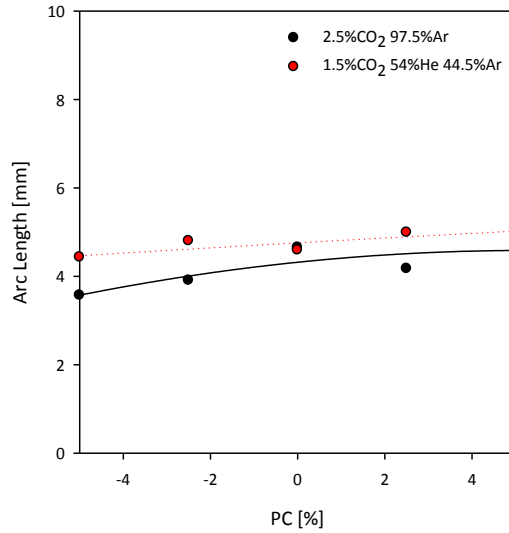


Figure VI.52 – Effect of PC on arc length for CMT-P, at different shielding gases.

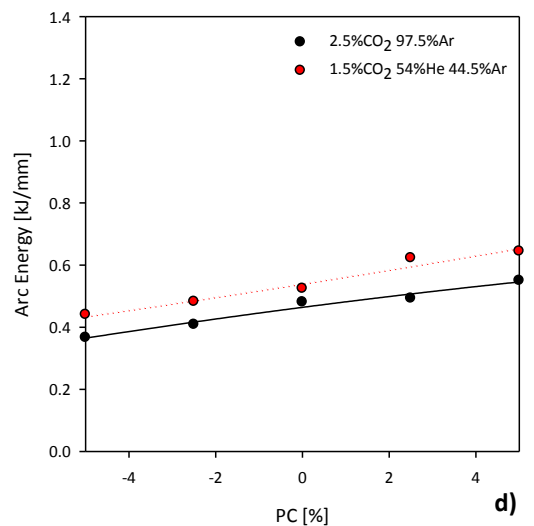
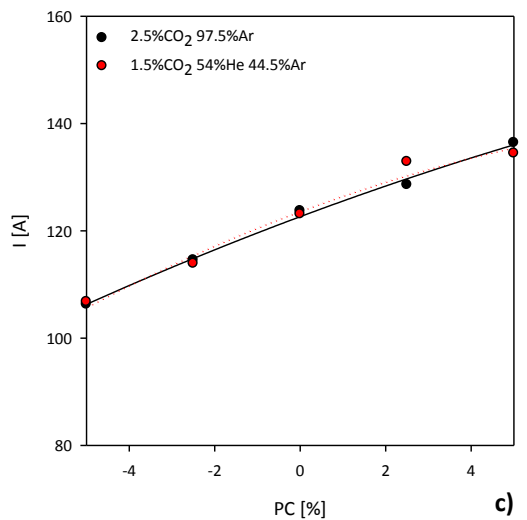
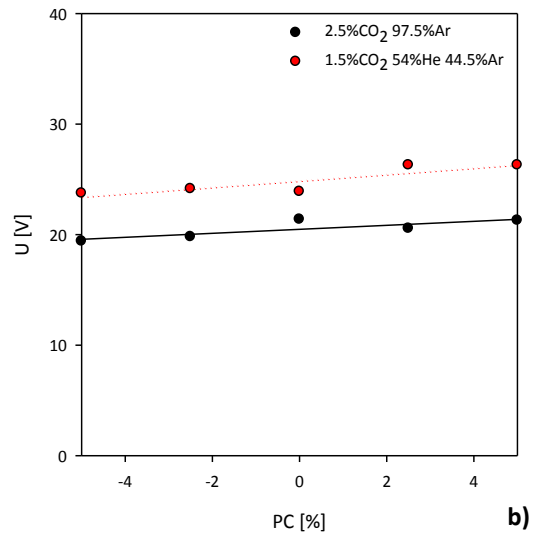
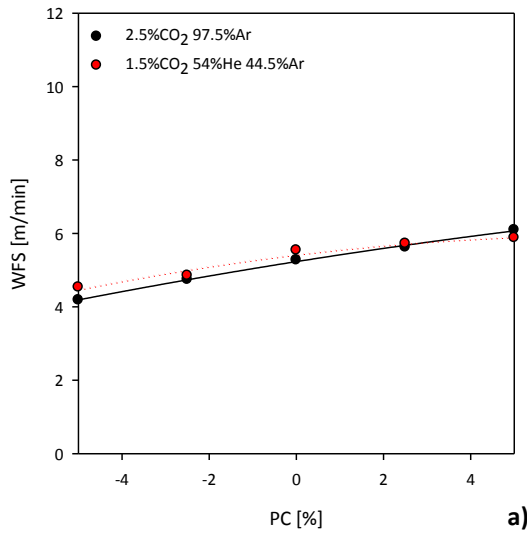


Figure VI.53 – Effect of ALC on waveform characteristics for CMT-P, at different shielding gases: a) measured WFS; b) arc voltage; c) arc current and d) arc energy.

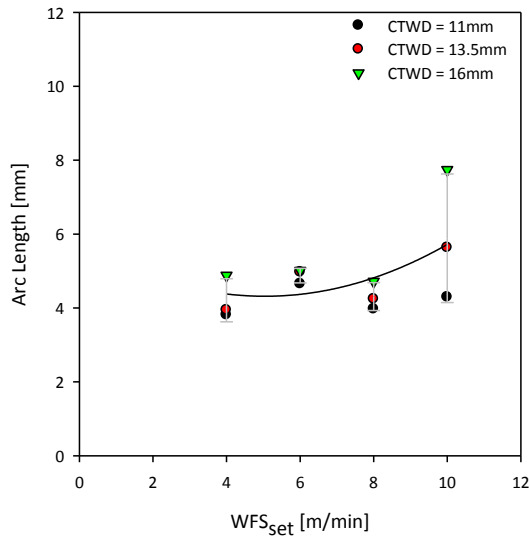


Figure VI.54 – Effect of the variation of CTWD on arc length for CMT-P, at different WFS levels.

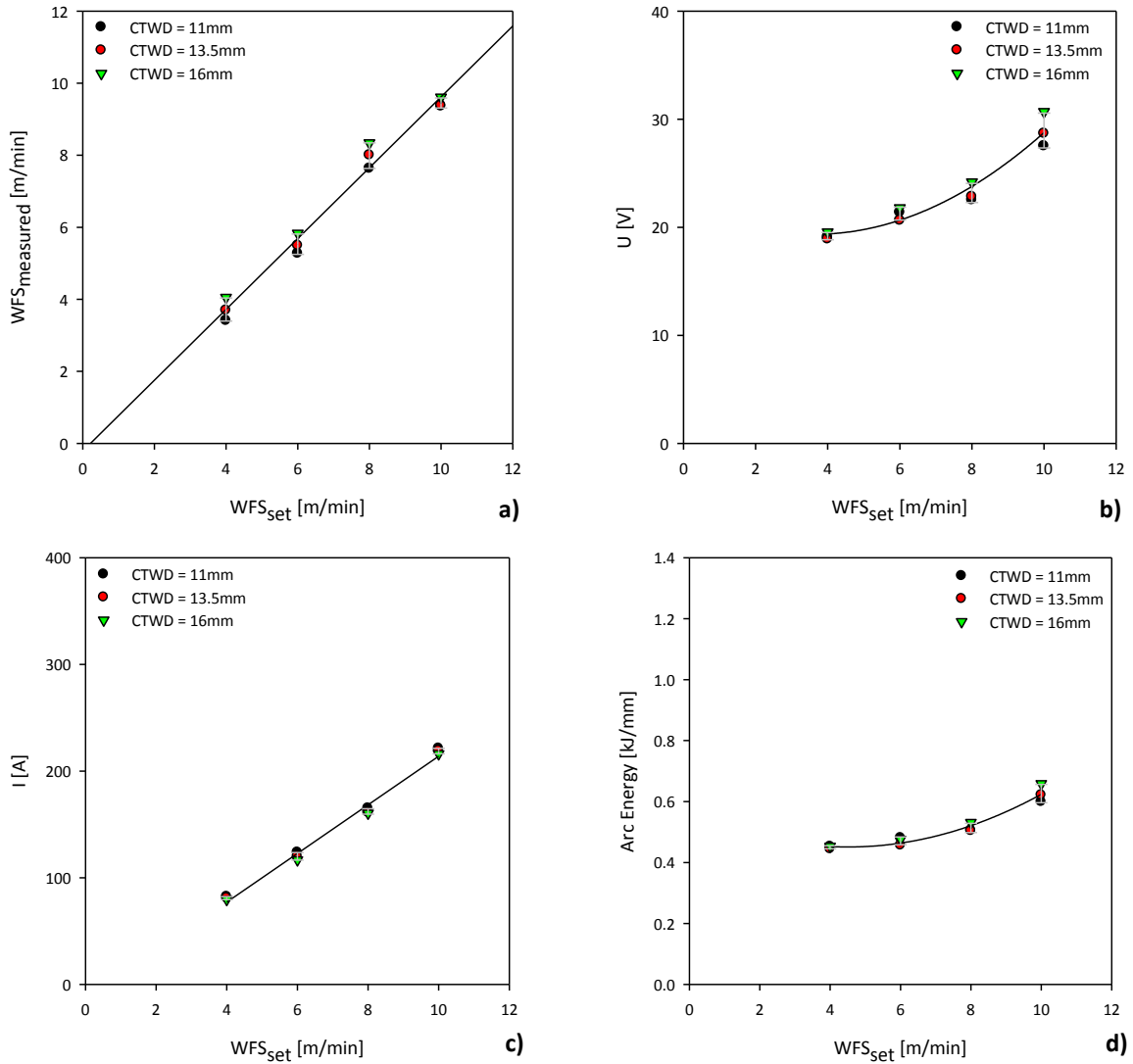


Figure VI.55 – Effect of the variation of CTWD on waveform characteristics for CMT-P, at different WFS levels: a) measured WFS; b) arc voltage; c) arc current; d) arc energy.

VI.6. Characterization of Waveform Characteristics and Arc Length for FastROOT

The effect of WFS was also evaluated for FastROOT and the results obtained are presented in the Figure VI.56 and VI.57.

The effect of Base Current (BC) from -50 to +50 was analysed for different WFS levels and at WFS (6m/min). The results obtained are illustrated from the Figure VI.58 to VI.61.

The effect of changing the Forming Pulse (FP) setting from -30 to +30 was analysed at constant WFS (8m/min) and the results presented in the Figure VI.62 and VI.63.

The effect of CTWD was also evaluated, and the results are illustrated in the Figure VI.64 and VI.65.

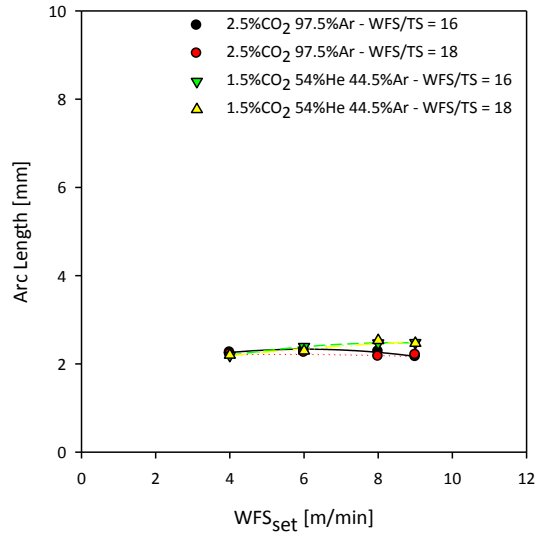


Figure VI.56 – Effect of WFS on arc length to FastROOT, at different WFS/TS ratios and shielding gases.

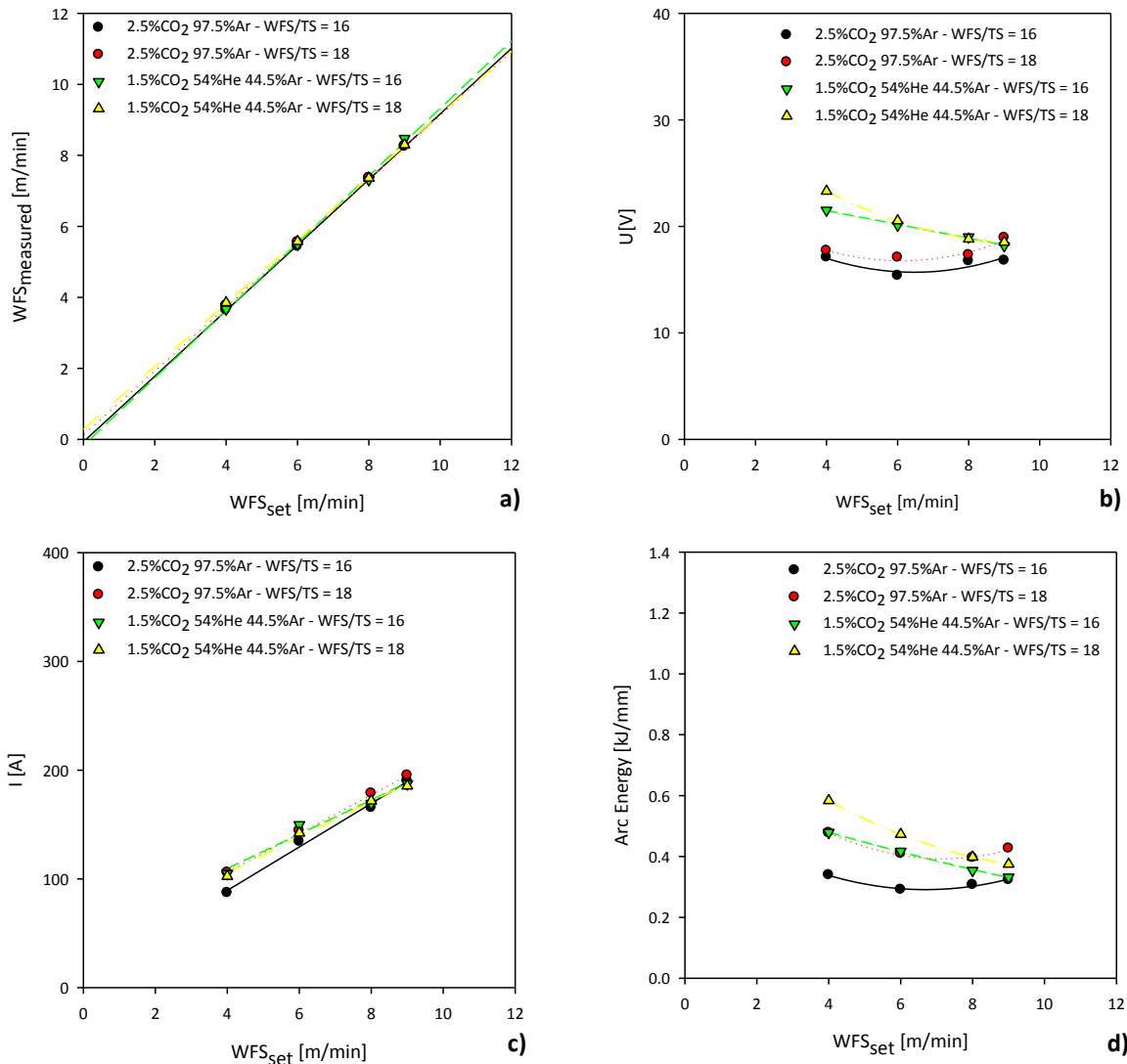


Figure VI.57 – Effect of WFS on waveform characteristics for FastROOT, at different WFS/TS ratios and shielding gases: a) measured WFS; b) arc voltage; c) arc current; d) arc energy.

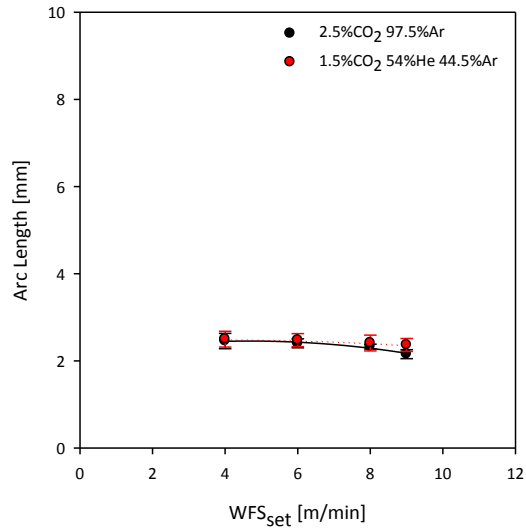


Figure VI.58 – Effect of BC on arc length for FastROOT, at different WFS levels and shielding gases.

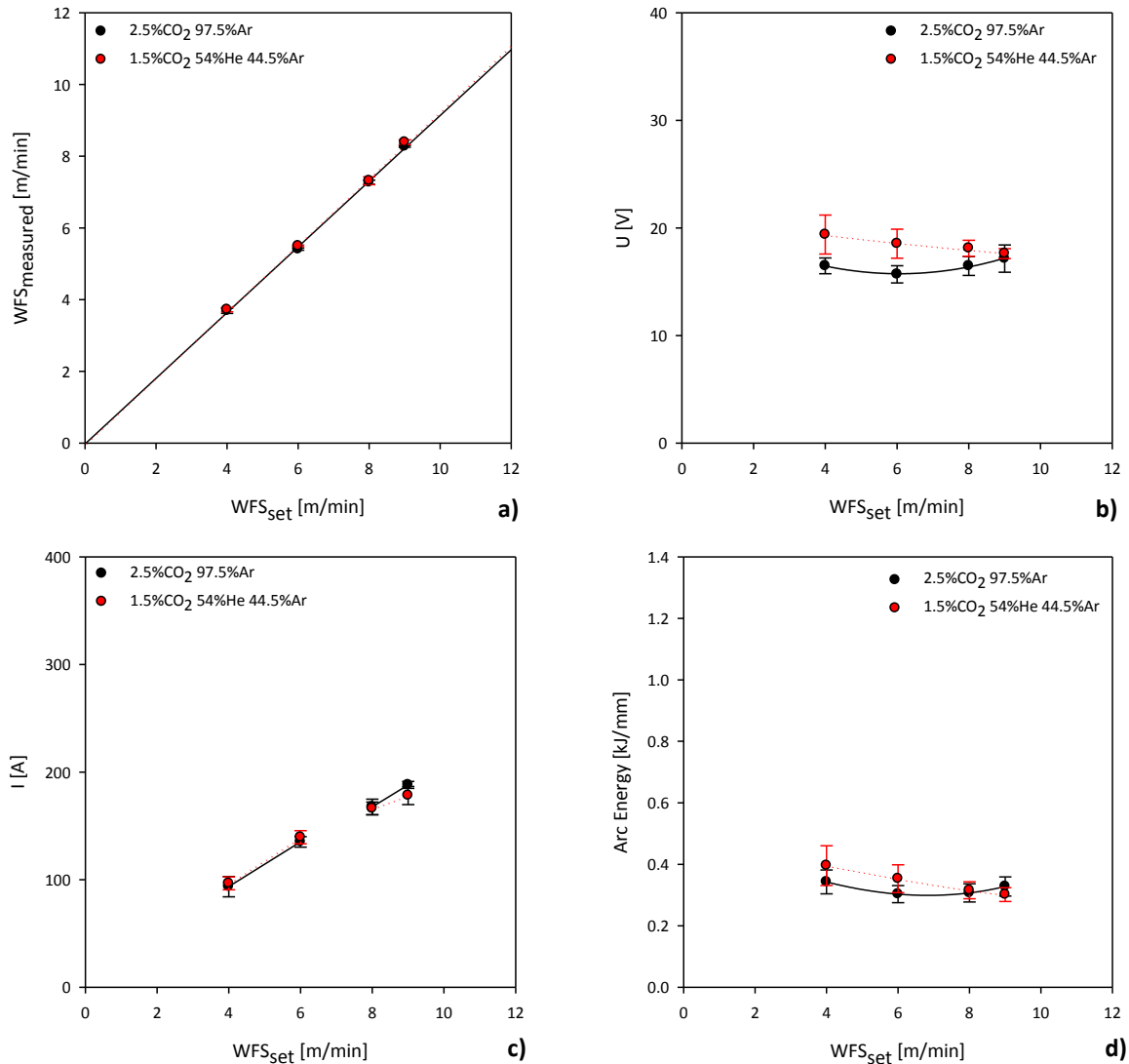


Figure VI.59 – Effect of BC on waveform characteristics for FastROOT, at different WFS levels and shielding gases: a) measured WFS; b) arc voltage; c) arc current; d) arc energy.

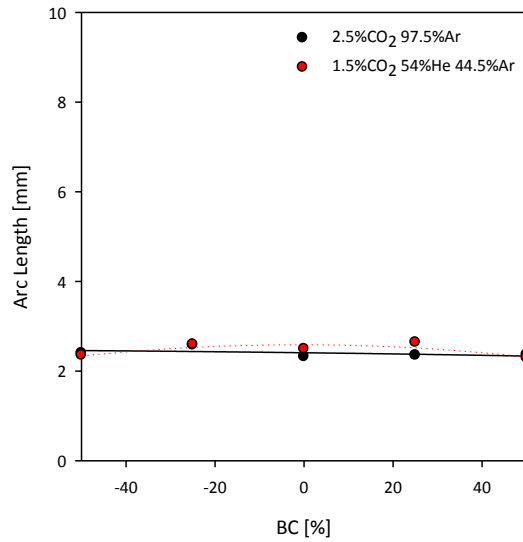


Figure VI.60 – Effect of BC on arc length to FastROOT, at different shielding gases.

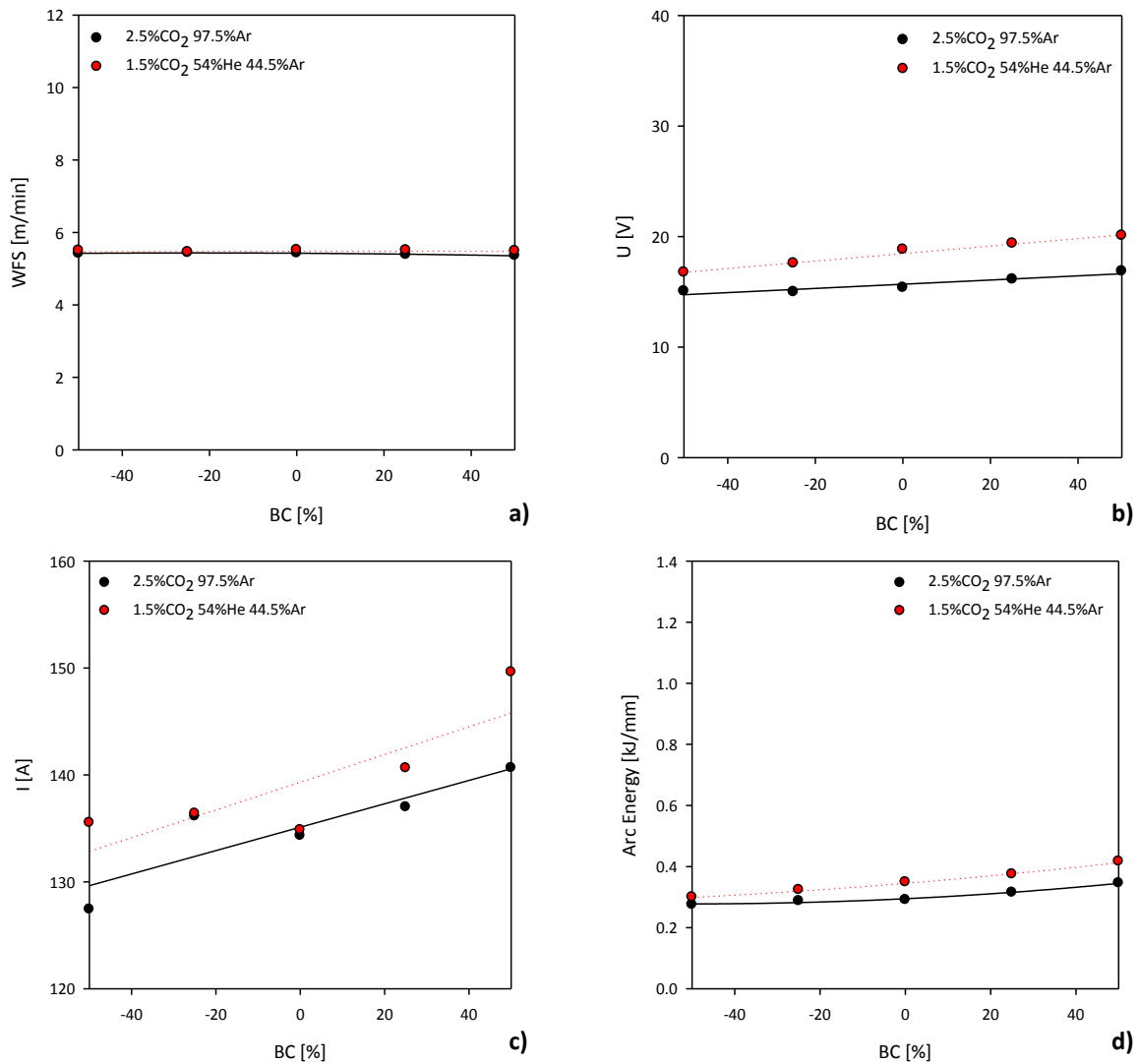


Figure VI.61 – Effect of BC on waveform characteristics for FastROOT, at different shielding gases: a) measured WFS; b) arc voltage; c) arc current; d) arc energy.

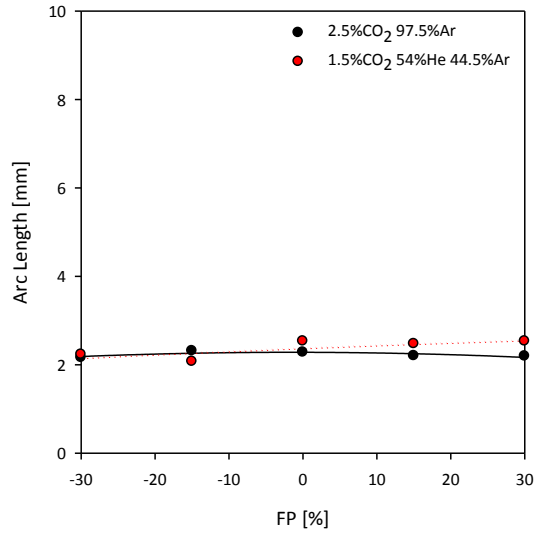


Figure VI.62 – Effect of FP on arc length to FastROOT, at different shielding gases.

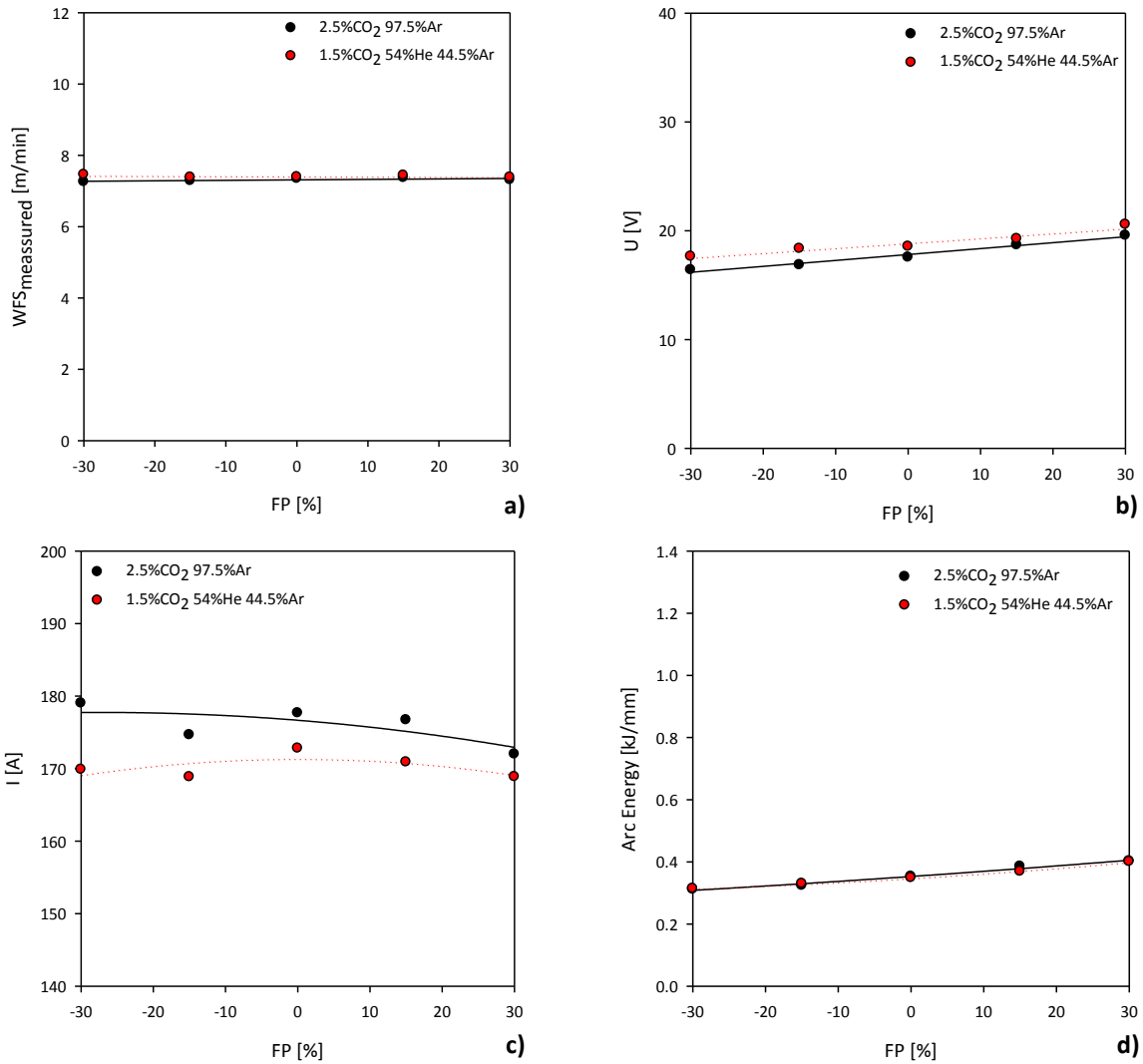


Figure VI.63 – Effect of FP on waveform characteristics for FastROOT, at different shielding gases: a) measured WFS; b) arc voltage; c) arc current; d) arc energy.

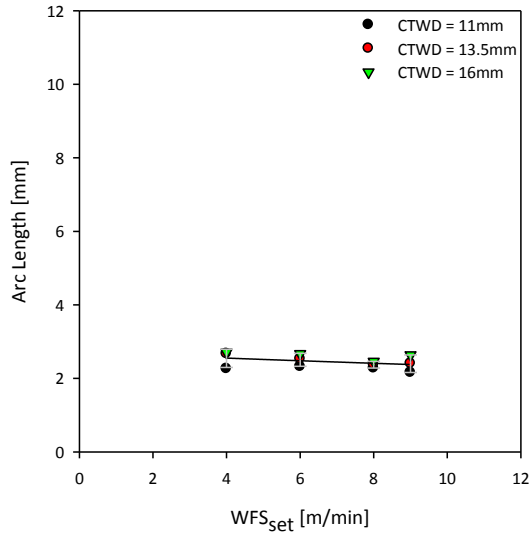


Figure VI.64 – Effect of the variation of CTWD on arc length for FastROOT, at different WFS levels.

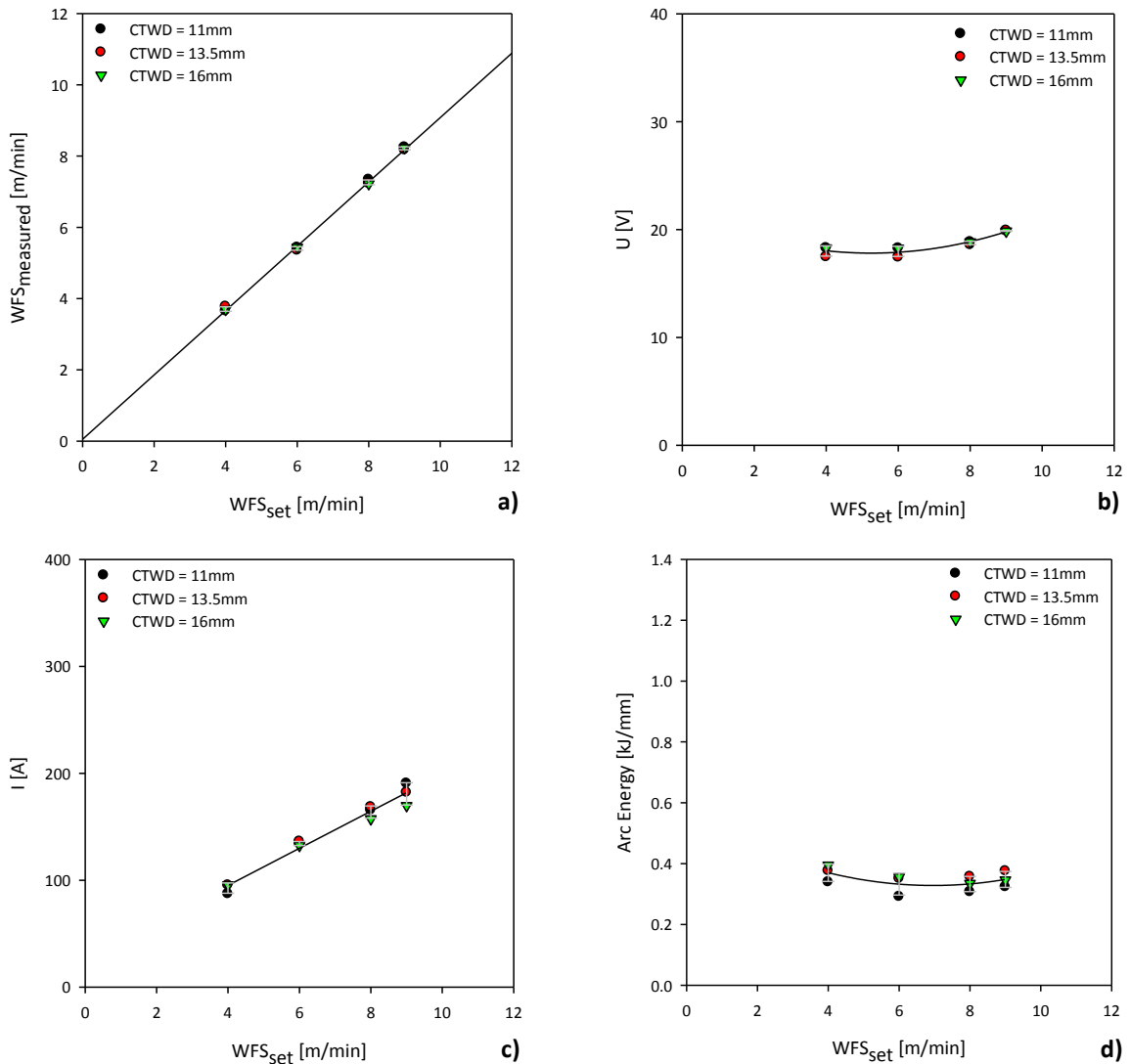


Figure VI.65 – Effect of variation of CTWD on waveform characteristics for FastROOT, at different WFS levels: a) measured WFS; b) arc voltage; c) arc current; d) arc energy.

VII. GRAPHICAL ANALYSIS OF THE EFFECT OF SETTING PROCESS PARAMETERS ON WAVEFORM PARAMETERS

The different waveforms under research are characterized by variations in the waveform parameters. This appendix includes the analysis of the effect of setting process parameters on waveform parameters, i.e., peak and background current (I_p and I_b), peak, step and background voltage (U_p , U_{step} and U_b), and peak and background time (relative to the arc current) (t_p and t_b). The identification of the waveform parameters is shown in the typical waveform presented in Figure VII.1.

The influence on pulse and short-circuiting frequency (f_p and f_{sc}) (when applied) and duty cycle (DC), i.e. the measure of the peak time ratio during the full cycle time, will be also characterized. The numerical results obtained in this research study were previously presented in Appendix V.

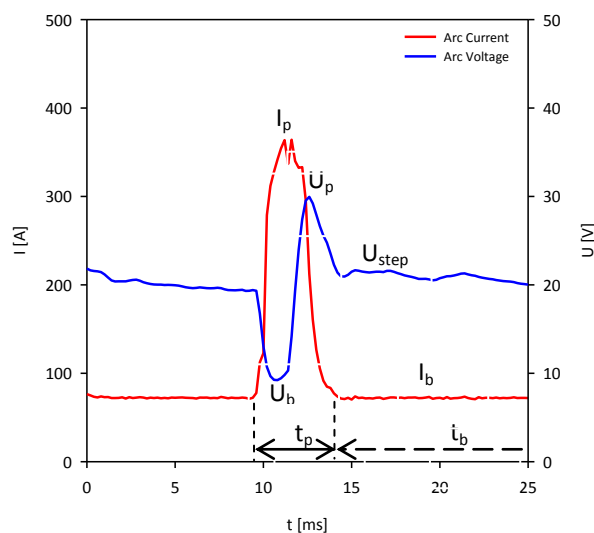


Figure VII.1 – Identification of the waveform parameters in a typical waveform design.

The experimental conditions applied to this research (unless otherwise indicated) were similar those in Appendix VI.

VII.1. Characterization of Waveform Parameters for GMAW-P

The effect of WFS is illustrated for GMAW-P in from the Figures VII.2 to VII.4.

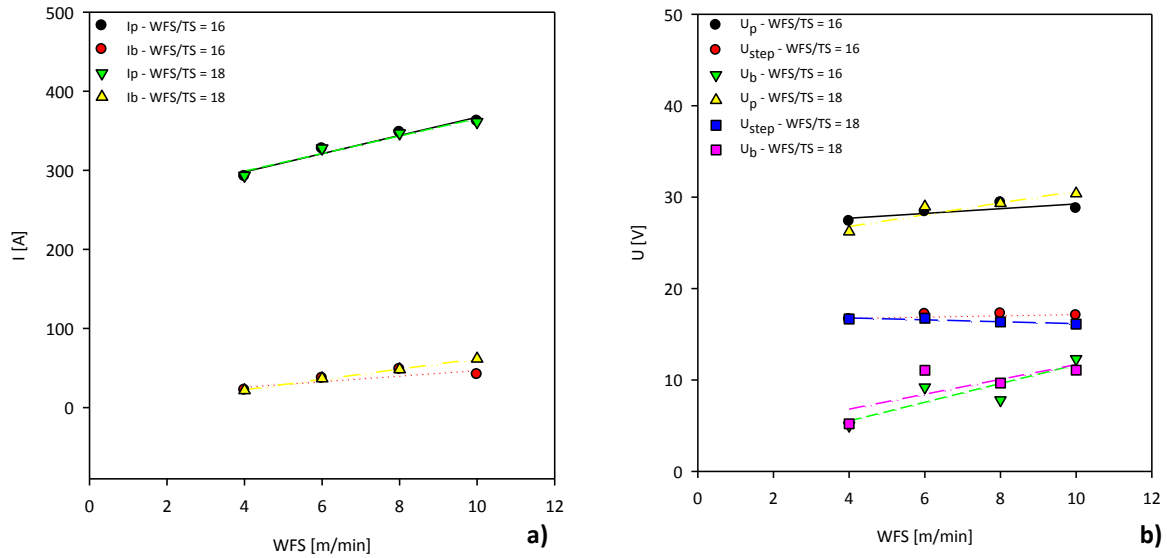


Figure VII.2 – Effect of WFS on background and peak parameters for GMAW-P, at different WFS/TS ratios: a) arc current; b) arc voltage.

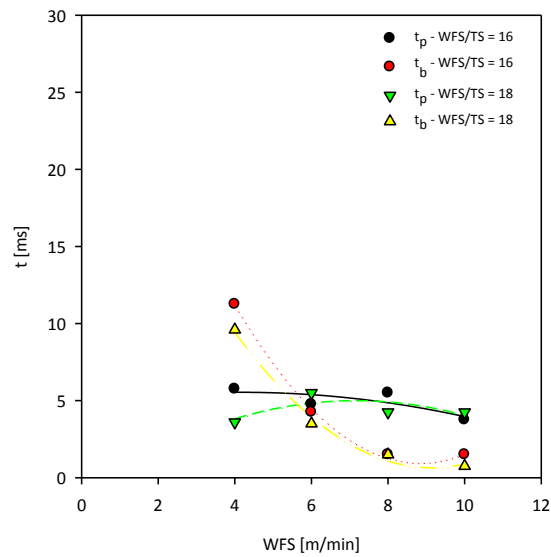


Figure VII.3 – Effect of WFS on background and peak time for GMAW-P, at different WFS/TS ratios.

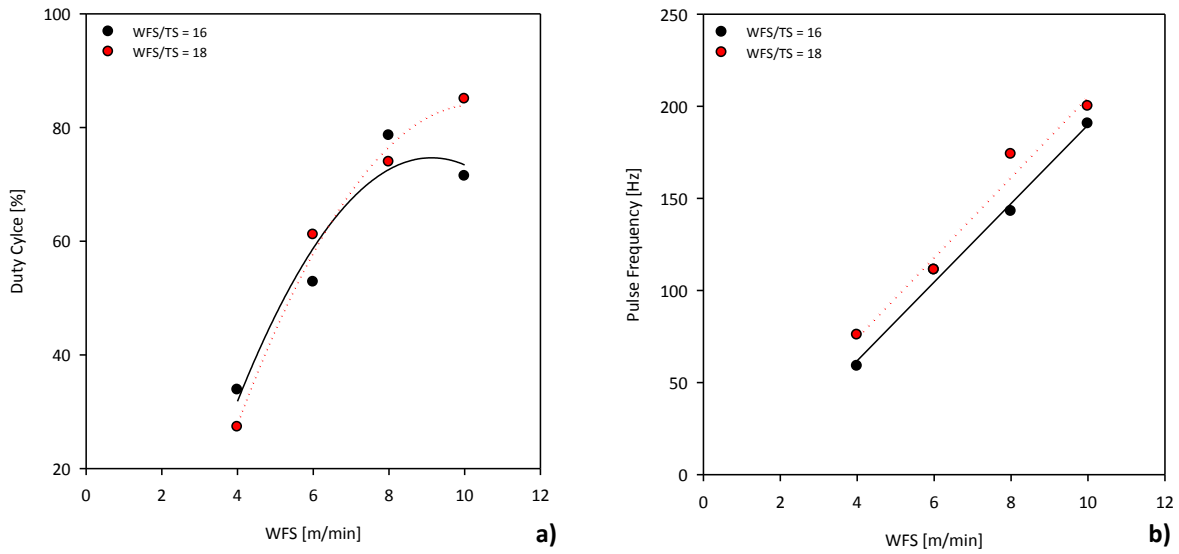


Figure VII.4 – Effect of WFS on duty cycle (a) and pulse frequency (b) for GMAW-P, at different WFS/TS ratios.

The effect of shielding gas composition was also evaluated and the most significant results are presented in the Figure VII.5.

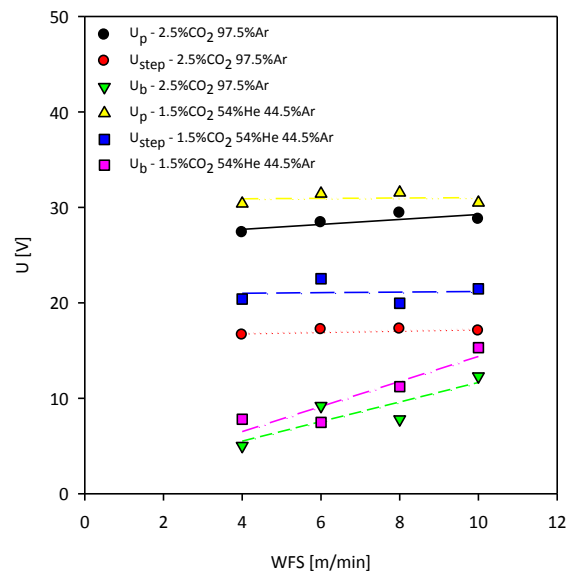


Figure VII.5 – Effect of WFS on arc voltage waveform parameters for GMAW-P, at different shielding gases.

The effect of trim is illustrated in the Figure VII.6.

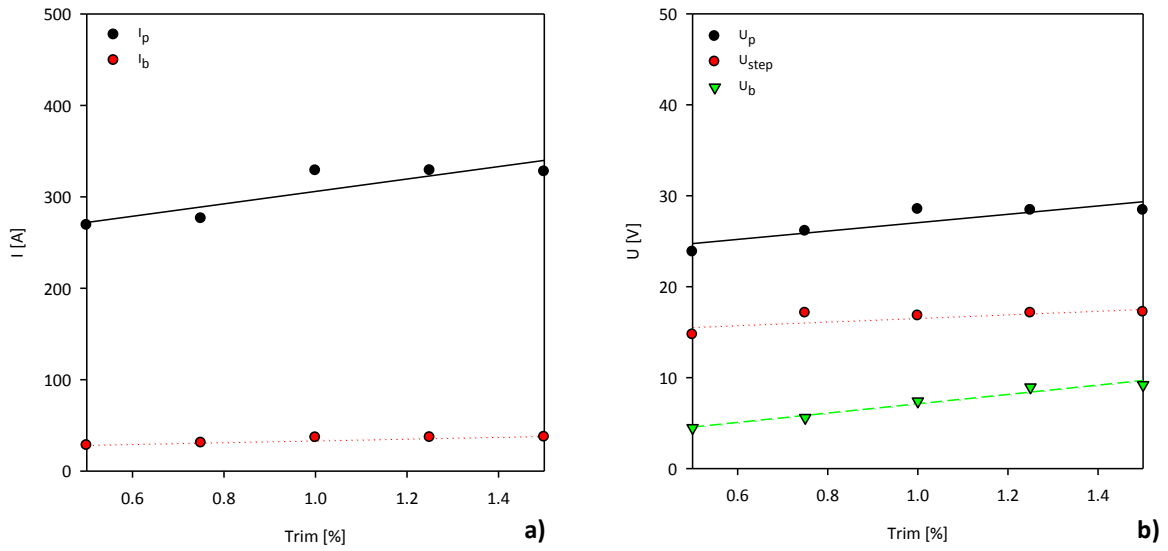


Figure VII.6 – Effect of trim on waveform parameters for GMAW-P: a) arc current and b) arc voltage.

CTWD was also evaluated for GMAW-P and the results are illustrated in the Figure VII.7.

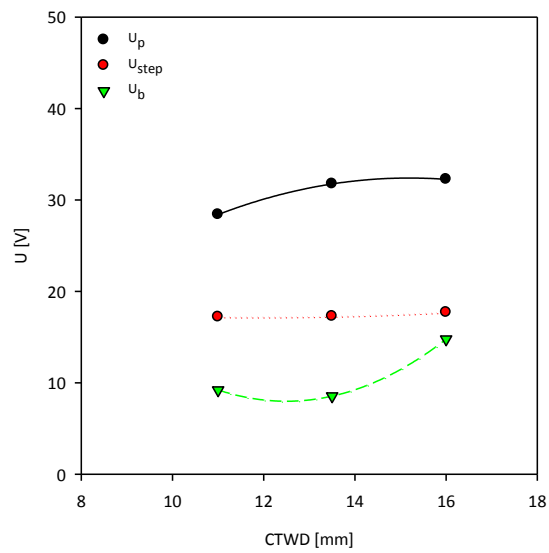


Figure VII.7 – Effect of CTWD on arc voltage waveform parameters to GMAW-P.

VII.2. Characterization of Waveform Parameters for RapidArc

The effect of WFS was also studied for RapidArc at different WFS/TS ratios. The results are presented from Figure VII.8 to VII.10.

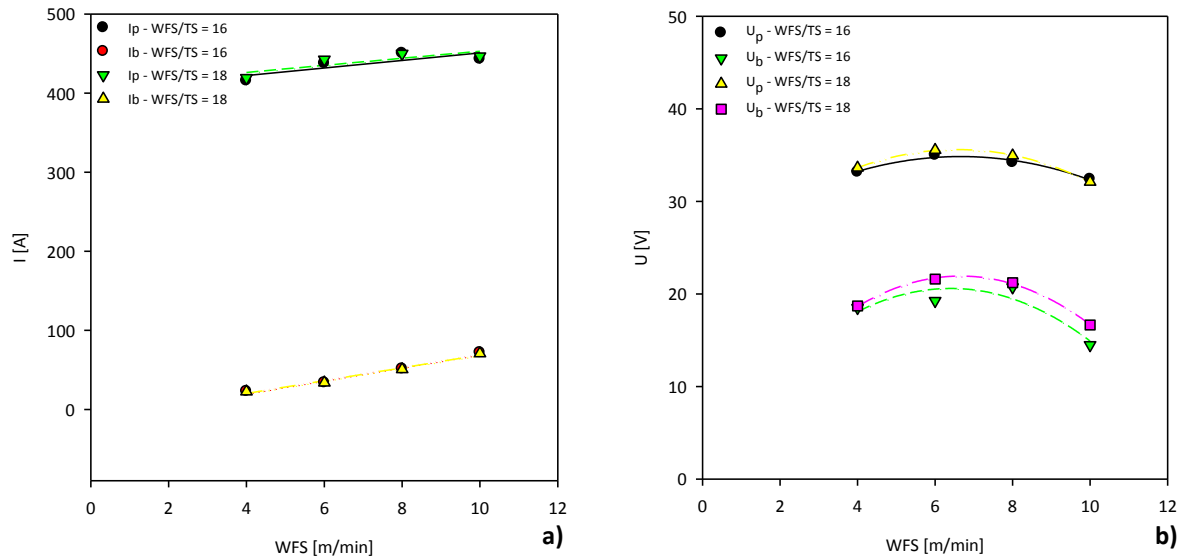


Figure VII.8 – Effect of WFS on background and peak parameters for RapidArc, at different WFS/TS ratios: a) arc current; b) arc voltage.

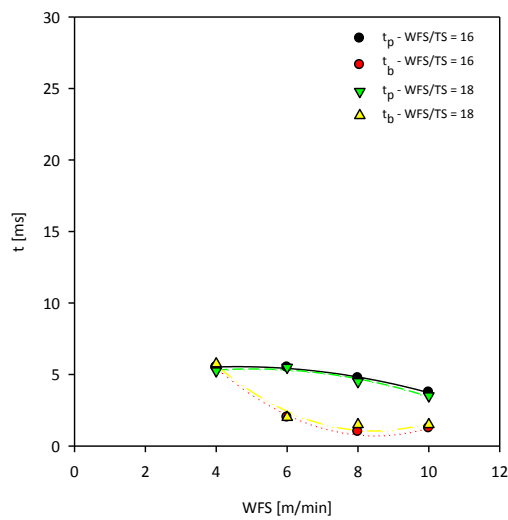


Figure VII.9 – Effect of WFS on background and peak time for RapidArc, at different WFS/TS ratios.

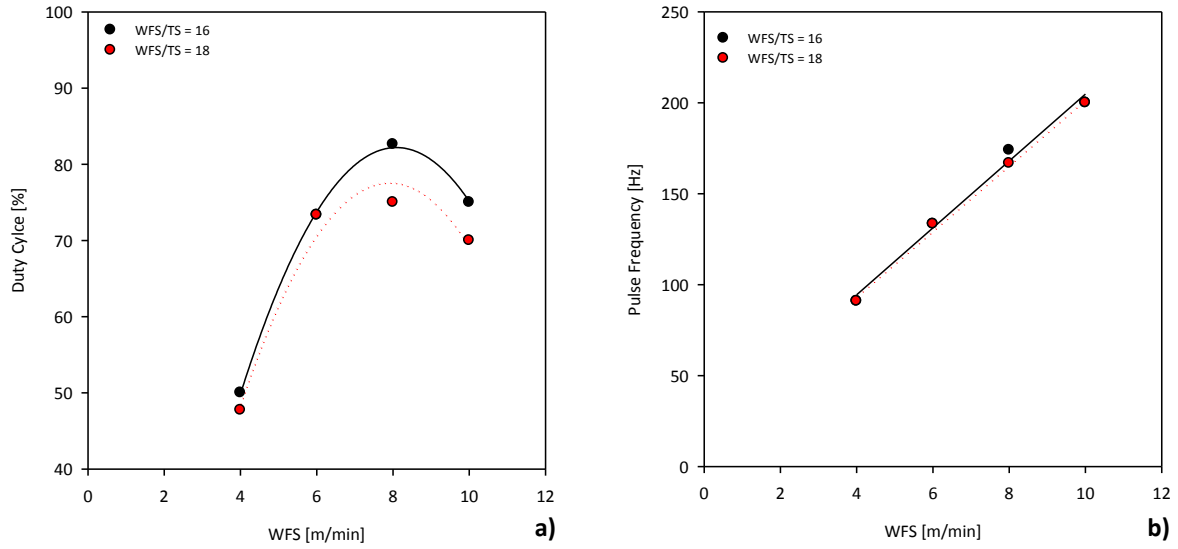


Figure VII.10 – Effect of WFS on duty cycle (a) and pulse frequency (b) to RapidArc, at different WFS/TS ratios.

The effect of shielding gas composition is illustrated in the Figure VII.11.

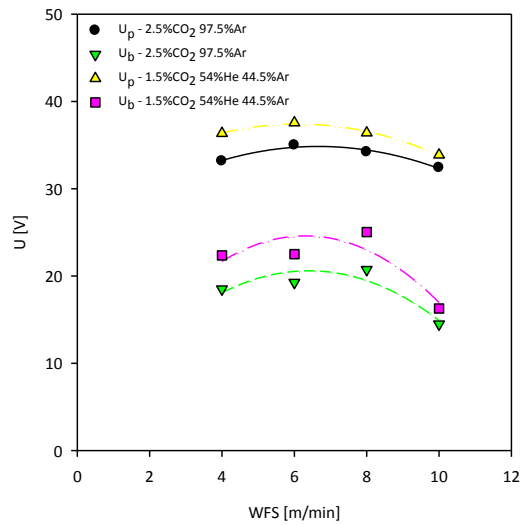


Figure VII.11 – Effect of WFS on arc voltage waveform parameters for RapidArc, at different shielding gases.

The effect of trim was also analysed for RapidArc and the most significant results are illustrated in the Figure VII.12.

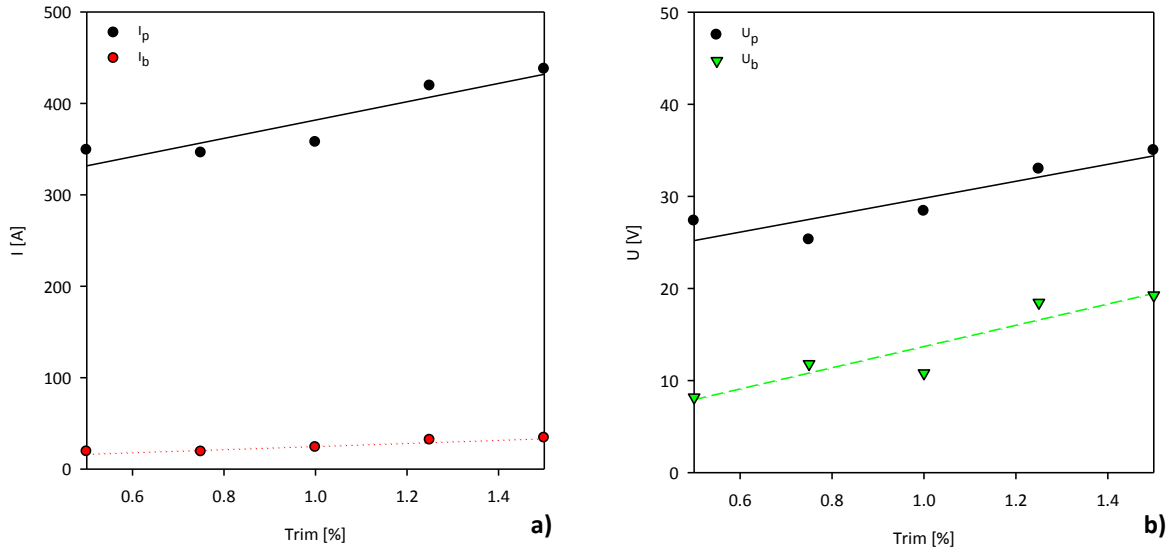


Figure VII.12 – Effect of trim on waveform parameters for RapidArc: a) arc current and b) arc voltage.

CTWD was also evaluated for RapidArc and the noteworthy results are presented in the Figure VII.13.

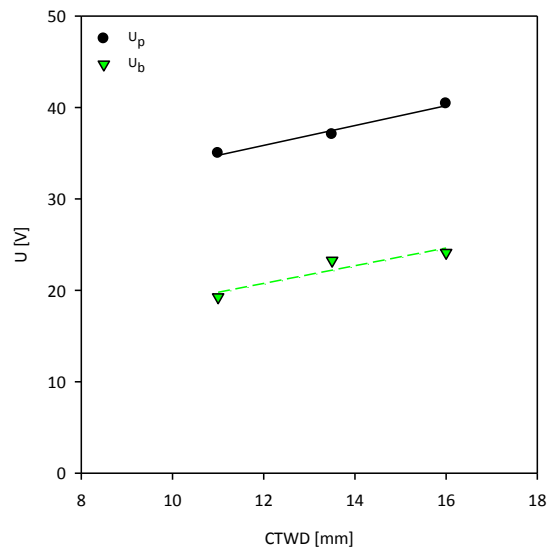


Figure VII.13 – Effect of CTWD on arc voltage parameters for RapidArc.

VII.3. Characterization of Waveform Parameters for STT

The effect of WFS was assessed for STT, at different WFS/TS ratios, and the results are illustrated from the Figure VII.14 to VII.16.

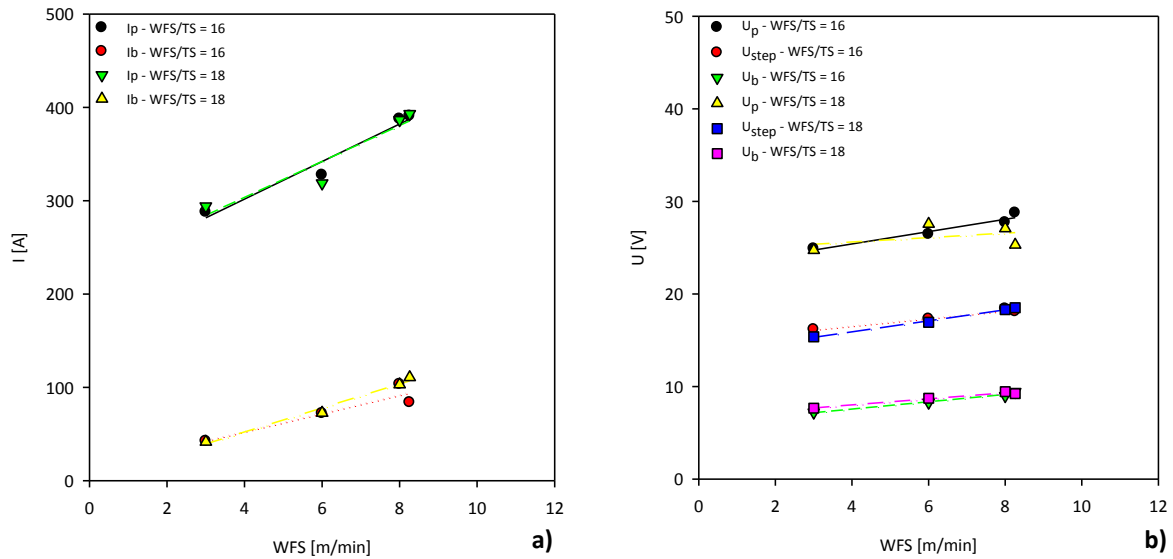


Figure VII.14 – Effect of WFS on background and peak parameters for STT, at different WFS/TS ratios: a) arc current; b) arc voltage.

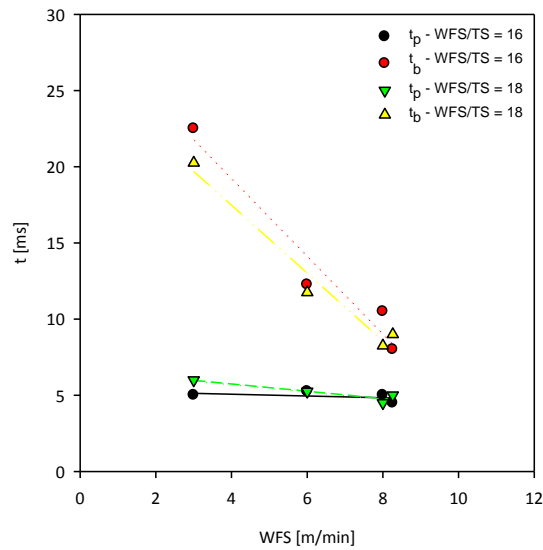


Figure VII.15 – Effect of WFS on background and peak time for STT, at different WFS/TS ratios.

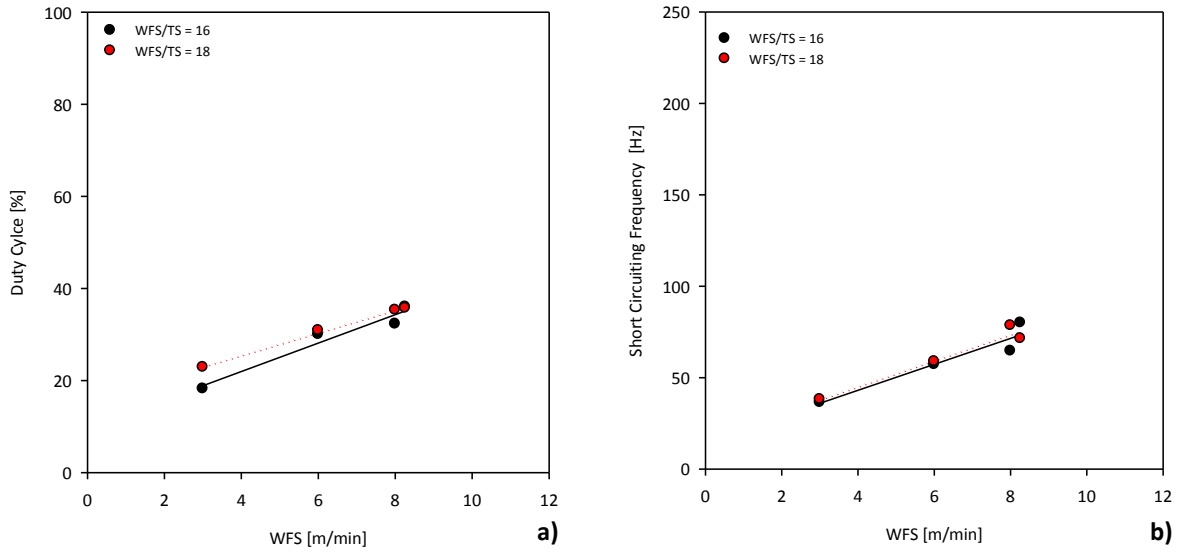


Figure VII.16 – Effect of WFS on duty cycle (a) and short circuiting frequency (b) for STT, at different WFS/TS ratios.

The effect of shielding gas composition was also evaluated for STT and the results are illustrated in the Figure VII.17.

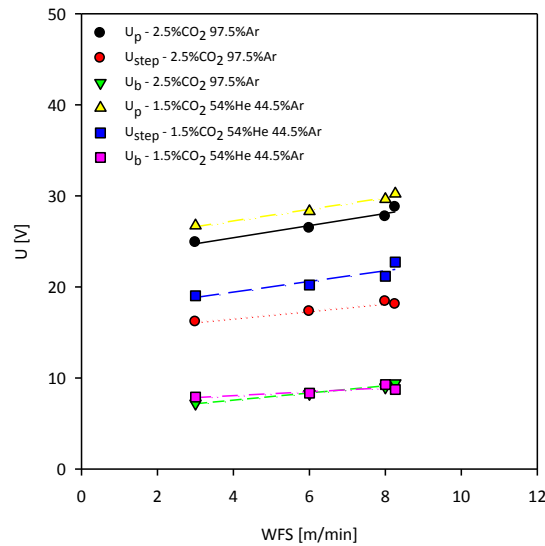


Figure VII.17 – Effect of WFS on arc voltage waveform parameters for STT, at different shielding gases.

The effect of trim was analysed for STT and the results are presented in the Figure VII.18.

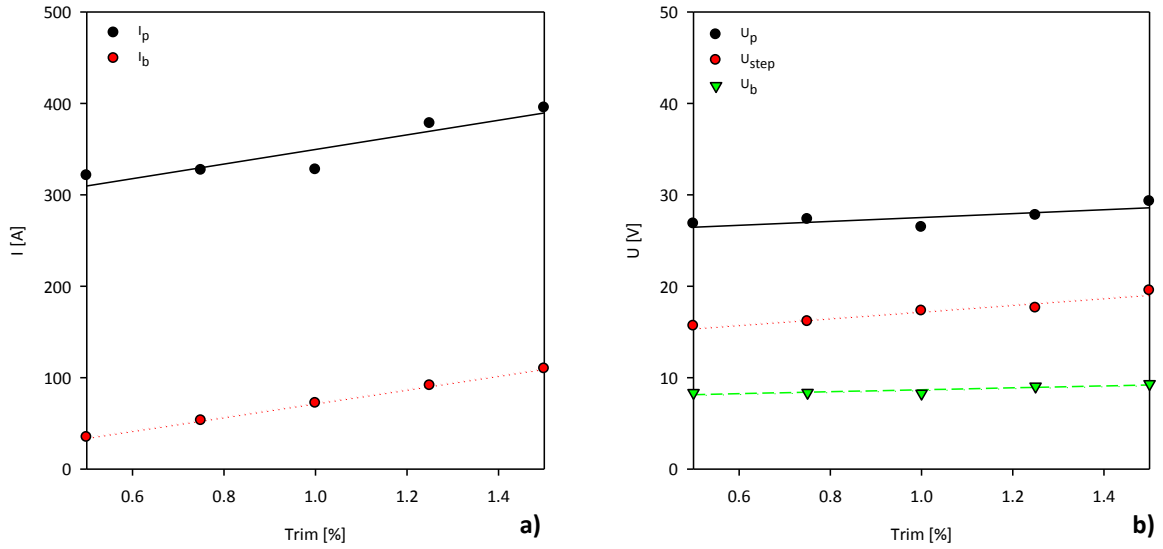


Figure VII.18 – Effect of trim on waveform parameters to RapidArc: a) arc current and b) arc voltage.

The results obtained in the analyses of CTWD are presented in the Figure VII.19 and VII.20.

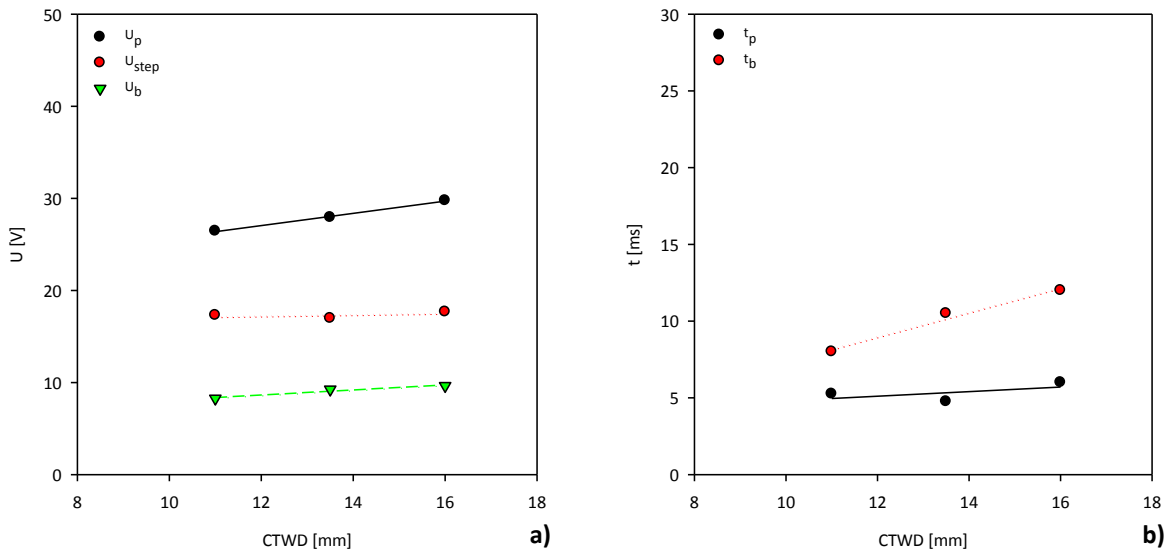


Figure VII.19 – Effect of CTWD on arc voltage waveform parameters (a) and time (b) for STT.

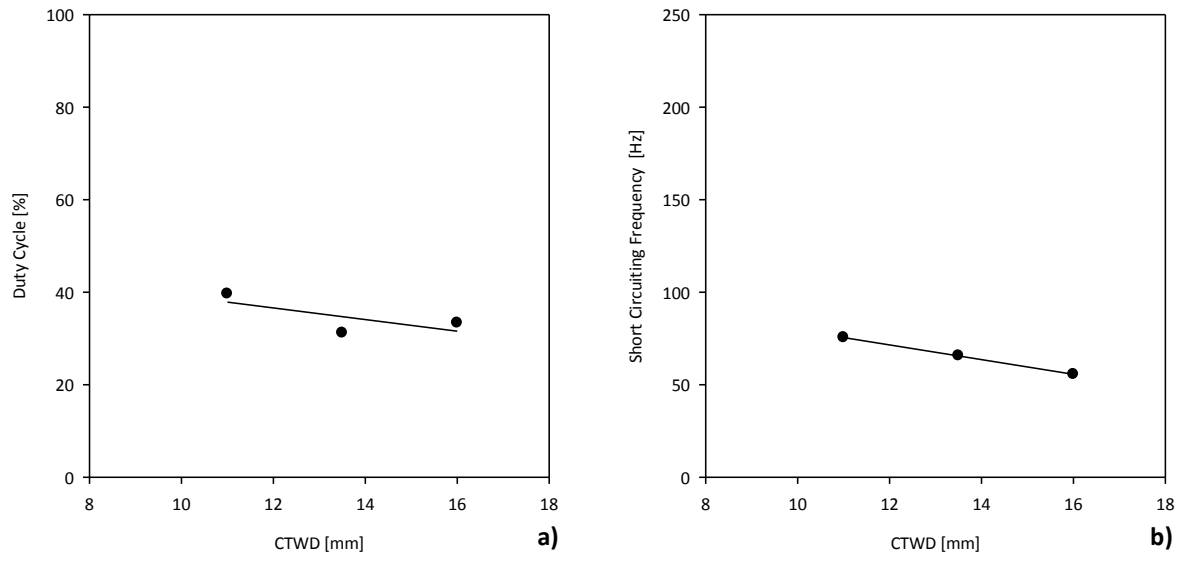


Figure VII.20 – Effect of CTWD on duty cycle (a) and short circuiting frequency (b) for STT.

VII.4. Characterization of Waveform Parameters to CMT

The effect of WFS was evaluated for CMT, at different WFS/TS ratios, and the results are illustrated from the Figure VII.21 to VII.23.

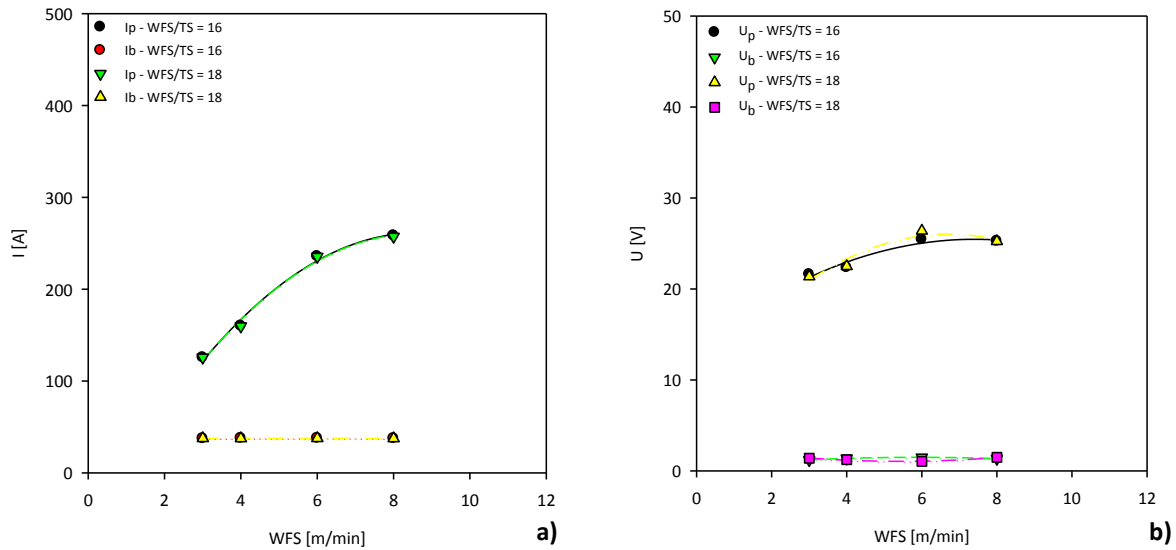


Figure VII.21 – Effect of WFS on background and peak waveform parameters for CMT, at different WFS/TS ratios: a) arc current waveform; b) arc voltage waveform.

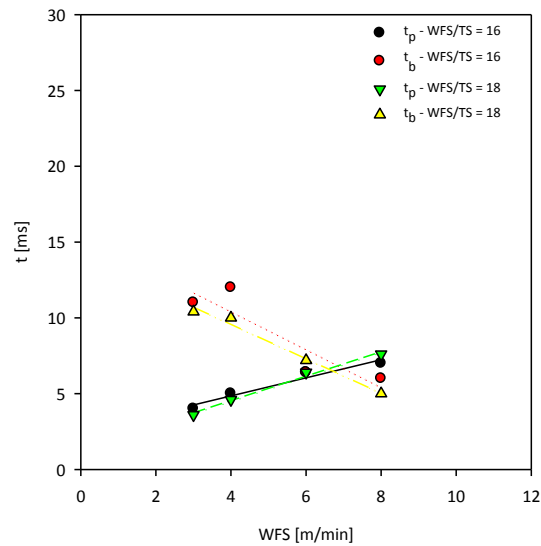


Figure VII.22 – Effect of WFS on the background and peak time for CMT, at different WFS/TS ratios.

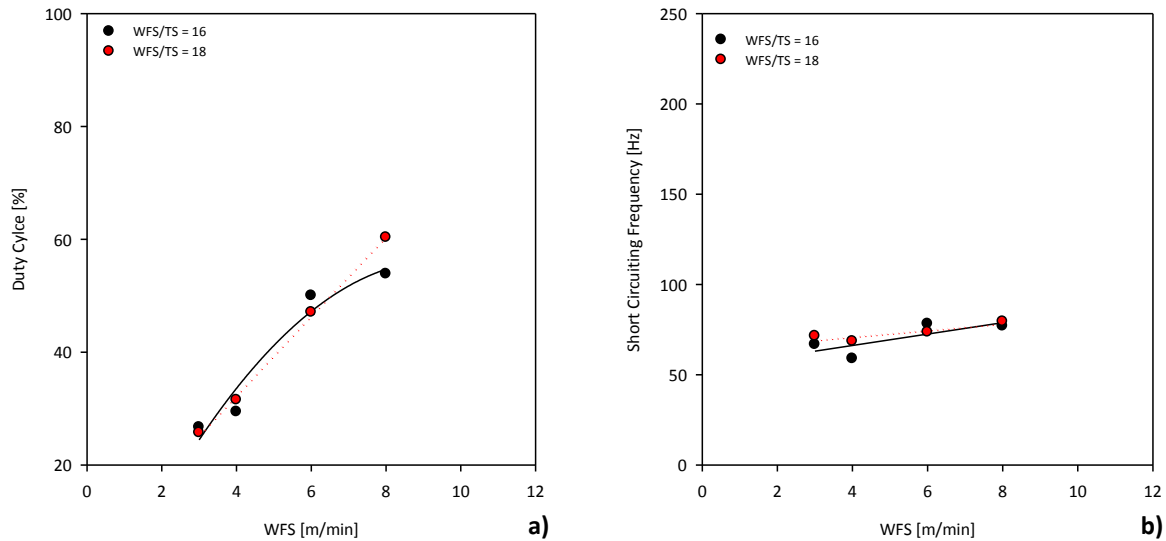


Figure VII.23 – Effect of WFS on duty cycle (a) and short circuiting frequency (b) for CMT, at different WFS/TS ratios.

The effect of shielding gas composition was also assessed for CMT as illustrated in the Figure VII.24.

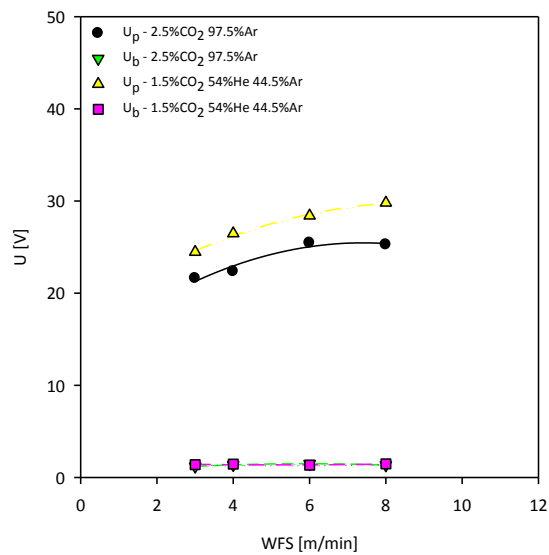


Figure VII.24 – Effect WFS on arc voltage waveform parameters to CMT, at different of shielding gases.

The effect of ALC is illustrated for CMT in the Figures VII.25 and VII.26.

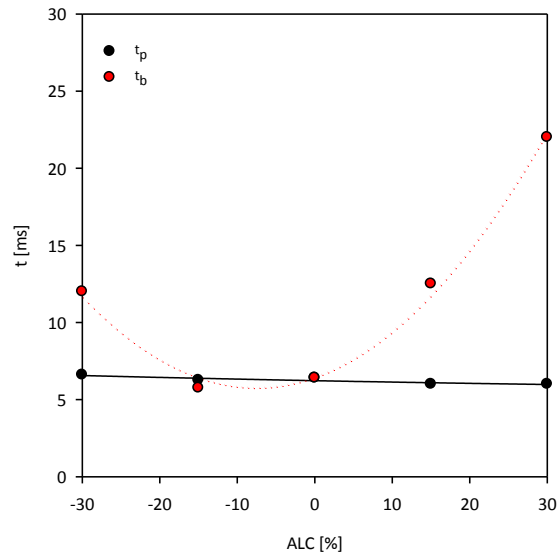


Figure VII.25 – Effect of ALC on the time parameters for CMT.

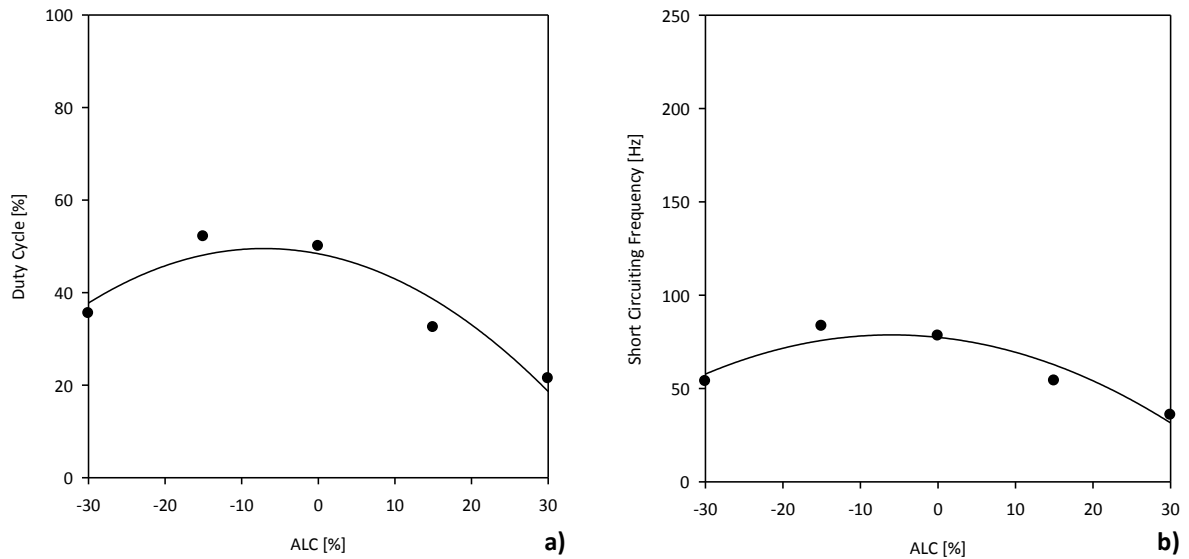


Figure VII.26 – Effect of ALC on duty cycle (a) and short circuiting frequency (b) for CMT.

The effect of Dynamic Control (DC) was evaluated for CMT and the results are illustrated in the Figure VII.27.

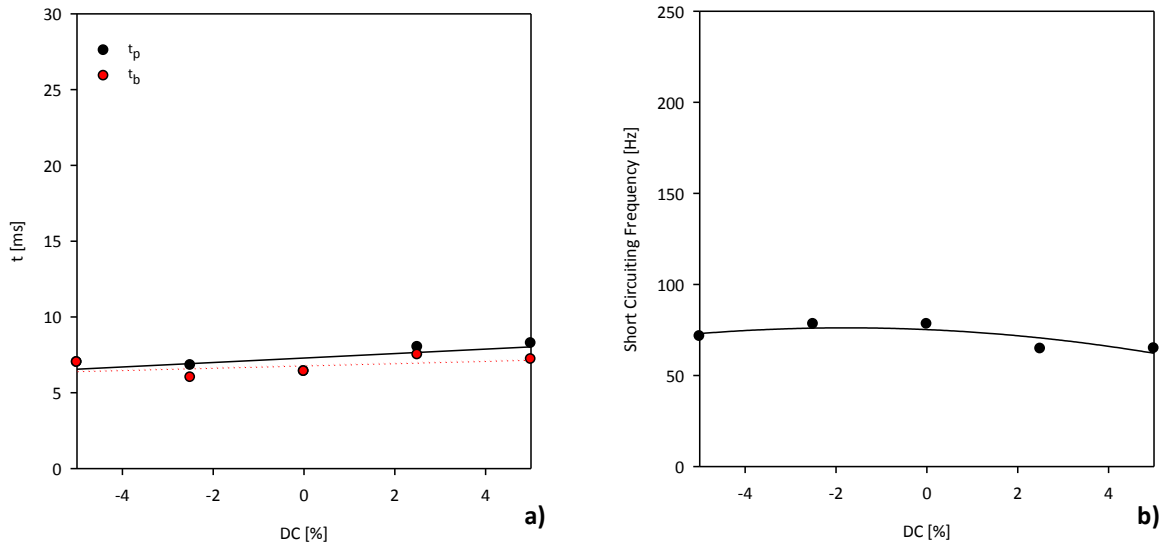


Figure VII.27 – Effect of DC on time (a) and short circuiting frequency (b) in CMT.

The effect of CTWF for CMT is shown in the Figure VII.28, below.

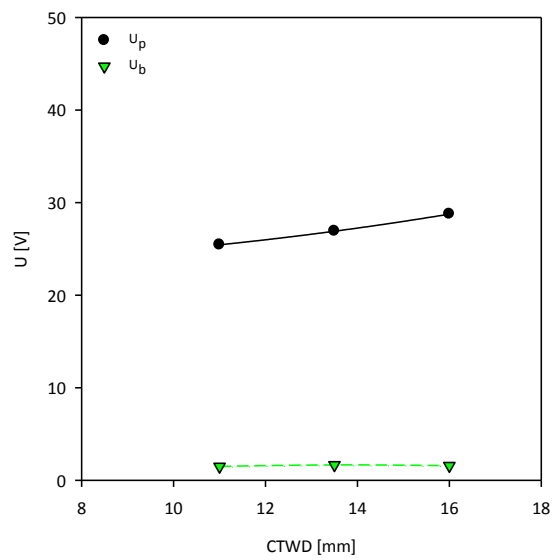


Figure VII.28 – Effect of CTWD on arc voltage waveform parameters for CMT.

VII.5. Characterization of Waveform Parameters for CMT-P

The effect of WFS is illustrated from the Figure VII.29 to VII.31.

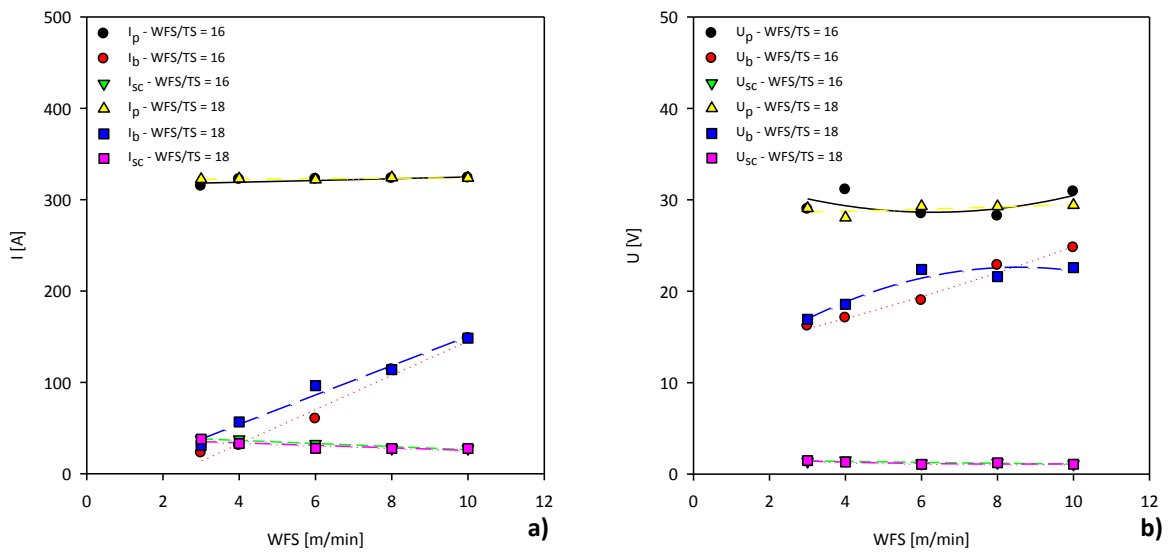


Figure VII.29 – Effect of WFS on waveform parameters for CMT-P, at different WFS/TS ratios: a) arc current waveform; b) arc voltage waveform.

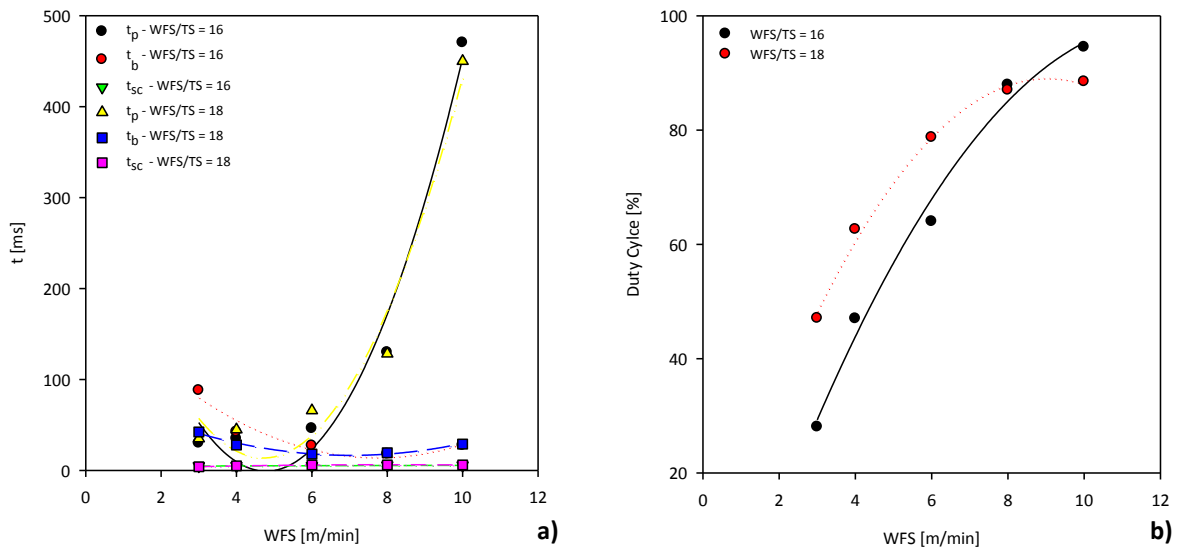


Figure VII.30 – Effect of WFS on time (a) and duty cycle (b) for CMT-P, at different WFS/TS ratios.

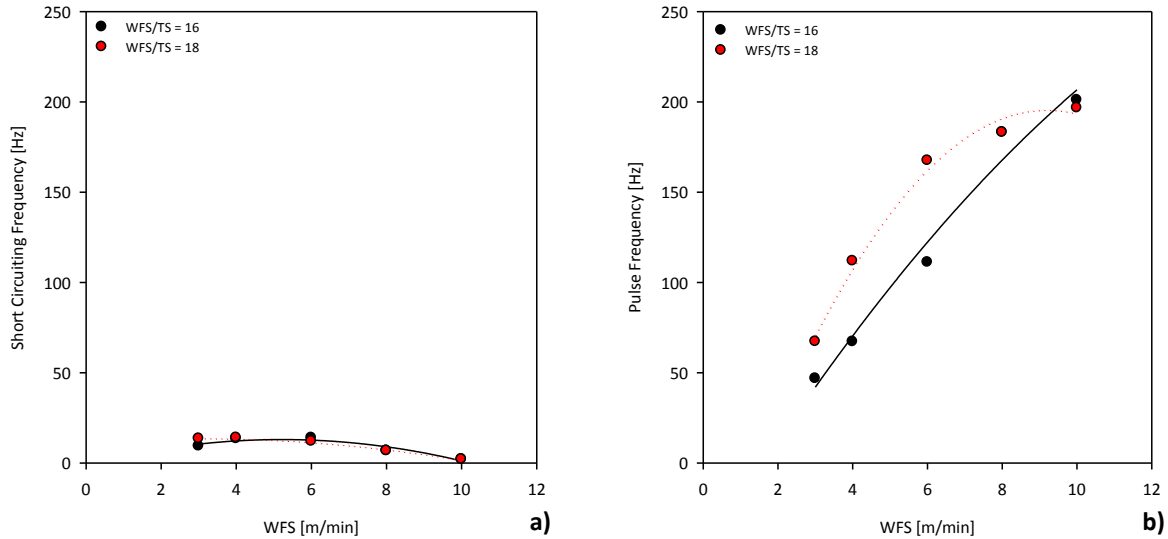


Figure VII.31 – Effect of WFS on short circuiting frequency (a) and pulse frequency (b) for CMT-P, at different WFS/TS ratios.

The effect of shielding gas composition was also evaluated as illustrated in the Figure VII.32.

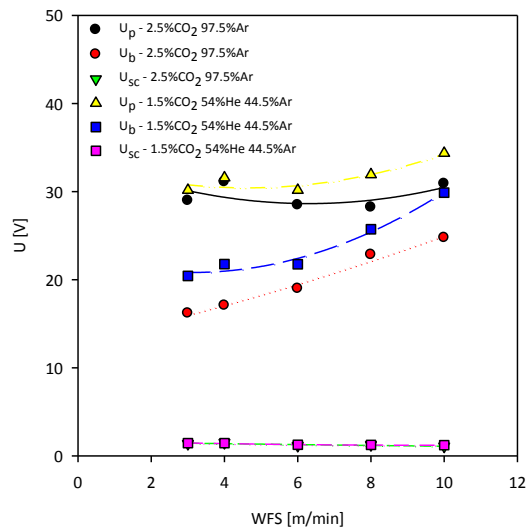


Figure VII.32 – Effect of WFS on arc voltage waveform parameters for CMT-P, at different shielding gases.

The effect of ALC for CMT-P is illustrated in the Figure VII.33.

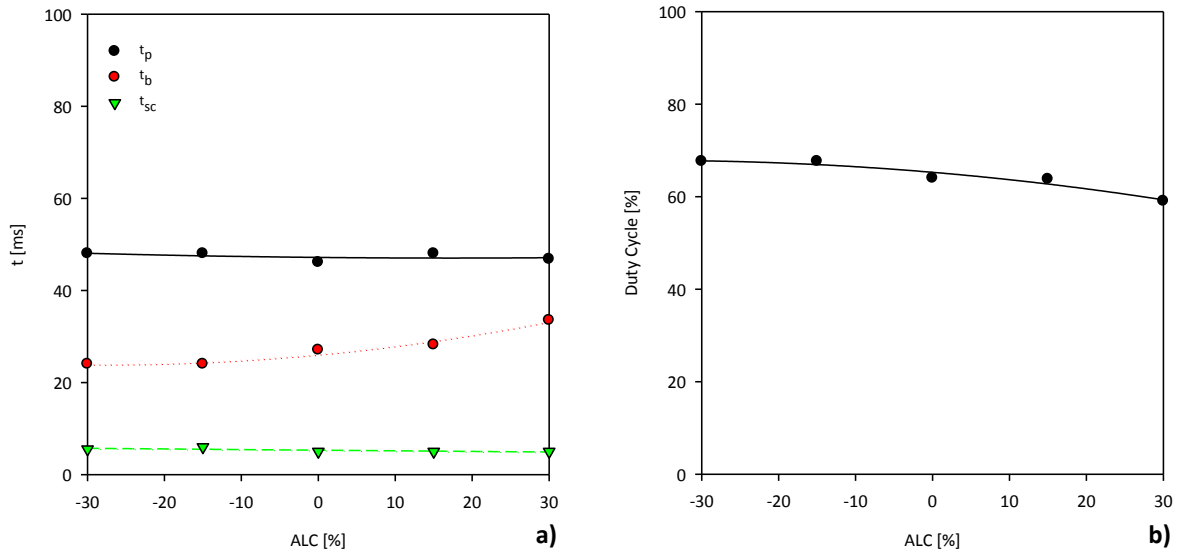


Figure VII.33 – Effect of ALC on time parameters (a) and duty cycle (b) for CMT-P.

The effect of PC (pulse control) for CMT-P is shown in the Figure VII.34.

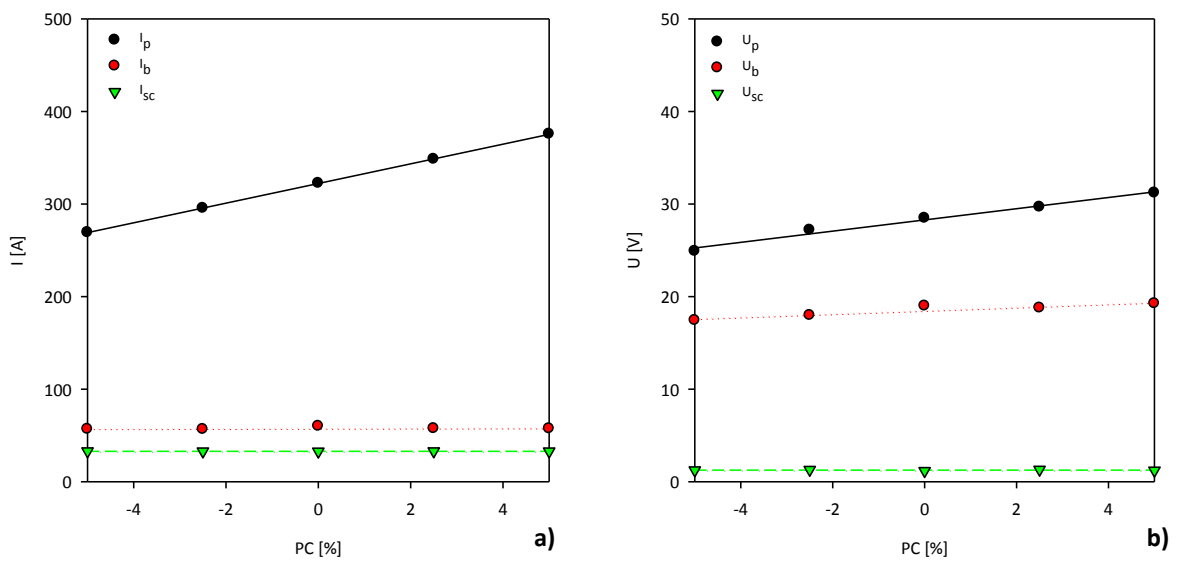


Figure VII.34 – Effect of PC on the waveform parameters to CMT-P: a) arc current; b) arc voltage.

The effect of CTWD was obtained for CMT-P and is presented in the Figure VII.35.

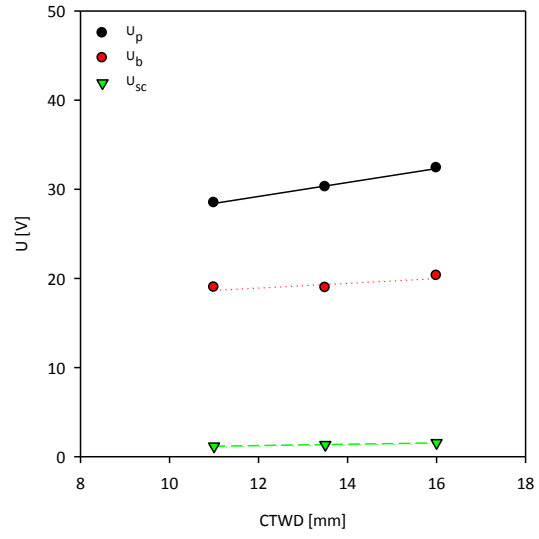


Figure VII.35 – Effect of CTWD on arc voltage waveform parameters for CMT-P.

VII.6. Characterization of Waveform Parameters for FastROOT

The effect of WFS was assessed for FastROOT, and the results are presented in Figures VII.36 to VII.38.

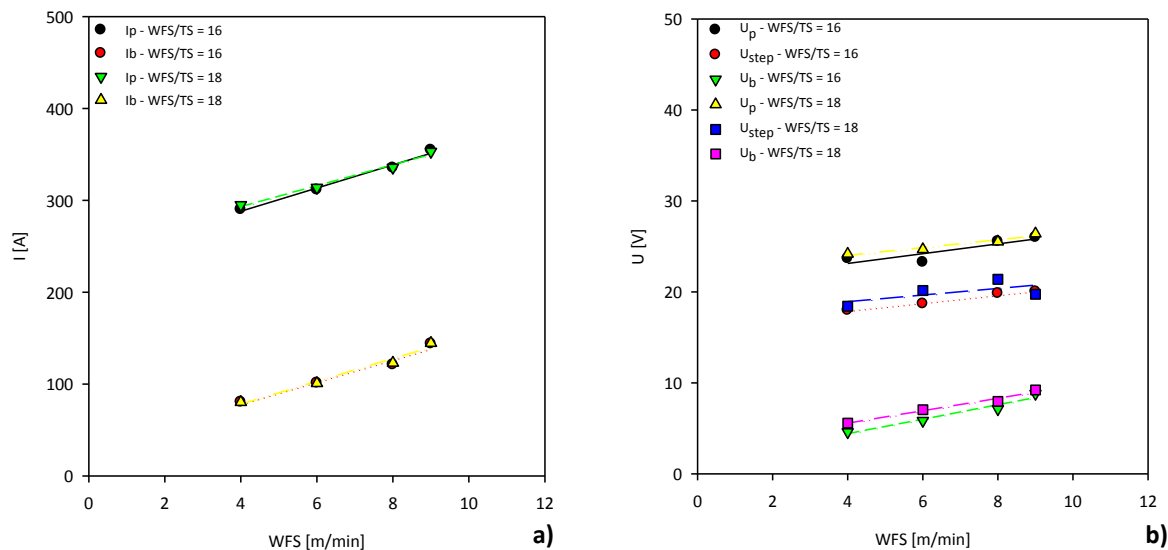


Figure VII.36 – Effect of WFS on background and peak waveform parameters for FastROOT, at different WFS/TS ratios: a) arc current waveform; b) arc voltage waveform.

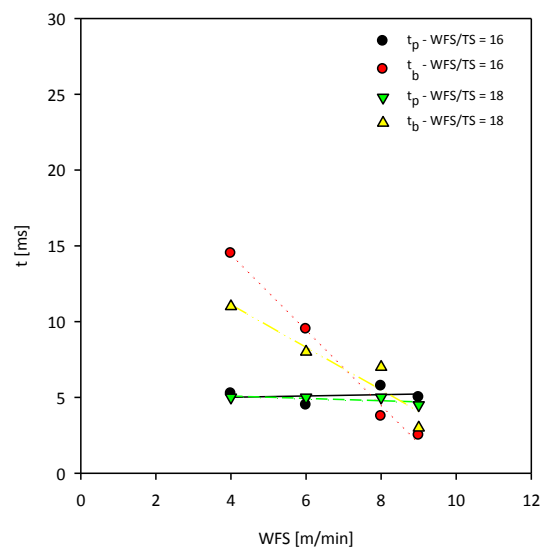


Figure VII.37 – Effect of WFS on background and peak time for FastROOT, at different WFS/TS ratios.

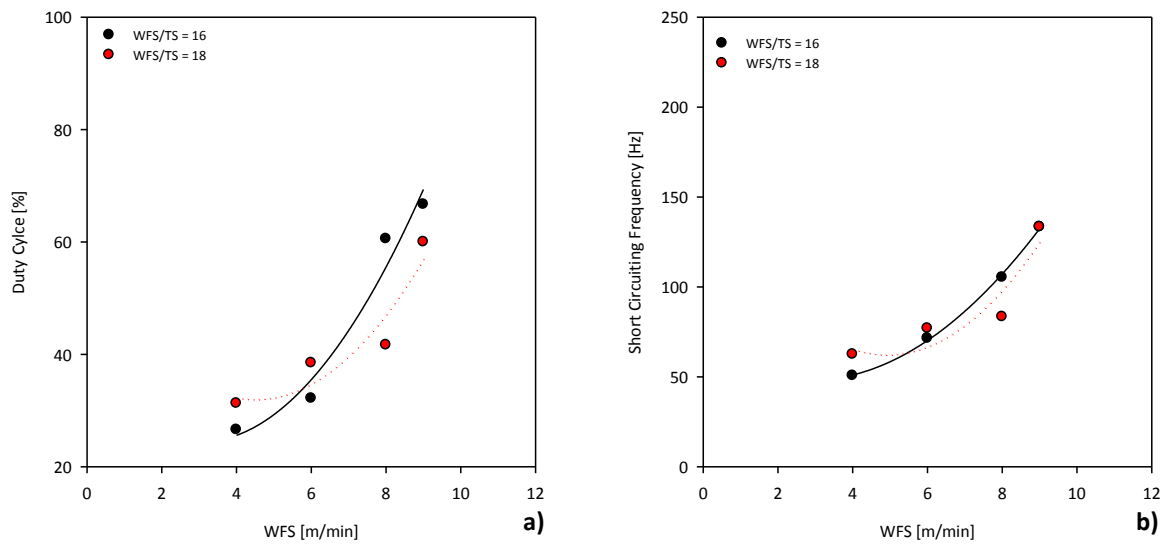


Figure VII.38 – Effect of WFS on duty cycle (a) and pulse frequency (b) for FastROOT, at different WFS/TS ratios.

The effect of shielding gas composition was also evaluated and the results are presented in the Figure VII.39 and VII.40.

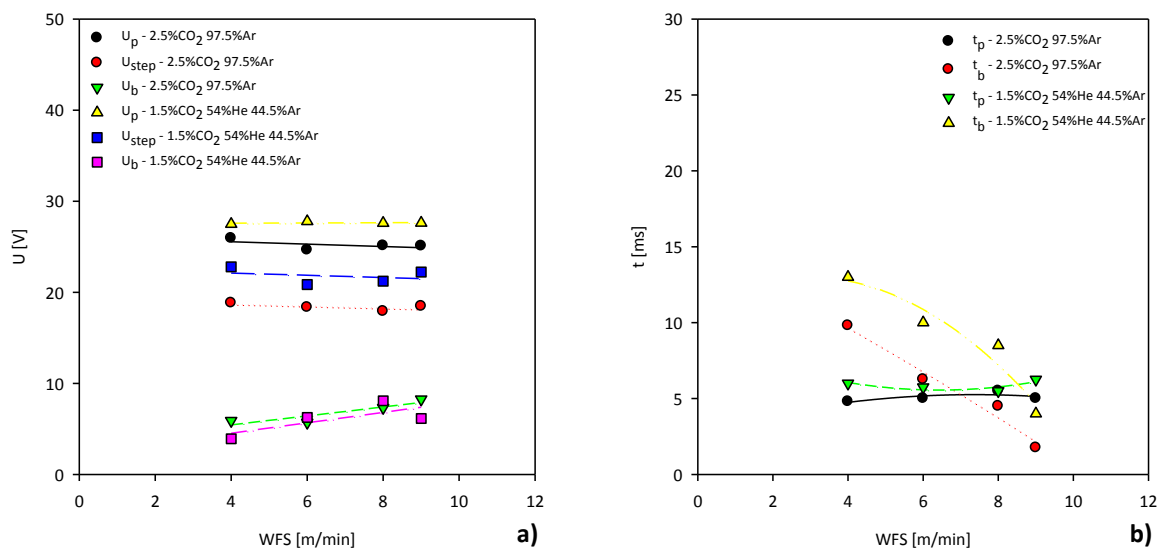


Figure VII.39 – Effect of WFS on waveform parameters for FastROOT, at different shielding gases: a) arc voltage parameters; b) time parameters.

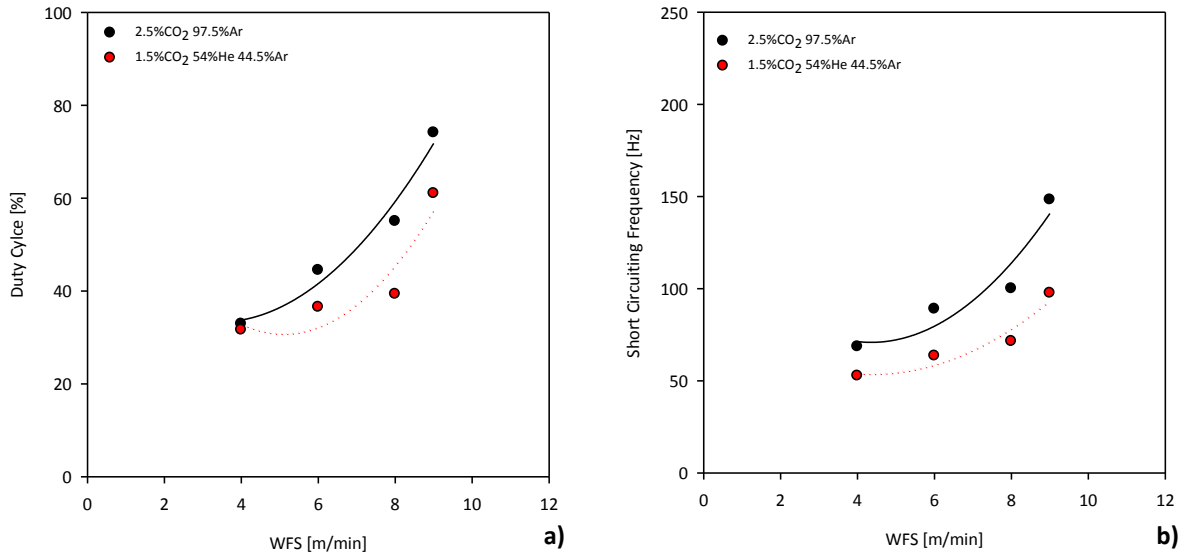


Figure VII.40 – Effect of WFS on duty cycle (a) and short circuiting frequency (b) for FastROOT, at different shielding gases.

The effect of Base Current (BC) was evaluated for FastROOT and the results are presented in the Figure VII.41 and VII.42.

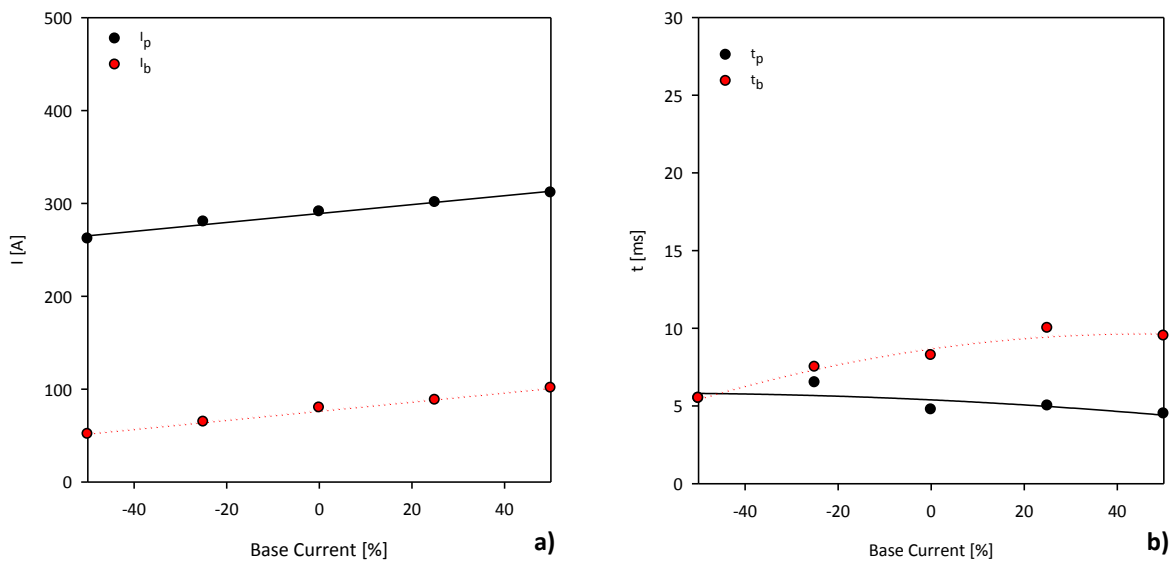


Figure VII.41 – Effect of Base Current on waveform parameters for FastROOT: a) arc current and b) time parameters.

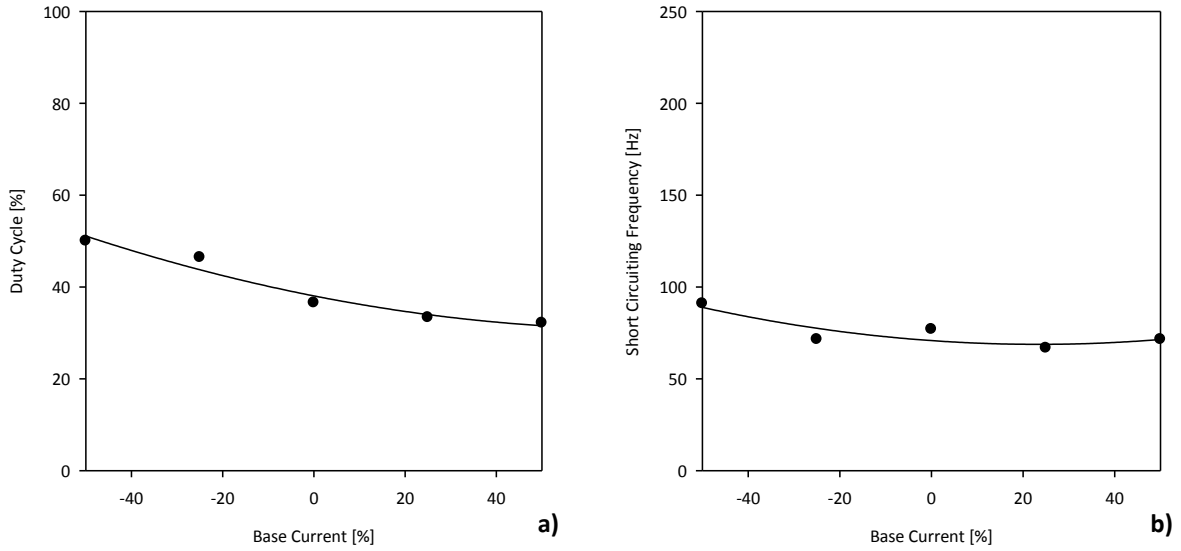


Figure VII.42 – Effect of Base Current on duty cycle (a) and short circuiting frequency (b) for FastROOT.

The effect of Forming Pulse (FP) was assessed to FastROOT as shown in Figure VII.43.

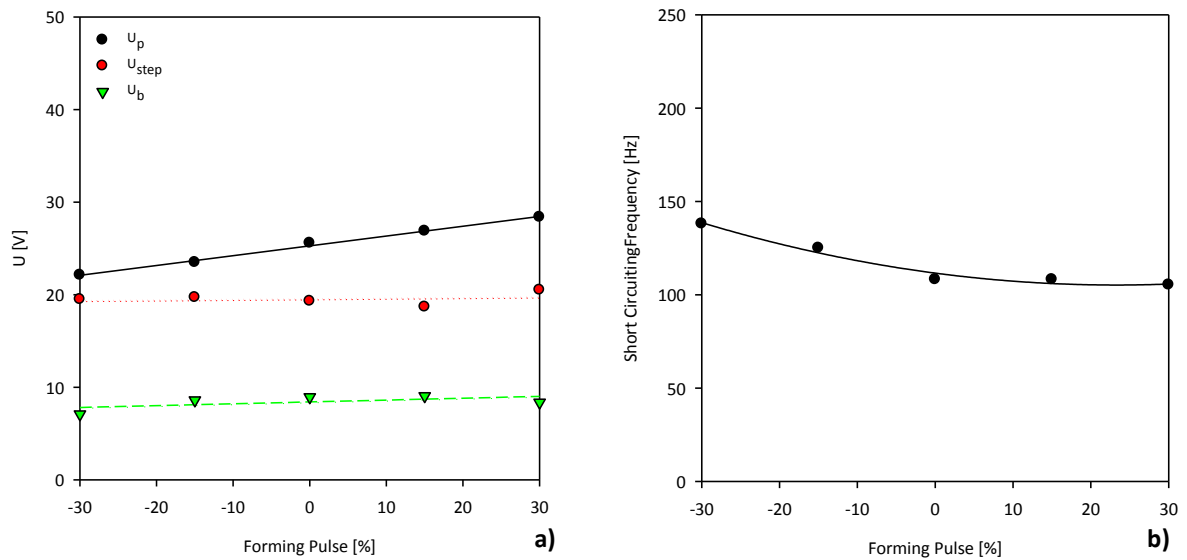


Figure VII.43 – Effect of Forming Pulse on arc voltage parameters (a) and short circuiting frequency (b) for FastROOT.

CTWD was also assessed for FastROOT and the results are presented from the Figure VII.44 to VII.46.

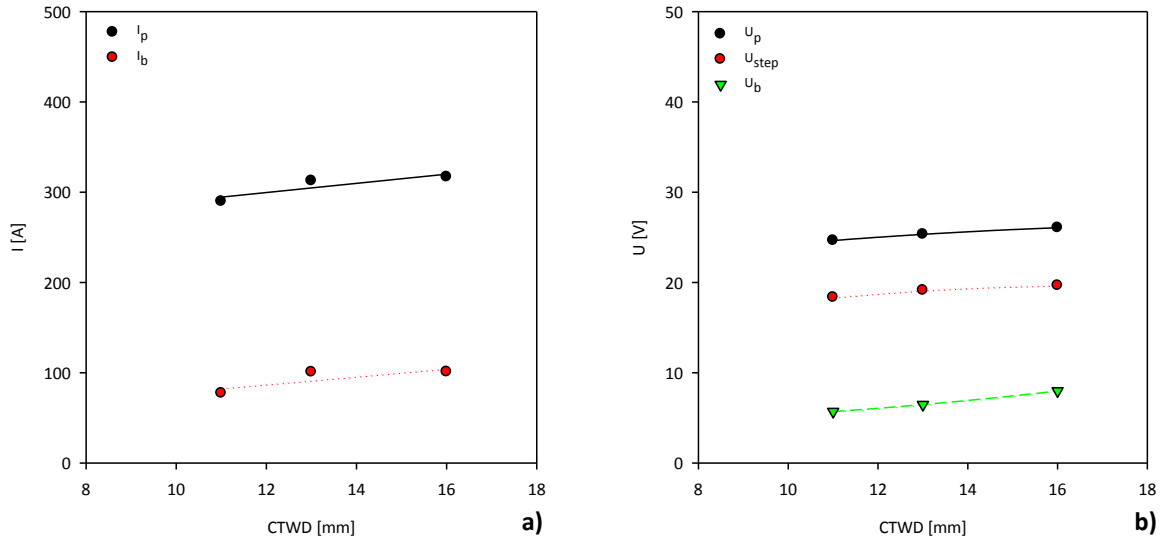


Figure VII.44 – Effect of CTWD on waveform parameters for FastROOT: a) arc current; b) arc voltage.

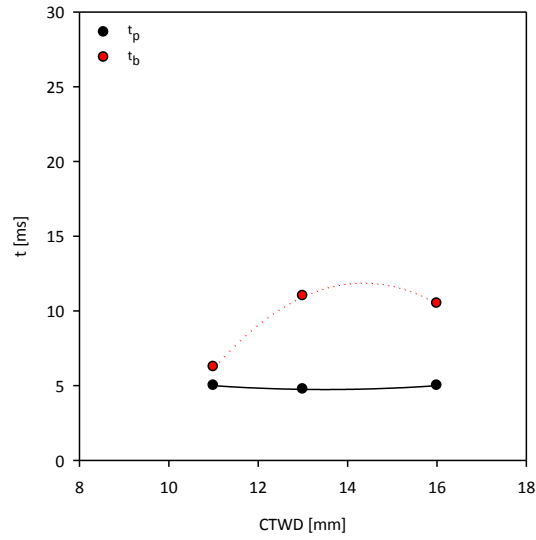


Figure VII.45 – Effect of CTWD on time parameters for FastROOT.

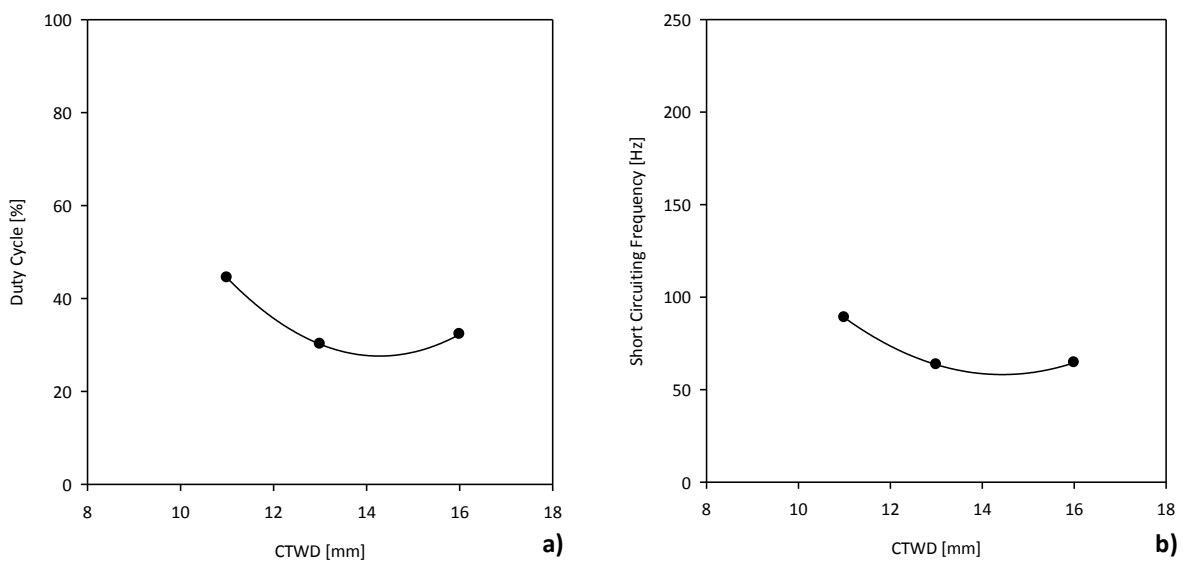


Figure VII.46 – Effect of CTWD on duty cycle (a) and short circuiting frequency (b) for FastROOT.

VIII. ARC CURRENT AND VOLTAGE WAVEFORMS

The first 5000 frames (100ms) of the arc current and arc voltage waveforms for different setting conditions will be presented in the following pages. At least the first 1000 frames (25ms) were ignored to these analyses due to the instability phenomena identified at the start of the weld.

Table VIII.1 – Signal of arc voltage and current waveforms obtained for GMAW-P.

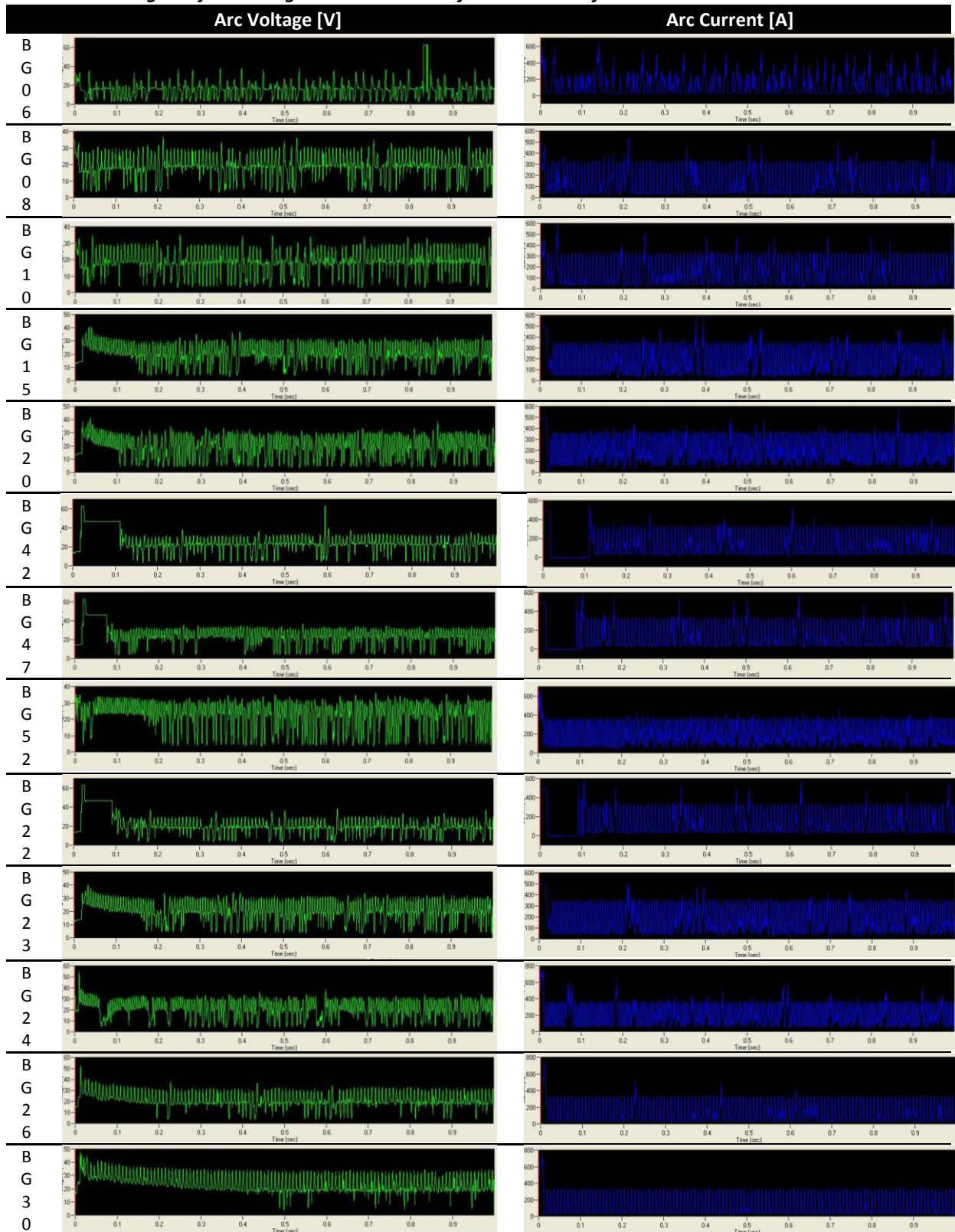


Table VIII.2 – Signal of arc voltage and current waveforms obtained for RapidArc.

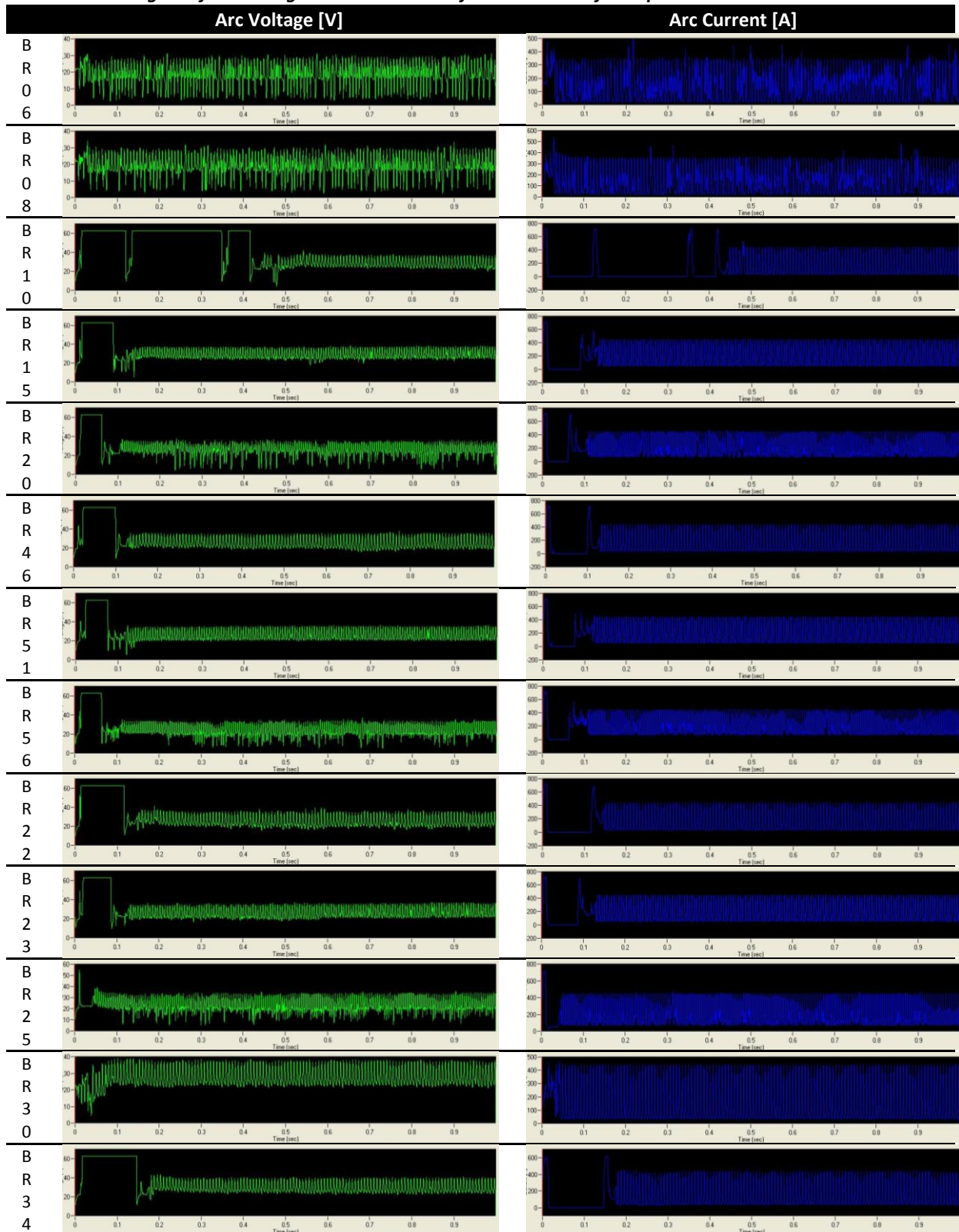


Table VIII.3 – Signal of arc voltage and current waveforms obtained for STT.

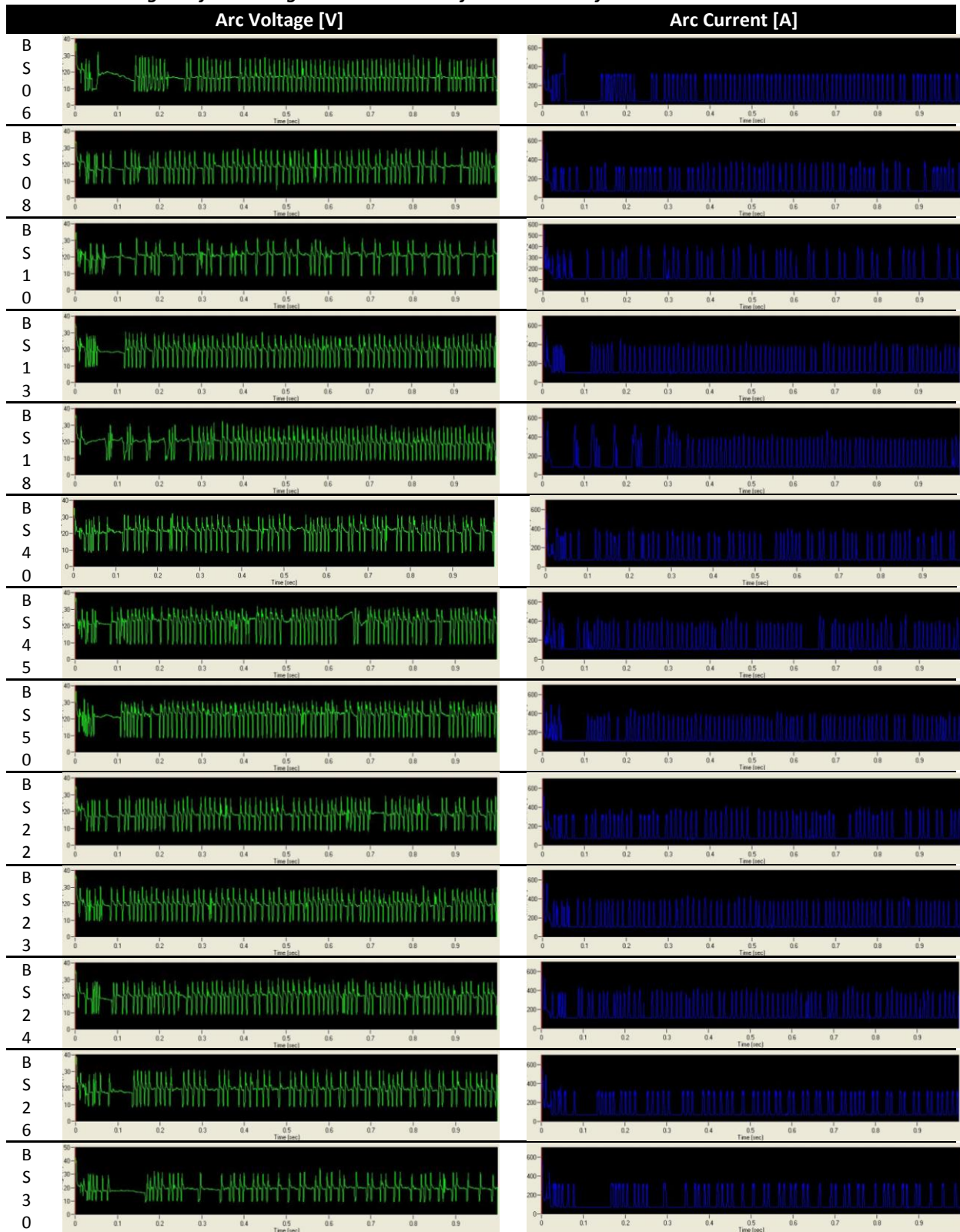


Table VIII.4 – Signal of arc voltage and current waveforms obtained for CMT.

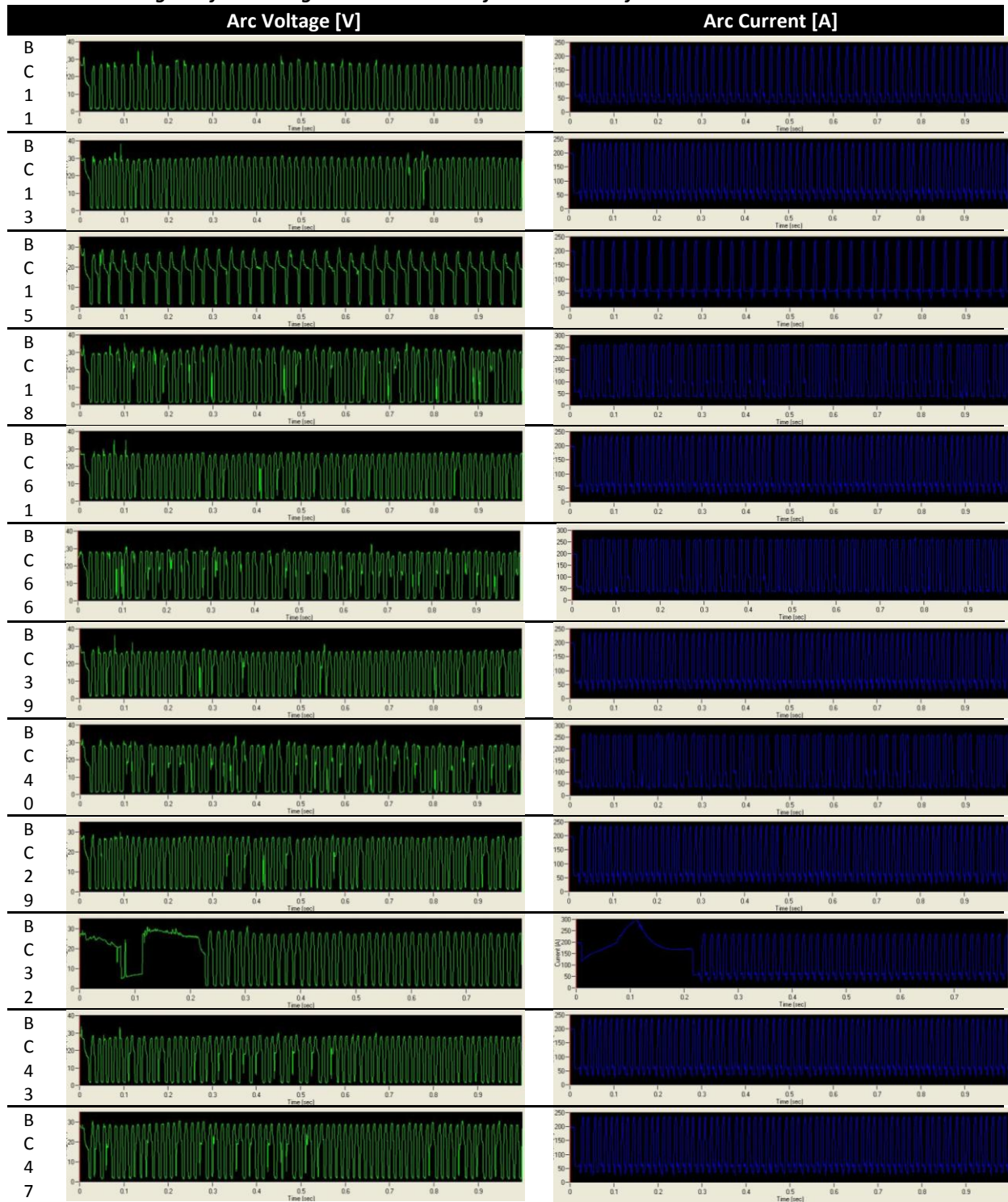


Table VIII.5 – Signal of arc voltage and current waveforms obtained for CMT-P.

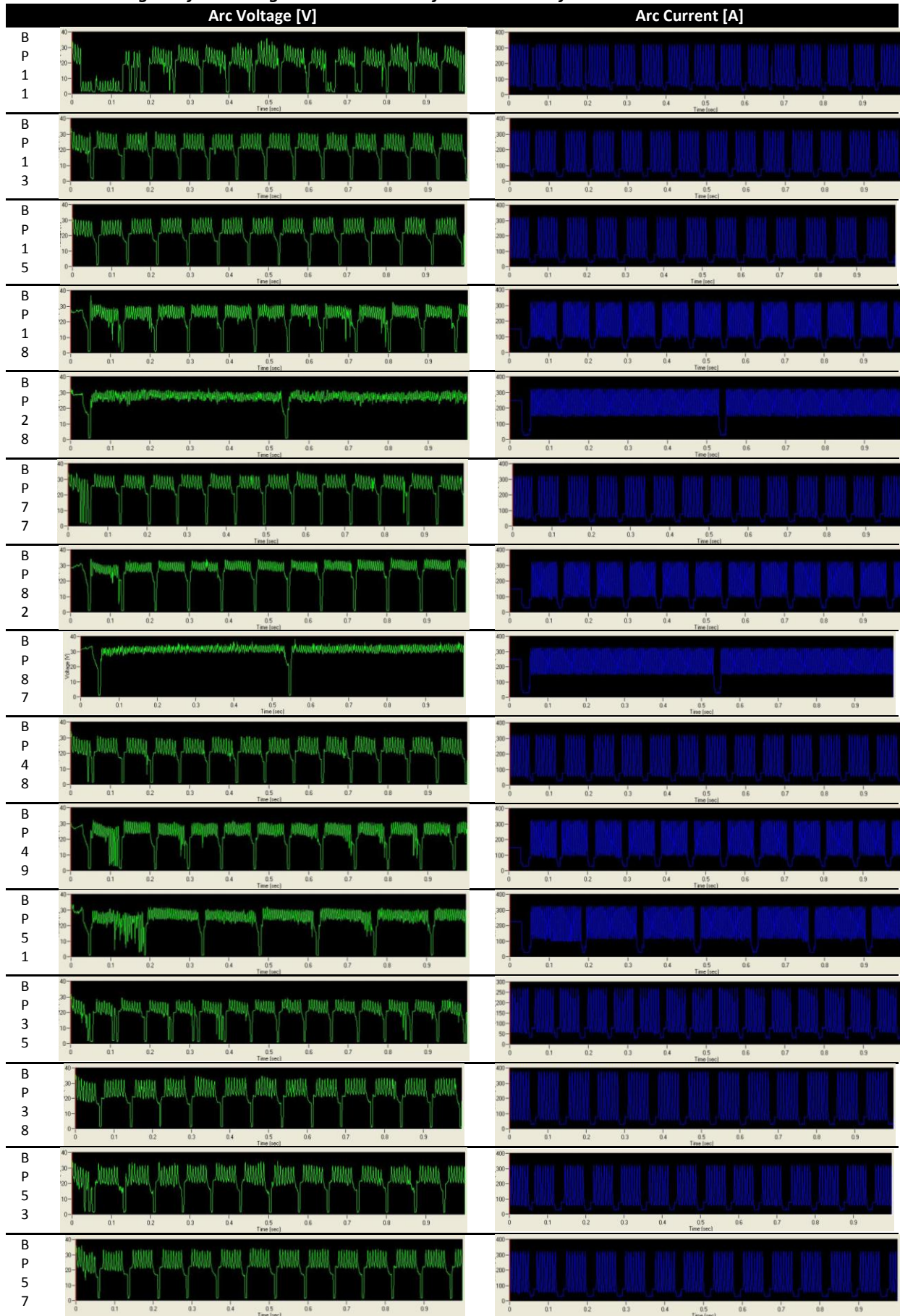
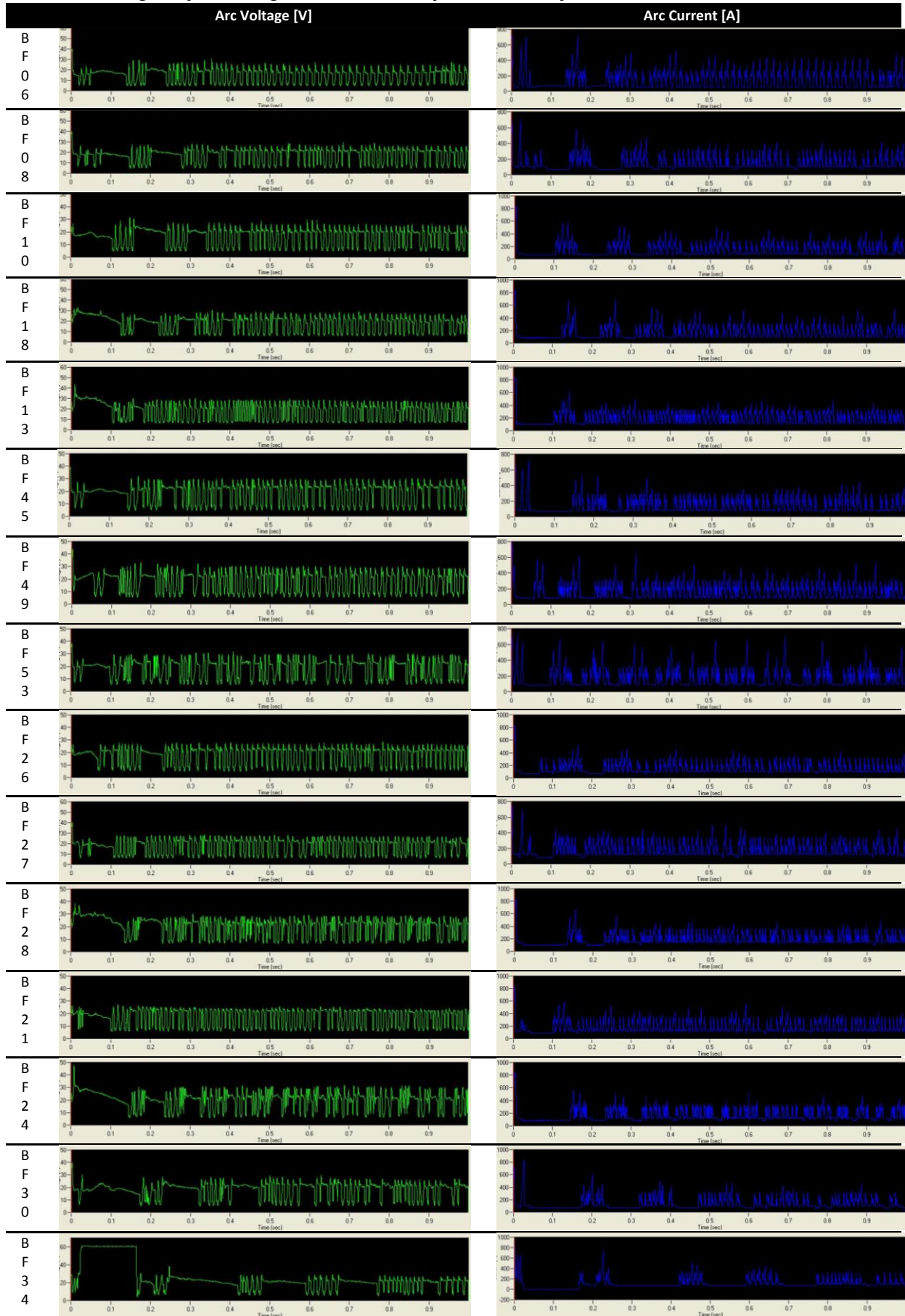


Table VIII.6 – Signal of arc voltage and current waveforms obtained for FastROOT.



IX. BEAD SHAPE CHARACTERISTICS FOR BEAD ON PIPE TESTS

The bead shape characteristics were determined for all the experimental tests performed and are described in the tables present in this section, as follow:

- Penetration bead;
- Height bead;
- Width bead;
- Dilution area;
- Height to Width Ratio;
- Dilution Ratio;
- Reinforcement Ratio.

Table IX.1 – Bead shape characteristics obtained for GMAW-P, using 2.5%CO₂, 97.5%Ar.

Run	Depth of Penetration [mm]	Height Bead [mm]	Width Bead [mm]	Dilution Area [mm ²]	Height/ Width Ratio [%]	Dilution Ratio [%]	Reinforcement Ratio [%]
BG01	0.410	3.91	6.96	1.03	56.2	5.47	94.5
BG02	-	-	-	-	-	-	-
BG03	1.26	3.48	5.13	3.60	67.8	24.4	75.6
BG04	1.19	3.07	6.62	3.21	46.4	22.3	77.7
BG05	1.25	3.68	5.81	3.70	63.3	21.1	78.9
BG06	0.700	3.39	5.91	1.46	57.4	10.1	89.9
BG07	1.03	3.55	7.96	1.99	44.6	11.3	88.7
BG08	1.67	3.26	7.55	6.20	43.2	30.5	69.5
BG09	2.25	2.97	6.13	6.38	48.5	32.5	67.5
BG10	-	-	-	-	-	-	-
BG11	0.680	3.45	6.41	2.09	53.8	14.9	85.1
BG12	1.42	3.00	7.40	3.09	40.5	18.8	81.2
BG13	2.42	2.61	6.78	6.96	38.5	38.2	61.8
BG14	1.71	3.32	8.33	5.89	39.9	24.1	75.9
BG15	1.77	3.00	7.77	5.72	38.6	26.8	73.2
BG16	0.260	3.55	5.66	0.65	62.7	4.94	95.1
BG17	0.900	3.32	6.28	2.25	52.9	14.0	86.0
BG18	2.07	2.93	7.80	8.80	37.6	37.9	62.1
BG19	2.52	2.80	6.06	8.12	46.2	39.9	60.1
BG20	2.12	3.23	7.43	6.19	43.5	28.2	71.8
BG21	1.13	4.03	7.34	3.54	54.9	15.1	84.9
BG22	1.71	3.19	6.93	6.40	46.0	29.1	70.9
BG23	2.22	2.94	7.83	8.46	37.5	36.4	63.6
BG24	2.16	3.26	8.05	8.86	40.5	35.8	64.2
BG25	1.29	3.51	5.72	2.51	61.4	16.2	83.8
BG26	1.97	3.06	6.19	6.30	49.4	31.2	68.8
BG27	2.56	2.51	6.31	9.75	39.8	49.5	50.5
BG28	2.13	3.03	7.43	7.39	40.8	32.8	67.2
BG29	1.35	3.13	4.94	2.54	63.4	18.0	82.0
BG30	2.28	2.81	6.12	6.53	45.9	35.9	64.1
BG31	2.51	2.78	6.31	7.89	44.1	39.7	60.3
BG32	2.23	2.84	7.53	7.11	37.7	32.5	67.5

Table IX.2 – Bead shape characteristics obtained for GMAW-P, using 1.5%CO₂, 54%He 44.5%Ar.

Run	Depth of Penetration [mm]	Height Bead [mm]	Width Bead [mm]	Dilution Area [mm ²]	Height/ Width Ratio [%]	Dilution Ratio [%]	Reinforcement Ratio [%]
BG33	0.610	3.08	6.63	2.00	46.5	13.3	86.7
BG34	1.13	2.79	6.91	2.59	40.4	17.2	82.8
BG35	1.45	3.31	6.63	4.07	49.9	23.8	76.2
BG36	1.39	3.21	6.16	3.64	52.1	22.5	77.5
BG37	1.52	2.95	6.38	5.06	46.2	31.1	68.9
BG38	0.740	3.34	7.41	2.24	45.1	14.5	85.5
BG39	0.750	3.08	6.88	1.71	44.8	12.2	87.8
BG40	1.76	2.75	6.97	6.67	39.5	35.4	64.6
BG41	1.85	2.66	7.41	7.53	35.9	37.0	63.0
BG42	1.94	2.66	6.91	7.56	38.5	38.6	61.4
BG43	0.71	2.79	7.97	2.44	35.0	14.8	85.2
BG44	1.06	2.74	7.40	2.45	37.0	16.3	83.7
BG45	2.49	2.58	7.31	9.62	35.3	40.9	59.1
BG46	2.51	2.68	7.25	10.05	37.0	42.9	57.1
BG47	2.55	2.87	7.27	11.27	39.5	44.4	55.6
BG48	0.420	2.93	6.00	1.66	48.8	13.7	86.3
BG49	1.23	2.74	7.03	3.90	39.0	24.0	76.0
BG50	2.15	2.78	7.09	9.21	39.2	40.7	59.3
BG51	2.25	2.71	7.52	7.96	36.0	35.5	64.5
BG52	2.36	2.51	6.58	10.62	38.1	48.9	51.1
BG53	1.67	3.49	6.53	4.55	53.4	22.6	77.4
BG54	1.88	2.93	6.84	6.60	42.8	29.8	70.2
BG55	2.77	2.81	6.96	11.45	40.4	45.9	54.1
BG56	2.84	2.74	6.87	11.48	39.9	48.1	51.9
BG57	1.67	3.10	6.50	5.59	47.7	30.4	69.6
BG58	2.58	2.87	6.19	8.64	46.4	40.0	60.0
BG59	2.80	3.10	6.37	11.25	48.7	47.1	52.9
BG60	2.09	2.84	7.65	8.98	37.1	38.1	61.9
BG61	1.49	3.19	5.88	4.59	54.3	28.0	72.0
BG62	2.58	3.10	5.84	7.24	53.1	34.4	65.6
BG63	1.54	4.13	5.35	3.77	77.2	18.7	81.3
BG64	2.94	3.16	7.18	11.19	44.0	42.8	57.2

Table IX.3 – Bead shape characteristics obtained for RapidArc, using 2.5%CO₂ 97.5%Ar.

Run	Depth of Penetration [mm]	Height bead [mm]	Width Bead [mm]	Dilution Area [mm²]	Height/ Width Ratio [%]	Dilution Ratio [%]	Reinforcement Ratio [%]
BR01	1.61	3.39	5.32	4.22	63.7	24.8	75.2
BR02	1.45	3.26	5.50	4.81	59.3	29.6	70.4
BR03	1.74	2.71	5.84	5.23	46.4	33.2	66.8
BR04	1.86	2.81	6.28	4.77	44.7	27.4	72.6
BR05	2.00	2.87	6.72	5.53	42.7	29.3	70.7
BR06	2.13	2.90	6.87	7.82	42.2	40.0	60.0
BR07	1.26	3.58	7.65	3.99	46.8	17.6	82.4
BR08	-	-	-	-	-	-	-
BR09	2.48	2.94	7.55	7.80	38.9	34.2	65.8
BR10	2.44	2.91	7.65	8.08	38.0	38.1	61.9
BR11	1.74	2.84	7.18	6.63	39.6	34.4	65.6
BR12	1.61	2.74	6.31	5.25	43.4	32.1	67.9
BR13	-	-	-	-	-	-	-
BR14	2.03	3.84	7.52	7.31	51.1	26.0	74.0
BR15	2.87	2.32	7.52	8.85	30.9	43.6	56.4
BR16	1.71	2.87	6.62	6.08	43.4	34.8	65.2
BR17	1.74	3.19	6.76	6.52	47.2	33.1	66.9
BR18	2.20	2.74	7.40	8.63	37.0	40.1	59.9
BR19	2.68	2.64	7.87	8.76	33.5	40.5	59.5
BR20	1.52	3.64	7.87	8.41	46.3	40.0	60.0
BR21	1.97	3.06	7.52	6.25	40.7	28.4	71.6
BR22	2.68	2.87	7.93	8.54	36.2	36.9	63.1
BR23	3.18	2.74	8.67	12.1	31.6	45.5	54.5
BR24	2.71	2.97	8.30	10.3	35.8	39.8	60.2
BR25	2.91	2.84	8.12	11.4	35.0	43.5	56.5
BR26	3.29	3.03	7.37	12.3	41.1	46.1	53.9
BR27	3.23	3.03	7.28	9.46	41.6	39.0	61.0
BR28	3.77	3.97	6.25	11.2	63.5	40.0	60.0
BR29	1.16	3.97	7.49	2.52	53.0	10.1	89.9
BR30	2.33	3.06	7.27	8.79	42.1	39.7	60.3
BR31	2.68	3.00	8.59	9.49	34.9	40.5	59.5
BR32	2.91	2.64	8.15	11.5	32.4	48.9	51.1
BR33	1.23	4.22	6.75	3.07	62.5	12.2	87.8
BR34	1.77	3.52	4.90	6.78	71.8	28.2	71.8
BR35	1.75	3.06	5.69	5.70	53.8	31.1	68.9
BR36	1.45	3.00	6.75	4.75	44.4	27.8	72.2

Table IX.4 – Bead shape characteristics obtained for RapidArc, using 1.5%CO₂ 54%He 44.5%Ar.

Run	Depth of Penetration [mm]	Height bead [mm]	Width Bead [mm]	Dilution Area [mm ²]	Height/ Width Ratio [%]	Dilution Ratio [%]	Reinforcement Ratio [%]
BR37	0.900	3.16	8.08	2.10	39.1	11.1	88.9
BR38	1.19	3.00	7.40	2.42	40.5	14.7	85.3
BR39	1.81	2.77	6.94	5.74	39.9	31.4	68.6
BR40	1.97	2.74	8.46	7.69	32.4	35.6	64.4
BR41	2.19	2.45	7.59	6.39	32.3	32.6	67.4
BR42	1.38	2.81	8.36	4.91	33.6	24.2	75.8
BR43	1.77	2.55	6.87	7.49	37.1	39.7	60.3
BR44	1.84	2.64	7.56	7.05	34.9	35.9	64.1
BR45	2.90	2.74	7.31	11.3	37.5	45.3	54.7
BR46	2.36	2.61	8.98	8.83	29.1	36.6	63.4
BR47	1.74	2.29	8.15	6.81	28.1	38.0	62.0
BR48	1.77	2.71	8.21	6.47	33.0	29.5	70.5
BR49	2.58	2.51	7.74	13.1	32.4	50.3	49.7
BR50	-	-	-	-	-	-	-
BR51	3.10	2.39	9.67	13.5	24.7	51.0	49.0
BR52	1.77	2.42	7.59	7.02	31.9	39.1	60.9
BR53	1.88	2.42	8.08	6.61	30.0	32.7	67.3
BR54	1.96	2.55	7.37	7.69	34.6	38.0	62.0
BR55	2.97	2.48	7.99	13.0	31.0	50.0	50.0
BR56	2.94	2.48	8.02	12.1	30.9	48.7	51.3
BR57	1.58	3.03	9.70	7.12	31.2	26.2	73.8
BR58	2.67	2.52	9.58	13.2	26.3	48.6	51.4
BR59	3.35	2.42	10.26	14.3	23.6	48.5	51.5
BR60	2.35	2.84	8.08	12.7	35.1	47.0	53.0
BR61	2.25	3.23	9.08	10.2	35.6	33.7	66.3
BR62	2.96	2.78	8.24	12.9	33.7	47.2	52.8
BR63	3.22	2.87	8.02	11.4	35.8	41.5	58.5
BR64	4.06	3.32	6.78	12.8	49.0	47.4	52.6
BR65	1.58	2.81	7.83	4.24	35.9	23.9	76.1
BR66	2.00	2.52	8.12	7.76	31.0	39.7	60.3
BR67	2.90	2.42	8.49	12.8	28.5	50.4	49.6
BR68	2.90	2.48	9.23	10.9	26.9	44.1	55.9
BR69	1.65	3.03	7.43	5.03	40.8	25.1	74.9
BR70	2.29	2.42	7.46	7.44	32.4	38.3	61.7
BR71	2.81	2.48	8.33	10.1	29.8	41.4	58.6
BR72	3.09	2.55	9.20	12.4	27.7	47.7	52.3

Table IX.5 – Bead shape characteristics obtained for STT, using 2.5%CO₂, 97.5%Ar.

Run	Depth of Penetration [mm]	Height bead [mm]	Width Bead [mm]	Dilution Area [mm ²]	Height/ Width Ratio [%]	Dilution Ratio [%]	Reinforcement Ratio [%]
BS01	0.190	3.13	5.29	0.484	59.2	3.91	96.1
BS02	0.450	3.32	4.97	1.36	66.8	10.3	89.7
BS03	0.870	3.61	4.79	1.64	75.4	13.1	86.9
BS04	0.450	4.35	5.35	1.46	81.3	7.94	92.1
BS05	1.00	3.77	4.94	2.74	76.3	15.3	84.7
BS06	0.160	2.84	6.47	0.379	43.9	3.07	96.9
BS07	0.610	2.97	6.19	1.31	48.0	10.9	89.1
BS08	1.36	3.19	6.81	4.52	46.8	25.9	74.1
BS09	2.23	2.48	6.03	6.68	41.1	42.3	57.7
BS10	1.87	3.03	6.12	7.79	49.5	37.5	62.5
BS11	0.590	3.09	6.62	1.57	46.7	11.2	88.8
BS12	0.900	2.87	7.43	3.80	38.6	24.7	75.3
BS13	1.74	2.74	7.68	6.94	35.7	35.8	64.2
BS14	2.36	2.77	6.34	8.53	43.7	42.8	57.2
BS15	1.80	2.84	6.62	8.94	42.9	42.2	57.8
BS16	0.650	3.22	6.56	1.84	49.1	12.2	87.8
BS17	1.03	2.90	7.55	3.34	38.4	20.6	79.4
BS18	1.87	2.58	7.55	5.76	34.2	30.0	70.0
BS19	2.22	2.87	6.16	8.86	46.6	42.7	57.3
BS20	2.42	2.61	6.47	9.01	40.3	43.6	56.4
BS21	1.10	3.51	4.23	2.53	83.0	19.4	80.6
BS22	1.52	3.09	4.67	5.11	66.2	27.1	72.9
BS23	1.71	2.90	6.28	6.73	46.2	33.7	66.3
BS24	1.80	2.84	5.97	6.17	47.6	32.8	67.2
BS25	0.550	3.87	4.70	1.02	82.3	6.97	93.0
BS26	1.55	3.22	5.85	5.68	55.0	31.5	68.5
BS27	1.26	3.31	5.34	4.78	62.0	28.0	72.0
BS28	1.75	3.21	6.22	5.80	51.6	29.8	70.2
BS29	1.07	3.66	5.16	3.80	70.9	24.4	75.6
BS30	1.49	3.31	6.44	4.19	51.4	23.3	76.7
BS31	1.72	3.11	7.38	7.25	42.1	32.9	67.1
BS32	1.77	2.92	6.61	6.72	44.2	35.0	65.0

Table IX.6 – Bead shape characteristics obtained for STT, using 1.5%CO₂, 54%He 44.5%Ar.

Run	Depth of Penetration [mm]	Height Bead [mm]	Width Bead [mm]	Dilution Area [mm ²]	Height/ Width Ratio [%]	Dilution Ratio [%]	Reinforcement Ratio [%]
BS33	0.290	3.03	5.01	0.352	60.5	3.06	96.9
BS34	1.09	3.13	5.29	2.88	59.2	22.4	77.6
BS35	0.580	3.64	5.69	1.85	64.0	12.1	87.9
BS36	0.900	3.78	6.00	3.07	63.0	16.2	83.8
BS37	0.580	3.13	7.37	0.815	42.5	4.96	95.0
BS38	0.480	2.81	7.62	1.22	36.9	7.96	92.0
BS39	1.09	2.71	7.28	4.01	37.2	23.4	76.6
BS40	1.87	2.71	6.53	6.03	41.5	32.8	67.2
BS41	2.13	2.61	6.78	5.86	38.5	30.4	69.6
BS42	2.55	2.77	6.31	9.52	43.9	42.3	57.7
BS43	0.520	2.87	5.41	1.18	53.0	10.5	89.5
BS44	1.78	2.48	7.27	5.93	34.1	33.6	66.4
BS45	2.19	2.61	6.69	7.09	39.0	37.3	62.7
BS46	2.25	2.68	5.91	9.18	45.3	44.2	55.8
BS47	2.55	2.58	7.06	11.2	36.5	50.2	49.8
BS48	0.900	2.84	7.24	3.06	39.2	19.4	80.6
BS49	1.52	2.61	7.43	5.80	35.1	32.0	68.0
BS50	2.10	2.71	8.05	7.57	33.7	37.6	62.4
BS51	2.35	2.81	7.12	11.0	39.5	48.0	52.0
BS52	1.65	2.90	8.96	9.72	32.4	37.4	62.6
BS53	0.720	3.48	5.75	1.22	60.5	7.09	92.9
BS54	1.87	2.81	6.72	5.53	41.8	30.8	69.2
BS55	1.90	2.84	8.64	8.47	32.9	35.7	64.3
BS56	2.13	2.68	8.12	10.2	33.0	41.7	58.3
BS57	1.22	3.42	5.32	3.73	64.3	22.9	77.1
BS58	1.90	2.97	6.81	6.85	43.6	32.4	67.6
BS59	2.07	2.61	7.37	6.99	35.4	35.2	64.8
BS60	2.06	2.55	6.50	8.12	39.2	42.4	57.6
BS61	1.16	3.42	5.72	3.04	59.8	19.2	80.8
BS62	1.64	2.97	8.36	4.31	35.5	20.6	79.4
BS63	2.28	2.68	7.68	7.65	34.9	34.7	65.3
BS64	2.00	2.90	8.24	7.51	35.2	32.6	67.4

Table IX.7 – Bead shape characteristics obtained for CMT, using Gas 2.5%CO₂ 97.5%Ar.

Run	Depth of Penetration [mm]	Height Bead [mm]	Width Bead [mm]	Dilution Area [mm ²]	Height/ Width Ratio [%]	Dilution Ratio [%]	Reinforcement Ratio [%]
BC01	0.190	4.10	2.58	0.475	159	3.10	96.9
BC02	0.290	4.39	3.86	0.603	114	3.50	96.5
BC03	0.840	3.19	3.58	1.15	89.1	9.70	90.3
BC04	0.680	3.22	4.38	1.74	73.5	13.4	86.6
BC05	1.16	3.03	4.14	3.02	73.2	23.1	76.9
BC06	0.510	3.81	2.89	1.05	132	9.40	90.6
BC07	0.610	3.81	2.8	0.858	136	7.40	92.6
BC08	0.770	3.39	3.26	1.81	104	15.7	84.3
BC09	1.25	3.10	4.01	3.57	77.3	27.6	72.4
BC10	1.16	2.61	3.89	2.92	67.1	28.4	71.6
BC11	0.740	4.13	4.17	1.97	99.0	10.7	89.3
BC12	1.64	3.10	5.63	4.89	55.1	28.8	71.2
BC13	1.52	2.87	6.12	4.39	46.9	28.8	71.2
BC14	1.67	2.97	5.54	4.58	53.6	29.2	70.8
BC15	1.98	2.87	4.88	4.16	58.8	32.5	67.5
BC16	0.680	2.84	5.07	1.91	56.0	17.3	82.7
BC17	1.09	3.13	6.06	3.32	51.7	21.6	78.4
BC18	1.55	3.03	6.53	6.22	46.4	32.3	67.7
BC19	1.71	2.35	5.81	4.98	40.4	37.5	62.5
BC20	2.23	2.48	4.73	6.14	52.4	43.2	56.8
BC21	0.840	3.03	3.92	1.87	77.3	16.5	83.5
BC22	0.670	3.84	2.61	0.64	147	5.20	94.8
BC23	1.17	3.35	3.73	2.82	89.8	21.1	78.9
BC24	1.00	3.55	3.67	2.87	96.7	20.1	79.9
BC25	0.830	3.49	3.48	2.03	100	16.1	83.9
BC26	0.910	3.61	3.58	1.80	101	12.9	87.1
BC27	0.870	3.42	3.70	1.54	92.4	12.0	88.0
BC28	0.780	3.35	4.63	1.67	72.4	12.2	87.8
BC29	1.71	2.77	6.53	5.35	42.4	31.6	68.4
BC30	1.90	2.58	6.53	5.63	39.5	33.9	66.1
BC31	-	-	-	-	-	-	-
BC32	-	-	-	-	-	-	-
BC33	-	-	-	-	-	-	-
BC34	-	-	-	-	-	-	-
BC35	-	-	-	-	-	-	-
BC36	-	-	-	-	-	-	-
BC37	0.840	3.29	3.54	1.59	92.9	13.1	86.9
BC38	0.740	3.29	3.48	1.19	94.5	11.6	88.4
BC39	1.94	2.90	6.19	6.82	46.8	36.0	64.0
BC40	1.65	2.80	6.35	6.05	44.1	36.4	63.6
BC41	-	-	-	-	-	-	-
BC42	-	-	-	-	-	-	-
BC43	-	-	-	-	-	-	-
BC44	-	-	-	-	-	-	-
BC45	-	-	-	-	-	-	-
BC46	-	-	-	-	-	-	-
BC47	-	-	-	-	-	-	-
BC48	-	-	-	-	-	-	-

Table IX.8 – Bead shape characteristics obtained for CMT, using 1.5%CO₂ 54%He 44.5%Ar.

Run	Depth of Penetration [mm]	Height Bead [mm]	Width Bead [mm]	Dilution Area [mm ²]	Height to Width Ratio [%]	Dilution Ratio [%]	Reinforcement Ratio [%]
BC49	0	3.18	1.62	0	196	0.00	100
BC50	0.750	3.34	3.47	0.768	96.3	7.09	92.9
BC51	0.780	3.05	4.31	1.32	70.8	11.3	88.7
BC52	0.780	2.66	5.94	2.93	44.8	21.5	78.5
BC53	0.910	2.59	4.53	2.00	57.2	18.5	81.5
BC54	0.160	3.76	3.34	0.55	113	3.81	96.2
BC55	0.810	3.40	3.97	2.10	85.6	16.0	84.0
BC56	0.060	3.7	3.91	0.51	94.6	2.99	97.0
BC57	0.390	3.18	4.75	1.08	66.9	7.74	92.3
BC58	0.770	2.37	5.25	2.14	45.1	20.2	79.8
BC59	0.320	3.24	4.91	0.752	66.0	5.42	94.6
BC60	0.710	2.95	7.22	1.55	40.9	8.46	91.5
BC61	1.10	2.95	6.69	2.37	44.1	14.2	85.8
BC62	1.11	3.01	6.25	3.46	48.2	19.9	80.1
BC63	1.75	2.20	5.22	4.25	42.1	35.1	64.9
BC64	0.420	3.06	6.56	1.35	46.6	8.89	91.1
BC65	1.03	2.81	7.43	3.48	37.8	22.6	77.4
BC66	1.68	2.51	7.52	5.49	33.4	31.3	68.7
BC67	1.97	2.45	8.15	8.83	30.1	40.9	59.1
BC68	2.03	2.35	6.03	8.52	39.0	48.9	51.1
BC69	0.810	2.71	4.85	3.03	55.9	24.3	75.7
BC70	0.880	2.80	4.97	2.67	56.3	20.9	79.1
BC71	0.640	2.81	4.91	1.76	57.2	13.8	86.2
BC72	1.03	2.97	4.41	3.10	67.3	22.3	77.7
BC73	0.130	3.48	5.17	0.309	67.3	2.00	98.0
BC74	0.680	2.90	4.23	1.54	68.6	12.5	87.5
BC75	0.740	2.87	6.09	2.31	47.1	16.2	83.8
BC76	0.870	2.84	5.44	3.00	52.2	21.4	78.6
BC77	1.78	2.87	6.50	6.15	44.2	33.9	66.1
BC78	1.94	2.74	6.22	5.75	44.1	32.3	67.7
BC79	2.00	2.71	6.13	5.82	44.2	33.4	66.6
BC80	2.09	2.81	5.97	8.20	47.1	40.9	59.1
BC81	1.68	2.51	8.24	5.50	30.5	29.8	70.2
BC82	1.91	2.64	7.84	6.62	33.7	35.0	65.0
BC83	1.65	3.06	8.55	5.06	35.8	24.0	76.0
BC84	1.80	2.68	7.71	5.54	34.8	30.6	69.4
BC85	0.810	3.03	4.48	1.55	67.6	11.9	88.1
BC86	0.870	2.81	6.37	2.51	44.1	16.9	83.1
BC87	1.26	3.00	8.64	3.91	34.7	18.0	82.0
BC88	1.58	3.16	8.86	6.03	35.7	26.1	73.9
BC89	0.710	2.84	5.16	1.25	55.0	9.60	90.4
BC90	0.910	2.77	5.07	1.53	54.6	12.4	87.6
BC91	1.90	2.61	6.87	5.73	38.0	31.7	68.3
BC92	1.68	2.64	7.72	5.51	34.2	30.5	69.5
BC93	0.640	2.97	4.60	1.21	64.5	9.10	90.9
BC94	0.870	2.90	5.44	2.20	53.3	15.6	84.4
BC95	1.90	2.97	6.03	5.12	49.3	27.7	72.3
BC96	1.55	2.81	7.90	3.97	35.6	22.0	78.0

Table IX.9 – Bead shape characteristics obtained for CMT-P, using 2.5%CO₂, 97.5%Ar.

Run	Depth of Penetration [mm]	Height Bead [mm]	Width Bead [mm]	Dilution Area [mm ²]	Height/ Width Ratio [%]	Dilution Ratio [%]	Reinforcement Ratio [%]
BP01	1.84	3.13	5.41	4.87	57.9	27.9	72.1
BP02	1.52	3.09	5.50	4.55	56.2	26.9	73.1
BP03	1.55	3.03	5.78	5.23	52.4	31.9	68.1
BP04	1.64	3.07	5.16	4.06	59.5	26.7	73.3
BP05	1.29	3.26	5.35	3.65	60.9	23.8	76.2
BP06	2.00	3.13	6.56	6.67	47.7	34.8	65.2
BP07	2.22	3.29	6.53	7.71	50.4	34.7	65.3
BP08	2.19	3.03	6.16	7.17	49.2	37.6	62.4
BP09	1.83	3.30	6.19	5.87	53.3	30.9	69.1
BP10	2.19	3.03	5.97	5.62	50.8	31.4	68.6
BP11	2.36	3.22	6.31	6.78	51.0	31.0	69.0
BP12	2.71	3.42	6.44	9.96	53.1	43.1	56.9
BP13	1.95	3.42	6.78	9.52	50.4	42.1	57.9
BP14	2.42	2.97	6.53	10.09	45.5	48.2	51.8
BP15	1.87	3.42	7.90	6.08	43.3	25.8	74.2
BP16	2.32	3.26	6.87	7.04	47.5	33.9	66.1
BP17	2.91	2.71	7.52	11.63	36.0	48.1	51.9
BP18	2.90	2.68	7.71	8.95	34.8	41.9	58.1
BP19	2.19	3.45	8.49	7.07	40.6	28.2	71.8
BP20	2.45	3.32	8.55	10.67	38.8	39.1	60.9
BP21	1.49	2.77	7.12	4.64	38.9	22.7	77.3
BP22	1.74	3.87	8.43	9.50	45.9	31.1	68.9
BP23	2.87	2.42	6.75	11.38	35.9	53.0	47.0
BP24	2.23	3.29	7.68	9.93	42.8	35.3	64.7
BP25	2.75	3.35	7.18	12.23	46.7	42.4	57.6
BP26	1.10	3.22	10.0	8.44	32.1	30.3	69.7
BP27	2.30	3.76	8.09	10.13	46.5	34.0	66.0
BP28	3.59	2.37	8.35	14.87	28.4	55.9	44.1
BP29	3.12	2.33	7.16	12.09	32.5	52.0	48.0
BP30	2.33	3.50	9.41	9.28	37.2	34.3	65.7
BP31	2.21	2.59	7.19	14.01	36.0	45.5	54.5
BP32	1.36	3.05	5.06	4.58	60.3	30.1	69.9
BP33	1.23	4.15	7.66	4.01	54.2	16.7	83.3
BP34	1.26	4.44	8.38	2.26	53.0	8.3	91.7
BP35	1.81	3.18	7.47	5.15	42.6	26.8	73.2
BP36	2.56	3.21	7.22	7.07	44.5	33.5	66.5
BP37	0.810	2.82	6.88	4.28	41.0	28.8	71.2
BP38	3.05	2.85	7.28	9.96	39.1	44.3	55.7
BP39	2.53	2.59	5.94	8.17	43.6	43.7	56.3
BP40	2.20	2.56	7.75	8.25	33.0	39.7	60.3
BP41	2.76	2.98	8.97	11.45	33.2	42.3	57.7
BP42	3.12	2.88	6.34	12.71	45.4	64.7	35.3
BP43	0.220	2.31	6.06	0.84	38.1	8.5	91.5
BP44	2.86	2.82	9.06	13.23	31.1	46.6	53.4
BP45	3.21	2.95	9.06	14.06	32.6	47.6	52.4
BP46	3.12	3.50	9.44	12.51	37.1	41.2	58.8
BP47	1.68	3.05	7.22	9.13	42.2	40.6	59.4
BP48	2.30	3.14	6.56	6.44	47.9	34.5	65.5
BP49	2.91	2.66	8.03	10.57	33.1	45.7	54.3
BP50	2.11	2.98	5.81	12.39	51.3	36.5	63.5
BP51	2.75	3.31	6.84	14.81	48.4	43.5	56.5
BP52	2.78	2.92	8.44	7.70	34.6	45.9	54.1
BP53	3.54	2.79	8.41	7.03	33.2	50.2	49.8
BP54	3.43	2.69	9.72	10.72	27.7	52.9	47.1
BP55	3.30	2.92	8.97	13.14	32.6	46.6	53.4
BP56	1.56	3.53	6.56	5.46	53.8	28.3	71.7
BP57	2.69	3.21	7.06	9.11	45.5	40.3	59.7
BP58	2.66	3.11	8.91	8.37	34.9	35.3	64.7

Table IX.10 – Bead shape characteristics obtained for CMT-P, using 1.5%CO₂, 54%He 44.5%Ar.

Run	Depth of Penetration [mm]	Height Bead [mm]	Width Bead [mm]	Dilution Area [mm ²]	Height/ Width Ratio [%]	Dilution Ratio [%]	Reinforcement Ratio [%]
BP60	1.58	2.61	7.49	4.85	34.8	27.8	72.2
BP61	1.23	2.61	7.06	3.21	37.0	20.7	79.3
BP62	1.52	2.35	7.18	4.64	32.7	28.5	71.5
BP63	1.74	2.39	6.93	4.75	34.5	28.0	72.0
BP64	1.48	2.55	6.62	4.04	38.5	24.8	75.2
BP65	2.35	2.55	6.65	8.45	38.3	41.4	58.6
BP66	2.26	2.64	7.65	7.62	34.5	36.1	63.9
BP67	2.03	2.29	7.62	7.01	30.1	36.8	63.2
BP68	1.87	2.20	8.30	5.08	26.5	28.9	71.1
BP69	1.81	2.74	7.80	3.57	35.1	19.9	80.1
BP70	1.38	3.10	9.95	5.73	31.2	24.0	76.0
BP71	1.71	3.13	8.24	9.74	38.0	38.2	61.8
BP72	2.36	2.64	7.80	11.18	33.8	46.7	53.3
BP73	1.78	2.93	8.61	6.18	34.0	28.4	71.6
BP74	1.71	2.55	8.36	7.25	30.5	37.4	62.6
BP75	2.42	2.74	8.83	11.53	31.0	43.5	56.5
BP76	2.78	2.51	9.51	13.11	26.4	48.5	51.5
BP77	2.74	2.55	9.80	11.15	26.0	45.1	54.9
BP78	2.74	2.58	8.77	9.01	29.4	42.4	57.6
BP79	2.45	2.61	8.42	8.53	31.0	42.2	57.8
BP80	0.870	3.23	8.21	3.31	39.3	15.8	84.2
BP81	1.93	3.68	9.86	5.20	37.3	26.2	73.8
BP82	3.22	2.58	8.49	15.37	30.4	54.0	46.0
BP83	3.03	2.61	8.39	12.46	31.1	50.3	49.7
BP84	2.90	2.26	8.58	10.46	26.3	51.3	48.7
BP85	-	-	-	-	-	-	-
BP86	-	-	-	-	--	-	-
BP87	3.42	2.35	9.45	18.77	24.9	63.0	37.0
BP88	2.49	2.87	9.89	9.23	29.0	35.1	64.9
BP89	2.22	2.84	7.56	10.14	37.6	46.8	53.2
BP90	1.32	2.26	5.01	4.55	45.1	35.6	64.4
BP91	1.90	2.74	5.41	6.04	50.6	37.2	62.8
BP92	1.42	3.58	8.95	3.34	40.0	13.7	86.3
BP93	2.19	3.32	7.87	9.20	42.2	39.8	60.2
BP94	1.87	2.32	7.46	9.09	31.1	48.0	52.0
BP95	2.39	2.61	7.40	9.16	35.3	45.3	54.7
BP96	2.58	2.77	8.87	10.20	31.2	40.9	59.1
BP97	1.32	3.97	10.7	5.91	37.1	19.3	80.7
BP98	1.87	2.97	8.27	6.09	35.9	26.7	73.3
BP99	2.93	2.71	7.12	12.92	38.1	51.4	48.6
BP100	3.16	3.00	7.93	16.97	37.8	57.3	42.7
BP101	2.22	3.84	9.48	9.86	40.5	31.6	68.4
BP102	0.46	2.22	6.00	1.62	37.0	14.5	85.5
BP103	3.09	2.71	9.36	13.38	29.0	48.4	51.6
BP104	2.71	3.45	10.1	11.13	34.3	33.7	66.3
BP105	2.68	3.35	9.26	13.97	36.2	41.5	58.5
BP106	1.52	3.06	8.58	4.48	35.7	21.6	78.4
BP107	1.68	3.16	9.64	5.94	32.8	23.9	76.1
BP108	2.93	2.84	10.1	14.51	28.2	48.2	51.8
BP109	3.28	2.97	10.3	14.23	28.9	45.6	54.4
BP110	4.16	2.58	10.5	19.29	24.5	56.6	43.4
BP111	1.68	3.06	8.33	7.61	36.7	33.0	67.0
BP112	1.45	3.77	9.05	6.89	41.7	23.6	76.4
BP113	3.26	2.45	7.80	12.05	31.4	51.1	48.9
BP114	2.93	2.97	9.86	14.63	30.1	47.9	52.1
BP115	1.77	3.32	8.33	6.05	39.9	28.5	71.5
BP116	1.10	3.19	7.71	5.32	41.4	24.3	75.7
BP117	2.65	2.93	9.27	11.90	31.6	44.5	55.5

Table IX.11 – Bead shape characteristics obtained for FastROOT, using 2.5%CO₂ 97.5%Ar.

Run	Depth of Penetration [mm]	Height Bead [mm]	Width Bead [mm]	Dilution Area [mm ²]	Height/ Width Ratio [%]	Dilution Ratio [%]	Reinforcement Ratio [%]
BF01	0.710	3.71	4.88	2.01	76.0	13.5	86.5
BF02	0.740	3.64	4.32	1.50	84.3	10.2	89.8
BF03	1.03	3.32	4.91	2.57	67.6	17.0	83.0
BF04	1.16	3.22	5.29	3.11	60.9	21.2	78.8
BF05	1.67	3.52	5.19	5.11	67.8	28.1	71.9
BF06	0.650	3.64	4.57	2.55	79.6	18.0	82.0
BF07	0.940	3.80	5.44	2.65	69.9	16.2	83.8
BF08	1.16	3.61	5.32	3.90	67.9	22.3	77.7
BF09	1.32	3.10	5.44	3.40	57.0	24.1	75.9
BF10	1.65	3.19	5.53	4.70	57.7	25.1	74.9
BF11	0.900	4.00	5.53	1.68	72.3	10.3	89.7
BF12	1.04	4.09	6.37	2.58	64.2	13.6	86.4
BF13	1.29	3.22	6.03	3.00	53.4	18.7	81.3
BF14	1.19	3.10	6.84	4.01	45.3	24.5	75.5
BF15	1.64	3.29	6.65	5.30	49.5	25.6	74.4
BF16	1.16	3.45	5.85	3.87	59.0	23.2	76.8
BF17	1.22	3.39	5.69	3.13	59.6	18.0	82.0
BF18	1.90	3.29	5.88	5.66	56.0	29.4	70.6
BF19	2.22	3.13	5.60	6.65	55.9	33.0	67.0
BF20	2.23	3.06	6.28	8.16	48.7	37.4	62.6
BF21	1.32	3.45	5.44	3.52	63.4	21.1	78.9
BF22	1.51	3.16	5.69	4.99	55.5	28.1	71.9
BF23	2.20	3.06	6.13	6.82	49.9	33.9	66.1
BF24	1.81	3.00	7.06	7.40	42.5	36.2	63.8
BF25	1.38	3.68	5.69	3.63	64.7	19.4	80.6
BF26	1.35	3.55	6.22	3.57	57.1	20.2	79.8
BF27	1.97	3.64	5.94	6.28	61.3	28.3	71.7
BF28	2.42	3.29	6.07	7.73	54.2	34.5	65.5
BF29	1.77	3.39	4.66	4.53	72.7	25.7	74.3
BF30	1.87	3.26	5.60	4.79	58.2	27.4	72.6
BF31	2.23	3.55	5.38	7.41	66.0	34.5	65.5
BF32	2.41	2.97	5.29	7.45	56.1	38.1	61.9
BF33	1.61	3.55	4.45	4.76	79.8	27.8	72.2
BF34	1.39	3.90	4.69	3.59	83.2	20.2	79.8
BF35	1.87	3.39	4.76	5.98	71.2	35.6	64.4
BF36	2.13	3.32	4.57	6.51	72.6	37.4	62.6

Table IX.12 – Bead shape characteristics obtained for FastROOT, using 1.5%CO₂, 54%He 44.5%Ar.

Run	Depth of Penetration [mm]	Height Bead [mm]	Width Bead [mm]	Dilution Area [mm ²]	Height/ Width Ratio [%]	Dilution Ratio [%]	Reinforcement Ratio [%]
BF37	0.640	3.29	6.19	1.82	53.2	12.4	87.6
BF38	0.930	3.55	5.69	1.99	62.4	12.1	87.9
BF39	1.16	3.13	5.44	2.97	57.5	18.8	81.2
BF40	1.06	3.03	6.12	2.63	49.5	16.7	83.3
BF41	0.970	3.16	5.38	3.05	58.7	18.7	81.3
BF42	0.800	3.55	5.41	2.31	65.6	15.0	85.0
BF43	1.00	3.35	5.66	2.78	59.2	18.8	81.2
BF44	1.45	3.16	6.22	3.71	50.8	22.8	77.2
BF45	1.71	3.03	6.75	6.48	44.9	32.6	67.4
BF46	1.42	3.16	6.37	4.88	49.6	25.2	74.8
BF47	0.580	3.32	6.31	2.23	52.6	14.7	85.3
BF48	0.840	3.32	6.22	1.85	53.4	12.4	87.6
BF49	0.930	3.42	6.06	2.17	56.4	13.9	86.1
BF50	1.48	2.90	6.56	3.56	44.2	22.2	77.8
BF51	1.91	2.93	7.25	7.20	40.4	34.6	65.4
BF52	0.610	3.26	6.44	1.36	50.6	8.61	91.4
BF53	0.870	3.19	5.63	2.66	56.7	18.3	81.7
BF54	1.10	3.22	5.56	2.34	57.9	15.5	84.5
BF55	1.39	3.19	5.69	3.39	56.1	21.1	78.9
BF56	1.25	3.13	6.06	4.79	51.7	25.1	74.9
BF57	0.740	3.61	5.66	2.94	63.8	16.7	83.3
BF58	1.42	3.35	6.50	4.70	51.5	24.5	75.5
BF59	1.75	2.77	5.78	4.16	47.9	27.0	73.0
BF60	2.04	3.06	6.78	8.21	45.1	36.6	63.4
BF61	1.48	3.26	6.47	6.45	50.4	30.1	69.9
BF62	1.84	3.09	6.90	5.63	44.8	26.4	73.6
BF63	1.64	3.13	6.22	5.37	50.3	28.4	71.6
BF64	1.64	3.10	6.53	5.14	47.5	27.1	72.9
BF65	0.930	3.26	5.91	3.33	55.2	17.7	82.3
BF66	2.16	2.97	6.03	6.77	49.3	33.2	66.8
BF67	1.87	3.45	5.60	5.78	61.6	30.1	69.9
BF68	1.74	3.71	6.31	6.08	58.8	26.3	73.7
BF69	1.45	3.19	5.53	5.27	57.7	28.3	71.7
BF70	1.61	3.00	5.29	5.36	56.7	30.8	69.2
BF71	1.75	3.06	5.69	5.70	53.8	31.1	68.9
BF72	1.45	3.00	6.75	4.75	44.4	27.8	72.2

X. GRAPHICAL ANALYSIS OF THE EFFECT OF SETTING PROCESS PARAMETERS ON BEAD SHAPE CHARACTERISTICS

Measured bead shape characteristics result from the waveform design and welding setting parameters applied. During this research project the penetration bead, height bead, width bead, height to width ratio (also called convexity index), dilution and reinforcement ratio were analysed. The waveforms studied were evaluated in respect to:

- The effect of WFS, at different WFS/TS ratios and shielding gases;
- The effect of adjusting arc length setting parameters (trim, ALC or BC);
- The effect of adjusting dynamic setting parameters, when applied (DC, PC, FP);
- The effect of CTWD.

The experimental conditions applied to this research (unless otherwise indicated) were as follows: WFS of 6m/min, WFS/TS of 16, trim of 1.0 (STT) or 1.5 (GMAW-P and RapidArc), WaveControl of 10 (GMAW-P, RapidArc and STT), ALC of 0% (CMT and CMT-P), DC of 0% (CMT), PC of 0% (CMT-P), BC and FP of 0% (FastROOT), CTWD of 11mm, and shielding gas composition 2.5%CO₂ 97.5%Ar. The following subsections will present the results obtained for the different waveforms studied.

X.1. Characterization of Bead Shape Characteristics for GMAW-P

The effect of WFS on the bead shape characteristics was investigated for GMAW-P using different WFS/TS ratios and shielding gases, as illustrated in the Figures X.1 and X.2.

The effect of trim was evaluated for GMAW-P in respect to the variation of the bead shape characteristics, at different WFS levels and shielding gases, and its effect on them, at constant WFS. The results are presented from the Figure X.3 to X.5.

The effect of CTWD was evaluated to GMAW-P at three different levels (from 11 to 16mm) in respect to the variation of the bead shape characteristics, at different WFS levels and shielding gases, and its effect on the bead on shape characteristics at constant WFS. The results are presented from the Figure X.6 to X.8.

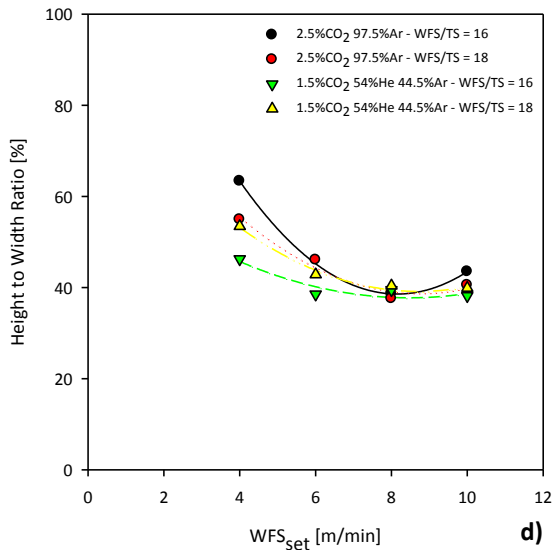
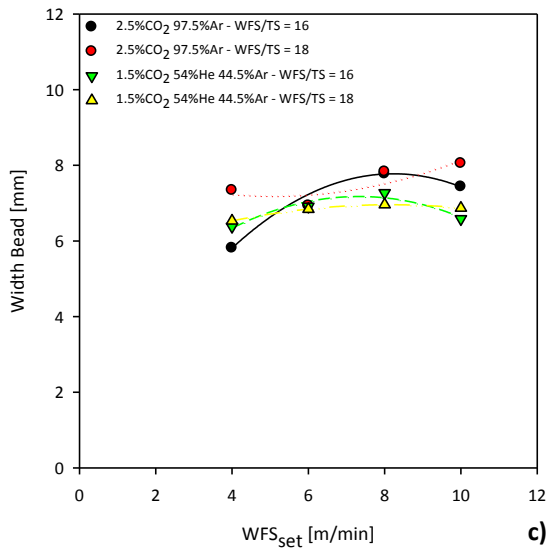
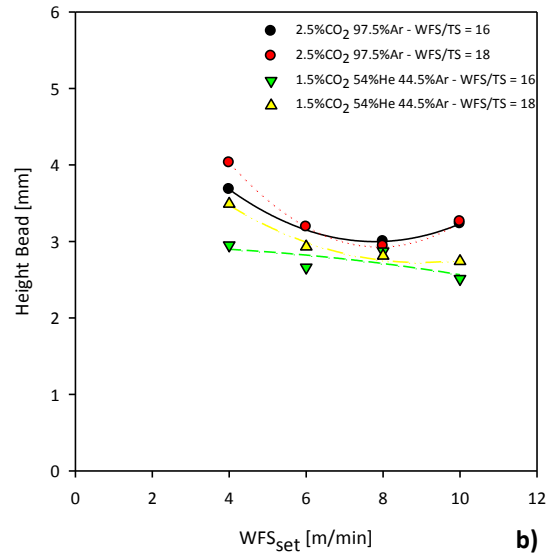
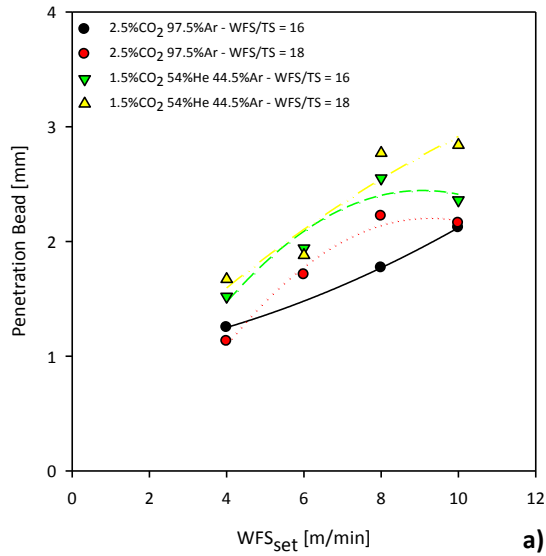


Figure X.1 – Effect of WFS on bead shape characteristics for GMAW-P, at different WFS/TS ratios and shielding gases: a) penetration bead; b) height bead; c) width bead; and d) height to width ratio.

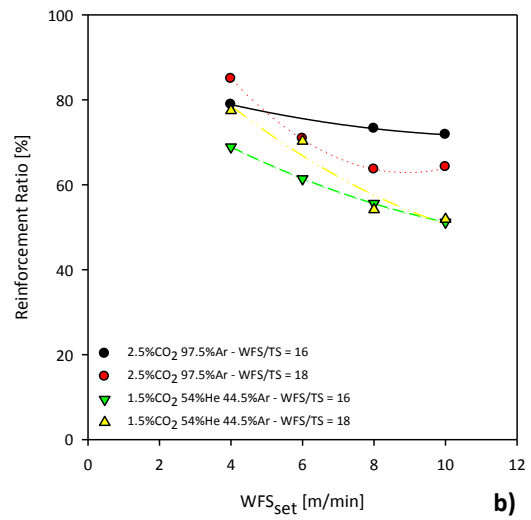
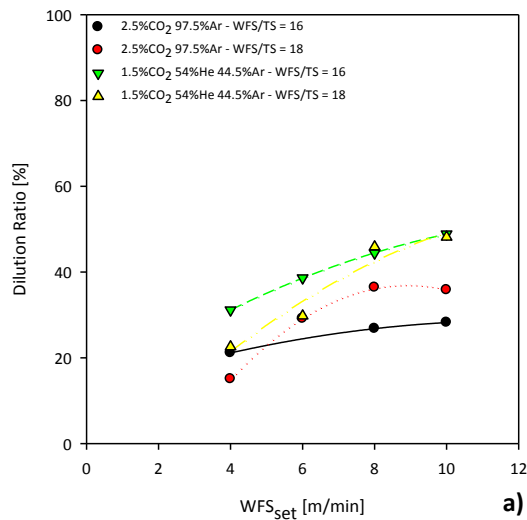


Figure X.2 – Effect of WFS on dilution (a) and reinforcement ratio (b) for GMAW-P, at different WFS/TS ratios and shielding gases.

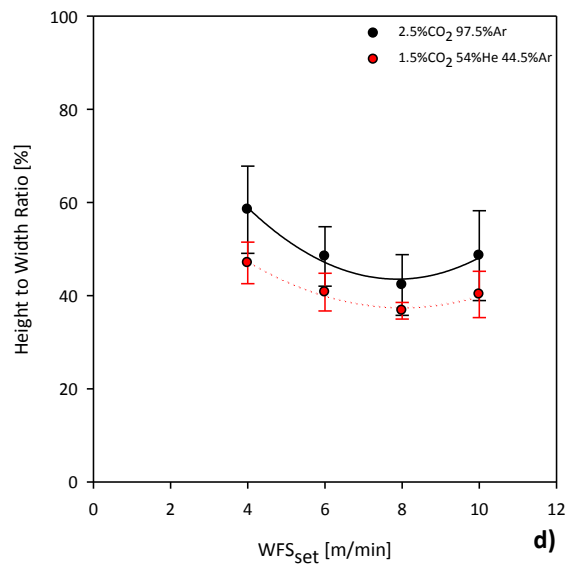
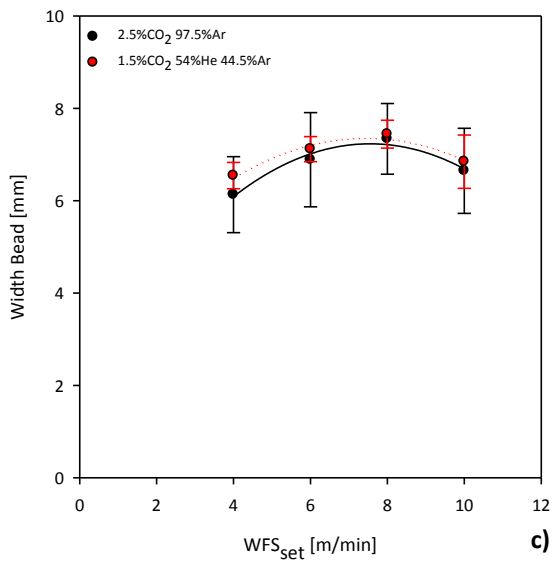
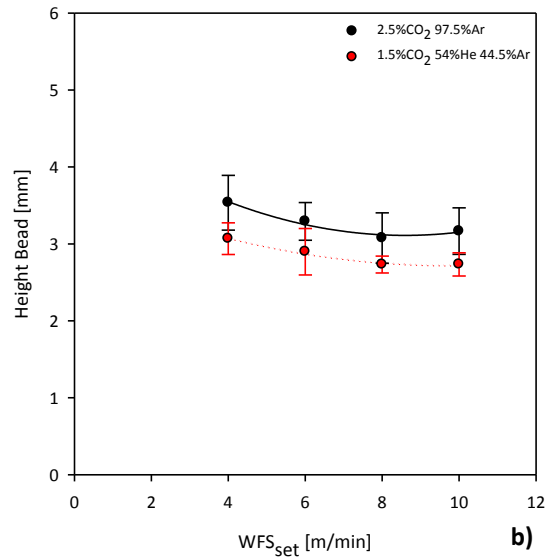
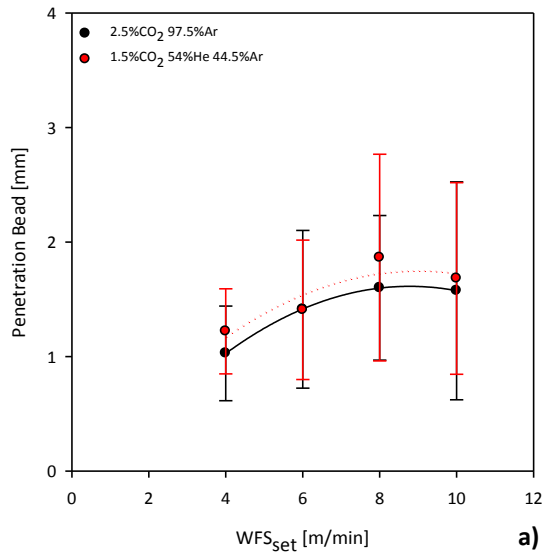


Figure X.3 – Effect of the variation of trim on bead shape characteristics for GMAW-P, at different WFS levels and shielding gases: a) penetration bead; b) height bead; c) width bead; and d) height to width ratio.

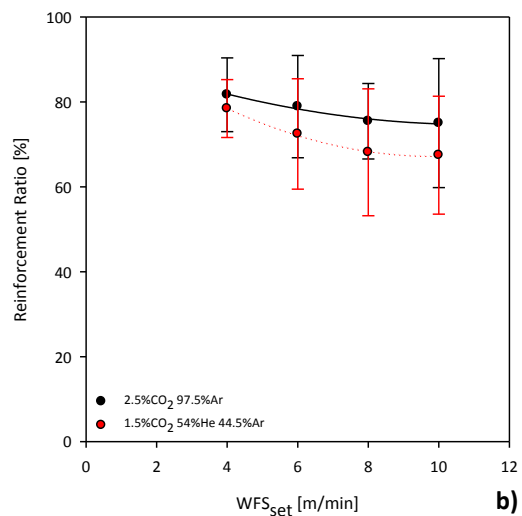
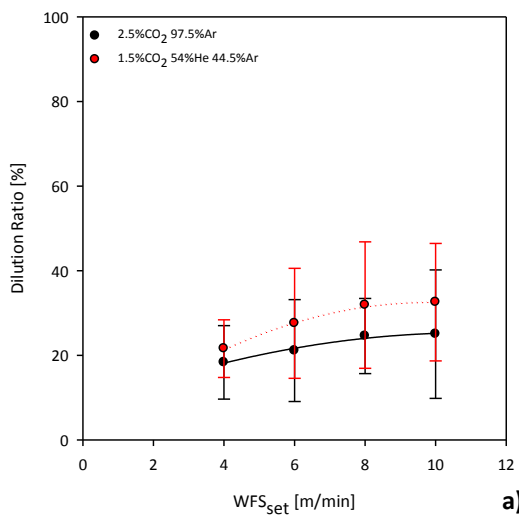


Figure X.4 – Effect of the variation of trim on dilution ratio (a) and reinforcement ratio (b) for GMAW-P, at different WFS levels and shielding gases.

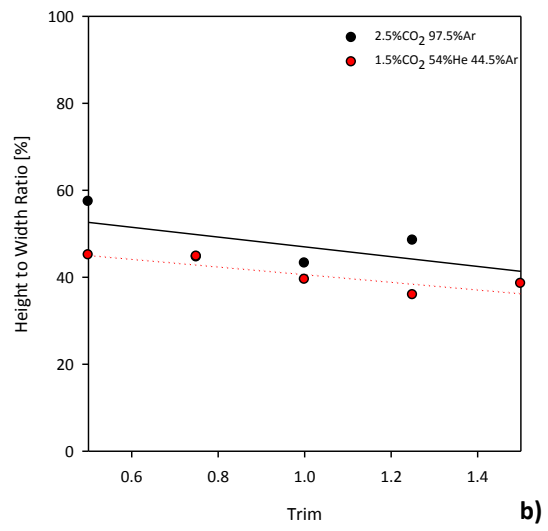
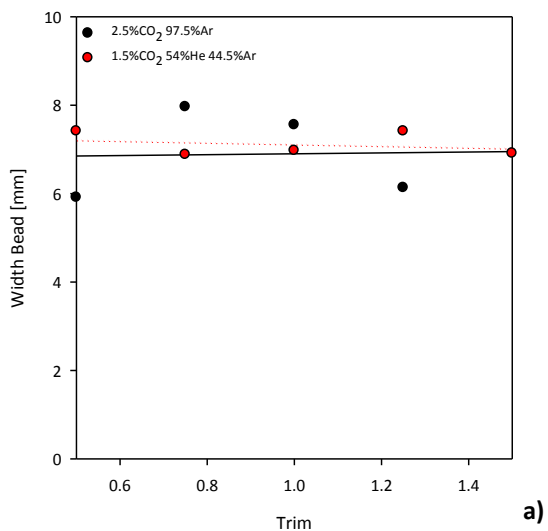
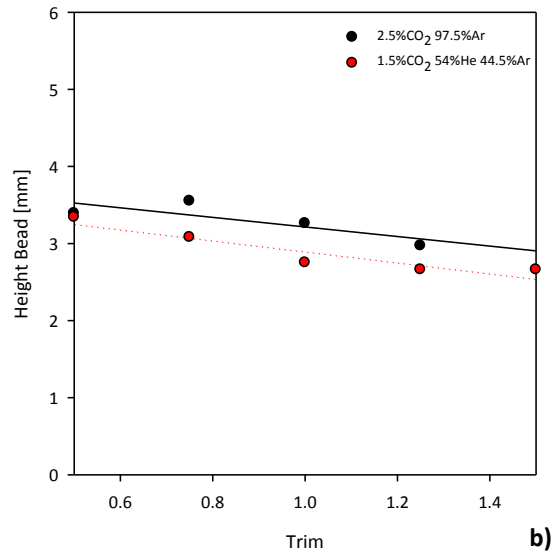
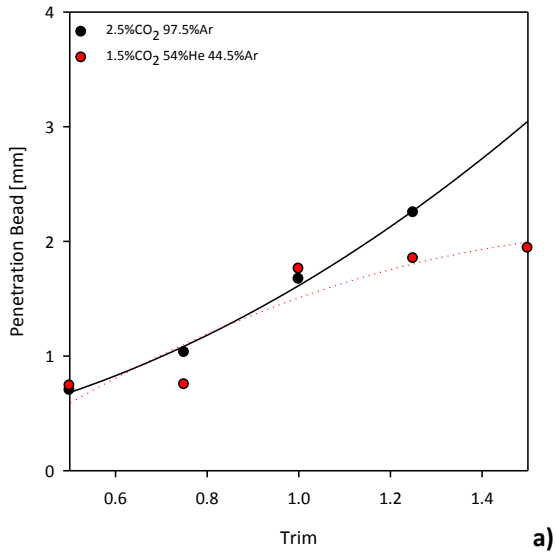


Figure X.5 – Effect of trim on bead shape characteristics for GMAW-P, at different shielding gases: a) penetration bead; b) height bead; c) width bead; and d) height to width ratio.

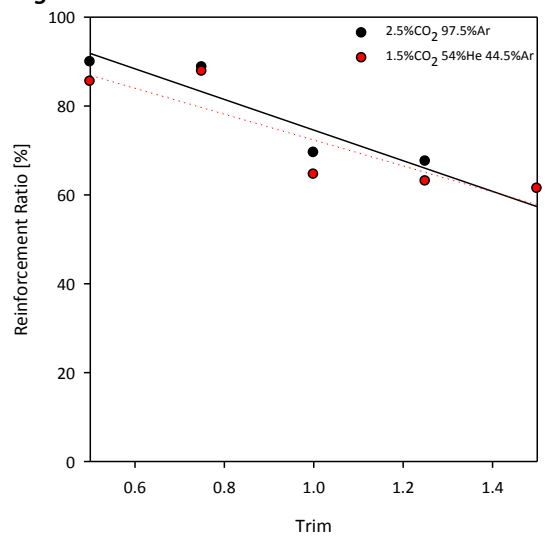
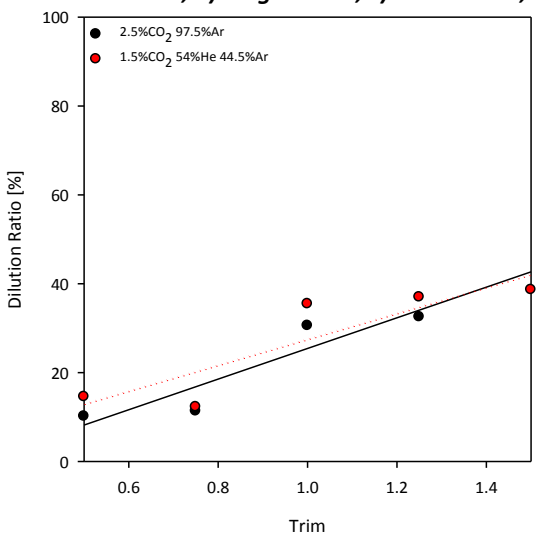


Figure X.6 – Effect of trim on the dilution ratio (a) and reinforcement ratio (b) for GMAW-P at different shielding gases.

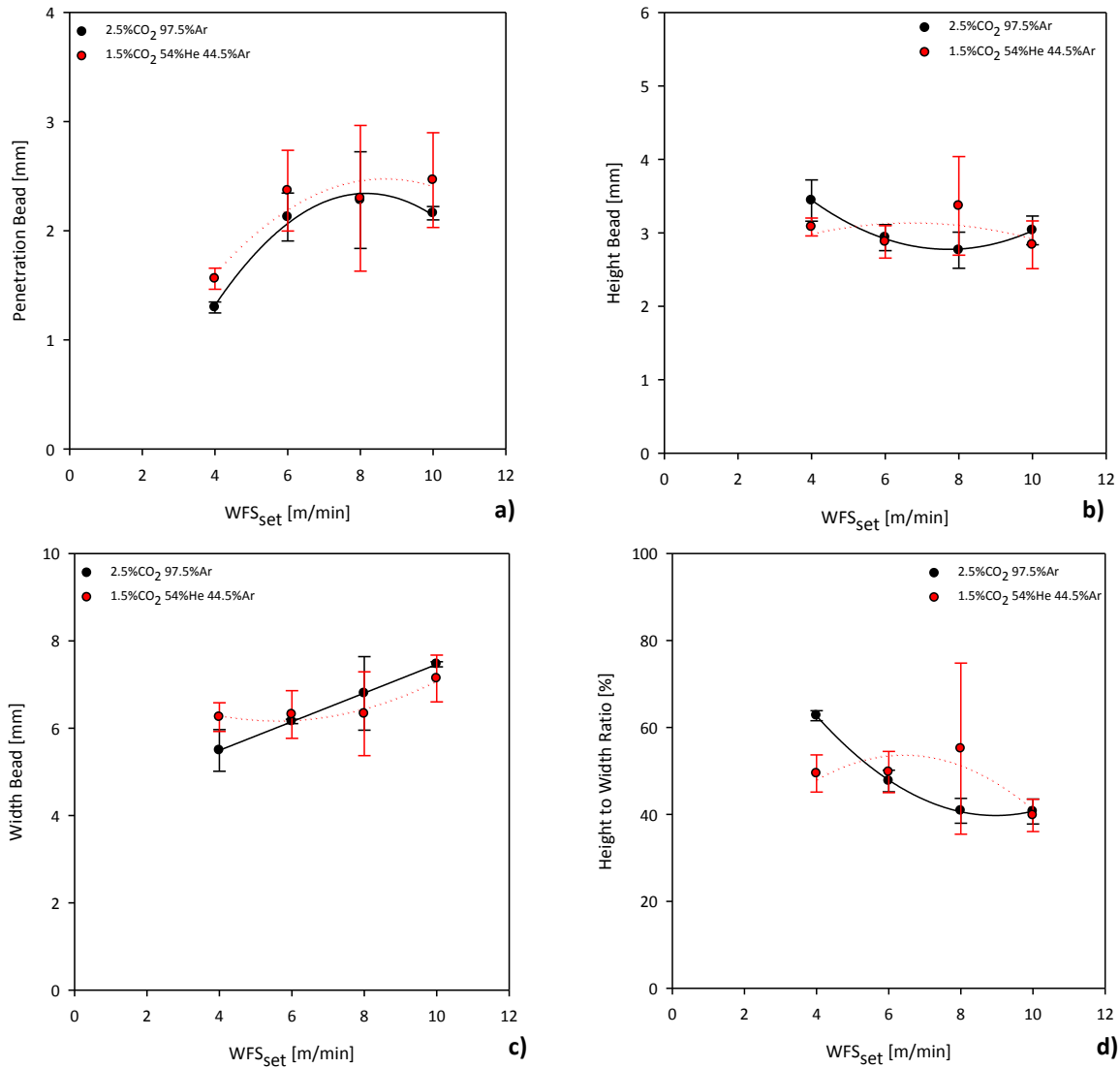


Figure X.7 – Effect of the variation of CTWD on bead shape characteristics for GMAW-P, at different WFS levels and shielding gases: a) penetration bead; b) height bead; c) width bead; and d) height to width ratio.

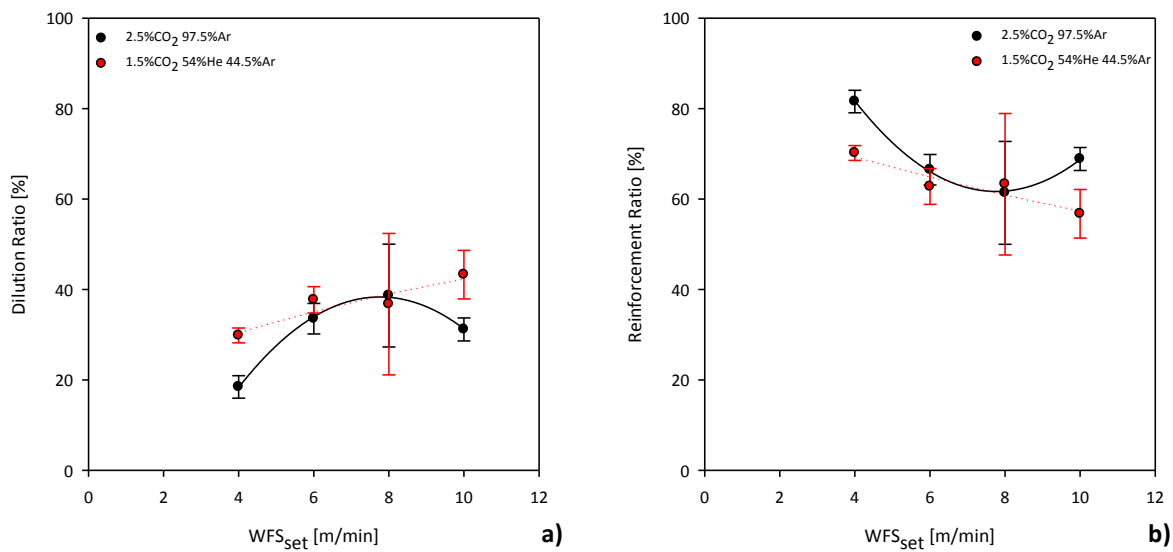


Figure X.8 – Effect of the variation of CTWD on dilution (a) and reinforcement ratio (b) for GMAW-P, at different WFS levels and shielding gases.

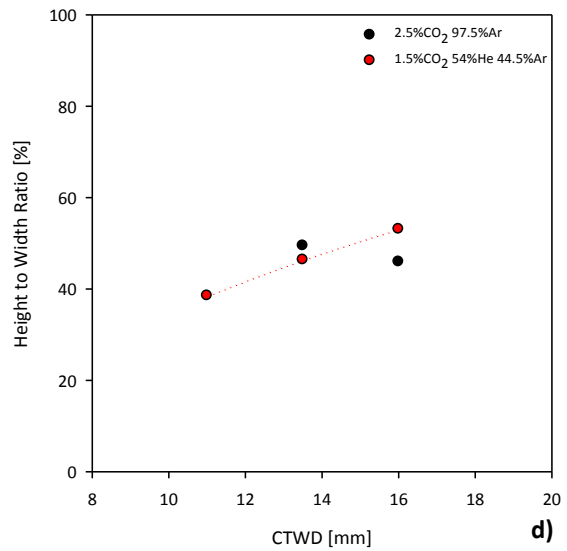
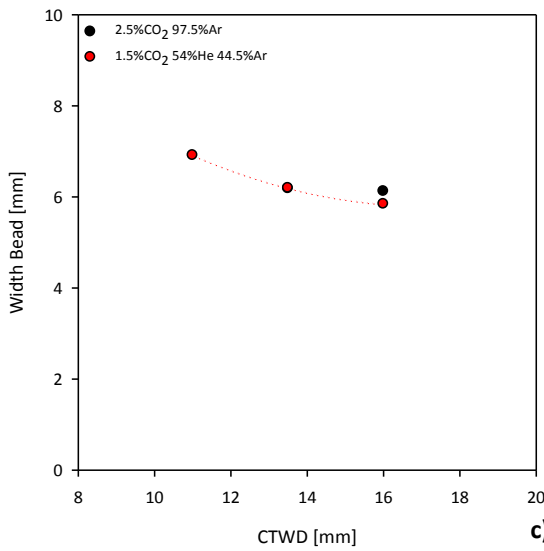
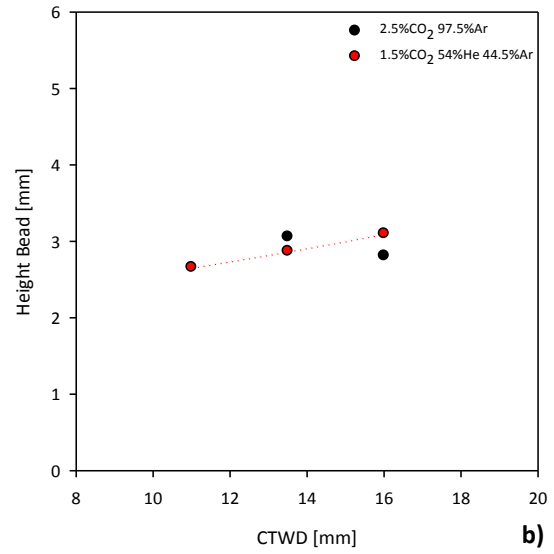
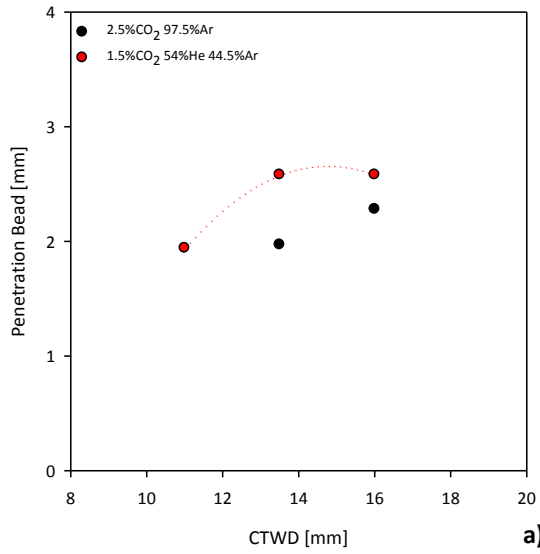


Figure X.9 – Effect of CTWD on bead shape characteristics for GMAW-P, at different shielding gases: a) penetration bead; b) height bead; c) width bead; and d) height to width ratio.

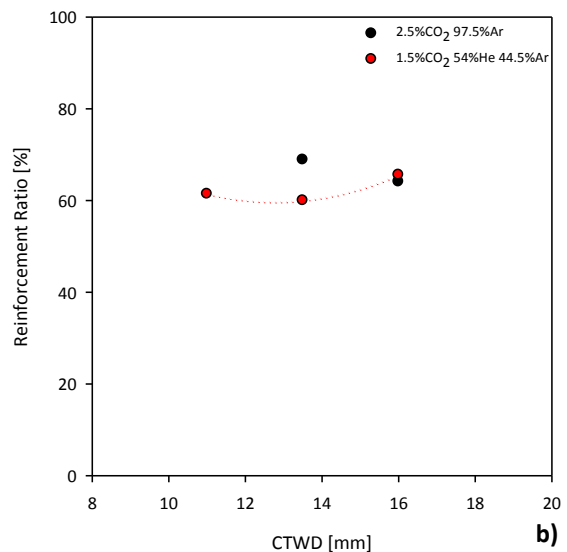
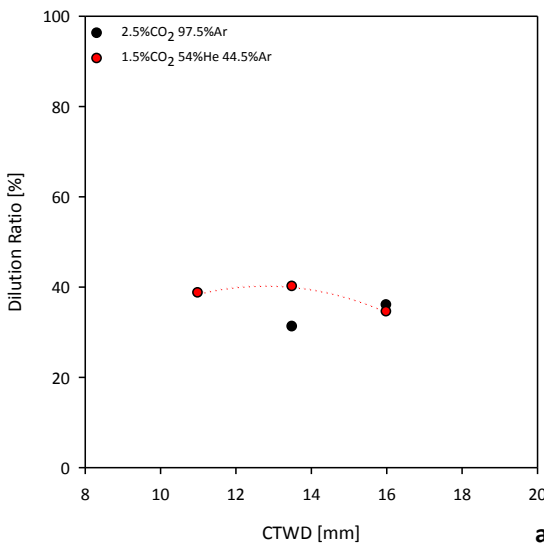


Figure X.10 – Effect of CTWD on dilution ratio (a) and reinforcement ratio (b) for GMAW-P, at different shielding gases.

X.2. Characterization of Bead Shape Characteristics for RapidArc

The effect of WFS on the bead shape characteristics was also investigated for RapidArc using different WFS/TS ratios and shielding gases, as illustrated in Figures X.11 and X.12.

The effect of trim was also evaluated for RapidArc in respect to the variation of bead shape characteristics, at different WFS levels and shielding gases, and its effect on them at constant WFS (6m/min). The results are illustrated from the Figure X.13 to X.16.

The effect of CTWD was evaluated for RapidArc in a similar way as was performed for trim. The results obtained are shown from the Figure X.17 to X.20.

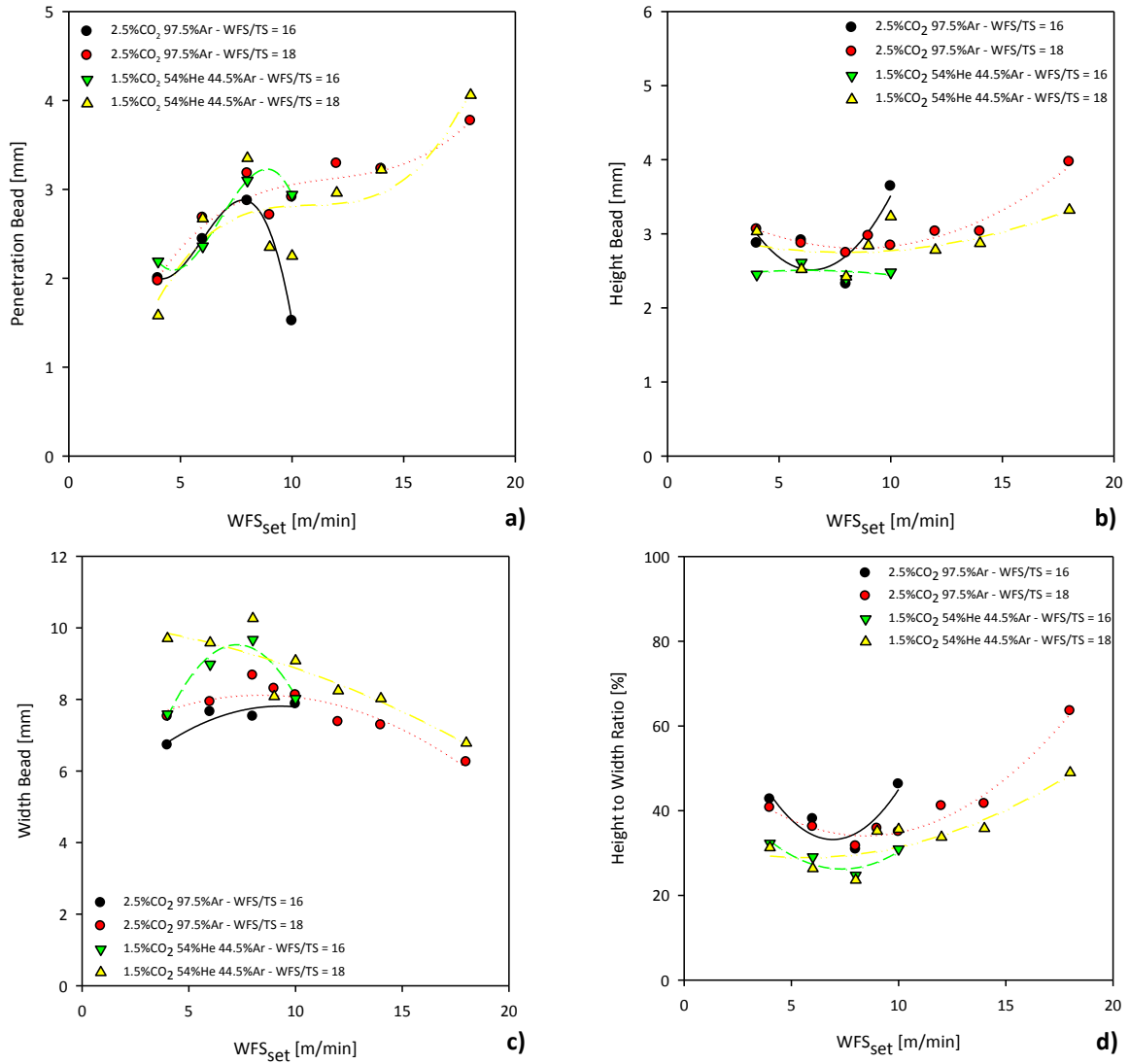


Figure X.11 – Effect of WFS on bead shape characteristics for RapidArc, at different WFS/TS ratios and shielding gases: a) penetration bead; b) height bead; c) width bead; and d) height to width ratio.

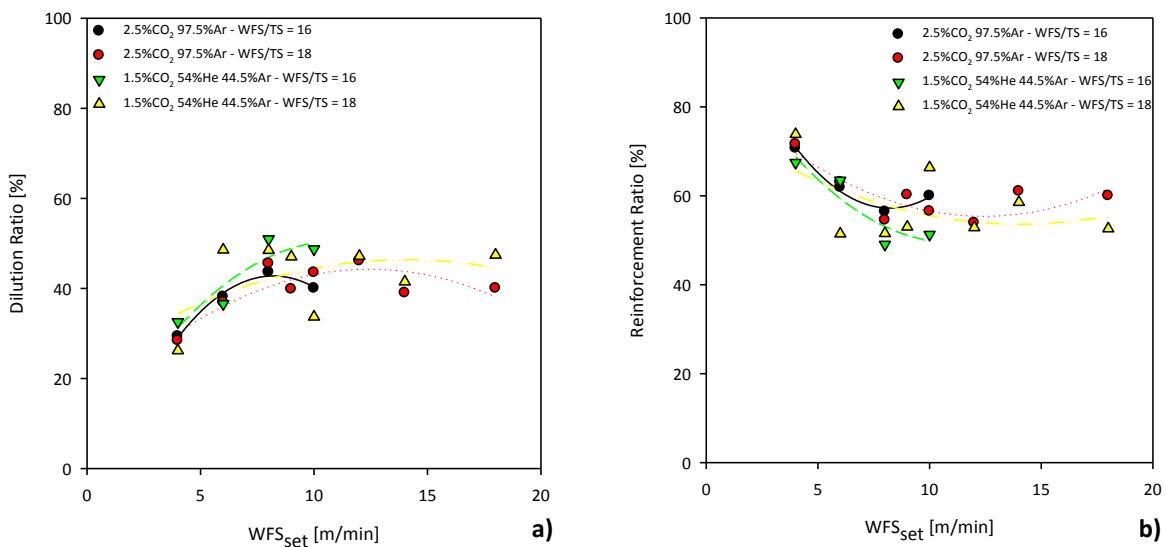


Figure X.12 – Effect of WFS on dilution ratio (a) and reinforcement ratio (b) for RapidArc, at different WFS/TS ratios and shielding gases.

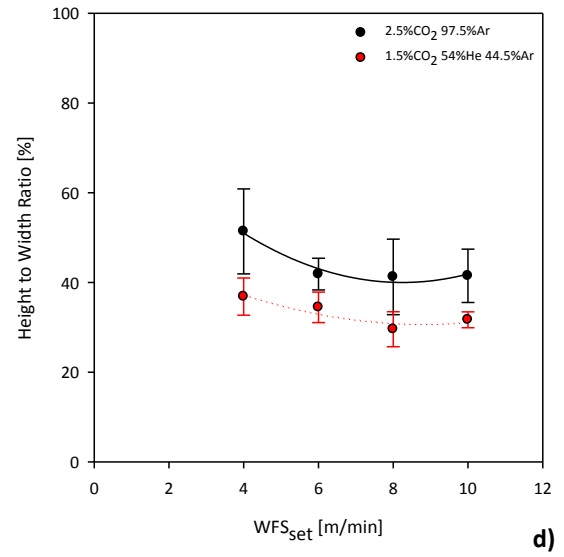
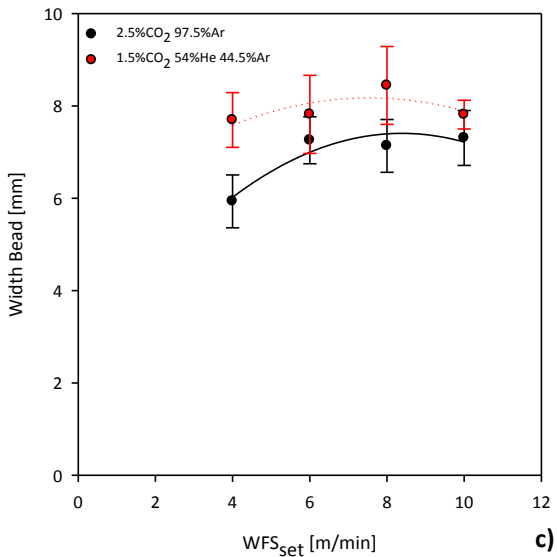
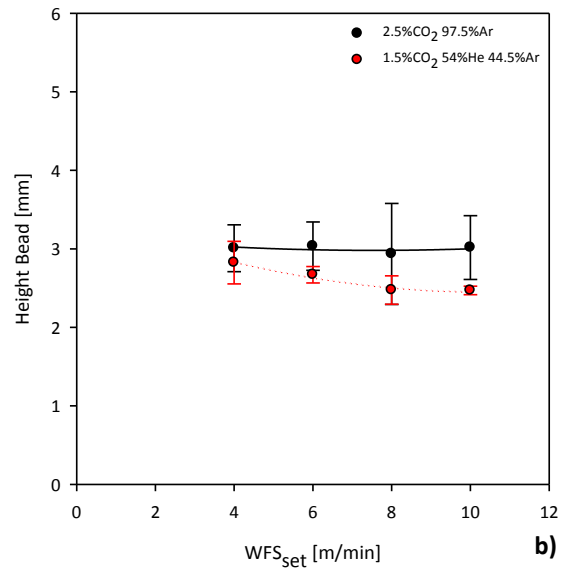
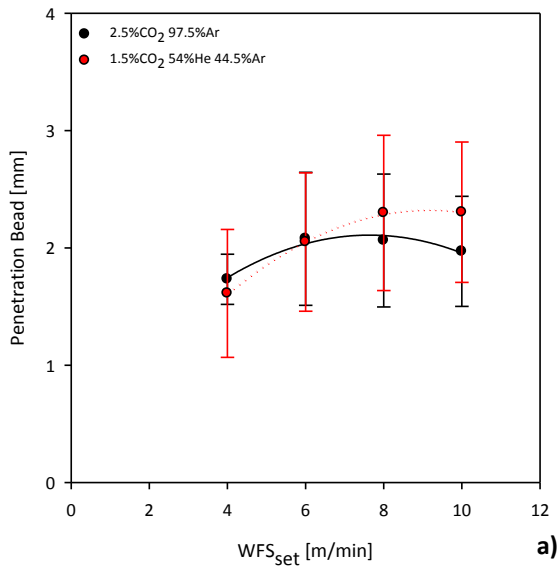


Figure X.13 – Effect of the variation of trim on bead shape characteristics for RapidArc, at different WFS levels and shielding gases: a) penetration bead; b) height bead; c) width bead; and d) height to width ratio.

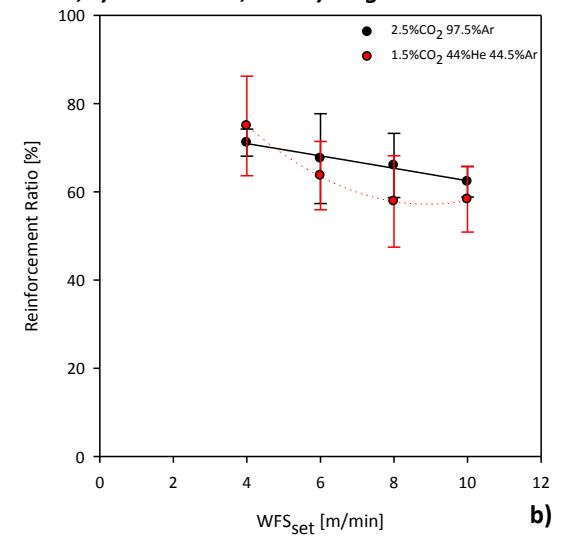
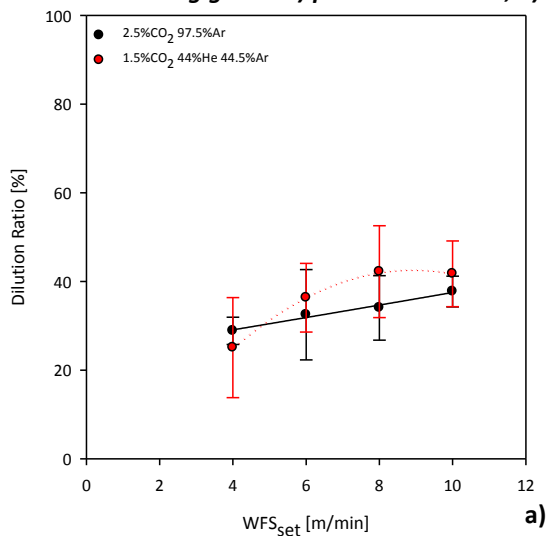


Figure X.14 – Effect of the variation of trim on dilution (a) and reinforcement ratio (b) for RapidArc, at different WFS levels and shielding gases.

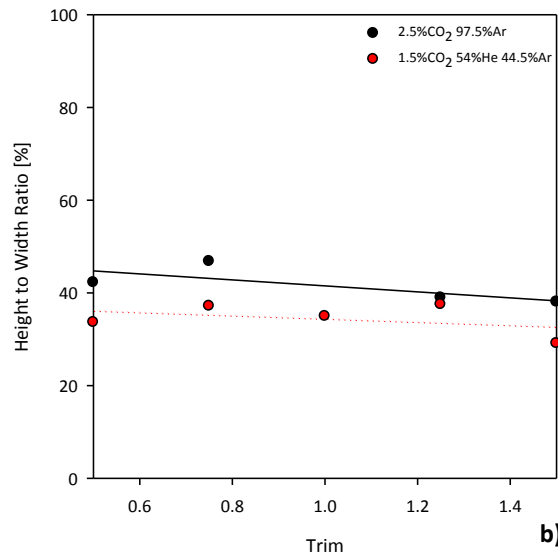
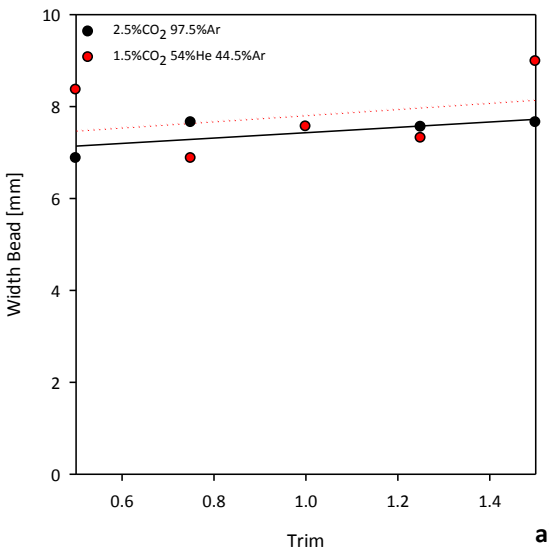
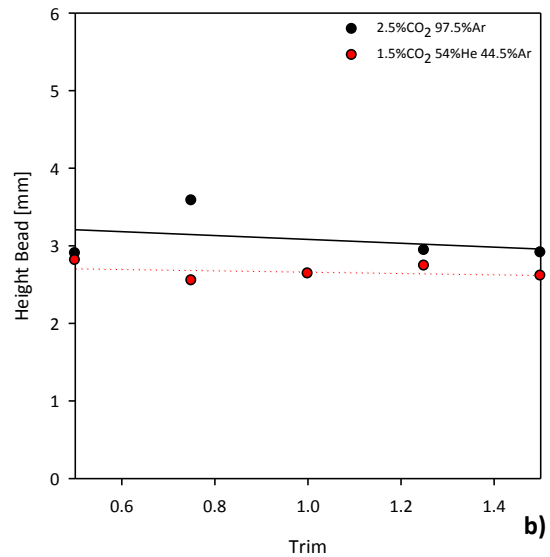
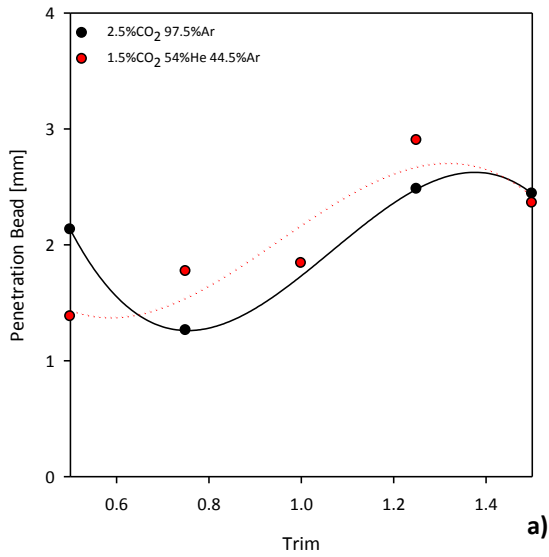


Figure X.15 – Effect of trim on bead shape characteristics for RapidArc, at different shielding gases: a) penetration bead; b) height bead; c) width bead; and d) height to width ratio.

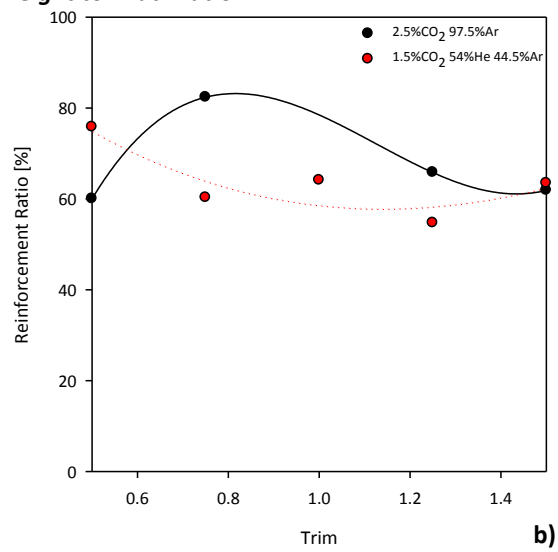
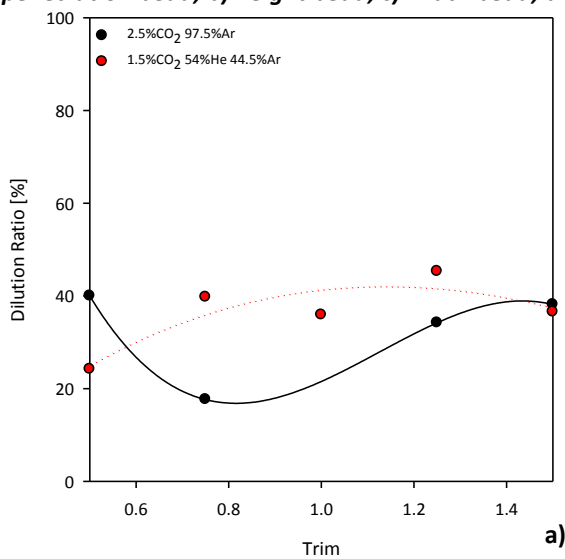


Figure X.16 – Effect of trim on dilution ratio (a) and reinforcement ratio (b) for RapidArc, at different shielding gases.

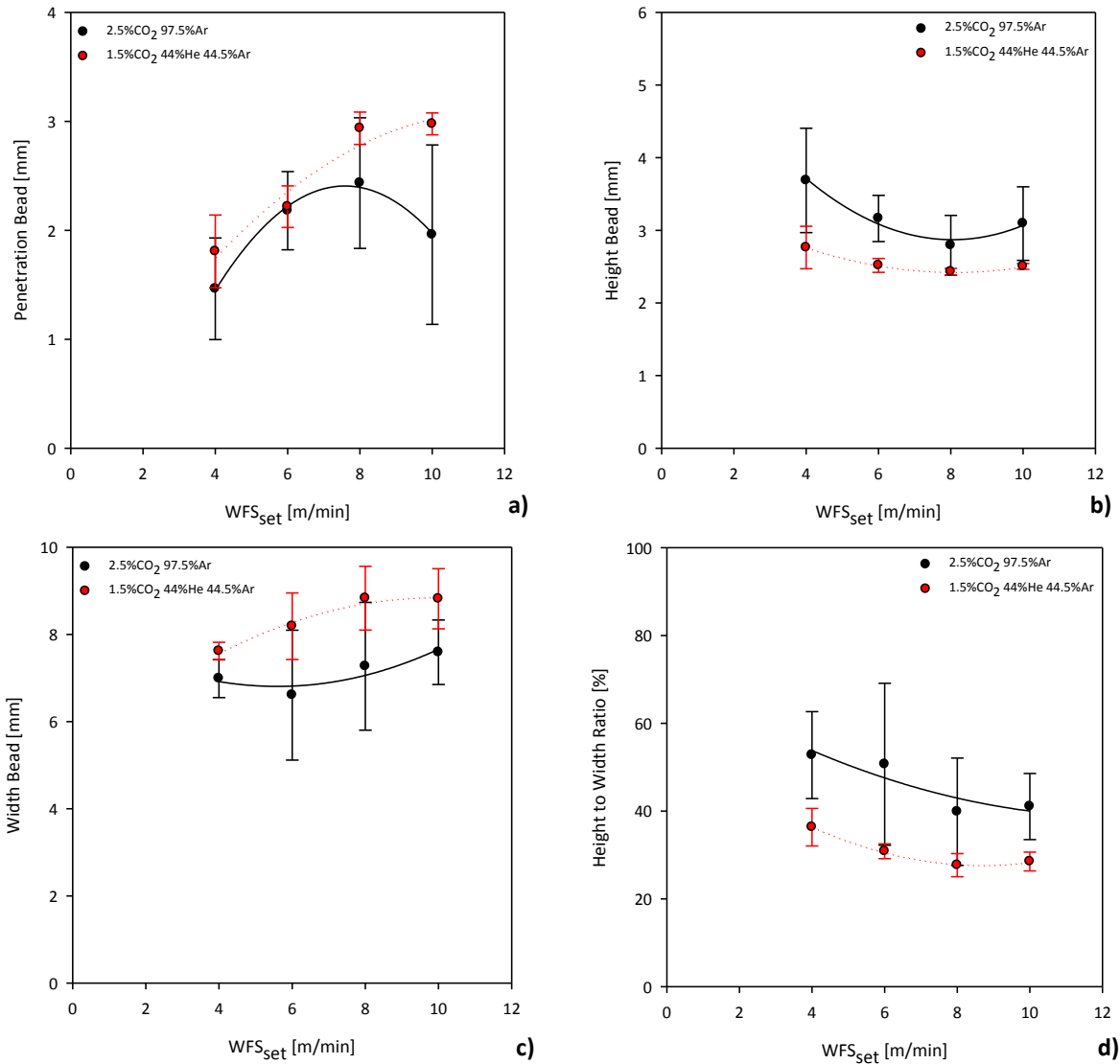


Figure X.17 – Effect of the variation of CTWD on bead shape characteristics for RapidArc, at different WFS levels and shielding gases: a) penetration bead; b) height bead; c) width bead; and d) height to width ratio.

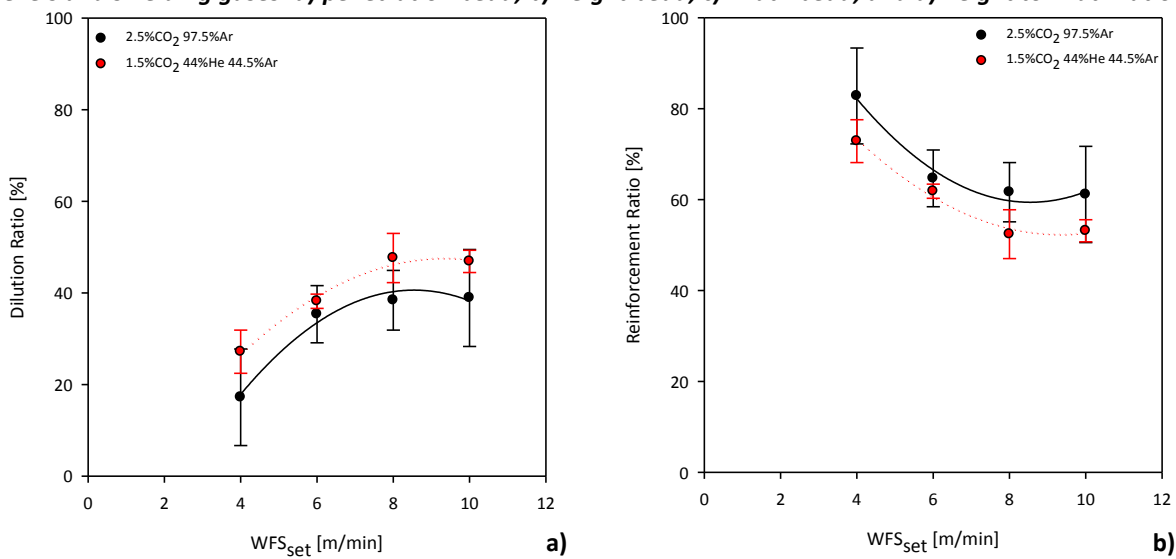


Figure X.18 – Effect of the variation of CTWD on dilution ratio (a) and reinforcement ratio (b) for RapidArc, at different WFS levels and shielding gases.

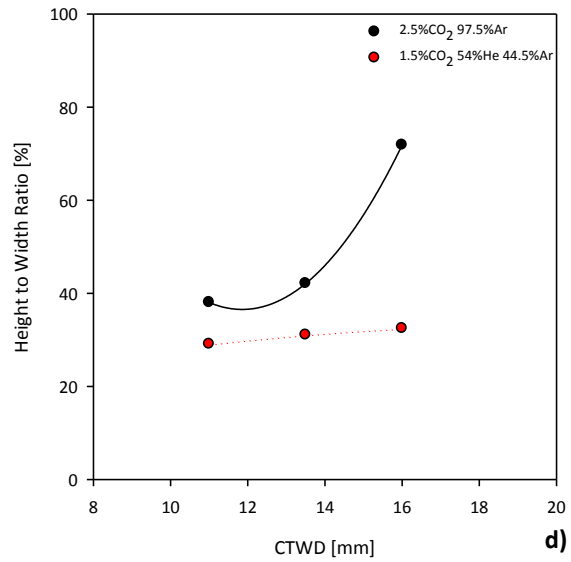
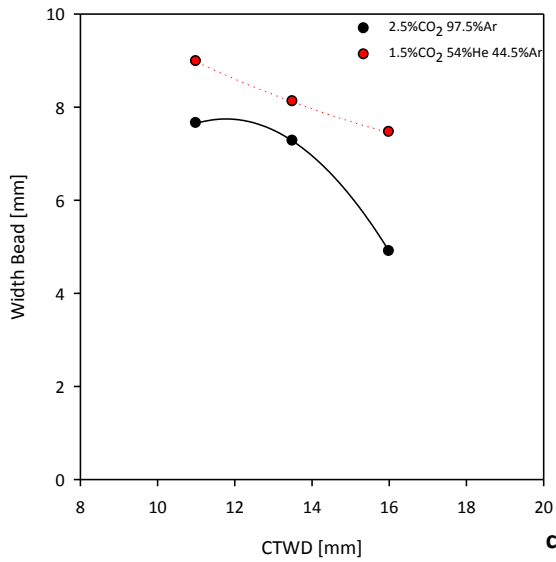
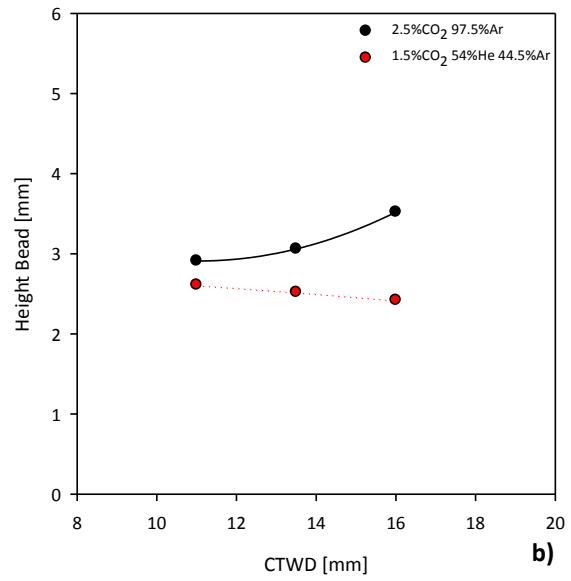
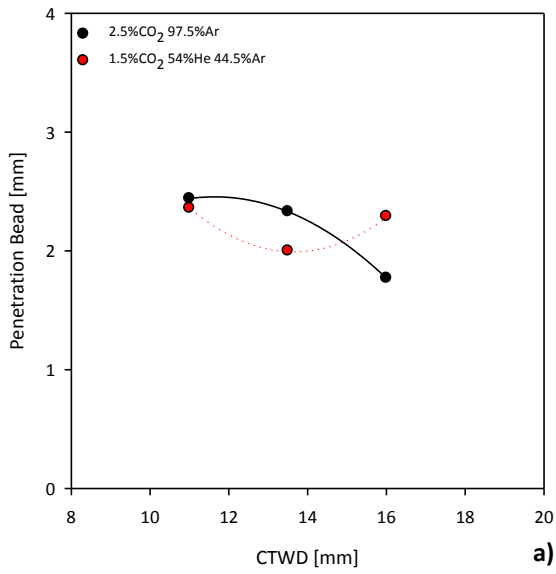


Figure X.19 – Effect of CTWD on bead shape characteristics for RapidArc, at different shielding gases: a) penetration bead; b) height bead; c) width bead; and d) height to width ratio.

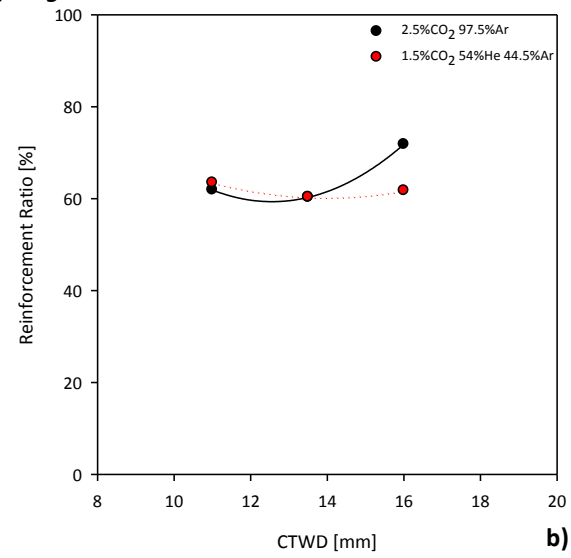
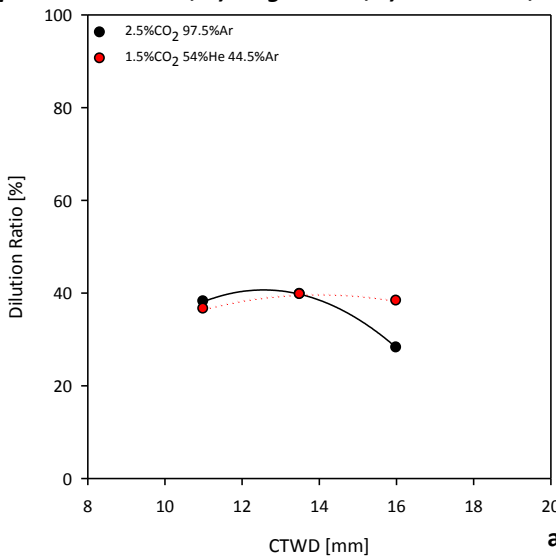


Figure X.20 – Effect of CTWD on dilution ratio (a) and reinforcement ratio (b) for RapidArc, at different shielding gases.

X.3. Characterization of Bead Shape Characteristics for STT

The effect of WFS on the bead shape characteristics was also investigated for STT using different WFS/TS ratios and shielding gases. The results are presented in Figure X.21 and X.22.

The effect of trim was also evaluated for STT in terms of the variation of bead shape characteristics, at different WFS levels and shielding gases, and its effect on them at constant WFS (6m/min). The results are illustrated from Figure X.23 to X.26.

The effect of CTWD was evaluated for STT in a similar way as was performed for trim. The results are shown from Figure X.27 to X.30.

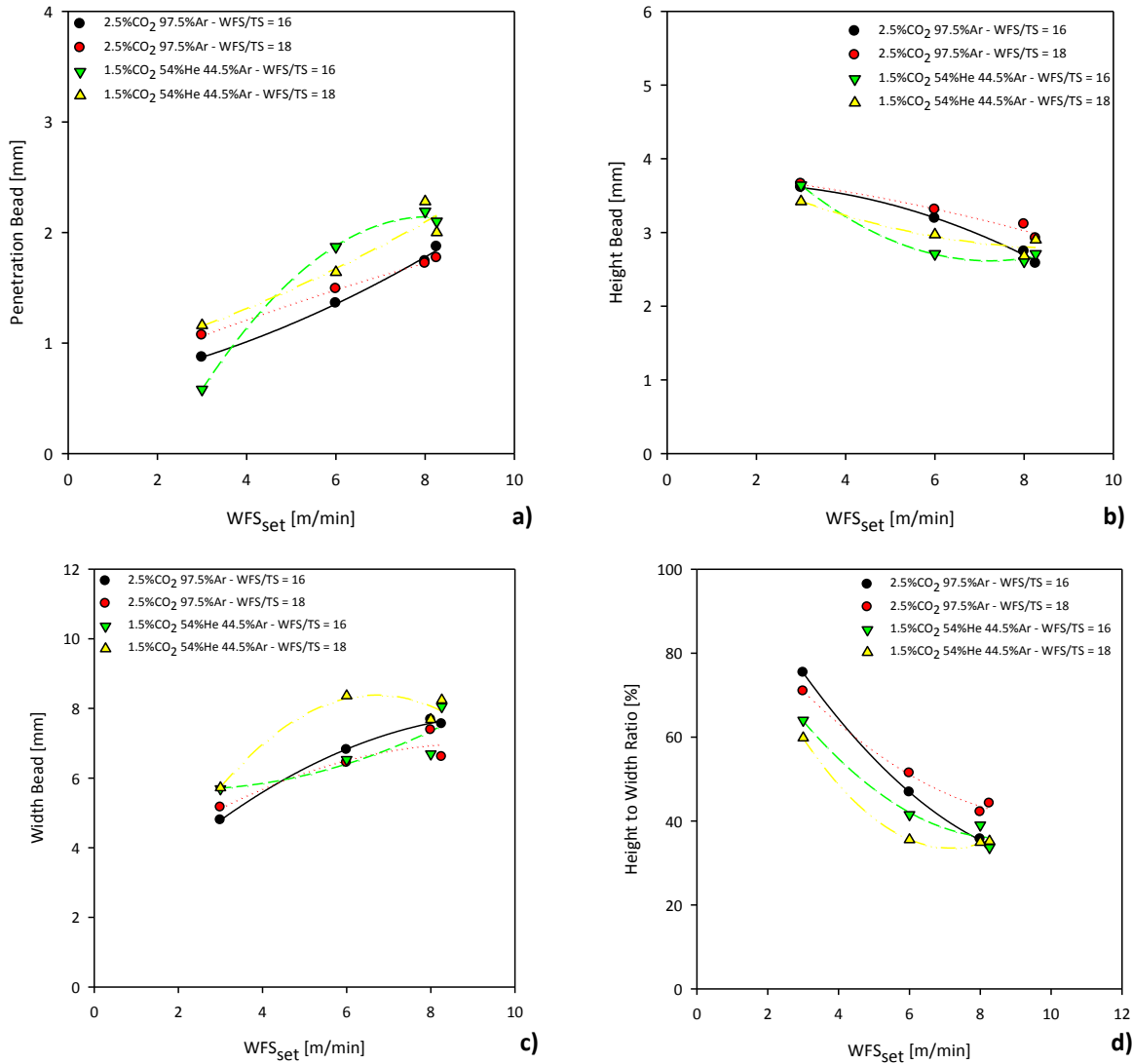


Figure X.21 – Effect of WFS on bead shape characteristics for STT, at different WFS/TS ratios and shielding gases: a) penetration bead; b) height bead; c) width bead; and d) height to width ratio.

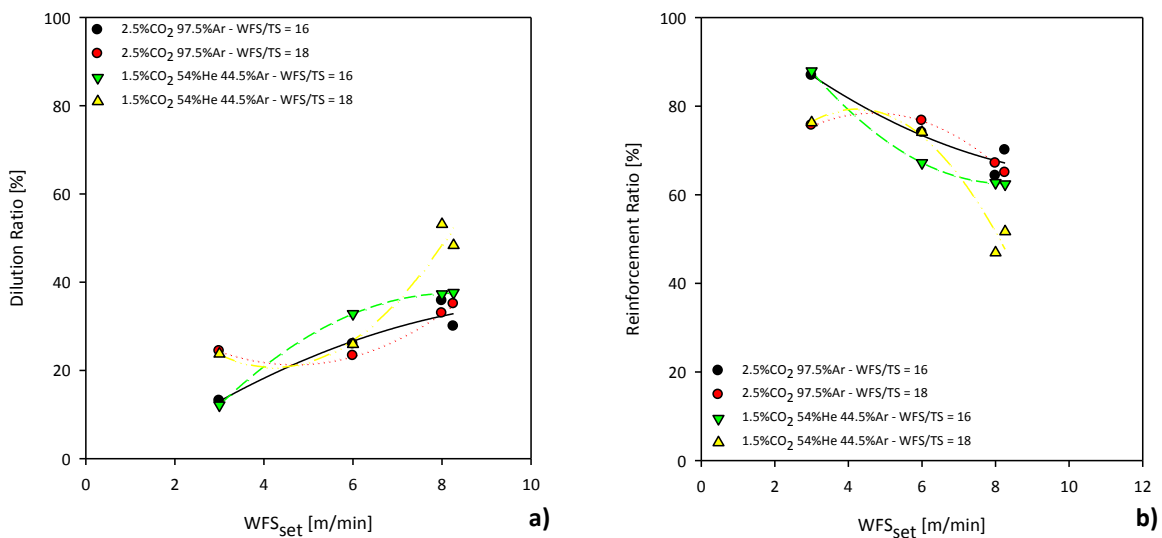


Figure X.22 – Effect of WFS on dilution ratio (a) and reinforcement ratio (b) for STT, at different WFS/TS ratios and shielding gases.

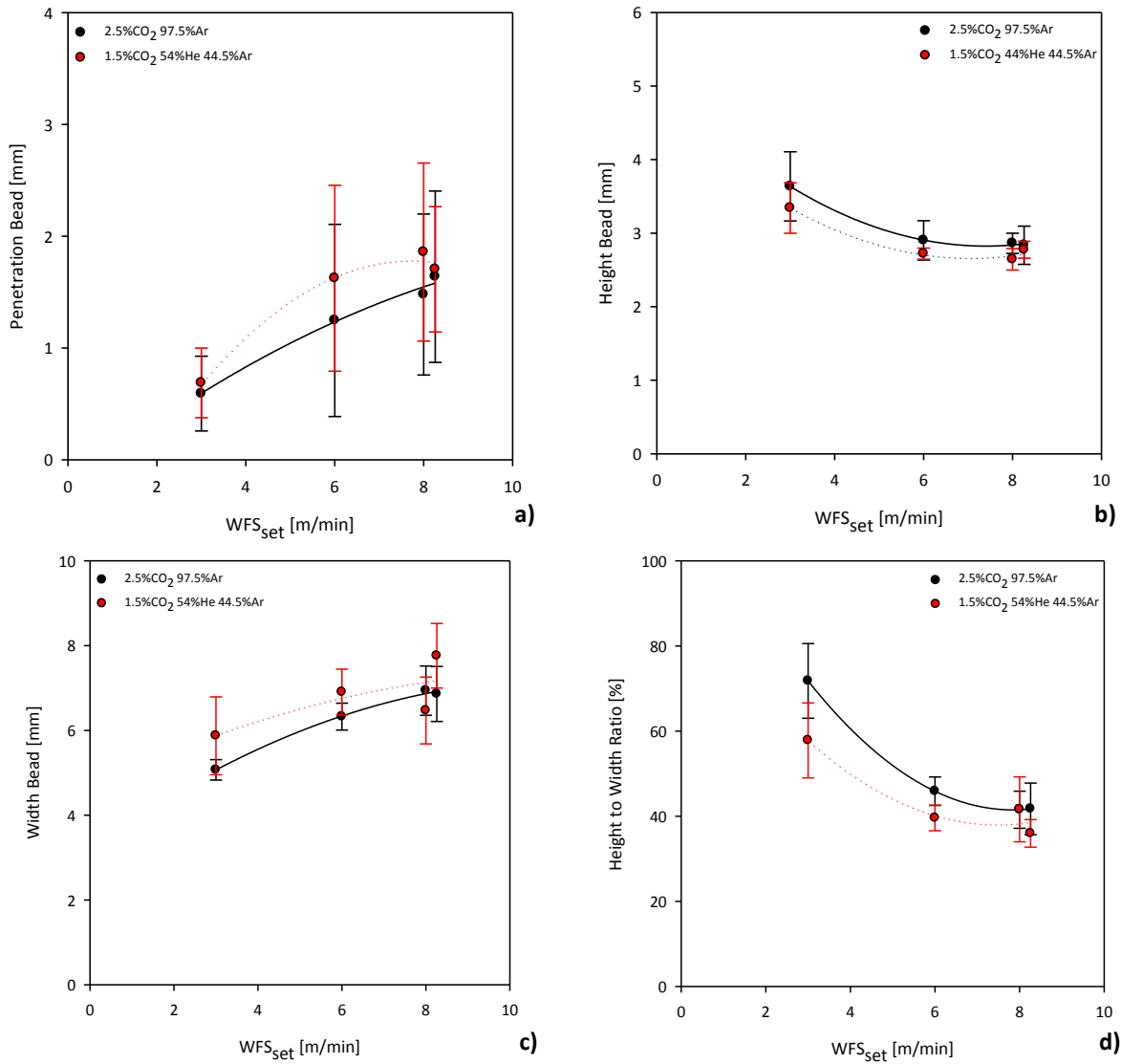


Figure X.23 – Effect of the variation of trim on bead shape characteristics for STT, at different WFS levels and shielding gases: a) penetration bead; b) height bead; c) width bead; and d) height to width ratio.

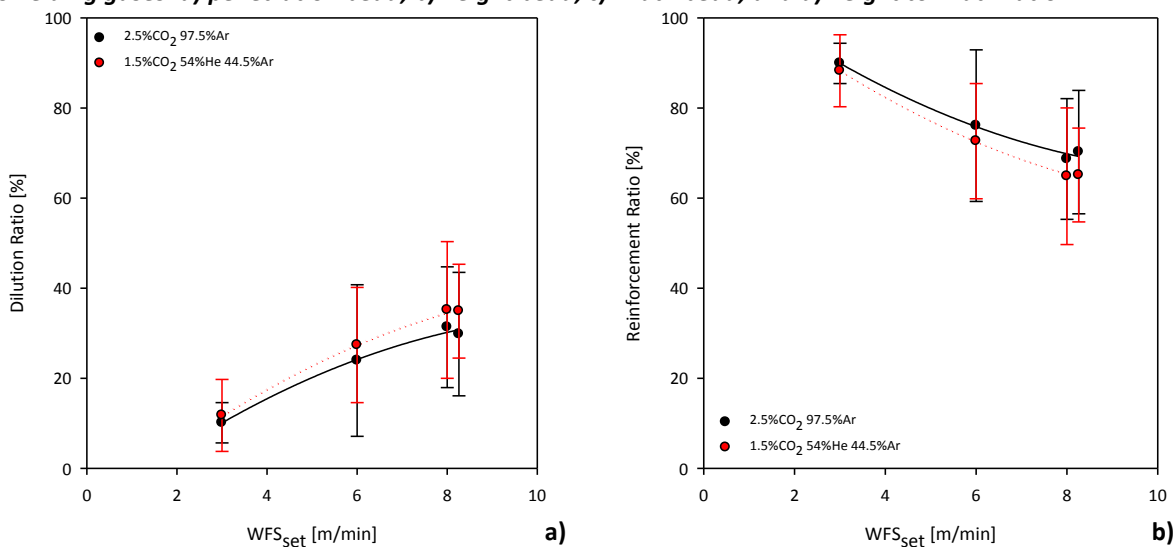


Figure X.24 – Effect of the variation of trim on dilution ratio (a) and reinforcement ratio (b) for STT, at different WFS levels and shielding gases.

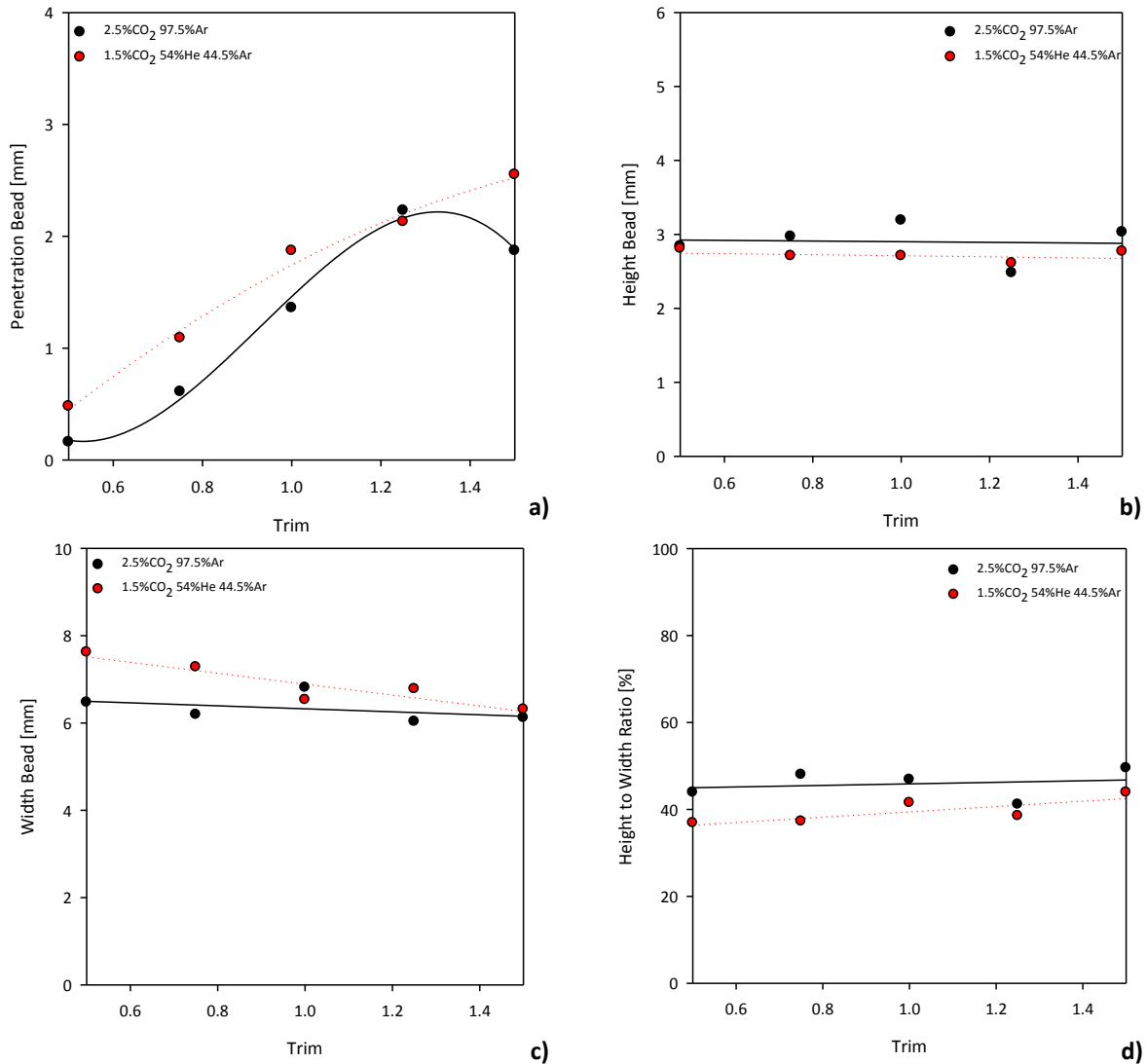


Figure X.25 – Effect of trim on bead shape characteristics for STT, at different shielding gases: a) penetration bead; b) height bead; c) width bead; and d) height to width ratio.

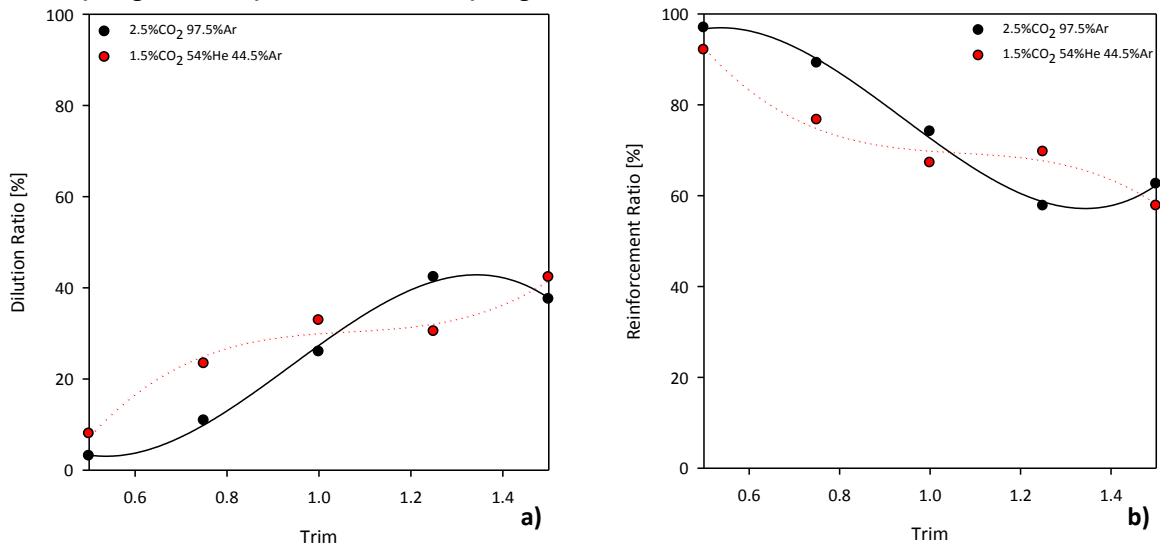


Figure X.26 – Effect of trim on dilution ratio (a) and reinforcement ratio (b) for STT, at different shielding gases.

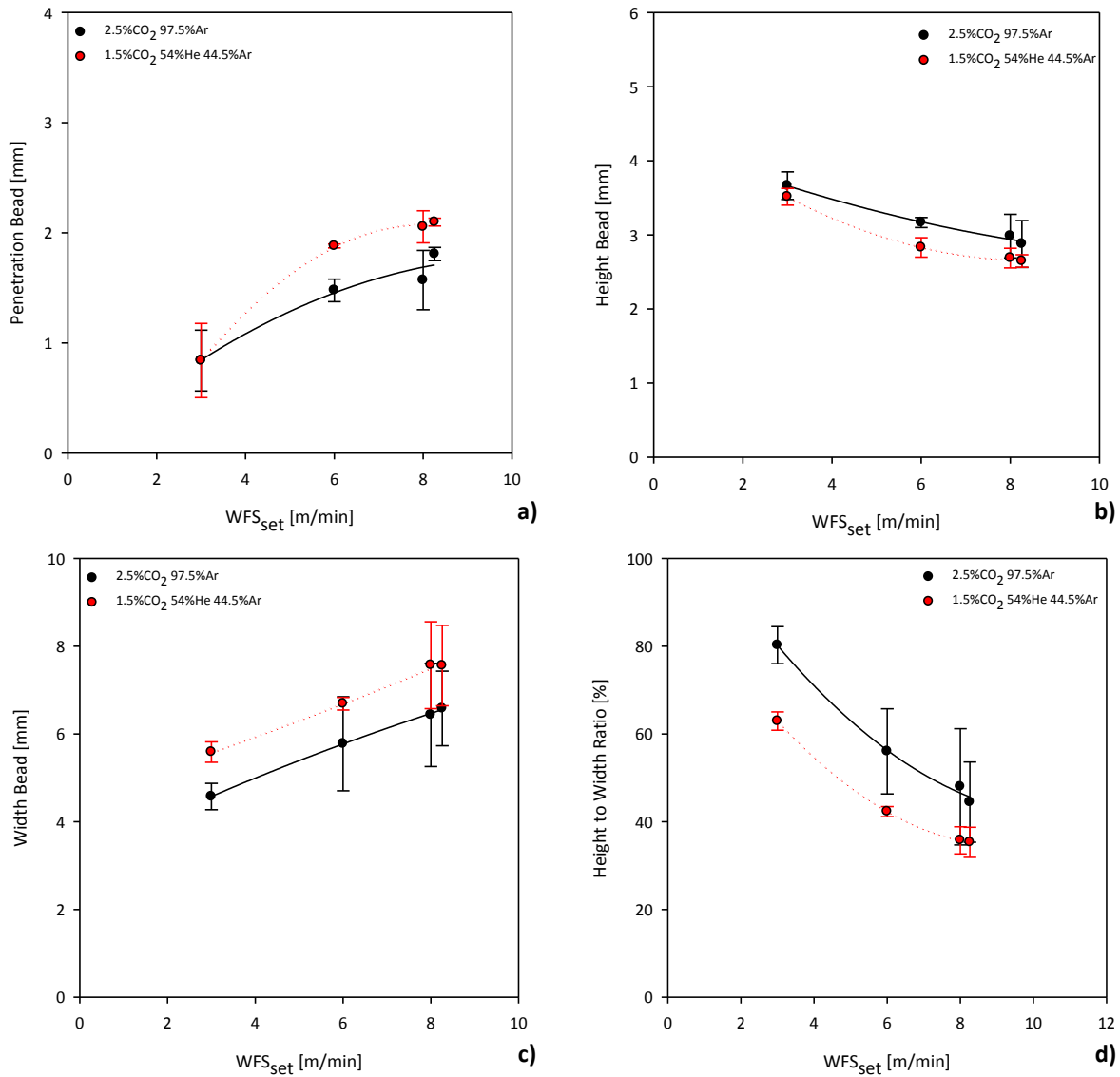


Figure X.27 – Effect of the variation of CTWD on bead shape characteristics for STT, at different WFS levels and shielding gases: a) penetration bead; b) height bead; c) width bead; and d) height to width ratio.

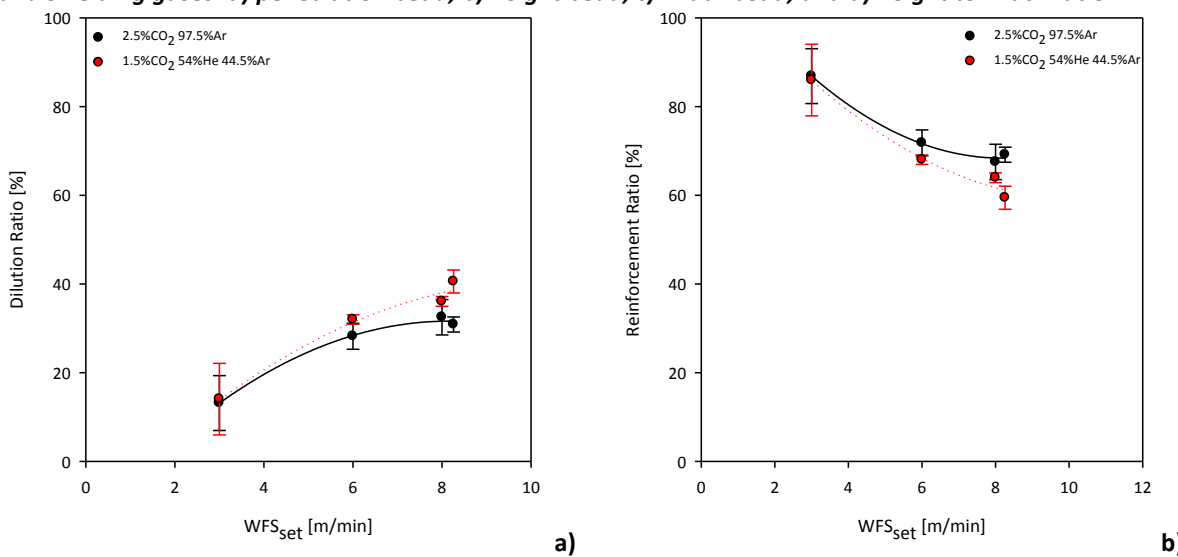


Figure X.28 – Effect of the variation of CTWD on dilution ratio (a) and reinforcement ratio (b) for STT, at different WFS levels and shielding gases.

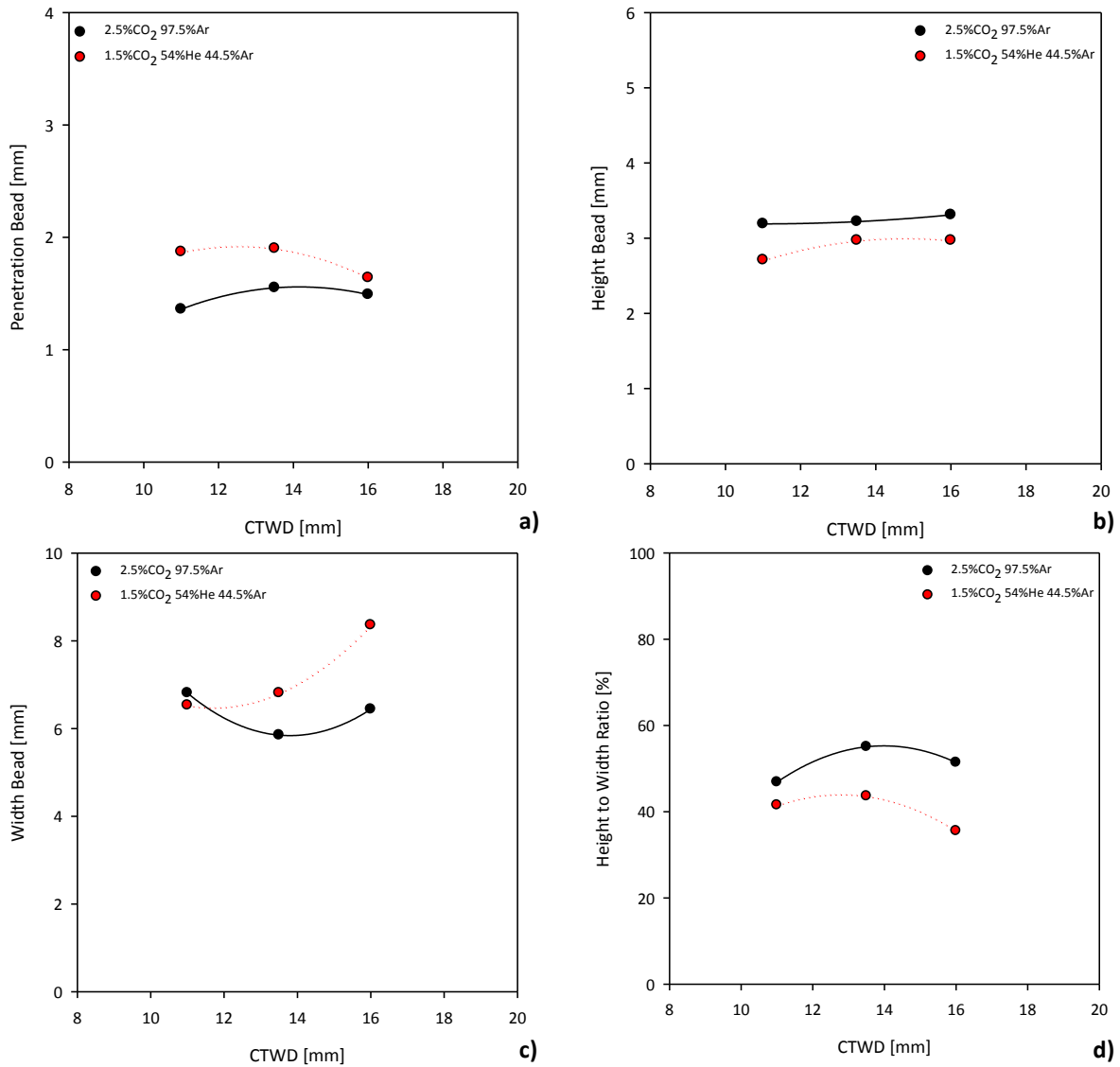


Figure X.29 – Effect of CTWD on bead shape characteristics for STT, at different shielding gases: a) penetration bead; b) height bead; c) width bead; and d) height to width ratio.

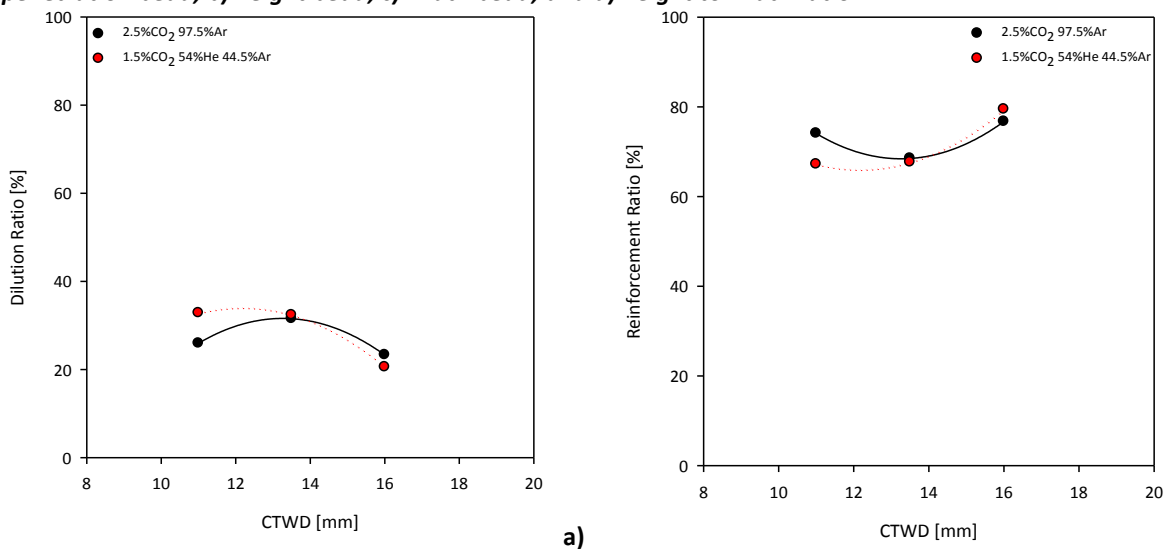


Figure X.30 – Effect of CTWD on dilution ratio (a) and reinforcement ratio (b) for STT at different shielding gases.

X.4. Characterization of Bead Shape Characteristics for CMT

The effect of WFS on the bead shape characteristics was also investigated for CMT using different WFS/TS ratios and shielding gases. The results are presented in the Figure X.31 and X.32.

The effect of arc length correction (ALC) was evaluated for CMT in terms of the variation of bead shape characteristics, at different WFS levels and shielding gases, and its effect on them at constant WFS (6m/min). The results are illustrated from Figure X.33 to X.36.

The effect of CTWD was evaluated for CMT in similar way as was performed for ALC. The results are shown from Figure X.37 to X.40

The analysis of the effect of dynamic control (DC) was evaluated for CMT at constant WFS (6m/min), Figure X.41 and X.42.

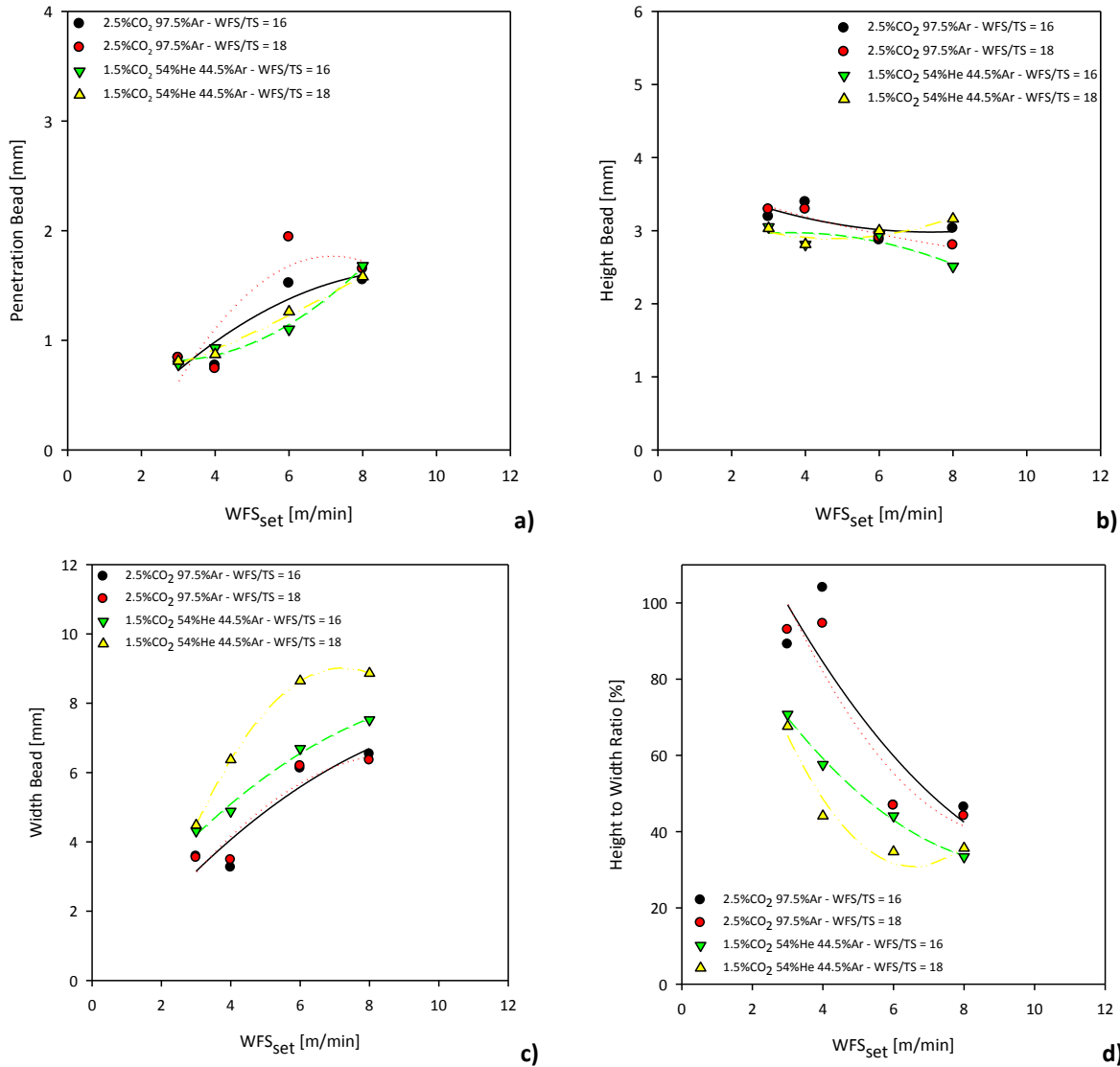


Figure X.31 – Effect of WFS on bead shape characteristics for CMT, at different WFS/TS ratios and shielding gases: a) penetration bead; b) height bead; c) width bead; and d) height to width ratio.

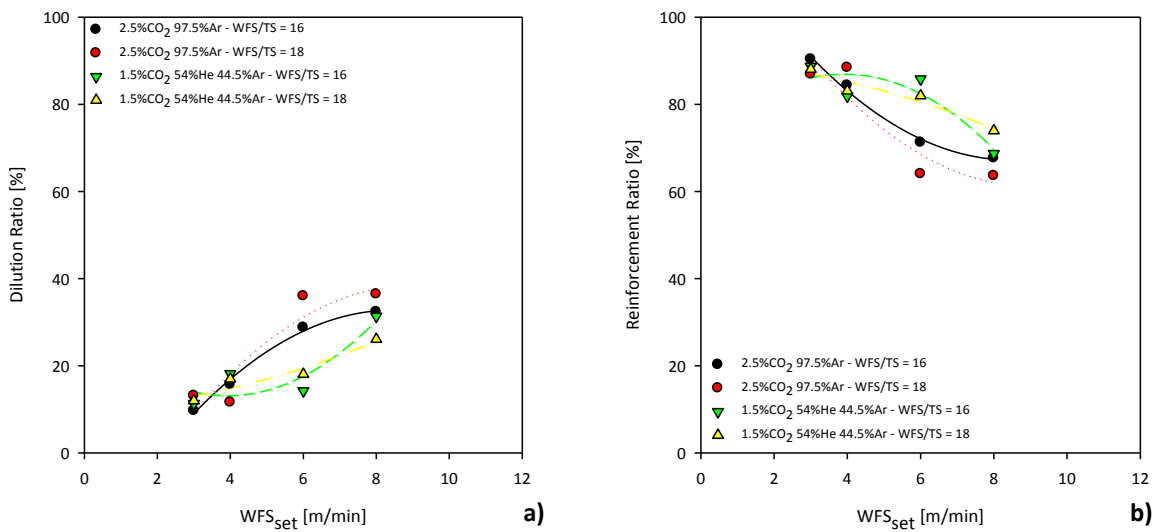


Figure X.32 – Effect of WFS on dilution ratio (a) and reinforcement ratio (b) for CMT, at different WFS/TS ratios and shielding gases.

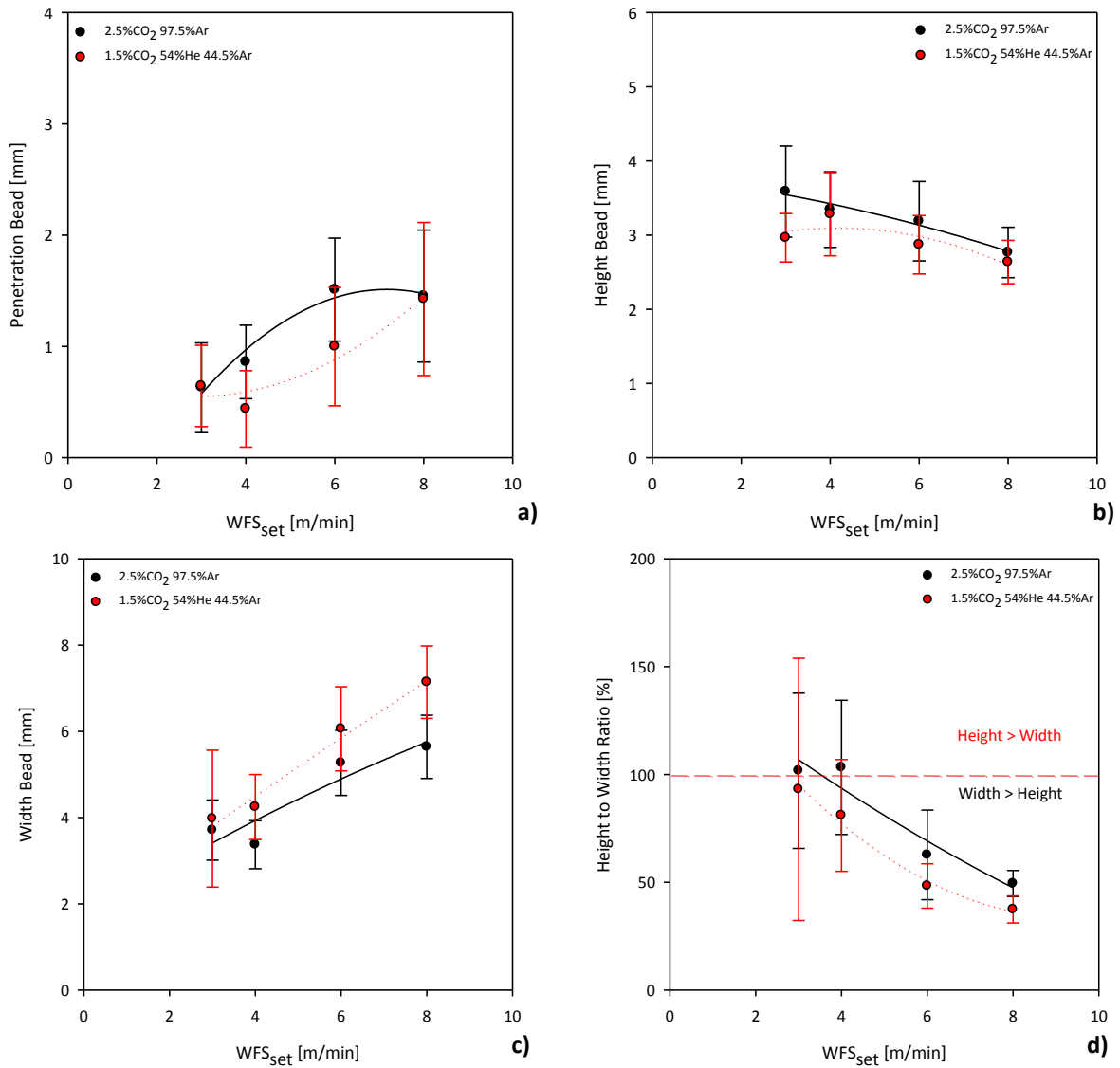


Figure X.33 – Effect of the variation of ALC on bead shape characteristics for CMT, at different WFS levels and shielding gases: a) penetration bead; b) height bead; c) width bead; d) height to width ratio.

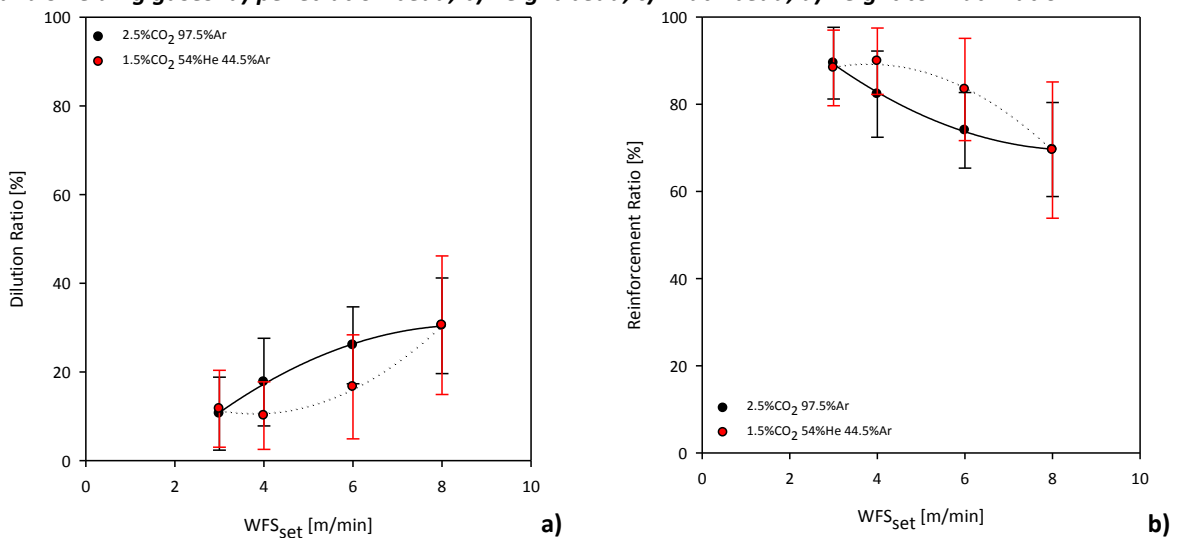


Figure X.34 – Effect of the variation of ALC on dilution ratio (a) and reinforcement ratio (b) for CMT, at different WFS levels and shielding gases.

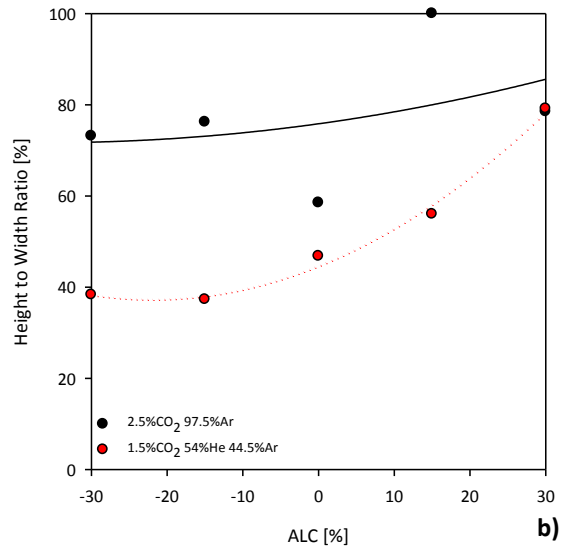
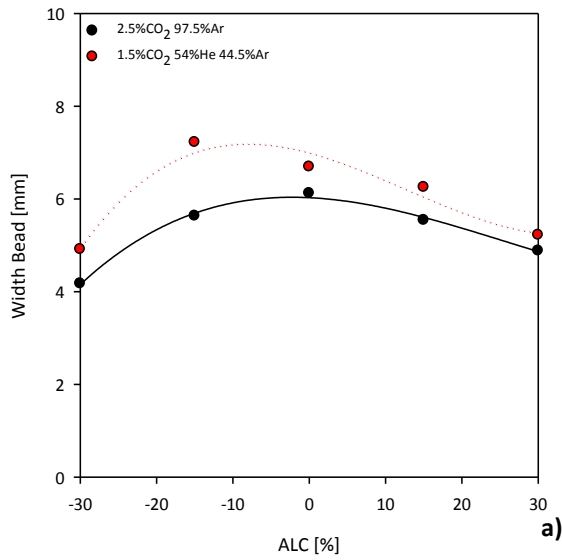
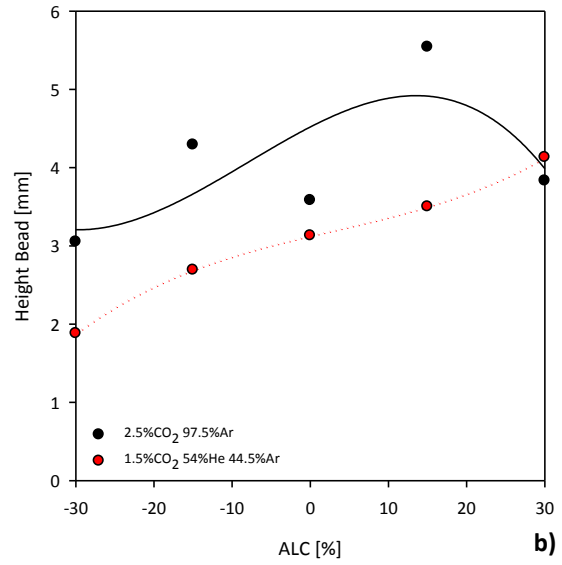
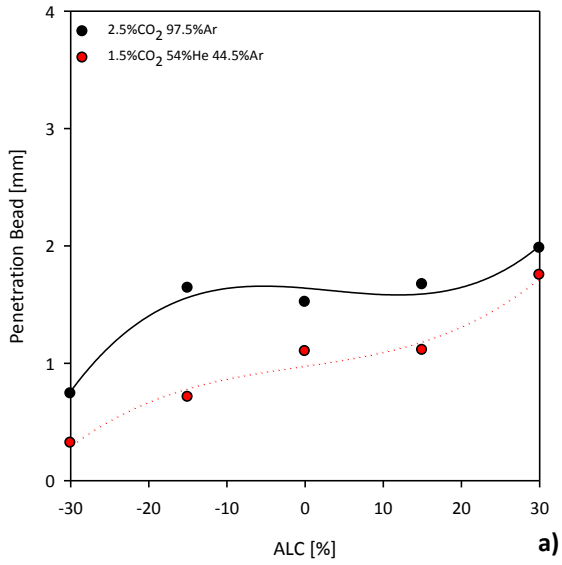


Figure X.35 – Effect of arc length correction (ALC) on bead shape characteristics for CMT, at different shielding gases: a) penetration bead; b) height bead; c) width bead; and d) height to width ratio.

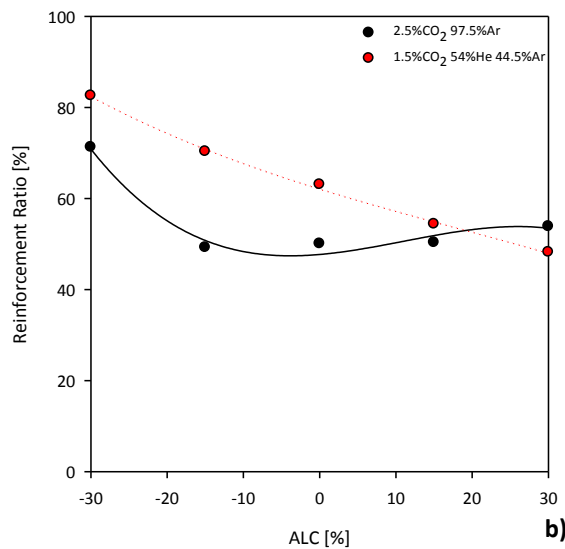
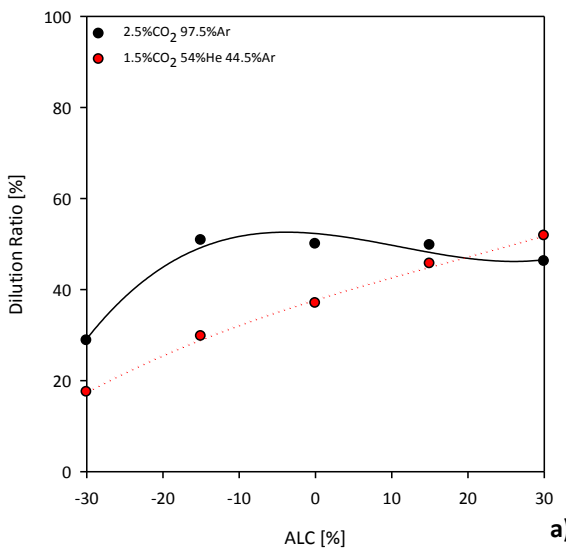


Figure X.36 – Effect of arc length correction (ALC) on dilution ratio (a) and reinforcement ratio (b) for CMT, at different shielding gases.

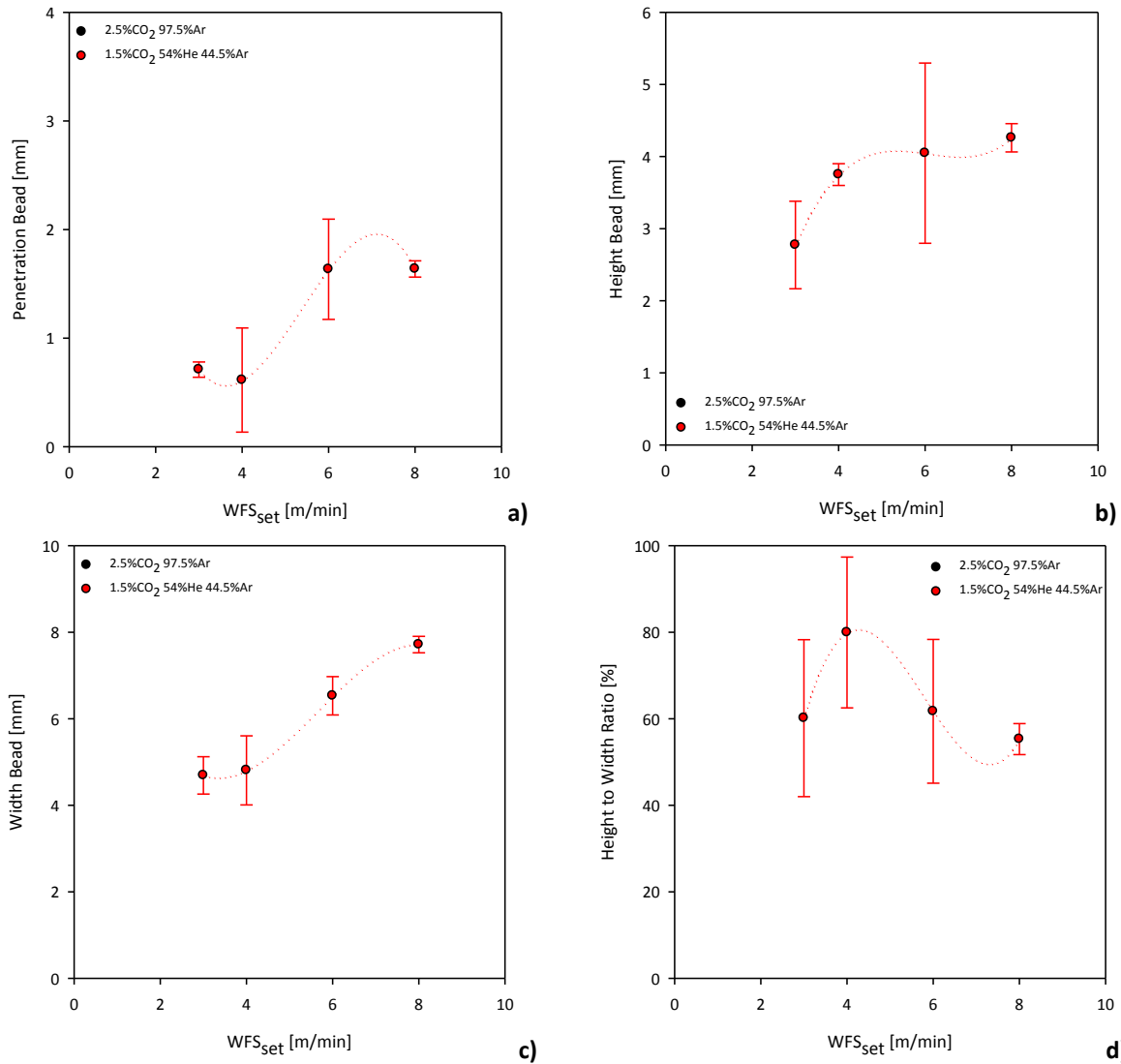


Figure X.37 – Effect of the variation of CTWD on bead shape characteristics with CTWD for CMT, using 1.5%CO₂ 54%He 44.5%Ar, at different WFS levels: a) penetration bead; b) height bead; c) width bead; and d) height to width ratio.

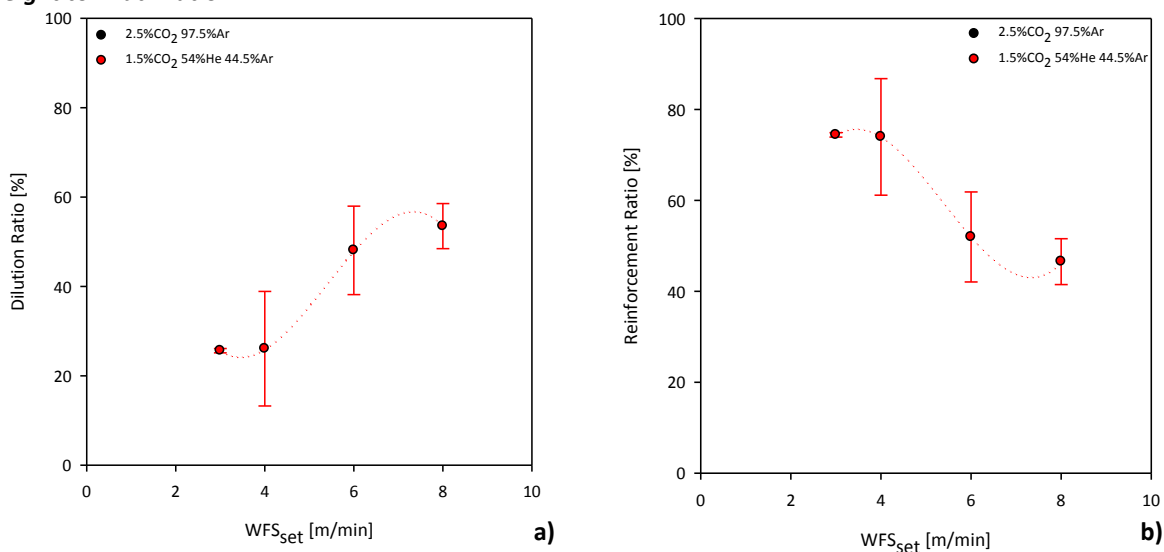


Figure X.38 – Effect of the variation of CTWD on dilution ratio (a) and reinforcement ratio (b) for CMT, using 1.5%CO₂ 54%He 44.5%Ar, at different WFS level.

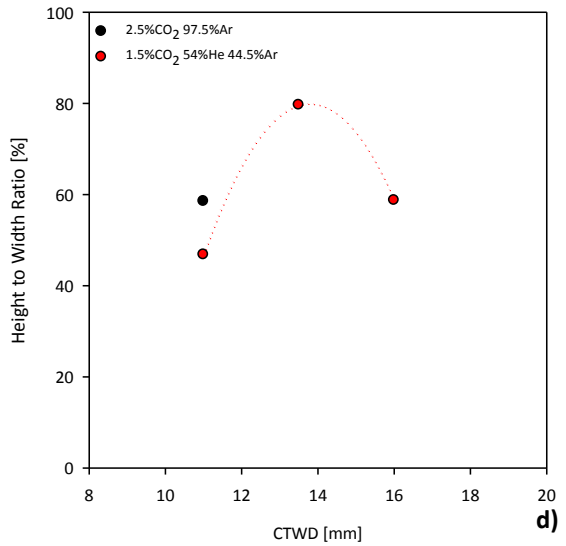
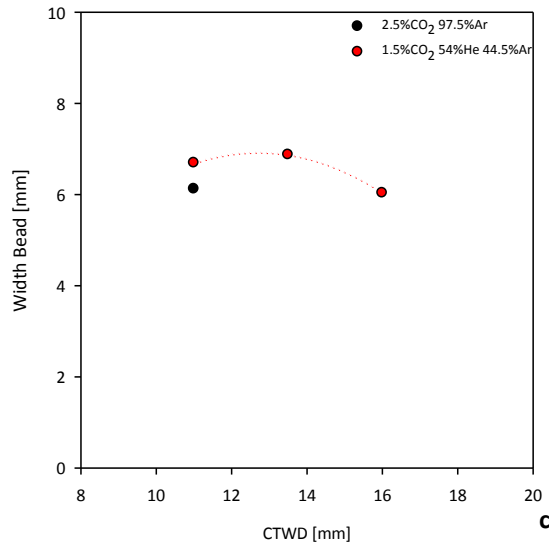
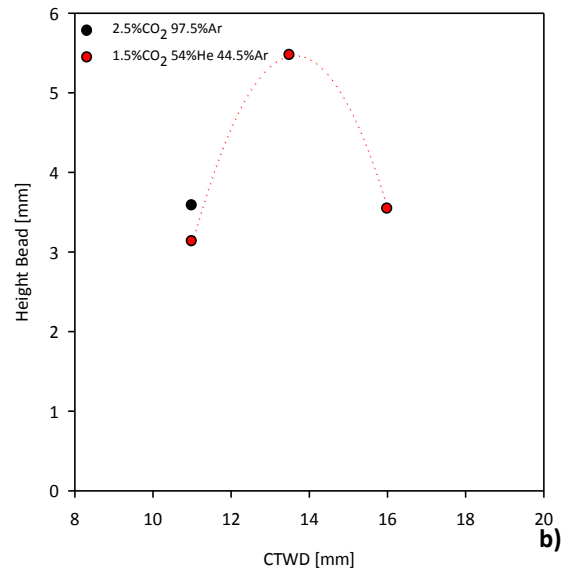
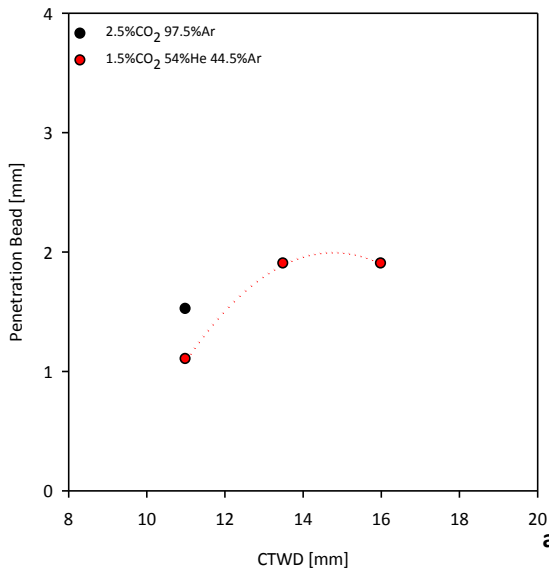


Figure X.39 – Effect of CTWD on bead shape characteristics for CMT at different shielding gases: a) penetration bead; b) height bead; c) width bead; and d) height to width ratio.

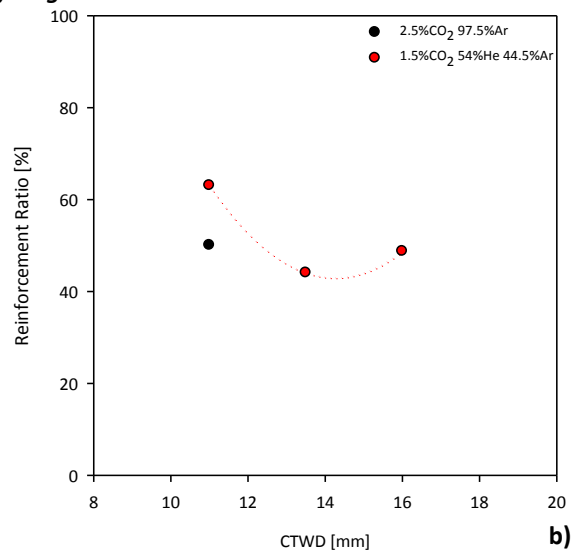
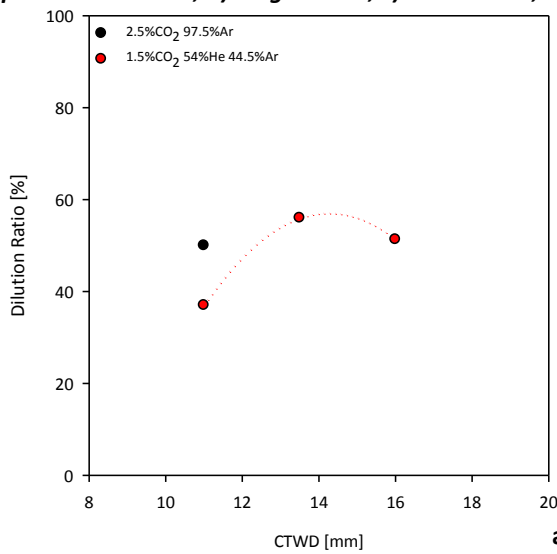


Figure X.40 – Effect of CTWD on dilution ratio (a) and reinforcement ratio (b) for CMT, at different shielding gases.

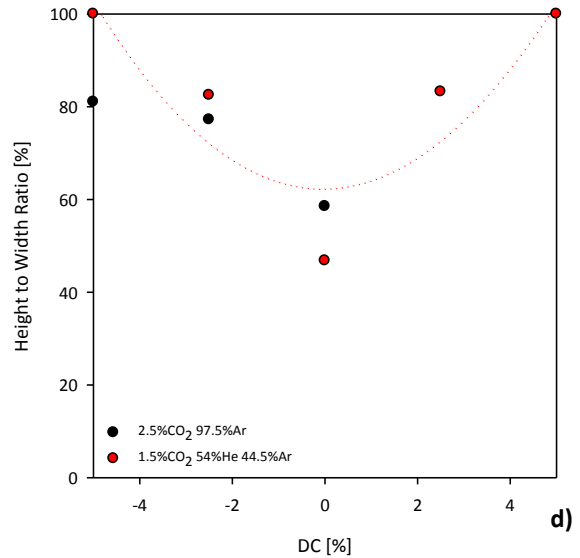
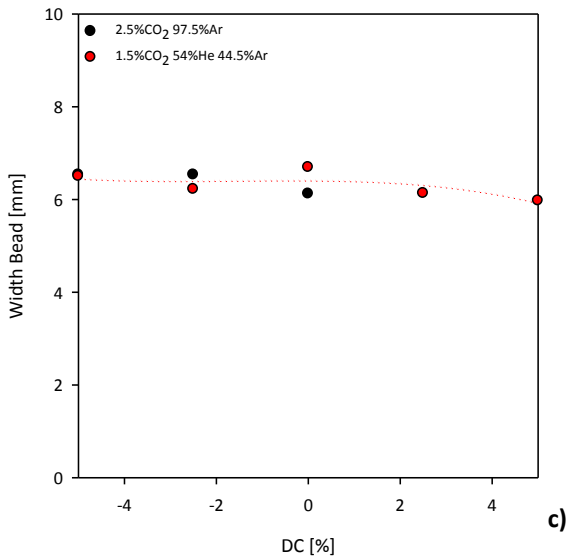
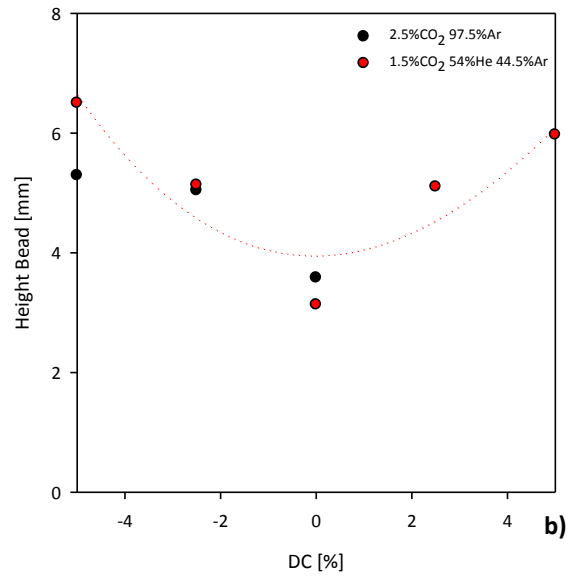
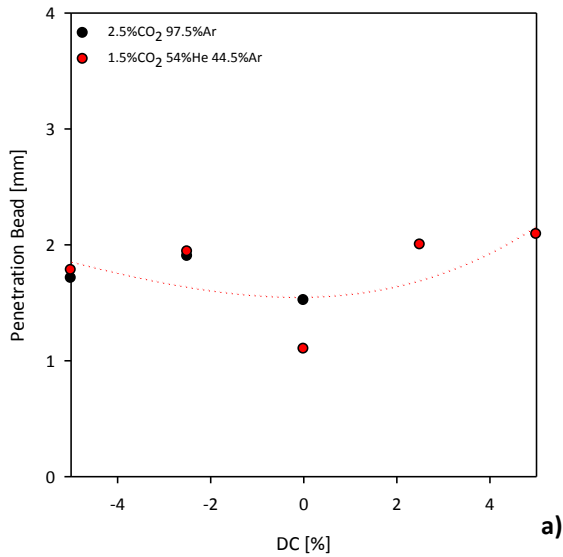


Figure X.41 – Effect of dynamic control (DC) on bead shape characteristics for CMT, at different shielding gases: a) penetration bead; b) height bead; c) width bead; and d) height to width ratio.

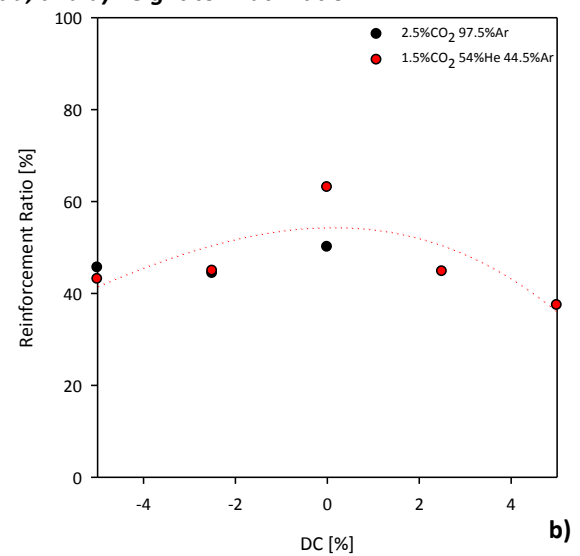
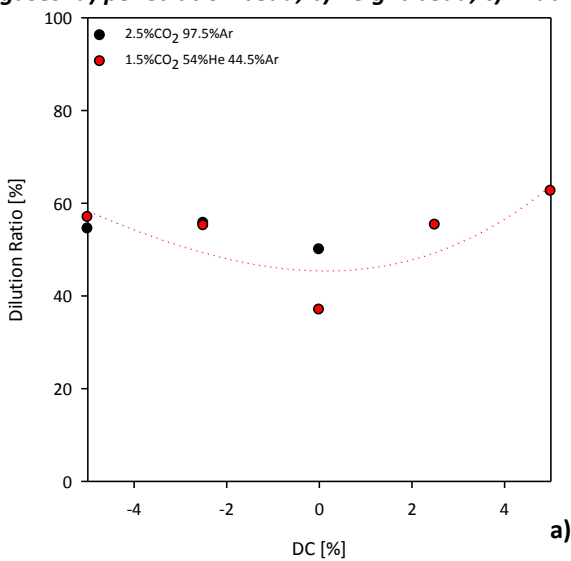


Figure X.42 – Effect of dynamic control (DC) on dilution ratio (a) and reinforcement ratio (b) for CMT, at different shielding gases.

V.5. Characterization of Bead Shape Characteristics for CMT-P

The effect of WFS on the bead shape characteristics was also investigated for CMT-P using different WFS/TS ratios and shielding gases. The results are presented in Figure X.43 and X.44.

The analysis of effect of arc length correction (ALC) for CMT-P was also performed in terms of the variation of bead shape characteristics, at different WFS levels and shielding gases, and its effect on them, at constant WFS (6m/min). The results are illustrated from Figure X.45 to X.48.

The effect of CTWD was also evaluated for CMT-P in similar way as was performed for ALC. The results are shown from Figure X.49 to X.52.

The analysis of the effect of pulse control (PC) was performed for CMT-P, and the results are illustrated in Figure X.53.

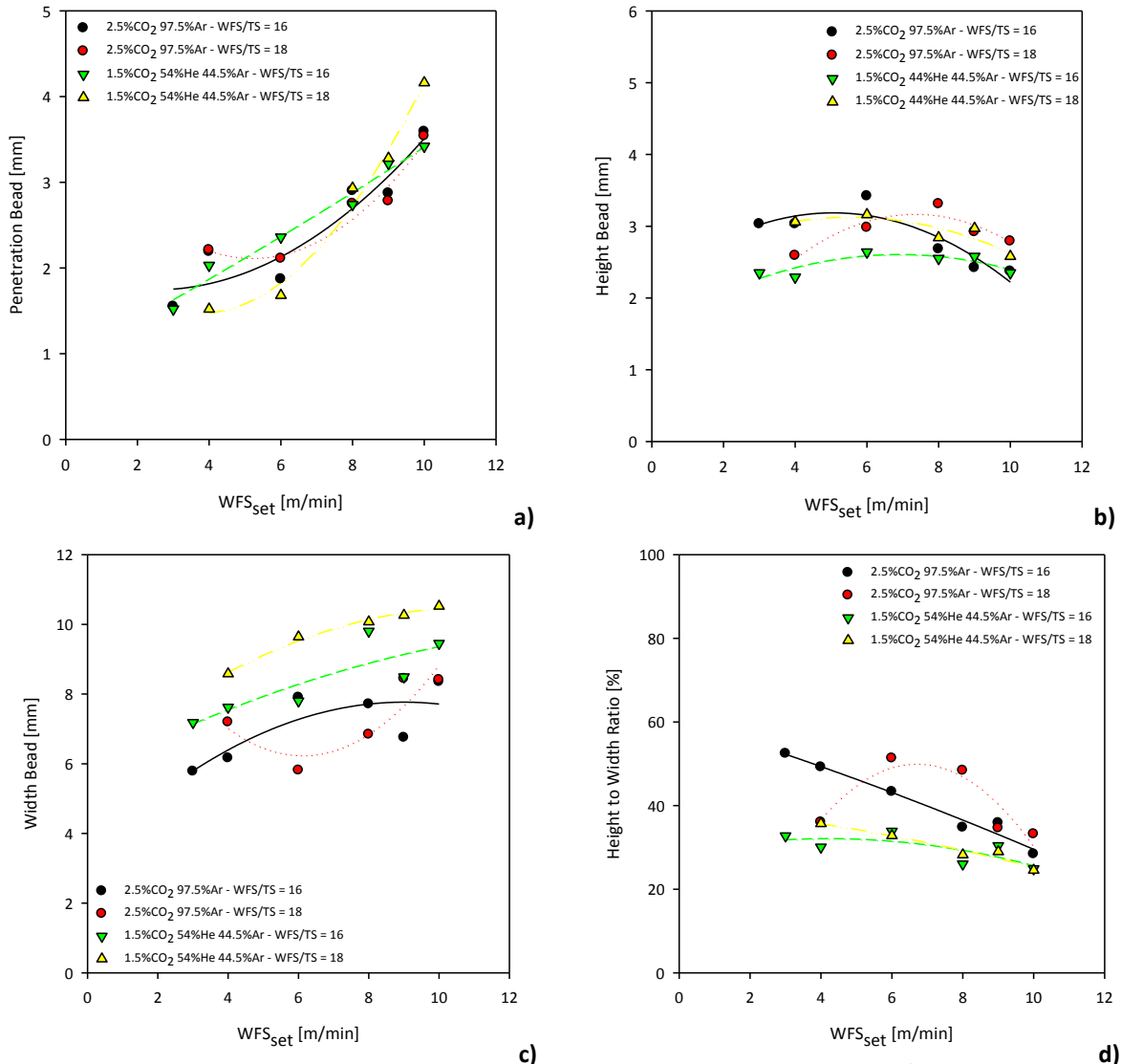


Figure X.43 – Effect of WFS on bead shape characteristics for CMT-P, at different WFS/TS ratios and shielding gases: a) penetration bead; b) height bead; c) width bead; and d) height to width ratio.

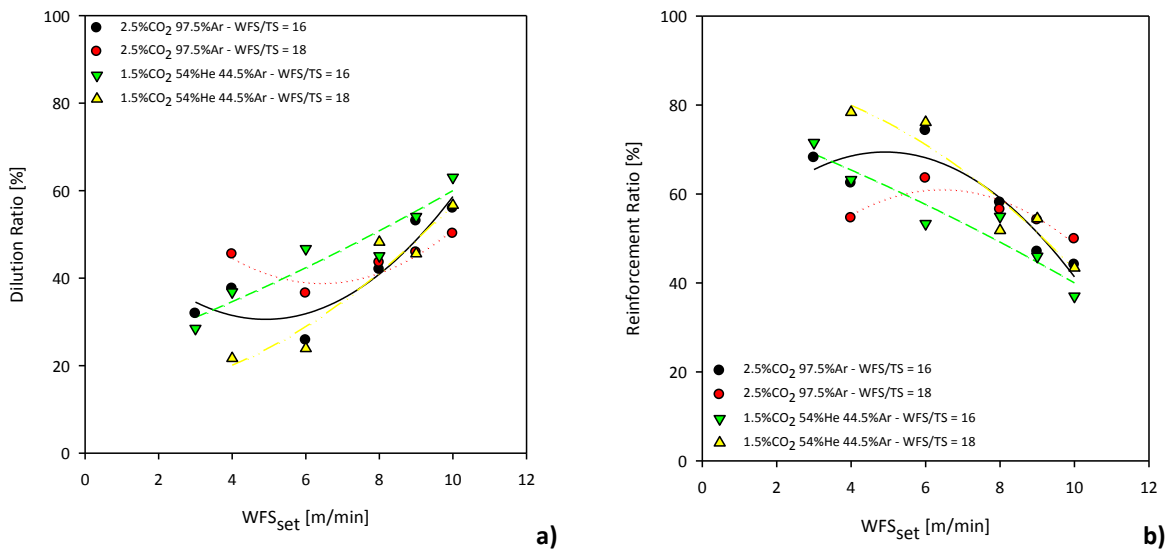


Figure X.44 – Effect of WFS on dilution ratio (a) and reinforcement ratio (b) for CMT-P, at different WFS/TS ratios and shielding gases.

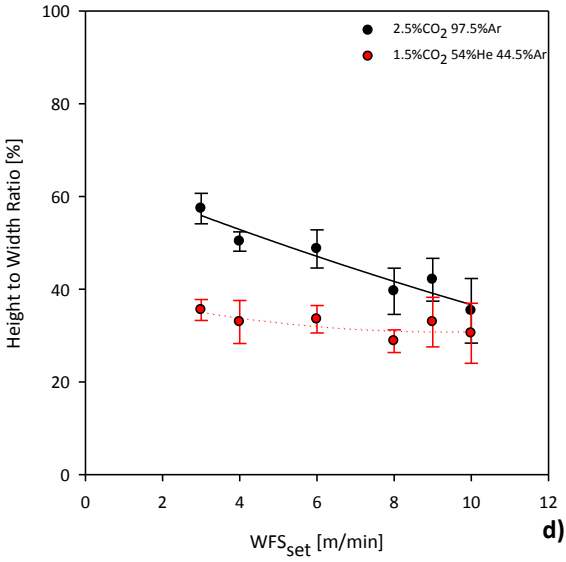
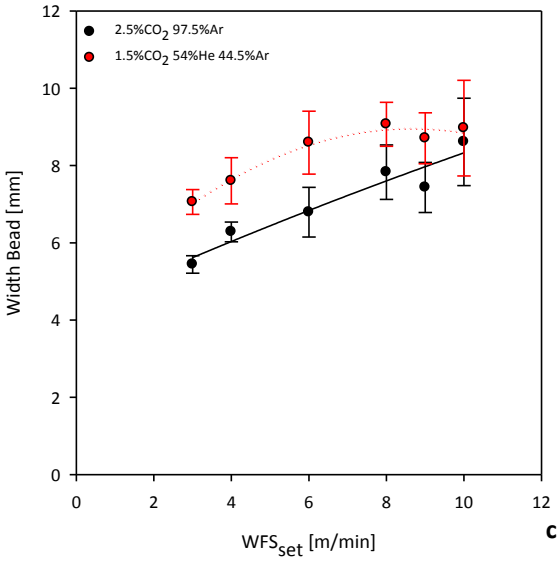
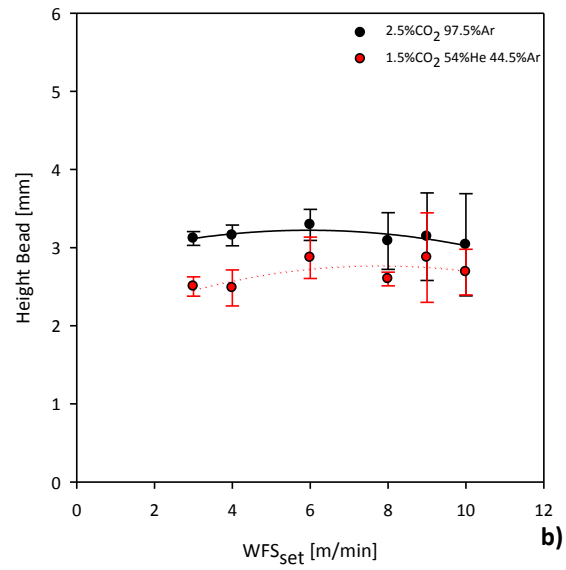
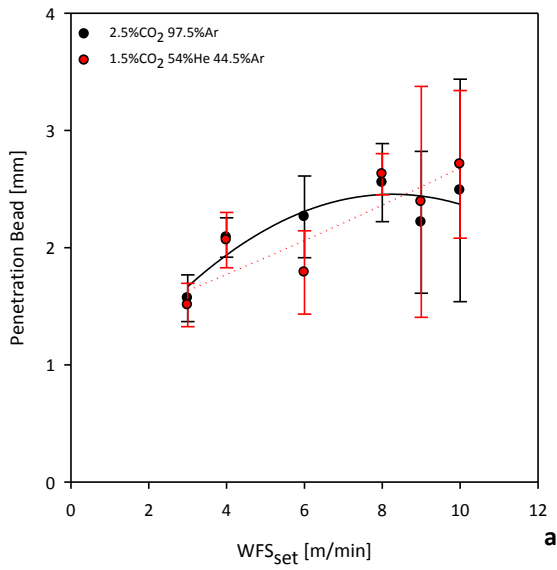


Figure X.45 – Effect of the variation of ALC on bead shape characteristics for CMT-P, at different WFS levels and shielding gases: a) penetration bead; b) height bead; c) width bead; d) height to width ratio.

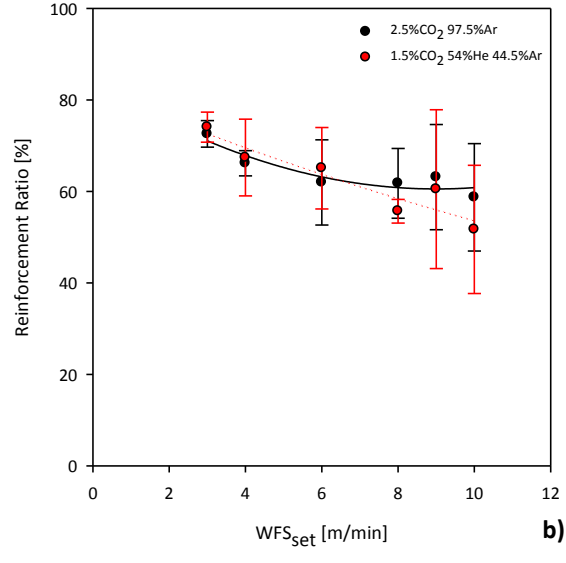
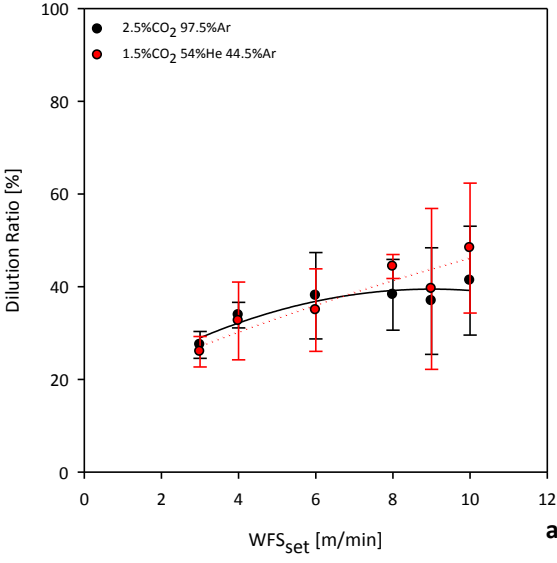


Figure X.46 – Effect of the variation of ALC on dilution ratio (a) and reinforcement ratio (b) for CMT-P, at different WFS levels and shielding gases.

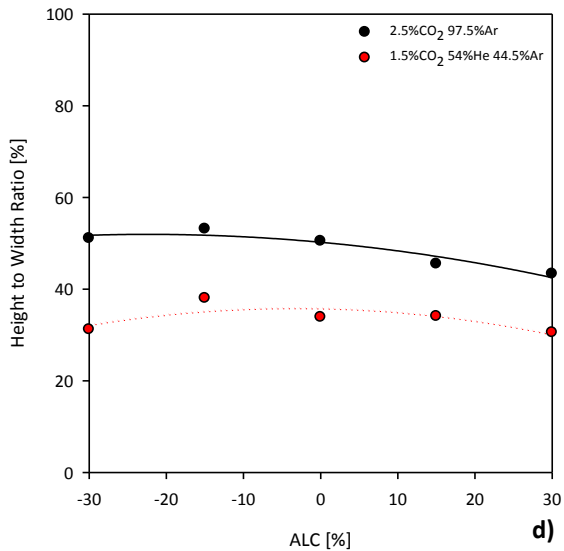
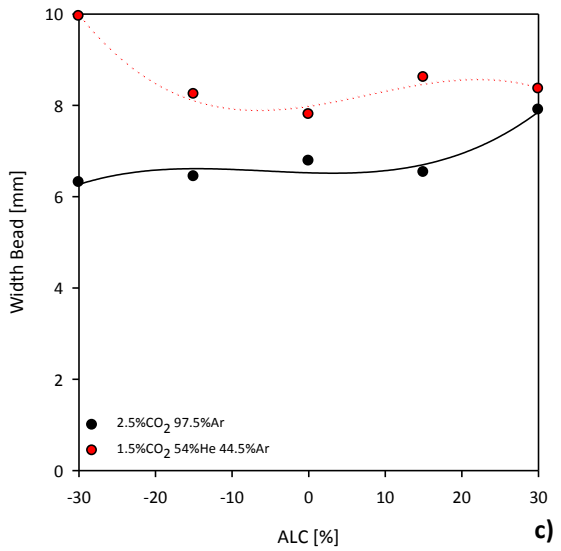
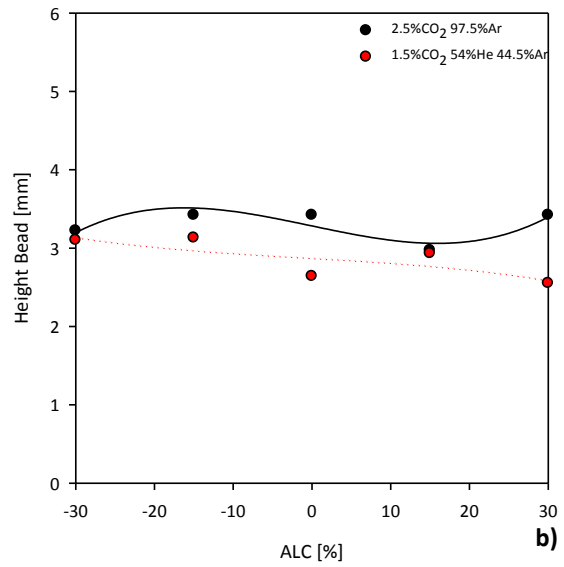
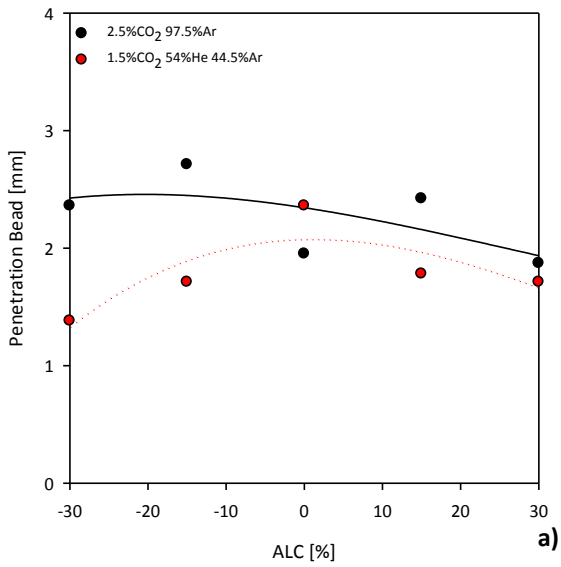


Figure X.47 – Effect of arc length correction (ALC) on bead shape characteristics for CMT-P, at different shielding gases: a) penetration bead; b) height bead; c) width bead; and d) height to width ratio.

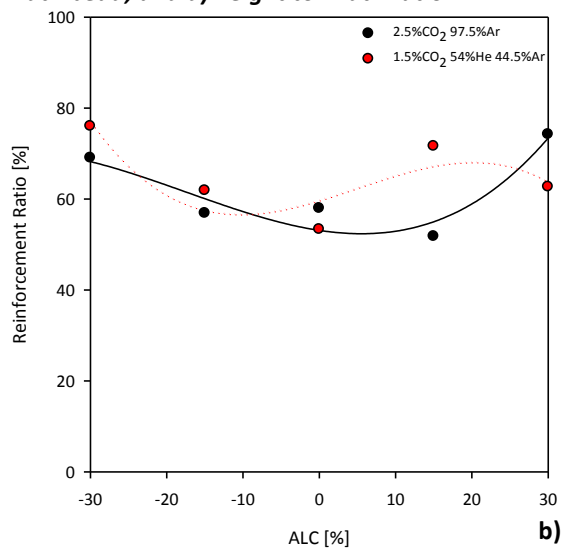
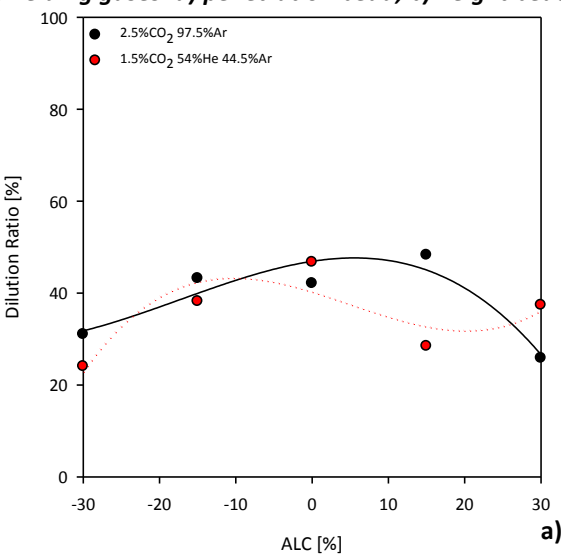


Figure X.48 – Effect of arc length correction (ALC) on dilution ratio (a) and reinforcement ratio (b) for CMT-P at different shielding gases.

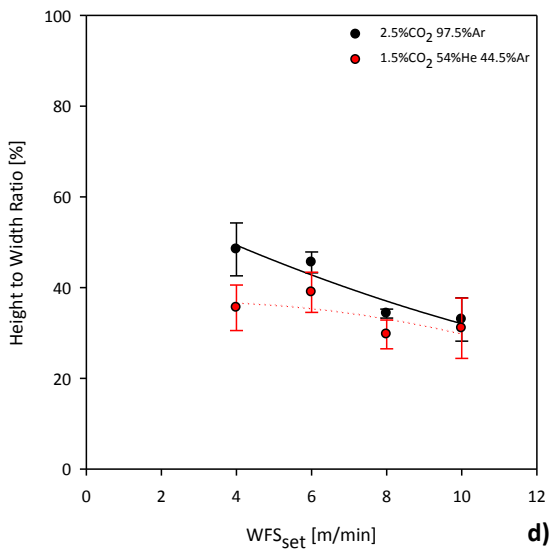
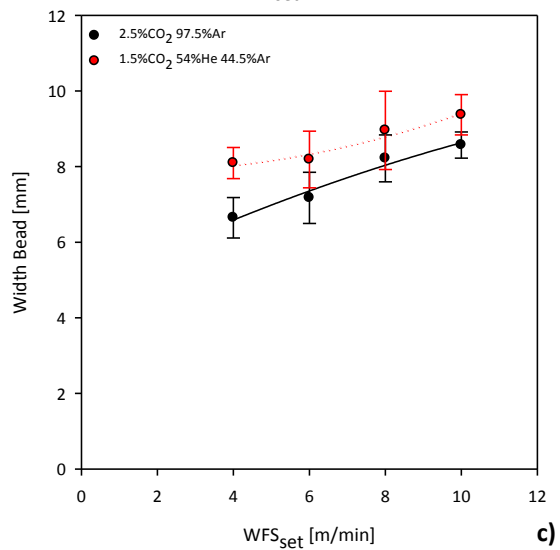
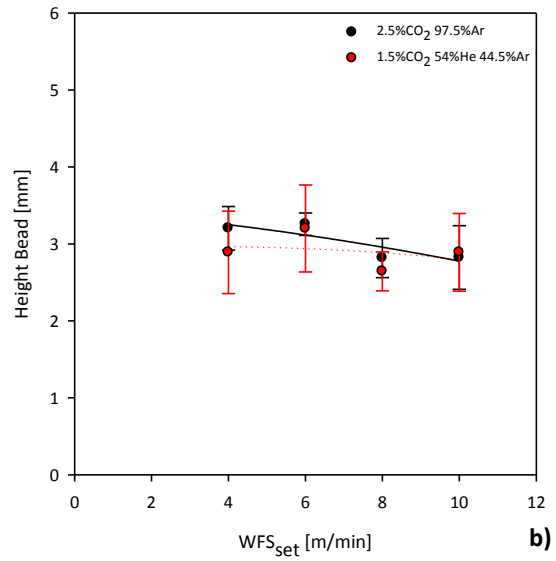
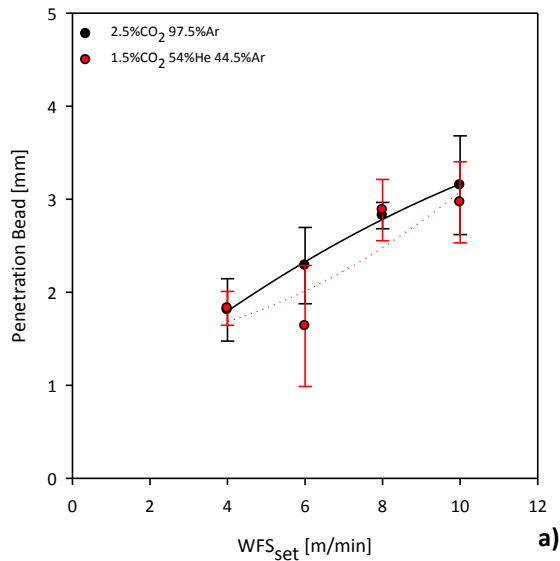


Figure X.49 – Effect of the variation of CTWD on bead shape characteristics for CMT-P, at different WFS levels and shielding gases: a) penetration bead; b) height bead; c) width bead; and d) height to width ratio.

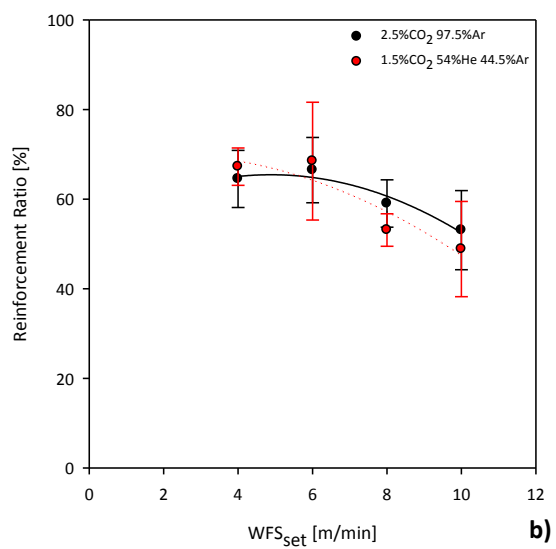
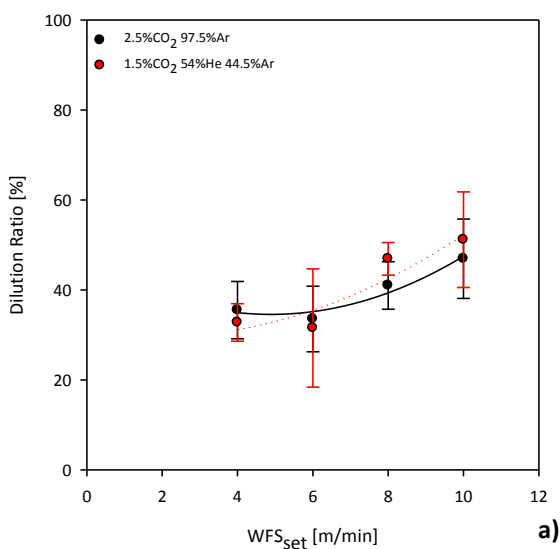


Figure X.50 – Effect of the variation of CTWD on dilution ratio (a) and reinforcement ratio (b) for CMT-P, at different WFS levels and shielding gases.

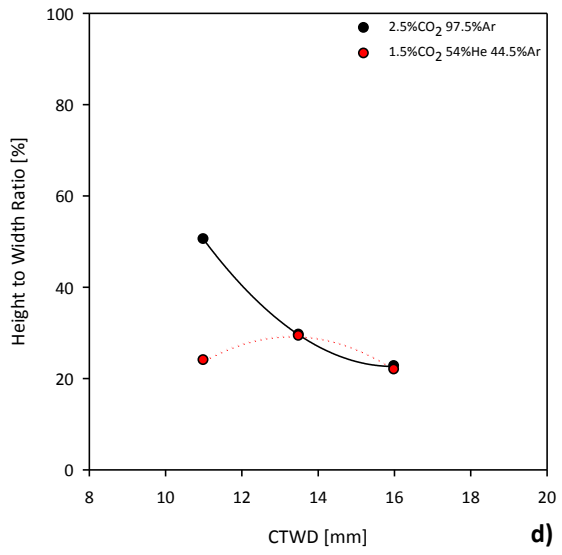
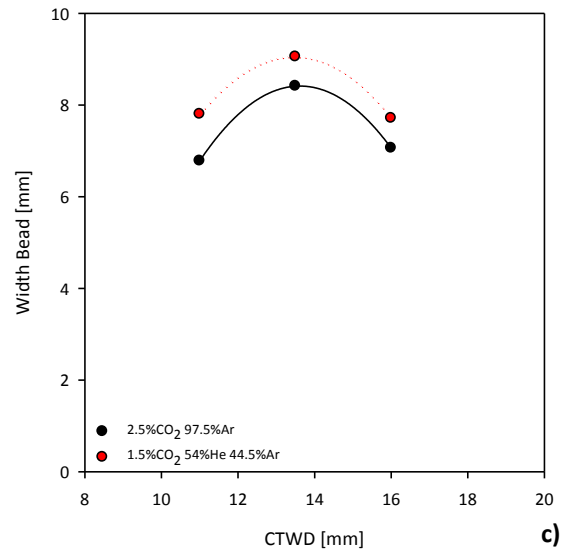
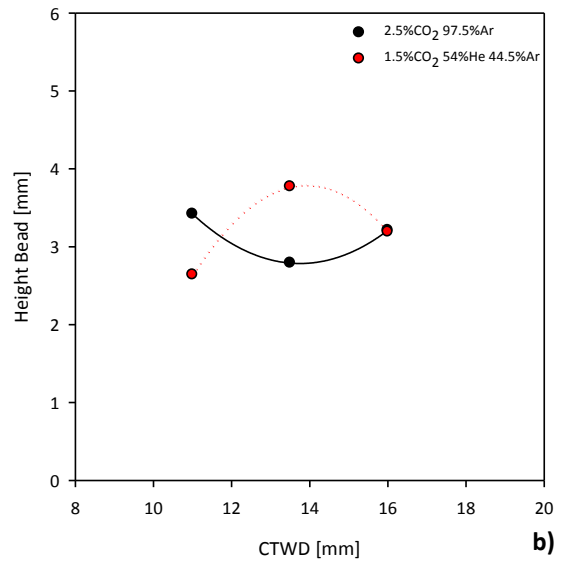
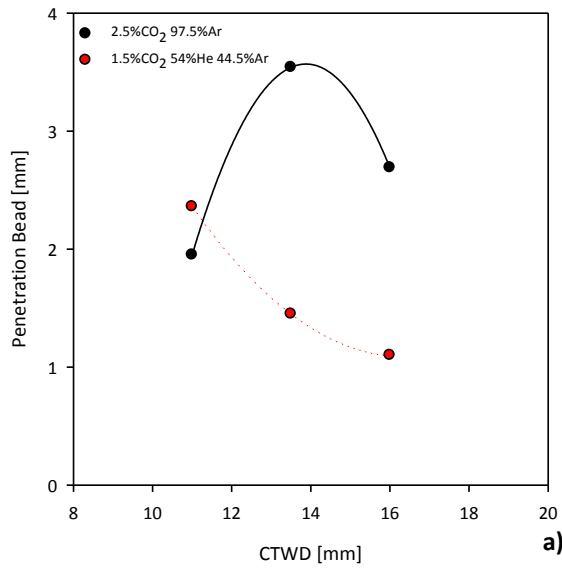


Figure X.51 – Effect of CTWD on bead shape characteristics for CMT-P at different shielding gases: a) penetration bead; b) height bead; c) width bead; and d) height to width ratio.

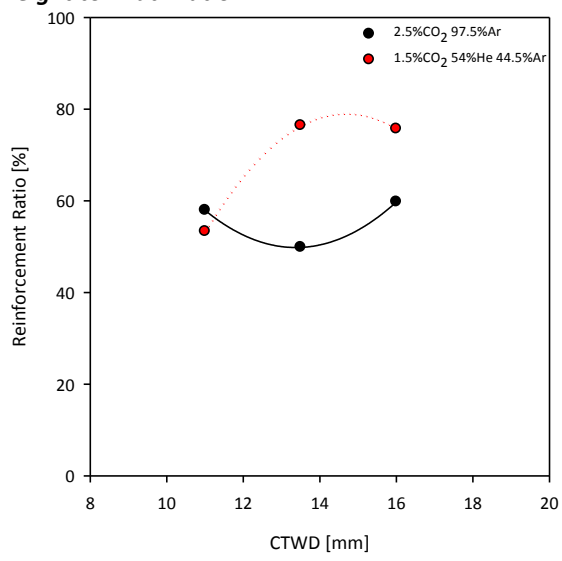
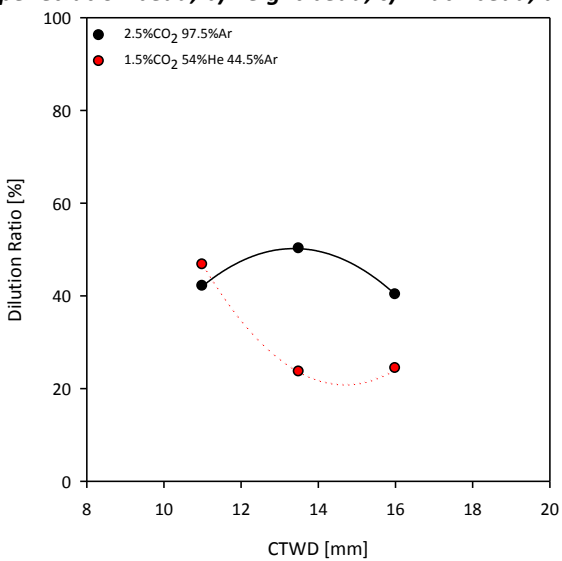


Figure X.52 – Effect of CTWD on dilution ratio (a) and reinforcement ratio (b) for CMT-P, at different shielding gases.

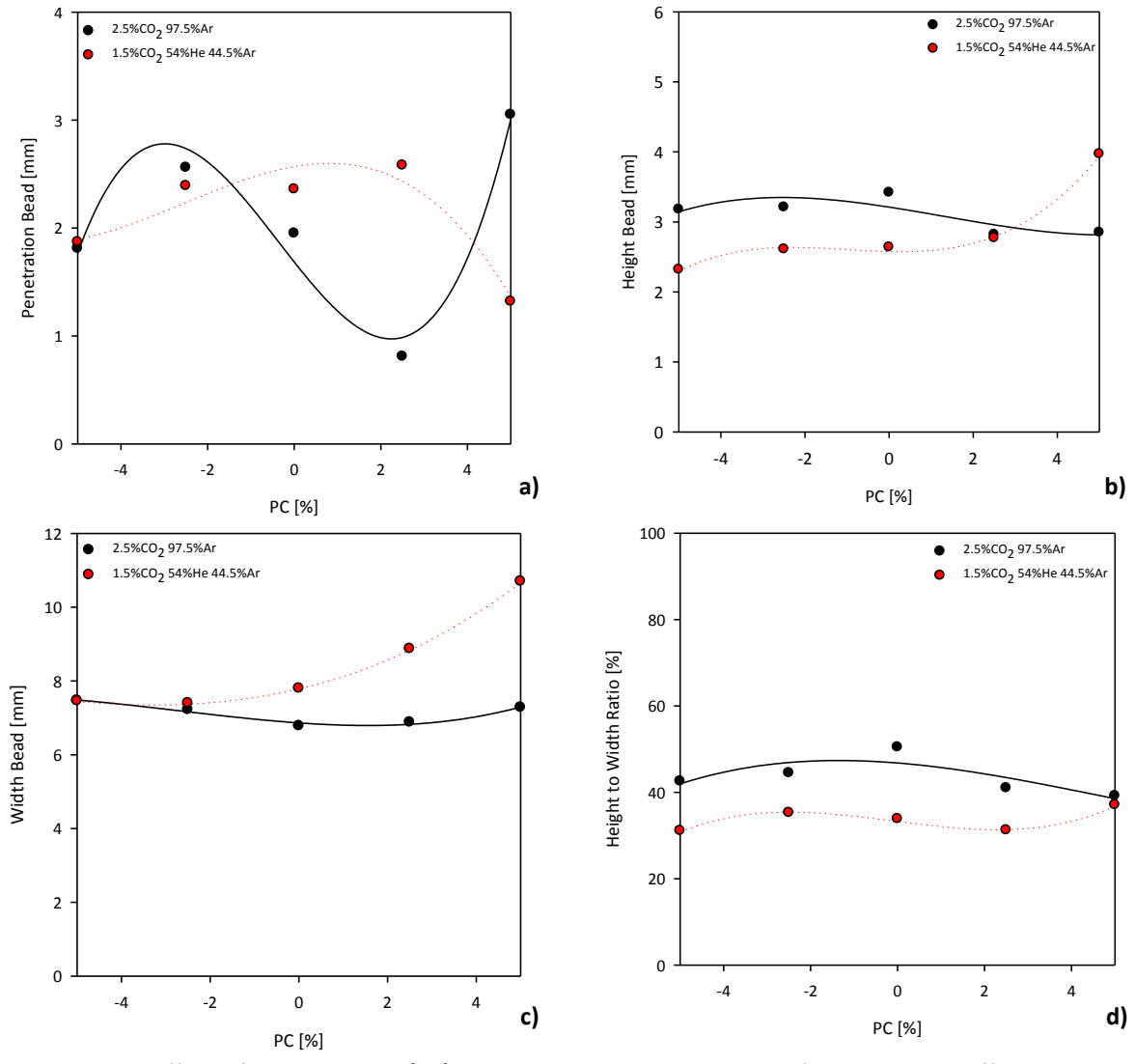


Figure X.53 – Effect of pulse control (PC) on bead shape characteristics for CMT-P, at different shielding gases: a) penetration bead; b) height bead; c) width bead; and d) height to width ratio.

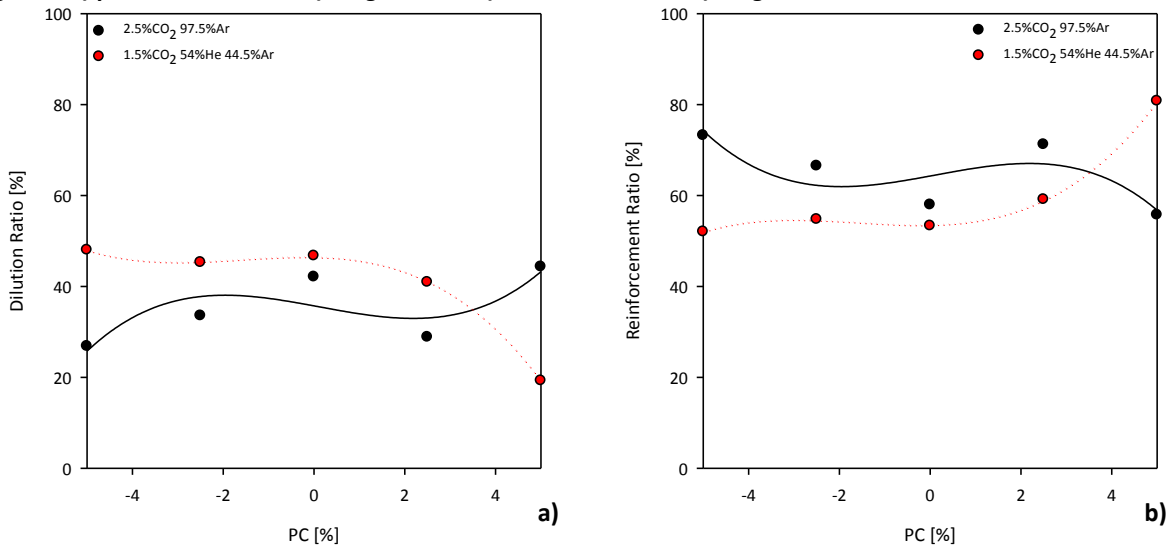


Figure X.54 – Effect of pulse control (PC) on dilution ratio (a) and reinforcement ratio (b) for CMT-P, at different shielding gases.

X.6. Characterization of Bead Shape Characteristics for FastROOT

The effect of WFS on the bead shape characteristics was also investigated for FastROOT using different WFS/TS ratios and shielding gases. The results are presented in the Figure X.55 and X.56.

The effect of base current (BC) was evaluated for FastROOT in terms of the variation of bead shape characteristics, at different WFS levels and shielding gases, and its effect on them at constant WFS (6m/min). The results are illustrated from Figure X.57 to X.60.

The effect of CTWD was also evaluated for FastROOT in a similar way as was performed for BC. The results are shown from Figure X.61 to X.64.

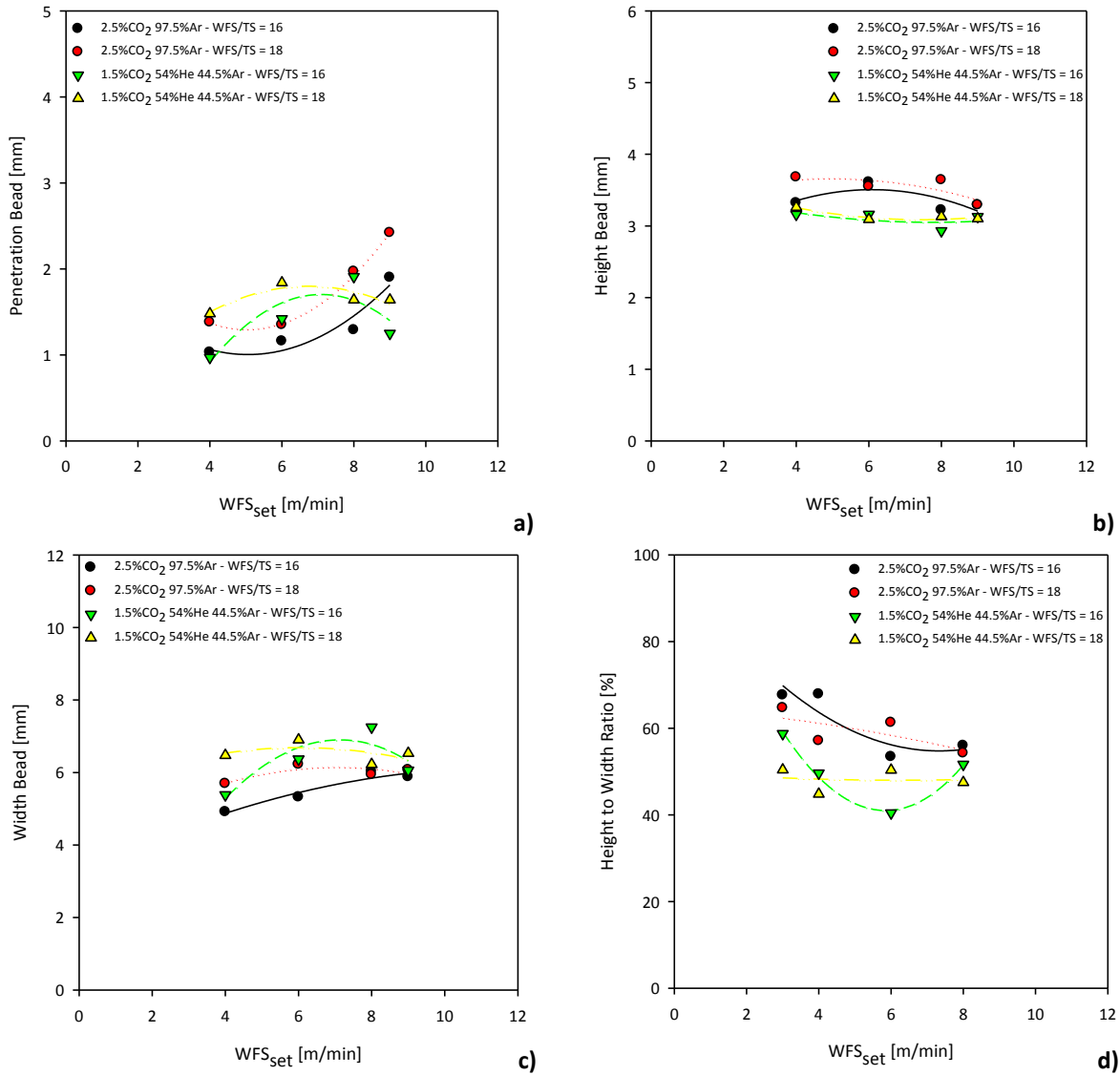


Figure X.55 – Effect of WFS on bead shape characteristics for FastROOT, at different WFS/TS ratios and shielding gases: a) penetration bead; b) height bead; c) width bead; and d) height to width ratio.

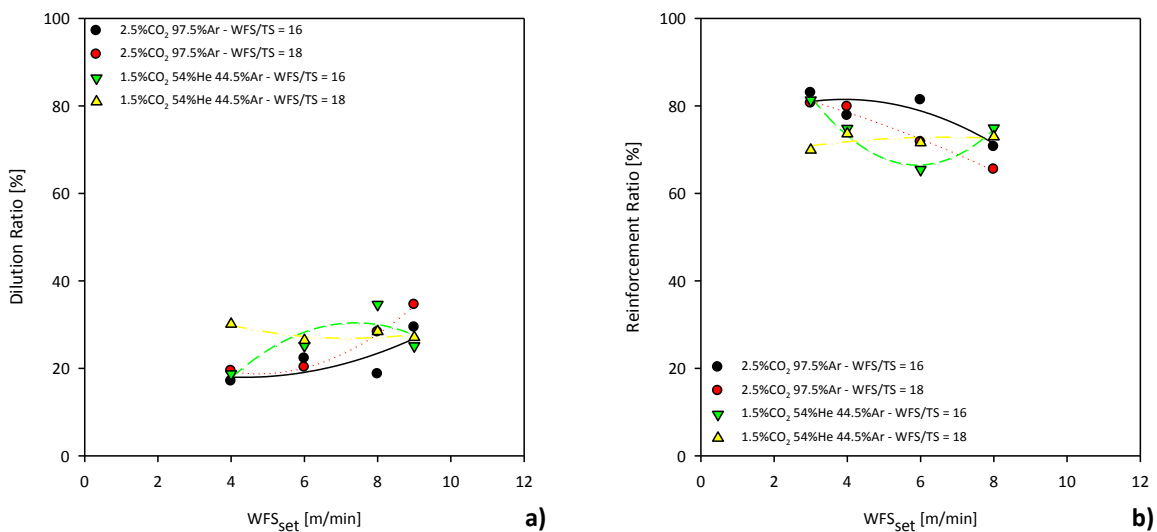


Figure X.56 – Effect of WFS, at different WFS/TS ratios and shielding gas composition, on bead shape characteristics for FastROOT: a) dilution ratio; and b) reinforcement ratio.

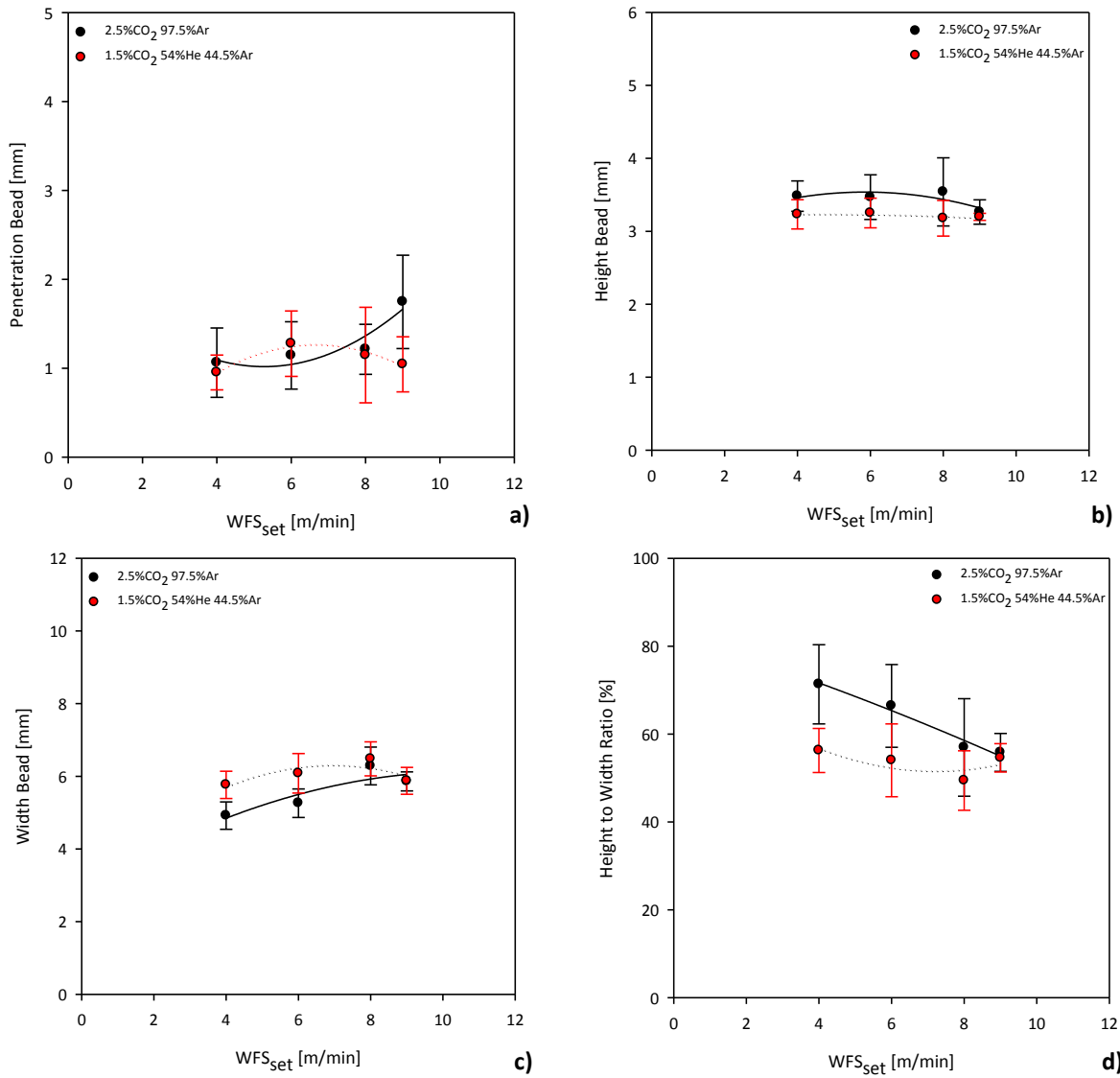


Figure X.57 – Effect of the variation of base current (BC) on bead shape characteristics for FastROOT, at different WFS levels and shielding gases: a) penetration bead; b) height bead; c) width bead; and d) height to width ratio.

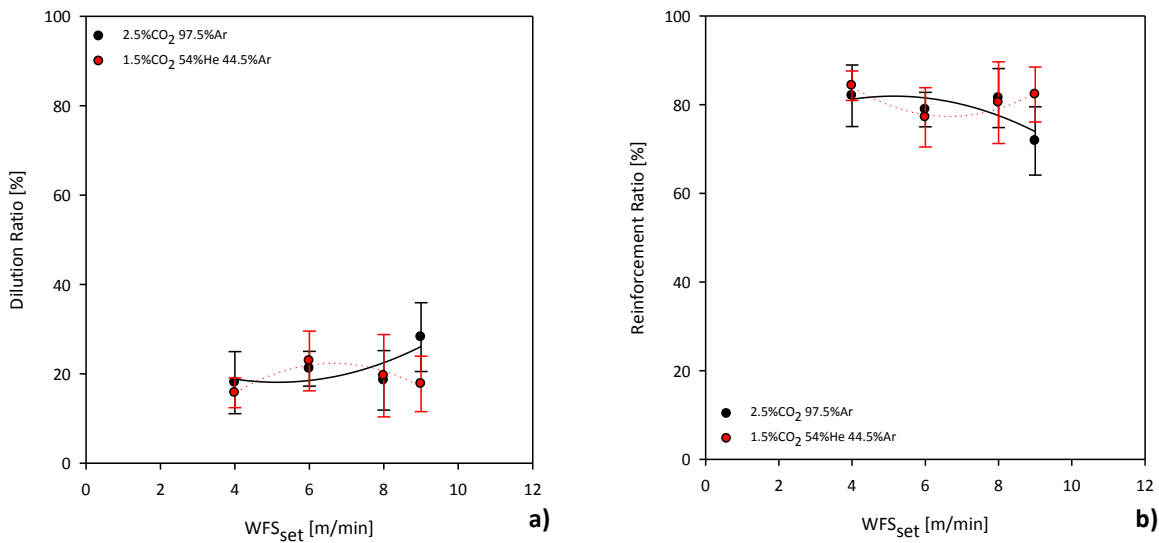


Figure X.58 – Variation of dilution ratio (a) and reinforcement ratio (b) with base current (BC) for FastROOT, at different WFS levels and shielding gases.

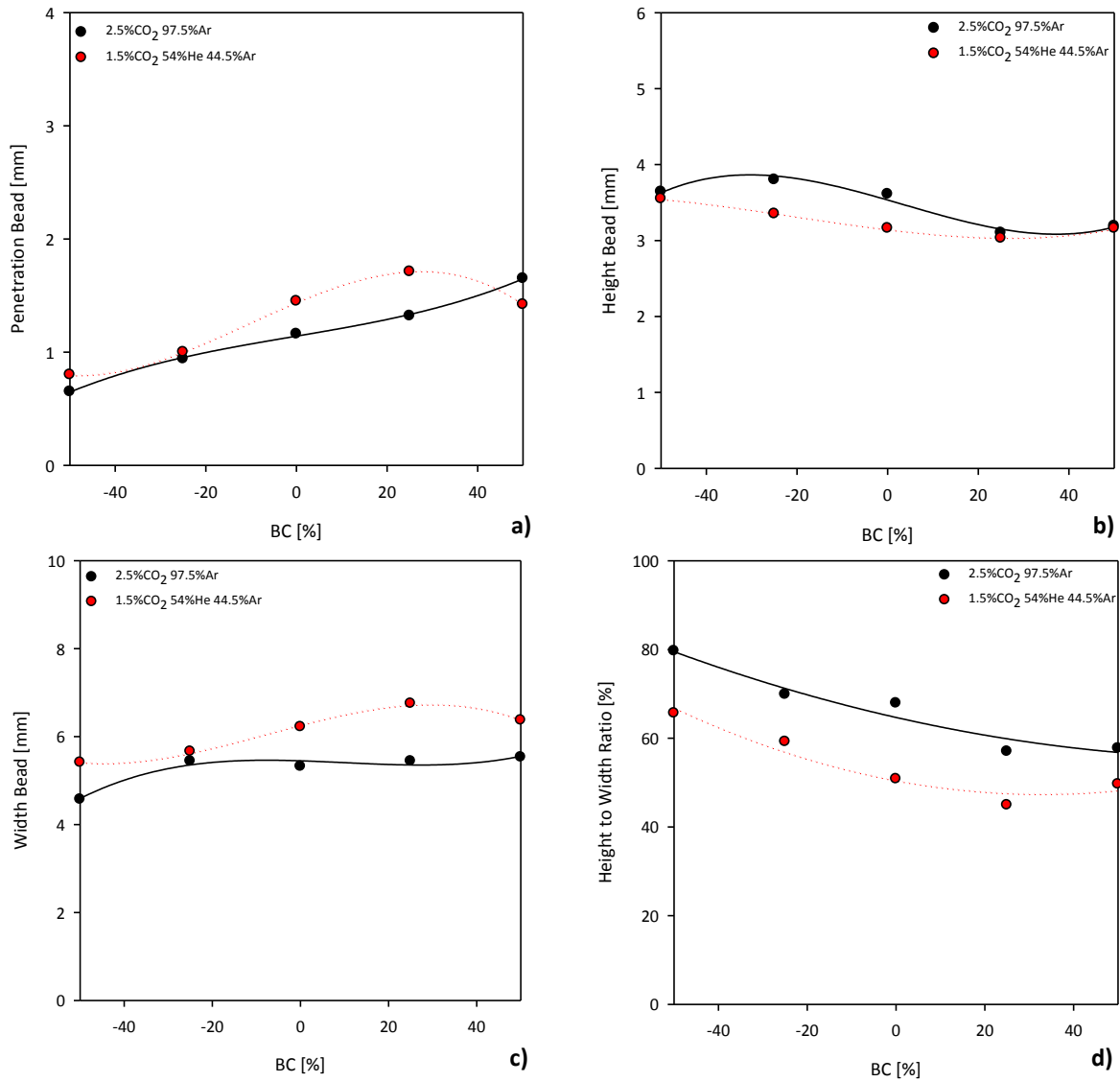


Figure X.59 – Effect of base current (BC) on bead shape characteristics for FastROOT, at different shielding gases: a) penetration bead; b) height bead; c) width bead; and d) height to width ratio.

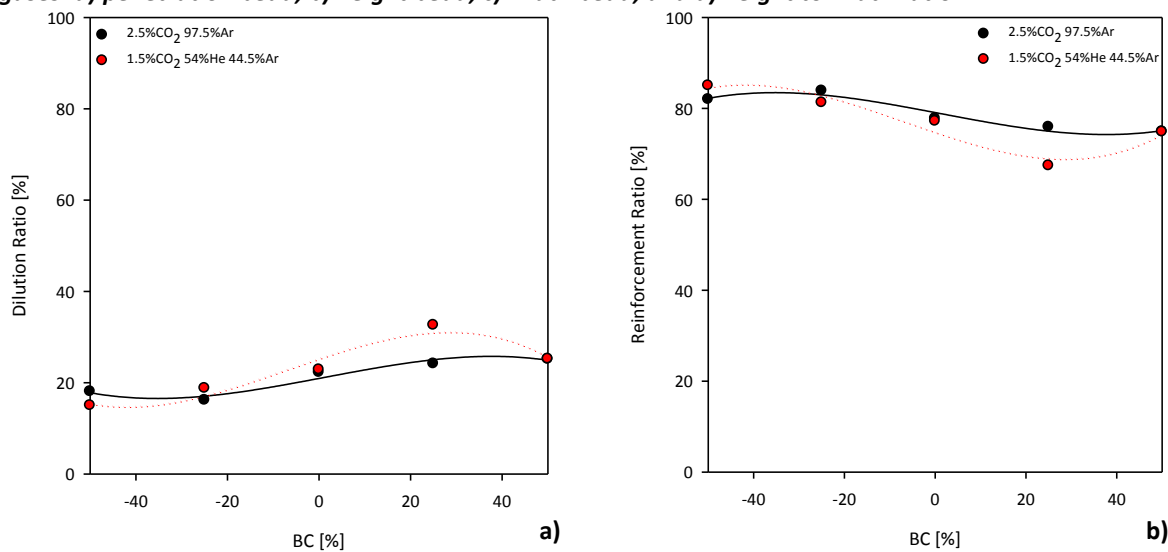


Figure X.60 – Effect of base current (BC) on dilution ratio (a) and reinforcement ratio (b) for FastROOT, at different shielding gases.

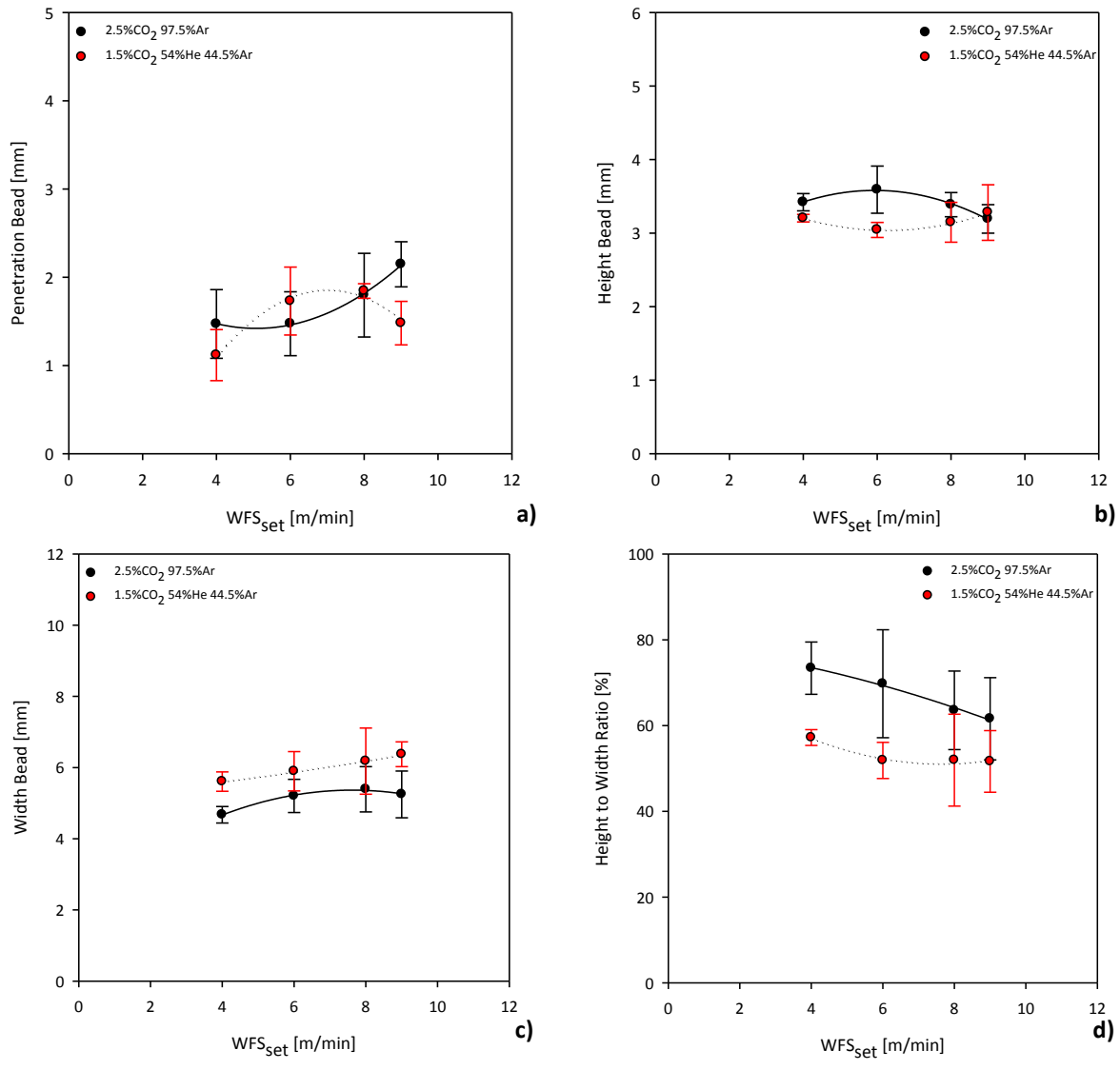


Figure X.61 – Effect of the variation of CTWD on bead shape characteristics for FastROOT, at different WFS levels and shielding gases: a) penetration bead; b) height bead; c) width bead; and d) height to width ratio.

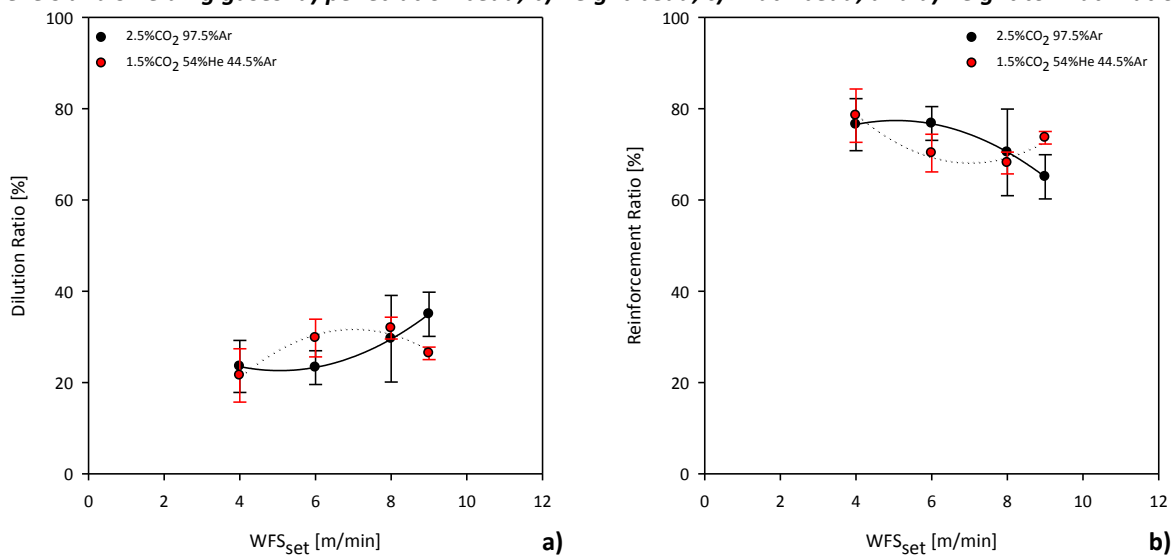


Figure X.62 – Effect of the variation of CTWD on dilution ratio (a) and reinforcement ratio (b) for FastROOT, at different WFS levels and shielding gases.

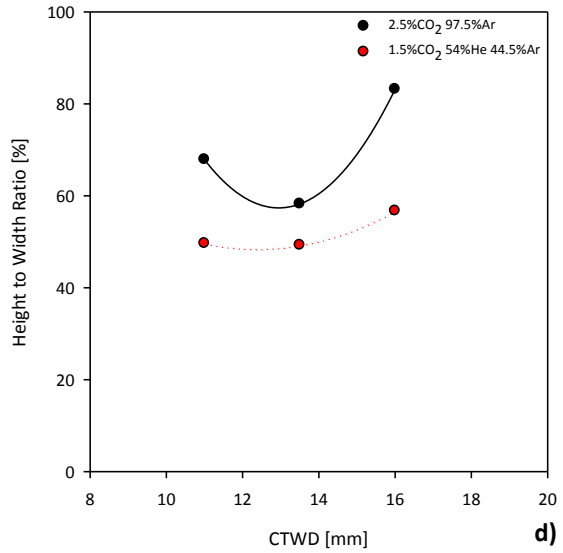
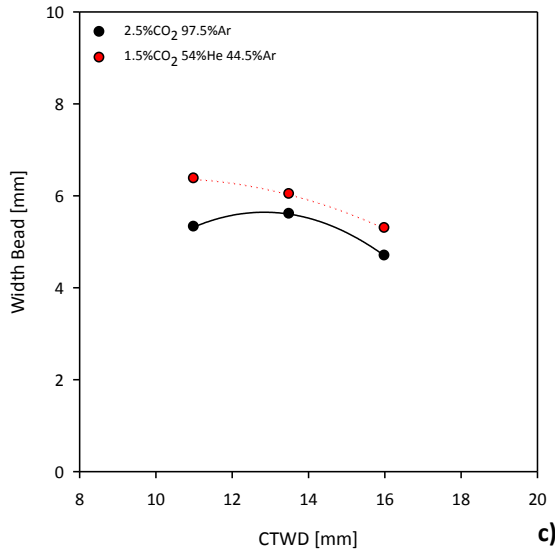
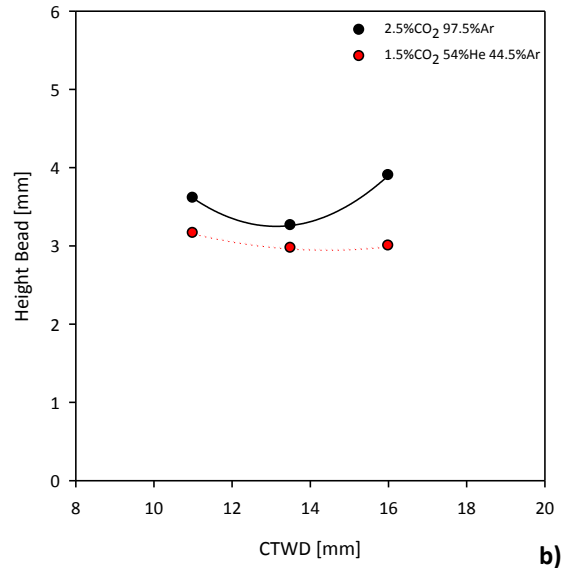
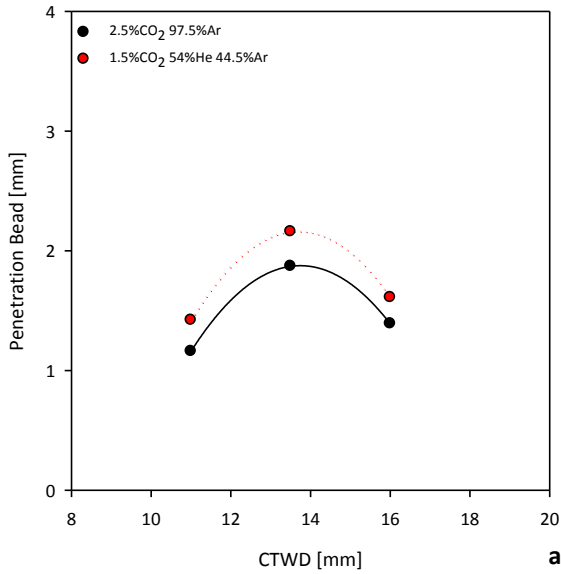


Figure X.63 – Effect of CTWD on bead shape characteristics for FastROOT, at different shielding gases: a) penetration bead; b) height bead; c) width bead; and d) height to width ratio.

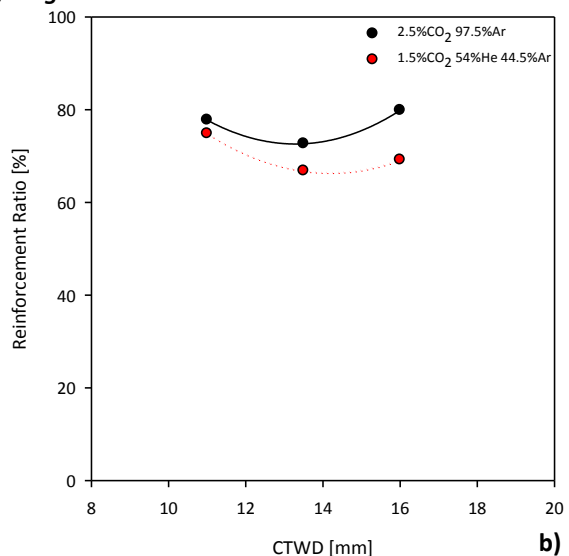
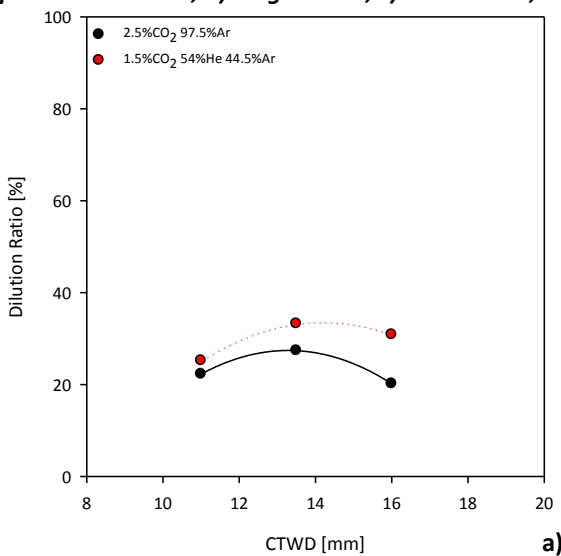


Figure X.64 – Effect of CTWD on dilution ratio (a) and reinforcement ratio (b) for FastROOT, at different shielding gases.

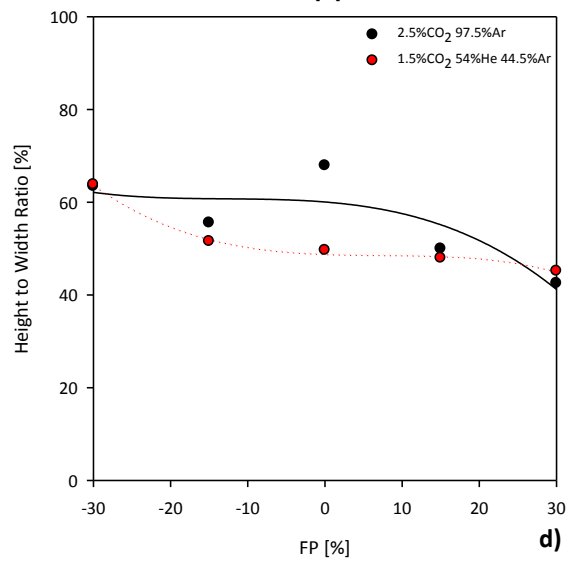
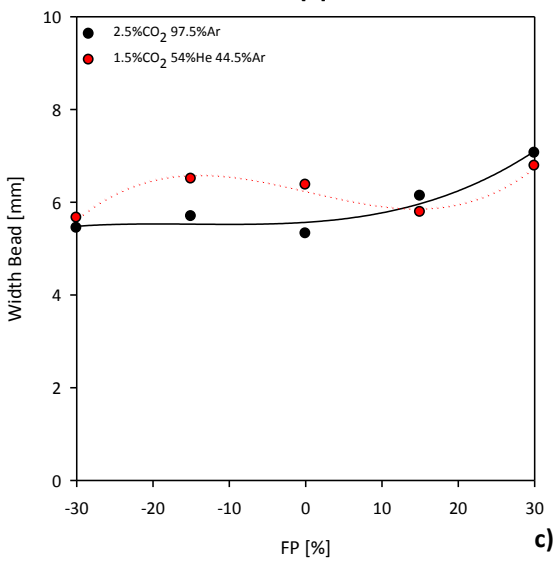
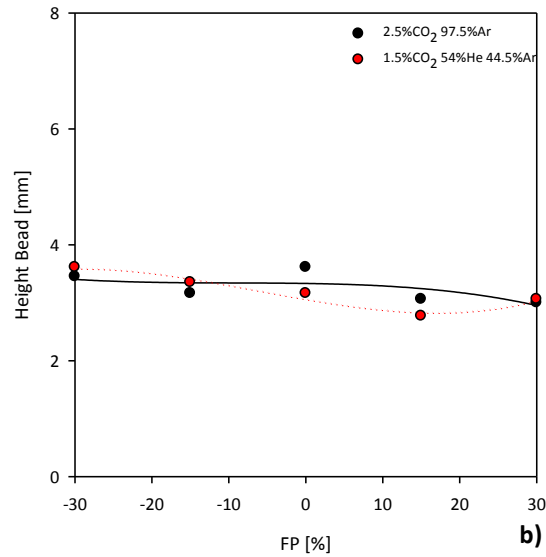
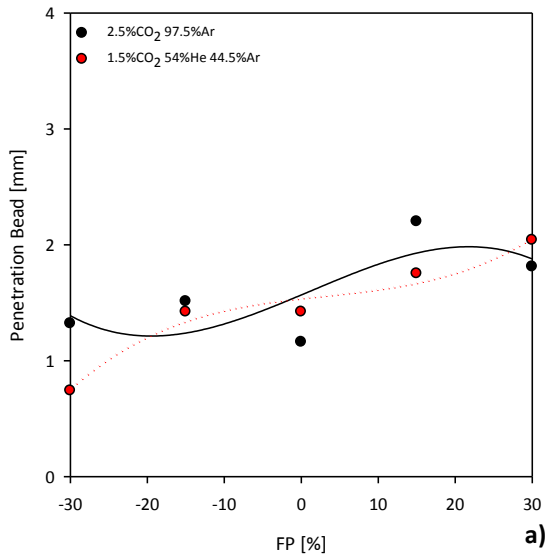


Figure X.65 – Effect of forming pulse (FP) on bead shape characteristics for FastROOT, at different shielding gases: a) penetration bead; b) height bead; c) width bead; and d) height to width ratio.

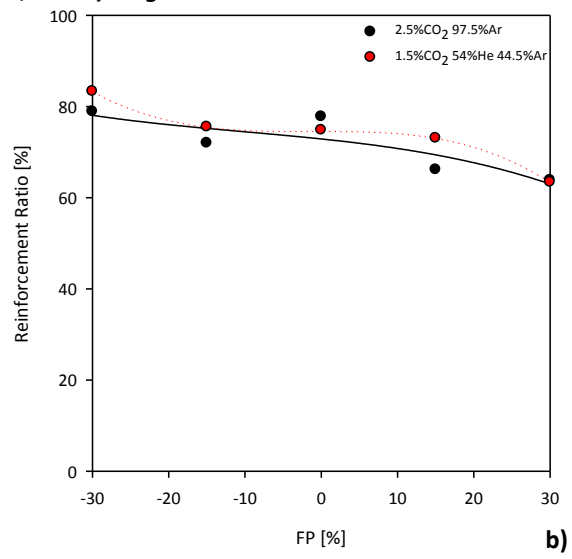
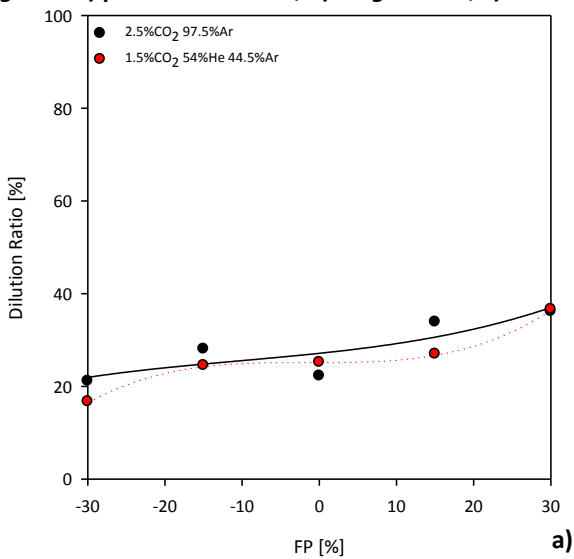


Figure X.66 – Effect of forming pulse (FP) on dilution ratio (a) and reinforcement ratio (b) for FastROOT, at different shielding gases.

XI. RESULTS OF BEAD SHAPE CHARACTERISTICS OBTAINED FOR NARROW GROOVE WELDING

Table XI.1 – Responses measured from the narrow groove welds and applied to the model analysis for GMAW-P using 2.5%CO₂ 97.5%Ar.

Run	WFS [m/min]	WFS/TS Ratio	Depth of Penetration [mm]	Height Ratio	Root Width [mm]	Top Width [mm]	Dilution Ratio [%]
PG1	4	23.5	-1.49	0.798	0.00	6.12	12.4
PG2	6	27.3	1.55	0.841	2.31	6.12	36.6
PG3	6	26.1	0.75	0.767	2.33	6.21	30.0
PG4	6	24.0	0.80	0.741	2.59	6.02	30.6
PG5	6	22.2	0.58	0.772	2.03	5.88	31.1
PG6	6	20.0	0.68	0.760	1.98	5.67	36.5
PG7	6	18.2	0.44	0.576	1.82	4.86	39.2
PG8	6	15.8	0.15	0.716	1.31	5.58	36.8
PG9	6	14.0	-0.73	0.771	0.00	5.58	23.7
PG10	8	18.2	0.39	0.606	3.71	5.53	46.2
PG11	8	16.0	0.02	0.707	3.08	5.09	40.2
PG12	8	14.0	0.27	0.694	2.55	4.74	36.9
PG13	8	10.0	-0.20	0.783	0.00	4.83	38.3
PG14	8	8.0	-0.65	0.783	0.00	4.88	47.1
PG15	10	20.0	0.70	0.789	3.69	5.88	41.7
PG16	10	17.9	0.53	0.770	3.60	5.67	30.2
PG17	10	15.9	0.65	0.801	2.34	5.49	38.1
PG18	10	14.1	0.53	0.688	2.57	5.18	38.5
PG19	10	12.0	0.12	0.596	1.38	4.55	55.5
PG20	10	12.0	0.10	0.742	1.63	4.62	41.2
PG21	10	10.0	0.07	0.710	1.28	4.67	35.8
PG22	10	8.0	-0.44	0.750	0.00	4.65	49.1

Figure XI.1 – Responses measured from the narrow groove welds and applied to the model analysis for GMAW-P using 1.5%CO₂, 54%He 44.5%Ar.

Run	WFS [m/min]	WFS/TS Ratio	Depth of Penetration [mm]	Height Ratio	Root Width [mm]	Top Width [mm]	Dilution Ratio [%]
PG23	4	23.5	-1.21	0.852	0.00	5.84	8.0
PG24	6	15.8	0.41	0.688	2.36	5.11	35.7
PG25	6	14.0	0.34	0.621	1.98	4.65	37.9
PG26	6	12.0	0.53	0.777	2.43	5.84	42.5
PG27	6	10.0	-0.41	0.771	0.00	5.02	27.6
PG28	8	22.2	0.56	0.734	4.34	5.56	38.5
PG29	8	22.2	1.02	0.809	4.65	6.00	49.5
PG30	8	18.2	0.44	0.851	3.25	5.77	36.1
PG31	8	16.0	0.39	0.830	2.80	5.60	38.1
PG32	8	14.0	0.44	0.784	2.90	5.39	41.9
PG33	8	11.9	0.31	0.817	2.08	5.51	33.9
PG34	8	11.6	0.41	0.783	1.96	5.37	27.5
PG35	8	10.0	-0.39	0.664	0.00	5.14	30.1
PG36	8	8.0	-0.75	0.796	0.00	4.55	34.5
PG37	10	22.2	0.82	0.786	4.18	5.70	40.8
PG38	10	20.0	0.90	0.648	3.69	5.77	40.3
PG39	10	20.0	0.90	0.712	3.76	5.77	40.1
PG40	10	14.1	0.68	0.830	2.59	5.04	27.2
PG41	10	14.1	0.63	0.845	2.59	5.42	25.7
PG42	10	12.0	0.27	0.929	1.91	5.18	32.2

Table XI.2 - Responses measured from the narrow groove welds and applied to the model analysis for RapidArc using 2.5%CO₂ 97.5%Ar.

Run	WFS [m/min]	WFS/TS Ratio	Depth of Penetration [mm]	Height Ratio	Root Width [mm]	Top Width [mm]	Dilution Ratio [%]
PR1	8	16.0	0.08	0.306	3.56	4.19	50.7
PR2	8	10.0	0.00	0.340	2.09	3.38	44.0
PR3	8	8.0	0.13	0.723	1.28	2.59	57.1
PR4	8	6.0	-0.55	0.275	0.00	2.41	7.7
PR5	9	18.0	0.00	0.426	2.78	4.81	41.9
PR6	9	18.0	0.03	0.533	3.88	5.31	55.7
PR7	9	16.1	0.36	1.104	3.78	6.34	23.8
PR8	9	10.0	0.02	1.318	2.34	5.34	53.6
PR9	9	8.0	0.00	0.821	2.09	5.03	59.6
PR10	9	6.0	-0.49	0.892	0.00	4.56	58.5
PR11	10	15.9	0.01	0.448	3.59	4.87	48.0
PR12	10	10.0	0.23	0.672	2.57	4.56	50.9
PR13	10	8.0	0.01	1.132	1.88	4.81	43.6
PR14	10	6.0	-0.62	0.731	0.00	4.34	62.1

Table XI.3 – Responses measured from the narrow groove welds and applied to the model analysis for RapidArc using 1.5%CO₂ 54%He 44.5%Ar.

Run	WFS [m/min]	WFS/TS Ratio	Depth of Penetration [mm]	Height Ratio	Root Width [mm]	Top Width [mm]	Dilution Ratio [%]
PR15	6	24.0	0.01	1.173	5.31	7.28	41.8
PR16	6	18.2	0.01	0.409	3.41	3.97	37.4
PR17	6	14.0	0.01	0.420	2.81	4.81	46.9
PR18	6	12.0	0.08	0.421	2.22	4.57	47.4
PR19	6	10.0	-0.68	0.171	0.00	1.82	18.1
PR20	8	18.2	0.01	1.375	4.25	6.53	54.1
PR21	8	16.0	0.12	0.430	3.75	3.87	37.5
PR22	8	16.0	-0.05	1.386	3.85	6.59	50.5
PR23	8	16.0	0.00	1.525	3.16	6.50	47.6
PR24	8	11.9	0.00	0.601	3.00	5.41	57.4
PR25	8	10.0	0.16	0.453	2.06	4.81	36.0
PR26	8	8.0	0.02	0.482	1.50	4.22	60.0
PR27	8	6.0	-0.65	0.505	0.00	3.09	38.2
PR28	9	18.0	0.15	0.745	5.32	5.81	48.0
PR29	9	18.0	-0.18	1.031	5.19	6.00	49.8
PR30	9	16.1	0.00	0.653	3.50	5.63	55.7
PR31	9	14.1	-0.10	1.306	3.75	5.88	55.9
PR32	9	10.0	0.14	1.401	2.85	4.84	57.9
PR33	9	8.0	0.19	0.787	1.60	4.94	45.5
PR34	9	6.0	0.01	1.136	0.91	5.00	46.4
PR35	10	20.0	0.00	0.964	6.13	6.19	57.4
PR36	10	15.9	0.07	0.731	4.78	5.63	51.3
PR37	10	14.1	0.08	0.865	4.88	5.41	56.0
PR38	10	10.0	0.16	1.221	3.19	5.66	50.1
PR39	10	8.0	0.02	1.176	2.16	5.44	39.8
PR40	10	6.0	-0.39	1.007	0.00	4.88	45.7

Table XI.4 - Responses measured from the narrow groove welds and applied to the model analysis for STT using 2.5%CO₂ 97.5%Ar.

Run	WFS [m/min]	WFS/TS Ratio	Depth of Penetration [mm]	Height Ratio	Root Width [mm]	Top Width [mm]	Dilution Ratio [%]
PS1	4	23.5	0.91	0.541	2.00	5.25	26.3
PS2	4	22.2	-1.49	0.703	0.00	5.88	8.3
PS3	4	22.2	-1.43	0.735	0.00	5.97	4.7
PS4	4	16.0	-1.50	0.739	0.00	5.66	7.0
PS5	4	14.8	-1.50	0.661	0.00	5.34	6.3
PS6	6	30.0	0.65	0.676	4.94	6.38	38.5
PS7	6	30.0	0.97	0.823	1.47	6.22	24.3
PS8	6	26.1	0.49	0.736	1.06	6.00	21.0
PS9	6	24.0	-0.84	0.733	0.00	5.84	13.9
PS10	8	24.2	0.94	0.772	2.47	5.88	28.0
PS11	8	20.0	0.49	0.778	1.56	5.94	27.3
PS12	8	18.2	0.03	0.805	1.12	5.81	20.7
PS13	8.26	24.3	0.78	0.696	2.59	5.53	27.9
PS14	8.26	21.7	0.49	0.813	1.53	5.97	21.2
PS15	8.26	20.1	0.36	0.737	1.81	5.78	27.8

Table XI.5 – Responses measured from the narrow groove welds and applied to the model analysis for STT using 1.5%CO₂ 54%He 44.5%Ar.

Run	WFS [m/min]	WFS/TS Ratio	Depth of Penetration [mm]	Height Ratio	Root Width [mm]	Top Width [mm]	Dilution Ratio [%]
PS16	4	23.5	1.00	0.777	2.59	5.91	28.9
PS17	4	22.2	0.81	0.757	2.72	5.81	31.3
PS18	4	20.0	-1.51	0.736	0.00	5.84	11.1
PS19	6	24.0	0.75	0.730	2.41	5.91	23.0
PS20	6	22.2	-1.17	0.634	0.00	5.78	21.0
PS21	6	22.2	-1.04	0.770	0.00	5.88	19.6
PS22	8	23.5	1.13	0.733	3.56	5.63	33.6
PS23	8	20.0	0.78	0.734	2.84	5.72	46.5
PS24	8	18.2	0.42	0.678	2.19	5.38	31.1
PS25	8	16.0	0.40	0.807	2.03	5.47	34.1
PS26	8	14.0	-0.65	1.133	0.00	4.72	28.1
PS27	8.26	15.9	0.05	1.449	1.31	5.34	38.2
PS28	8.26	14.0	-0.01	0.754	0.44	5.25	31.5
PS29	8.26	12.0	-0.41	0.794	0.00	5.37	29.0

Table XI.6 - Responses measured from the narrow groove welds and applied to the model analysis for CMT using 2.5%CO₂ 97.5%Ar.

Run	WFS [m/min]	WFS/TS Ratio	Depth of Penetration [mm]	Height Ratio	Root Width [mm]	Top Width [mm]	Dilution Ratio [%]
PC1	4	22.2	-1.39	0.260	0.00	3.92	6.9
PC2	6	24.0	0.48	0.395	2.15	4.57	28.8
PC3	6	20.0	0.42	0.432	1.87	3.92	25.1
PC4	6	18.2	0.39	0.353	1.56	3.61	25.1
PC5	6	15.8	0.29	0.435	1.21	3.67	23.6
PC6	6	14.0	-0.19	0.362	0.00	3.20	24.5
PC7	8	24.2	0.90	0.543	3.61	5.10	55.1
PC8	8	20.0	0.23	0.440	2.80	5.10	45.7
PC9	8	16.0	0.20	0.557	2.27	4.91	46.0
PC10	8	11.9	0.19	0.582	1.37	5.04	23.3
PC11	8	10.0	-0.20	0.589	0.00	3.98	25.0

Table XI.7 – Responses measured from the narrow groove welds and applied to the model analysis for CMT using 1.5%CO₂ 54%He 44.5%Ar.

Run	WFS [m/min]	WFS/TS Ratio	Depth of Penetration [mm]	Height Ratio	Root Width [mm]	Top Width [mm]	Dilution Ratio [%]
PC12	3	15.8	-1.13	0.143	0.00	3.64	14.7
PC13	4	22.2	-1.26	0.085	0.00	3.58	9.7
PC14	6	26.1	0.02	0.296	1.83	4.69	37.1
PC15	6	24.0	0.01	0.280	1.65	3.98	34.5
PC16	6	22.2	0.07	0.442	1.90	5.19	31.9
PC17	6	20.0	0.05	0.344	1.77	4.39	29.4
PC18	6	18.2	0.29	0.338	1.59	3.76	24.9
PC19	6	15.8	0.01	0.484	1.08	3.82	61.0
PC20	8	24.2	1.06	0.905	2.74	6.22	22.7
PC21	8	20.0	0.58	0.661	3.26	5.07	56.5
PC22	8	16.0	0.32	0.729	1.87	5.19	50.6
PC23	8	11.9	0.23	0.679	1.49	5.41	38.2
PC24	8	10.0	0.06	0.601	0.56	4.51	48.8

Table XI.8 - Responses measured from the narrow groove welds and applied to the model analysis for CMT-P using 2.5%CO₂ 97.5%Ar.

Run	WFS [m/min]	WFS/TS Ratio	Depth of Penetration [mm]	Height Ratio	Root Width [mm]	Top Width [mm]	Dilution Ratio [%]
PP1	4	22.22	0.39	0.52	2.97	5.00	37.7
PP2	4	18.18	0.52	0.28	1.84	2.72	18.4
PP3	4	13.79	0.22	0.31	1.12	2.62	18.2
PP4	4	12.12	0.23	0.42	1.44	3.22	23.0
PP5	6	22.22	0.23	0.81	3.47	6.00	39.9
PP6	6	18.18	0.11	0.55	3.44	4.72	51.3
PP7	6	12.00	0.24	0.41	2.06	3.19	23.1
PP8	6	8.57	0.23	0.45	1.09	2.16	44.8
PP9	6	8.00	-0.55	0.29	0.00	2.34	11.5
PP10	8	16.00	0.00	1.27	2.84	5.97	36.0
PP11	8	8.00	0.23	0.57	0.94	2.38	48.9
PP12	8	6.02	-0.52	0.43	0.00	2.95	37.7
PP13	9	18.00	0.00	0.46	3.31	4.91	42.0
PP14	9	12.00	0.01	1.26	2.44	5.56	49.3
PP15	9	7.96	0.12	0.54	1.56	3.94	29.9
PP16	9	6.00	-0.25	0.52	0.00	2.75	32.8
PP17	10	20.00	0.00	1.11	4.28	7.22	49.0
PP18	10	12.05	0.40	0.54	2.97	4.63	42.4
PP19	10	10.00	-0.28	0.46	0.00	2.03	40.8
PP20	10	8.00	-1.20	0.30	0.00	5.53	17.4

Table XI.9 – Responses measured from the narrow groove welds and applied to the model analysis for CMT-P using 1.5%CO₂ 54%He 44.5%Ar.

Run	WFS [m/min]	WFS/TS Ratio	Depth of Penetration [mm]	Height Ratio	Root Width [mm]	Top Width [mm]	Dilution Ratio [%]
PP21	4	22.2	0.12	0.35	3.00	4.44	30.5
PP22	4	13.8	0.23	0.31	1.38	2.53	21.7
PP23	4	12.1	-0.84	0.33	0.00	3.31	19.0
PP24	6	22.2	-0.02	1.39	3.50	6.31	44.2
PP25	6	18.2	0.01	1.22	3.38	5.97	43.2
PP26	6	12.0	0.44	0.48	2.50	3.00	45.2
PP27	6	10.0	0.32	0.45	1.69	2.63	43.1
PP28	6	8.0	0.02	0.58	0.82	2.47	53.2
PP29	8	16.0	-0.01	1.11	3.41	6.47	31.9
PP30	8	8.0	0.08	0.62	1.53	2.91	33.9
PP31	8	6.0	-0.65	0.32	0.00	2.81	18.6
PP32	9	18.0	0.00	1.21	3.16	6.78	44.5
PP33	9	12.0	0.01	0.36	2.25	4.25	38.8
PP34	9	8.0	0.00	2.09	1.78	3.88	39.6
PP35	9	6.0	-0.36	0.49	0.00	2.13	33.6
PP36	10	20.0	-0.02	0.52	4.13	5.97	52.0
PP37	10	12.1	-0.65	0.62	0.00	4.56	32.1

Table XI.10 - Responses measured from the narrow groove welds and applied to the model analysis for FastROOT using 2.5%CO₂ 97.5%Ar.

Run	WFS [m/min]	WFS/TS Ratio	Depth of Penetration [mm]	Height Ratio	Root Width [mm]	Top Width [mm]	Dilution Ratio [%]
PF1	4	20.0	0.46	0.431	0.82	3.92	28.9
PF2	4	18.2	0.27	0.305	1.98	2.87	21.5
PF3	4	16.0	-1.21	0.403	0.00	4.25	12.1
PF4	4	16.0	-1.11	0.577	0.00	5.58	4.8
PF5	6	22.2	0.36	0.735	2.84	5.94	28.7
PF6	6	20.0	0.29	0.791	1.78	5.50	19.8
PF7	6	18.2	0.28	0.798	1.72	5.59	19.2
PF8	6	15.8	-1.23	0.315	0.00	3.64	13.0
PF9	8	18.2	0.45	0.606	2.66	4.94	25.5
PF10	8	16.0	0.36	0.719	2.47	5.59	28.2
PF11	8	11.9	-0.97	0.637	0.00	5.06	18.8
PF12	9	22.0	0.80	0.641	4.13	5.42	42.1
PF13	9	20.0	0.41	0.691	3.92	5.98	46.1
PF14	9	18.0	0.58	0.761	3.53	5.63	35.2
PF15	9	16.1	0.29	0.726	2.41	5.41	26.0
PF16	9	12.0	0.00	0.746	0.81	5.41	23.7

Table XI.11 – Responses measured from the narrow groove welds and applied to the model analysis for FastROOT using 1.5%CO₂ 54%He 44.5%Ar.

Run	WFS [m/min]	WFS/TS Ratio	Depth of Penetration [mm]	Height Ratio	Root Width [mm]	Top Width [mm]	Dilution Ratio [%]
PF17	4	23.5	0.42	0.873	1.94	5.91	24.7
PF18	4	22.2	0.02	0.633	1.06	5.84	20.8
PF19	4	20.0	-0.39	0.712	0.00	5.72	26.3
PF20	6	22.2	0.68	0.814	3.94	5.81	34.6
PF21	6	20.0	0.84	0.841	4.38	6.19	37.2
PF22	6	18.2	0.55	0.774	3.19	5.78	38.5
PF23	6	15.8	0.36	0.684	3.19	5.00	41.8
PF24	6	14.0	-0.05	0.805	0.12	5.69	25.0
PF25	6	12.0	-0.88	0.571	0.00	4.82	23.0
PF26	8	18.2	0.91	0.678	2.28	5.59	36.7
PF27	8	16.0	0.52	0.745	1.59	5.41	20.6
PF28	8	14.0	-0.65	0.688	0.00	5.38	28.4
PF29	8	11.9	-1.04	0.680	0.00	5.41	28.0
PF30	9	18.0	0.97	0.727	3.16	5.13	32.7
PF31	9	16.1	0.55	0.797	1.25	5.69	22.6
PF32	9	14.1	0.01	0.649	1.06	4.41	31.0
PF33	9	12.0	-0.01	0.821	0.56	5.47	22.8

XII. EQUATION MODELS OBTAINED FOR THE DIFFERENT WELDING WAVEFORMS, RESPONSES AND SHIELDING GAS MIXTURES APPLIED

It was defined that Gas A = 2.5%CO₂ 97.5%Ar and Gas B = 1.5%CO₂ 54%He 44.5%Ar in all equations presented in the sub-sections below.

XII.1. Equation Models obtained for GMAW-P

Final Equation for Depth of Penetration (DP) in terms of Actual Factors (Gas A)

$$\begin{aligned}
 DP = & -38.83384 + 11.84820 \times WFS + 1.12240 \times \frac{WFS}{TS} \\
 & -0.099381 \times WFS \times \frac{WFS}{TS} - 1.36593 \times WFS^2 - 0.032039 \times \frac{WFS}{TS^2} \\
 & +4.46331 \times 10^{-3} \times WFS^2 \times \frac{WFS}{TS} + 3.11027 \times 10^{-4} \times WFS \times \frac{WFS}{TS^2} \\
 & +0.053571 \times WFS^3 + 5.11642 \times 10^{-4} \times \frac{WFS}{TS^3}
 \end{aligned} \tag{XII.1}$$

Final Equation for Depth of Penetration (DP) in terms of Actual Factors (Gas B)

$$\begin{aligned}
 DP = & -34.57479 + 10.99147 \times WFS + 1.10699 \times \frac{WFS}{TS} \\
 & -0.083497 \times WFS \times \frac{WFS}{TS} - 1.33349 \times WFS^2 - 0.035928 \times \frac{WFS}{TS^2} \\
 & +4.46331 \times 10^{-3} \times WFS^2 \times \frac{WFS}{TS} + 3.11027 \times 10^{-4} \times WFS \times \frac{WFS}{TS^2} \\
 & +0.053571 \times WFS^3 + 5.11642 \times 10^{-4} \times \frac{WFS}{TS^3}
 \end{aligned} \tag{XII.2}$$

Final Equation for Height Ratio (HR) in terms of Actual Factors (Gas A)

$$\begin{aligned}
 HR = & +0.25878 + 0.056138 \times WFS + 0.025263 \times \frac{WFS}{TS} \\
 & -3.10248 \times 10^{-3} \times WFS \times \frac{WFS}{TS}
 \end{aligned} \tag{XII.3}$$

Final Equation for Height Ratio (HR) in terms of Actual Factors (Gas B)

$$\begin{aligned}
 HR = & +0.32219 + 0.056138 \times WFS + 0.025263 \times \frac{WFS}{TS} \\
 & -3.10248 \times 10^{-3} \times WFS \times \frac{WFS}{TS}
 \end{aligned} \tag{XII.4}$$

Final Equation for Root Width (RW) in terms of Actual Factors (Gas A)

$$\begin{aligned}
 RW = & -17.75683 + 2.76823 \times WFS + 0.70294 \times \frac{WFS}{TS} \\
 & +6.95749 \times 10^{-3} \times WFS \times \frac{WFS}{TS} - 0.15358 \times WFS^2 - 0.015260 \times \frac{WFS}{TS^2}
 \end{aligned} \tag{XII.5}$$

Final Equation for Root Width (RW) in terms of Actual Factors (Gas B)

$$\begin{aligned} RW = & -15.24498 + 2.56985 \times WFS + 0.67346 \times \frac{WFS}{TS} \\ & + 6.95749 \times 10^{-3} \times WFS \times \frac{WFS}{TS} - 0.15358 \times WFS^2 - 0.015260 \times \frac{WFS}{TS^2} \end{aligned} \quad \text{(XII.6)}$$

Final Equation for Top Width (TW) in terms of Actual Factors (Gas A)

$$\begin{aligned} TW = & +4.65542 - 0.089288 \times WFS + 0.053647 \times \frac{WFS}{TS} \\ & + 4.0562 \times 10^{-3} \times WFS \times \frac{WFS}{TS} \end{aligned} \quad \text{(XII.7)}$$

Final Equation for Root Width (TW) in terms of Actual Factors (Gas B)

$$\begin{aligned} TW = & +4.92218 - 0.052296 \times WFS + 0.026257 \times \frac{WFS}{TS} \\ & + 4.0562 \times 10^{-3} \times WFS \times \frac{WFS}{TS} \end{aligned} \quad \text{(XII.8)}$$

XII.2. Equation Models obtained for RapidArc

Final Equation for Depth of Penetration (DP) in terms of Actual Factors (Gas A)

$$\begin{aligned} DP = & -11.21136 + 0.18391 \times WFS + 2.42001 \times \frac{WFS}{TS} \\ & - 0.30156 \times WFS \times \frac{WFS}{TS} + 0.21018 \times (WFS)^2 - 0.077094 \times \left(\frac{WFS}{TS}\right)^2 \\ & + 0.012551 \times WFS^2 \times \frac{WFS}{TS} + 3.3833 \times 10^{-3} \times WFS \times \left(\frac{WFS}{TS}\right)^2 \\ & - 0.014752 \times (WFS)^3 + 9.27492 \times 10^{-4} \times \left(\frac{WFS}{TS}\right)^3 \end{aligned} \quad \text{(XII.9)}$$

Final Equation for Depth of Penetration (DP) in terms of Actual Factors (Gas B)

$$\begin{aligned} DP = & -16.72961 + 1.38663 \times WFS + 2.42037 \times \frac{WFS}{TS} \\ & - 0.31618 \times WFS \times \frac{WFS}{TS} + 0.15412 \times (WFS)^2 - 0.073473 \times \left(\frac{WFS}{TS}\right)^2 \\ & + 0.012551 \times WFS^2 \times \frac{WFS}{TS} + 3.3833 \times 10^{-3} \times WFS \times \left(\frac{WFS}{TS}\right)^2 \\ & - 0.014752 \times (WFS)^3 + 9.27492 \times 10^{-4} \times \left(\frac{WFS}{TS}\right)^3 \end{aligned} \quad \text{(XII.10)}$$

Final Equation for Height Ratio (HR) in terms of Actual Factors (Gas A)

$$\begin{aligned} \ln(HR) = & -5.78042 + 0.62398 \times WFS + 0.25428 \times \frac{WFS}{TS} \\ & - 0.031380 \times WFS \times \frac{WFS}{TS} \end{aligned} \quad \text{(XII.11)}$$

Final Equation for Height Ratio (HR) in terms of Actual Factors (Gas B)

$$\begin{aligned} \ln(HR) = & -6.52423 + 0.69164 \times WFS + 0.29478 \times \frac{WFS}{TS} \\ & - 0.031380 \times WFS \times \frac{WFS}{TS} \end{aligned} \quad \text{(XII.12)}$$

Final Equation for Root Width (RW) in terms of Actual Factors (Gas A)

$$\begin{aligned} RW = & -30.51371 + 2.04318 \times WFS + 5.29344 \times \frac{WFS}{TS} \\ & - 0.69363 \times WFS \times \frac{WFS}{TS} + 0.32961 \times (WFS)^2 - 0.12417 \times \left(\frac{WFS}{TS}\right)^2 \\ & + 0.034370 \times WFS^2 \times \frac{WFS}{TS} + 2.89383 \times 10^{-3} \times WFS \times \left(\frac{WFS}{TS}\right)^2 \\ & - 0.030386 \times (WFS)^3 + 1.67271 \times 10^{-3} \times \left(\frac{WFS}{TS}\right)^3 \end{aligned} \quad \text{(XII.13)}$$

Final Equation for Root Width (RW) in terms of Actual Factors (Gas B)

$$\begin{aligned} RW = & -31.55742 + 2.83250 \times WFS + 4.56980 \times \frac{WFS}{TS} \\ & -0.64068 \times WFS \times \frac{WFS}{TS} + 0.27052 \times (WFS)^2 - 0.11027 \times \left(\frac{WFS}{TS}\right)^2 \\ & +0.034370 \times WFS^2 \times \frac{WFS}{TS} + 2.89383 \times 10^{-3} \times WFS \times \left(\frac{WFS}{TS}\right)^2 \\ & -0.030386 \times (WFS)^3 + 1.67271 \times 10^{-3} \times \left(\frac{WFS}{TS}\right)^3 \end{aligned} \quad \text{(XII.14)}$$

Final Equation for Top Width (TW) in terms of Actual Factors (Gas A)

$$\begin{aligned} TW = & -8.46966 + 1.29517 \times WFS + 0.06320 \times \frac{WFS}{TS} \\ & -0.054255 \times WFS \times \frac{WFS}{TS} \end{aligned} \quad \text{(XII.15)}$$

Final Equation for Root Width (TW) in terms of Actual Factors (Gas B)

$$\begin{aligned} TW = & -6.76112 + 1.16928 \times WFS + 0.61198 \times \frac{WFS}{TS} \\ & -0.054255 \times WFS \times \frac{WFS}{TS} \end{aligned} \quad \text{(XII.16)}$$

XII.3. Equation Models obtained for STT

Final Equation for Depth of Penetration (DP) in terms of Actual Factors (Gas A)

$$DP = -7.91749 + 1.11429 \times WFS + 0.27696 \times \frac{WFS}{TS} - 0.038416 \times WFS \times \frac{WFS}{TS} \quad (\text{XII.17})$$

Final Equation for Depth of Penetration (DP) in terms of Actual Factors (Gas B)

$$DP = -10.33193 + 1.05268 \times WFS + 0.42570 \times \frac{WFS}{TS} - 0.038416 \times WFS \times \frac{WFS}{TS} \quad (\text{XII.18})$$

Final Equation for Height Ratio (HR) in terms of Actual Factors (Gas A)

$$(HR)^{-1.54} = +1.74285 + 6.35498 \times 10^{-3} \times WFS + 0.031305 \times \frac{WFS}{TS} - 5.72140 \times 10^{-3} \times WFS \times \frac{WFS}{TS} \quad (\text{XII.19})$$

Final Equation for Height Ratio (HR) in terms of Actual Factors (Gas B)

$$(HR)^{-1.54} = -0.38230 + 0.12635 \times WFS + 0.089482 \times \frac{WFS}{TS} - 5.72140 \times 10^{-3} \times WFS \times \frac{WFS}{TS} \quad (\text{XII.20})$$

Final Equation for Root Width (RW) in terms of Actual Factors (Gas A)

$$\text{Log}_{10}(RW + 0.05) = -6.96450 + 1.04769 \times WFS + 0.22388 \times \frac{WFS}{TS} - 0.035387 \times WFS \times \frac{WFS}{TS} \quad (\text{XII.21})$$

Final Equation for Root Width (RW) in terms of Actual Factors (Gas B)

$$\text{Log}_{10}(RW + 0.05) = -10.57973 + 1.00888 \times WFS + 0.41155 \times \frac{WFS}{TS} - 0.035387 \times WFS \times \frac{WFS}{TS} \quad (\text{XII.22})$$

Final Equation for Top Width (TW) in terms of Actual Factors (Gas A)

$$TW = +4.51282 + 0.090474 \times WFS + 0.048458 \times \frac{WFS}{TS} - 2.57167 \times 10^{-3} \times WFS \times \frac{WFS}{TS} \quad (\text{XII.23})$$

Final Equation for Root Width (TW) in terms of Actual Factors (Gas B)

$$TW = +4.54612 - 3.30533 \times 10^{-3} \times WFS + 0.072207 \times \frac{WFS}{TS} - 2.57167 \times 10^{-3} \times WFS \times \frac{WFS}{TS} \quad (\text{XII.24})$$

XII.4. Equation Models obtained for CMT

Final Equation for Depth of Penetration (DP) in terms of Actual Factors (Gas A)

$$DP = +0.43346 + 0.61846 \times WFS - 0.33524 \times \frac{WFS}{TS} + 0.043086 \times WFS \times \frac{WFS}{TS} - 0.091317 \times WFS^2 + 2.09113 \times 10^{-3} \times \frac{WFS^2}{TS} \quad (\text{XII.25})$$

Final Equation for Depth of Penetration (DP) in terms of Actual Factors (Gas B)

$$DP = +0.77771 + 0.63917 \times WFS - 0.36043 \times \frac{WFS}{TS} + 0.043086 \times WFS \times \frac{WFS}{TS} - 0.091317 \times WFS^2 + 2.09113 \times 10^{-3} \times \frac{WFS^2}{TS} \quad (\text{XII.26})$$

Final Equation for Height Ratio (HR) in terms of Actual Factors (Gas A)

$$\text{Sqrt}(HR) = +1.14757 - 0.054813 \times WFS - 0.041981 \times \frac{WFS}{TS} + 5.39617 \times 10^{-3} \times WFS \times \frac{WFS}{TS} \quad (\text{XII.27})$$

Final Equation for Height Ratio (HR) in terms of Actual Factors (Gas B)

$$\text{Sqrt}(HR) = +0.66134 + 0.013842 \times WFS - 0.039061 \times \frac{WFS}{TS} + 5.39617 \times 10^{-3} \times WFS \times \frac{WFS}{TS} \quad (\text{XII.28})$$

Final Equation for Root Width (RW) in terms of Actual Factors (Gas A)

$$RW = +0.017620 - 0.24882 \times WFS - 0.13740 \times \frac{WFS}{TS} + 0.047796 \times WFS \times \frac{WFS}{TS} \quad (\text{XII.29})$$

Final Equation for Root Width (RW) in terms of Actual Factors (Gas B)

$$RW = +2.32393 - 0.37413 \times WFS - 0.21734 \times \frac{WFS}{TS} + 0.047796 \times WFS \times \frac{WFS}{TS} \quad (\text{XII.30})$$

Final Equation for Top Width (TW) in terms of Actual Factors (Gas A)

$$TW = +0.30841 + 0.42411 \times WFS + 0.062360 \times \frac{WFS}{TS} \quad (\text{XII.31})$$

Final Equation for Root Width (TW) in terms of Actual Factors (Gas B)

$$TW = +0.68295 + 0.42411 \times WFS + 0.062360 \times \frac{WFS}{TS} \quad (\text{XII.32})$$

XII.5. Equation Models obtained for CMT-P

Final Equation for Depth of Penetration (DP) in terms of Actual Factors (Gas A)

$$(DP + 1.32)^{2.13} = +2.42915 - 0.14300 \times WFS + 0.048392 \times \frac{WFS}{TS} \quad (\text{XII.33})$$

Final Equation for Depth of Penetration (DP) in terms of Actual Factors (Gas B)

$$(DP + 1.32)^{2.13} = +2.11461 - 0.14300 \times WFS + 0.048392 \times \frac{WFS}{TS} \quad (\text{XII.34})$$

Final Equation for Height Ratio (HR) in terms of Actual Factors (Gas A)

$$\frac{1}{HR} = +4.49585 - 0.21021 \times WFS - 0.066045 \times \frac{WFS}{TS} \quad (\text{XII.35})$$

Final Equation for Height Ratio (HR) in terms of Actual Factors (Gas B)

$$\frac{1}{HR} = +4.26432 - 0.21021 \times WFS - 0.066045 \times \frac{WFS}{TS} \quad (\text{XII.36})$$

Final Equation for Root Width (RW) in terms of Actual Factors (Gas A)

$$RW = -7.57947 + 1.51482 \times WFS + 0.36403 \times \frac{WFS}{TS} \\ + 0.011204 \times WFS \times \frac{WFS}{TS} - 0.10602 \times WFS^2 - 6.55375 \times 10^{-3} \times \left(\frac{WFS}{TS}\right)^2 \quad (\text{XII.37})$$

Final Equation for Root Width (RW) in terms of Actual Factors (Gas B)

$$RW = -6.92998 + 1.46271 \times WFS + 0.34227 \times \frac{WFS}{TS} \\ + 0.011204 \times WFS \times \frac{WFS}{TS} - 0.10602 \times WFS^2 - 6.55375 \times 10^{-3} \times \left(\frac{WFS}{TS}\right)^2 \quad (\text{XII.38})$$

Final Equation for Top Width (TW) in terms of Actual Factors (Gas A)

$$TW = -2.14798 + 0.39675 \times WFS + 0.25017 \times \frac{WFS}{TS} \quad (\text{XII.39})$$

Final Equation for Root Width (TW) in terms of Actual Factors (Gas B)

$$TW = -2.00961 + 0.39675 \times WFS + 0.25017 \times \frac{WFS}{TS} \quad (\text{XII.40})$$

XII.6. Equation Models obtained for FastROOT

Final Equation for Depth of Penetration (DP) in terms of Actual Factors (Gas A)

$$DP = -4.11186 + 0.20197 \times WFS + 0.15615 \times \frac{WFS}{TS} \quad (\text{XII.41})$$

Final Equation for Depth of Penetration (DP) in terms of Actual Factors (Gas B)

$$DP = -3.86007 + 0.20197 \times WFS + 0.15615 \times \frac{WFS}{TS} \quad (\text{XII.42})$$

Final Equation for Height Ratio (HR) in terms of Actual Factors (Gas A)

$$(HR)^{2.57} = -0.23858 + 0.036349 \times WFS + 0.018176 \times \frac{WFS}{TS} \quad (\text{XII.43})$$

Final Equation for Height Ratio (HR) in terms of Actual Factors (Gas B)

$$(HR)^{2.57} = -0.092287 + 0.036349 \times WFS + 0.018176 \times \frac{WFS}{TS} \quad (\text{XII.44})$$

Final Equation for Root Width (RW) in terms of Actual Factors (Gas A)

$$\text{sqrt}(RW + 0.04) = -3.09656 + 0.20794 \times WFS + 0.16430 \times \frac{WFS}{TS} \quad (\text{XII.45})$$

Final Equation for Root Width (RW) in terms of Actual Factors (Gas B)

$$\text{sqrt}(RW + 0.04) = -3.08923 + 0.20794 \times WFS + 0.16430 \times \frac{WFS}{TS} \quad (\text{XII.46})$$

Final Equation for Top Width (TW) in terms of Actual Factors (Gas A)

$$TW = +2.39215 + 0.15041 \times WFS + 0.092901 \times \frac{WFS}{TS} \quad (\text{XII.47})$$

Final Equation for Root Width (TW) in terms of Actual Factors (Gas B)

$$TW = +2.88406 + 0.15041 \times WFS + 0.092901 \times \frac{WFS}{TS} \quad (\text{XII.48})$$

XIII. VALIDATION ANALYSIS

Prediction and Actual values for depth of penetration models were compared using the plots obtained from DOE software.

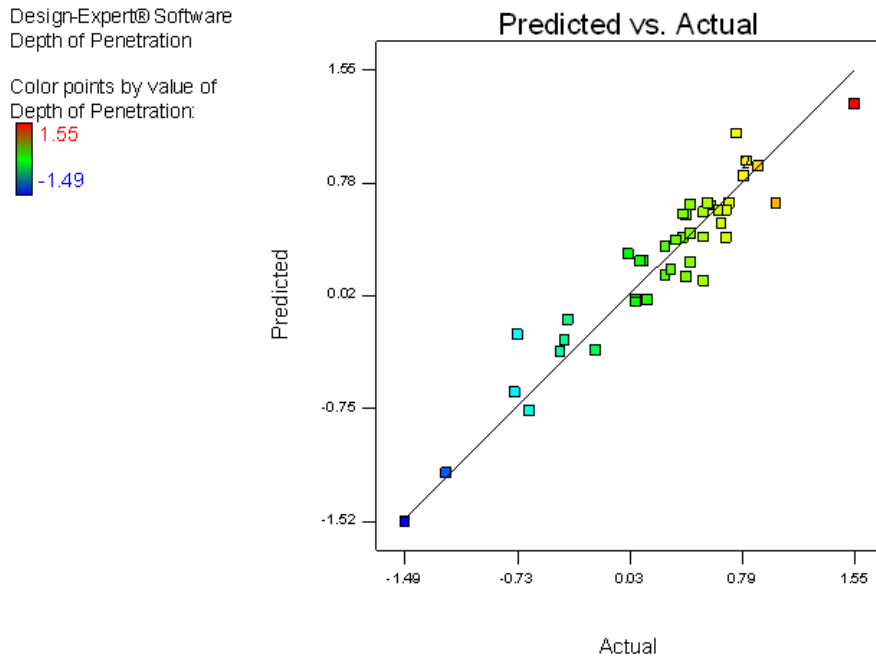


Figure XIII.1 – Validation plot obtained for the penetration models for GMAW-P.

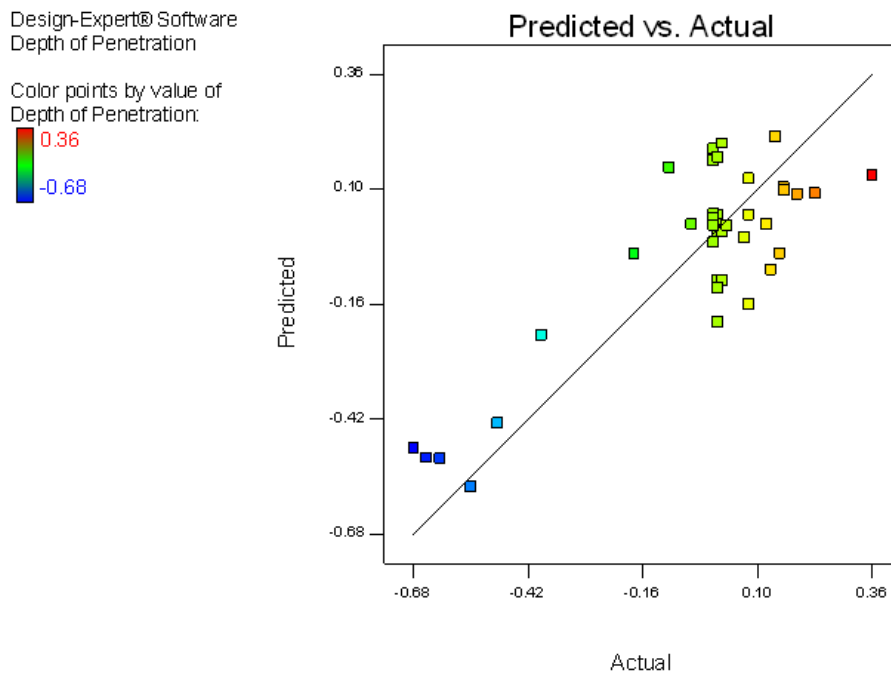


Figure XIII.2 – Validation plot obtained for the depth of penetration models for RapidArc.

Design-Expert® Software
Depth of Penetration

Color points by value of
Depth of Penetration:

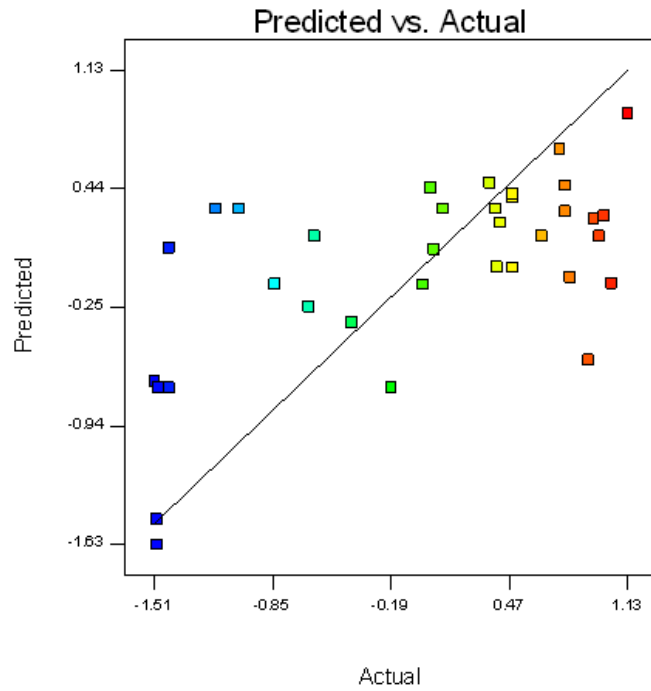


Figure XIII.3 – Validation plot obtained for the depth of penetration models for STT.

Design-Expert® Software
Depth of Penetration

Color points by value of
Depth of Penetration:

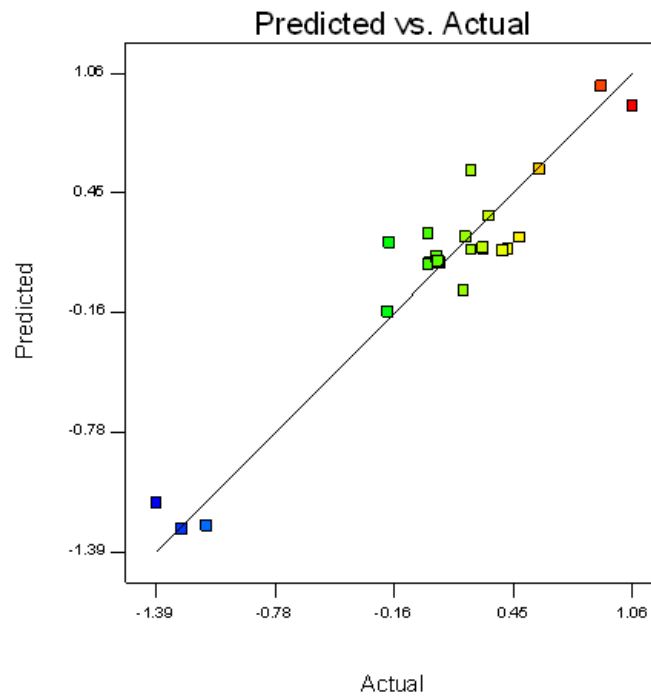


Figure XIII.4 – Validation plot obtained for the depth of penetration models for CMT.

Design-Expert® Software
(Depth of Penetration + 1.32)^{2.13}

Color points by value of
(Depth of Penetration + 1.32)^{2.13}:

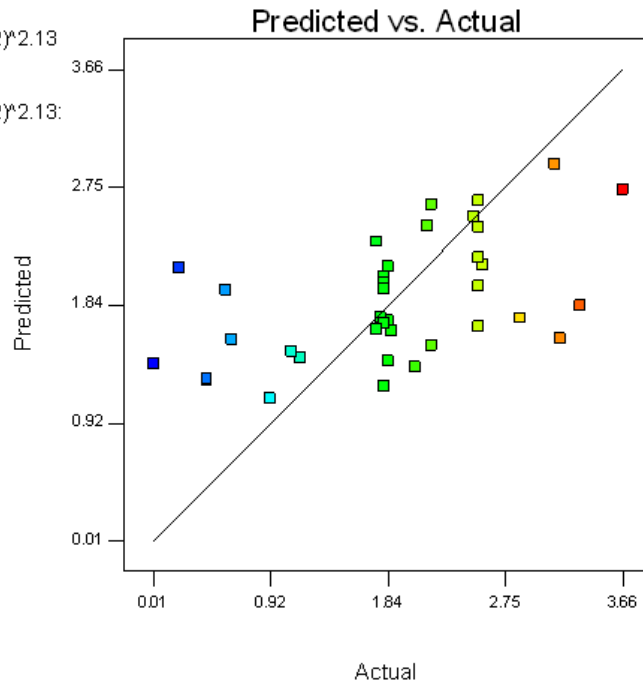


Figure XIII.5 – Validation plot obtained for the depth of penetration models for CMT.

Design-Expert® Software
Depth of Penetration

Color points by value of
Depth of Penetration:

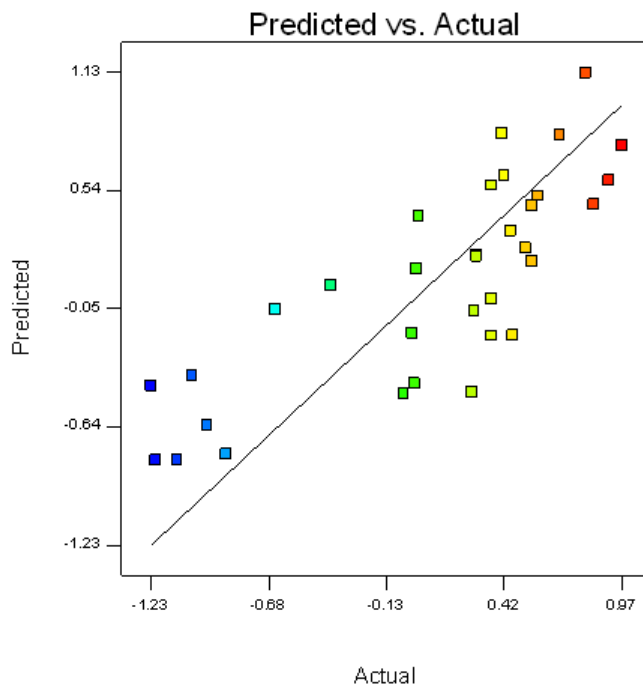


Figure XIII.6 – Validation plot obtained for the depth of penetration models for FastROOT.

XIV. GRAPHICAL ANALYSIS OBTAINED FROM THE STATISTICAL MODELLING

XIV.1. Graphical Results Obtained for the Depth of Penetration (DP) Model Responses

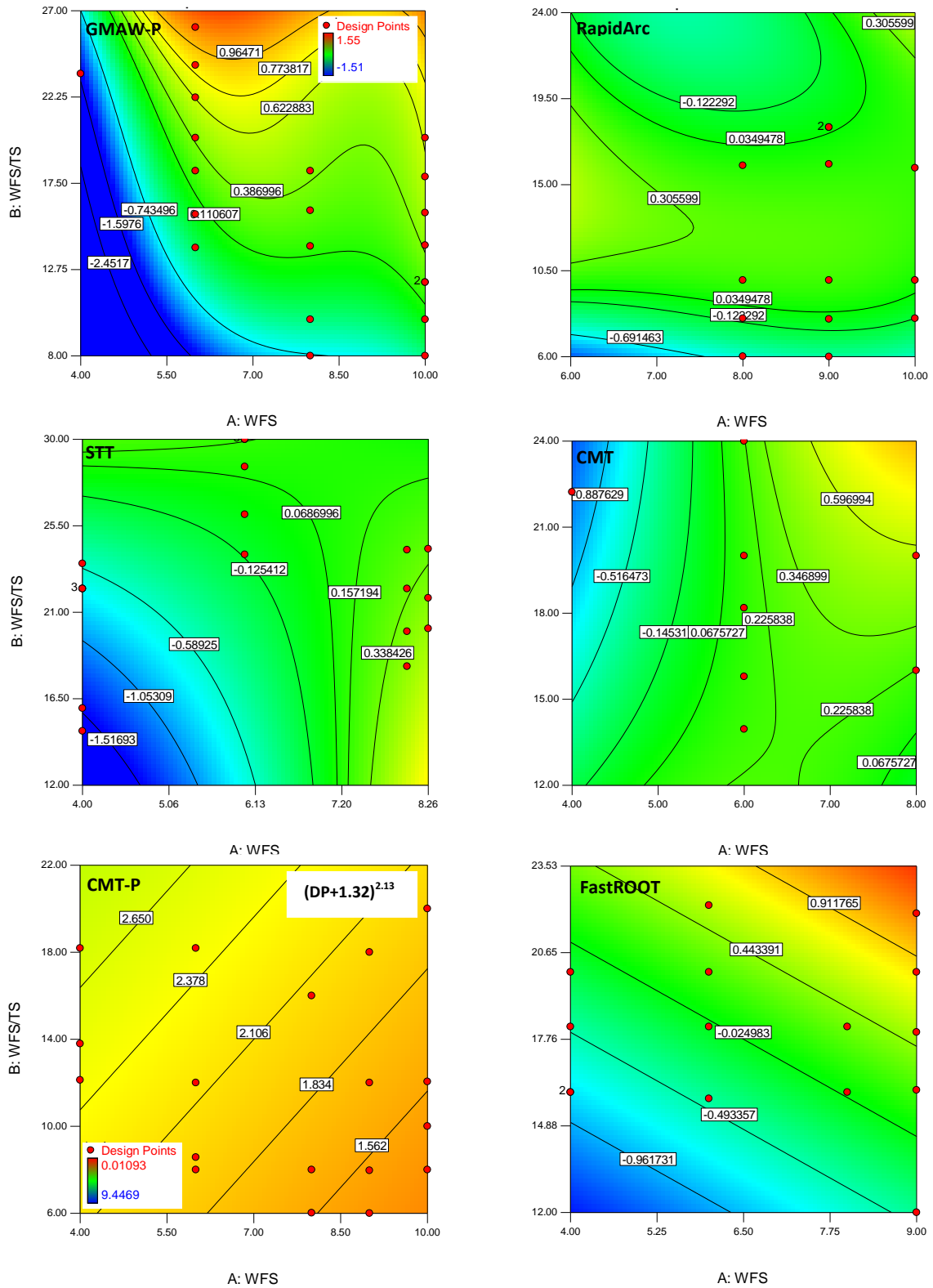
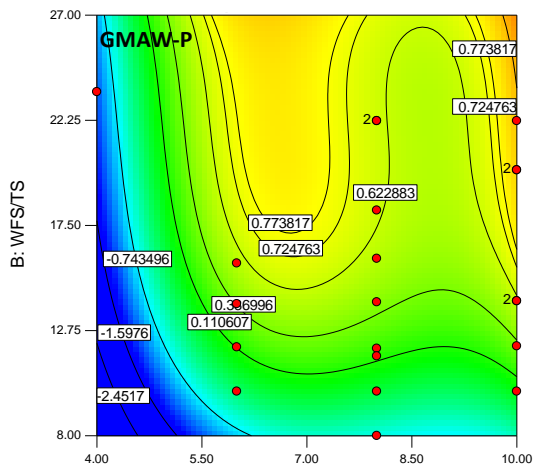
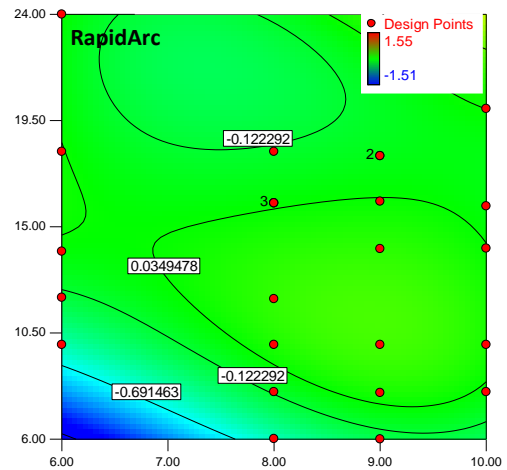


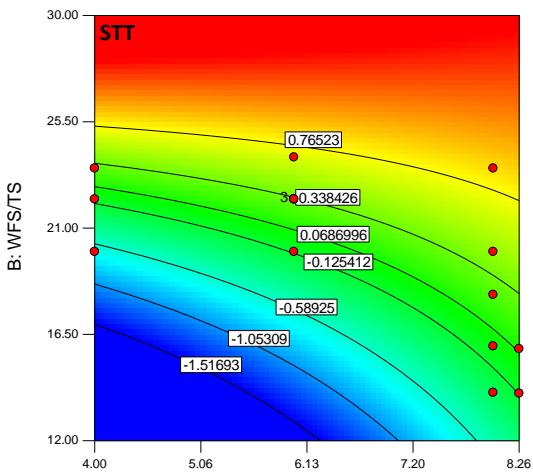
Figure XIV.1 – Contour plots for the variation of depth of penetration (DP) with WFS and WFS/TS ratio for different waveforms, using 2.5%CO₂ 97.5%Ar (scale allocated in GMAW-P plot). The CMT-P was analysed according to the mathematical function and scale and presented on its own figure.



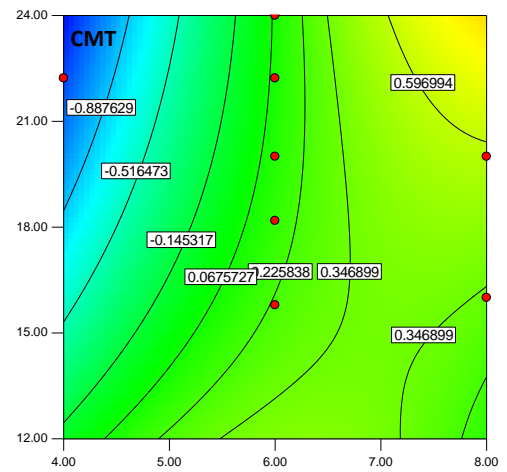
A: WFS



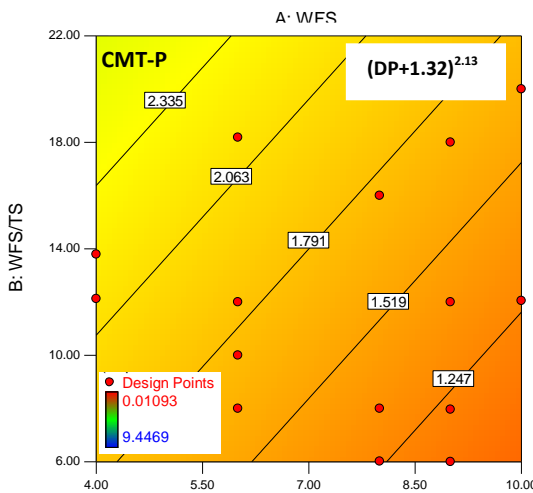
A: WFS



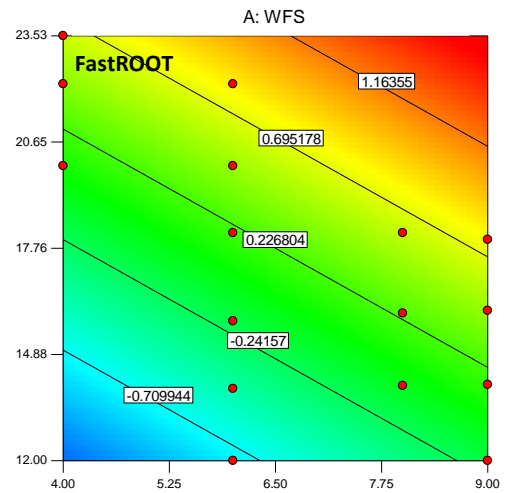
A: WFS



A: WFS



A: WFS



A: WFS

Figure XIV.2 – Contour plots for the variation of depth of penetration (DP) with WFS and WFS/TS ratio for different waveforms, using 1.5%CO₂ 54%He 44.5%Ar (scale allocated in RapidArc plot). CMT-P was analysed according to the mathematical function and scale and presented on its own picture.

XIV.2. Graphical Results Obtained for the Height Ratio (HR) Model Responses

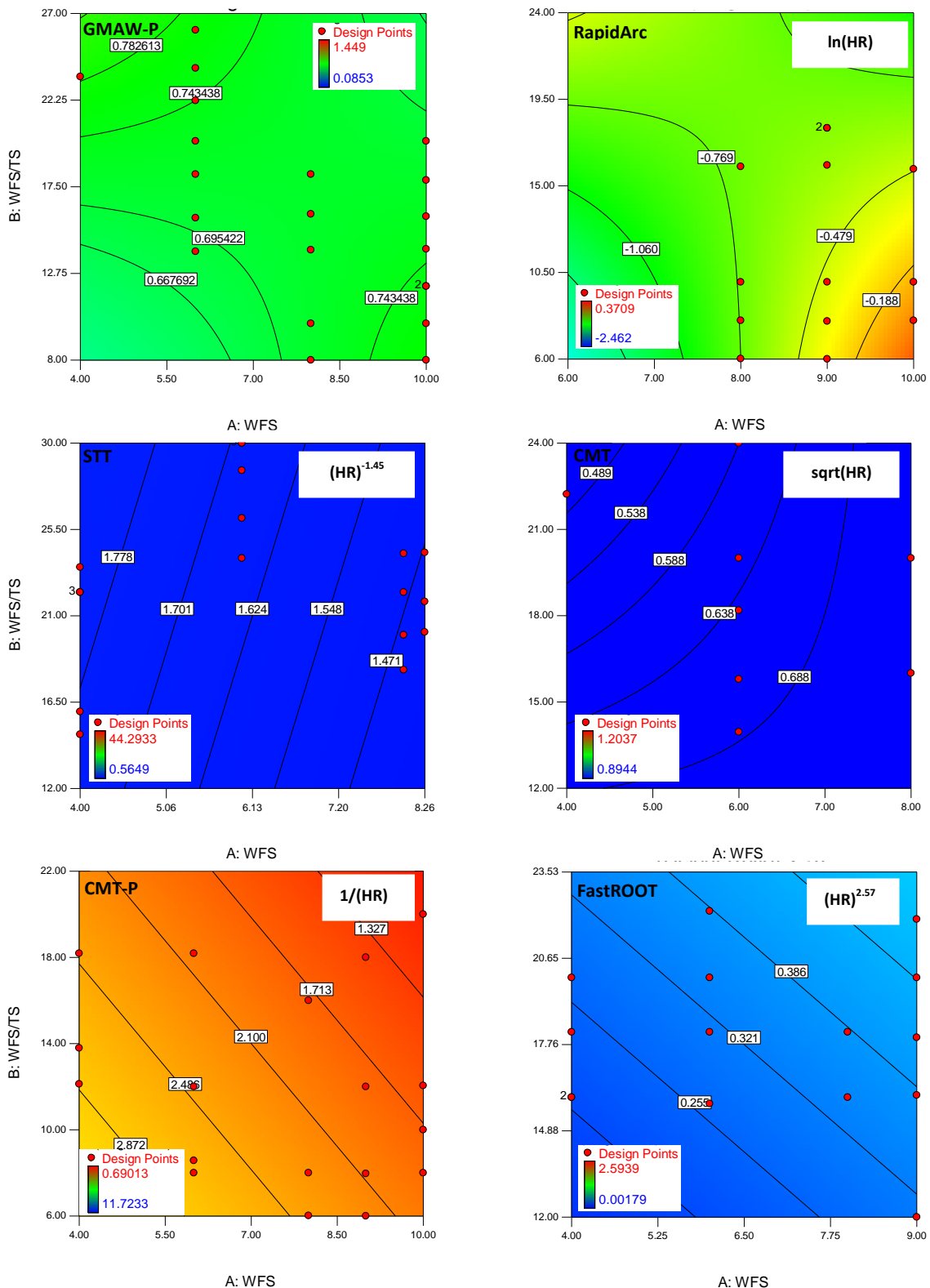


Figure XIV.3 – Contour plots for the variation of height ratio (HR) with WFS and WFS/TS ratio for different waveforms, using 2.5%CO₂ 97.5%Ar (scale allocated in GMAW-P plot). The waveforms where transformations occurred are shown with their own scale and function.

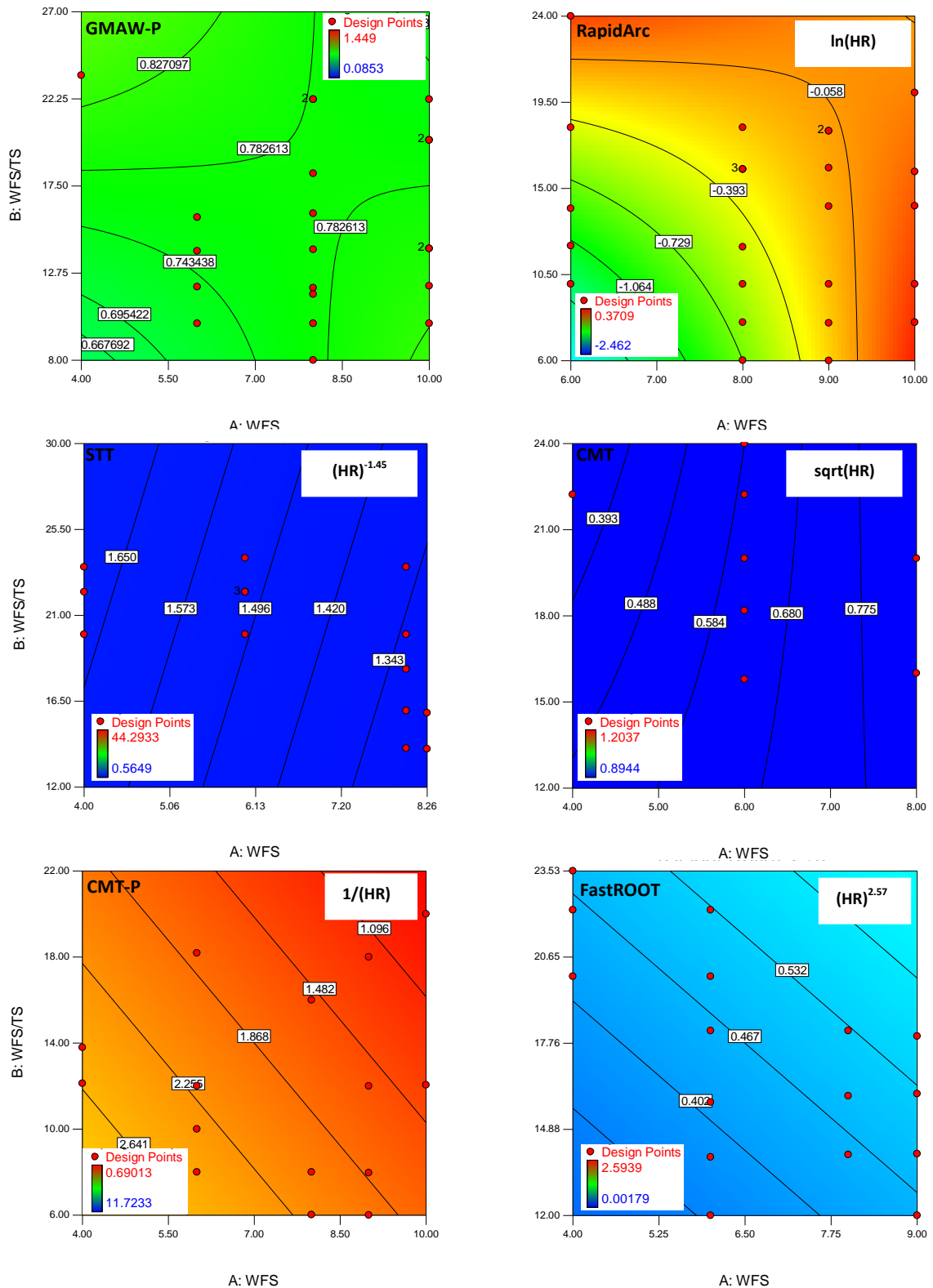


Figure XIV.4 – Contour plots to the variation of height ratio (HR) with WFS and WFS/TS ratio for different waveforms, using 1.5%CO₂ 54%He 44.5%Ar (scale allocated in GMAW-P plot). The waveforms where transformations occurred are shown with their own scale and function.

XIV.3. Graphical Results Obtained for the Root Width (RW) Model Responses

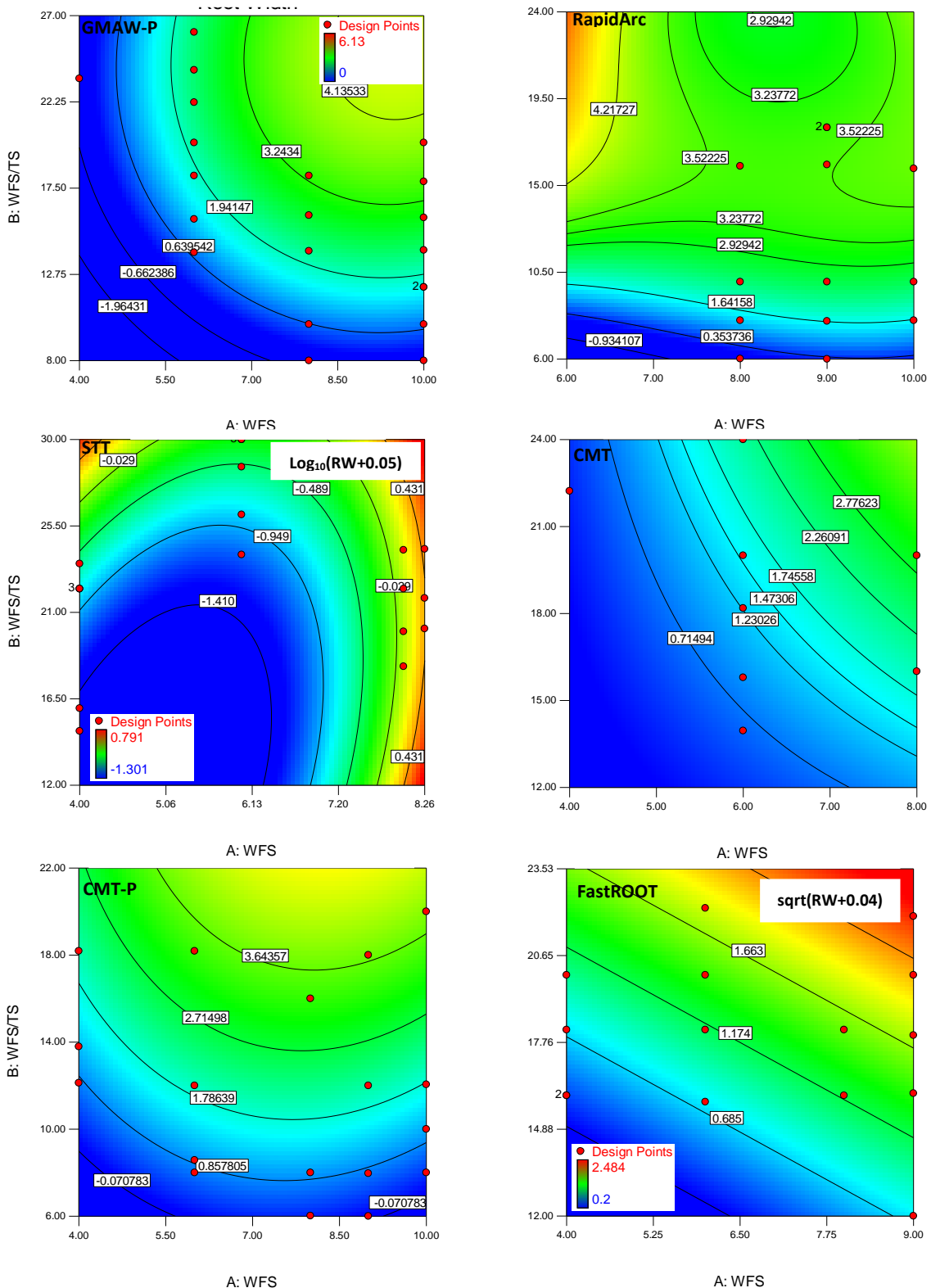


Figure XIV.5 – Contour plots to the variation of root width (RW) with WFS and WFS/TS ratio for different waveforms, using 2.5%CO₂ 97.5%Ar (scale allocated in GMAW-P plot). The waveforms where transformations occurred are shown with their own scale and function.

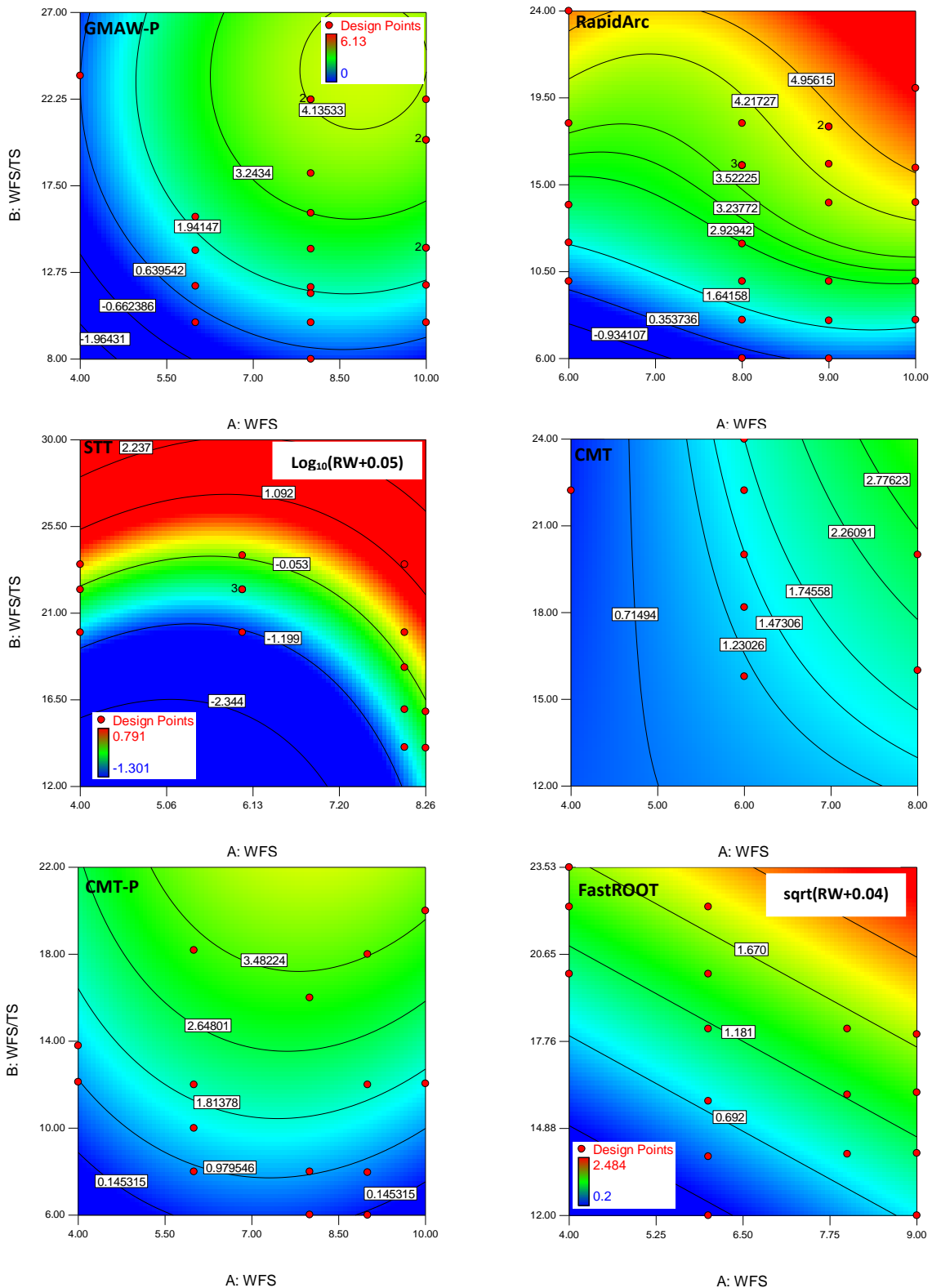


Figure XIV.6 – Contour plots to the variation of root width (RW) with WFS and WFS/TS ratio for different waveforms, using 1.5%CO₂ 54%He 44.5%Ar (scale allocated in GMAW-P plot). The waveforms where transformations occurred are shown with their own scale and function.

XIV.4. Graphical Results Obtained for the Top Width (TW) Model Responses

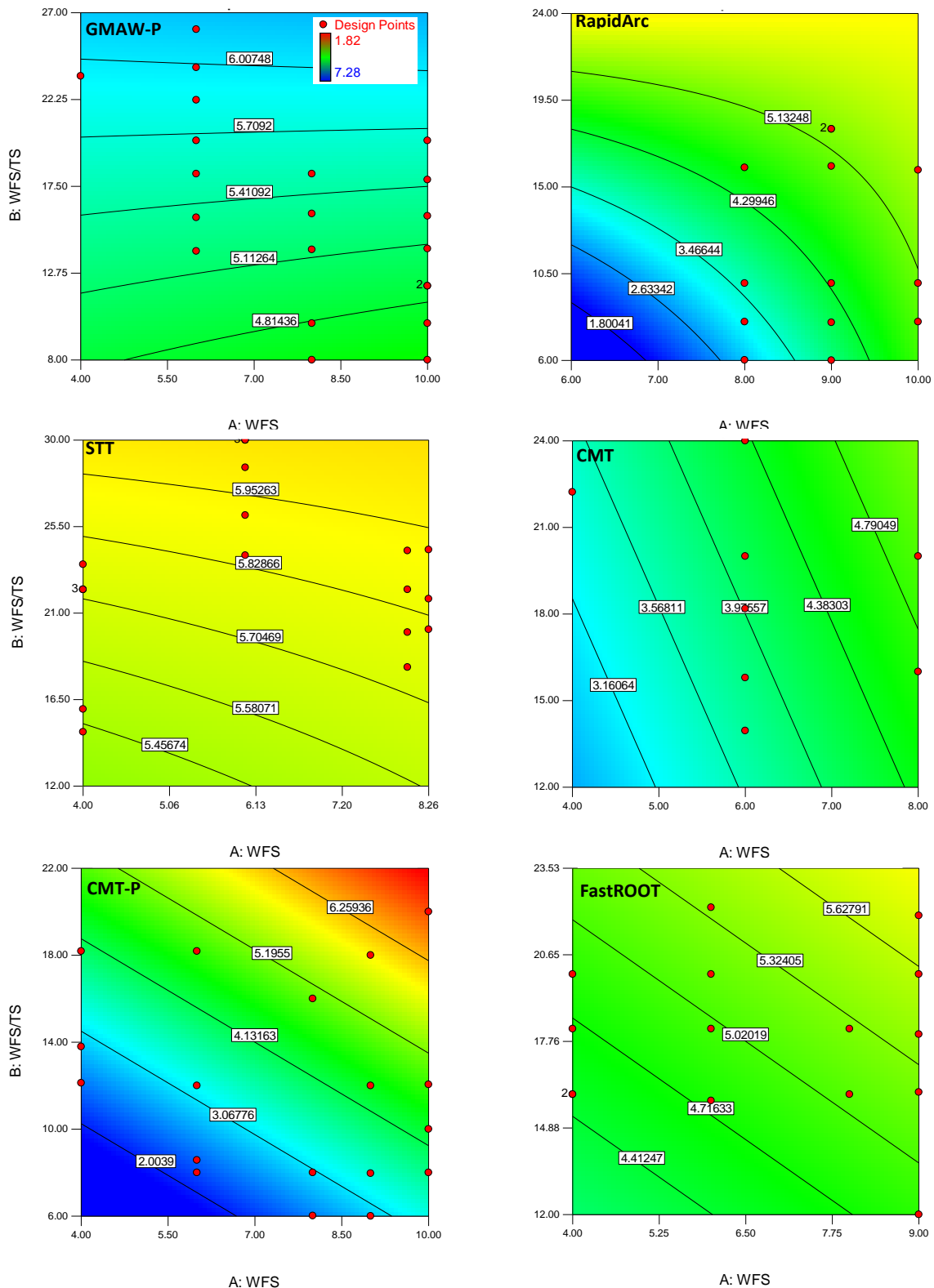
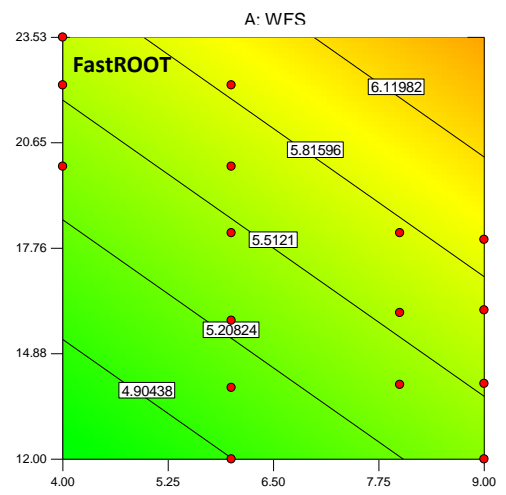
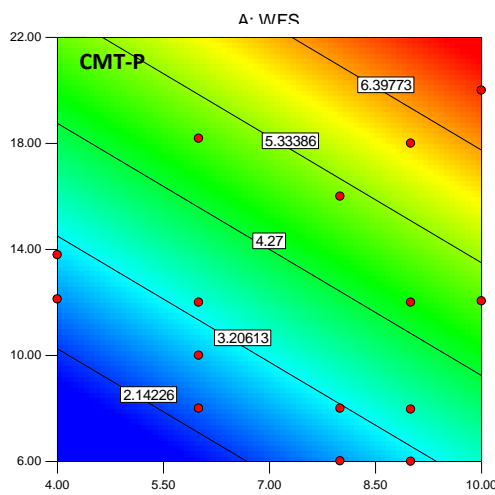
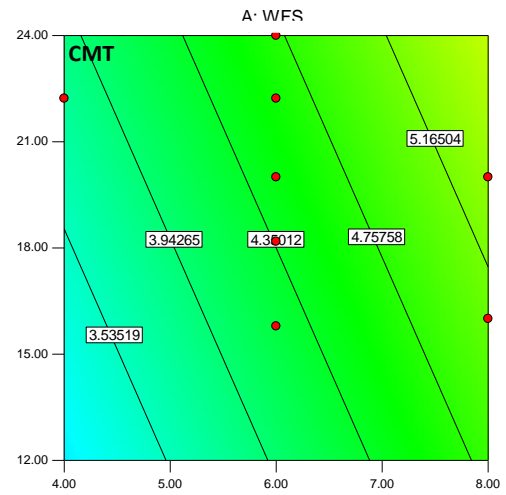
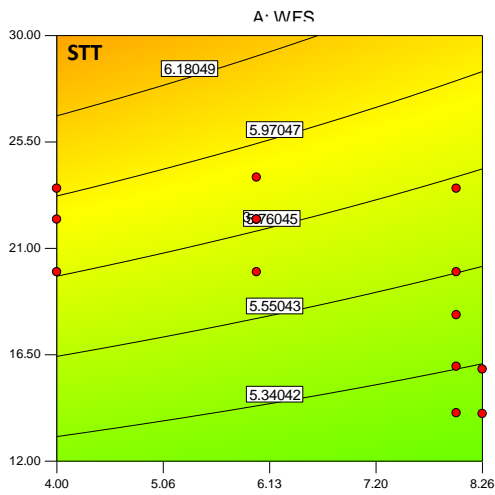
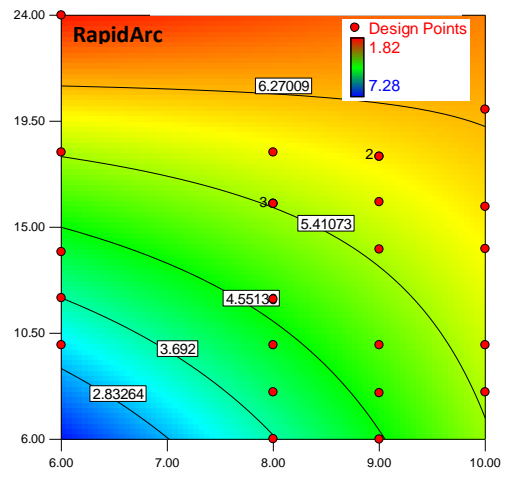
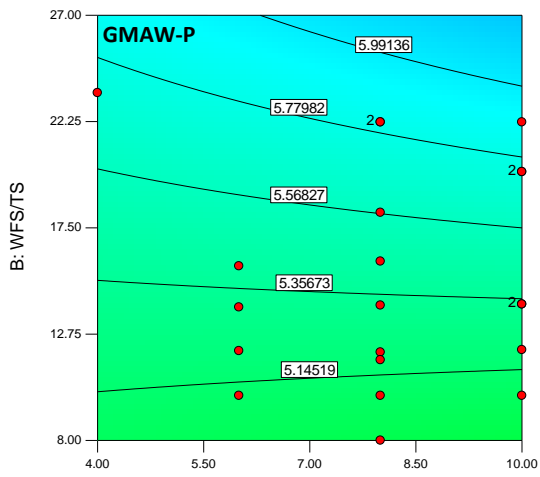


Figure XIV.7 – Contour plots to the variation of top width (RW) with WFS and WFS/TS ratio for different waveforms, using 2.5%CO₂ 97.5%Ar (scale allocated in GMAW-P plot).



A: WFS

A: WFS

Figure XIV.8 – Contour plots for the variation of top width (RW) with WFS and WFS/TS ratio for different waveforms, using 1.5%CO₂ 54%He 44.5%Ar (scale allocated in RapidArc plot).

XV. Diagrams of the Desirability Criteria Applied for different Waveforms

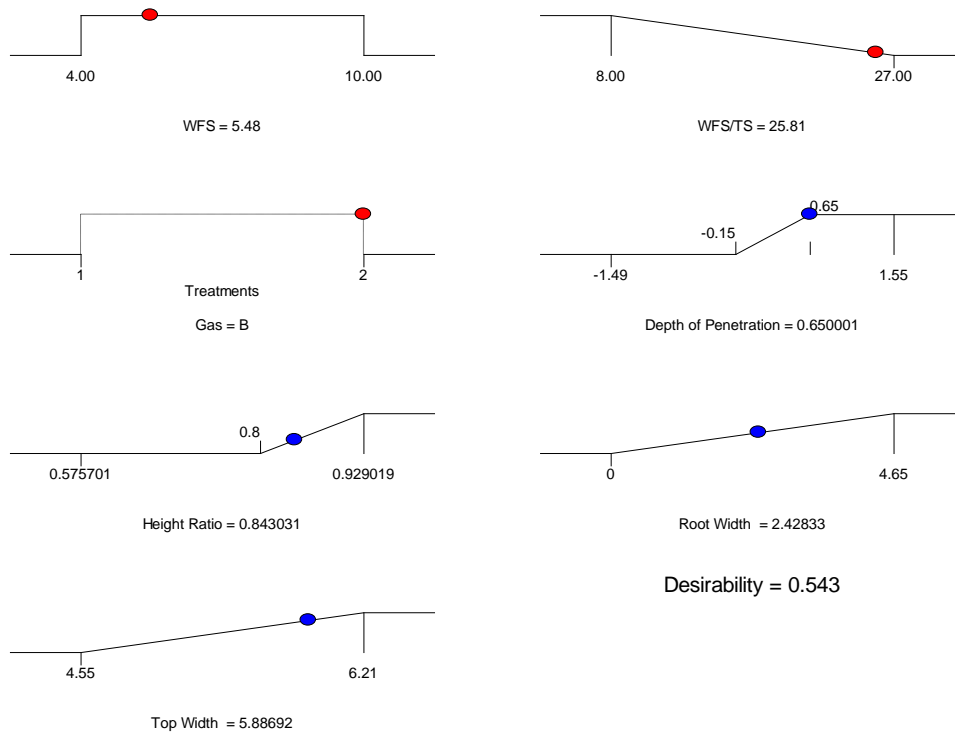


Figure XV.1 – Desirability conditions set for GMAW-P waveform.

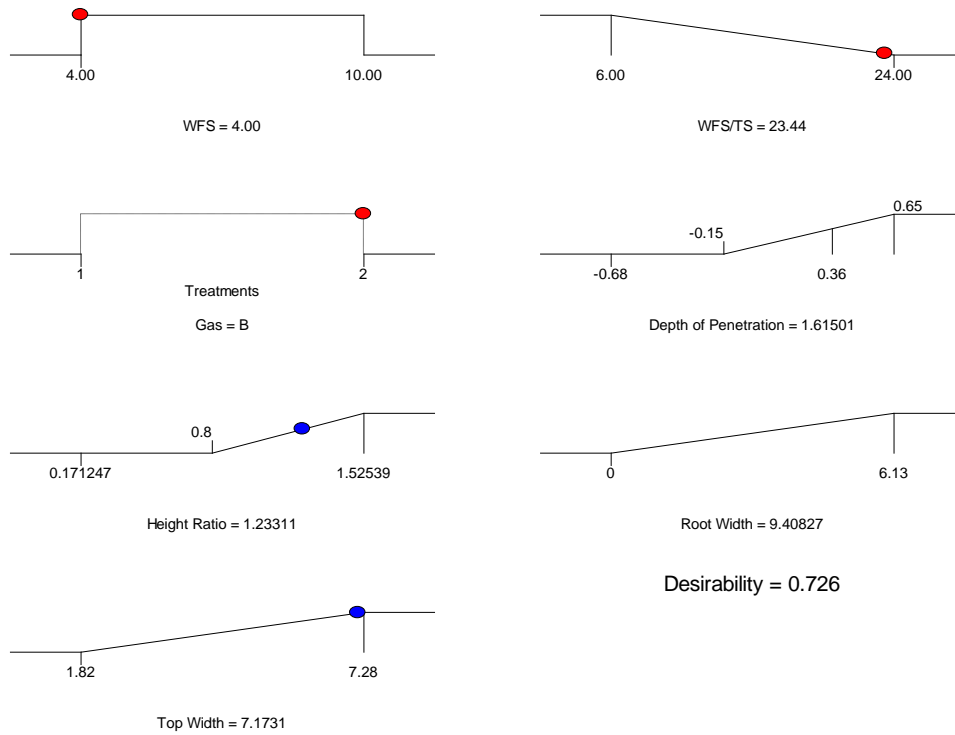


Figure XV.2 – Desirability conditions set for RapidArc waveform.

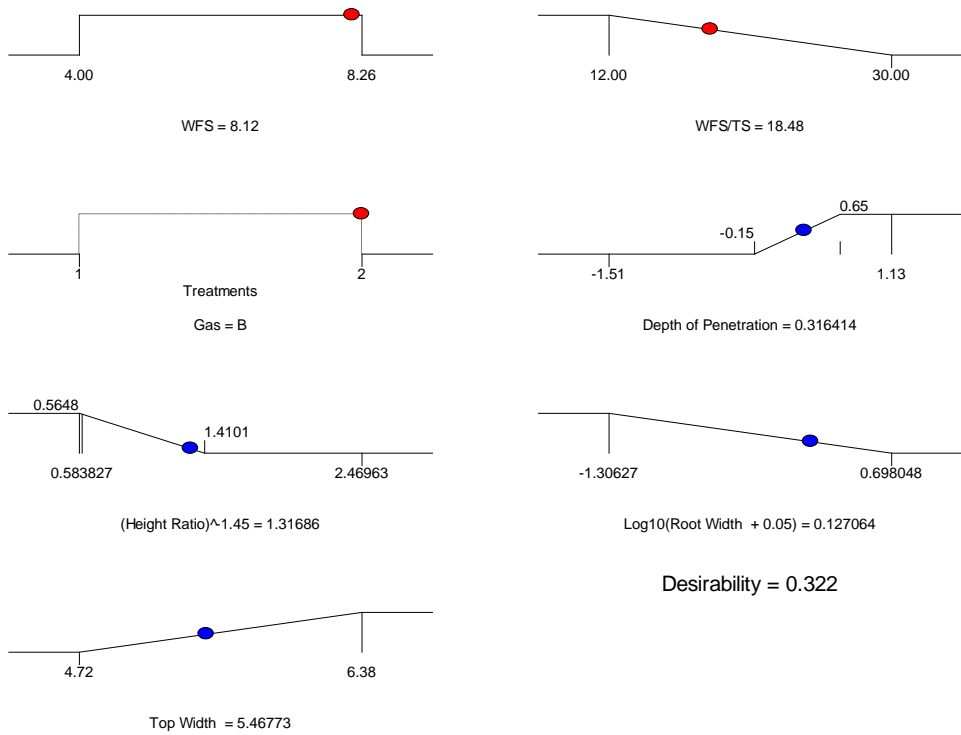


Figure XV.3 – Desirability conditions set for STT waveform.

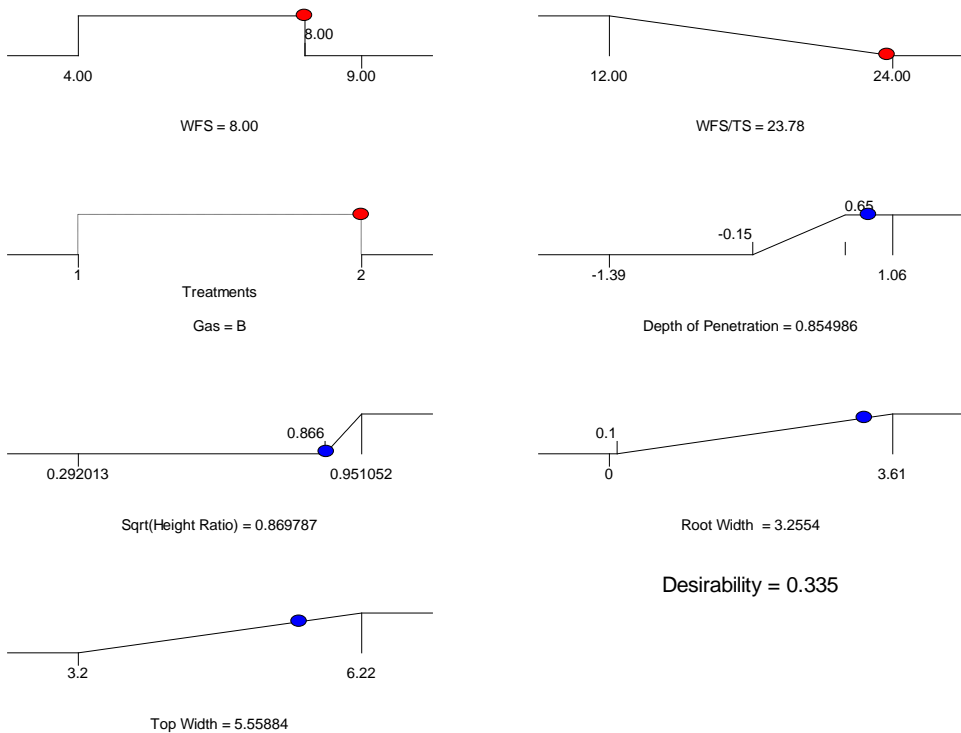


Figure XV.4 – Desirability conditions set for CMT waveform.

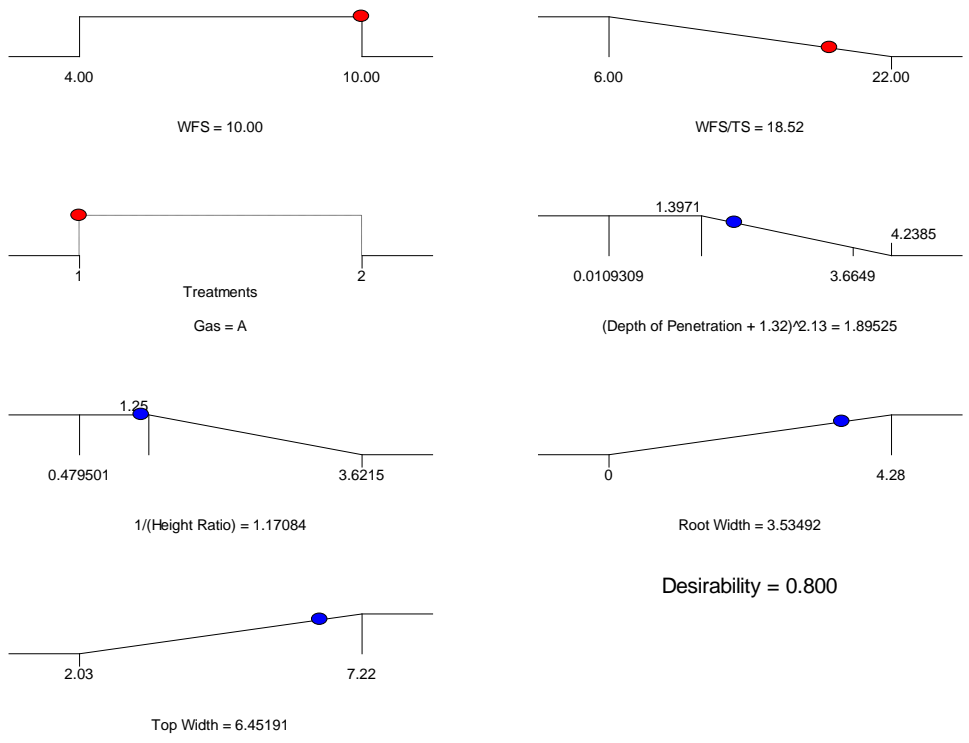


Figure XV.5 – Desirability conditions set for CMT-P waveform.

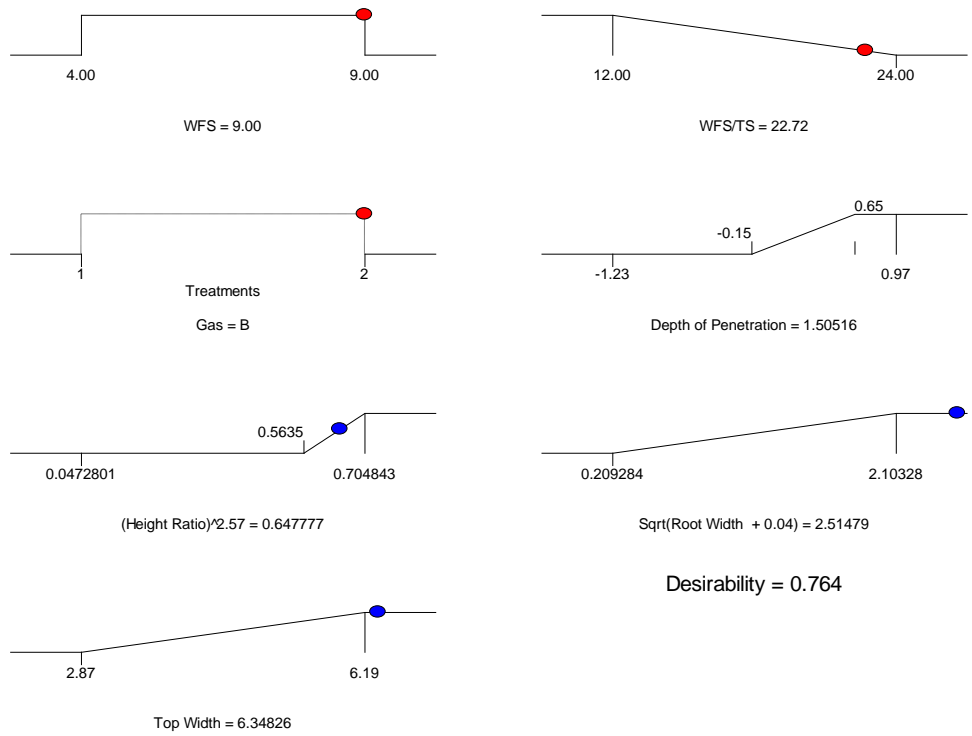


Figure XV.6 – Desirability conditions set for FastROOT waveform.

XVI. DESIRABILITY GRAPHIC ANALYSIS OBTAINED FROM STATISTICAL MODELLING

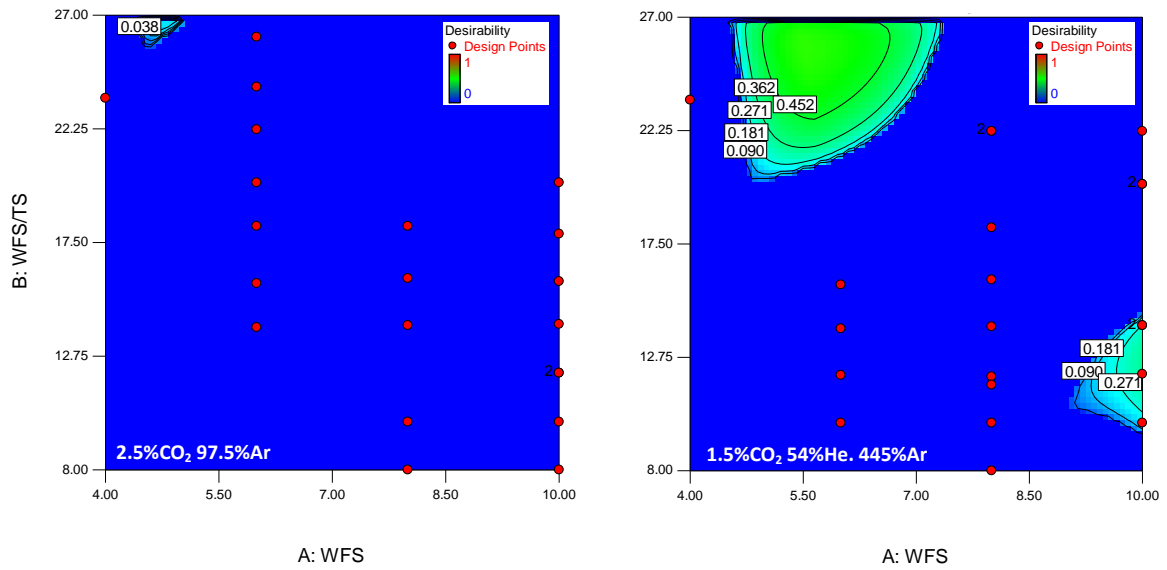


Figure XVI.1 – Desirability areas for work under the desirable conditions defined for GMAW-P.

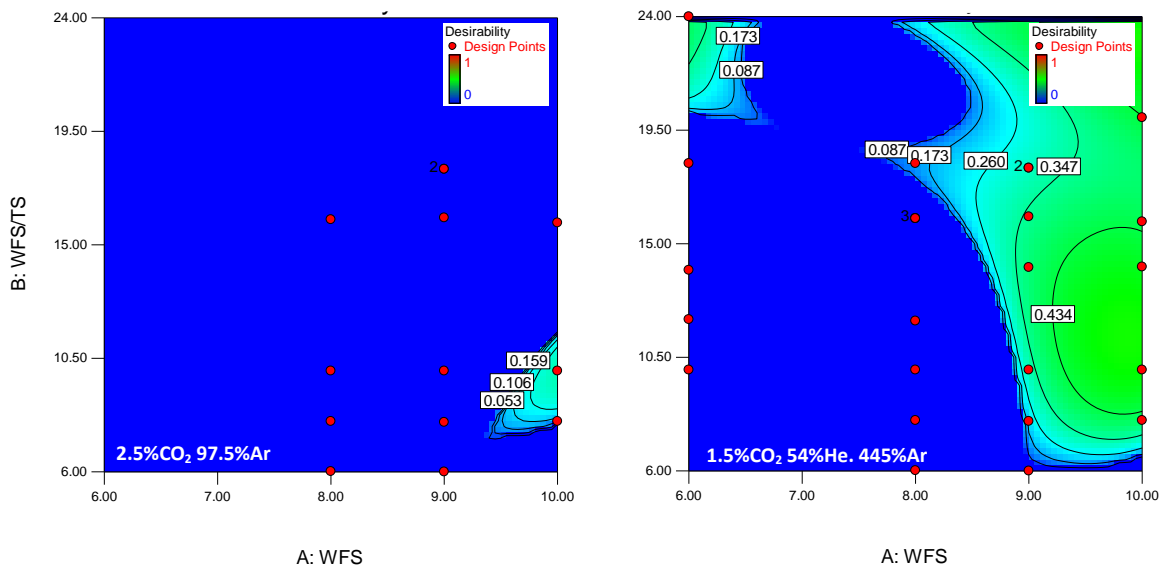
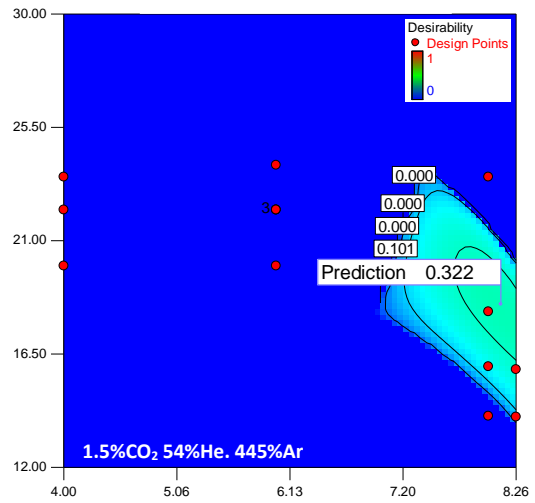
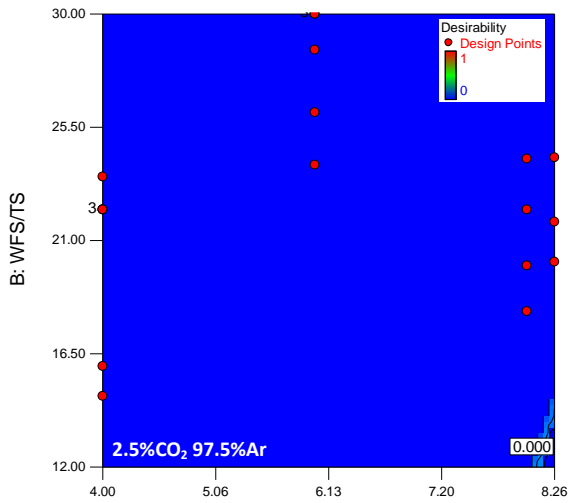


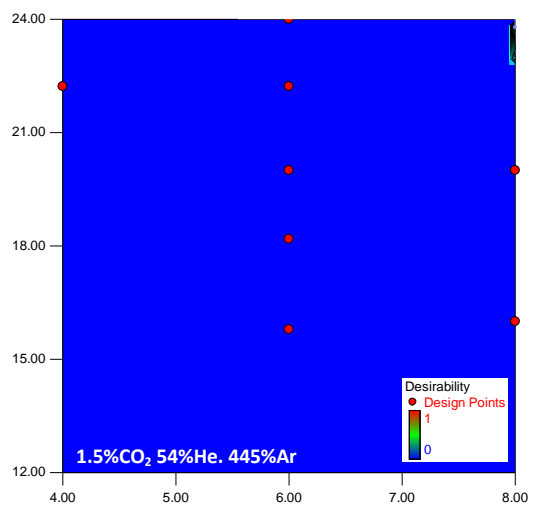
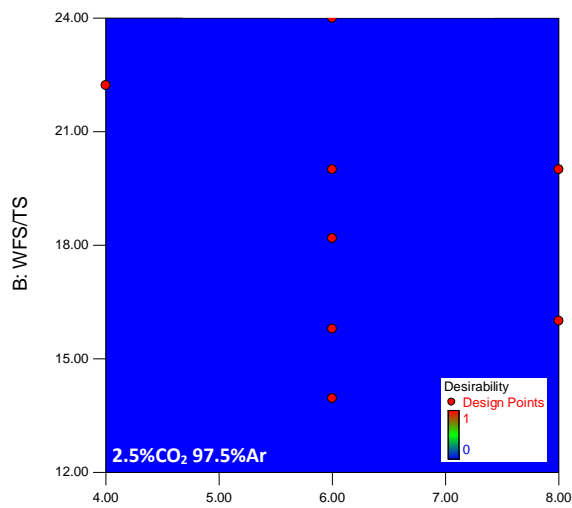
Figure XVI.2 – Desirability areas for work under the desirable conditions defined for RapidArc.



A: WFS

A: WFS

Figure XVI.3 – Desirability areas for work under the desirable conditions defined for STT.



A: WFS

A: WFS

Figure XVI.4 – Desirability areas for work under the desirable conditions defined for CMT.

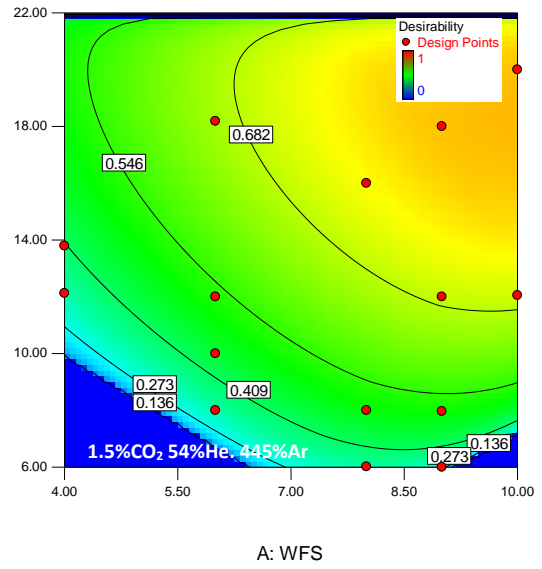
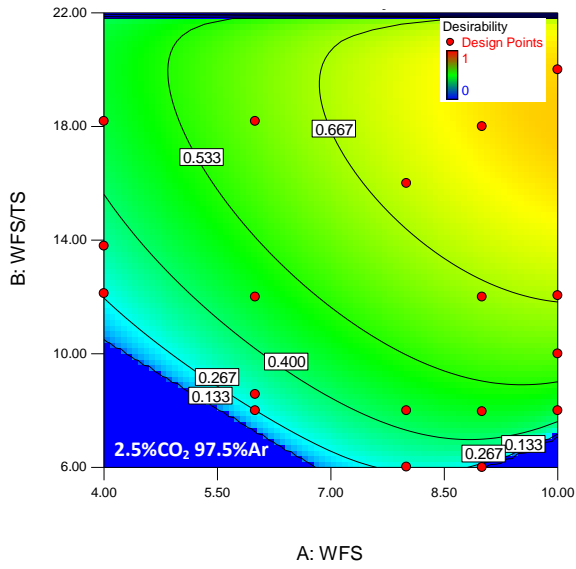


Figure XVI.5 – Desirability areas for work under the desirable conditions defined for CMT-P.

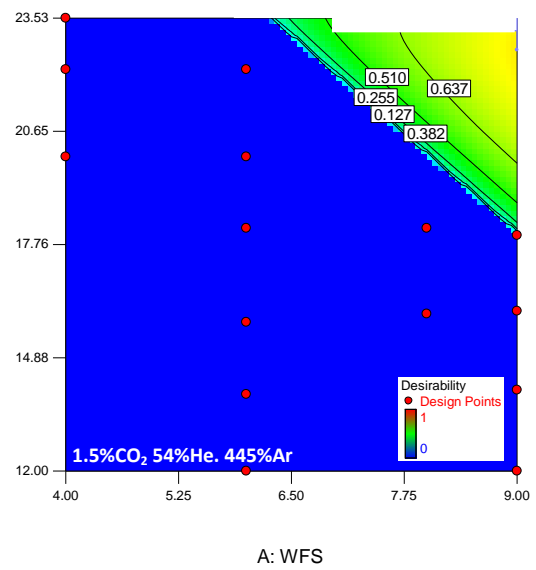
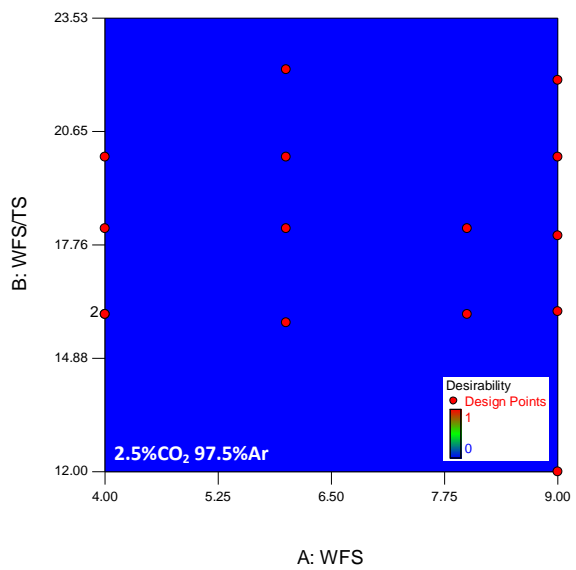


Figure XVI.6 – Desirability areas for work under the desirable conditions defined for FastROOT.

XVII. ARC LENGTH MEASUREMENTS

Table XVII.1 – Arc length measurements obtained for RapidArc.

Run	Shielding Gas (%)			Trim	Arc Length (mm)
	CO ₂	He	Ar		
GR1	1	0	99	1.25	3.45
GR2	1	0	99	1.25	3.49
GR3	1	0	99	1.25	3.39
GR4	1	0	99	1.5	3.32
GR5	1	14	85	1.25	3.75
GR6	1	14	85	1.5	3.55
GR7	1	31	68	1.25	3.33
GR8	1	31	68	1.25	3.22
GR9	1	31	68	1.5	3.81
GR10	1	56	43	1.5	3.49
GR11	1	70	29	1.15	3.29
GR12	1	70	29	1.25	3.60
GR13	1	70	29	1.25	3.15
GR14	1	70	29	1.3	2.82
GR15	1	70	29	1.5	3.40
GR16	1.5	20.5	78	1.25	3.59
GR17	1.5	20.5	78	1.35	3.41
GR18	1.5	20.5	78	1.5	3.47
GR19	1.5	39.5	59	1.25	4.16
GR20	1.5	39.5	59	1.35	3.52
GR21	1.5	39.5	59	1.5	4.06
GR22	1.5	44	44.5	1.25	2.84
GR23	1.5	44	44.5	1.25	3.18
GR24	1.5	44	44.5	1.35	3.21
GR25	1.5	44	44.5	1.5	3.28
GR26	1.5	44	44.5	1.5	3.10
GR27	2.5	0	97.5	1.25	3.62
GR28	2.5	0	97.5	1.25	3.47
GR29	2.5	0	97.5	1.35	3.41
GR30	2.5	0	97.5	1.5	3.38
GR31	2.5	0	97.5	1.5	3.35
GR32	3	8	89	1.25	3.79
GR33	3	8	89	1.35	3.26
GR34	3	8	89	1.5	3.46
GR35	3	34	63	1.25	3.29
GR36	3	34	63	1.25	3.07
GR37	3	34	63	1.25	3.44
GR38	3	34	63	1.25	3.44
GR39	3	34	63	1.5	3.67
GR40	3	34	63	1.5	3.07
GR41	5	7	88	1.25	3.45
GR42	5	7	88	1.25	3.66
GR43	5	7	88	1.35	3.33
GR44	5	7	88	1.5	2.91
GR45	5	45	50	1.5	3.36

Table XVIII.1 – Arc length measurements obtained for RapidArc (cont.)

Run	Shielding Gas (%)			Trim	Arc Length (mm)
	CO ₂	He	Ar		
GR46	5	45	50	1.35	3.54
GR47	5	62	33	1	2.38
GR48	5	62	33	1.25	3.08
GR49	5	62	33	1.43	3.40
GR50	5	62	33	1.5	2.98
GR51	5	62	33	1.5	3.41
GR52	5	62	33	1.5	2.97

Table XVII.2 – Arc length measurements obtained for CMT-P.

Run	Shielding Gas (%)			Arc Length Correction (%)	Arc Length (mm)
	CO ₂	He	Ar		
GP1	1	0	99	0	4.39
GP2	1	0	99	15	4.39
GP3	1	0	99	15	4.48
GP4	1	0	99	15	4.27
GP5	1	0	99	30	5.71
GP6	1	14	85	0	4.39
GP7	1	14	85	15	5.08
GP8	1	14	85	30	6.00
GP9	1	31	68	0	4.43
GP10	1	31	68	15	4.98
GP11	1	31	68	15	4.12
GP12	1	31	68	30	6.38
GP13	1	56	43	0	3.31
GP14	1	56	43	15	5.18
GP15	1	56	43	30	6.08
GP16	1	70	29	0	4.29
GP17	1	70	29	15	4.42
GP18	1	70	29	15	4.34
GP19	1	70	29	15	4.59
GP20	1	70	29	25	4.41
GP21	1.5	20.5	78	5	4.52
GP22	1.5	20.5	78	15	5.30
GP23	1.5	20.5	78	15	5.08
GP24	1.5	20.5	78	22	4.10
GP25	1.5	39.5	59	5	4.28
GP26	1.5	39.5	59	15	4.49
GP27	1.5	39.5	59	20	4.10
GP28	1.5	44	44.5	5	4.73
GP29	1.5	44	44.5	5	3.36
GP30	1.5	44	44.5	15	4.30
GP31	1.5	44	44.5	15	3.75
GP32	1.5	44	44.5	20	5.59
GP33	1.5	44	44.5	20	3.93
GP34	2.5	0	97.5	5	3.34
GP35	2.5	0	97.5	5	4.42
GP36	2.5	0	97.5	15	4.00
GP37	2.5	0	97.5	15	3.61
GP38	2.5	0	97.5	20	3.45
GP39	2.5	0	97.5	20	4.10
GP40	3	8	89	5	3.83
GP41	3	8	89	15	4.10
GP42	3	8	89	20	4.00
GP43	3	34	63	5	5.01
GP44	3	34	63	15	4.40
GP45	3	34	63	15	4.42
GP46	3	34	63	15	4.26

Table XVIII.2 – Arc length measurements obtained for CMT-P (cont.)

Run	Shielding Gas (%)			Arc Length Correction (%)	Arc Length (mm)
	CO ₂	He	Ar		
GP47	3	34	63	15	4.46
GP48	3	34	63	15	4.55
GP49	3	34	63	20	4.10
GP50	5	7	88	5	4.32
GP51	5	7	88	15	5.06
GP52	5	7	88	15	4.70
GP53	5	7	88	15	3.95
GP54	5	7	88	20	3.73
GP55	5	45	50	5	4.14
GP56	5	45	50	15	4.45
GP57	5	45	50	20	6.15
GP58	5	62	33	5	5.08
GP59	5	62	33	15	3.88
GP60	5	62	33	15	4.26
GP61	5	62	33	15	4.13
GP62	5	62	33	20	3.64

Table XVII.3 – Average and Standard Deviation of Arc length measurements obtained to all shielding gas mixture for RapidArc.

Ref.	Shielding Gas Composition [%]			Arc Length [mm]	
	CO ₂	He	Ar	Average	Standard Deviation
1	1	0	99	3.41	0.08
2	1	14	85	3.65	0.14
3	1	31	68	3.45	0.32
4	1	56	43	3.49	-
5	1	70	29	3.25	0.29
6	1.5	20.5	78	3.49	0.09
7	1.5	39.5	59	3.91	0.34
8	1.5	54	44.5	3.12	0.17
9	2.5	0	97.5	3.45	0.11
10	3	8	89	3.50	0.27
11	3	34	63	3.33	0.23
12	5	7	88	3.34	0.32
13	5	45	50	3.45	0.13
14	5	62	33	3.04	0.38

Table XVII.4 – Average and Standard Deviation of Arc length measurements obtained to all shielding gas mixture for CMT-P.

Ref.	Shielding Gas Composition [%]			Arc Length [mm]	
	CO ₂	He	Ar	Average	Standard Deviation
1	1	0	99	4.65	0.60
2	1	14	85	5.16	0.81
3	1	31	68	4.98	1.00
4	1	56	43	4.86	1.41
5	1	70	29	4.41	0.12
6	1.5	20.5	78	4.75	0.54
7	1.5	39.5	59	4.29	0.19
8	1.5	54	44.5	4.19	0.80
9	2.5	0	97.5	3.82	0.42
10	3	8	89	3.98	0.14
11	3	34	63	4.46	0.29
12	5	7	88	4.35	0.54
13	5	45	50	4.91	1.08
14	5	62	33	4.20	0.55

XVIII. BEAD SHAPE CHARACTERISTICS OBTAINED FOR RAPIDARC AND CMT-P

Table XVIII.1 – Bead shape characteristics applied to the mixtures design for RapidArc.

Run	Shielding Gas (%)			Depth of Penetration (mm)	Height Ratio	Root Width (mm)	Top Width (mm)
	CO ₂	He	Ar				
GR01	1	0	99	-0.03	1.000	4.72	6.00
GR02	1	0	99	-0.04	1.000	4.72	6.07
GR03	1	0	99	0.01	0.773	4.20	5.56
GR05	1	14	85	0.00	1.000	5.23	5.88
GR08	1	31	68	0.05	0.937	4.30	6.05
GR10	1	56	43	0.22	0.814	4.72	5.49
GR12	1	70	29	-0.03	1.031	4.67	6.20
GR13	1	70	29	0.23	0.888	5.74	5.98
GR18	1.5	20.5	78	0.31	0.744	5.35	5.56
GR20	1.5	39.5	59	0.41	0.688	4.48	5.91
GR25	1.5	54	44.5	0.17	0.816	6.05	6.12
GR26	1.5	54	44.5	0.24	0.751	4.72	5.93
GR28	2.5	0	97.5	0.02	0.828	4.62	6.10
GR34	3	8	89	0.48	0.748	4.00	5.86
GR35	3	34	63	0.44	0.675	4.69	5.58
GR36	3	34	63	0.46	0.827	4.83	6.28
GR37	3	34	63	0.20	0.835	5.56	6.12
GR38	3	34	63	0.34	0.863	5.16	6.12
GR41	5	7	88	0.34	0.667	5.93	5.51
GR42	5	7	88	0.41	0.839	5.37	5.46
GR46	5	45	50	0.48	0.695	5.60	6.30
GR49	5	62	33	0.34	0.729	5.77	6.02

Table XVIII.2 – Bead shape characteristics applied to the mixtures design for CMT-P.

Run	Shielding Gas (%)			Depth of Penetration (mm)	Height Ratio	Root Width (mm)	Top Width (mm)	Undercutting (mm)
	CO ₂	He	Ar					
GP02	1	0	99	-0.15	0.958	3.44	6.30	0.23
GP03	1	0	99	0.01	1.005	3.81	6.02	0.11
GP04	1	0	99	0.01	0.811	3.26	6.47	0.56
GP06	1	14	85	0.00	1.066	2.87	6.14	0.00
GP10	1	31	68	-0.14	0.617	3.58	6.47	0.35
GP11	1	31	68	0.00	0.690	3.61	5.68	0.40
GP14	1	56	43	-0.20	0.674	3.86	6.70	0.51
GP17	1	70	29	-0.12	0.727	3.89	6.29	0.84
GP18	1	70	29	-0.10	0.679	3.63	6.88	0.95
GP19	1	70	29	-0.16	0.829	4.00	7.05	1.07
GP22	1.5	20.5	78	0.00	0.829	3.86	6.16	0.75
GP23	1.5	20.5	78	-0.01	0.759	4.09	6.59	0.47
GP26	1.5	39.5	59	0.01	0.735	3.93	6.98	0.77
GP30	1.5	54	44.5	-0.09	0.633	3.93	6.84	0.74
GP31	1.5	54	44.5	-0.10	0.775	4.07	6.74	0.57
GP36	2.5	0	97.5	-0.04	1.172	4.16	6.21	0.05
GP37	2.5	0	97.5	0.00	0.920	3.70	6.14	0.09
GP41	3	8	89	0.09	0.808	3.37	6.74	0.18
GP44	3	34	63	0.02	0.670	3.86	6.93	0.67
GP45	3	34	63	0.12	0.791	3.81	6.70	0.56
GP46	3	34	63	0.00	0.737	4.28	6.79	0.89
GP47	3	34	63	0.01	0.651	4.12	6.64	0.77
GP51	5	7	88	0.00	0.767	4.23	6.80	0.48
GP52	5	7	88	0.13	0.734	3.74	7.02	0.31
GP56	5	45	50	0.07	0.606	3.35	6.70	0.61
GP59	5	62	33	0.19	0.590	3.75	7.28	0.98
GP60	5	62	33	0.04	0.583	4.07	6.98	1.05
GP61	5	62	33	0.06	0.625	3.63	7.12	0.47

XIX. EQUATION MODELS OBTAINED FOR GAS MIXTURES STUDY

XIX.1. Equation Models obtained for the Mixtures Design with RapidArc

Final Equation for Depth of Penetration (DP) in terms of Actual Components

$$DP = -1.55335 \times CO_2 - 3.37694 \times 10^{-3} \times He - 2.22801 \times 10^{-3} \times Ar + 0.016916 \times CO_2 \times He + 0.017506 \times CO_2 \times Ar + 1.29148 \times 10^{-4} \times He \times Ar \quad \text{(XIX.1)}$$

Final Equation for Height Ratio (HR) in terms of Actual Components

$$HR = +0.88697 - 0.041418 \times CO_2 + 5.20744 \times 10^{-4} \times Ar \quad \text{(XIX.2)}$$

Final Equation for Root Width (TW) in terms of Actual Components

$$RW = +0.22620 \times CO_2 + 0.051872 \times He + 0.043282 \times Ar \quad \text{(XIX.3)}$$

XIX.2. Equation Models obtained for the Mixtures Design with CMT-P

Final Equation for Depth of Penetration (DP) in terms of Actual Components

$$DP = +0.042183 \times CO_2 - 1.80613 \times 10^{-3} \times He - 8.47547 \times 10^{-4} \times Ar \quad \text{(XIX.1)}$$

Final Equation for Height Ratio (HR) in terms of Actual Components

$$(HR)^{-2.11} = +8.04401 \times CO_2 + 0.010218 \times He + 0.014358 \times Ar \\ -0.082136 \times CO_2 \times He - 0.084352 \times CO_2 \times Ar + 4.83944 \times 10^{-4} \times He \times Ar \quad \text{(XIX.2)}$$

Final Equation for Top Width (TW) in terms of Actual Components

$$TW = +0.18764 \times CO_2 + 0.068319 \times He + 0.060604 \times Ar \quad \text{(XIX.3)}$$

Final Equation for Undercutting (U) in terms of Actual Components

$$U = +0.020118 \times CO_2 + 0.011566 \times He + 1.89570 \times 10^{-3} \times Ar \quad \text{(XIX.4)}$$

XX. DESIRABILITY CRITERIA ESTABLISHED FOR THE MIXTURE DESIGNS

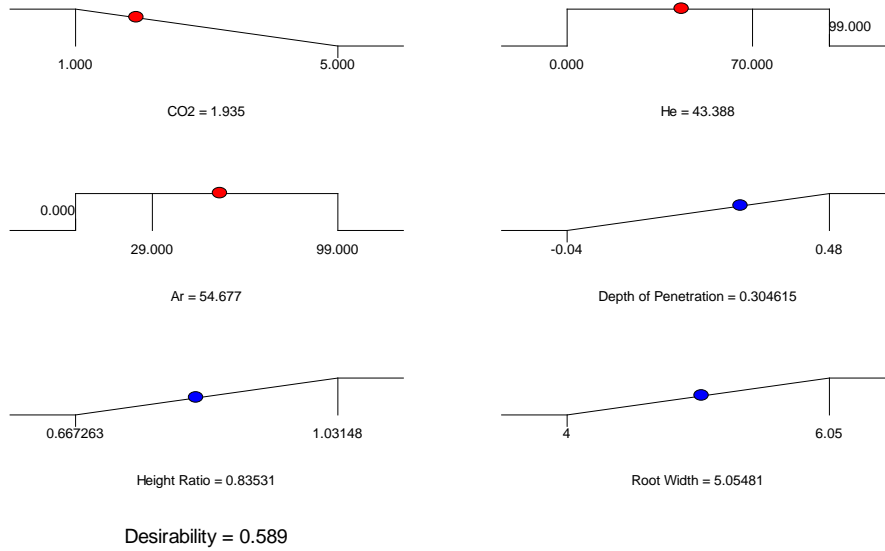


Table XX.1 – Desirability criteria established for RapidArc gas mixture design.

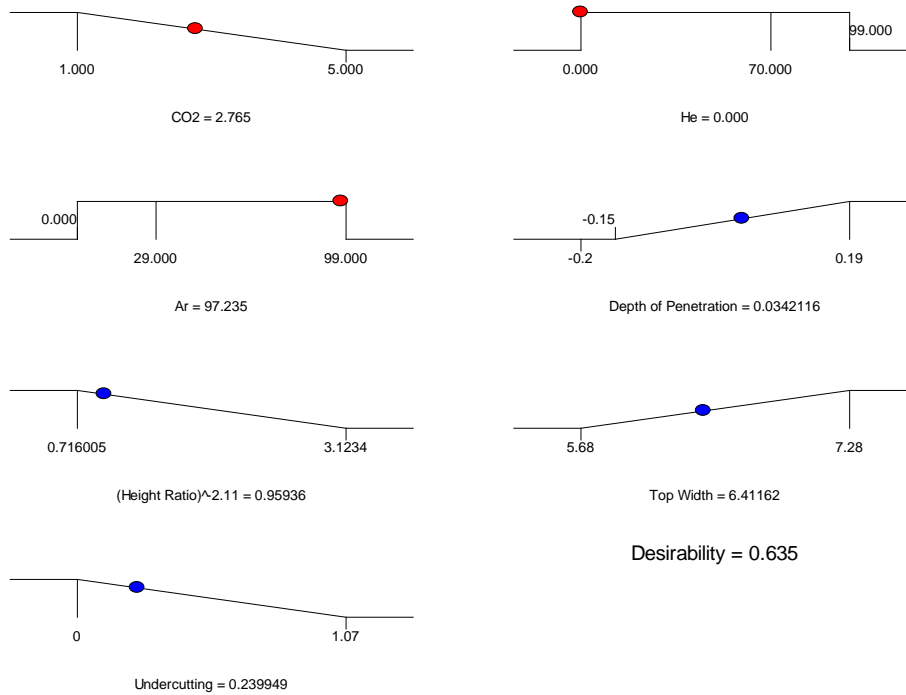


Table XX.2– Desirability criteria established for CMT-P gas mixture design.